University of Tehran

Print ISSN: 2322-2093

Online ISSN: 2423-6691

Volume 56, Number 1, June 2023

Civil Engineering Infrastructures Journal

CEIJ

Available online at
http://ceij.ut.ac.ir/

Civil Engineering Infrastructures Journal (CEIJ)

Volume 56, Number 1, June 2023

Civil Engineering Infrastructures Journal (CEIJ)
Semiannual Publication

Published by:

University of Tehran
College of Engineering

Indexed by:

Web of Science (ESCI)

Scopus

Civil Engineering Infrastructures Journal (CEIJ)
College of Engineering
University of Tehran
P.O. Box: 11155-4563
Tehran, Iran.
Tel/ Fax: +98-21-88956097
Email: ceij@ut.ac.ir
Web Site: www.ceij.ir

Editorial Board

Advisory Board

CONTENTS
Volume 56, Number 1, June 2023

Civil Engineering Infrastructures Journal 2023, 56(1): 1-18
DOI: 10.22059/CEIJ.2022.339592.1820

REVIEW PAPER

The Effect of Recycled Steel Fibers from Waste Tires on Concrete Properties

Modarres, Y.[1] and Ghalehnovi, M.[2]*

[1] Ph.D. Candidate, Department of Civil Engineering, Ferdowsi University of Mashhad, Mashhad, Iran.
[2] Professor, Department of Civil Engineering, Ferdowsi University of Mashhad, Mashhad, Iran.

Received: 23 Feb. 2022; Revised: 09 Oct. 2022; Accepted: 05 Nov. 2022

ABSTRACT: One of the most severe environmental problems in the world is how to dispose of waste tires properly. Many tires are dumped or thrown away worldwide every year, severely threatening the environment. Most waste tires are used as fuel by some industries, but as we know, this type of waste use has a dangerous effect. The use of synthetic fibers, especially industrial steel fibers, which is very common today and requires high raw materials and energy, negatively impacts the environment by emitting CO_2 during manufacturing. Therefore, finding fibers that perform similarly to industrial steel fibers is essential. This article presents a comprehensive overview of the methods of recycling steel fibers from waste tires, the characteristics of recycled fibers, and their application in producing different cement-based composites. The effect of these recycled fibers on fresh concrete properties, including workability and porosity, has been investigated. The effect of these fibers on the concrete's mechanical characteristics, including compressive strength, splitting tensile strength, flexural strength, impact resistance, and durability, is also discussed. According to recent research, using recycled steel fibers to strengthen concrete can be a suitable alternative to industrial steel fibers, which have fewer adverse effects on the environment and reduced recycling costs.

Keywords: Fiber Reinforced Concrete, Fresh Properties, Mechanical Properties, Recycled Steel Fiber, Waste Tire.

1. Introduction

One of the most popular building materials, concrete, due to temperature and relative humidity changes, always has internal micro-cracks that lead to low tensile strength and consequently, brittle failure concrete (Awolusi et al., 2021). Adding natural or synthetic fibers to the concrete mix is one of the most efficient strategies for improving and strengthening the brittle matrix and preventing cracking (Jamshaid and Mishra, 2016). Fibers have been used for a long time as reinforcements for construction materials and composites; according to studies and research, the use of natural and synthetic fibers has shown promising results (Mohajerani et al., 2019); because their use has advantages and significant improvements in the mechanical

* Corresponding author E-mail: ghalehnovi@um.ac.ir

and physical characteristics of the composite material (Ghanbari and Bayat, 2022). Natural fibers (such as straw, coconut, sisal, etc.) are readily available, save energy, and reduce environmental impacts (Mohajerani et al., 2019; Laborel et al., 2016). They are also biodegradable, renewable, and lightweight. Natural fibers can replace synthetic fibers for some applications (Mohajerani et al., 2019); however, natural fibers are less durable and degrade over time in alkaline environments (Saha et al., 2016).

Synthetic fibers can reduce construction costs by substituting traditional reinforcements such as steel mesh and rebars, which are much heavier and require more energy, resources, and time to produce (Yin et al., 2015). Industrial Steel Fibers (ISF) are concrete's most commonly utilized synthetic fibers. Of course, it is essential to note that steel fibers and rebars have distinct but complementary roles in increasing concrete performance. Similar to steel reinforcements, the main feature of steel fibers is their high tensile capacity (Yin et al., 2015). Steel fibers have been extensively studied in concrete applications; hence, they are commonly used to enhance the mechanical characteristics of concrete. Steel fibers help improve concrete behavior in terms of cracking, shrinkage, ductility, toughness, and energy absorption (Yin et al., 2015).

However, synthetic fibers are manufactured and require raw materials and energy; they are challenging to recycle and show the adverse effects of CO_2 emissions during production (Frazão, 2019). Climate change due to increasing concentrations of greenhouse gas emissions and air pollution is considered one of the most critical challenges for humanity in the current century (De Wilde and Coley, 2012). As mentioned above, the construction sector is also one of the main factors in the phenomena, which significantly impacts global warming and accounts for 39% of the relevant CO_2 emissions in 2017 (Frazão, 2019). In recent years, the scientific community has tried to reduce CO_2 emissions and their adverse environmental effects through several measures focused on the sustainability of materials and the environment based on the minimization and reuse of waste (Onuaguluchi and Banthia, 2018).

In particular, using recycled materials as sustainable constituents of cementitious materials has become a promising environmental and technical solution (Sabzi et al., 2022); one of the waste materials used in construction materials is vehicle tires (Bulei et al., 2018). Research on utilizing these waste tires in construction has recently been carried out. Rubber powder, crumb rubber, steel fibers, nylon fibers, and nylon pellets are just a few of the items that may be extracted from tires (Bulei et al., 2018). Recycled Steel Fibers (RSF) from waste tires can be a suitable replacement for ISF (Awolusi et al., 2021; Bulei et al., 2018).

Briefly, this review article focuses on the following issues:

- Investigating waste tire recycling methods and comparing the properties of RSF according to the recycling method in Section 2.
- Investigating the effect of RSF on fresh concrete properties in Section 3.
- Investigating the effect of RSF on concrete's mechanical characteristics, such as compressive strength, tensile strength, flexural strength, impact, and durability, in Section 4.
- Presenting a general conclusion of the studies conducted and presenting the challenges and studies needed for the future in Section 5.

Such information will help gain up-to-date knowledge of fiber properties and stimulate further research into its practical applications.

2. Methods of Recycling Tires and Characteristics of Recycled Steel Fibers

Waste tires are dumped or disposed of worldwide, severely threatening the

environment (Liew and Akbar, 2020). Most waste tires are used as fuel by some industries, but as we know, this type of waste use has a dangerous effect due to the production of greenhouse gases (Liew and Akbar, 2020). On the other hand, the excessive disposal of large waste tires has proven to be a significant environmental concern due to their non-biodegradable nature (especially in developing countries) (Frazão, 2019). Tire recycling methods are divided into branches, mechanical and chemical (Tlemat, 2004). In the mechanical method, the tire is divided into smaller pieces. Shredders and mills do this in several stages (Tlemat, 2004). Each step of this method produces different products used in various industries. Finally, the steel fibers, rubber components, and granules obtained during the shredding process are separated using an electromagnetic technique. Some industries use coarse granules, and others require very soft rubber powder; Shredded Recycled Steel Fiber (SRSF) refers to steel fibers obtained through shredding. Figure 1 summarizes the shredding process to recycle tires (Tlemat et al., 2003).

A technique for crumbling is cryogenic fragmentation which involves shredding tires and cooling them to temperatures below minus 80 degrees Celsius (Tlemat, 2004). After that, the chips are pounded in a hammermill to separate the parts. However, much energy is needed to maintain such low temperatures (Tlemat et al., 2003). In the chemical method, either the tire is burned or pyrolysis (Tlemat, 2004). Tire burning can be replaced by pyrolysis to reduce harmful emissions. In a sealed chamber, the tires are heated without air, producing oil and fuel gases as well as carbon and steel leftovers (Tlemat, 2004). Pyrolysed Recycled Steel Fiber (PRSF) is the name for recovered steel fibers through pyrolysis.

The fibers have varied forms and diameters depending on the main source and recycling procedure. Studies have shown that the shredding method is mainly used to recycle the steel fibers of waste tires, and the fibers are recycled in various diameters and lengths (Liew and Akbar, 2020). The type of tire determines the diameter of the RSF, while the recycling method has a more significant effect on the length of the fibers (Caggiano et al., 2015). RSF obtained by the cryogenic method has no significant rubber particles compared to recycled fibers using the shredding method (Awolusi et al., 2021; Caggiano et al., 2015). In the thermal analysis, longer fibers can be recycled and shortened to the required uniform length, while recycled fibers have small variable lengths using the shredding method (Frazão, 2019). Figure 2 shows the recycled fibers from the thermal and cryogenic methods. Statistical analysis is necessary for a specific group of sample fibers to disperse the fibers' frequency and average size due to the vast range of geometric differences in RSF.

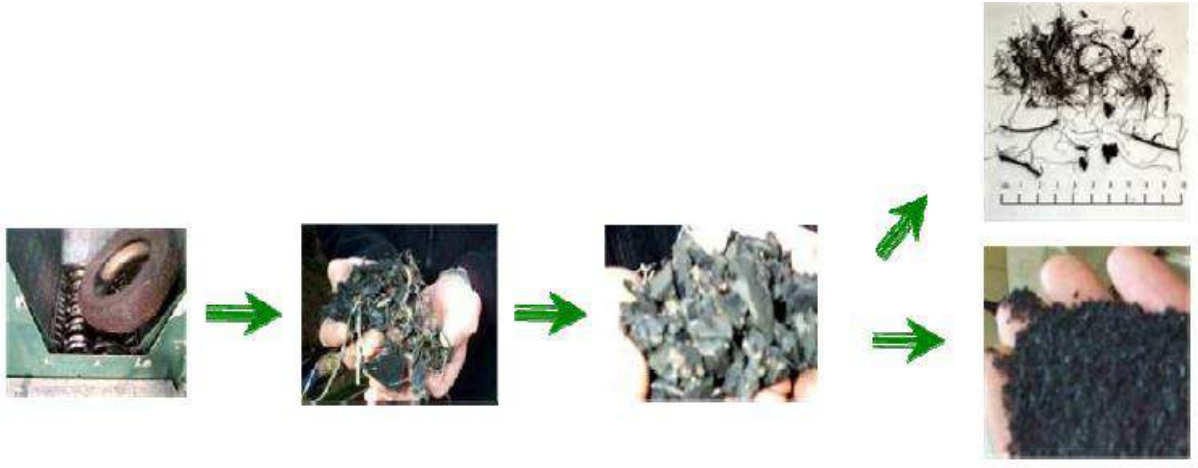

Fig. 1. Shredding process and production of SRSF (Tlemat, 2004)

(a) **(b)**

Fig. 2. The recycled fibers from: a) The thermal (Tlemat et al., 2003); and b) Cryogenic (Zamanzadeh et al., 2015) methods

For example, Shi et al. (2020) randomly selected 500 fibers to describe the RSFs' size distribution and manually measured their diameter and length with the help of a micrometer (Figure 3). The histograms of length, diameter, and fiber aspect ratio (length-to-diameter ratio) are displayed in Figure 4. According to research, most fibers have a diameter of less than 0.5 mm, with an average of 0.32 mm. Most fiber lengths fall between 5 and 25 mm, with a length of 14.9 mm on average. One crucial variable is the aspect ratio which could directly correlate with the fresh and hardened properties of the fiber-reinforced concrete (FRC). Most samples of RSF have aspect ratios between 20 and 70, and the average for the studied samples is 55.

3. Fresh Properties of Concrete with Recycled Steel Fibers

3.1. Workability (Slump)

Workability is one of the significant limitations of FRC for better performance of hardened concrete (Liew and Akbar, 2020). The kind and volume of RSF significantly impact the workability of concrete, which is the main criterion. Although the slump test is regarded as a standard test for quantifying the performance of a concrete mix, the slump test, in the opinion of many experts, needs to provide more details about the quantitative measurement of FRC performance. However, it is acceptable as a quality control technique to achieve uniformity in the performance of different concrete categories (Liew and Akbar, 2020). The workability and homogeneity of the freshly mixed concrete are both impacted by the high proportion of RSF (Awolusi et al., 2021). The aspect ratio and geometric properties of the fibers, in addition to the volume content of the fibers, significantly impact the workability and homogeneity of freshly mixed concrete with steel fibers (Alsaif et al., 2018b). The workability of fiber reinforcements depends mainly on achieving homogeneous dispersion of fibers in the concrete matrix. According to the obtained results, the geometry of RSF has a similar effect on the uniform distribution of fibers and the workability of concrete compared to ISF (Alsaif et al., 2018b). Numerous studies have found that fibers reduce the workability of concrete.

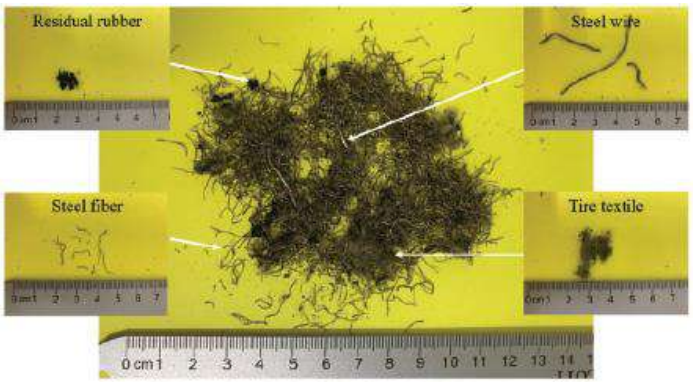

Fig. 3. Scrap tire recycled steel fiber (Shi et al., 2020)

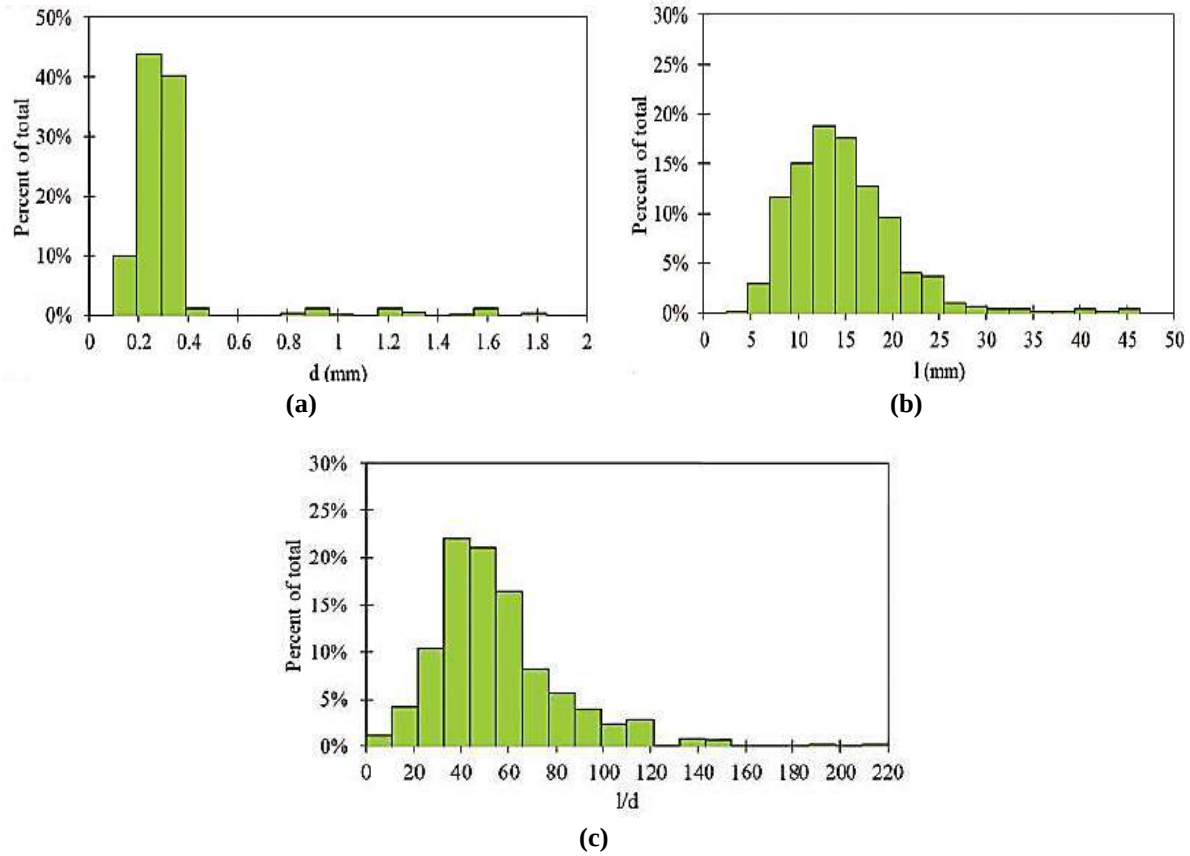

Fig. 4. Recycled steel fiber dimensions: a) Diameter, b) Length; and c) Aspect ratio (Shi et al., 2020)

Wafa (1990) observed that FRC slump values decrease from 0 to 2% with increasing fiber content. Rossli and Ibrahim (2012) investigated the effect of RSF from waste tires in the concrete mix. With increasing fiber content, the freshly mixed concrete's workability declined. In a study by Sengul (2016), the results showed that for fibers with a fixed length of 50 mm, increasing the fiber content from 10 to 40 kg/m^3 reduces the slump from 10 to 0 cm. In addition, the findings indicated that increasing the aspect ratio of the fibers (smaller fiber diameter) reduced the slump. Bedewi (2009) examined the influence of length (20, 40, and 60 mm) and volume (0%, 0.5%, 1%, and 1.5%) of recycled fibers on concrete slump values. In general, the findings showed that the slump decreases significantly with the increase in the length and volume of fibers. So that the specimen was reinforced with fibers 60 mm long, and a volume percentage of 1.5% had 0 slumps. A summary of the slump results of various studies is shown in Table 1.

3.2. Porosity

Workability in FRC can be attained by adding more water to the mix, but this additional water can lead to more pore volume inside the concrete matrix (Liew and Akbar, 2020). In addition, rubber on recycled fiber surfaces may prevent appropriate interaction with the surrounding cement matrix, which increases porosity and thus reduces mechanical performance (Yang et al., 2019). The porosity and homogeneity of RSF in concrete can be determined using Ultrasonic Pulse Velocity (UPV) testing (Yang et al., 2019; Mastali et al., 2018a). Steel fibers make it difficult to compact concrete in its fresh state, which leads to a decrease in workability; thus, the concrete becomes more porous, which is demonstrated by a reduction in UPV (Mehdipour et al., 2020; Mastali et al., 2018a). Results from UPV showed that by including a 2% volume of RSF, UPV is reduced by 3% to 7% (Liew and Akbar, 2020; Abdul Awal et al., 2015). In a study

on self-consolidation concrete, the findings indicated that by using a combination of RSF and ISF, increasing the volume percentage of ISF led to an increase in UPV. (Mastali et al., 2018a). The findings reflect that the lowest and highest UPV reduction in specimens containing 1% ISF and 0.5% RSF, and 0.5% ISF and 1% RSF, compared to the UPV in the control mixture, was obtained about 3% and 12%, respectively.

The studies conducted on microstructure and UPV investigation for recycled fibers are generally limited. Most of the available information is related to industrial fibers. Figure 5 shows some studies' UPV results for specimens reinforced with RSF and ISF. The numbers written in front of each of the abbreviations indicate the volume percentage of the fibers. Where REF stands for Reference concrete, ISF stands for Industrial steel fiber reinforced concrete, RSF stands for Recycled steel fiber reinforced concrete, and PP stands for Polypropylene fiber reinforced concrete. In general, the abbreviations used are mentioned in the captions of all figures.

Table 1. Results of slump values obtained from using RSF

Reference	RSF Content	Diameter (mm)	Length (mm)	Concrete class	W/C	Slump (mm)
Rossli and Ibrahim (2012)	0%	0.2-1.139	20-99	C40	0.53	55
	0.2%					60
	0.4%					30
	0.6%					10
	0.8%					30
	1%					10
Sengul (2016)	0 kg/m^3	-	-	C60	0.5	14
	10 kg/m^3	0.6	50			10
	20 kg/m^3					4
Bedewi (2009)	0%	-	-	C25	0.53	79
	0.5%	0.89	20			64
	1%					56
	1.5%					47
	0.5%	0.89	40			38
	1%					11
	1.5%					6
	0.5%	0.89	60			31
	1%					5
	1.5%					0

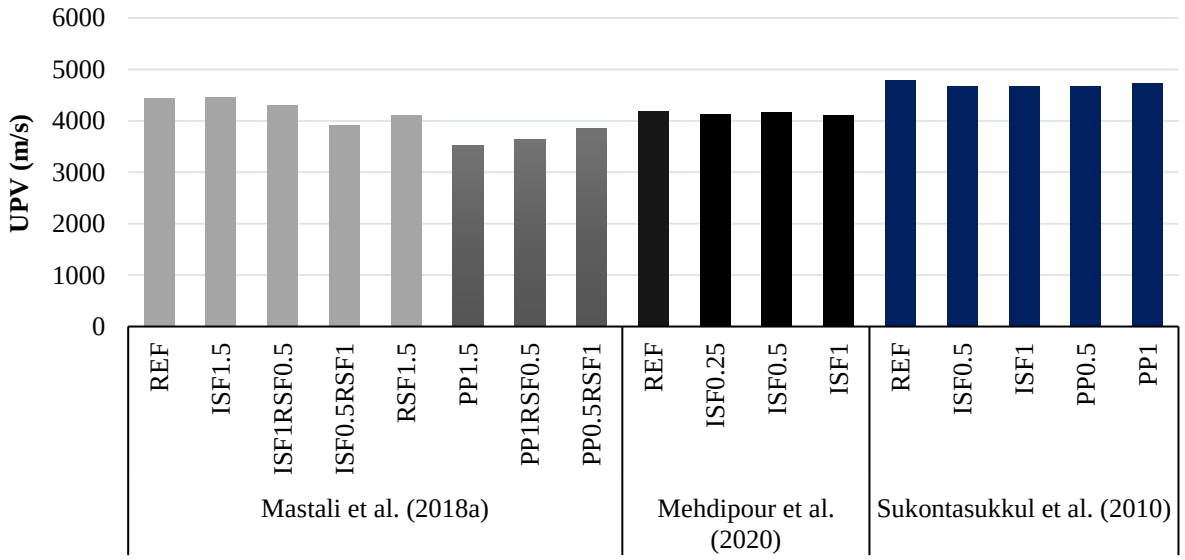

Fig. 5. UPV results for specimens reinforced with fibers (REF: Reference concrete, ISF: Industrial steel fiber reinforced concrete, RSF: Recycled steel fiber reinforced concrete, PP: Polypropylene fiber reinforced concrete)

4. Mechanical Properties of Hardened Concrete with Recycled Steel Fibers

4.1. Compressive Strength

The presence of RSF can positively affect the compressive strength of concrete. However, if a large volume of fibers is used, excess water to solve workability problems can damage the concrete's compressive strength due to increased porosity (Awolusi et al., 2021; Liew and Akbar, 2020). Concrete failure can be delayed using RSF because these fibers cause ductile failure. Fiber content dramatically impacts the response of concrete to compressive loads (Liew and Akbar, 2020). According to the study, despite the minimal amount of fibers present, there was no discernible increase in the compressive strength of concrete. (Yang et al., 2019). It can be assumed that in a small volume content of RSF, the compressive strength of concrete depends mainly on the structure of the internal matrix. Mastali et al. (2018a) examined the impact of hybrid fibers in self-consolidating concrete, which had various fibers (including ISF, RSF, and PP) and different volumes content. In this research, an average length of more than 50 mm and a diameter of 0.15 ± 0.05 mm was measured for RSF. As a result of the fibers' ability to prevent crack propagation, the findings demonstrated that mixtures containing fibers have compressive strengths that are higher than those of the reference mixture. The increase in compressive strength was measured by almost 60% (80 MPa) in the reinforced mixture with 1.5% ISF and about 40% (70 MPa) with 1.5% RSF. The compressive strength increased by around 50% in the specimen with 1% ISF and 0.5% RSF. Mastali et al. (2018b) investigated the topography and morphology of recycled and industrial fiber surfaces, which showed that recycled fibers contain deeper grooves and a rougher surface. The interaction between the fibers and matrix may be enhanced by these deeper grooves and improve the bonding properties at the interface. Due to the ability of fibers to limit crack development and bridging cracks, mixes containing fibers have greater compressive strength than the reference mixture. Figure 6 shows the morphology and topography of recycled and industrial fiber surfaces.

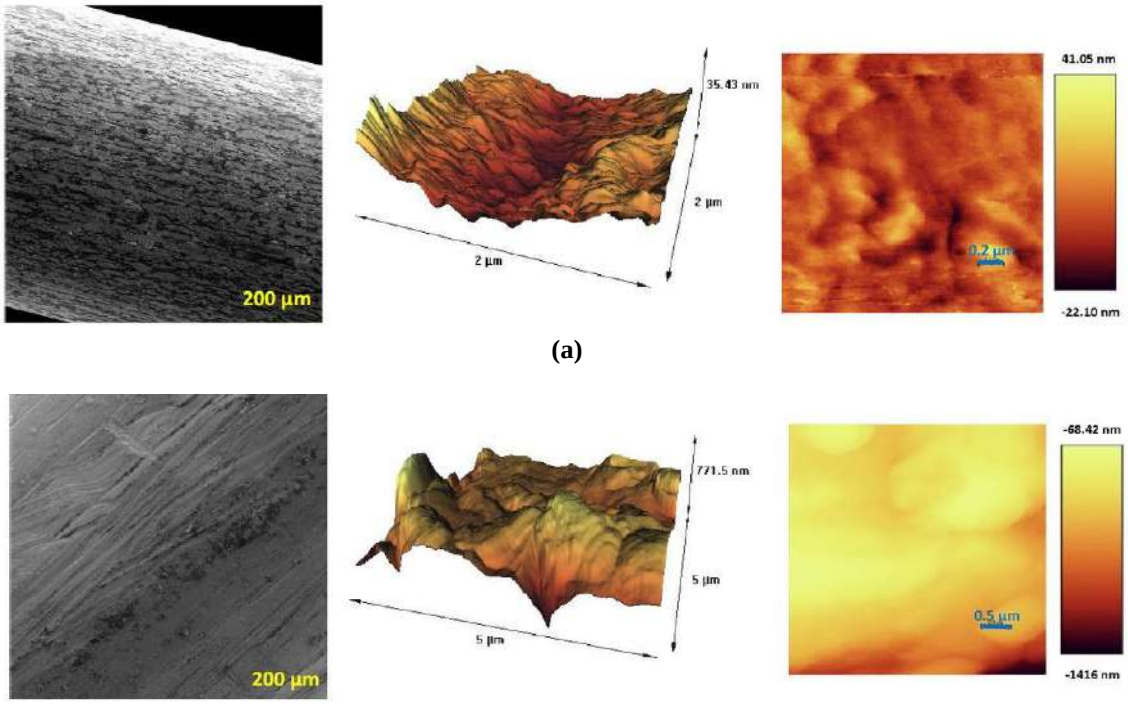

Fig. 6. SEM and AFM images of the fiber surfaces: a) Industrial steel fibers; and b) Recycled steel fibers (Mastali et al. 2018b)

According to the reference mixture, Caggiano et al. (2017) showed that RSF with variable lengths and diameters increase compressive strength between 5% and 10%. The existence of fibers has a minor impact on the final compressive strength of FRC. To a certain extent, additional fibers (or rising aspect ratios) can increase the compressive strength of concrete, which is mainly determined by the quality of the cementitious matrix and the aggregates. Dehghanpour and Yılmaz (2018) also show that for fibers with a fixed length of 25 mm, concrete's compressive strength is improved by increasing the fiber content from 0% to 2%. While increasing the content by more than 2% harms compressive strength. This is because large voids formed between the fibers during compaction due to increased RSF in the mortar mixture. Bedewi (2009) examined how the volumetric fraction and fiber length affected the compressive strength of concrete reinforced with steel fibers obtained from used tires. The volumetric content was varied at 0%, 0.5%, 1%, and 1.5%, while the fiber length was varied at 20 mm, 40 mm, and 60 mm. Figure 7 briefly shows Bedewi's (2009) results regarding the effect of recycled fibers with volume percentage and lengths on the compressive strength of concrete with different strength values. The results have shown that the compressive strength increases with the volume percentage of fibers. Increasing the length of fibers up to 40 mm has also improved the compressive strength, but using fibers with a length of 60 mm has decreased strength. Based on the findings, it was found that 1.5% volumetric content with a fiber length of 40 mm provided the highest compressive strength. Details of previous studies for maximum compressive strength are presented in Table 2.

Concrete's compressive strength is also greatly influenced by the surface morphology, amount of rubber attached to the RSF, and fiber shape. Some research has suggested that the existence of rubber adhered to the steel fibers' surface harms the compressive strength of concrete (Rossli and Ibrahim, 2012). Rubber particles' hydrophobicity and insufficient bonding with the surrounding cement matrix negatively impact the concrete's performance (Figure 8) (Yang et al., 2019).

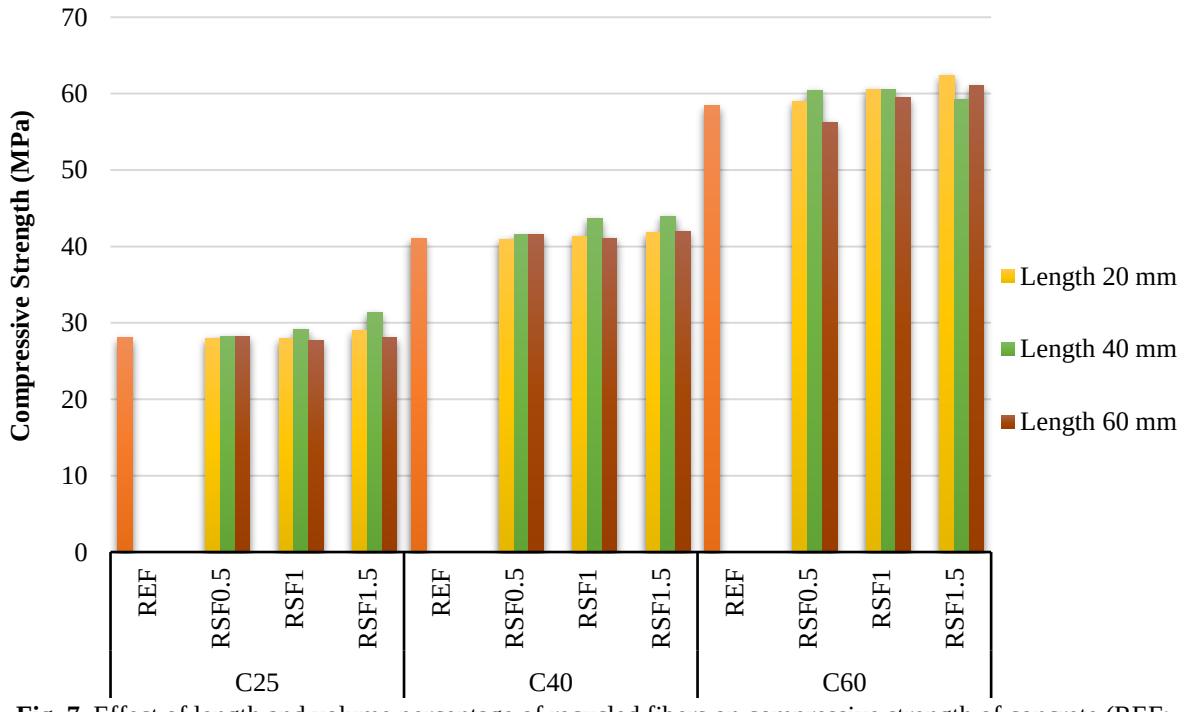

Fig. 7. Effect of length and volume percentage of recycled fibers on compressive strength of concrete (REF: Reference concrete, RSF: Recycled steel fiber reinforced concrete, C: Concrete class)

Table 2. Results of compressive strength obtained from using RSF

Reference	RSF Content	Diameter (mm)	Length (mm)	W/C	CS of PC[1] (MPa)	CS of FRC (MPa)
Mastali et al. (2018a)	1.5%	0.15	Over 50	0.76	50	70
Caggiano et al. (2017)	0.75%	0.11-0.44	6-74	0.49	22	24
Dehghanpour and Yılmaz (2018)	1%	0.26	25	0.5	57.16	62.74
	1.5%					66.62
	2%					70.5
	2.5%					64.55
Bedewi (2009)-C40[2]	0.5%	0.89	20	0.42	41.03	40.92
	1%					41.32
	1.5%					41.78
	0.5%	0.89	40	0.42		41.51
	1%					43.66
	1.5%					43.94
	0.5%	0.89	60	0.42		41.58
	1%					41.06
	1.5%					41.97

[1] CS- Compressive Strength. PC-Plain Concrete
[2] C40- Concrete class

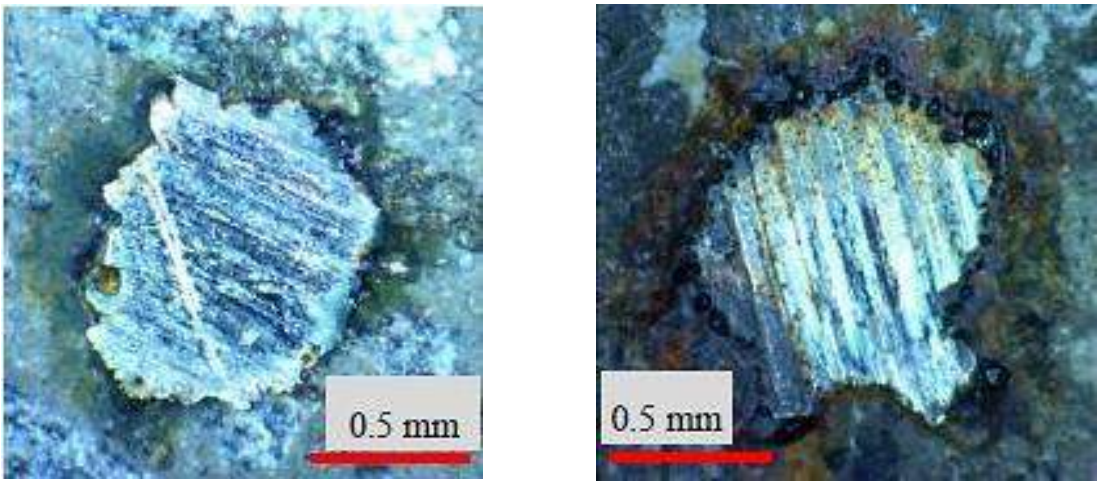

(a) **(b)**

Fig. 8. Observations of the interface zones between fiber and concrete matrix by an optical microscope: a) RSF without rubber; and b) RSF with rubber (Yang et al., 2019)

The findings revealed a decline in compressive strength from 135.5 to 130.2 MPa; in contrast, the samples' compressive strength was raised from 135.5 to 141.3 MPa by using RSF without rubber on the surface (Yang et al., 2019). In the study by Frazão (2019), the results obtained from the stress-strain curve show that the compressive strength and elastic modulus increase with the age of the specimens. However, RSF-reinforced specimens' compressive strength is lower compared to the reference specimen. Meanwhile, the elastic modulus of specimens reinforced with recycled fibers is higher than the control specimen. According to Figure 9, the fiber-reinforced specimens' ultimate strain is greater than the control specimen, indicating the specimens' better ductility and performance. RSFRC stands for Recycled steel fiber reinforced concrete. The number written with a percentage sign in front of it indicates the percentage of fibers, and the second number after the dash indicates the casting number of the specimen. Six castings were performed in this study. Figure 10 briefly compares the impact of RSF and ISF on the compressive strength of concrete in different studies. The numbers written in front of each of the abbreviations indicate the volume percentage of the fibers.

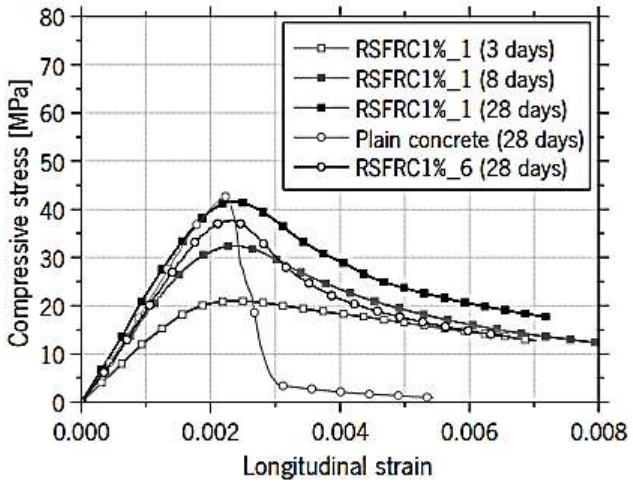

Fig. 9. Average compressive stress-longitudinal strain curve (Frazão, 2019)

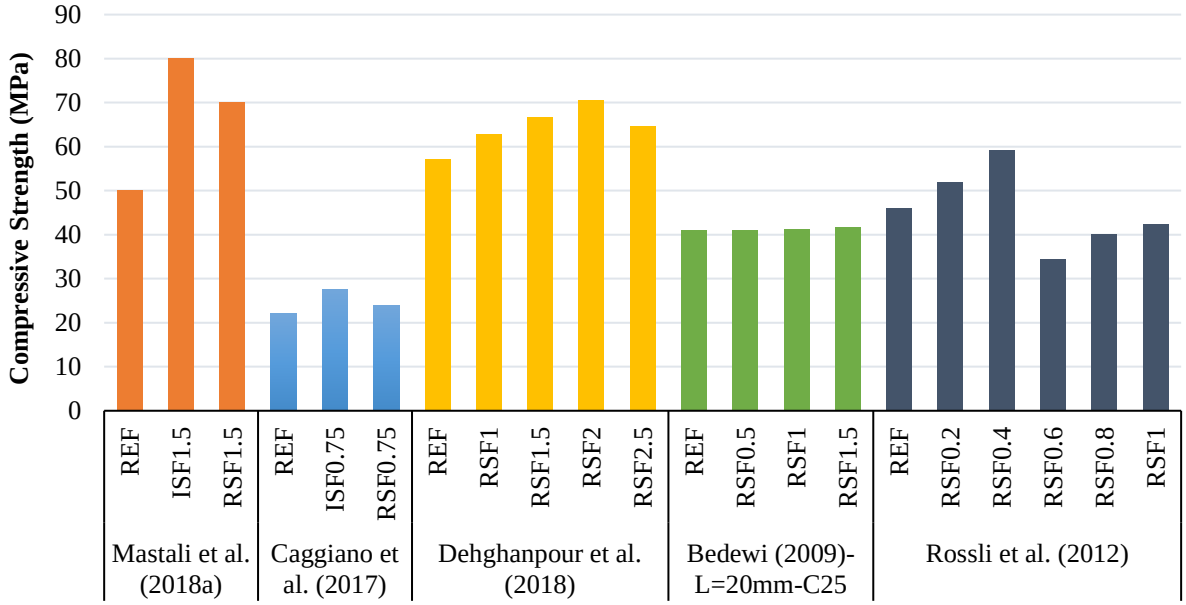

Fig. 10. Compressive strength results for specimens reinforced with recycled and industrial fibers (REF: Reference concrete, ISF: Industrial steel fiber reinforced concrete, RSF: Recycled steel fiber reinforced concrete, C: Concrete class)

4.2. Splitting Tensile Strength

Various studies have reported contradictory results on using RSF from tires on the tensile strength of concrete (Caggiano et al., 2015). Some studies have reported that rubber particles bonded to RSF reduce concrete's splitting tensile strength. Compared to the surrounding dense cement matrix, the rubber's softness leads to elastic imbalance and acts as cavities that provide little load resistance (Liew and Akbar, 2020). Sengul (2016) studied the effect of RSF from tires with different aspect ratios on the splitting tensile strength of concrete. Using RSF did not result in a noticeable increase in tensile strength. However, some studies have shown the opposite result.

Mastali et al. (2018a) examined the impact of hybrid fibers containing RSF longer than 50 mm on the splitting tensile strength of self-consolidating concrete. The findings show that fibers have a positive impact on splitting tensile strength. Like compressive strength, fiber bridging and an increase in splitting tensile strength were caused by the high potential of fibers to stop further crack propagation. Comparing the specimen reinforced with RSF to the plain mixture, a tensile strength increase of

roughly 25% was observed. Interestingly, using recycled and industrial steel fibers together provided beneficial results. As previously indicated, ISF were shown to be the most effective at bridging action, followed by RSF. Therefore, in the mixture supplemented with 1% ISF and 0.5% RSF, the most remarkable improvement in splitting tensile strength for the hybrid RSF and ISF was 27%.

Yang et al. (2019) investigated the effect of RSF from tires with and without rubbers attached to the surface on the splitting tensile strength of Ultra-High Performance Concrete (UHPC). In this study, the fiber length was 40 mm, and the fiber diameter was 1 mm. The results showed that the fibers with and without rubber attached to the surface increased the splitting tensile strength by 50% and 40%, respectively, in comparison to the reference specimen. The lower impact of non-rubber steel fibers attached to the surface may be due to the carbon black on the surface of these fibers. Compared to concrete that contained ISF with a tensile strength similar to that of RSF, a study found that the carbon black on the surface of RSF reduced the flexural strength of concrete by around 15% (Yang et al., 2019; Tlemat, 2004). Further study is required to determine how carbon black affects the mechanical characteristics and pore microstructure of UHPC. Rossli and Ibrahim (2012) investigated the effect of volume content (0%, 0.2%, 0.4%, 0.6%, 0.8%, 1%) and the length of randomly distributed fibers ranging from 20 mm to 99 mm on splitting tensile strength. The findings indicate that the splitting tensile strength is optimum at 1% volume content. Table 3 shows the results for splitting tensile strength using RSF.

4.3. Flexural Strength

FRC's post-peak behavior is influenced by the volume, type, and quality of the fibers used in the mixture (Awolusi et al., 2021). RSF can bridge cracks and stop cracking to enhance the post-cracking behavior of concrete. Regarding energy absorption and residual resistance after cracking brought on by flexural loading, RSF can perform similarly to ISF (Aiello et al., 2009). Mastali et al. (2018a) examined the impact of hybrid fibers containing recycled fibers longer than 50 mm on the flexural strength of self-consolidating concrete. For this purpose, the three-point bending test evaluated prismatic beams with dimensions of $420 \times 80 \times 60$ mm^3. The findings indicated that the type of fiber impacts the flexural strength, ductility, flexural stiffness, post-peak residual strength, and ultimate deflection corresponding to the maximum load. The flexural and post-peak residual strengths increased by increasing the fiber mechanical anchorage while the flexural stiffness was reduced. Figure 11 shows that plain, fiber-free concrete has no resistance to energy absorption and crack expansion after maximum load and suddenly fails due to bending load. Conversely, concrete with 1.5% ISF demonstrates better post-cracking performance by preventing crack development. When steel fibers are recycled, some of them are damaged. The loose particles attached to the surface reduce the peak energy response in the energy absorption compared to the ISF with a smooth surface (Mastali et al., 2018a). The insufficient response of RSF can also be related to their irregular geometry (Martinelli et al., 2015). According to the findings, when compared to ordinary self-consolidating concrete, the flexural strengths of mixtures improved in reinforced self-consolidating concrete independent of the fiber combination. Additionally, the hybrid combination of ISF and RSF showed the highest flexural strength among the mixtures reinforced with hybrid fibers (about 35%).

Caggiano et al. (2017) studied the impact of RSF on the flexural behavior of prismatic beams with dimensions of $600 \times 150 \times 150$ mm^3. Prism-shaped specimens were notched in the middle for a depth of around 45 mm prior to the four-point bending tests. As a result of the initial crack's growth, the

plain concrete exhibits brittle failure. However, the ISF mix exhibits a post-cracking response (under bending loads) that is distinguished by a notable increase in toughness. The analysis emphasizes the effects of entirely substituting RSF with an equivalent amount of ISF. The results in ductility indices highlight that RSF slightly reduce the FRC toughness. The presence of RSF moves the post-cracking behavior from hardening to plastic (with values varying from 0.9 to 1.1 in every instance where RSF were used).

Dehghanpour and Yilmaz (2018) investigated the effect of recycled fibers on the flexural behavior of prismatic beams with dimensions of 160 × 40 × 40 mm^3. Mortar specimens reinforced with RSF showed higher flexural strength than specimens without fibers. Additionally, the specimens reinforced with 2.0% and 2.5% RSF exhibited the best maximum flexural strength value among the results of the flexural tests. As shown in Figure 12, there was no observable change between specimens reinforced with 1.0% RSF and unreinforced specimens. While the specimens containing 1.5%, 2.0%, and 2.5% RSF compared to the unreinforced specimen, the area under the curves increased by 10, 13, and 18 times, respectively.

Bedewi (2009) examined the impact of volume content and fiber length on the flexural strength of concrete reinforced with RSF. Fiber lengths of 20 mm, 40 mm, and 60 mm and volumes of 0, 0.5%, 1%, and 1.5% were considered. The results obtained in each volume content showed that the maximum fiber length (60 mm) was observed for the maximum flexural strength. Table 4 summarises the results of various research' examinations of flexural strength.

Table 3. Results of splitting tensile strength obtained from using RSF

Reference	RSF Content	Diameter (mm)	Length (mm)	W/C	TS of PC* (MPa)	TS of FRC (MPa)
Sengul (2016)	10 kg/m^3	0.6	50	0.5	6.7	6
Mastali et al. (2018a)	1.5%	0.15	Over 50	0.76	3.5	4.3
Yang et al. (2019)	30 kg/m^3	1	40	0.18	6.91	11.8
Rossli and Ibrahim (2012)	0.2%	0.2-1.39	20-99	0.53	3.88	3.39
	0.4%					3.98
	0.6%					3.90
	0.8%					3.50
	1%					4.44
Onuaguluchi and Banthia (2018)	0.35%	0.2-0.3	15	0.5	3.35	3.98
	0.5%					3.91

*TS- Tensile Strength. PC-Plain Concrete

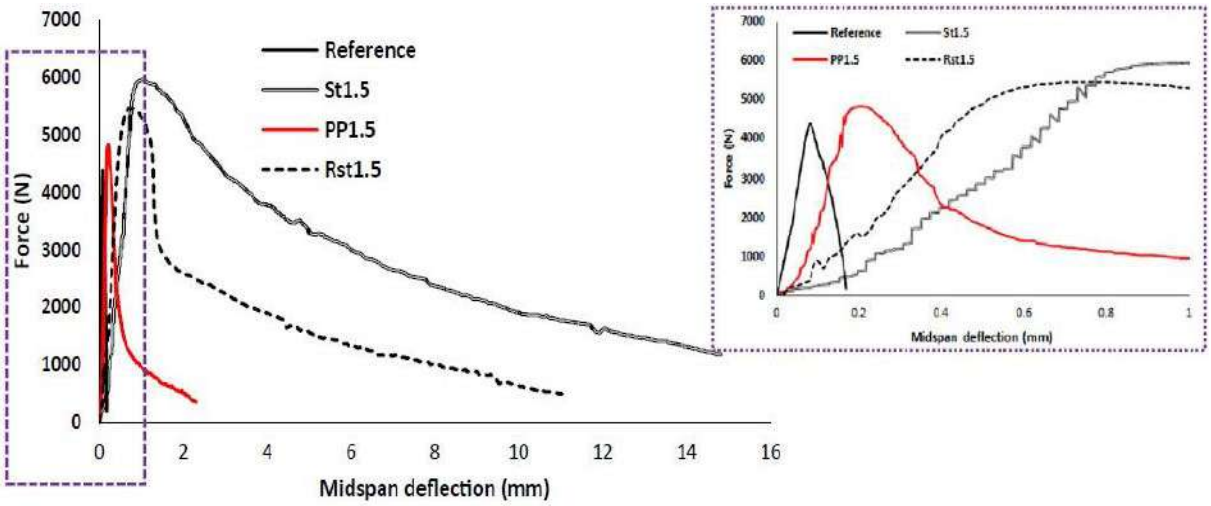

Fig. 11. Force-deflection responses of specimens reinforced with mono-fiber (Mastali et al., 2018a)

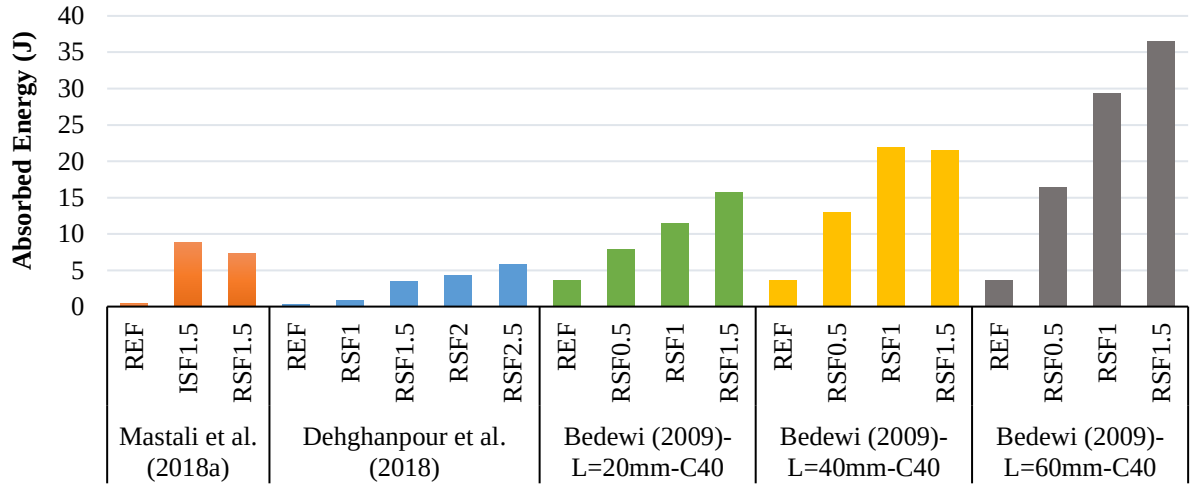

Fig. 12. Amounts of absorbed energy presented in different studies (REF: Reference concrete, ISF: Industrial steel fiber reinforced concrete, RSF: Recycled steel fiber reinforced concrete, L: Fiber length, C: Concrete class)

Table 4. Results of flexural strength obtained from using RSF

Reference	RSF Content	Diameter (mm)	Length (mm)	W/C	FS of PC* (MPa)	FS of FRC (MPa)
Mastali et al. (2018a)	1.5%	0.15	Over 50	0.76	5	6.5
Caggiano et al. (2017)	0.75%	0.11-0.44	6-74	0.49	3	3.68
Dehghanpour and Yilmaz (2018)	1%	0.26	25	0.5	5.21	6.83
	1.5%					7.34
	2%					8.09
	2.5%					8.19
Bedewi (2009)	0.5%	0.89	20	0.53	6.18	6.84
	1%					7.17
	1.5%					8.07
	0.5%	0.89	40	0.53		6.96
	1%					7.89
	1.5%					8.64
	0.5%	0.89	60	0.53		8.19
	1%					10.08
	1.5%					13.71

*FS- Flexural Strength. PC-Plain Concrete

4.4. Impact Resistance

One of FRC's distinctive features is its impact resistance. It has generally been observed that fibers increase fracture energy and maximum load under the impact (Ndayambaje, 2018; Soufeiani et al., 2016; Mastali and Dalvand, 2016). Following the ACI Committee's recommendations, impact resistance should be quantified for repeated blows that the test specimen receives. (ACI Committee, 1996). The number of blows needed to produce the initially visible cracks is considered the first impact resistance. In contrast, the number of blows determines the final resistance that causes the test specimen to fail. Steel fibres' presence positively affects impact resistance because it improves the fracture energy, maximum load, abrasion resistance, and impact resistance. Mastali et al. (2018a) investigated the effect of hybrid fibers containing recycled fibers longer than 50 mm on the impact resistance in self-consolidating concrete. The findings demonstrated that adding fibers enhanced impact resistance due to fiber bridging action regardless of the fiber combination. Also, increasing mechanical anchorage of fibers resulted in a more notable enhancement in impact resistance. Accordingly, the reinforced specimens with 1.5% ISF were found to have the highest impact resistance of discs, with first crack and ultimate crack resistance of 73 and 115 blows, respectively. The first and ultimate cracks increased by more than 4 and 6 times as much as the plain concrete disc. Maximum impact resistance for hybrid

fibers was observed as 67 and 101 blows for the first and ultimate crack, respectively; the cementitious disk contributed 1% ISF and 0.5% RSF. Figure 13a shows the number of blows required for ultimate failure in different studies.

Dehghanpour and Yılmaz (2018) investigated the effect of RSF on the impact resistance of concrete. The findings demonstrated that the increased RSF volume fraction improved the ultimate energy values up to the ultimate failure of the RSF-reinforced mortar specimen slabs at 40 mm thickness. For instance, although the slabs without RSF required 30.96 Joules of energy to collapse, the specimens with 2.5% RSF incorporated required an average of 313.80 joules of energy to fail. With the increased RSF volume, a more effective composite material is obtained against stresses due to forming more bridges in the matrix. Energy absorption increases with increasing failure duration (Yahaghi et al., 2016). Impact resistance depends on the length and volume of the fibers in the concrete mix (Mastali et al., 2019). Bedewi (2009) investigated the effect of different lengths of 20 mm, 40 mm, and 60 mm and volumes of 0, 0.5%, 1%, and 1.5% recycled fibers on the impact resistance. The obtained results showed that the number of blows required for the final cracking of the test specimens increases with the fibers' length and volume content. The highest number of impacts was observed in the length of 60 mm and volume of 1.5%, which indicates the highest impact resistance. Figure 13b briefly shows the results of Bedewi's study (2009) regarding the effect of the length and volume percentage of fibers in addition to the concrete strength class.

4.5. Durability

The fiber incorporation increases the permeability of the specimens, and this increase in permeability is maintained as the fiber content rises (Ramezani and Esfahani, 2018). Concrete with RSF has improved crack propagation, impact resistance, and shrinkage behavior (Mastali and Dalvand, 2017; Al-Kamyani et al., 2018). Diffusion, capillary transfer, and permeation are the three main modes of corrosive agents entering concrete (Toghroli et al., 2018). Controlling the propagation of crack width reduces the penetration of hazardous chemicals into the concrete structure, thus reducing the concrete's deterioration and structural steel fibers (Caldentey et al., 2016). Only surface fiber damage in the corrosive medium was seen by restricting the crack thickness to 0.3 mm (Graeff et al., 2009). Corrosion significantly affects the interaction of fibers and cement matrix (Frazão et al., 2016). Electrochemical results showed that for RSF in a 3.5% NaCl solution, the probability of corrosion was 90%, and RSF were more vulnerable to corrosion than ISF (Balouch et al., 2010). The corrosion resistance of RSF is not seriously affected by the presence of rubber on the surface of the fibers. It has a negligible effect on concrete reinforced with RSF in terms of corrosion resistance (Frazão et al., 2019). The results showed that combining ISF and RSF increases the durability of concrete (Alsaif et al., 2018a).

In the study conducted by Bjegovic et al. (2012), the effect of steel fibers, textile fibers, and rubber crumb (as an aggregate substitute) recycled from waste tires in freeze-thaw cycles was investigated. The results showed that the presence of by-products from the mechanical recycling of waste tires complies with all criteria and can meet the criteria of water permeability and wear resistance. In a study by Graeff et al. (2009), the effect of RSF and ISF with wet-dry methods to accelerate corrosion was investigated. The findings revealed that when the specimens were exposed to 5 months of continuous wet-dry cycles, the corrosion of the fibers was visible only on the outside. Both types of fibers showed limited signs of corrosion. This study's compressive and flexural results showed that specimens with 2% industrial fibers have the same performance as specimens with 6% recycled fibers.

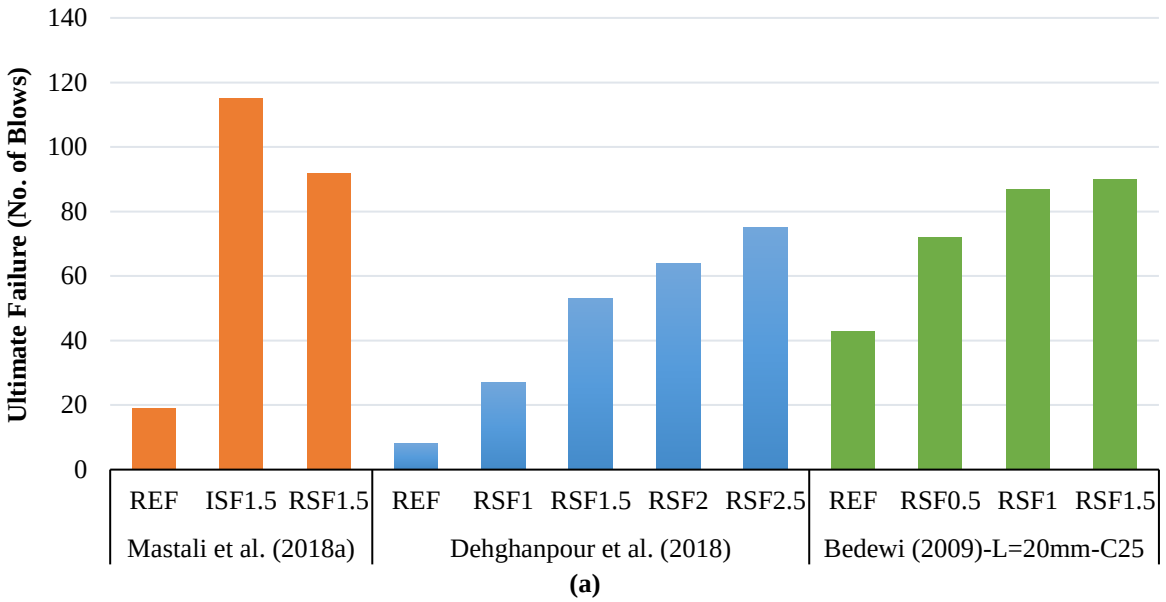

(a)

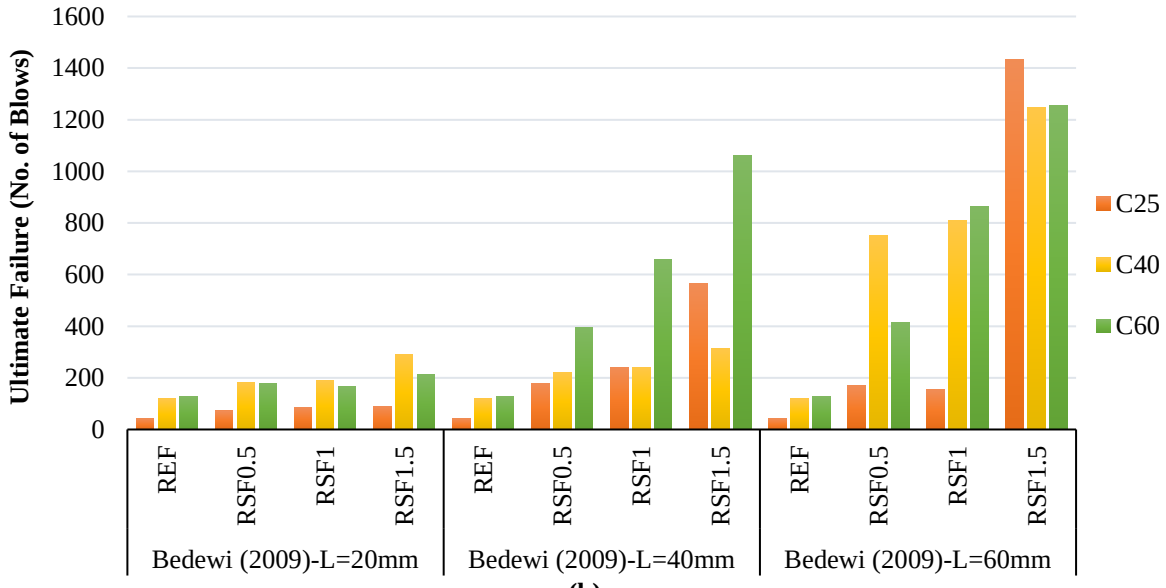

(b)

Fig. 13. The number of blows required for ultimate failure: a) Compare different studies; and b) Bedewi's study (2009) regarding the effect of the length and volume percentage of fibers (REF: Reference concrete, ISF: Industrial steel fiber reinforced concrete, RSF: Recycled steel fiber reinforced concrete, L: Fiber length, C: Concrete class)

5. Conclusions

Studies have extensively identified the possibility of reusing waste tire debris as a source of RSF to achieve a sustainable environment and an alternative to ISF. RSF have different lengths, diameters, and tensile strengths depending on the recycling method. As a result, a significant range in the characteristics of fresh and hardened concrete that contained tire waste-derived RSF was noted. Studies show that RSF can provide comparable mechanical properties to ISF if added under optimal conditions. It needs to be determined how RSF may affect compressive strength.

More research is required to comprehend better how the matrix interacts with the fibers and behaves under compressive pressures. Better resistance against structural loads is provided by using hybrid fibers consisting of RSF and ISF. Concrete reinforced with RSF can provide desirable results under bending loads compared to

ISF. Therefore, improving concrete's mechanical characteristics by using RSF in the construction industry can be economical and environmentally friendly.

Based on the available studies, some current challenges and the studies needed for the future are mentioned below:

- RSF from waste tires have rubber attached to the surface and textiles. Therefore, it is essential to investigate the interaction and bonding of fibers with the concrete matrix. In studies, the microstructure of concrete has rarely been investigated, and mostly the surface morphology of fibers has been investigated. Therefore, more studies are needed to understand better the fibers' interaction with the matrix and its behavior under mechanical loads.
- The behavior of these fibers at high temperatures has yet to be studied. Concrete spalling behavior has been investigated only in one case study. Therefore, investigating the effect of these fibers at high temperatures on concrete's mechanical properties is a critical challenge for future work.
- The studies conducted on the effect of these fibers and rubber and textiles on concrete durability issues are also limited and still need more work and study.

6. References

Abdul Awal, A.S.M., Kadir, M.A.A., Yee, L.L. and Memon, N. (2015). "Strength and deformation behaviour of concrete incorporating steel fibre from recycled tyre", In *InCIEC 2014* (pp. 109-117), Springer, Singapore, https://doi.org/10.1007/978-981-287-290-6_10.

ACI Committee 544. (1996). *State-of-the-art report on fiber reinforced concrete*. ACI Committee 544 report 544.1R-96, Detroit.

Aiello, M.A., Leuzzi, F., Centonze, G. and Maffezzoli, A. (2009). "Use of steel fibres recovered from waste tyres as reinforcement in concrete: Pull-out behaviour, compressive and flexural strength", *Waste Management*, 29(6), 1960-1970, https://doi.org/10.1016/j.wasman.2008.12.002.

Al-Kamyani, Z., Figueiredo, F.P., Hu, H., Guadagnini, M. and Pilakoutas, K. (2018). "Shrinkage and flexural behaviour of free and restrained hybrid steel fibre reinforced concrete", *Construction and Building Materials*, 189, 1007-1018.

Alsaif, A., Bernal, S.A., Guadagnini, M. and Pilakoutas, K. (2018a). "Durability of steel fibre reinforced rubberised concrete exposed to chlorides", *Construction and Building Materials*, 188, 130-142, https://doi.org/10.1016/j.conbuildmat.2018.08.122.

Alsaif, A., Garcia, R., Guadagnini, M. and Pilakoutas, K. (2018b). "Behaviour of FRP-confined rubberised concrete with internal recycled tyre steel fibres", In *High Tech Concrete: Where Technology and Engineering Meet*, (pp. 233-241), Springer, Cham, https://doi.org/10.1007/978-3-319-59471-2_29.

Awolusi, T.F., Oke, O.L., Atoyebi, O.D., Akinkurolere, O.O., and Sojobi, A.O. (2021). "Waste tires steel fiber in concrete: A review", *Innovative Infrastructure Solutions*, 6(1), 1-12, https://doi.org/10.1007/s41062-020-00393-w.

Balouch, S.U., Forth, J.P. and Granju, J.L. (2010). "Surface corrosion of steel fibre reinforced concrete", *Cement and Concrete Research*, 40(3), 410-414, https://doi.org/10.1016/j.cemconres.2009.10.001.

Bedewi, N. (2009). "Steel fiber reinforced concrete made with fibers extracted from used tyres", MSc Thesis in Civil Engineering, Addis Ababa University, Addis Ababa, Ethiopia.

Bjegovic, D., Baricevic, A. and Lakusic, S. (2012). "Innovative low cost fibre-reinforced concrete. Part I: Mechanical and durability properties", *Concrete Repair, Rehabilitation and Retrofitting III, CRC Press/Balkema*, 199-203.

Bulei, C., Todor, M.P., Heput, T. and Kiss, I. (2018). "Directions for material recovery of used tires and their use in the production of new products intended for the industry of civil construction and pavements", In *IOP Conference Series: Materials Science and Engineering* (Vol. 294, No. 1, p. 012064), IOP Publishing, https://doi.org/10.1088/1757-899X/294/1/012064.

Caggiano, A., Folino, P., Lima, C., Martinelli, E. and Pepe, M. (2017). "On the mechanical response of hybrid fiber reinforced concrete with recycled and industrial steel fibers", *Construction and Building Materials*, 147, 286-295.

Caggiano, A., Xargay, H., Folino, P. and Martinelli, E. (2015). "Experimental and numerical characterization of the bond behavior of steel fibers recovered from waste tires embedded in cementitious matrices", *Cement and Concrete Composites*, 62, 146-155, https://doi.org/10.1016/j.conbuildmat.2017.04.160.

Caldentey, A.P., Vila, J.G., González, J.O. and Rodríguez, F. (2016). "Contributing to sustainability of concrete by using steel fibres from recycled tyres in water retaining structures", In *Ii International Conference on Concrete Sustainability-Iccs16*, 84-93.

De Wilde, P. and Coley, D. (2012). "The implications of a changing climate for buildings", *Building and environment*, 55, 1-7, https://doi.org/10.1016/j.buildenv.2012.03.014.

Dehghanpour, H., and Yilmaz, K. (2018). "Mechanical and impact behavior on recycled steel fiber reinforced cementitious mortars", *Scientific Herald of the Voronezh State University of Architecture and Civil Engineering*, 39(3), 67-84.

Frazão, C.M.V. (2019). "Recycled steel fiber reinforced concrete for structural elements subjected to chloride attack: Mechanical and durability performance", PhD Thesis, University of Minho.

Frazão, C., Barros, J., Camões, A., Alves, A.C. and Rocha, L. (2016). "Corrosion effects on pullout behavior of hooked steel fibers in self-compacting concrete", *Cement and Concrete Research*, 79, 112-122, https://doi.org/10.1016/j.cemconres.2015.09.005.

Frazão, C., Díaz, B., Barros, J., Bogas, J.A. and Toptan, F. (2019). "An experimental study on the corrosion susceptibility of Recycled Steel Fiber Reinforced Concrete", *Cement and Concrete Composites*, 96, 138-153, https://doi.org/10.1016/j.cemconcomp.2018.11.011.

Ghanbari, M. and Bayat, M. (2022). "Effectiveness of reusing steel slag powder and polypropylene fiber on the enhanced mechanical behavior of cement-stabilized sand", *Civil Engineering Infrastructures Journal*, 55(2), 241-257, https://doi.org/10.22059/CEIJ.2021.319310.1742.

Graeff, Â.G., Pilakoutas, K., Lynsdale, C., and Neocleous, K. (2009). "Corrosion durability of recycled steel fibre reinforced concrete", *Intersectii/Intersections*, 6(4), 77-89.

Jamshaid, H. and Mishra, R. (2016). "A green material from rock: basalt fiber, A review", *The Journal of The Textile Institute*, 107(7), 923-937, https://doi.org/10.1080/00405000.2015.1071940.

Laborel-Préneron, A., Aubert, J.E., Magniont, C., Tribout, C. and Bertron, A. (2016). "Plant aggregates and fibers in earth construction materials: A review", *Construction and building materials*, 111, 719-734, https://doi.org/10.1016/j.conbuildmat.2016.02.119.

Liew, K.M., and Akbar, A. (2020). "The recent progress of recycled steel fiber reinforced concrete", *Construction and Building Materials*, 232, 117232, https://doi.org/10.1016/j.conbuildmat.2019.117232.

Martinelli, E., Caggiano, A. and Xargay, H. (2015). "An experimental study on the post-cracking behaviour of Hybrid Industrial/Recycled Steel Fibre-Reinforced Concrete", *Construction and Building Materials*, 94, 290-298, https://doi.org/10.1016/j.conbuildmat.2015.07.007.

Mastali, M. and Dalvand, A. (2016). "Use of silica fume and recycled steel fibers in self-compacting concrete (SCC)", *Construction and Building Materials*, 125, 196-209, https://doi.org/10.1016/j.conbuildmat.2016.08.046.

Mastali, M. and Dalvand, A. (2017). "Fresh and hardened properties of self-compacting concrete reinforced with hybrid recycled steel-polypropylene fiber", *Journal of Materials in Civil Engineering*, 29(6), 04017012, https://doi.org/10.1061/(ASCE)MT.1943-5533.0001851.

Mastali, M., Dalvand, A., Sattarifard, A.R., Abdollahnejad, Z. and Illikainen, M.J.C.P.B.E. (2018a). "Characterization and optimization of hardened properties of self-consolidating concrete incorporating recycled steel, industrial steel, polypropylene and hybrid fibers", *Composites Part B: Engineering*, 151, 186-200, https://doi.org/10.1016/j.compositesb.2018.06.021.

Mastali, M., Dalvand, A., Sattarifard, A.R. and Illikainen, M. (2018b). "Development of eco-efficient and cost-effective reinforced self-consolidation concretes with hybrid industrial/recycled steel fibers", *Construction and Building Materials*, 166, 214-226, https://doi.org/10.1016/j.conbuildmat.2018.01.147.

Mastali, M., Dalvand, A., Sattarifard, A.R., Abdollahnejad, Z., Nematollahi, B., Sanjayan, J. G. and Illikainen, M. (2019). "A comparison of the effects of pozzolanic binders on the hardened-state properties of high-strength cementitious composites reinforced with waste tire fibers", *Composites Part B: Engineering*, 162, 134-153, https://doi.org/10.1016/j.compositesb.2018.10.100.

Mehdipour, S., Nikbin, I.M., Dezhampanah, S., Mohebbi, R., Moghadam, H., Charkhtab, S. and Moradi, A. (2020). "Mechanical properties, durability and environmental evaluation of rubberized concrete incorporating steel fiber and metakaolin at elevated temperatures", *Journal of Cleaner Production*, 254, 120126, https://doi.org/10.1016/j.jclepro.2020.120126.

Mohajerani, A., Hui, S.Q., Mirzababaei, M., Arulrajah, A., Horpibulsuk, S., Abdul Kadir, A., Rahman, M.T. and Maghool, F. (2019). "Amazing types, properties, and applications of fibres in construction materials", *Materials*, 12(16), 2513, https://doi.org/10.3390/ma12162513.

Ndayambaje, J.C. (2018). "Structural performance and impact resistance of rubberized concrete", Ph.D. Thesis, Pan-African University for Basic Science, Technology and Inovation, Juja, Kenya.

Onuaguluchi, O. and Banthia, N. (2018). "Scrap tire steel fiber as a substitute for commercial steel fiber in cement mortar: Engineering properties and cost-benefit analyses", *Resources, Conservation and Recycling*, 134, 248-256, https://doi.org/10.1016/j.resconrec.2018.03.014.

Ramezani, A. and Esfahani, M. (2018). "Evaluation of Hybrid Fiber Reinforced Concrete exposed to severe environmental conditions", *Civil Engineering Infrastructures Journal*, 51(1), 119-130, https://doi.org/10.7508/CEIJ.2018.01.007.

Rossli, S. and Ibrahim, I. (2012). *Mechanical properties of recycled steel tire fibres in concrete*, Technical Report, Faculty of Civil Engineering, University Technology Malaysia.

Sabzi, J., Asadi Shamsabadi, E., Ghalehnovi, M., Hadigheh, S.A., Khodabakhshian, A. and Brito, J.D. (2021). "Mechanical and durability properties of mortars incorporating red mud, ground granulated blast furnace slag, and electric arc furnace dust", *Applied Sciences*, 11(9), 4110. https://doi.org/10.3390/app11094110.

Saha, P., Chowdhury, S., Roy, D., Adhikari, B., Kim, J.K. and Thomas, S. (2016). "A brief review on the chemical modifications of lignocellulosic fibers for durable engineering composites", *Polymer Bulletin*, 73(2), 587-620, https://doi.org/10.1007/s00289-015-1489-y.

Sengul, O. (2016). "Mechanical behavior of concretes containing waste steel fibers recovered from scrap tires", *Construction and Building Materials*, 122, 649-658, https://doi.org/10.1016/j.conbuildmat.2016.06.113.

Shi, X., Brescia-Norambuena, L., Grasley, Z. and Hogancamp, J. (2020). "Fracture properties and restrained shrinkage cracking resistance of cement mortar reinforced by recycled steel fiber from scrap tires", *Transportation Research Record*, 2674(8), 581-590, https://doi.org/10.1177/0361198120924407.

Sukontasukkul, P., Pomchiengpin, W. and Songpiriyakij, S. (2010). "Post-crack (or post-peak) flexural response and toughness of fiber reinforced concrete after exposure to high temperature", *Construction and Building Materials*, 24(10), 1967-1974, https://doi.org/10.1016/j.conbuildmat.2010.04.003.

Soufeiani, L., Raman, S.N., Jumaat, M.Z.B., Alengaram, U.J., Ghadyani, G., and Mendis, P. (2016). "Influences of the volume fraction and shape of steel fibers on fiber-reinforced concrete subjected to dynamic loading, A review", *Engineering Structures*, 124, 405-417, https://doi.org/10.1016/j.engstruct.2016.06.029.

Tlemat, H. (2004). "Steel fibres from waste tyres to concrete: testing, modelling and design", PhD Thesis, University of Sheffield.

Tlemat, H., Pilakoutas, K. and Neocleous, K. (2003). "Pull-out behaviour of steel fibres recycled from used tyres", *Proceedings of International Symposia on Celebrating Concrete: People and Practice (in Role of Concrete in Sustainable Development)*, Dundee, (pp. 175-184).

Toghroli, A., Shariati, M., Sajedi, F., Ibrahim, Z., Koting, S., Mohamad, E.T. and Khorami, M. (2018). "A review on pavement porous concrete using recycled waste materials", *Smart Structures and System*, 22(4), 433-440. https://doi.org/10.12989/sss.2018.22.4.433.

Wafa, F.F. (1990). "Properties and applications of Fiber Reinforced Concrete", *Engineering Sciences*, 2, 49-63.

Yahaghi, J., Muda, Z.C. and Beddu, S.B. (2016). "Impact resistance of oil palm shells concrete reinforced with polypropylene fibre", *Construction and Building Materials*, 123, 394-403, https://doi.org/10.1016/j.conbuildmat.2016.07.026.

Yang, J., Peng, G.F., Shui, G.S. and Zhang, G. (2019). "Mechanical properties and anti-spalling behavior of ultra-high performance concrete with recycled and industrial steel fibers", *Materials*, 12(5), 783, https://doi.org/10.3390/ma12050783.

Yin, S., Tuladhar, R., Shi, F., Combe, M., Collister, T. and Sivakugan, N. (2015). "Use of macro plastic fibres in concrete: A review", *Construction and Building Materials*, 93, 180-188, https://doi.org/10.1016/j.conbuildmat.2015.05.105.

Zamanzadeh, Z., Lourenço, L. and Barros, J. (2015). "Recycled steel fibre reinforced concrete failing in bending and in shear", *Construction and Building Materials*, *85*, 195-207, https://doi.org/10.1016/j.conbuildmat.2015.03.070.

Civil Engineering Infrastructures Journal 2023, 56(1): 19-32
DOI: 10.22059/CEIJ.2021.327968.1778

RESEARCH PAPER

Validation of Modified Driver Behavior Questionnaire Considering Mobile Phone Usage While Driving

Parishad, N.[1], Aghabayk, K.[2*], Bayat, M.[1] and Shiwakoti, N.[3]

[1] M.Sc., School of Civil Engineering, College of Engineering, University of Tehran, Tehran, Iran.
[2] Assistant Professor, School of Civil Engineering, College of Engineering, University of Tehran, Tehran, Iran.
[3] Assistant Professor, Senior Lecturer, School of Engineering, RMIT University, Melbourne, Australia.

Received: 29 Jul. 2021; Revised: 17 Sep. 2021; Accepted: 26 Sep. 2021

ABSTRACT: Although the existing Driver Behavior Questionnaire (DBQ) covers a wide range of drivers' aberrant behaviors, advances in technology have made some questions out of date. These advancements could lead to human errors while driving, and therefore some items of DBQ need to be updated to reflect the influence of technology on driving behavior such as mobile phone usage while driving. This study aims to modify the widely used DBQ by including "mobile phone usage while driving" items and validate it in Iranian context. The impact of demographic items on each factor scale is also investigated. A shortened DBQ that include drivers' aberrant behaviors and additional questions on mobile phone usage while driving was developed. A total of 298 drivers (168 males and 130 females) between the ages of 18 and 60 participated in this study. Results showed that the mean score of two mobile phone usage items is significantly correlated with violation behaviors. Besides, younger drivers, male drivers, and drivers who were involved in an accident in the past three years behave more aberrant. Statistical analysis shows that drivers who use their mobile phones while driving are more likely to be involved in a traffic crash. Moreover, mobile phone usage while driving decreases significantly by age and males use their mobile phones more than females while driving.

Keywords: Driver Behavior Questionnaire (DBQ), Driver Distraction, Error, Factor Analysis, Mobile Phone Usage, Violation.

1. Introduction

Traffic accidents are a critical issue that has been the concern of researchers for many years (Vajari et al., 2020). Previous studies have shown that as compared to the developed countries, the Middle East countries are more vulnerable in road safety due to the higher number of vehicle crashes or severity of road traffic injury and fatality (Besharati et al., 2020; Heydari et al., 2019; Rezaei et al., 2014; Bener et al., 2008). Tehran, the capital city of Iran, with a population of about 9 million and an average 19 million daily trips, is considered as one of the most populated cities in the

* Corresponding author E-mail: kayvan.aghabayk@ut.ac.ir

Middle East (Tehran Traffic and Transportation Organization (TTTO), 2018). According to TTTO (2018), 660 people were killed by traffic crashes in 2018 in the city of Tehran. Besides, the crash fatality rate per 100,000 populations in Tehran province increased from 8.7 people in 2016 to 9.7 people in 2018 (TTTO, 2018). Therefore, the study of traffic injuries and their causes in Tehran is of great importance.

Previous studies have considered different methods to investigate traffic accidents and their causes. One of these methods is the evaluation and analysis of road users' injury and fatality information (Nasri and Aghabayk, 2020). The study of the relationship between drivers' aberrant behavior and crash involvement is another approach (Wang and Xu, 2019; Deng et al., 2019; Gueho et al., 2014). The 50-items Driver Behavior Questionnaire (DBQ) that was developed by Reason et al. (1990) is one of the most widely used instruments to evaluate the drivers' aberrant behaviors. The questionnaire classified drivers' aberrant behaviors into three factors namely: Violations (deliberate acts), Errors (failure of planned action), and Slips and Lapses (unintentional acts). The violations category has been further refined by Lawton et al. (1997) into ordinary violations and aggressive violations. The aggressive violations concern hostile behaviors toward other users. Besides, a study by Aberg and Rimmö (1998) presented another classification of driver's aberrant behavior where they divided the errors into three types, namely dangerous errors, errors due to inattention and errors due to inexperience.

To take into account the country-specific variations and solutions and also different driving cultures, the DBQ has been applied and calibrated in several countries. Further, attempts have been made to shorten the DBQ to reduce the time required for the completion of the questionnaire and subsequently increase the completion rate (Martinussen et al., 2013). Over the years, the DBQ has been applied in Australia (Stephens and Fitzharris, 2016), France (Gueho et al., 2014), Denmark (Martinussen et al., 2017), America (Owsley et al., 2003), Canada (Koppel et al., 2019, 2018), China (Xu et al., 2018; Qu et al., 2016), Sweden (Åberg and Warner, 2008), Greece (Ersan et al., 2020; Kontogiannis et al., 2002), Netherland (Lajunen et al., 1999), Spain (Gras et al., 2006), New Zealand (Sullman et al., 2019; Sullman et al., 2000) and UK (Rowe et al., 2015; Reason et al., 1990). Furthermore, researchers in Iran (Parishad et al., 2020), Turkey (Özkan and Lajunen, 2005), Oman (Al Azri et al., 2017), Qatar, and UAE (Bener et al., 2008) conducted similar studies in the Middle East countries.

Moreover, due to the advancement of technology in recent years, some of the 50-items DBQ questions might be out of date (e.g. "attempt to drive away from traffic lights in third gear" or "lock yourself out of your car with the keys still inside"). On the other hand, some questions could be added to the DBQ to consider the influence of new technology on drivers' behaviors. Besides, technological advances could lead to the formation of new questions that may indicate human errors that may not have been captured in the previous questionnaire. Therefore, the driver behavior questionnaire needs to be updated considering the current context. For example, mobile phone usage while driving could be correlated to drivers' aberrant behaviors. A study by Arvin et al. (2016) showed that almost 10 percent of Iranian drivers use their cell phones while driving. Due to the development of mobile phone applications and social networks, and consequently increasing mobile phone usage while driving, recent studies concentrated more on investigating the impact of mobile phone usage while driving as a variable that affects traffic crashes (Qu et al., 2020; Lipovac et al., 2017). Previous studies depicted that the risk of being involved in a traffic accident could be increased by using a mobile phone while

driving (Mohammadi, 2009). Furthermore, studies by Lansdown and Stephens (2013), and Holland and Rathod (2013) showed that mobile phone use while driving can lead to distraction and reduce driving performance. In Finland, Korpinen and Pääkönen (2012) showed that younger drivers and male drivers more likely to be involved in road crashes while using a mobile phone. Besides, the probability of cellphone usage while driving decreases by aging (Arvin et al., 2016). A study by Isa et al. (2012) showed that almost 70 percent of Indonesian drivers using their mobile phones while driving do not use a hands-free device. Although many drivers perceived that using hands-free devices has advantages to hand-held mobile phone use, previous studies showed that hands-free device reduces driving performance as well (Lipovac et al., 2017).

The focus of recent studies is more on investigating mobile phone usage while driving from behavioral aspects that attempt to elucidate the relation between mobile phone usage and crash involvement (Qu et al., 2020; Hill et al., 2019). Nevertheless, mobile phone usage while driving as a deliberate act which violates the driving laws has not been categorized in any drivers' aberrant behaviors subscales in the past DBQ researches. Furthermore, although the study by Parishad et al. (2020) calibrated the DBQ for Iran and presented a shortened DBQ, the reliability of the shortened version has not been tested and validated. It should be noted that the DBQ calibrated by Parishad et al. (2020) has been used in other studies as well (Aghabayk et al., 2020). Moreover, aberrant behaviors were assessed for other types of road users such as pedestrians (Esmaili et al., 2021) and motorcycle drivers (Haqverdi et al., 2015). However, none of them investigate the impact of mobile phone usage while driving.

The goal of this study is threefold. First, the shortened version of DBQ presented by Parishad et al. (2020) for the city of Tehran was validated. Second, the DBQ was updated using "mobile phone usage while driving" questions and the impact of mobile phone usage while driving from a behavioral aspect was investigated. Finally, the effect of the demographic variables (age, gender, crash history, average driving time per day) will be assessed for various driver behaviors.

2. Method

2.1. Survey Instrument

To assess the reliability of the shortened version of the DBQ on Iranian sample and update the DBQ, a survey instrument was used with three sections: demographic questions (4 items), a shortened version of drivers' aberrant behaviors questions (24 questions), and mobile phone usage while driving questions (2 questions).

The first part of the questionnaire consists of some demographic questions including the participants' age, gender, crash history in three past years, and average driving time per day. The second section contains the DBQ questions. The study by Parishad et al. (2020) provided a shortened version of DBQ for Iranian drivers using the conceptual framework of 50-items Manchester drivers' aberrant behaviors (Reason et al., 1990). The shortened version consists of 20 items that are extracted in four factors namely; Violations (6-items), Errors (6-items), Lapses (6-items), and Aggressive behaviors (2-items). The shortened version that was used in this study has 24 items including 20 items extracted by Parishad et al. (2020) and four additional aggressive behavior questions developed by Lawton et al. (1997). These four additional aggressive behavior questions are: 1) "stay in a lane that you know will be closed", 2) "pull out of a junction", 3) "sound your horn", and 4) "race away from traffic lights". The participants were asked to answer questions on a six-point Likert scale (1: very infrequently, 2: quite infrequently, 3: infrequently, 4: frequently, 5: quite frequently, 6: very often). The third section

was designed to update the questionnaire and investigate the mobile phone usage while driving from the behavioral aspect. This section includes two questions related to using a mobile phone while driving. Since calling, texting and using mobile phone apps are the most frequent activities while driving, the participants were asked to answer 1) "How often do you use your mobile phone for calling or texting while driving?", and 2) "How often do you use your mobile phone applications (e.g., bank, navigation, games, etc.) while driving?". These questions were answered on the 6-point Likert scale as well. The survey instrument was translated into Farsi using the back-translation method. It was first translated into Farsi, then back to English again to assure similar meaning. Moreover, a pilot study was conducted on 10 people to evaluate participants' reactions to the translated questionnaire and eliminate possible problems. The complete survey questionnaire is attached in the Appendix.

2.2. Data Collection

A study by Mundfrom et al. (2005) stated that the required sample size for a factor analysis depends on the ratio of variables to factors (p/f). Since the p/f ratio in the present study is equal to six, the maximum sample size recommended by Mundfrom et al. (2005) equals to 260 people. Moreover, according to a rule of thumb, 5 to 10 samples are needed for each variable. Since there are 26 variables in this study, the maximum required sample size equals to 260 people. Therefore, to collect the data, 325 questionnaires were divided equally between five different districts of the city (center, east, west, north, and south parts of the city) to represent various drivers of Tehran. The questionnaires were distributed during a week in five different malls of the city in November 2019. The participants were provided with the information necessary to make voluntary informed decisions about participating in the survey, how the data will be stored and used, and what are their rights and responsibilities as participants before conducting the questionnaire survey. The survey took, on an average, eight minutes to complete. At first, participants were asked about their driving time per day and whether they hold a driving license. Participants who responded that they do not have a car driving license or drive less than 15 minutes per day on average were excluded from the study. Since this study needs just participants' general impressions or perceptions (Reason et al., 1990), they were asked to provide the first response that came to their minds and answer the questions accordingly. Out of 325 participants, 27 participants' responses were omitted from analysis because of a high number of missing data (more than six questions) or low standard deviation of answers (less than 0.2). Finally, the analysis was conducted with 298 participants.

The sample includes 168 male and 130 female participants. The age of participants ranged from 18 to 60 (M = 34.18, SD = 10.91). Among 298 participants, 91 (30.5%) participants reported that they were involved in car accidents as a driver in the past three years, while most of the participants (69.2%) reported that they drive less than 2 hours per day. Table 1 shows the data description.

3. Results

The model development was conducted using AMOS version 24.0 (IBM, 2016). In addition, the effect of demographic variables and mobile phone usage on each factor scores were examined using SPSS version 25.0 (IBM, 2017).

Table 2 depicts the descriptive statistics, Means (M), and Standard Deviations (SD), ranked in descending order by the mean value for 24 behavioral items plus two mobile phone usage items. The most frequently reported behaviors (mean response ≥ 3) involved mobile phone usage: i) "calling/texting while driving", and ii) "using mobile apps while driving". The most frequent driver aberrant behavior

reported are violations and aggressive violations respectively: i) "Become impatient with a slow driver in the outer lane and overtake on the inside", and ii) "Race away from traffic lights with the intention of beating the driver next to you". Moreover, the least frequently reported behaviors on the errors were related to other road users: i) "Fail to notice pedestrians crossing when turning into a side street from a main road", and ii) "Misjudge speed of oncoming vehicle when overtaking".

Table 1. Sample size by gender, car ownership, crash history, and average driving time per day for each age groups

Variables		Age group			Total
		18-30	30-45	More than 45	
Gender	Male	68	59	41	168
	Female	59	48	23	130
Car ownership	Yes	70	91	57	218
	No	57	16	7	80
Crash history	Involved	49	29	13	91
	Not involved	78	78	51	207
Average driving time per day	Less than 1 hr	56	38	15	109
	1-2 hr	38	27	32	97
	2-4 hr	27	31	13	71
	More than 4 hr	6	11	4	21

Table 2. Means and standard deviations of the DBQ behavior items (n = 298)

Pedestrian behavior item (How often do you …)	M	SD
Use your mobile phone for calling/texting while driving	3.18	1.517
Use your mobile phone applications (bank, navigation, games, …) while driving	3.02	1.624
Become impatient with a slow driver in the outer lane and overtake on the inside	2.98	1.577
Race away from traffic lights with the intention of beating the driver next to you	2.74	1.508
Sound your horn to indicate your annoyance to another driver	2.66	1.466
Miss your exit on a motorway and have to make a lengthy detour	2.64	1.093
Overtake a slow-moving vehicle on the inside lane or hard shoulder of a motorway	2.55	1.428
Distracted or preoccupied, realize belatedly that the vehicle ahead has slowed, and have to slam on the brakes to avoid a collision	2.46	1.152
'Wake up' to realize that you have no clear recollection of the road along which you have just travelled	2.42	1.243
Have an aversion to a particular class of road user, and indicate your hostility by whatever means you can	2.42	1.361
Deliberately disregard the speed limits late at night or very early in the morning	2.35	1.490
Stay in a lane that you know will be closed ahead until the last minute before forcing your way into the other lane	2.26	1.262
Forget where you left your car in a multi-level car park	2.22	1.342
Intending to drive to destination A, you 'wake up' to find yourself en route to B, where the latter is the more usual journey	2.20	1.198
Pull out of a junction so far that the driver with right of way has to stop and let you out	2.20	1.343
Deliberately drive the wrong way down a deserted one-way street	2.13	1.225
Fail to notice someone stepping out from behind a bus or parked vehicle until it is nearly too late	2.12	1.237
Get involved in unofficial 'races' with other drivers	2.12	1.457
Hit something when reversing that you had not previously seen	2.10	1.146
Intend to switch on the windscreen wipers, but switch on the lights instead, or vice versa	2.08	1.273
Overtake a single line of stationary or slow-moving vehicles, only to discover that they were queueing to get through a one lane gap or roadwork lights	2.07	1.315
Misjudge your crossing interval when turning right and narrowly miss collision	2.05	1.198
In a queue of vehicles turning left on to a main road, pay such close attention to the traffic approaching from the right that you nearly hit the car in front	2.00	1.203
Angered by another driver's behavior, you give chase with the intention of giving him/her a piece of your mind	2.00	1.361
Fail to notice pedestrians crossing when turning into a side street from a main road	1.97	1.069
Misjudge speed of oncoming vehicle when overtaking	1.93	1.183

3.1. DBQ Validation

Confirmatory factor analysis (CFA) was conducted for the four-factor structure presented by Parishad et al. (2020). Since previous studies used the maximum likelihood estimation procedure (Gueho et al., 2014; Stephens and Fitzharris, 2016), the authors conducted a similar approach in the present study. Modification indices, factors load estimation, and standardized residual covariance were used to improve the model fit. Due to the low factor loading (less than 0.4), one of the aggressive behavior items was dropped from the model: "race away from traffic lights with the intention of beating the driver next to you". Besides, the standardized residual covariance suggested eliminating another aggressive behavior item due to a high correlation with the violation questions: "sound your horn to indicate your annoyance to another driver". The modification indices suggested adding error covariance between items V5 and V6, L4, and L5. This can be due to the similarity of the content of these items. After applying these minor changes, the model fit indices showed better results. Model fit outcomes presented in Table 3 in terms of a) absolute fit, using the Root Mean Square Error of Approximation (RMSEA); b) the chi-square test statistic comparative fit, using the Comparative Fit Index (CFI); and c) parsimonious fit, using parsimony normed CFI (PCFI) as were used in previous studies (Deb et al., 2017).

Figure 1 displays the model structure and standard regression weights. The factor loadings (standard regression weight) for all 22 items are statistically significant ($p < 0.0001$). Given the good fit of the model, four composite scores were computed by calculating the mean score of responses for each of the subscales for driver behavior. Besides, the internal reliability of the resulting subscales was tested using Cronbach's alpha (α). The alpha values were found as: Violations (6 items) = 0.823, Errors (6 items) = 0.836, Lapses (6 items) = 0.733, Aggressive violations (4 items) = 0.769. Based on a study by George and Mallery (2003), these values indicated that all the scales had acceptable internal reliability ($0.7 \leq \alpha \leq 0.9$).

Table 3. Model fit indices of the confirmatory factor analysis

Model	χ2	df	χ2/df	Absolute fit RMSEA	Comparative fit CFI	Parsimonious fit PCFI
Model: Violations, Aggressive, Lapses, Errors	385.5	201	1.918	0.056	0.92	0.81

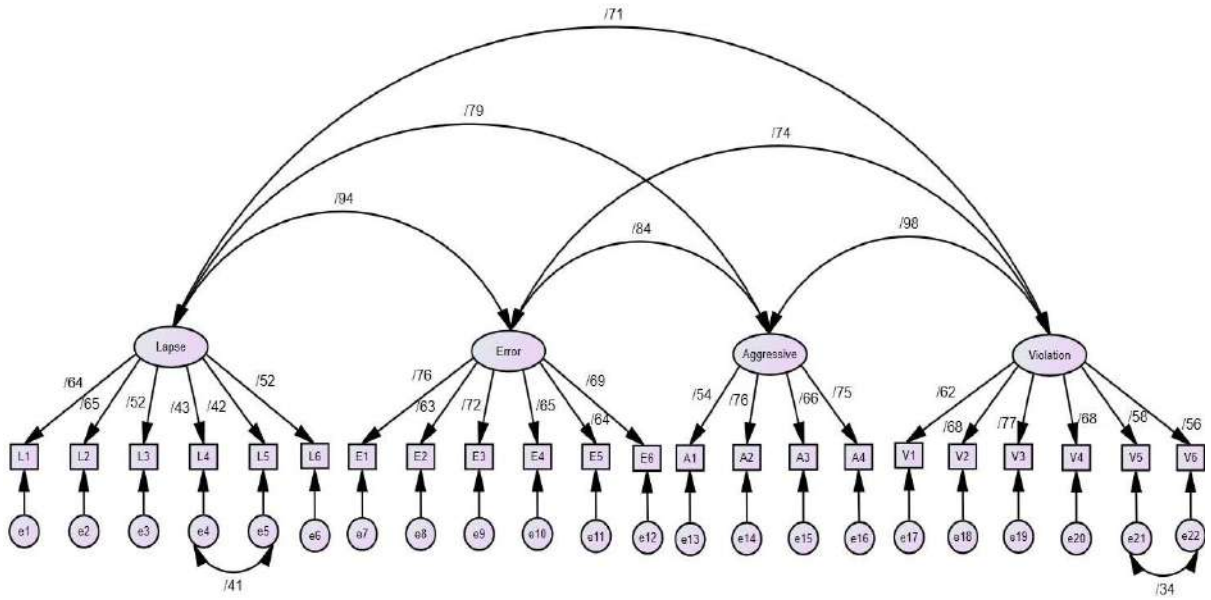

Fig. 1. Standardized solution for the four-factor confirmatory factor model

3.2. Mobile Phone Usage

For updating the DBQ using "mobile phone usage while driving" questions, the association between mobile phone usage items score and various behavioral subscales scores were assessed. After that, a new model containing mobile phone usage items was developed to assess the reliability and validity of the new model including the added items.

3.2.1. Effect of Mobile Phone Usage While Driving on Drivers' Aberrant Behavior

To investigate the relationship of drivers' aberrant behaviors and mobile phone usage questions, bivariate Pearson's correlation was calculated between each of the four subscale scores and the mobile phone usage score. Since mobile phone usage while driving, is a deliberate deviation of laws, it is expected to correlate more with violation questions. As was expected, Table 4 shows that the mean score of two mobile phone usage items is more correlated with violation behaviors. Furthermore, all of the correlations are statistically significant ($p < 0.0001$).

3.2.2 Development of New DBQ Including Mobile Phone Usage Items

Considering mobile phone usage questions as violations, another CFA was conducted. Modification indices suggested adding an error covariance between two mobile phone usage questions due to the similarity of the content of these items. Figure 2 illustrates the model structure and Table 5 exhibits the model fit outcomes. Cronbach's alpha (α) was calculated for new violations (containing mobile phone usage) to test internal reliability ($\alpha = 0.87$). Results show that two added items are valid ($p < 0.0001$). Moreover, adding two mobile phone items in violation subscale increased the reliability of subscale, and improved the model fit indices as well.

Table 4. Bivariate Pearson's correlation results

Driver aberrant behavior	Mobile phone usage
Violation	0.668*
Error	0.407*
Lapse	0.330*
Aggressive	0.527*

*$p < 0.0001$

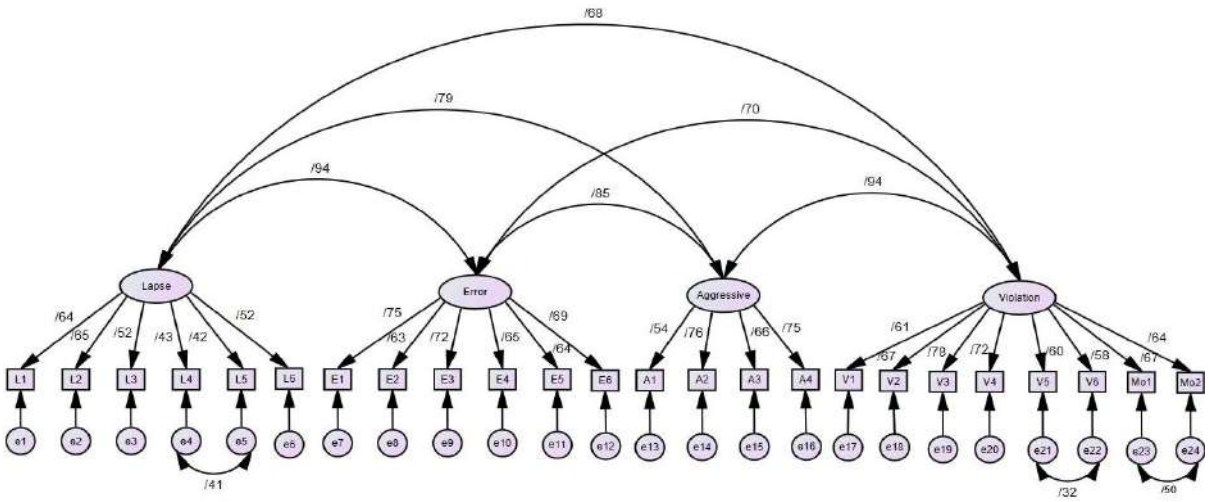

Fig. 2. Standardized solution for the four-factor confirmatory factor model containing mobile phone usage items

Table 5. Model fit indices of confirmatory factor analysis on a shortened version of DBQ containing mobile phone items

Model	χ^2	df	χ^2/df	Absolute fit RMSEA	Comparative fit CFI	Parsimonious fit PCFI
Model: Violations, Aggressive, Lapses, Errors	457	243	1.882	0.054	0.93	0.82

3.3. Effect of Demographic Variables

3.3.1. Analysis of Variance (ANOVA) Test

Analysis of Variance (ANOVA) was conducted to determine the impact of age (3 levels: 18-30, 31-46, and 45+), gender (2 levels: male and female), crash history (2 levels: involved, not involved), and driving time per day (4 levels: less than 1 hour, 1-2 hours, 2-4 hours, more than 4 hours) on each of the four subscale scores.

The ANOVA test revealed a significant influence of age and crash history on all the subscale scores. The results show that there are no statistically significant differences between males and females on violation and lapses scores. However, the mean score of errors and aggressive behaviors are statistically different by gender ($p < 0.05$). Moreover, investigating the impact of driving time on each factor scores shows that prolonged driving does not have a statistically significant impact on lapses score, while long time driving can affect errors and aggressive behaviors ($p < 0.05$). Although driving time has no significant impact on violations scores at a 95% level, it is significant at a 90% level of confidence ($p < 0.1$). Table 6 presents the ANOVA results.

3.3.2. T-Test Analysis

The means and standard deviations of each subscale score for gender, age, crash history, and driving time groups are presented in Table 7. According to Table 7, male drivers have more score in all the subscales than females. However, errors and aggressive behaviors are only statistically significant ($p < 0.05$). It means that male participants have more aggressive behavior and do more errors while driving.

Furthermore, using an independent sample t-test, the mean score of elder drivers (+45) on entire subscales is significantly lower than middle-aged and young drivers ($p < 0.001$). Moreover, the mean score of middle-aged participants is lower than young participants on entire subscales ($p < 0.001$). It means that aging significantly decreases drivers' aberrant behaviors ($p < 0.001$). Table 7 shows that those drivers who were involved in a crash accident in the past three years have significantly higher factor score on entire aberrant behaviors ($p < 0.001$).

Furthermore, the driving time has a direct relationship with all of the factor scores, and driving more per day can lead to more aberrant behavior. However, the independent sample t-test depicted that the mean score of drivers who drive less than one hour per day and drivers who drive more than four hours per day in violations, errors, and aggressive behaviors are only statistically different at a 95% level of confidence.

Table 6. ANOVA results

Demographics	F statistics from ANOVA (p-value)			
	Violations	Errors	Lapses	Aggressive behaviors
Gender	2.18 (0.14)	4.26 (0.04)	1.32 (0.25)	3.693 (0.04)
Age	39.43 (< 0.001)	16.21 (< 0.001)	7.72 (0.001)	17.07 (< 0.001)
Crash history	42.74 (< 0.001)	12.98 (< 0.001)	6.18 (0.013)	33.7 (< 0.001)
Driving time	2.24 (0.065)	2.41 (0.04)	1.7 (0.148)	2.87 (0.023)

Table 7. Means (standard deviation) of all subscale scores

Variables	Subgroup (n)	Mean (Standard deviation)			
		Violations	Errors	Lapses	Aggressive behaviors
Gender	Male (168)	2.57 (1.122)	2.12 (0.909)	2.38 (0.762)	2.32 (1.081)
	Female (130)	2.38 (0.965)	1.91 (0.806)	2.28 (0.842)	2.09 (0.935)
Age	18-30 (127)	3.04 (1.069)	2.34 (0.871)	2.54 (0.777)	2.59 (1.035)
	30-45 (107)	2.15 (0.833)	1.80 (0.793)	2.23 (0.752)	1.98 (0.880)
	45+ (64)	1.94 (0.845)	1.77 (0.803)	2.11 (0.834)	1.86 (0.993)
Crash history	Involved (91)	3.05 (1.016)	2.30 (0.903)	2.51 (0.761)	2.71 (1.129)
	Not involved (207)	2.24 (0.980)	1.91 (0.804)	2.26 (0.804)	2.00 (0.895)
Driving time	Less than 1hr (109)	2.33 (0.987)	1.90 (0.752)	2.24 (0.825)	2.03 (0.881)
	1-2 hr (97)	2.43 (1.042)	2.01 (0.910)	2.33 (0.795)	2.25 (1.049)
	2-4 hr (71)	2.69 (1.152)	2.11 (0.910)	2.39 (0.712)	2.27 (1.087)
	More than 4 hr (21)	2.86 (1.035)	2.51 (0.992)	2.65 (0.903)	2.81 (1.180)

3.3.3. Effect of Mobile Phone Usage

To investigate the impact of mobile phone usage as a demographic variable, the mean score of two mobile phone usage items was calculated. According to Table 8, drivers who were involved in a crash in three past years, use their mobile phones more while driving as compared to the drivers who were not involved in a traffic crash ($p < 0.0001$). Furthermore, there are significant differences between the mean score of mobile phone usage while driving by young (18-30 years), middle-aged (30-45 years), and elder (+ 45 years) drivers. Table 8 shows that mobile phone usage while driving decreases significantly by age ($p < 0.0001$). Besides, males use their mobile phones more while driving than females. However, this is not statistically significant at 95% level of confidence.

4. Discussions

Consistent with previous studies, the most frequent response to the 24 items of DBQ was "quite infrequently" (Reason et al., 1990; Stephens and Fitzharris, 2016). However, in general, the mean responses of Iranian drivers were higher than European countries such as England (Reason et al., 1990), Australia (Stephens and Fitzharris, 2016), France (Gueho et al., 2014) and Turkey (Özkan and Lajunen, 2005). Furthermore, four-factor-solution supports previous studies in Iran (Mehdizadeh et al., 2018). Moreover, the mean response of two mobile phone usage items was “infrequently”. This shows the necessity of investigating mobile phone usage while driving. Table 2 depicted that, the most frequent responses are violations and aggressive behaviors, while the least frequent responses were related to the errors and lapses questions. This means that although Iranian drivers tend to violate the traffic rules and drive aggressively, they are conscious while driving.

The results of confirmatory factor analysis show that, although the shortened version of DBQ is reliable and valid, it could be further shortened due to the error covariance suggested by modification indices. These covariances are suggested to apply between the two lapses items (“'Wake up' to realize that you have no clear recollection of the road along which you have just traveled” and “Forget where you left your car in a multi-level car park”) and two violations items (“Become impatient with a slow driver in the outer lane and overtake on the inside” and “Overtake a slow-moving vehicle on the inside lane or hard shoulder of a motorway”). This can be due to the similarity of the content of these items.

It was observed that aggressive behaviors factor is highly correlated with violations and errors factor is strongly interrelated with lapses. Therefore, two second-order underlying factors may exist. However, additional second-order CFA analysis showed less model fit indices than the first-order four-factor structure model. Therefore, the results of the second-order model were not shown. Moreover, another model structure with the two first-order underlying factors (errors and lapses united in one factor, and violations and aggressive behaviors united in one factor) also showed less model fit indices.

Table 8. The mean (standard deviations) of mobile phone usage items in each demographic subgroup

Variable	Subgroup	Mean score of mobile phone usage
Gender	Male	3.04 (1.602)
	Female	2.83 (1.508)
Age	Young	3.59 (1.559)*
	Middle	2.66 (1.438)*
	Elder	2.17 (1.250)*
Crash history	Involved	3.52 (1.562)*
	Not involved	2.69 (1.499)*

*$p < 0.0001$

The results show that participants who declared to be involved in a crash in three past years use their mobile phones more while driving. It supports previous findings by Mohammadi (2009) that increasing mobile phone usage while driving could increase the risk of being involved in a traffic accident. Furthermore, younger drivers and male drivers use their mobile phones more while driving. These results also support previous findings of Korpinen and Pääkönen (2012) and Arvin et al. (2016).

It should be noted that given the results of the behavioral assessment are based on the drivers' perceptions, there could be a difference between the drivers' perceptions and reality. A study conducted by van Huysduynen et al. (2018) depicted that there is a moderate correlation between self-reported driving style and the driver behavior in the driving simulator. Therefore, updating the DBQ by increasing indicators of errors and violations in a way that be more consistent with daily events can increase the correlation between self-reported driver behaviors and real-life observations.

5. Conclusions

The primary aim of this article was to validate the shortened version of the driver behavior questionnaire that included mobile phone usage. The results of this study confirmed four-factor structure presented by Parsihad et al. (2020). Moreover, four additional aggressive behaviors questions that were developed by Lawton et al. (1997), and not considered in the study by Parishad et al. (2020), were included and assessed in our model. Two of them were added to the final model. The final model consists of four subscales, namely, Violations (6 items), Errors (6 items), Lapses (6 items), and Aggressive behaviors (4 items). The results showed that young drivers, male drivers, drivers who were involved in a traffic crash in the past three years, and drivers who drive more during the day behave more aberrantly.

Furthermore, due to technology advancement, the other goal of this study was to improve and update the DBQ. As a new addition, mobile phone usage while driving was assessed from the behavioral aspect. Bivariate Pearson's' correlation depicts that mobile phone usage while driving is highly correlated to violations subscale as was expected. Placing mobile phone usage items in the violations subscale, a new model was developed, and presented a better model fit indices and subscale reliability. The results showed that mobile phone usage while driving as a deliberate act, which violates the driving laws, could be assessed on the violations subscale and impact on drivers' aberrant behaviors. Moreover, supporting previous studies (Mohammadi, 2009; Korpinen and Pääkönen, 2012; Arvin et al., 2016), the results of this study showed that young drivers, male drivers, and drivers who were involved in a traffic crash in the past three years use their mobile phones more than the others while driving. As vehicle technology evolves with an increase in the level of automation, in the future, the DBQ may need to be modified and adapted to suit the drivers' behaviors in a highly automated vehicle.

6. Limitations and Future Studies

A conducted study by Özkan and Lajunen (2005) developed a new driver behavior scale namely positive behaviors. The positive behaviors focus on "taking care of smooth traffic flow or paying attention to other road users" (Özkan and Lajunen, 2005). Since this study used the 50-items Manchester drivers' aberrant behaviors (Reason et al., 1990), the positive behaviors scale was not assessed in the present study. Therefore, investigating the positive behaviors in future studies is suggested.

Since the impact of mobile phone usage from a behavioral aspect was not addressed in the literature, this study considered the drivers' perceptions on the influence of

mobile phone usage on their driving behavior. It was observed that there is an error covariance between the two mobile phone usage items. It means people do not differentiate between those two mobile phone usage items a lot. Therefore, the author(s) suggest developing other additional items for mobile phone usage in future studies. Furthermore, the effect of other car technology advancements such as radar cruise control, Bluetooth technology, assisted steering, blind-spot monitoring, head-up displays, voice command, the autonomous cars technology, etc. can be investigated in future studies.

7. References

Åberg, L. and Rimmo, P.A. (1998). "Dimensions of aberrant driver behavior", *Ergonomics*, 41(1), 39-56, https://doi.org/10.1080/001401398187314.

Åberg, L. and Warner, H.W. (2008). "Speeding-deliberate violation or involuntary mistake?", *European Review of Applied Psychology*, 58(1), 23-30, https://doi.org/10.1016/j.erap.2005.09.014.

Aghabayk, K., Mashhadizade, L. and Moridpour, S. (2020). "Need safer taxi drivers? Use psychological characteristics to find or train!", *Sustainability*, 12(10), 4206, https://doi.org/10.3390/su12104206.

Al Azri, M., Al Reesi, H., Al-Adawi, S., Al Maniri, A. and Freeman, J. (2017). "Personality of young drivers in Oman: Relationship to risky driving behaviors and crash involvement among Sultan Qaboos University students", *Traffic Injury Prevention*, 18(2), 150-156, https://doi.org/10.1080/15389588.2016.1235269.

Arvin, R., Khademi, M. and Razi-Ardakani, H. (2017). "Study on mobile phone use while driving in a sample of Iranian drivers", *International Journal of Injury Control and Safety Promotion*, 24(2), 256-262, https://doi.org/10.1080/17457300.2016.1175480.

Bener, A., Özkan, T. and Lajunen, T., (2008). "The driver behaviour questionnaire in Arab gulf countries: Qatar and United Arab Emirates", *Accident Analysis and Prevention*, 40(4), 1411-1417, https://doi.org/10.1016/j.aap.2008.03.003.

Besharati, M.M., Kashani, A.T., Li, Z., Washington, S. and Prato, C.G. (2020). "A bivariate random effects spatial model of traffic fatalities and injuries across provinces of Iran", *Accident Analysis and Prevention*, 136, 105394, https://doi.org/10.1016/j.aap.2019.105394.

Deb, S., Strawderman, L., DuBien, J., Smith, B., Carruth, D.W. and Garrison, T.M. (2017). "Evaluating pedestrian behavior at crosswalks: Validation of a pedestrian behavior questionnaire for the US population", *Accident Analysis and Prevention*, 106, 191-201, https://doi.org/10.1016/j.aap.2017.05.020.

Deng, Z., Chu, D., Wu, C., He, Y. and Cui, J. (2019). "Curve safe speed model considering driving style based on driver behaviour questionnaire", *Transportation Research Part F: Traffic Psychology and Behaviour*, 65, 536-547, https://doi.org/10.1016/j.trf.2018.02.007.

Ersan, Ö., Üzümcüoğlu, Y., Azık, D., Fındık, G., Kaçan, B., Solmazer, G., Özkan, T., Lajunen, T., Öz, B., Pashkevich, A., Pashkevich, M., Mylona, V.D., Georgogianni, D., Krasniqi, B.E., Krasniqi, M., Makris, E., Shubenkova, K. and Xheladini, G. (2020). "Cross-cultural differences in driver aggression, aberrant, and positive driver behaviors", *Transportation Research Part F: Traffic Psychology and Behaviour*, 71, 88-97, https://doi.org/10.1016/j.trf.2020.03.020.

Esmaili, A., Aghabayk, K., Parishad, N. and Stephens, A.N. (2021). "Investigating the interaction between pedestrian behaviors and crashes through validation of a pedestrian behavior questionnaire (PBQ)", *Accident Analysis and Prevention*, 153, 106050, https://doi.org/10.1016/j.aap.2021.106050.

Gras, M.E., Sullman, M.J., Cunill, M., Planes, M., Aymerich, M. and Font-Mayolas, S. (2006). "Spanish drivers and their aberrant driving behaviours", *Transportation Research Part F: Traffic Psychology and Behaviour*, 9(2), 129-137, https://doi.org/10.1016/j.trf.2005.09.004.

George, D. and Mallery, P. (2003). *SPSS for Windows step by step: A simple guide and reference*, 11.0 update (4th ed.), Boston: Allyn and Bacon.

Gueho, L., Granie, M.A. and Abric, J.C. (2014). "French validation of a new version of the Driver Behavior Questionnaire (DBQ) for drivers of all ages and level of experiences", *Accident Analysis and Prevention*, 63, 41-48, https://doi.org/10.1016/j.aap.2013.10.024.

Haqverdi, M.Q., Seyedabrishami, S. and Groeger, J.A. (2015). "Identifying psychological and socio-economic factors affecting motorcycle helmet use", *Accident Analysis and Prevention*, 85, 102-110, https://doi.org/10.1016/j.aap.2015.09.007.

Heydari, S., Hickford, A., McIlroy, R., Turner, J. and Bachani, A.M. (2019). "Road safety in low-income countries: state of knowledge and future directions", *Sustainability*, 11(22), 6249, https://doi.org/10.3390/su11226249.

Hill, T., Sullman, M.J.M. and Stephens, A.N.

(2019). “Mobile phone involvement, beliefs, and texting while driving in Ukraine”, *Accident Analysis and Prevention*, 125, 124-131, https://doi.org/10.1016/j.aap.2019.01.035.

Holland, C. and Rathod, V. (2013). “Influence of personal mobile phone ringing and usual intention to answer on driver error”, *Accident Analysis and Prevention*, 50, 793-800, https://doi.org/10.1016/j.aap.2012.07.004.

Koppel, S., Stephens, A.N., Charlton, J.L., Di Stefano, M., Darzins, P., Odell, M. and Marshall, S. (2018). “The Driver Behaviour Questionnaire for older drivers: Do errors, violations and lapses change over time?”, *Accident Analysis and Prevention*, 113, 171-178, https://doi.org/10.1016/j.aap.2018.01.036.

Koppel, S., Stephens, A.N., Bedard, M., Charlton, J.L., Darzins, P., Di Stefano, M., Gagnon, S., Gelinas, I., Hua, P., Macleay, L., Man-Son-Hing, M., Mazer, B., Myers, A., Naglie, G., Odell, M., Potter, M. M., Rapoport, M. J., Stinchcombe, A., Tuokko, H., Vrkjlan, B. and Marshall, S. (2019). “Self-reported violations, errors and lapses for older drivers: measuring the change in frequency of aberrant driving behaviours across five time-points”, *Accident Analysis and Prevention*, 123, 132-139, https://doi.org/10.1016/j.aap.2018.11.009.

IBM. (2016). *IBM SPSS Amos user’s guide*, Version 24.0.0, Armonk, NY: IBM Corp.

IBM. (2017). *IBM SPSS Statistics Base: User’s Guide*, Version 25.0.0, Armonk, NY: IBM Corp.

Isa, K.A.M., Masuri, M.G., Abd Aziz, N.A., Isa, N.N.M., Hazali, N., Tahir, M.P.M., Noor, S.H., Danis, A. and Fansuri, H. (2012). “Mobile phone usage behaviour while driving among educated young adults in the urban university”, *Procedia-Social and Behavioral Sciences*, 36, 414-420, https://doi.org/10.1016/j.sbspro.2012.03.045.

Kontogiannis, T., Kossiavelou, Z. and Marmaras, N. (2002). “Self-reports of aberrant behaviour on the roads: Errors and violations in a sample of Greek drivers”, *Accident Analysis and Prevention*, 34(3), 381-399, https://doi.org/10.1016/S0001-4575(01)00035-5.

Korpinen, L. and Pääkkönen, R. (2012). “Accidents and close call situations connected to the use of mobile phones”, *Accident Analysis and Prevention*, 45, 75-82, https://doi.org/10.1016/j.aap.2011.11.016.

Lajunen, T., Parker, D. and Summala, H. (1999). “Does traffic congestion increase driver aggression?”, *Transportation Research Part F: Traffic Psychology and Behaviour*, 2(4), 225-236, https://doi.org/10.1016/S13698478(00)00003-6.

Lansdown, T.C. and Stephens, A.N. (2013). “Couples, contentious conversations, mobile telephone use and driving”, *Accident Analysis and Prevention*, 50, 416-422, https://doi.org/10.1016/j.aap.2012.05.015.

Lawton, R., Parker, D., Stradling, S.G. and Manstead, A.S. (1997). “Predicting road traffic accidents: The role of social deviance and violations”, *British Journal of Psychology*, 88(2), 249-262, https://doi.org/10.1111/j.20448295.1997.tb02633.x.

Lipovac, K., Đerić, M., Tešić, M., Andrić, Z. and Marić, B. (2017). “Mobile phone use while driving-literary review”, *Transportation Research Part F: Traffic Psychology and Behaviour*, 47, 132-142, https://doi.org/10.1016/j.trf.2017.04.015.

Martinussen, L.M., Lajunen, T., Møller, M. and Özkan, T. (2013). “Short and user-friendly: The development and validation of the Mini-DBQ”, *Accident Analysis and Prevention*, 50, 1259-1265, https://doi.org/10.1016/j.aap.2012.09.030.

Martinussen, L.M., Møller, M., Prato, C.G. and Haustein, S. (2017). “How indicative is a self-reported driving behaviour profile of police registered traffic law offences?”, *Accident Analysis and Prevention*, 99, 1-5, https://doi.org/10.1016/j.aap.2016.10.031.

Mehdizadeh, M., Shariat-Mohaymany, A. and Nordfjaern, T. (2018). “Accident involvement among Iranian lorry drivers: Direct and indirect effects of background variables and aberrant driving behavior”, *Transportation Rresearch Part F: Traffic Psychology and Behaviour*, 58, 39-55, https://doi.org/10.1016/j.trf.2018.05.029.

Mohammadi, G. (2009). “Mobile phone and seat belt usage and its impact on road accident fatalities and injuries in southeast Iran”, *International Journal of Crashworthiness*, 14(4), 309-314, https://doi.org/10.1080/13588260802671423.

Mundfrom, D.J., Shaw, D.G. and Ke, T.L. (2005). “Minimum sample size recommendations for conducting factor analyses”, *International Journal of Testing*, 5(2), 159-168, https://doi.org/10.1207/s15327574ijt0502_4.

Nasri, M. and Aghabayk, K. (2020). “Assessing risk factors associated with urban transit bus involved accident severity: A case study of a Middle East country”, *International Journal of Crashworthiness*, 1-11, https://doi.org/10.1080/13588265.2020.1718465.

Owsley, C., McGwin Jr, G. and McNeal, S.F. (2003). “Impact of impulsiveness, venturesomeness, and empathy on driving by older adults”, *Journal of Safety Research*, 34(4), 353-359, https://doi.org/10.1016/j.jsr.2003.09.013.

Özkan, T. and Lajunen, T. (2005). “A new addition to DBQ: Positive driver behaviours scale”, *Transportation Research Part F: Traffic*

Psychology and Behaviour, 8(4-5), 355-368, https://doi.org/10.1016/j.trf.2005.04.018.

Parishad, N., Aghabayk, K., Rezaie, R., Samerei, A. and Mohammadi, A., (2020). "Validation of the Driver Behavior Questionnaire in a representative sample of Iranian drivers", *Civil Engineering Infrastructures Journal*, 53(1), 161-171, https://doi.org/10.22059/CEIJ.2019.283780.1593.

Parker, D., Reason, J.T., Manstead, A.S. and Stradling, S.G. (1995). "Driving errors, driving violations and accident involvement", *Ergonomics*, 38(5), 1036-1048, https://doi.org/10.1080 /00140139508925170.

Qu, W., Ge, Y., Guo, Y., Sun, X. and Zhang, K. (2020). "The influence of WeChat use on driving behavior in China: A study based on the theory of planned behavior", *Accident Analysis and Prevention*, 144, 105641, https://doi.org/10.1016/j.aap.2020.105641.

Qu, W., Zhang, Q., Zhao, W., Zhang, K. and Ge, Y. (2016). "Validation of the driver stress inventory in China: Relationship with dangerous driving behaviors", *Accident Analysis and Prevention*, 87, 50-58, https://doi.org/10.1016/j.aap.2015.11.019.

Reason, J., Manstead, A., Stradling, S., Baxter, J. and Campbell, K. (1990). "Errors and violations on the roads: A real distinction?", *Ergonomics*, 33(10-11), 1315-1332, https://doi.org/10.1080/00140139008925335.

Rezaei, S., Nafar, H. and Behbahani, H. (2014). "Prioritizing roads safety based on the Quasi-Induced Exposure Method and utilization of the Analytical Hierarchy Process", *Civil Engineering Infrastructures Journal*, 47(1), 43-58, https://doi.org/10.7508/ceij.2014.01.004.

Rowe, R., Roman, G.D., McKenna, F.P., Barker, E. and Poulter, D. (2015). "Measuring errors and violations on the road: A bifactor modeling approach to the Driver Behavior Questionnaire", *Accident Analysis and Prevention*, 74, 118-125, https://doi.org/10.1016/j.aap.2014.10.012.

Stephens, A.N. and Fitzharris, M. (2016). "Validation of the driver behaviour questionnaire in a representative sample of drivers in Australia", *Accident Analysis and Prevention*, 86, 186-198, https://doi.org/10.1016/j.aap.2015.10.030.

Sullman, M.J., Meadows, M.L. and Pajo, K.B. (2002). "Aberrant driving behaviours amongst New Zealand truck drivers", *Transportation Research Part F: Traffic Psychology and Behaviour*, 5(3), 217-232, https://doi.org/10.1016/S1369-8478(02)00019-0.

Sullman, M.J., Stephens, A.N. and Taylor, J.E. (2019). "Dimensions of aberrant driving behaviour and their relation to crash involvement for drivers in New Zealand", *Transportation Research Part F: Traffic Psychology and Behaviour*, 66, 111-121, https://doi.org/10.1016/j.trf.2019.08.024.

Tehran Traffic and Transportation Organization (TTTO). (2018). Office of Transportation Research, In: Annual Statistical Report of Tehran Transportation, Tehran, Iran.

Vajari, M.A., Aghabayk, K., Sadeghian, M. and Shiwakoti, N. (2020). "A multinomial logit model of motorcycle crash severity at Australian intersections", *Journal of Safety Research*, 73, 17-24, https://doi.org/10.1016/j.jsr.2020.02.008.

van Huysduynen, H.H., Terken, J. and Eggen, B. (2018). "The relation between self-reported driving style and driving behaviour, A simulator study", *Transportation Research Part F: Traffic Psychology and Behaviour*, 56, 245-255, https://doi.org/10.1016/j.trf.2018.04.017.

Wang, X. and Xu, X. (2019). "Assessing the relationship between self-reported driving behaviors and driver risk using a naturalistic driving study", *Accident Analysis and Prevention*, 128, 8-16, https://doi.org/10.1016/j.aap.2019.03.009.

Xu, J., Liu, J., Sun, X., Zhang, K., Qu, W. and Ge, Y. (2018). "The relationship between driving skill and driving behavior: Psychometric adaptation of the Driver Skill Inventory in China", *Accident Analysis and Prevention*, 120, 92-100, https://doi.org/10.1016/j.aap.2018.07.032.

Appendix

Shortened Driver Behavior Questionnaire

Lapses (L)

1) Distracted or preoccupied, realize belatedly that the vehicle ahead has slowed, and have to slam on the brakes to avoid a collision.
2) Intend to switch on the windscreen wipers, but switch on the lights instead, or vice versa.
3) Intending to drive to destination A, you 'wake up' to find yourself in route to B, where the latter is the more usual journey.
4) 'Wake up' to realize that you have no clear recollection of the road along which you have just travelled.
5) Forget where you left your car in a multi-level car park.
6) Miss your exit on a motorway and have to make a lengthy detour.

Errors (E)

1) Misjudge your crossing interval when turning right and narrowly miss collision.
2) Hit something when reversing that you had not previously seen.
3) Fail to notice pedestrians crossing when turning into a side street from a main road.
4) In a queue of vehicles turning left on to a main road, pay such close attention to the traffic approaching from the right that you nearly hit the car in front.
5) Fail to notice someone stepping out from behind a bus or parked vehicle until it is nearly too late.
6) Misjudge speed of oncoming vehicle when overtaking.

Violations (V)

1) Deliberately drive the wrong way down a deserted one-way street.
2) Overtake a single line of stationary or slow-moving vehicles, only to discover that they were queueing to get through a one lane gap or roadwork lights.
3) Get involved in unofficial 'races' with other drivers.
4) Deliberately disregard the speed limits late at night or very early in the morning.
5) Become impatient with a slow driver in the outer lane and overtake on the inside.
6) Overtake a slow-moving vehicle on the inside lane or hard shoulder of a motorway.

Aggressive violations (AV)

1) Have an aversion to a particular class of road user, and indicate your hostility by whatever means you can.
2) Angered by another driver's behavior, you give chase with the intention of giving him/her a piece of your mind.
3) stay in a lane that you know will be closed ahead until the last minute before forcing your way into the other lane.
4) Pull out of a junction so far that the driver with right of way has to stop and let you out.
5) sound your horn to indicate your annoyance to another driver.
6) race away from traffic lights with the intention of beating the driver next to you.

Mobile phone usage (MU)

1) Use your mobile phone for calling/texting while driving.
2) Use your mobile phone applications (bank, navigation, games, …) while driving.

Civil Engineering Infrastructures Journal 2023, 56(1): 33-49
DOI: 10.22059/CEIJ.2022.330606.1790

RESEARCH PAPER

A New Damage Detection Approach Under Variable Environmental or Operational Conditions

Jalalifar, F.[1], Esfahani, M.R.[2*] and Shahabian Moghadam, F.[2]

[1] Ph.D. Candidate, Civil Engineering Department, Faculty of Engineering, Ferdowsi University of Mashhad, Mashhad, Iran.
[2] Professor, Civil Engineering Department, Faculty of Engineering, Ferdowsi University of Mashhad, Mashhad, Iran.

Received: 13 Sep. 2021; Revised: 09 Sep. 2022; Accepted: 05 Nov. 2022

ABSTRACT: The basic idea of vibration-based damage identification approaches is that damage causes change in vibration response of structure. So monitoring the vibration response characteristics can be helpful in damage detection. The main limitation in such methods is that these characteristics are also affected by the Environmental and Operational Variability (EOV) that can be incorrectly known as structural damage or sometimes cover actual damages. This paper aims to propose an innovative approach to detect and locate damage considering the EOV conditions. In this regard, an Independent Component Analysis (ICA) based Blind Source Separation (BSS) approach is employed to remove the EOV influences from the time history response of the structure. The beneficial of using the ICA-based BSS method is that there is no need to measure the environmental/operational conditions. Moreover, it is able to remove EOV influences using a limited group of response data monitored during different environmental and operational conditions. Time series analysis is then performed to extract damage-sensitive features. Finally, a statistical tool is employed to damage identification and localization by using EOV independent features. Two recognized benchmark structures are employed for verifying the accuracy of the proposed approach. Results indicate that the proposed method is a time-saving tool and efficiently successful in damage assessment of structures under EOV.

Keywords: Bhattacharyya Measure, Blind Source Separation, Damage Detection, Environmental and Operational Variability, Time Series Analysis.

1. Introduction

Monitoring structural damage plays a critical role in the maintenance of civil structures and has several economic benefits. Several methods such as thermography, optical methods, ultrasonic testing, acoustic emission, and vibration-based methods have been developed to diagnose structural damage (Avci et al., 2021). Among these methods, vibration-based methods are of great importance as they can detect damage remotely by sensors.

Utilizing the statistical pattern recognition techniques in vibration-based

* Corresponding author E-mail: esfahani@um.ac.ir

damage detection methods leads to an effective data-driven methodology which have attracted much attention in Structural Health Monitoring (SHM) applications. These methods consist of using vibration time domain responses, feature extraction by time series analysis, and damage identification through statistical decision making (Entezami, 2021). Roy et al. (2015) employed different time series models to obtain damage-sensitive features using output-only measurements. They used a statistical distance test for damage localization. Datteo et al. (2017) employed the principal component analysis of AutoRegressive (AR) parameters to condition assessment of a stand of the Giuseppe Meazza stadium in Milan during a long-term vibration monitoring. Razavi et al. (2021) proposed a data-driven method for vibration-based damage detection. In the proposed method, feature extraction is based on time series analysis and then damage is localized by two statistical distance measure called Jeffery's and Smith's distances. More applications of statistical pattern recognition techniques to SHM can be found in (Zhang and Song, 2018; Entezami et al., 2019; Daneshvar et al., 2021; Kordi and Mahmoudi, 2022).

The damage detection in vibration-based methods is based on the assumption that damage affects the structural dynamic properties that change the vibration response characteristic (Limongelli et al., 2021). However, the responses measured in these methods are sensitive not only to damage but also to EOV (Vamvoudakis-Stefanou et al., 2018). In SHM literature, the sensitivity of structural responses has been reported to environmental and operational items including temperature, wind, humidity, traffic and water level within the dam (Bayraktar et al., 2014; Comanducci et al., 2016; Nguyen et al., 2017; Hu W-H, 2018; Cunha et al., 2019; Kullaa, 2020). Consequently, before extracting damage sensitive features, the effects of the EOV must be considered. Cross (2012) introduced this issue as the data normalization problem. A literature review presents different approaches proposed for dealing with the EOV effects. Some of these approaches try to model the effect of EOV on monitoring parameters or damage sensitive features (Spiridonakos et al., 2016; Cai et al., 2021; Shan et al., 2018). Therefore, the prediction error is a robust indicator of a structural condition that is insensitive to EOV. The simplest approach to model the effects of EOV on damage-sensitive features contains the linear regression model (Cross et al., 2013; Dervilis et al., 2015). Several approaches containing neural networks and support vector machines can be found in the literature dealing with the modeling the effect of EOV (Zhang et al., 2018). The primary restriction of such approaches is due to a set of changing conditions that must be identified and accurately measured. Nevertheless, these approaches may not be a good choice when several environmental or operational items are considered.

Several alternative strategies have been investigated when it is not feasible to measure the environmental/operational conditions. The most popular of these strategies rely on using a group of response data monitored during a long enough time period to span all the possible normal conditions. Handling a huge amount of data is the main limitation of this strategy. Furthermore, having a large database from normal conditions may reduce features sensitivity to damage (Cross, 2012).

Considering the above-mentioned practical difficulties, this paper aims to employ a Blind Source Separation technique (BSS) to suggest a new approach for data normalization. BSS technique has been accepted as an effective solution for analysis of traffic-induced vibrations (Chen et al., 2015), modal identification (Yu, 2019; Sadhu et al., 2017), and condition monitoring (Guo and Kareem, 2016). Sadhu and Hazra (2013) proposed a new damage detection method including BSS technique and time-series analysis. In this algorithm, the modal response is estimated from the

vibration measurements utilizing the BSS technique and then one-step-ahead prediction of the modal response is performed by means of time-series analysis. Rainieri et al. (2019) employed the Second-Order Blind Identification (SOBI) to model the variability of natural frequency estimates under EOV. In this paper, an ICA-based BSS method is employed to remove the EOV influences from the time history response of the structure.

In the damage assessment approach proposed in this paper, a BSS approach is employed to remove the effects of the EOV on the time history response of the structure in the presence of unmeasured EOV. Then, time series analysis is applied to extract damage sensitive feature from the EOV independent response of the structure. Finally, a statistical tool called Bhattacharyya measure is introduced for damage identification and localization.

This paper includes different sections as follows: Section 2 indicates the novelty and importance of the present work. Section 3 describes the mathematical foundations of techniques used in the proposed approach. Section 4 presents the steps of the proposed damage assessment approach. In Section 5, the proposed method is applied to data acquired from two benchmark structures. A comparative study also is conducted to demonstrate the capability of the proposed approach. Finally, Section 6 provides the conclusion.

2. Research Significance

This paper proposes a statistical pattern recognition approach to detect and locate damage in structures considering the EOV conditions. The effect of EOV on the system's vibration signal is a challenging issue in application of vibration-based damage detection methods. This paper employs an ICA-based BSS method to suggest a new approach to remove the EOV influences from the time history response of the structure. This approach is able to remove EOV influences using a limited group of response data monitored during different environmental and operational conditions. It is worth to mention that in the proposed method, the measurement of environmental or operational items is unnecessary.

In the proposed damage detection method, a time series analysis is applied to extract damage sensitive feature from the EOV independent response of the structure. In this method, in contrary with model based methods, there is no need to analytical or physical modeling of the structure and only use time-domain data.

Finally, a novel statistical method named as Bhattacharyya measure is introduced to measure the degree of similarity between damage sensitive features obtained in different conditions of structure for damage detection.

In calculating the Bhattacharyya measure, feature vector is divided into several subdivisions and the numerical information of them, like the number of total subdivisions and the number of samples within each subdivision, are used. In the other word, the features is not directly involved in the Bhattacharyya measure calculation. Therefore, it can be able to be regarded as a solution for the issue of large data or high-dimensional features.

3. Theoretical Background

The algorithm developed in this paper employs the BSS method to eliminate the effects of EOV from the structural responses. After that, time series analysis is employed to extract damage sensitive features. Finally, Bhattacharyya measure is used for damage detection and localization. Theoretical background of BSS method, time series analysis and Bhattacharyya measure are included herein.

3.1. Blind Source Separation (BSS)

The objective of BSS technique is to retrieve the unobserved source signals from the mixture observations carried out by an array of sensors. In this paper, the sources

refer to the responses of the structure to unmeasured environmental and operational conditions that cause the responses of the structure in a certain state be uncertain. Figure 1 shows a BSS problem.

$$\begin{bmatrix} s_1 \\ \vdots \\ s_n \end{bmatrix} = s \rightarrow A \overset{x}{\rightarrow} U \rightarrow y = \begin{bmatrix} y_1 \\ \vdots \\ y_n \end{bmatrix} = \hat{s}$$

Fig. 1. Mixing and separating; Unknown sources: *s*, Observations: *x*, Estimated sources: *ŝ*, Mixing matrix: *A*, Demixing matrix: *U* (Jain and Rai, 2012)

The BSS model considers the N source signals and the M observations as $s(t) = (s_1(t), \dots, s_N(t))^T$ and $x(t) = (x_1(t), \dots, x_M(t))^T$ respectively. Now, the BSS model can be expressed as,

$$\begin{aligned} x(t) &= As(t) \\ \hat{S}(t) &= Ux(t) \end{aligned} \quad (1)$$

BSS methods' purpose is to find the demixing matrix *U* and the sources *ŝ(t)* based on observations of the *x(t)* alone. A literature review reveals several BSS approaches. In this paper, Independent Component Analysis (ICA) is applied to remove the EOV effect.

3.1.1. Independent Component Analysis (ICA)

Independent Component Analysis is greatly utilized in various fields such as blind separation of mixed voices or images, biomedical signal processing, data communication and several others. Recently ICA is extended for damage detection and condition monitoring (Jiang et al., 2019; Wang et al., 2020). There are different ICA algorithms in the literature (for example Joint Approximate Diagonalization of Eigenmatrices (JADE) and Natural Gradient algorithms). The proposed approach in this paper utilizes the JADE algorithm.

Cardoso and Souloumica (1993) proposed the JADE as an algorithm for ICA by a joint approximate diagonalization of eigenmatrices. The approach combines second and fourth order statistics to perform BSS of the mixtures. Due to space limitation, fundamental steps of JADE algorithm are indicated. The reader can refer to Cardoso (1999) for further detail.

Referring to Eq. (1), *X*: is a set of observations and *A*: is an unknown mixing matrix. The goal is then to estimate a demixing matrix, $U = A^{-1}$. Supposing that the sources are independent, four fundamental steps are needed to obtain the demixing matrix.

1. Estimating a whitening matrix *W* and calculating the whitened matrix Z which $Z = WX$.
2. Estimating the cumulant matrices $\{Q_i^Z\}$.
3. Estimating the matrix *V* using joint approximate diagonalization (JAD) algorithm as

$$V = argmin \sum\nolimits_i 0ff\left(V^T Q_i^2 V\right) \quad (2)$$

4. Estimating the demixing matrix $[U]$ and the sources $\{s(t)\}$which

$$\begin{aligned} [U] &= [V]^T[W] \\ \{s(t)\} &= [U]\{x(t)\} \end{aligned} \quad (3)$$

3.2. Time Series Analysis

Time series analysis is a statistical way trying to fit a mathematical model over time-series observations in order to determine specific statistics. There are several model for analyzing the time series data. Entezami and Shariatmadar (2019) suggested that when the measured response of the structure is resulting from the ambient excitations, it should be better to model the structural response by applying time series models that contain a polynomial equation into the error term. In this regard, the ARMA and ARARX models can be efficiently employed for modeling the time history measurements under the ambient excitations. If time series signal is an AR process in nature, the ARARX model is a better choice (Ljung, 1999). To determine the nature of time series data, the Box-Jenkins methodology

can be used efficiently (Box et al., 2015). In the benchmark structures considered in this paper, the ARARX model is used.

Suppose that *x(t)* is a stationary and linear time series, then AR(*p*) model is indicated as:

$$x(t) = \sum_{j=1}^{p} \varphi_{xj} x(t-j) + e_x(t) \quad (4)$$

in which $e_x(t)$: is the random error, φ_{xj}: denotes the AR coefficients, and *p*: is the order of the model. Structurally, the ARX model and the AR model are identical. The difference is that the ARX model contain a regression term for an external input *e(t)*. In the employment of an ARARX model, the residuals of the AR model are applied as the external input in the ARX model.

$$x(t) = \sum_{i=1}^{a} \alpha_i x(t-i) + \sum_{j=1}^{b} \beta_j e_x(t-j) + \varepsilon_x(t) \quad (5)$$

where α_i and β_j: are the ARX coefficients, $\varepsilon_x(t)$: is the ARX random error, and *a* and *b*: are the order of the model.

In application, damage sensitive feature might be selected from particular characteristics of the residuals achieved by fitting a model from reference condition *x(t)* to *y(t)* measured from an unknown condition.

$$y(t) = \sum_{j=1}^{p} \phi_{yj} y(t-j) + e_y(t) \quad (6)$$

$$\varepsilon_y(t) = y(t) - \sum_{i=1}^{a} \alpha_i y(t-i) + \sum_{j=1}^{b} \beta_j e_y(t-j) \quad (7)$$

3.3. Bhattacharyya Measure

Bhattacharyya measure reflects the degree of similarity between any two statistical samples. Suppose that *p(i)* and *p'(i)* are two samples, including N partitions with respective probabilities *p(i = 1), . . . , p(i = N)* and *p'(i = 1), . . . , p'(i = N)*. The Bhattacharyya measure is defined as:

$$\rho(p, p') = \sum_{i=1}^{N} \sqrt{p(i)p'(i)} \quad (8)$$

From the geometric view, the Bhattacharyya measure is the cosine of the angle between the vectors $\left(\sqrt{p(i)} \ldots\ldots \sqrt{p(N)}\right)^T$ and $\left(\sqrt{p'(i)} \ldots\ldots \sqrt{p'(N)}\right)^T$. To obtain Bhattacharyya measure between two damage-sensitive feature vectors, each vector should be divided into N partitions, after determining the probability of each partition, the Bhattacharyya measure is calculated according to Eq. (8).

4. Proposed Method

Suppose that there is a significant amount of variability in the measured data from an undamaged structure due to EOV. The proposed method takes advantage of the JADE algorithm to filter the confounding effects of EOV. The JADE algorithm makes the measured data independent of one another and obtains the sources. Therefore, if in a time period, the data from the undamaged structure subject to EOV conditions are recorded, one can acquire the independent sources. Discarding the sources that account for significant amounts of variability in the data, the confounding effects of EOV are filtered.

A critical aspect of the application of the JADE algorithm is the determination of the number of sources (*m*). Like the PCA, a smaller number of measured data are responsible for the total variability in data. This happens when some of the eigenvalues of the covariance matrix become equal to zero. In practical applications, owing to the noise and numerical precision issues, the eigenvalues do not become exactly equal to zero. Instead, the number of sources, which

account for most of the variabilities, can be determined when a clear drop in the eigenvalues is observed. Here, the following indicator is used to determine *m*:

$$I = \frac{\sum_{i=1}^{m} \sigma_i^2}{\sum_{i=1}^{n} \sigma_i^2} \quad (9)$$

The steps of the proposed damage assessment framework are as follows. First, the JADE algorithm is applied into a set of acceleration time history measurements from an undamaged state (or reference state) measured in different environmental and operational conditions, and the sources are obtained. Concerning *m* in Eq. (9), the number of sources is determined as *m*+1. The last source is selected as an independent source from EOV effects. Then, the independent source is modeled using an appropriate time series model as presented in Subsection 2.2 and the residuals are calculated. With the arrival of acceleration time history measurements from the current state, the independent source is also obtained using the JADE algorithm. After that, the time series model applied in the reference state is used to model the independent source from the current state and the residuals are calculated. Finally, the Bhattacharyya measure is determined between the residuals from reference and current states and considered as a damage index. The flowchart of the suggested approach is showed in Figure 2.

5. Application

To support the proposed method and to demonstrate the usefulness of the JADE algorithm for compensating the influences of EOV, two well-known benchmark models in the SHM community are investigated. The first is a simulated beam structure under changing environmental and operational conditions. The second is a laboratory wooden bridge with actual environmental variability.

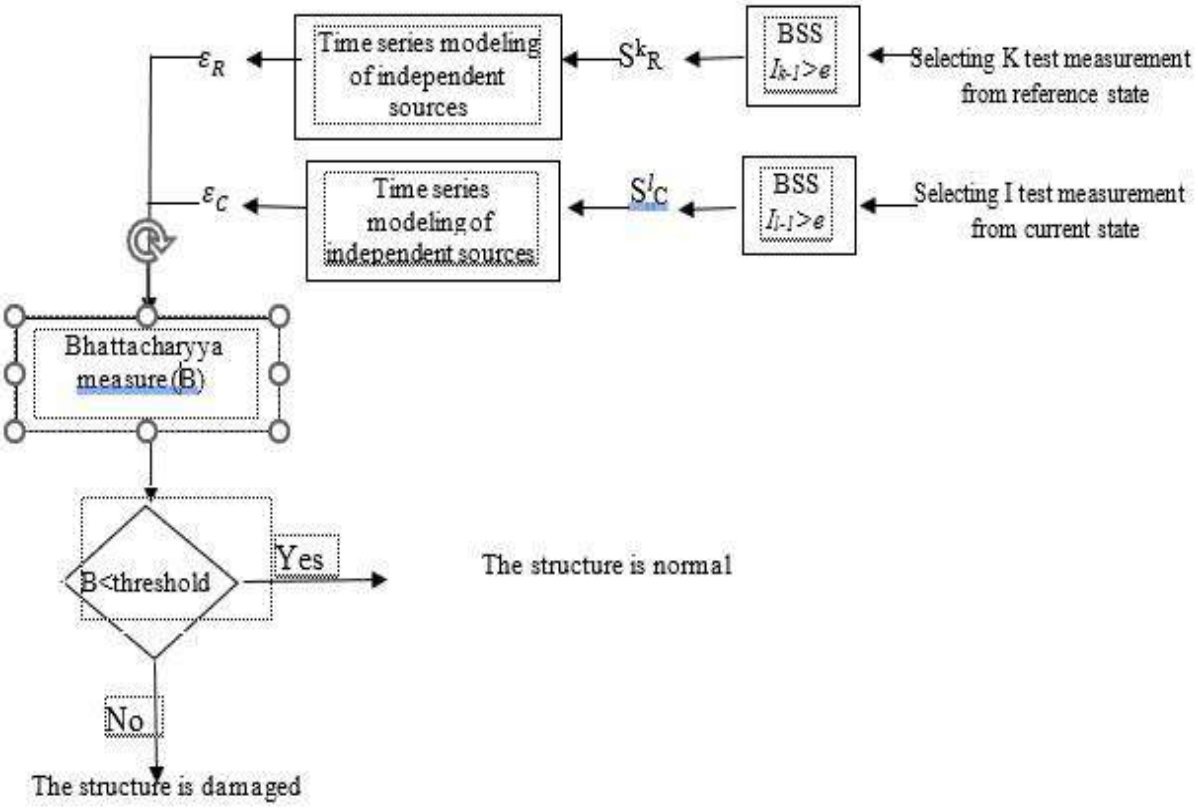

Fig. 2. Flowchart of the proposed method

5.1. Beam Structure with Environmental and Operational Changes

The considered structure is a simply-supported steel beam simulated by Kullaa (2014) and is showed in Figure 3. The length and cross-section of the beam is 1.4 m and 50 × 5 mm, respectively. According to Figure 3, the structure contains a spring in 612.5 mm from the support with spring constant k as:

$$k = k_0 + aT^3 \quad (10)$$

where k_0 = 100 kN/m, a = –0.8 (with compatible units), and T: is temperature with a uniform random distribution between -20 and +40 °C.

The beam consists of three equal length parts. The Young's modulus of each part E_i is:

$$E_i = E_0 + \sigma_i z_i, \qquad i = 1,2,3 \quad (11)$$

where E_0 = 207 GPa and z_i: is the environmental variable with standardized Gaussian distribution and the standard deviations (σ_i) of different parts are 5, 3 and 7 GPa, respectively.

Damage is simulated by the beam depth reduction on a length of 19.4 mm at the spring support. Sensor 21 is at the center of the damaged zone. The beam depth reduction differs in five levels: 0.5, 1, 1.5, 2, and 2.5 mm.

The proposed method is applied to the acceleration measurements of the beam structure. First, 10 measurements from the undamaged beam as a reference data set (R), 10 measurements from the undamaged beam as a health data set (H), and 10 measurements from each five damaged state as damaged data sets (D1, D2, D3, D4, and D5) are selected. Then, the sources are obtained from each dataset using the JADE algorithm. The 10th source is chosen as an independent source in each state. Based on Section 2.2, the ARARX model is selected for time series modeling. Finally, the Bhattacharyya measure is calculated between residuals of the reference state and those of each state. The mentioned steps are repeated for each Degree Of Freedom (DOF).

To determine the threshold value, after estimating the Bhattacharyya measure of health state in each DOF, the mean and standard deviation of them are obtained. Supposing normal distribution for Bhattacharyya measure, the threshold is set at the point under which 1% values occur. Here, the threshold value is 0.8059. The damage index beyond the threshold value means the structure is healthy and under that indicates a damaged state.

Figure 4 illustrates the Bhattacharyya measure in different structural states. As the number of DOF is too large, only odd DOFs are shown. As can be seen from Figure 4, the damage index in healthy states is beyond the threshold value in all DOFs. About the damaged states in DOF 11 to 29, the damage indices are under the threshold value except for a few errors. In few initial and final DOF, the damaged states D1 and D2 are not recognized due to be far from the damage location. In DOF 21, the Bhattacharyya measure in damaged states is lower than that of other DOFs showing damage location. In point of damage severity, the damage index decreased while damage severity increased as denoted in Figure 4. However, there are a few errors that it will be discussed later.

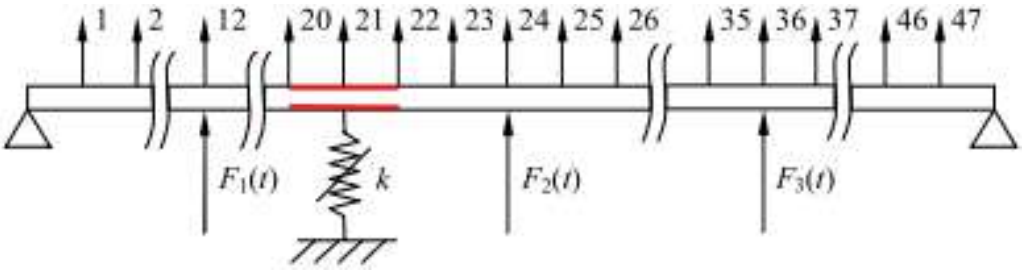

Fig. 3. Simply-supported beam (Kullaa, 2014)

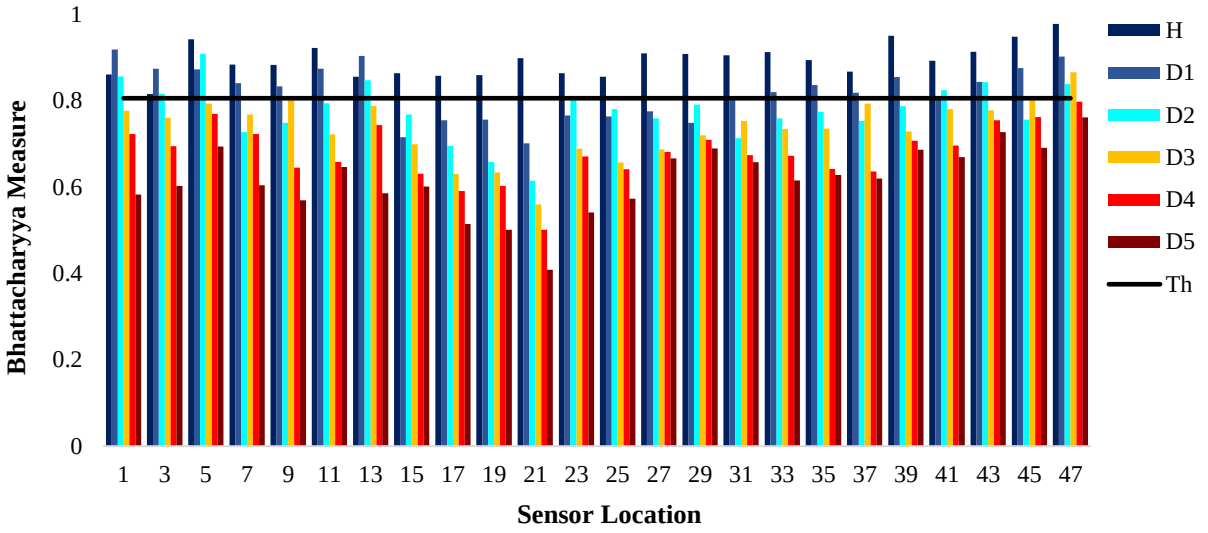

Fig. 4. The Bhattacharyya measure of odd DOFs of beam structure in different structural states

Investigating the cause of errors in Figure 4, the values of the indicator I in Eq. (9) are considered for m = 9. These values in each DOF and different damage states are shown in Table 1. As it is clear in all error cases, the indicator I is less than 0.97. This reveals that in such cases, the EOV effects have not been effectively eliminated and the obtained sources are not independent of EOV. So, in these cases, more data measurements are needed in a relevant data set. In Figure 5, the cases that $I < 0.97$ are deleted. In each DOF, as the damage severity increases, the damage index decreases.

It is notable to mention that the proposed method is able to identify the damage location even in the small damage scenarios like the states D1 and D2.

Table 1. The value of indicator I in Eq. (9) when m = 9

DOF	Structural state						
	R	H	D1	D2	D3	D4	D5
1	0.989	0.995	0.964	0.979	0.972	0.990	0.988
3	0.989	0.995	0.963	0.978	0.972	0.990	0.989
5	0.991	0.995	0.960	0.975	0.973	0.990	0.990
7	0.993	0.996	0.975	0.955	0.978	0.992	0.994
9	0.992	0.994	0.976	0.961	0.979	0.991	0.993
11	0.990	0.997	0.974	0.992	0.977	0.996	0.992
13	0.991	0.996	0.966	0.983	0.975	0.993	0.992
15	0.994	0.996	0.957	0.973	0.977	0.991	0.994
17	0.992	0.993	0.975	0.974	0.975	0.990	0.992
19	0.991	0.994	0.974	0.974	0.970	0.988	0.987
21	0.992	0.993	0.977	0.971	0.972	0.987	0.991
23	0.994	0.992	0.980	0.965	0.970	0.980	0.991
25	0.995	0.992	0.984	0.968	0.971	0.979	0.991
27	0.992	0.992	0.978	0.972	0.972	0.984	0.987
29	0.989	0.993	0.975	0.961	0.970	0.987	0.984
31	0.991	0.992	0.982	0.957	0.971	0.985	0.985
33	0.991	0.992	0.981	0.980	0.972	0.986	0.986
35	0.990	0.993	0.973	0.973	0.971	0.989	0.985
37	0.988	0.993	0.973	0.972	0.969	0.990	0.983
39	0.991	0.990	0.986	0.981	0.971	0.974	0.984
41	0.993	0.991	0.985	0.962	0.971	0.981	0.990
43	0.992	0.993	0.975	0.970	0.973	0.985	0.988
45	0.991	0.994	0.970	0.964	0.970	0.987	0.992
47	0.991	0.994	0.975	0.966	0.970	0.988	0.985

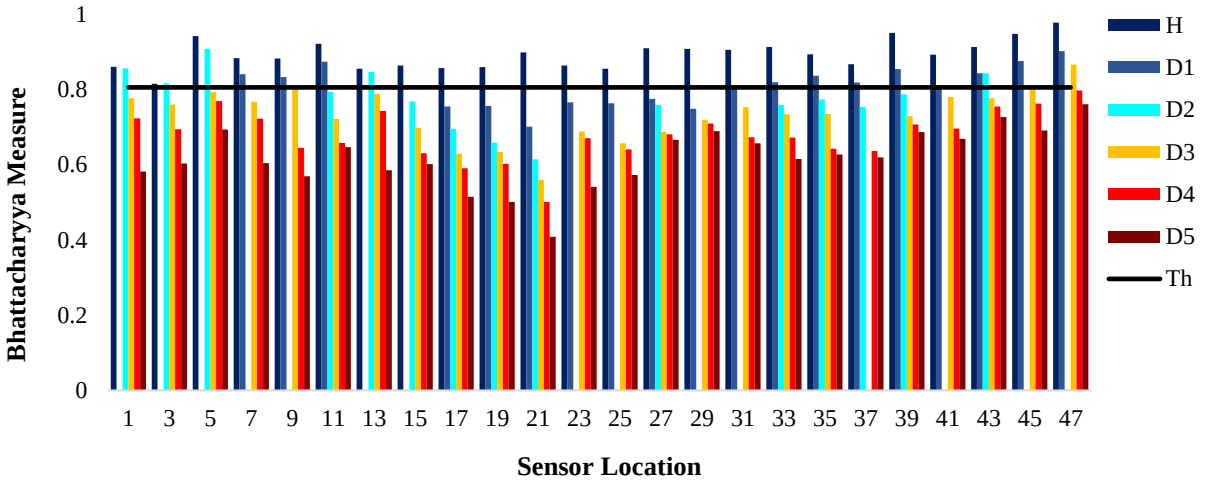

Fig. 5. The modified Bhattacharyya measure of beam structure in different structural states

To demonstrate the capabilities of the suggested approach, it is compared with the damage detection method suggested by Sohn and Farrer (2001). In Sohn and Farrer's method, an AR(*p*) model is applied to all measurements from a reference database. After estimating AR coefficients of the measurement *y(t)* from unidentified state, the reference dataset *x(t)* whose AR coefficients approximate those of *y(t)*, is chosen. Next, the chosen *x(t)* is modeled by an ARX (α,β). So, $\varepsilon_x(t)$ and $\varepsilon_y(t)$, the ARX residual of *x(t)* and *y(t)*, are estimated. Finally, the ratio $\sigma(\varepsilon_y)/\sigma(\varepsilon_x)$ is determined being the damage-sensitive feature, while $\sigma(\ )$ is the standard deviation. The increase in this ratio is monitored to detect damage and is anticipated to reach its peak value near the damage location. Furthermore, a hypothesis test is applied to examine if the new measurement *y(t)* and the baseline measurement *x(t)* are considerably different. A more detailed discussion of this method can be found in Sohn and Farrer (2001). To employ the indicated method, 40 measurements from the health state of the beam structure measured under EOV are chosen as the reference database. Next, from each structural state, 10 datasets are picked as test datasets. Table 2 presents the $\sigma(\varepsilon_y)/\sigma(\varepsilon_x)$ ratio for odd DOFs and all structural states. The values presented are the mean values of 10 sample standard deviation ratios for each structural state. Regarding Table 2 in damaged states, the highest increase in $\sigma(\varepsilon_y)/\sigma(\varepsilon_x)$ ratio is at DOF 21 (damage location). Moreover, as damage severity increases, the standard deviation ratio also increases as well.

The results of hypothesis tests are outlined in Table 3. The values in Table 3 show among all hypothesis tests how many null hypothesis are rejected. For example, 2/10 means that from 10 hypothesis test applied on data sets, the rejection number is 2. Normally, in the health condition the rejection numbers are low, though in damaged condition many rejections are reported. Besides, maximum value of the rejections shows the damage location.

Results show that Sohn and Farrer's method has been able to effectively determine structural state and damage location. Meanwhile, the reference database in this method contains 40 test measurements and in the proposed method there are only 10 test measurements. Besides, the analysis time by MATLAB in the Sohn and Farrer's method is 2328 s while it is 196 s in the proposed method. Once again, the beam structure is analyzed using Sohn and Farrer's method. This time the number of test measurements in the reference database is 10. In this case, the analysis time is 1663 s. Table 4 demonstrates the hypothesis test results in a healthy structure. Table 4, reveals that having a reference database with 10 test measurements, the Sohn and Farrer's

method is not successful in damage detection. As a conclusion from these analyses, it can be stated that the proposed method compared with Sohn and Farrer's method can present good results using fewer measurements from the reference state of the structure in a shorter analysis time.

5.2. Wooden Bridge with Actual Environmental Variability

The second considered structure is a wooden bridge under real environmental variability presented by Kulla (2011). Figure 6 shows the laboratory setup. The acceleration is measured by 15 sensors at three different longitudinal positions with a 256 Hz sampling frequency. The measurement is accomplished under temperature and humidity variations during several days. Damage is simulated by attaching point masses on the top flange close to sensor 4 (Figure 6). The weight of the masses varies in five sizes: 23.5, 47.0, 70.5, 123.2, and 193.7 g. With regard to the total weight of the structure (36 kg), the attaching point masses are very small.

Table 2. The mean value of $\sigma(\varepsilon_y)/\sigma(\varepsilon_x)$ in different structural states

Structural state	DOF 1	3	5	7	9	11	13	15	17	19	21	23
H	1.016	1.018	1.010	1.010	1.073	1.002	1.029	1.015	1.010	1.022	1.035	1.016
D1	1.015	1.022	1.016	1.019	1.028	1.016	1.019	1.427	1.353	1.895	2.088	1.782
D2	1.018	1.024	1.018	1.019	1.024	1.290	1.480	1.453	1.460	2.076	2.565	1.981
D3	1.020	1.018	1.024	1.306	1.264	1.427	1.667	1.800	2.228	2.588	3.259	2.733
D4	1.368	1.212	1.456	1.396	1.602	1.647	1.686	1.881	2.584	2.925	3.513	2.840
D5	1.397	1.351	1.414	1.431	1.653	1.621	1.792	2.420	3.138	3.735	4.349	3.414

Structural state	DOF 25	27	29	31	33	35	37	39	41	43	45	47
H	1.027	1.018	1.012	1.004	1.017	1.015	1.025	1.001	1.016	1.016	1.012	1.015
D1	1.704	1.508	1.550	1.334	1.029	1.020	1.025	1.017	1.019	1.015	1.016	1.030
D2	1.792	1.610	1.595	1.450	1.246	1.026	1.024	1.015	1.021	1.016	1.020	1.025
D3	2.045	1.695	1.653	1.501	1.321	1.398	1.353	1.214	1.022	1.020	1.025	1.015
D4	2.331	1.830	1.717	1.576	1.555	1.598	1.563	1.257	1.199	1.266	1.158	1.291
D5	2.930	2.256	2.173	2.055	1.930	1.958	1.893	1.475	1.498	1.469	1.546	1.400

Table 3. The result of hypothesis tests in different structural states

Structural state	DOF 1	3	5	7	9	11	13	15	17	19	21	23
H	0/10	1/10	0/10	0/10	1/10	0/10	0/10	0/10	0/10	0/10	0/10	0/10
D1	0/10	1/10	0/10	1/10	0/10	0/10	1/10	6/10	6/10	10/10	10/10	10/10
D2	1/10	2/10	1/10	1/10	1/10	4/10	7/10	6/10	7/10	10/10	10/10	10/10
D3	0/10	0/10	2/10	5/10	5/10	6/10	9/10	9/10	10/10	10/10	10/10	10/10
D4	6/10	3/10	7/10	6/10	8/10	8/10	9/10	10/10	10/10	10/10	10/10	10/10
D5	6/10	6/10	6/10	6/10	8/10	8/10	10/10	10/10	10/10	10/10	10/10	10/10

Structural state	DOF 25	27	29	31	33	35	37	39	41	43	45	47
H	1/10	0/10	0/10	0/10	0/10	0/10	1/10	0/10	0/10	0/10	0/10	0/10
D1	9/10	7/10	7/10	6/10	1/10	0/10	1/10	0/10	0/10	0/10	0/10	1/10
D2	10/10	8/10	8/10	7/10	5/10	1/10	1/10	0/10	1/10	0/10	1/10	1/10
D3	10/10	9/10	9/10	7/10	5/10	6/10	5/10	4/10	1/10	1/10	2/10	1/10
D4	10/10	10/10	10/10	7/10	7/10	7/10	7/10	5/10	4/10	5/10	3/10	4/10
D5	10/10	10/10	10/10	10/10	10/10	10/10	10/10	7/10	7/10	7/10	7/10	6/10

Table 4. The result of hypothesis tests in heath state with 10 measurements in the reference database

DOF	1	3	5	7	9	11	13	15	17	19	21	23
H	8/10	7/10	6/10	8/10	7/10	8/10	9/10	8/10	6/10	8/10	8/10	7/10
DOF	25	27	29	31	33	35	37	39	41	43	45	47
H	6/10	7/10	8/10	8/10	8/10	7/10	8/10	9/10	7/10	8/10	8/10	9/10

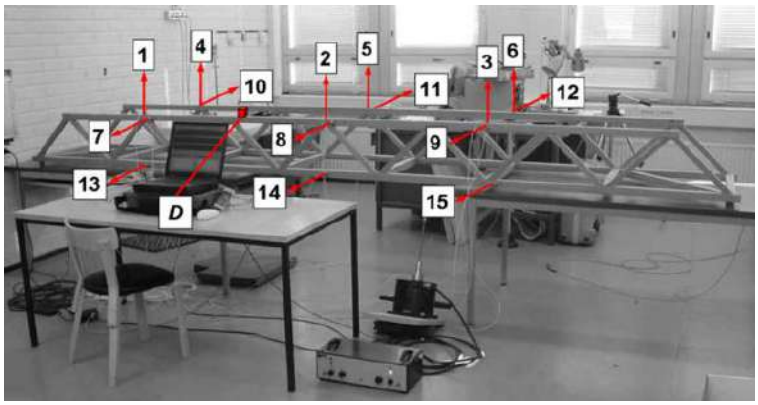

Fig. 6. Wooden bridge with the location of sensors and damage (*D*) (Kulla, 2011)

To apply the proposed method, 20 test measurements from the healthy state are accounted for a reference dataset (training phase) and 20 test measurements from each state (healthy state and 5 damage states) are considered as the current structural state (i.e., H, D1-D5). To determine the number of sources, the *I* indicator according to Eq. (9) is considered for $m = 1, 2, \ldots, 20$. These values for each structural state in DOF 1 are shown in Table 5. Regarding *I* values, the numbers of sources are chosen as 19, 20, 20, 18, 20, 19, and 14 for R, H, D1, D2, D3, D4, and D5 states, respectively. In each state, the last source is considered an independent source. Choosing fewer sources makes the last source not independent enough and the more sources lead to the disappearance of some structural information. For example, if 19 sources in D2 is chosen and the 19th source is considered as an independent source, this source cannot express the behavior of the structure. Figure 7 demonstrates the last source in DOF 1 when the number of sources is 18 and 19.

The AutoCorrelation Function (ACF) and Partial AutoCorrelation Function (PACF) are considered in order to determine a proper time series model. As an example, the ACF and PACF plot of the independent source in DOF 1 is shown in Figures 8 and 9. It can be seen that in Figure 8, the ACF approaches zero as time goes to infinity by damped wave sine and Figure 9 shows cut off at PACF.

So, according to Box-Jenkins approach, the nature of this time series is an AR process and thus, according to what is explained in Section 2.2, the ARARX model is selected.

Table 5. The *I* indicator in DOF 1 for each structural states of wooden bridge

M Values	Structural states						
	R	**H**	**D1**	**D2**	**D3**	**D4**	**D5**
1	0.1173	0.0850	0.1032	0.1512	0.1021	0.1026	0.1483
2	0.1976	0.1648	0.1777	0.2353	0.1746	0.1772	0.2618
3	0.2746	0.2361	0.2447	0.3032	0.2463	0.2494	0.3691
4	0.3430	0.3065	0.3075	0.3692	0.3112	0.3100	0.4727
5	0.4095	0.3733	0.3687	0.4329	0.3725	0.3703	0.5658
6	0.4751	0.4381	0.4269	0.4927	0.4316	0.4263	0.6554
7	0.5393	0.4988	0.4816	0.5485	0.4876	0.4813	0.7242
8	0.6000	0.5580	0.5350	0.6024	0.5426	0.5339	0.7762
9	0.6553	0.6132	0.5878	0.6532	0.5945	0.5852	0.8258
10	0.7063	0.6664	0.6379	0.7014	0.6454	0.6349	0.8726
11	0.7539	0.7158	0.6852	0.7469	0.6935	0.6839	0.9187
12	0.7907	0.7626	0.7306	0.7900	0.7402	0.7315	0.9623
13	0.8269	0.8037	0.7747	0.8309	0.7846	0.7782	0.9999
14	0.8604	0.8384	0.8174	0.8703	0.8248	0.8223	1.0000
15	0.8924	0.8722	0.8587	0.9068	0.8630	0.8648	1.0000
16	0.9232	0.9043	0.8982	0.9409	0.8995	0.9050	1.0000
17	0.9532	0.9324	0.9336	0.9745	0.9341	0.9399	1.0000
18	0.9802	0.9588	0.9679	1.0000	0.9676	0.9711	1.0000
19	1.0000	0.9833	0.9999	1.0000	0.9999	0.9999	1.0000
20	1.0000	1.0000	1.0000	1.0000	1.0000	1.0000	1.0000

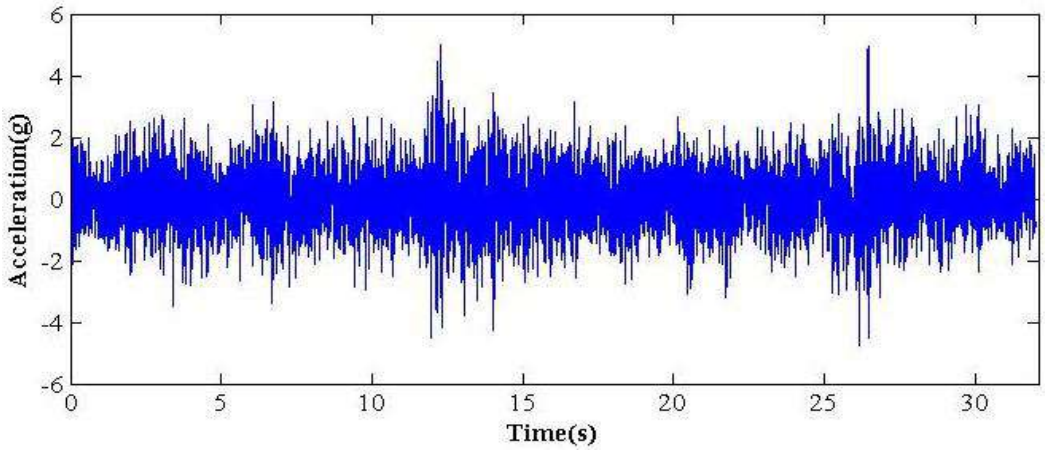

(a)

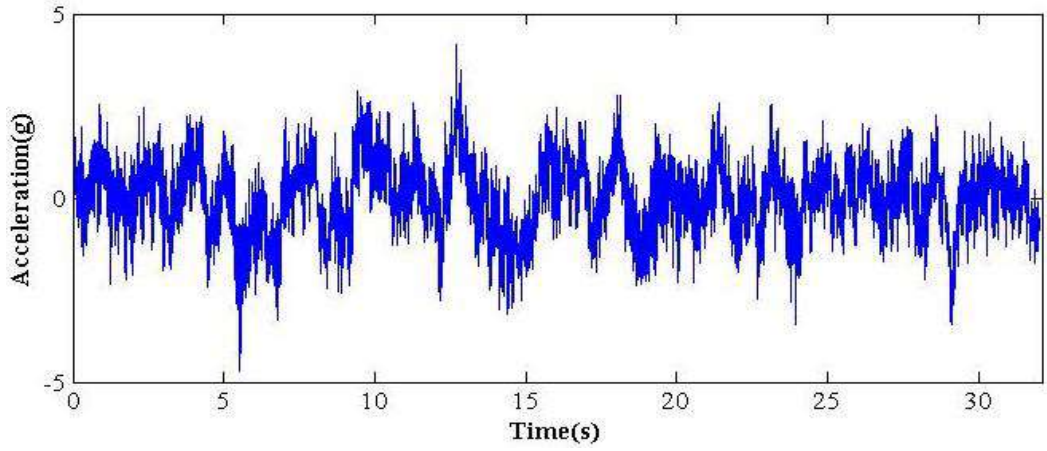

(b)

Fig. 7. The last source in DOF 1 when the number of sources is: a) 18; and (b) 19

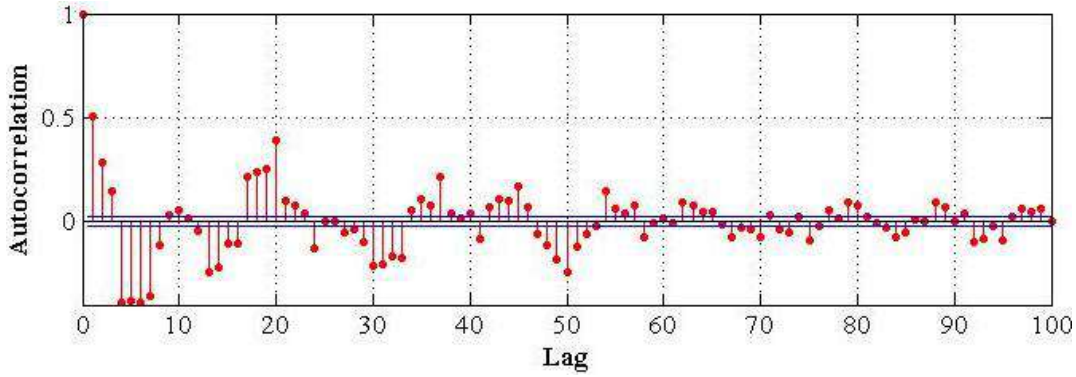

Fig. 8. The ACF plot of the independent source in DOF 1

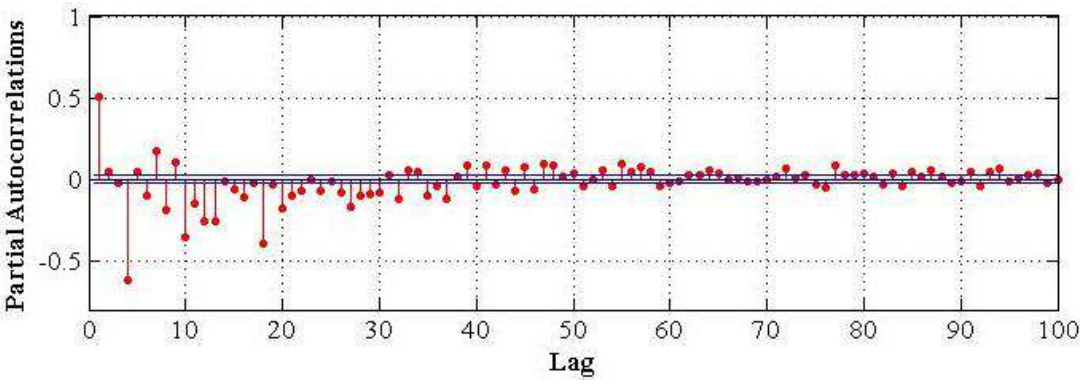

Fig. 9. The PACF plot of the independent source in DOF 1

The AR model order is estimated using the Akaike Information Criterion (AIC). For example, Figure 10 exhibits the AIC estimates in DOF 1. The optimal order is found to be 70, as shown in Figure 10. To determine the ARX model order, according to Ljung (1999) recommendation, the sum of α and β (ARX order) should be kept smaller than AR order p (i.e. $\alpha + \beta \leq p$). In this way, the ARARX model order is determined in each DOF and structural state.

As the structure is under the ambient vibrations, the acceleration data are supposed to be linear stationary signals. This assumption is examined by the ACF of the residuals of the ARARX model and is shown in Figure 11. The plot specifies no significant trend in the residuals and so the residuals are independent and identically distributed.

After specifying the ARARX model parameters in each DOF, the model is applied to the independent source in each structural state. Then, the Bhattacharyya measure is obtained between the residuals of the current state and reference state. To define the threshold value, a similar procedure as indicated in Section 4.1 is employed (Figure 12). A close look at Figure 12 reveals that the damage index in the health state in all DOFs is greater than the threshold limits. Also, it shows that between DOFs 4 to 6, which are in the same direction, DOF 4 has the lowest damage index. Similarly, between DOFs 10 to 12, DOF 10 has the lowest damage index. This localizes the damage which is near the sensors 4 and 10. Furthermore, in most DOFs, as the severity of damage increases, the Bhattacharyya measure decreases. In DOFs 13 to 15, there are some errors due to being away from the damage location; besides, all damage scenarios are small as mentioned earlier.

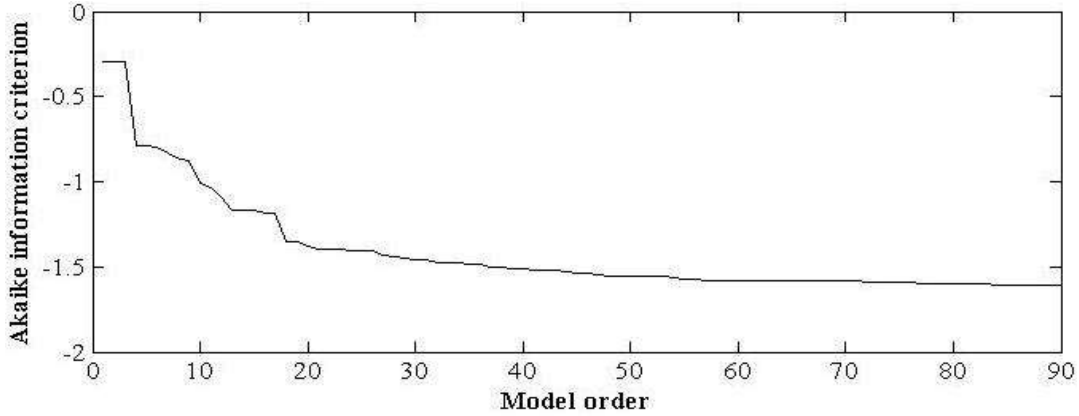

Fig. 10. Determination of the AR model order by the AIC method in DOF 1

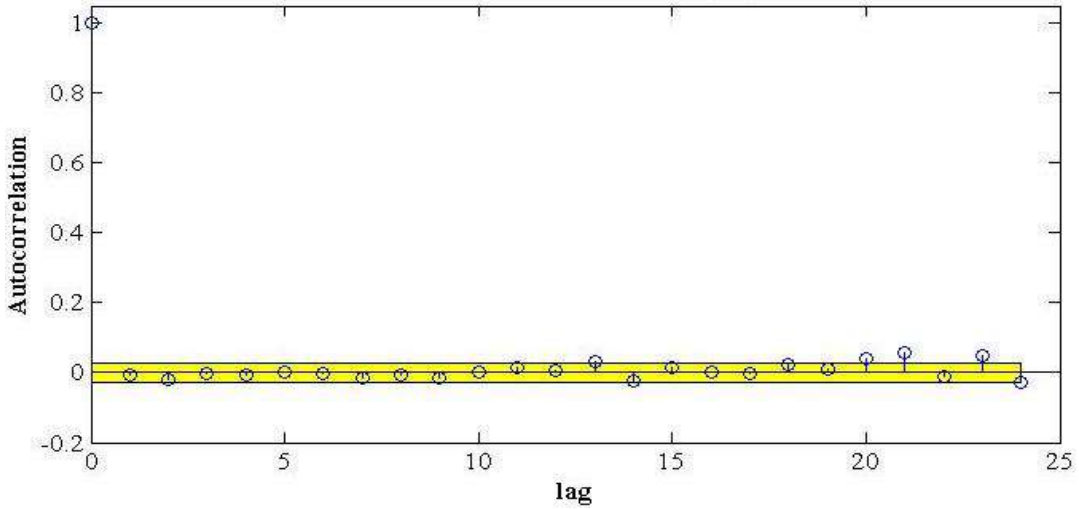

Fig. 11. ACF of residuals in DOF 1

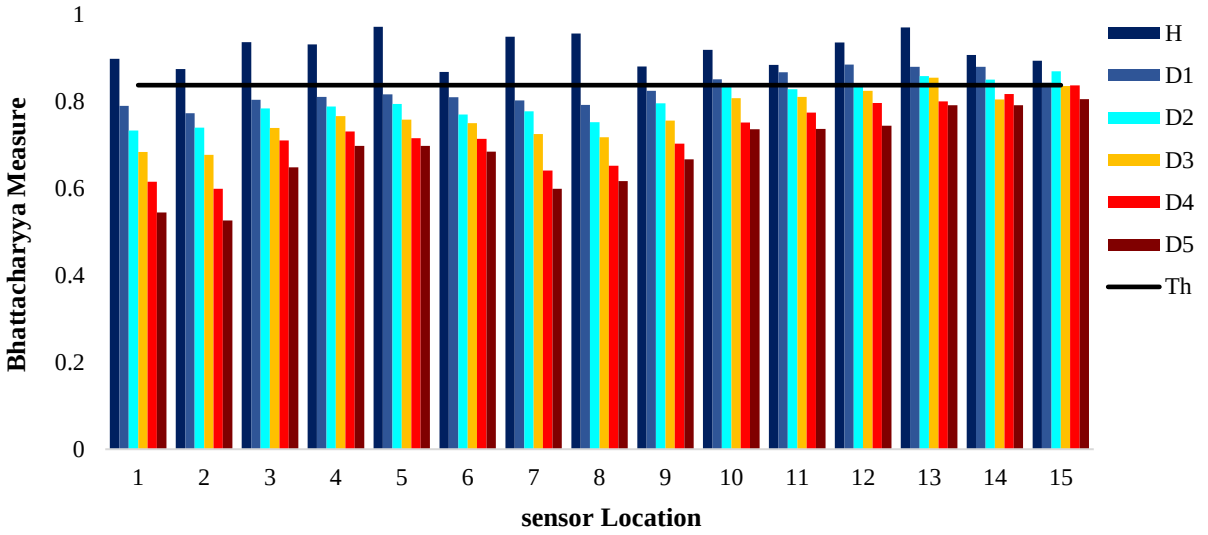

Fig. 12. The Bhattacharyya measure of odd DOF of beam structure in in each structural state

6. Discussion and Conclusion

In this paper, an innovative approach was proposed to detect and locate damage under the EOV conditions. In this approach, the ICA-based BSS approach was initially employed to acquire the time history response of the structure that is independent of unmeasured EOV. Then, time series analysis was applied to extract damage sensitive features. Finally, a novel statistical tool called Bhattacharyya measure was introduced to damage identification and localization using EOV independent features. The accuracy of the proposed techniques was validated by two useful benchmark structures under the simulated and actual EOV.

The first benchmark structure was a numerical beam structure under simulated EOV. The proposed method was applied to the acceleration measurements of the beam structure. Supposing normal distribution for Bhattacharyya measure in healthy state, the threshold value was defined. The damage index beyond the threshold value means that the structure is healthy and under that indicates a damaged state. Result showed that the proposed method could detect and localize damage. However, there were a few errors in results. Investigating the cause of errors revealsed that in all error cases, the indicator *I* was less than 0.97. It means that in these cases, the EOV effects have not been effectively eliminated and the obtained sources are not independent of EOV. Therefore, in these cases, more data measurements are needed in a relevant data set. The results showed as the damage severity increases, the damage index decreases; so the proposed approach could evaluate damage severity qualitatively. Furthermore, the proposed method was capable of damage localization even in the small damage scenarios. It showed that the proposed method was successful in early damage detection. As a result, if there are enough test measurements in each structural state, the proposed method can detect, localize damage, and evaluate damage severity qualitatively. Then a comparative study was conducted to indicate the capability of the suggested approach.

In this study, the structural state was analyzed based on the method proposed by Sohn and Farrer. The results showed that this method is also successful in damage diagnosis. However, the test measurements under EOV, which are needed in the training phase in the proposed method (10 test measurements), are much fewer than those in Sohn and Farrer's method (40 test measurements). Furthermore, the analysis time in the proposed method was about 12 times shorter.

The second benchmark structure was an experimental beam structure under actual EOV. In this beam structure, the steps of the

proposed approach were considered in details. Firstly, the importance of proper estimation of the number of sources in BSS implementation was investigated. It showed that to determine the number of sources, the amount of *I* indicator should be considered. According to this study, the indicator *I* must be greater than 0.97. Furthermore, in the cases that with increasing the number of sources (m) the change in indicator *I* is negligible, the smallest m is chosen as the number of sources. Choosing fewer sources makes the last source not independent enough and the more sources lead to the disappearance of some structural information. Then, the process of determining the appropriate time series model and the order of chosen model was discussed in details. Finally, the results showed that although the damage severity was small, the proposed method was successful in damage detection and localization. It could also qualitatively evaluate the damage severity at the damaged area.

Based on the analysis of this study, it can be concluded that:

- The ICA-based BSS technique employed in the proposed method is effectively able to remove the EOV influence from the time history response of the structure under unmeasured EOV.
- The suggested approach uses a limited group of response data for extracting the independent damage-sensitive features in the training phase. This significant advantage grants the suggested approach, in comparison with the conventional approach, to be a more time-saving and effective tool for damage assessment of structures with reliable results.
- The introduced Bhattacharyya measure is a powerful tool in decision making for damage identification and localization. It can also qualitatively evaluate the severity of damage.
- The proposed method can be effectively employed in the issues of early damage identification.

7. References

Avci, O., Abdeljaber, O., Kiranyaz, S., Hussein, M., Gabbouj, M. and Inman, D.J. (2021). "A review of vibration-based damage detection in civil structures: From traditional methods to Machine Learning and Deep Learning applications", *Mechanical Systems and Signal Processing*, 147, (15 January), 107077, https://doi.org/10.1016/j.ymssp.2020.107077.

Bayraktar, A., Altunişik, A.C., Sevim, B. and Özşahin, T. (2014). "Environmental effects on the dynamic characteristics of the Gülburnu Highway Bridge", *Civil Engineering and Environmental Systems*, 31(4), 347-366, https://doi.org/10.1080/10286608.2014.916697.

Box, G.E., Jenkins, G.M., Reinsel, G.C. and Ljung, G.M. (2015). *Time series analysis: Forecasting and control*, John Wiley & Sons.

Cai, Y., Zhang, K., Ye, Zh. Liu, Ch., Lu, K. and Wang, L. (2021). "Influence of temperature on the natural vibration characteristics of simply Supported reinforced concrete beam", *Sensors*, 21, 21(12), 4242, https://doi.org/10.3390/s21124242.

Cardoso, J.F. (1999). "High-order contrasts for independent component analysis", *Neural Computation*, 11(1), 157-192, https://doi.org/10.1162/089976699300016863.

Cardoso, J.F. and Souloumiac, A. (1993). "Blind beamforming for non-Gaussian signals", *IEE Proceedings F (Radar and Signal Processing)*, 140(6), 362-370, https://doi.org/10.1049/ip-f-2.1993.0054.

Chen, S-F., Hung, T-Y and Loh, C-H. (2015). "Analysis of traffic-induced vibration and damage detection by blind source separation with application to bridge monitoring", *Proceedings of SPIE 9435, Sensors and Smart Structures Technologies for Civil, Mechanical, and Aerospace Systems*, California, United States, https://doi.org/10.1117/12.2084084.

Comanducci, G., Magalhães, F., Ubertini, F. and Cunha, Á. (2016). "On vibration-based damage detection by multivariate statistical techniques: Application to a long-span arch bridge", *Structural Health Monitoring*, 15(5), 505-524, https://doi.org/10.1177/1475921716650630.

Cross, E. (2012). "On structural health monitoring in changing environmental and operational conditions", PhD Thesis, University of Sheffield.

Cross, E.J., Koo, K.Y., Brownjohn, J.M.W. and Worden, K. (2013). "Long-term monitoring and data analysis of the Tamar Bridge", *Mechanical Systems and Signal Processing*, 35(1-2), 16-34, https://doi.org/10.1016/j.ymssp.2012.08.026.

Cunha, A., Caetano, E., Moutinho, C. and Magalhães, F. (2019). "Continuous dynamic monitoring program of large civil infrastructures", *Proceedings of the 7th*

International Conference on Computational Methods in Structural Dynamics and Earthquake Engineering (COMPDYN 2015), 13-47, Crete Island, Greece, https://doi.org/10.7712/120119.6901.20156.

Datteo, A, and Lucà, F. (2017). "Statistical pattern recognition approach for long-time monitoring of the G. Meazza stadium by means of AR models and PCA", *Engineering Structures*, 153, (15 December), 317-333, https://doi.org/10.1016/j.engstruct.2017.10.022..

Daneshvar, M.H, Gharighoran, A., Zareei, S.A. and Karamodin, A. (2021). "Structural health monitoring using high-dimensional features from time series modeling by innovative hybrid distance-based methods", *Journal of Civil Structural Health Monitoring*, 11(2), 537-557, https://doi.org/10.1007/s13349-020-00466-5.

Dervilis, N., Worden, K. and Cross, E. (2015). "On robust regression analysis as a means of exploring environmental and operational conditions for SHM data", *Journal of Sound and Vibration*, 347(7 July), 279-96, https://doi.org/10.1016/j.jsv.2015.02.039.

Entezami A. (2021), *Structural health monitoring by time series analysis and statistical distance measures*, Cham: Springer International Publishing, https://doi.org/10.1007/978-3-030-66259-2.

Entezami, A. and Shariatmadar, H. (2019). "Structural health monitoring by a new hybrid feature extraction and dynamic time warping methods under ambient vibration and non-stationary signal", *Measurement*, 134(February), 548-568, https://doi.org/10.1016/j.measurement.2018.10.095.

Entezami, A., Shariatmadar, H. and Karamodin, A. (2019). "Data-driven damage diagnosis under environmental and operational variability by novel statistical pattern recognition methods", *Structural Health Monitoring*, 18(5-6), 1416-1443, https://doi.org/10.1177/1475921718800306.

Guo, Y., and Kareem, A., (2016). "System identification through nonstationary data using time-frequency blind source separation", *Journal of Sound and Vibration*, 371(February), 110-131, https://doi.org/10.1016/j.jsv.2016.02.011.

Hu, W-H., Tang, D-H., Teng, J., Said, S. and Rohrmann, R.G. (2018). "Structural health monitoring of a prestressed concrete bridge based on statistical pattern recognition of continuous dynamic measurements over 14 years", *Sensors*, 18(12), 4117, https://doi.org/10.3390/s18124117.

Jain, S.N. and Rai, C. (2012). "Blind source separation and ICA techniques: A review", *International Journal of Engineering Science and Technology*, 4(4), 1490-1503, https://doi.org/10.1109/CISES54857.2022.9844373.

Jiang, S., Lin, P., Chen, Y., Tian, Ch. and Li, Y. (2019). "Mixed-signal extraction and recognition of wind turbine blade multiple-area damage based on improved Fast-ICA", *Optik*, 179(February), 1152-1159, https://doi.org/10.1016/j.ijleo.2018.10.137.

Kordi, A., and Mahmoudi, M. (2022). "Damage detection in truss bridges under moving load using time history response and members influence line curves", *Civil Engineering Infrastructures Journal*, 55(1), 183-194, https://doi.org/10.22059/ceij.2021.314109.1723.

Kullaa, J. (2011). "Distinguishing between sensor fault, structural damage, and environmental or operational effects in structural health monitoring", *Mechanical Systems and Signal Processing*, 25(8), 2976-2989, https://doi.org/10.1016/j.ymssp.2011.05.017.

Kullaa, J. (2014). "Benchmark data for structural health monitoring", *Proceedings of the EWSHM, 7th European Workshop on Structural Health Monitoring*, Nantes, France, https://inria.hal.science/hal-01021056.

Kullaa, J. (2020). "Robust damage detection in the time domain using Bayesian virtual sensing with noise reduction and environmental effect elimination capabilities", *Journal of Sound and Vibration*, 473, (12 May), 115232, https://doi.org/10.1016/j.jsv.2020.115232.

Limongelli, M.P., Manoach, E., Quqa, S., Giordano, P.F., Bhowmik, B., Pakrashi, V. and Cigada, F. (2021). "Vibration response-based damage detection", In: Sause, M.G.R., Jasiūnienė, E. (eds), *Structural Health Monitoring Damage Detection Systems for Aerospace*, Springer Aerospace Technology, Springer, Cham, https://doi.org/10.1007/978-3-030-72192-3_6.

Ljung, L. (1999). *System identification: Theory for the user*, PTR Prentice Hall, Upper Saddle River.

Nguyen, V., Mahowald, J., Schommer, S., Maas, S. and Zuerbes, A. (2017). "A study of temperature and aging effects on Eigenfrequencies of concrete bridges for health monitoring", *Engineering*, 9(5), 396-411, https://doi.org/10.4236/eng.2017.95023.

Rainieri, C., Magalhaes, F., Gargaro, D., Fabbrocino, G. and Cunha, A. (2019). "Predicting the variability of natural frequencies and its causes by Second-Order Blind Identification", *Structural Health Monitoring*, 18(2), 486-507, https://doi.org/10.1177/1475921718758629.

Razavi, B.S., Mahmoudkelayeh, M.R. and Razavi, S.S. (2021). "Damage identification under ambient vibration and unpredictable signal nature", *Journal of Civil Structural Health Monitoring*, 11(5), 1253-1273, https://doi.org/10.1007/s13349-021-00503-x.

Roy, K., Bhattacharya, B. and Ray-Chaudhuri, S. (2015). "ARX model-based damage sensitive features for structural damage localization using output-only measurements", *Journal of Sound and Vibration*, 349(4 August), 99-122, https://doi.org/10.1016/j.jsv.2015.03.038..

Sadhu, A. and Hazra, B. (2013). "A novel damage detection algorithm using time-series analysis-based blind source separation" *Shock and Vibration*, 20(3), 423-438, https://doi.org/10.3233/SAV-120759.

Sadhu, A., Narasimhan, S. and Antoni, J. (2017). "A review of output-only structural mode identification literature employing blind source separation methods", *Mechanical Systems and Signal Processing*, 94(15 September), 415-431, https://doi.org/10.1016/j.ymssp.2017.03.001.

Shan, W., Wang, X. and Jiao, Y. (2018). "Modeling of temperature effect on modal frequency of concrete beam based on field monitoring data", *Shock and Vibration*, 2018, Article ID. 8072843, 1-13, https://doi.org/10.1155/2018/8072843.

Sohn, H. and Farrar, C.R. (2001). "Damage diagnosis using time series analysis of vibration signals", *Smart Materials and Structures*, 10(3), 446, https://doi.org/10.1088/0964-1726/10/3/304.

Spiridonakos, M.D, Chatzi, E.N. and Sudret, B. (2016). "Polynomial Chaos Expansion models for the monitoring of structures under operational variability", *ASCE-ASME Journal of Risk and Uncertainty in Engineering Systems, Part A: Civil Engineering*, 2(3), B4016003, https://doi.org/10.1061/AJRUA6.0000872.

Vamvoudakis-Stefanou, K., Sakellariou, J. and Fassois, S. (2018). "Vibration-based damage detection for a population of nominally identical structures: Unsupervised Multiple Model (MM) statistical time series type methods", *Mechanical Systems and Signal Processing*, 111(October), 149-171, https://doi.org/10.1016/j.ymssp.2018.03.054.

Wang, K., Hao, Q., Zhang, X., Tang, Z., Wang, Y. and Shen, Y. (2020). "Blind source extraction of acoustic emission signals for rail cracks based on ensemble empirical mode decomposition and constrained independent component analysis", *Measurement*, 157(June), 107653, https://doi.org/10.1016/j.measurement.2020.107653.

Yu, G. (2019). "An underdetermined blind source separation method with application to modal identification", *Shock and Vibration*, 2019, Article ID. 1637163, https://doi.org/10.1155/2019/1637163.

Zhang, W., Li, C., Peng, G., Chen, Y. and Zhang, Z. (2018). "A deep convolutional neural network with new training methods for bearing fault diagnosis under noisy environment and different working load", *Mechanical System and Signal Processing*, 100(1 February), 439-453, https://doi.org/10.1016/j.ymssp.2017.06.022.

Zhang, X., Li, D. and Song, G. (2018). "Structure damage identification based on regularized ARMA time series model under environmental excitation", *Vibration*, 1(1), 138-156, https://doi.org/10.3390/vibration1010011.

Civil Engineering Infrastructures Journal 2023, 56(1): 51-78
DOI: 10.22059/CEIJ.2022.330788.1792

RESEARCH PAPER

An Explicit and Highly Accurate Runge-Kutta Family

Rezaiee-Pajand, M.[1*], Esfehani, S.A.H.[2] and Ehsanmanesh, H.[3]

[1] Professor, Civil Engineering Department, Faculty of Engineering, Ferdowsi University of Mashhad, Mashhad, Iran.
[2] M.Sc., Civil Engineering Department, Faculty of Engineering, Ferdowsi University of Mashhad, Mashhad, Iran.
[3] B.Sc., Department of Electrical Engineering, Faculty of Engineering, Ferdowsi University of Mashhad, Mashhad, Iran.

Received: 16 Sep. 2021; Revised: 14 May 2022; Accepted: 17 Jul. 2022

ABSTRACT: In this paper, an explicit family with higher-order of accuracy is proposed for dynamic analysis of structural and mechanical systems. By expanding the analytical amplification matrix into Taylor series, the Runge-Kutta family with n stages can be presented. The required coefficients (α) for different stages are calculated through a solution of nonlinear algebraic equations. The contribution of the new family is the equality between its accuracy order, and the number of stages used in a single time step (n). As a weak point, the stability of the proposed family is conditional, so that the stability domain for each of the first three orders ($n = 5$, 6, and 7) is smaller than that for the classic fourth-order Runge-Kutta method. However, as a positive point, the accuracy of the family boosts as the order of the family increases. As another positive point, any arbitrary order of the family can be easily achieved by solving the nonlinear algebraic equations. The robustness and ability of the authors' schemes are illustrated over several useful time integration methods, such as Newmark linear acceleration, generalized-α, and explicit and implicit Runge-Kutta methods. Moreover, various numerical experiments are utilized to show higher performances of the explicit family over the other methods in accuracy and computation time. The results demonstrate the capability of the new family in analyzing nonlinear systems with many degrees of freedom. Further to this, the proposed family achieves accurate results in analyzing tall building structures, even if the structures are under realistic loads, such as ground motion loads.

Keywords: Accuracy, Linear and Nonlinear Dynamic Systems, Stability, Tall Building Structure, Taylor Series.

1. Introduction

The ability of structural analysis can be regarded as one of the most important achievements on the engineering field (Haj Najafi and Tehranizadeh, 2016; Ghassemieh and Badrkhani Ajaei, 2018; Ezoddin et al., 2020; Kordi and Mahmoudi, 2022). Time integration methods offer numerous techniques to analyze structural and mechanical dynamic systems with high efficiency (Bathe, 1982; Goel et al., 2018; Rezaie et al., 2018). These techniques are implemented to calculate the dynamic

* Corresponding author E-mail: mrpajand@yahoo.com

responses of the motion in linear and nonlinear systems (Chang, 2013; Soares and Großeholz, 2018). It is well-known that Newmark's paper in 1959 is considered as one of the fundamental works in this scope (Newmark, 1959).

In time integration methods, time is divided into several time steps (Shutov et al., 2013), in which the length of time steps might be equal or different (Rossi et al., 2014). Time integration methods are typically classified as explicit or implicit. In explicit algorithms, the response at the end of each step is directly calculated based on the initial value of the response, as well as, the initial and current values of inputs (Kim, 2019). Some researchers developed their methods based on this idea (Hulbert and Chung, 1996; Soares, 2016). On the other hand, in implicit schemes, the response at the end of each time step not only depends on its initial value, but also on the response value at the end of the time step (Lee et al., 2017). In this manner, the response is usually obtained by solving an algebraic equation. Many researchers proposed various implicit time integrations to solve linear and nonlinear dynamic systems (Newmark, 1959; Ortigosa et al., 2020). By combining the explicit and implicit schemes, predictor-corrector methods have been developed. In these procedures, an explicit algorithm is deployed to approximate the initial solution of the response. In the next step, an implicit method is utilized to modify the obtained solution (Noels et al., 2006; Yaghoubi et al., 2016).

A large group of methods, known as Runge-Kutta schemes and their derivations, has been developed over decades to deal with dynamic equations. The first useful group is known as 2^{nd}-order and 4^{th}-order Runge-Kutta schemes, which were introduced by Heun (1900) and Kutta (1901), respectively. Thereafter, different methods have been proposed based on Runge-Kutta techniques (Izzo and Jackiewicz, 2017; Jørgensen et al., 2018). It is worth emphasizing that some of these methods are explicit, and some others are based on implicit techniques (Zhao and Wei, 2014; Grote et al., 2015). More to this, some researchers presented predictor-corrector Runge-Kutta algorithms (Gu and Zhu, 2021). Butcher (2016) proposed a general table to illustrate the majority of the Runge-Kutta schemes. Each Runge-Kutta method exploits a number of stages to achieve the response at the end of time step. The accuracy order of the scheme will be improved by increasing the number of stages. However, based on the results of Butcher's study, in order to achieve an accuracy order greater than 4 in an explicit Runge-Kutta scheme, the number of utilized stages should be larger than the desired accuracy order (Hairer et al., 2006). Fok (2016) proposed a 4^{th}-order of accuracy Runge-Kutta method. In his scheme, the length of time step is changed to control the error of response solution. Braś et al. (2017) suggested an explicit-implicit method to obtain a Runge-Kutta family with various orders of accuracy, from the first- to the fourth-order. In their technique, the number of stages is equal to the accuracy order of the method. Grote et al. (2015) proposed some explicit forms of the local time-stepping Runge-Kutta method up to the 4^{th}-order. Based on Runge-Kutta techniques, Zhao and Wei (2014) developed a new discrete Galerkin method for time integration. The highest order of accuracy provided by this approach, which is an implicit Runge-Kutta technique, is equal to 6. Many scholars offered some methods in which their order of accuracy varies between 1 and 5 (Izzo and Jackiewicz, 2017; Isherwood et al., 2018; Jørgensen et al., 2018; Martín-Vaquero and Kleefeld, 2019). However, some of the proposed procedures have a higher order of accuracy, which can only solve free vibration problems (Turaci and Öziş, 2018; Sun and Shu, 2019).

Some researchers use the expansion of the exponential matrix to develop their Runge-Kutta family. For example, Vejju et al. (2016) computed the state transition

matrix using Lagrange's interpolation formula for the general solution of linear dynamical systems. In their method, the exponential of a matrix is approximated by Lagrange's interpolation polynomials. However, the coefficients required for Lagrange's interpolation should be calculated for every dynamic system. Kassam and Trefethen (2005) proposed a modified exponential time difference fourth-order Runge-Kutta method to solve stiff nonlinear PDEs. Based on the experiments performed, the maximum order of accuracy of their method is 5. Zhang et al. (2020) invented an exponential Runge-Kutta method with second-order accuracy in space and fourth-order accuracy in time. In their algorithm, the product of a block Toeplitz matrix exponential and a vector is calculated by the shift-invert Lanczos method. A survey on the literature manifests that researchers have carried out a great deal of work concerning the dynamic analysis of structures. So far, various strategies have been proposed to increase the order of accuracy and stability of different methods. Nonetheless, the development of a family capable of furnishing any arbitrary order remains a significant challenge.

This paper presents a comprehensive explicit family of Runge-Kutta methods to deal with linear and nonlinear structural dynamic systems. In this manner, the amplification matrix of analytical solution is expanded into Taylor series, and by solving a system of nonlinear algebraic equations, coefficients required (α) for the stages of the Runge-Kutta family are obtained. One of the superiorities of the proposed formulation is the equality between the method accuracy order, and the number of stages used in a single time step. Aside from this, any arbitrary order of the family can be easily achieved by solving a system of algebraic equations.

2. Proposed Scheme

2.1. Linear Dynamic Systems

In linear structural dynamics, the equation of motion with initial values for displacement ($\boldsymbol{u}_0$) and velocity ($\dot{\boldsymbol{u}}_0$) is written in the following form.

$$\begin{aligned} &\mathbf{M}\ddot{\mathbf{u}}(t)+\mathbf{C}\dot{\mathbf{u}}(t)+\mathbf{K}\mathbf{u}(t)=\mathbf{f}(t) \\ &\mathbf{u}(0)=\mathbf{u}_0\ ,\dot{\mathbf{u}}(0)=\dot{\mathbf{u}}_0 \end{aligned} \tag{1}$$

where, $\boldsymbol{M}$, $\mathbf{C}$, and $\boldsymbol{K}$: are the mass, damping, and linear stiffness matrices of the structure, respectively. Also, $\boldsymbol{u}$,$\dot{\boldsymbol{u}}$,$\ddot{\boldsymbol{u}}$ and $\boldsymbol{f}$: are vectors showing the displacement, velocity, acceleration, and applied loads in different nodes of the structure at time *t*, respectively. Eq. (1) can be formulated in the form of state-space representation as follows:

$$\dot{\mathbf{x}}=\mathbf{M}\ \mathbf{x}+\mathbf{p} \tag{2}$$

in which, $\boldsymbol{x}$: is the state space vector of Eq. (2) and is given by:

$$\mathbf{x}=\begin{Bmatrix}\mathbf{u}\\ \dot{\mathbf{u}}\end{Bmatrix} \tag{3}$$

where, $\dot{\boldsymbol{x}}$, $\boldsymbol{p}$, and $\mathbf{M}$: are derivative of the state vector, input vector, and state coefficient matrix, respectively. The input vector $\boldsymbol{p}$ and state coefficient matrix $\mathbf{M}$ are expressed as follows.

$$\mathbf{p}=\begin{Bmatrix}0_{k\times 1}\\ \mathbf{M}^{-1}\mathbf{f}(\mathbf{t})\end{Bmatrix} \tag{4}$$

$$\mathbf{M}\ =\begin{bmatrix}0_{k\times k} & \mathbf{I}_{k\times k}\\ -\mathbf{M}^{-1}\mathbf{K} & -\mathbf{M}^{-1}\mathbf{C}\end{bmatrix} \tag{5}$$

where, $0_{k\times k}$ and $\boldsymbol{I}_{k\times k}$: represent zero and identity matrices, respectively, and k: shows the degrees of freedom for the structure with the equation of motion in Eq. (1). In the time integration process, the time-domain $[0,t]$ is divided into m subdomains, each having a length of Δt. These are called time steps. At each step, the values provided at the beginning of the step, and the input vector are used to calculate the responses at the end of the step. The value of the input vector at each step is defined as follows:

$$\mathbf{p}_i(\tau)=\mathbf{p}\big((i-1)\Delta t+\tau\big);\quad 0\le\tau\le\Delta t \tag{6}$$

where, i: shows the step number and τ: is a

time variable that varies in $[0, \Delta t]$. The exact solution of Eq. (2) at the end of the time step i is achievable as follows:

$$\mathbf{x}_{i+1} = e^{\mathbf{M}\,\Delta t}\mathbf{x}_i + \int_0^{\Delta t} e^{\mathbf{M}\,\tau}\mathbf{p}_i\left(\Delta t - \tau\right)d\tau \quad (7)$$

where $\boldsymbol{x}_i$ and $\boldsymbol{x}_{i+1}$: represent the initial and final values of the solution of Eq. (2) at ith time step. Taylor series expansion for the exponential matrix functions given in Eq. (7) (i.e. $e^{\mathbf{M}\,\Delta t}$ and $e^{\mathbf{M}\,\tau}$) can be represented in the following equations:

$$\begin{aligned} e^{\mathbf{M}\,\Delta t} &= \mathbf{I} + \frac{\mathbf{M}\,\Delta t}{1!} + \frac{\mathbf{M}^2\Delta t^2}{2!} + \frac{\mathbf{M}^3\Delta t^3}{3!} \\ &+ \ldots + \frac{\mathbf{M}^n\Delta t^n}{n!} + \ldots = \mathbf{I} + \sum_{s=1}^{\infty}\frac{\mathbf{M}^s\Delta t^s}{s!} \end{aligned} \quad (8)$$

$$\begin{aligned} e^{\mathbf{M}\,\tau} &= \mathbf{I} + \frac{\mathbf{M}\,\tau}{1!} + \frac{\mathbf{M}^2\tau^2}{2!} + \frac{\mathbf{M}^3\tau^3}{3!} \\ &+ \ldots + \frac{\mathbf{M}^n\tau^n}{n!} + \ldots = \mathbf{I} + \sum_{s=1}^{\infty}\frac{\mathbf{M}^s\tau^s}{s!} \end{aligned} \quad (9)$$

By substituting Eqs. (8) and (9) into Eq. (7), the exact solution of Eq. (2) at the ith step is rewritten in the below form:

$$\begin{aligned} \mathbf{x}_{i+1} &= \left(\mathbf{I} + \sum_{s=1}^{\infty}\frac{\mathbf{M}^s\Delta t^s}{s!}\right)\mathbf{x}_i \\ &+ \int_0^{\Delta t}\left(\mathbf{I} + \sum_{s=1}^{\infty}\frac{\mathbf{M}^s\tau^s}{s!}\right)\mathbf{p}_i\left(\Delta t - \tau\right)d\tau \end{aligned} \quad (10)$$

Similar to other Runge-Kutta schemes, the proposed formulation uses the initial value $\mathbf{x}_i$ to produce the increments of the variable $\mathbf{X}$ ($\boldsymbol{\Delta X}$) in some stages. In this manner, the increments are calculated as follows:

$$\begin{aligned} &\boldsymbol{X}_0 = \boldsymbol{x}_i \\ &\boldsymbol{X}_1 = \boldsymbol{X}_0 \\ &\boldsymbol{\Delta X}_1 = \mathcal{M}(\boldsymbol{X}_1 + \boldsymbol{P}_1)\Delta t \\ &\boldsymbol{X}_2 = \boldsymbol{X}_0 + \alpha_1\boldsymbol{\Delta X}_1 \\ &\boldsymbol{\Delta X}_2 = \mathcal{M}(\boldsymbol{X}_2 + \boldsymbol{P}_2)\Delta t \\ &\boldsymbol{X}_3 = \boldsymbol{X}_0 + \alpha_2\boldsymbol{\Delta X}_2 \\ &\boldsymbol{\Delta X}_3 = \mathcal{M}(\boldsymbol{X}_3 + \boldsymbol{P}_3)\Delta t \\ &\ldots \\ &\boldsymbol{X}_{n-1} = \boldsymbol{X}_0 + \alpha_{n-2}\boldsymbol{\Delta X}_{n-2} \\ &\boldsymbol{\Delta X}_{n-1} = \mathcal{M}(\boldsymbol{X}_{n-1} + \boldsymbol{P}_{n-1})\Delta t \\ &\boldsymbol{X}_n = \boldsymbol{X}_0 + \alpha_{n-1}\boldsymbol{\Delta X}_{n-1} \\ &\boldsymbol{\Delta X}_n = \mathcal{M}(\boldsymbol{X}_n + \boldsymbol{P}_n)\Delta t \end{aligned} \quad (11)$$

where n: denotes the number of the utilized stages. Eventually, using the initial values and weighted average of the increments ($\boldsymbol{\Delta X}$), the responses at the end of the time step i is achievable by using Eq. (12).

$$\begin{aligned} \mathbf{x}_{i+1} &= \mathbf{X}_0 + \mathbf{P}_0 + \\ &\frac{\boldsymbol{\Delta X}_1 + \frac{1}{\alpha_1}\boldsymbol{\Delta X}_2 + \ldots + \frac{1}{\alpha_{n-1}}\boldsymbol{\Delta X}_n}{1 + \frac{1}{\alpha_1} + \frac{1}{\alpha_2} + \ldots + \frac{1}{\alpha_{n-1}}} \end{aligned} \quad (12)$$

in which coefficients α_1 to α_{n-1} and vectors $\mathbf{P}_0$ to $\mathbf{P}_n$: represent the unknown quantities, which should be calculated. By using Eqs. (11) and (12), Eq. (13) is achieved.

$$\mathbf{x}_{i+1} = \mathbf{x}_i + \mathbf{P}_0 + \left(1 + \sum_{j=1}^{n-1}\frac{1}{\alpha_j}\right)^{-1}\mathbf{XP} \quad (13)$$

where, $\mathbf{XP}$ is defined as follows.

$$\begin{aligned} \mathbf{XP} = (&\left[1 + \sum_{j=1}^{n-1}\frac{1}{\alpha_j}\right]\mathbf{M}\,\Delta t + \left[n-1\right]\mathbf{M}^2\Delta t^2 + \\ &\left[\sum_{j=1}^{n-2}\alpha_j\right]\mathbf{M}^3\Delta t^3 + \left[\sum_{j=1}^{n-3}\alpha_j\alpha_{j+1}\right]\mathbf{M}^4\Delta t^4 + \\ &\left[\sum_{j=1}^{n-4}\alpha_j\alpha_{j+1}\alpha_{j+2}\right]\mathbf{M}^5\Delta t^5 + \\ &\left[\sum_{j=1}^{n-5}\prod_{v=0}^{3}\alpha_{j+v}\right]\mathbf{M}^6\Delta t^6 + \ldots + \left[\prod_{v=1}^{n-2}\alpha_v\right]\mathbf{M}^n\Delta t^n)\mathbf{x}_i \\ &+(\mathbf{M}\,\Delta t[\mathbf{P}_1 + \frac{1}{\alpha_1}\mathbf{P}_2 + \frac{1}{\alpha_2}\mathbf{P}_3 \\ &\quad + \ldots + \frac{1}{\alpha_{n-2}}\mathbf{P}_{n-1} + \frac{1}{\alpha_{n-1}}\mathbf{P}_n] \\ &+\mathbf{M}^2\Delta t^2\left[\mathbf{P}_1 + \mathbf{P}_2 + \mathbf{P}_3 + \ldots + \mathbf{P}_{n-2} + \mathbf{P}_{n-1}\right] \\ &+\mathbf{M}^3\Delta t^3\left[\alpha_1\mathbf{P}_1 + \alpha_2\mathbf{P}_2 + \ldots + \alpha_{n-2}\mathbf{P}_{n-2}\right] \\ &+\mathbf{M}^4\Delta t^4[\alpha_1\alpha_2\mathbf{P}_1 + \alpha_2\alpha_3\mathbf{P}_2 + \alpha_3\alpha_4\mathbf{P}_3 \\ &\quad + \ldots + \alpha_{n-4}\alpha_{n-3}\mathbf{P}_{n-4} + \alpha_{n-3}\alpha_{n-2}\mathbf{P}_{n-3}] \\ &+ \ldots \\ &+\mathbf{M}^{k+1}\Delta t^{k+1}[\alpha_1\ldots\alpha_{k-1}\mathbf{P}_1 + \alpha_2\ldots\alpha_k\mathbf{P}_2 \\ &\quad + \ldots + \alpha_{n-k}\ldots\alpha_{n-2}\mathbf{P}_{n-k}] \\ &+\mathbf{M}^{n-1}\Delta t^{n-1}\left[\alpha_1\ldots\alpha_{n-3}\mathbf{P}_1 + \alpha_2\ldots\alpha_{n-2}\mathbf{P}_2\right] \\ &+\mathbf{M}^n\Delta t^n\left[\alpha_1\ldots\alpha_{n-2}\mathbf{P}_1\right]) \end{aligned} \quad (14)$$

By substituting Eq. (14) into Eq. (13), Eq. (13) can be expanded in the following form.

$$\begin{aligned}\mathbf{x}_{i+1} &= \left(\mathbf{I}+\left(1+\sum_{j=1}^{n-1}\frac{1}{\alpha_j}\right)^{-1}\left[\left(1+\sum_{j=1}^{n-1}\frac{1}{\alpha_j}\right)\mathbf{M}\ \Delta t\right.\right.\\ &\left.+(n-1)\mathbf{M}^{\ 2}\Delta t^{2}+\ldots+\prod_{v=1}^{n-2}\alpha_v\mathbf{M}^{\ n}\Delta t^{n}\right]\Big)\mathbf{x}_i\\ &+\Big(\mathbf{P}_0+\left(1+\sum_{j=1}^{n-1}\frac{1}{\alpha_j}\right)^{-1}\\ &\left[\mathbf{M}\ \Delta t\left[\mathbf{P}_1+\frac{1}{\alpha_1}\mathbf{P}_2+\ldots+\frac{1}{\alpha_{n-1}}\mathbf{P}_n\right]\right.\\ &\left.+\ldots+\mathbf{M}^{\ n}\Delta t^{n}\left[\alpha_1\ldots\alpha_{n-2}\mathbf{P}_1\right]\right]\Big)\end{aligned} \tag{15}$$

According to Eq. (10), if the number of selected terms in the series is limited to *n*, one can arrive at:

$$\begin{aligned}\mathbf{x}_{i+1} &= \left(\mathbf{I}+\sum_{s=1}^{n}\frac{\mathbf{M}^{\ s}\Delta t^{s}}{s!}\right)\mathbf{x}_i+\\ &\int_0^{\Delta t}\left(\mathbf{I}+\sum_{s=1}^{n}\frac{\mathbf{M}^{\ s}\tau^{s}}{s!}\right)\mathbf{p}_i\left(\Delta t-\tau\right)d\tau\end{aligned} \tag{16}$$

Both Eqs. (15) and (16) consist of two parts corresponding to the initial value and the input vector at the time step i. By equating the part which is associated with the initial value of the step i in Eqs. (15) and (16), one can write:

$$\begin{aligned}&\mathbf{I}+\left(1+\sum_{j=1}^{n-1}\frac{1}{\alpha_j}\right)^{-1}\left[\left(1+\sum_{j=1}^{n-1}\frac{1}{\alpha_j}\right)\mathbf{M}\ \Delta t+\right.\\ &\left.(n-1)\mathbf{M}^{\ 2}\Delta t^{2}+\ldots+\prod_{v=1}^{n-2}\alpha_v\mathbf{M}^{\ n}\Delta t^{n}\right]\\ &=\mathbf{I}+\sum_{s=1}^{n}\frac{\mathbf{M}^{\ s}\Delta t^{s}}{s!}\end{aligned} \tag{17}$$

According to Eq. (17), the required relations for obtaining the unknown coefficients, α_1 to α_{n-1}, are as follows.

$$\begin{aligned}&\frac{1+\sum_{j=1}^{n-1}\frac{1}{\alpha_j}}{1+\sum_{j=1}^{n-1}\frac{1}{\alpha_j}}=\frac{1}{1!}\\ &\frac{n-1}{1+\sum_{j=1}^{n-1}\frac{1}{\alpha_j}}=\frac{1}{2!}\\ &\frac{\sum_{j=1}^{n-2}\alpha_j}{1+\sum_{j=1}^{n-1}\frac{1}{\alpha_j}}=\frac{1}{3!}\\ &\frac{\sum_{j=1}^{n-3}\alpha_j\alpha_{j+1}}{1+\sum_{j=1}^{n-1}\frac{1}{\alpha_j}}=\frac{1}{4!}\\ &\ldots\\ &\frac{\sum_{j=1}^{n-(k-1)}\prod_{v=0}^{k-3}\alpha_{j+v}}{1+\sum_{j=1}^{n-1}\frac{1}{\alpha_j}}=\frac{1}{k!}\\ &\ldots\\ &\frac{\prod_{v=1}^{n-2}\alpha_v}{1+\sum_{j=1}^{n-1}\frac{1}{\alpha_j}}=\frac{1}{n!}\end{aligned} \tag{18}$$

It is obvious that the values of all coefficients, α_1 to α_{n-1}, for any arbitrary *n*, can be available. The studies about the uniqueness and existence of the coefficients α_1 to α_{n-1} are presented in Appendix 1. These coefficients are outlined in Table 1 for n from 2 to 10. To obtain the unknown vectors of $\mathbf{P}_0$ to $\mathbf{P}_n$, the part of Eqs. (15) and (16) concerned with the input vector must be equated. In this manner, the corresponding equality can be expressed as:

$$\begin{aligned}&\mathbf{P}_0+\left(1+\sum_{j=1}^{n-1}\frac{1}{\alpha_j}\right)^{-1}\\ &\left[\mathbf{M}\ \Delta t\left[\mathbf{P}_1+\frac{1}{\alpha_1}\mathbf{P}_2+\ldots+\frac{1}{\alpha_{n-1}}\mathbf{P}_n\right]\right.\\ &\left.+\ldots+\mathbf{M}^{\ n}\Delta t^{n}[\alpha_1\ldots\alpha_{n-2}\mathbf{P}_1]\right]\\ &=\int_0^{\Delta t}\left(\mathrm{I}+\sum_{s=1}^{n}\frac{\mathbf{M}^{\ s}\tau^{s}}{s!}\right)\mathbf{P}_i\left(\Delta t-\tau\right)d\tau\end{aligned} \tag{19}$$

From Eq. (18), one can find out that the term $\left(1+\sum_{j=1}^{n-1}\frac{1}{\alpha_j}\right)$ is equal to $2(n-1)$. Using this equality and according to Eq. (19), one can use the equalities provided in Eq. (20) to calculate the unknown vectors $\mathbf{P}_0$ to $\mathbf{P}_n$.

Table 1. Values of coefficients $\alpha_{(1\ to\ n-1)}$ for $n = 2$ to 10

n	$\alpha_{(1\ to\ n-1)}$
2	$\alpha_1 = 1$
3	$\alpha_1 = \frac{2}{3}$, $\alpha_2 = \frac{2}{3}$
4	$\alpha_1 = \frac{1}{2}$, $\alpha_2 = \frac{1}{2}$, $\alpha_3 = 1$
5	$\alpha_1 = 0.276393202250021$, $\alpha_2 = \frac{1}{3}$, $\alpha_3 = 0.723606797749979$, $\alpha_4 = -1$
6	$\alpha_1 = 0.204201653860479$, $\alpha_2 = 0.230959413182896$, $\alpha_3 = 0.324788653084487$, $\alpha_4 = 0.906716946538805$, $\alpha_5 = -0.226824729490652$
7	$\alpha_1 = 0.164001419299363$, $\alpha_2 = 0.180945030752080$, $\alpha_3 = 0.224567849422043$, $\alpha_4 = 0.322442384424107$, $\alpha_5 = 1.108043316102407$, $\alpha_6 = -0.110121647194359$
8	$\alpha_1 = 0.138024395659493$, $\alpha_2 = 0.150377394128368$, $\alpha_3 = 0.177126116082260$, $\alpha_4 = 0.222065352065870$, $\alpha_5 = 0.321068289581217$, $\alpha_6 = 1.324671785816124$, $\alpha_7 = 1.324671785816124$
9	$\alpha_1 = 0.119669128822673$, $\alpha_2 = 0.129338229567660$, $\alpha_3 = 0.148026233263177$, $\alpha_4 = 0.175655856970635$, $\alpha_5 = 0.220533539633299$, $\alpha_6 = 0.319746278224780$, $\alpha_7 = 1.553697400184442$, $\alpha_8 = -0.045783116925874$
10	$\alpha_1 = 0.105907195963393$, $\alpha_2 = 0.113787598394926$, $\alpha_3 = 0.127824138883028$, $\alpha_4 = 0.147160952467405$, $\alpha_5 = 0.174797828444654$, $\alpha_6 = 0.219349289937336$, $\alpha_7 = 0.318322435005099$, $\alpha_8 = 1.792850560904159$, $\alpha_9 = -0.033525393846740$

$$
\begin{aligned}
&\mathbf{P}_0 = \int_0^{\Delta t} \mathbf{p}_i\left(\Delta t - \tau\right) d\tau \\
&\frac{1}{2(n-1)}\mathbf{M}\ \Delta t\,(\mathbf{P}_1 + \frac{1}{\alpha_1}\mathbf{P}_2 + \frac{1}{\alpha_2}\mathbf{P}_3 + \ldots \\
&\quad + \frac{1}{\alpha_{n-1}}\mathbf{P}_n) = \frac{\mathbf{M}}{1!}\int_0^{\Delta t} \tau\,\mathbf{p}_i\left(\Delta t - \tau\right) d\tau \\
&\frac{1}{2(n-1)}\mathbf{M}^{\ 2}\Delta t^{\,2}\left(\mathbf{P}_1 + \mathbf{P}_2 + \mathbf{P}_3 + \ldots + \mathbf{P}_{n-1}\right) = \\
&\quad \frac{\mathbf{M}^{\ 2}}{2!}\int_0^{\Delta t} \tau^2\mathbf{p}_i\,(\Delta t - \tau) d\tau \\
&\frac{1}{2(n-1)}\mathbf{M}^{\ 3}\Delta t^{\,3}(\alpha_1\mathbf{P}_1 + \alpha_2\mathbf{P}_2 + \alpha_3\mathbf{P}_3 + \ldots \\
&\quad + \alpha_{n-2}\mathbf{P}_{n-2}) = \frac{\mathbf{M}^{\ 3}}{3!}\int_0^{\Delta t} \tau^3\mathbf{p}_i\left(\Delta t - \tau\right) d\tau \\
&\quad \ldots \\
&\frac{1}{2(n-1)}\mathbf{M}^{\ n}\Delta t^{\,n}\left(\alpha_1\alpha_2\alpha_3\ldots\alpha_{n-2}\mathbf{P}_1\right) = \\
&\quad \frac{\mathbf{M}^{\ n}}{n!}\int_0^{\Delta t} \tau^n\mathbf{p}_i\left(\Delta t - \tau\right) d\tau
\end{aligned}
\tag{20}
$$

It would be cumbersome and rather impossible in some cases to calculate the above integrations in a general form. In order to reduce the complexity and make the solution straightforward, the Taylor series expansion of the term $\mathbf{p}_i\left(\Delta t - \tau\right)$ given in the following form can be utilized.

$$
\begin{aligned}
\mathbf{p}_i\left(\Delta t - \tau\right) \approx\ & \mathbf{p}_i\left(0\right) + \frac{\dot{\mathbf{p}}_i\left(0\right)}{1!}\left(\Delta t - \tau\right) + \\
& \frac{\ddot{\mathbf{p}}_i\left(0\right)}{2!}\left(\Delta t - \tau\right)^2 + \ldots + \frac{\mathbf{p}_i^{(n)}\left(0\right)}{n!}\left(\Delta t - \tau\right)^n
\end{aligned}
\tag{21}
$$

By substituting Eq. (21) into Eq. (20), the unknown vectors $\mathbf{P}_0$ to $\mathbf{P}_n$ will be achieved.

2.2. Nonlinear Dynamic Systems

The general form of a nonlinear dynamic equation is as follows:

$$\mathbf{M}\ddot{\mathbf{u}}(t)+\mathbf{F}\left(\mathbf{u}(t),\dot{\mathbf{u}}(t)\right)=\mathbf{f}(t) \quad (22)$$

The relation between $\ddot{\mathbf{u}}(t)$ and $\mathbf{u}(t)$, $\dot{\mathbf{u}}(t)$, and $\mathbf{f}(t)$, can be expressed as:

$$\ddot{\mathbf{u}}(t)=-\mathbf{M}^{-1}\times\mathbf{F}\left(\mathbf{u}(t),\dot{\mathbf{u}}(t)\right)+\mathbf{M}^{-1}\times\mathbf{f}(t) \quad (23)$$

By considering Eq. (3), the derivative of $\mathbf{X}$ is stated as below.

$$\dot{\mathbf{x}}=\begin{Bmatrix}\dot{\mathbf{u}}(t)\\ \ddot{\mathbf{u}}(t)\end{Bmatrix} \quad (24)$$

Based on Eqs. (23) and (24), the nonlinear dynamic system shown in Eq. (22) can be represented as Eq. (23) (Brogan, 1991).

$$\begin{aligned}\dot{\boldsymbol{x}}&=\begin{Bmatrix}\dot{\boldsymbol{u}}(t)\\ \ddot{\boldsymbol{u}}(t)\end{Bmatrix}\\&=\begin{Bmatrix}\dot{\boldsymbol{u}}(t)\\ -\boldsymbol{M}^{-1}\times\boldsymbol{F}\left(\boldsymbol{u}(t),\dot{\boldsymbol{u}}(t)\right)+\boldsymbol{M}^{-1}\times\boldsymbol{f}(t)\end{Bmatrix}\\&=\begin{Bmatrix}\dot{\boldsymbol{u}}\\ -\boldsymbol{M}^{-1}\times\boldsymbol{F}\left(\boldsymbol{u}(t),\dot{\boldsymbol{u}}(t)\right)\end{Bmatrix}+\begin{Bmatrix}0_{k\times1}\\ \boldsymbol{M}^{-1}\times\boldsymbol{f}(t)\end{Bmatrix}\end{aligned} \quad (25)$$

Eq. (23) has two sections that are separately related to the state variable $\mathbf{x}=\begin{Bmatrix}\mathbf{u}(t)\\ \dot{\mathbf{u}}(t)\end{Bmatrix}$ and the input vector $\mathbf{f}(t)$. Using $\mathbf{p}(t)$ and $\mathbf{G}(\mathrm{x})$ presented in Eqs. (26) and (27), Eq. (25) can be rewritten in a compact form, which is shown in Eq. (28).

$$\mathbf{p}(t)=\begin{bmatrix}0_{k\times1}\\ \mathbf{M}^{-1}\end{bmatrix}\mathbf{f}(t) \quad (26)$$

$$\mathbf{G}(\mathbf{x})=\mathbf{G}\left(\begin{Bmatrix}\mathbf{u}\\ \dot{\mathbf{u}}\end{Bmatrix}\right)=\begin{Bmatrix}\dot{\mathbf{u}}\\ -\mathbf{M}^{-1}\times\mathbf{F}(\mathbf{u},\dot{\mathbf{u}})\end{Bmatrix} \quad (27)$$

$$\dot{\mathbf{x}}=\mathbf{G}(\mathbf{x})+\mathbf{p}(t) \quad (28)$$

Similar to the procedure explained for linear dynamic systems, in order to obtain $\mathbf{x}_{i+1}=\begin{Bmatrix}\mathbf{u}_{i+1}\\ \dot{\mathbf{u}}_{i+1}\end{Bmatrix}$ at the time step i, the values of $\mathbf{x}_i=\begin{Bmatrix}\mathbf{u}_i\\ \dot{\mathbf{u}}_i\end{Bmatrix}$ and $\mathbf{P}_0$ to $\mathbf{P}_n$ are needed. The values of $\mathbf{P}_0$ to $\mathbf{P}_n$ are calculated by using $\mathbf{p}(t)$ and through the solution of Eq. (20). The procedure to obtain $\mathbf{X}_{i+1}$ is shown in Figure 1.

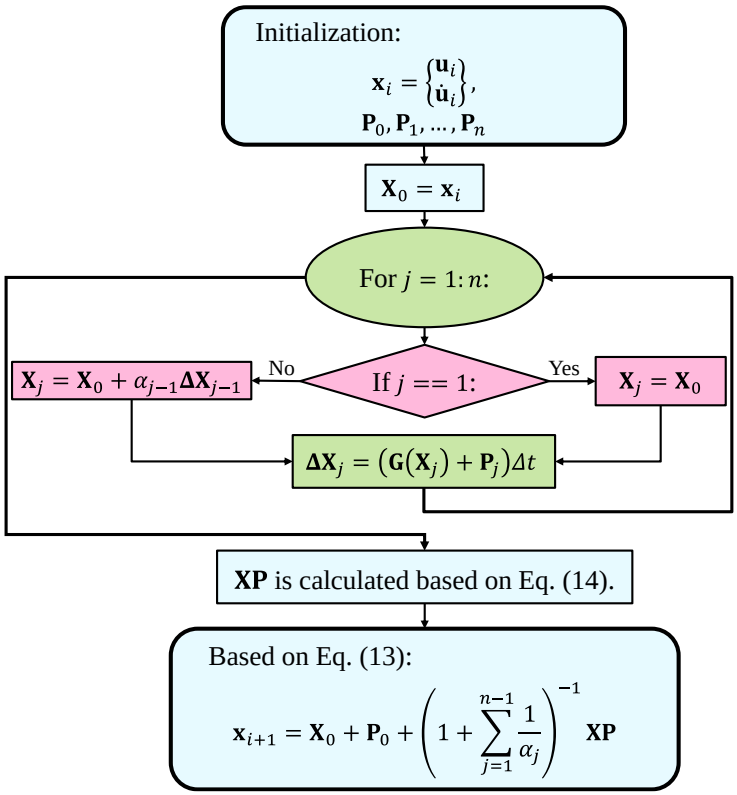

Fig. 1. The procedure for calculating $\mathbf{x}_{i+1}$ at the time step i

Based on the flowchart illustrated in Figure 1, at the beginning of the ith time step, the values of $\mathbf{x}_i$ and $\mathbf{P}_0$ to $\mathbf{P}_n$ are considered. At the first, $\mathbf{X}_0$ is set as $\mathbf{x}_i$. In the next step, using an iterative procedure, the increment $\mathbf{\Delta X}_j$ is calculated for $j=1$ to n. In each iteration, $\mathbf{\Delta X}_j$ is achieved by using $\mathbf{G}(.)$ function given in Eq. (27) and $\mathbf{P}_j$ provided at the beginning of the time step i. Finally, the value of $\mathbf{x}_{i+1}=\begin{Bmatrix}\mathbf{u}_{i+1}\\ \dot{\mathbf{u}}_{i+1}\end{Bmatrix}$ is achieved by using Eq. (13). Different increments of the variable $\mathbf{X(\Delta X}_j\mathbf{)}$ are obtained explicitly and there is no recursive solution to calculate them. Also, the values of $\mathbf{P}_0$ to $\mathbf{P}_n$ are explicitly achieved by using Eqs. (20) and (21). Therefore, the new family can be categorized into explicit time integration groups.

3. Amplification Matrix

To assess the stability and numerical accuracy of the proposed method, the amplification matrix should be obtained. This matrix is calculated for a linear structure having one degree of freedom, which is shown in Eq. (29).

$$\ddot{u}(t)+2\xi\omega\dot{u}(t)+\omega^2u(t)=0 \qquad (29)$$

where ω and ξ: refer to the natural frequency and damping ratio of the structure, respectively. When the new scheme is applied to find the solution of the above system in the time step i, the following relationship can be presented for the solutions at the beginning and end of the time steps i:

$$\begin{Bmatrix}u_{i+1}\\ \dot{u}_{i+1}\end{Bmatrix}=\mathbf{A}(\Delta t)\begin{Bmatrix}u_i\\ \dot{u}_i\end{Bmatrix} \qquad (30)$$

where **A**: is the amplification matrix of the new method and can be presented in the following form by using Eq. (16).

$$\mathbf{A}(\Delta t)=\mathbf{I}_{2\times2}+\sum_{s=1}^{n}\frac{\mathbf{M}^{\,s}\Delta t^s}{s!} \qquad (31)$$

Matrix **M** : is the state coefficient matrix introduced in Eq. (5) and can be obtained for the system of Eq. (29) as below.

$$\mathscr{M}=\begin{bmatrix}0_{1\times1} & I_{1\times1}\\ -(1)^{-1}(\omega^2) & -(1)^{-1}(2\xi\omega)\end{bmatrix}=\begin{bmatrix}0 & 1\\ -\omega^2 & -2\xi\omega\end{bmatrix} \qquad (32)$$

4. Numerical Stability

A method is called numerically stable if displacement and velocity at time t do not unlimitedly increase during the solution process. In a numerically stable technique, the physical conditions of the problem should not be intensified by the numerical procedures after several time steps. The stability of the proposed method is evaluated using the spectral radius of the amplification matrix. The spectral radius holds the following form for the amplification matrix $\mathbf{A}$ obtained in Eq. (31).

$$\rho(\mathbf{A})=\max\left(|\lambda_1|,|\lambda_2|\right) \qquad (33)$$

where λ_1 and λ_2: are the eigenvalues of the amplification matrix **A**, and $|.|$: is the absolute operator. The inequality $\rho(\mathbf{A})\le1$ must be satisfied for all values in Δt, to make sure that a numerical method is stable (Bathe and Wilson, 1972; Bathe, 1982; Rezaiee-Pajand et al., 2018). The spectral radius of the amplification matrix for the Newmark linear acceleration (NLA) method (Newmark, 1959), the 4th-order Runge-Kutta (RK4) technique (Kutta, 1901), and the 5th- to 7th-order of the proposed family are depicted in Figure 2. Moreover, Figure 3 presents the results for $n=1$ to 10 against $\frac{\Delta t}{T}$. In these two figures, the damping ratio is considered to be zero. Based on Figure 2, as a weak point, the stability of the various orders of the new family is conditional. According to Figure

2, the largest stability domain belongs to NLA, RK4, and NRKF7, respectively. However, as is illustrated in Figure 3, from a general point of view, the stability domain increases by raising the value of *n*.

5. Numerical Accuracy

It is a common way that the accuracy of any time integration method is evaluated by assessing the order of accuracy, period error, and amplitude decay (Chung and Hulbert, 1993; Rezaiee-Pajand et al., 2021). The order of accuracy of the authors' scheme will be examined in Section 6. Using the eigenvalue of the amplification matrix, one can be able to evaluate the numerical errors using the following relations (Bathe, 1982; Hughes, 2012).

$$\begin{aligned}
&\lambda_{1,2} = \bar{a} \pm i\bar{b} = e^{\left(-\bar{\xi}\bar{\omega} \pm i\bar{\omega}_d\right)\Delta t} \\
&\bar{\omega} = \frac{\arctan\left(\bar{a} / \bar{b}\right)}{\sqrt{1-\xi^2}\,\Delta t} \\
&\bar{\omega}_d = \bar{\omega}\sqrt{1-\xi^2} \\
&\bar{\xi} = -\frac{\ln\left(\bar{a}^2 + \bar{b}^2\right)\sqrt{1-\xi^2}}{2\arctan\left(\bar{b} / \bar{a}\right)}
\end{aligned} \tag{34}$$

in which $\bar{\xi}$: denotes the numerical damping ratio of a time integration method. Additionally, the numerical period can be calculated using $\bar{T} = \frac{2\pi}{\bar{\omega}}$. Period error is estimated by comparing $\bar{T}$ and the true period $T = \frac{2\pi}{\omega}$.

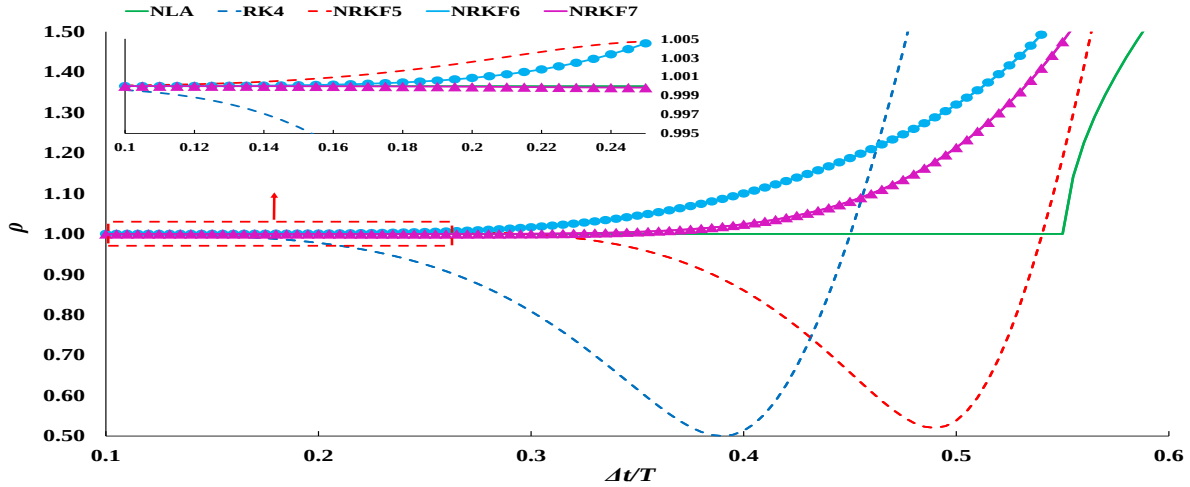

Fig. 2. The spectral radius for various schemes

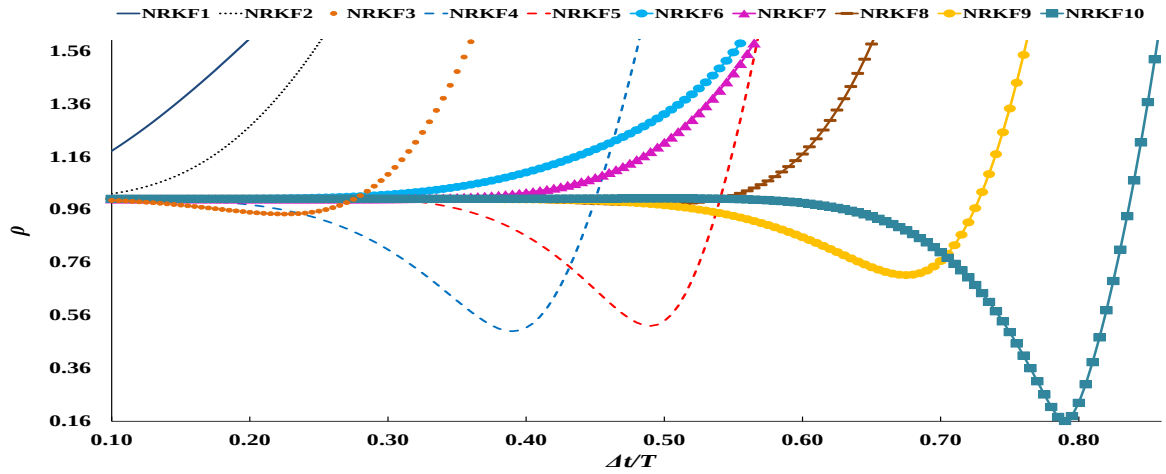

Fig. 3. The spectral radius for various orders of the new family

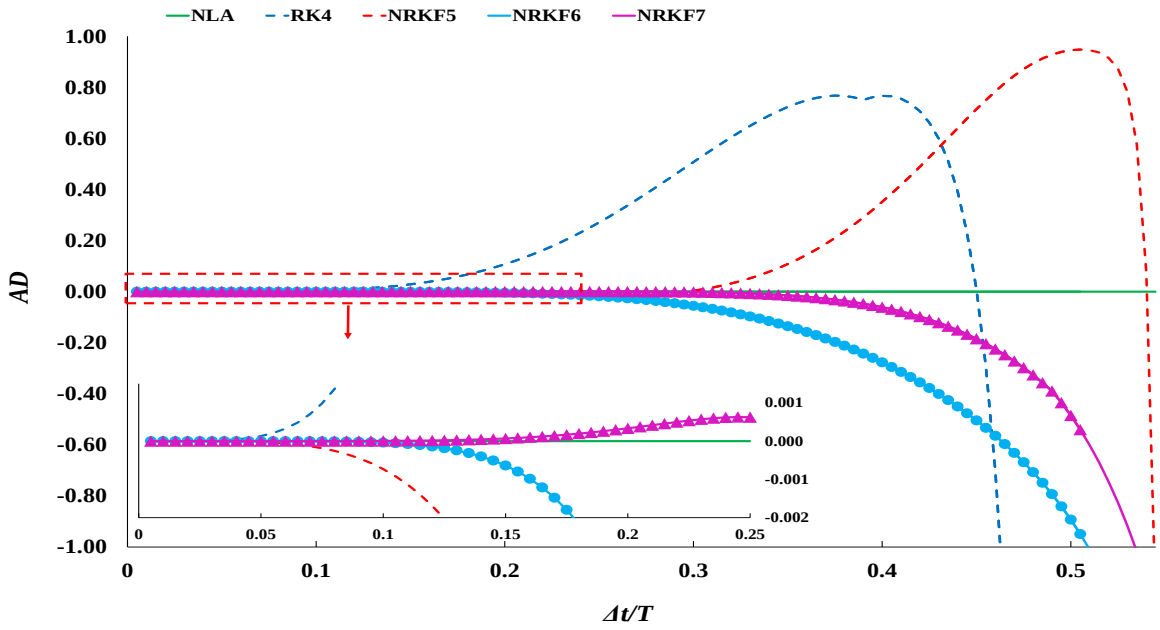

Fig. 4. Amplitude decay for various schemes

Figures 4 to 7 compare the amplitude decay and period error of the present scheme against those of the other solution techniques. Based on Figure 4, the NLA method has no elongation error, in the given domain. The proposed family method, having orders of 7, 6, and 5, and finally, the RK4 scheme possesses lower elongation errors, respectively. Figure 5 clearly indicates that an increment in the order of the presented family will lead the amplitude decay error to become nearly zero in a great interval of Δt.

According to the results shown in Figure 6, the nearest method in period error value to zero belongs to the proposed method with the order of 7. Then, the methods with the orders of 6 and 5, and the classic 4^{th}-order Runge-Kutta scheme have lower values in period error, respectively. The NLA scheme has more value in period error compared to all other proposed schemes. Figure 7 displays the values of period error among different orders of the new family. As it can be observed, the value of the period error decreases as the order of the family raises.

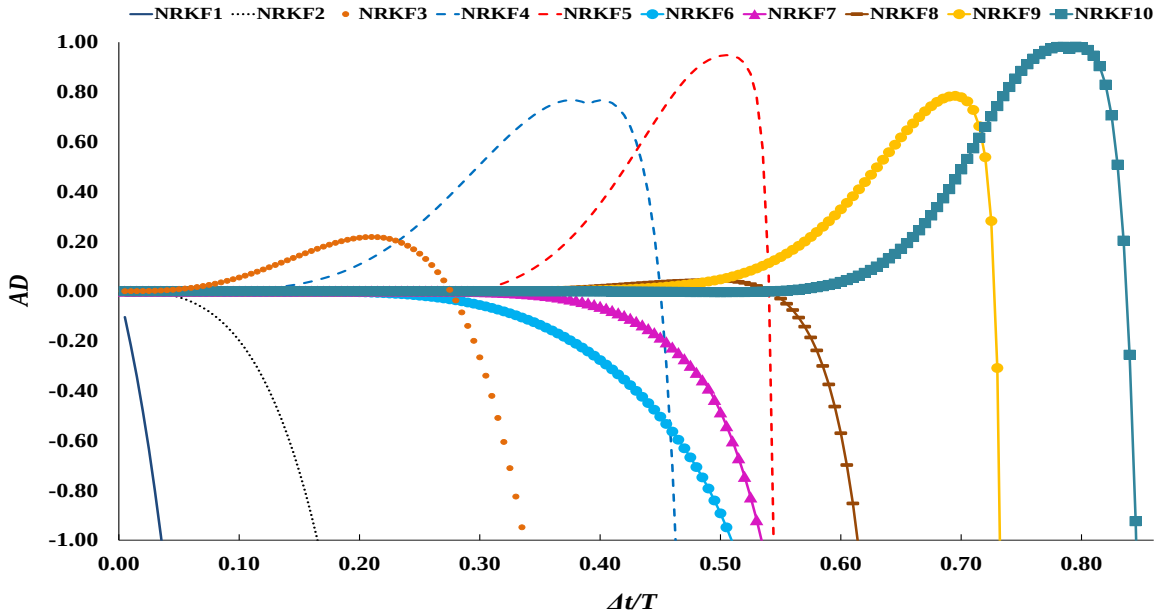

Fig. 5. Amplitude decay for various orders of the new family

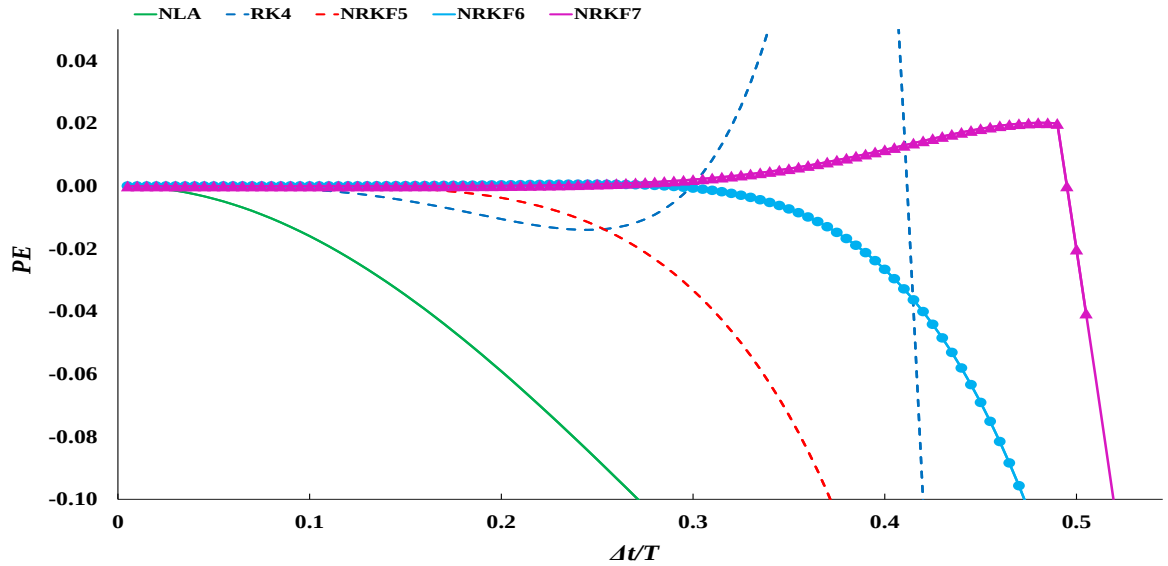

Fig. 6. Period error for various schemes

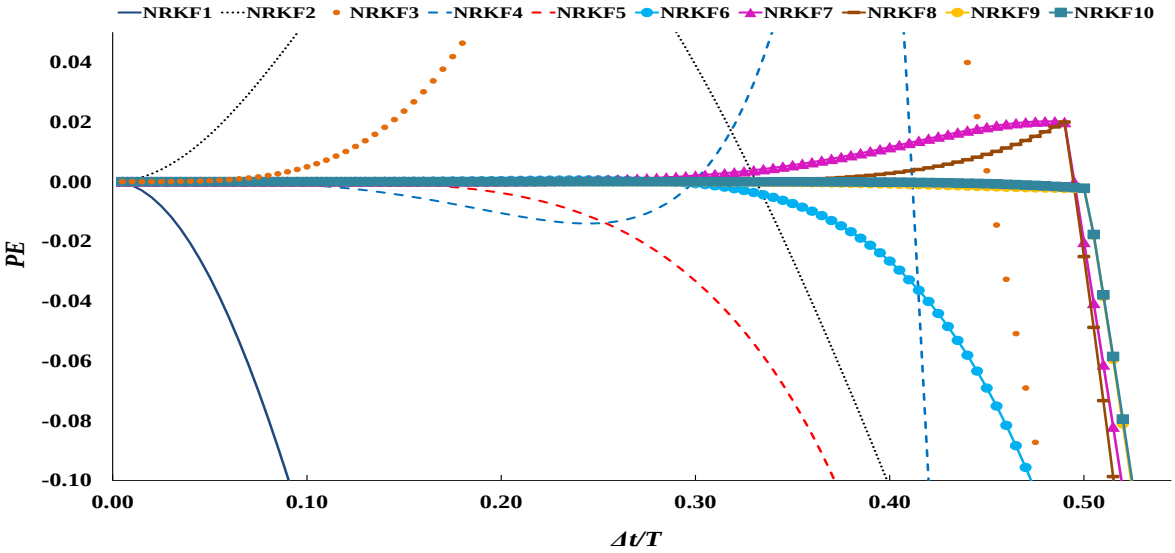

Fig. 7. Period error for various orders of the new family

6. Order of Accuracy

In order to determine the order of accuracy of the new time integration method, the amplification matrix of the proposed method should be compared with the analytical one (Hulbert and Hughes, 1987; Rezaiee-Pajand et al., 2021). To derive the analytical amplification matrix, the equation of motion given in Eq. (29) is considered. This equation can be changed into the subsequent equivalent first-order differential equation:

$$\dot{\mathbf{x}} = \mathbf{M}\, \boldsymbol{x} \tag{35}$$

where

$$\mathbf{x} = \begin{Bmatrix} u \\ \dot{u} \end{Bmatrix} \tag{36}$$

$$\mathbf{M} = \begin{bmatrix} 0 & 1 \\ -\omega^2 & -2\xi\omega \end{bmatrix} \tag{37}$$

The exact solution for Eq. (35) with the given initial vector $\mathbf{x}_0 = \begin{Bmatrix} u_0 \\ \dot{u}_0 \end{Bmatrix}$ can be expressed as follows (Turyn, 2013):

$$\mathbf{x} = e^{\mathbf{M}\, t}\mathbf{x}_0 \tag{38}$$

Therefore, the following recursive relationship is obtained.

$$\mathbf{x}_{i+1} = e^{\mathbf{M}\,\Delta t}\mathbf{x}_i \tag{39}$$

The matrix $e^{\mathbf{M}\,\Delta t}$, which is the analytical amplification matrix in the equation of motion given in Eq. (29), can be expanded into Taylor series, as below (Moler and Van Loan, 2003).

$$e^{\mathbf{M}\,\Delta t} = \mathbf{I} + \sum_{s=1}^{\infty} \frac{\mathbf{M}^{\,s}\Delta t^{s}}{s!} \tag{40}$$

By comparing the Taylor series expansion of the amplification matrix outlined in Eq. (31), which belongs to the proposed family, and that in Eq. (40), it is concluded that the order of accuracy of the present family is equal to n (the order of the proposed family).

7. Numerical Examples

In this section, numerical examples are presented to establish the accuracy and advantages of the proposed methods. Various problems in the scope of structural and mechanical engineering, including an undamped single degree of freedom oscillator, five stories shear building with non-classic damping, a structure with two degrees of freedom subjected to impact loading, a plane truss, a three-dimensional truss, and two nonlinear systems with many degrees of freedom, are employed. The nonlinear experiments include a nonlinear mass-spring-damper system with 100 Dofs and a tall shear building structure subjected to a realistic load, the El-Centro ground motion. All linear examples are analyzed and compared through different numerical schemes, including the Newmark Linear Acceleration (NLA) technique, the 4th-order classic Runge-Kutta (RK4) scheme, an implicit 4th-order Runge-Kutta method presented by Fok (2016) (CKRK), an implicit three-step method suggested by Zhao and Wei (2014) (SRK3), and the proposed family methods by the orders of 5, 6 and 7 (NRKF5, NRKF6, and NRKF7). The solution of the nonlinear mass-spring-damper structure is added to illustrate the capability of the new family in the analysis of nonlinear dynamic systems with many degrees of freedom. Furthermore, the example of a tall shear building structure is used to demonstrate the ability of the new family methods over broadly accepted methods such as the generalized-α method (Chung and Hulbert,1993), and the higher-order implicit method, SRK3, in comparison to dealing with many degrees of freedom nonlinear structures subjected to a realistic load.

7.1. Undamped Single Degree of Freedom Oscillator

In the first example, the following 2nd-order differential equation is considered. It should be reminded that this equation has been widely adopted in evaluating the accuracy of several time integration schemes (Bathe, 1982; Rezaiee-Pajand et al., 2018; Rezaiee-Pajand et al., 2021).

$$\ddot{u} + u = 0 \tag{41}$$

It is assumed that the initial values of u_0 and $\dot{u}_0$ are equal to 1000 and 0, respectively. The exact solution of Eq. (41) is given by $u_{ex} = 1000\cos(t)$. The time step in the numerical integration procedures is assumed as $\Delta t = 0.1$ s and the total time of the analysis is equal to $t = 10$ s. Figure 8 illustrates the logarithmic values of error for different methods in base 10.

According to the results demonstrated in Figure 8, the proposed family having an order of 7 gives the lowest value of error, while the NLA method possesses the highest error value. Figure 9 depicts the error values for two other techniques, the CKRK scheme and the new family method of order 5. Based on this figure, the suggested method of this paper leads to a lower error value compared to the CKRK scheme.

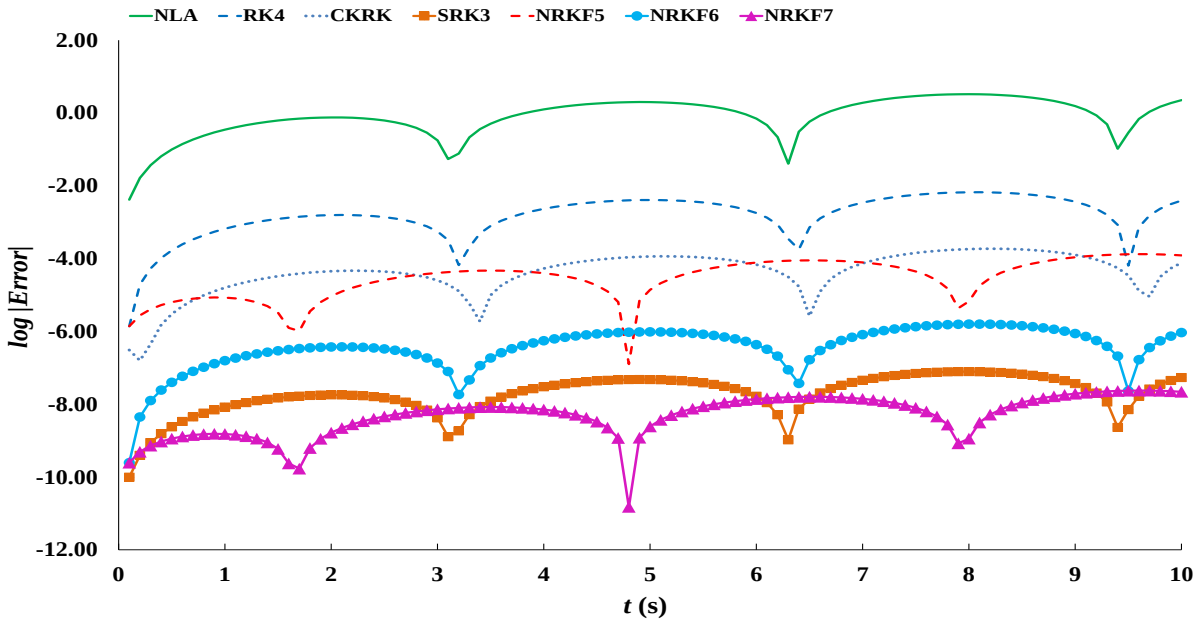

Fig. 8. Logarithmic error for different methods

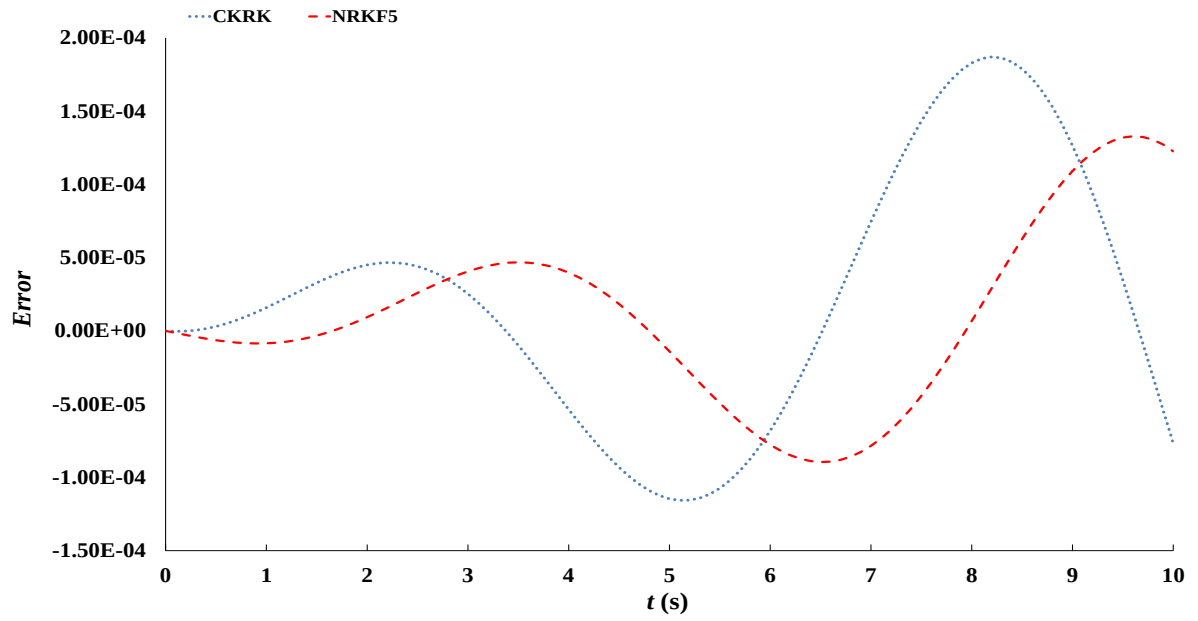

Fig. 9. Error comparison between the CKRK and NKRF5 schemes

According to Figure 8, the maximum values of the errors for the NRKF7 and SRK3 methods are equal to -7.625 and -7.105, respectively. Aside from this, as shown in Figure 9, the maximum values of errors are 1.328×10^{-3} and 1.870×10^{-3} for the NRKF5 and CKRK methods, respectively. In these comparisons, the NRKF5 and NRKF7 are explicit methods, although the CKRK and SRK3 methods are implicit schemes. The comparison between the maximum values of errors in these techniques illustrates that the proposed explicit family has higher abilities in solving undamped systems, compared to the implicit methods.

7.2. Five Stories Shear Building with Non-Classical Damping

Figure 10 depicts a shear frame building, which was investigated by Rezaiee-Pajand et al. (2018). All stories have an equal mass of 2.616×10^{6} Kg. The stiffness of the second to fifth stories is considered as 981×10^{6} N/m. The stiffness of the first story is 20% larger than that of the other stories.

It should be added that the first story is equipped with a damping device. In this regard, the damping matrix consists of two parts. The classic damping of the structure is obtained by $\mathbf{C}_c = 0.3\mathbf{M} + 0.002\mathbf{K}$. Aside from this, the term $20\,\mathbf{C}_c(1,1)$ is added to the damping of the first degree of freedom of the structure. As it is shown in Figure 10, five lateral forces are applied to the structure. The equation of these forces is given by:

$$\mathbf{f}(t) = 2.616\times10^6\{1,1,1,1,1\}^T \sin(\pi t) \qquad (42)$$

Selecting the time step as $\Delta t = 0.01$s, this example is analyzed using different techniques. The near-exact solution for this problem is obtained by the RK4 method with a very tiny time step equal to 0.00001 s. Figure 11 depicts the error of different methods in calculating the horizontal displacement of the fifth story compared to the near-exact solution.

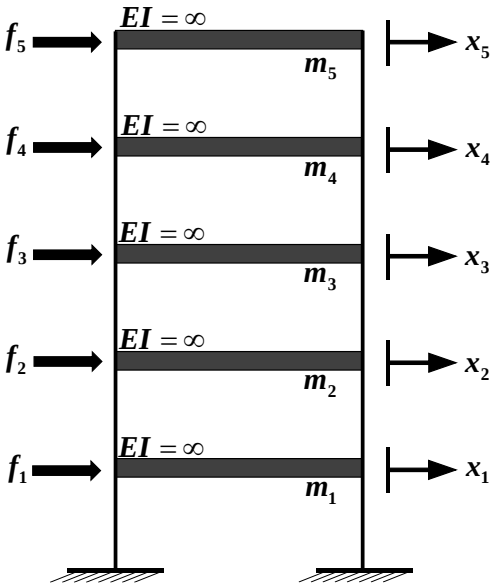

Fig. 10. Five stories shear building

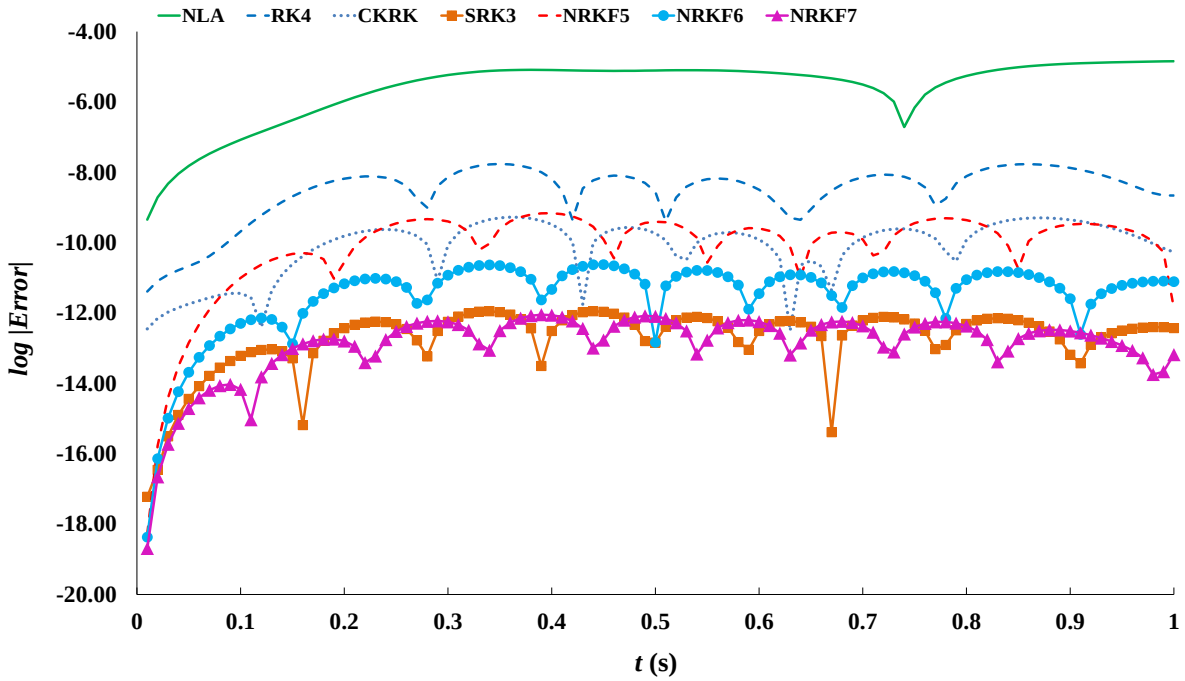

Fig. 11. Error of the horizontal displacement of the fifth story

Based on the results shown in Figure 11, the NRKF5 and CKRK methods have lower analysis errors compared to the NLA and RK4 schemes, which are more applicable time integration methods in civil engineering fields. The solution obtained by the NRKF6 is more accurate than the one from the implicit CKRK method. The 7th-order method of the new family and SRK3 technique furnished the best accuracy in the analysis. Figure 12 presents a more exact comparison between the error values of the NKRF7 and SRK3 methods. As it is illustrated in Figure 12, the value of error is larger in the SRK3 scheme compared to the NRKF7 method. The outcomes reveal that the accuracy of the proposed family in analyzing non-classic structural problems is better than the other methods.

7.3. A Structure with Two Degrees of Freedom Subjected to Impact Loading

Some researchers investigated a dynamic system with two degrees of freedom subjected to impact loading (Rezaiee-Pajand et al., 2018). The equilibrium equation of this system and the applied loads are expressed as follows.

$$\begin{bmatrix} m & 0 \\ 0 & 3m \end{bmatrix} \ddot{\boldsymbol{u}} + \begin{bmatrix} 3k & -2k \\ -2k & 6k \end{bmatrix} \boldsymbol{u} = \begin{bmatrix} 0 \\ 1 \end{bmatrix} \times f(t) \tag{43}$$

$$f(t) = \begin{cases} 1000(1-10t) & 0 \le t \le 0.1 \\ 0 & t \ge 0.1 \end{cases} \tag{44}$$

The values of stiffness k and mass m are equal to 1000 N/m and 0.5 Kg, respectively. The exact solution can be attained via modal analysis. By choosing a value of 0.001 s for the time step, the system is analyzed with different methods. The values of error for the time integration methods are shown in Figure 13. Based on the results obtained, the NLA method and the fourth-order classic Runge-Kutta lead to the highest errors in the analysis. The highest values of error for these methods are equal to -2.568 and -5.517, respectively. As it is demonstrated in the figure, the error of the analysis for the new family method decreases as the order of family increases. The highest values of error for the orders of 5, 6, and 7 are equal to -7.377, -9.309, and -11.290, respectively. Moreover, the NKRF7 method has better accuracy in comparison to the implicit SRK3 scheme. The results indicate that the proposed family is capable of analyzing structures subjected to impact loading over other techniques.

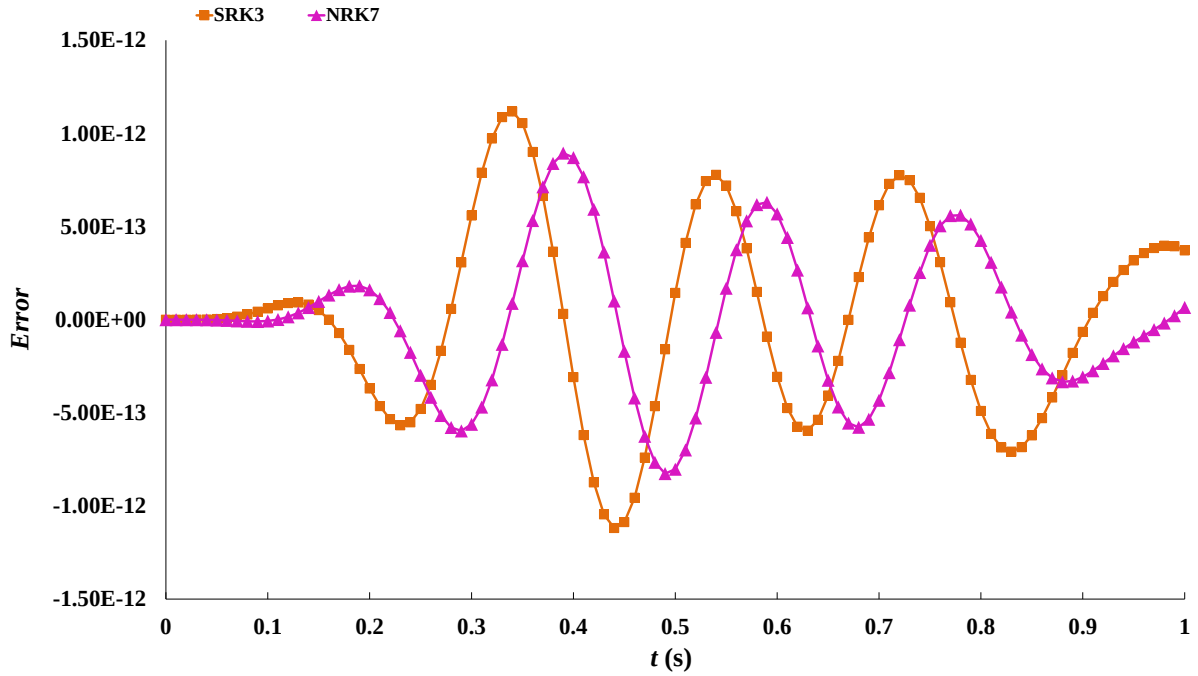

Fig. 12. Error comparison between the SRK3 and NRKF7 methods

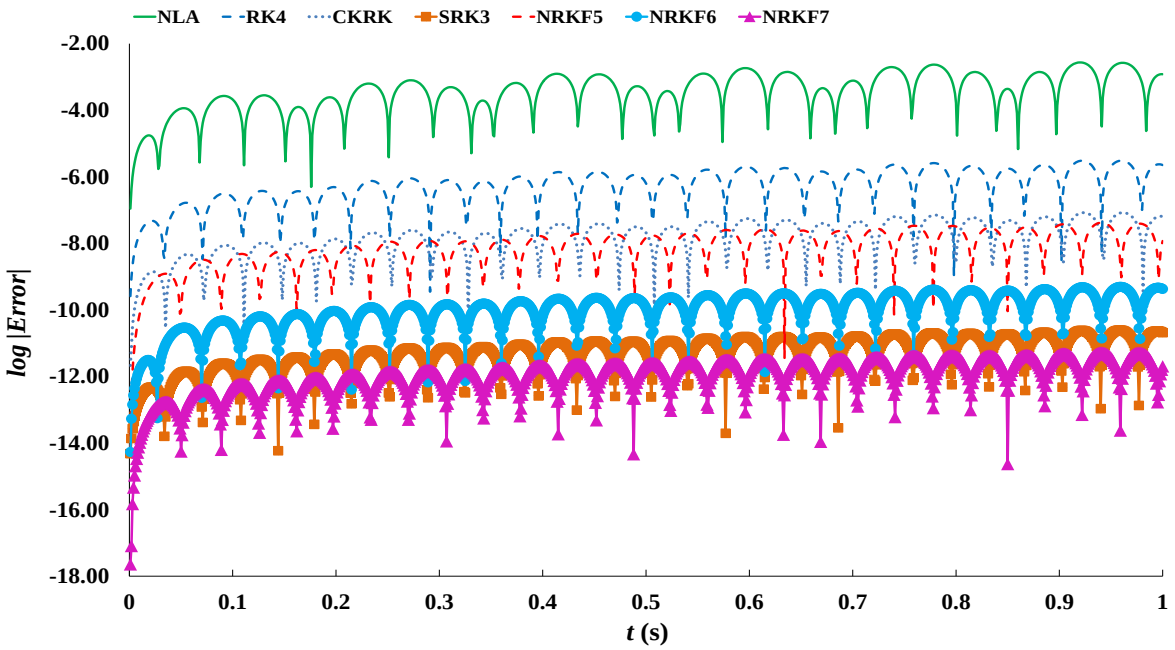

Fig. 13. Error of u_1 of 2Dof structure

7.4. Plane Truss

The plane truss represented in Figure 14 comprises three elements and 3 degrees of freedom (Paz and Kim, 2018). The characteristics of the members are outlined in Table 2. A constant horizontal force equal to 22241.108 N is applied to node 1. Figure 15 portrays the error value for horizontal displacement of this node in the final steps of the analysis. The related exact responses are obtained by using modal analysis.

The NRKF7 and NLA methods lead to the smallest and largest error values in the analysis, respectively. The maximum values of the error for these methods are equal to -11.030 and -3.539, respectively. The error values of NRKF5 and CKRK schemes are nearly equal. The maximum value of error for these methods is almost equal to -7.588. Based on the results, it is obvious that an increase in the order of the new family reduces the error of the analysis. The results of this example demonstrated in Figure 15 illustrate that the suggested family is capable of analyzing two-dimensional structures.

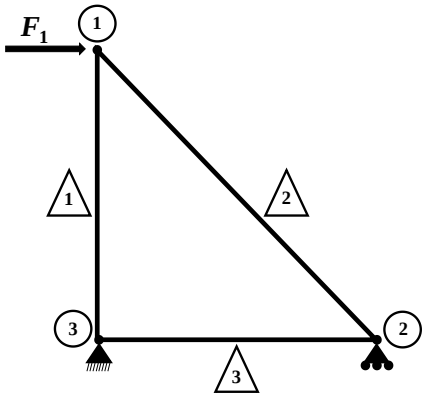

Fig. 14. Three members plane truss

Table 2. Characteristics of the plane truss

Member	Area (mm^2)	Length (mm)	E (N/m^2)	$\bar{m}$ (N.sec^2/m^2)
1	6451.6	1524.0	2.06844×10^{11}	689.48
2	6451.6	2155.3	2.06844×10^{11}	689.48
3	6451.6	1524.0	2.06844×10^{11}	689.48

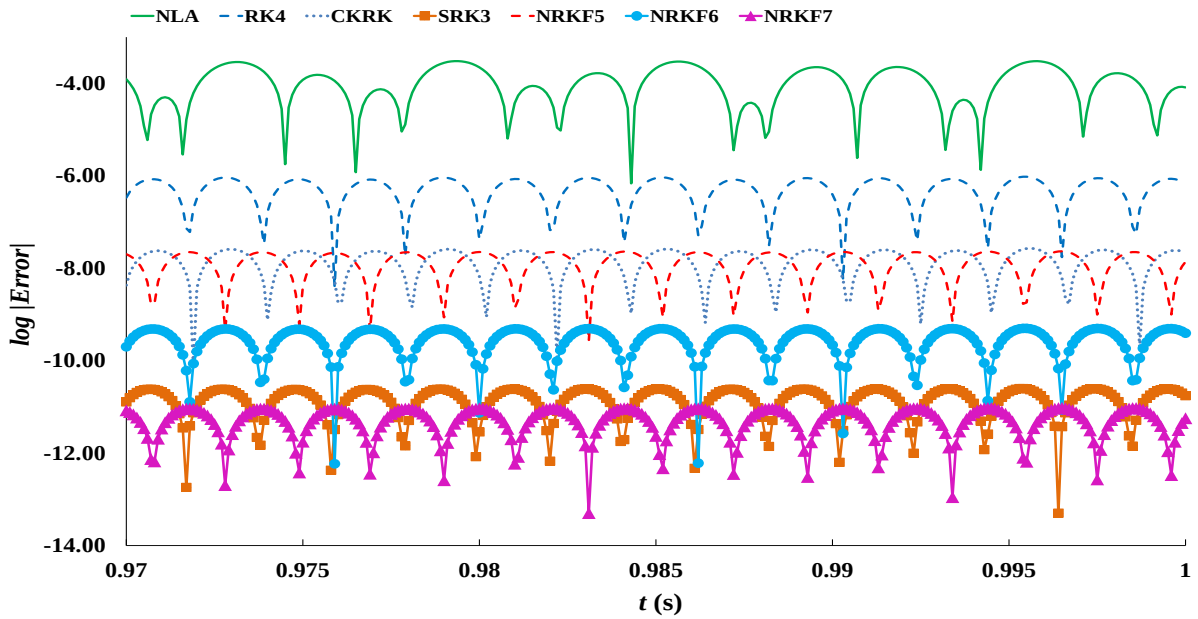

Fig. 15. The horizontal displacement error of node 1

7.5. Three-Dimensional Truss

The structure shown in Figure 16 illustrates a three-dimensional truss. The nodal coordinates are available in Table 3. The elastic modulus and density of members are given as $E = 2\times10^{11}$ N/m^2 and $\rho = 7850$ Kg/m^3, respectively. In this structure, the upper node is subjected to two forces in the X- and Y-directions. These forces are equal to $F_x = 4000$ kN and $F_y = 16000$ kN. The cross-sectional area of highlighted members indicated by *b* is equal to 1935 mm^2, and that of pale members named *a* is equal to 3870 mm^2. The smallest period of this structure is $T_{\min} = 2.59\times10^{-3}$ s. The responses of this structure are obtained up to $t = 1.25\times10^{6}\,T_{min}$ s by choosing the time steps of $\Delta t = 0.01T_{min}$ s. Figure 17 demonstrates the values of error in vertical tip displacement within the timeline $\left[1247.5\times10^{3} - 1250\times10^{3}\right]T_{min}$ s of the analysis. Moreover, the exact solution of the three-dimensional truss is available by using modal analysis.

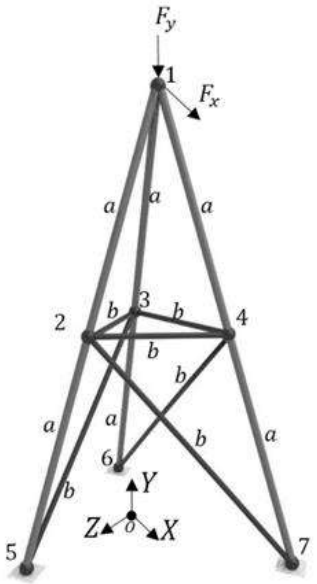

Fig. 16. The three-dimensional truss

Table 3. Characteristics of the three-dimensional truss

Node number	X (mm)	Y (mm)	Z (mm)
1	0	9144	0
2	0	4572	1524
3	-1219.2	4572	-914.4
4	1219.2	4572	-914.4
5	0	0	3048
6	-2438.4	0	-1828.8
7	2438.4	0	-1828.8

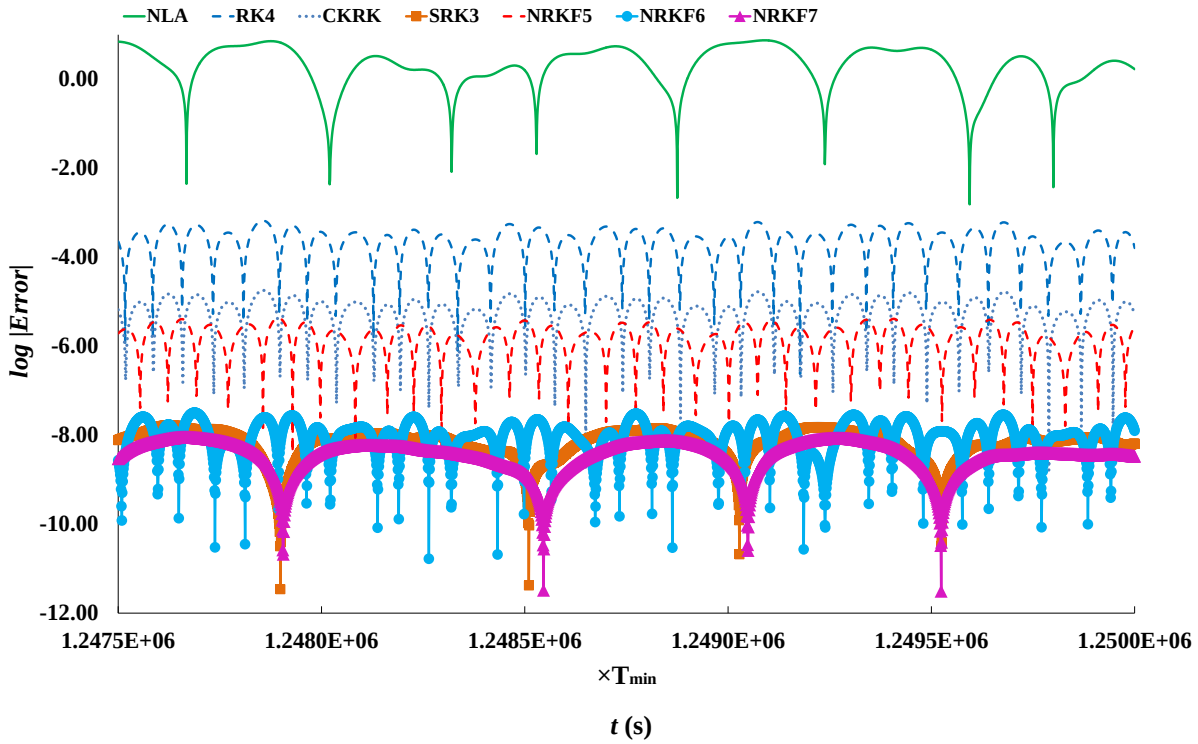

Fig. 17. Error of the top node vertical displacement

Error in each numerical integration method is calculated through Eq. (45).

$$Err = \sqrt{L_2 norm\left(x_{exact}\left(t\right) - x_{scheme}\left(t\right)\right)}$$
$$L_2 norm\left(x\left(t\right)\right) = \sum_t \left(x\left(t\right)\right)^2 \quad (45)$$

Values of *Err* for different time integration methods and CPU time of each method are reported in Table 4.

The results presented in Figure 17 and Table 4 indicate that the highest accuracy belongs to the 7th-order method of the new family, while the Newmark linear acceleration technique leads to the lowest precision. The values of *Err* for these schemes are equal to 2.69×10^{-6} and 2.34×10^{3}, respectively. Based on the results obtained in Table 4, the fourth-order Runge-Kutta method has the highest value in CPU time, which is equal to 146.11 s. On the other hand, the lowest value for CPU time with good accuracy is for the method NRKF5, which is equal to 69.53s. The NRKF7 method has a better performance compared to the SRK3 method in accuracy and CUP time. The values of *Err* and CPU time for the NRKF7 method are 2.69×10^{-6} and 84.84 s, and are 4.87×10^{-6} and 95.05 s for the SRK3 method. From the obtained results, one can conclude that the new explicit family has a good ability to analyze structural dynamic systems in low CPU time with acceptable accuracy. Furthermore, according to the outcomes, the present family methods show their ability in the analysis of three-dimensional problems.

7.6. A Nonlinear Mass-Spring-Damper System with 100 Dofs

Figure 18 illustrates a nonlinear system of masses, springs, and dampers with 100 Dofs. The relations for the forces applied due to nonlinear springs ($F_{k,i}(x)$) and nonlinear dampers ($F_{c,i}(\dot{x})$) are shown in Figure 19 (Rezaiee-Pajand and Karimi-Rad, 2017; Rezaiee-Pajnd et al., 2021). The values for the masses (M_i), and the coefficients K_i and C_i, are given in Table 5. The coefficients β_k and β_c are equal to 0.8. Also, for each nonlinear stiffness and damper, the values of u_x and $v_{\dot{x}}$ are equal to 1 m and 1 m/s, respectively.

No load is applied to the structure, and the initial displacement and velocity for all nodes are 0, except for the last node. The initial values for displacement and velocity of this node (x_{100} and $\dot{x}_{100}$) are 2 m and 2 m/s, respectively. The near-exact solution is achieved by the fourth-order Runge-Kutta with a very tiny time step $\Delta t_{ex} = \frac{\pi}{1.6\sqrt{3}} \times 10^{-3}$ s. Table 6 shows the results obtained by the various orders of the suggested family in the time interval of $\left[0 - \frac{100\pi}{1.6\sqrt{3}}\right]$ s. Due to the explicitly of the fourth-order Runge-Kutta method, as well as, the new family, there is no need for any iterative nonlinearity solution methods, such as Newton-Raphson iterations. The responses are obtained for three cases with different time steps (Δt). The value of $RMSE$, the root of mean squares of the errors for all Dofs, can be obtained by the following equation.

$$RMSE_{scheme} = \sqrt{\frac{1}{steps} \times \sum_{i=1}^{100} \sum_{j=1}^{steps} \left(\mathbf{x}_{i,exact}(t_j) - \mathbf{x}_{i,scheme}(t_j)\right)^2} \quad (46)$$

The results presented in Table 6 show that different orders of the new family can analyze properly nonlinear dynamic systems with many degrees of freedom. According to these results, as the order of the family increases, the value of $RMSE$ decreases. Based on the experiments in Case 1 ($\Delta t = 1000\Delta t_{ex}$), by increasing the order of the family, the solution becomes more stable. As shown by the numerical results, the NRKF5 method becomes unstable; however, the NRKF6 and NRKF7 schemes have more stable results. The results for Cases 2 and 3 reveal that for nonlinear dynamic analysis, the NRKF6 method can obtain solutions with low error, and even is more accurate than the NRKF7 method (Case 3). In this manner, the NRKF6 can be chosen as the optimum member of the new family, for nonlinear dynamic analysis.

Table 4. CPU time and error of various schemes

Scheme	NLA	RK4	CKRK	SRK3	NRKF5	NRKF6	NRKF7
CPU Time (s)	21.35	146.11	81.47	95.05	69.53	74.18	84.84
Err (mm)	2.34×10^{3}	2.01×10^{-1}	5.44×10^{-3}	4.87×10^{-6}	1.37×10^{-3}	8.88×10^{-6}	2.69×10^{-6}

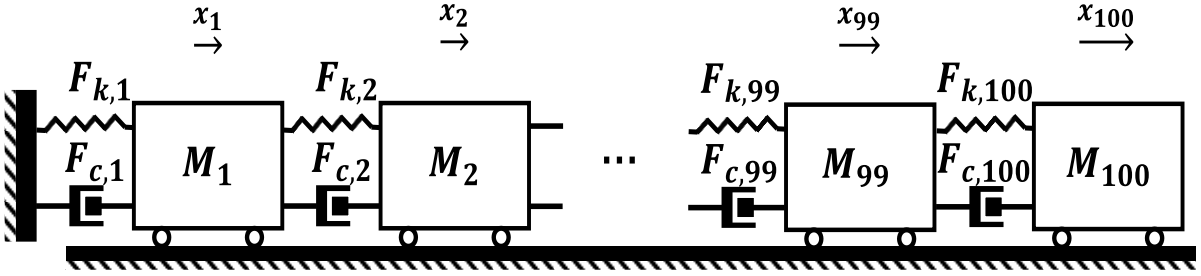

Fig. 18. The nonlinear mass-spring-damper system with 100 Dofs

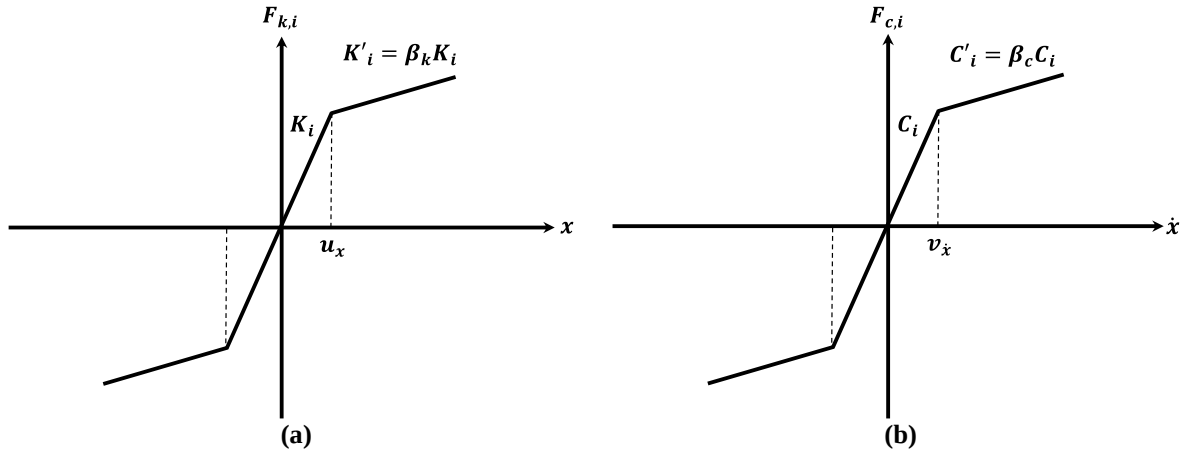

Fig. 19. Relations for stiffness and damping forces: a) Stiffness force; and b) Damping force

Table 5. The values of M_i, K_i and C_i for various nodes

Number	M_i (kg)	K_i (N/m)	C_i (N.s/m)
1-30	1	3	0.50
31-70	1	2	0.10
71-100	1	1	0.15

Table 6. The values of $RMSE$ for the suggested family

Case.	Δt	Steps	RMSE		
			NRKF5	NRKF6	NRKF7
1	$1000\Delta t_{ex}$	100	∞	4.194×10^{1}	3.521×10^{-2}
2	$500\Delta t_{ex}$	200	6.222×10^{-3}	3.569×10^{-3}	3.493×10^{-3}
3	$100\Delta t_{ex}$	1000	3.809×10^{-4}	2.910×10^{-4}	2.926×10^{-4}

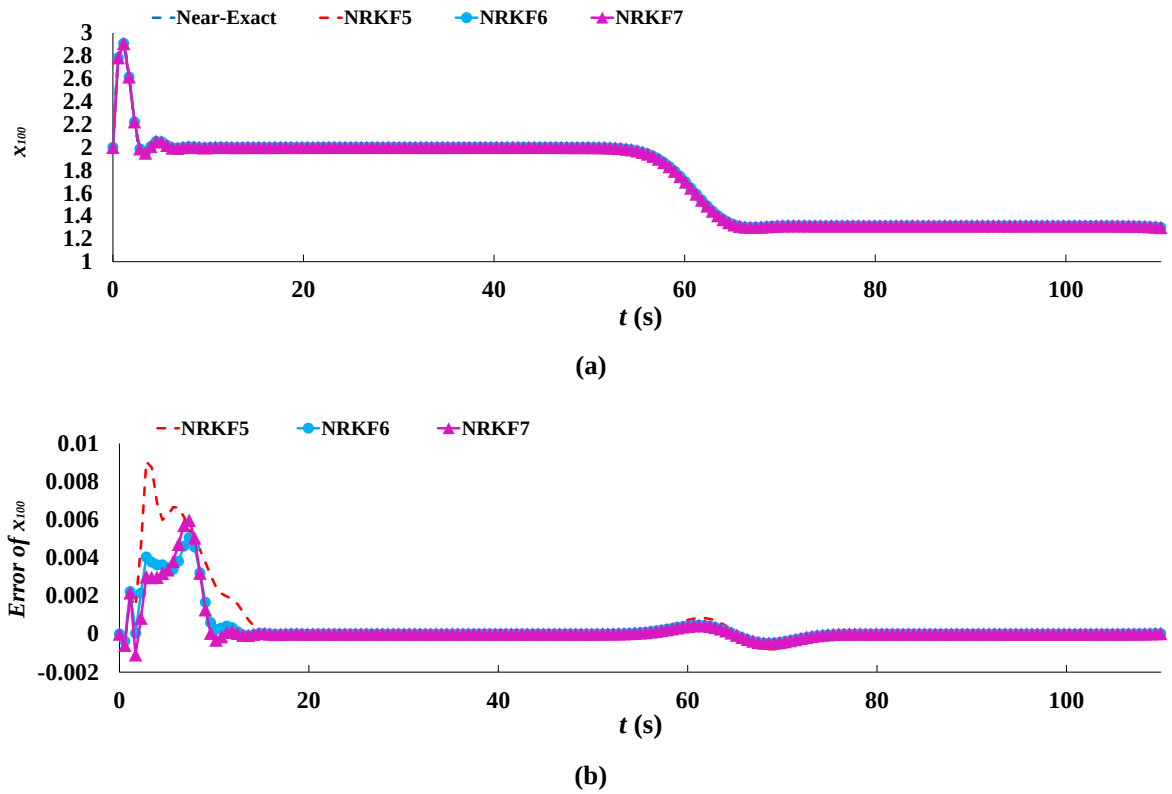

Fig. 20. Solutions of x_{100} from various orders of the new family: a) The values of x_{100}; and b) The errors of the solutions

Further to this, Figure 20 shows solutions of x_{100} by various orders of the new family obtained in the condition of Case 2. As shown in Figure 20, all orders of the new family have a good performance in achieving accurate results for nonlinear systems with many degrees of freedom. It is noteworthy that the smallest period of this structure is equal to 2.565 s and the time step chosen to analyze the system as shown in Case 2, is equal to 0.567 s ($500\,\Delta t_{ex}$), which means the time step used is not a very small value. Therefore, one can conclude that various orders of the new family have the capability in solving nonlinear systems with many degrees of freedom, in the case of using a logical time step.

7.7. A Tall Shear Building Subjected to El-Centro Ground Motion

In this example, the dynamics of a tall shear building subjected to a realistic ground motion are analyzed. This shear building shown in Figure 21 is a fifty-story structure. The nonlinear behavior of the structure has been assumed as the bilinear model demonstrated in Figure 22. The elastic stiffness is $K_1 = 3.404\times10^5$ N/m and the post-elastic stiffness is $K_2 = 3.404\times10^4$ N/m. u_x is considered as 0.012 m. The story mass is $m = 245.6\times10^3$ Kg. The mentioned characteristics are the same for all stories.

Since the dynamic response of structures due to earthquake excitations is very important in earthquake engineering, the fifty-story shear building is analyzed when it is subjected to the El-Centro earthquake. Figure 23 shows the time history of the North-South component of this ground motion.

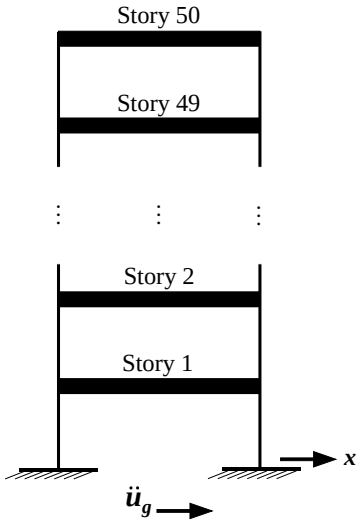

Fig. 21. A tall shear building with fifty stories

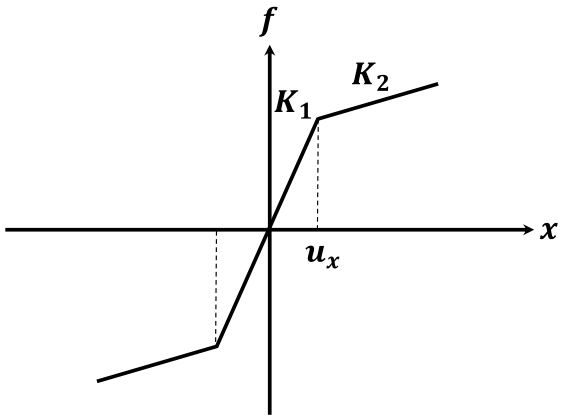

Fig. 22. Nonlinear relation between deformation and force

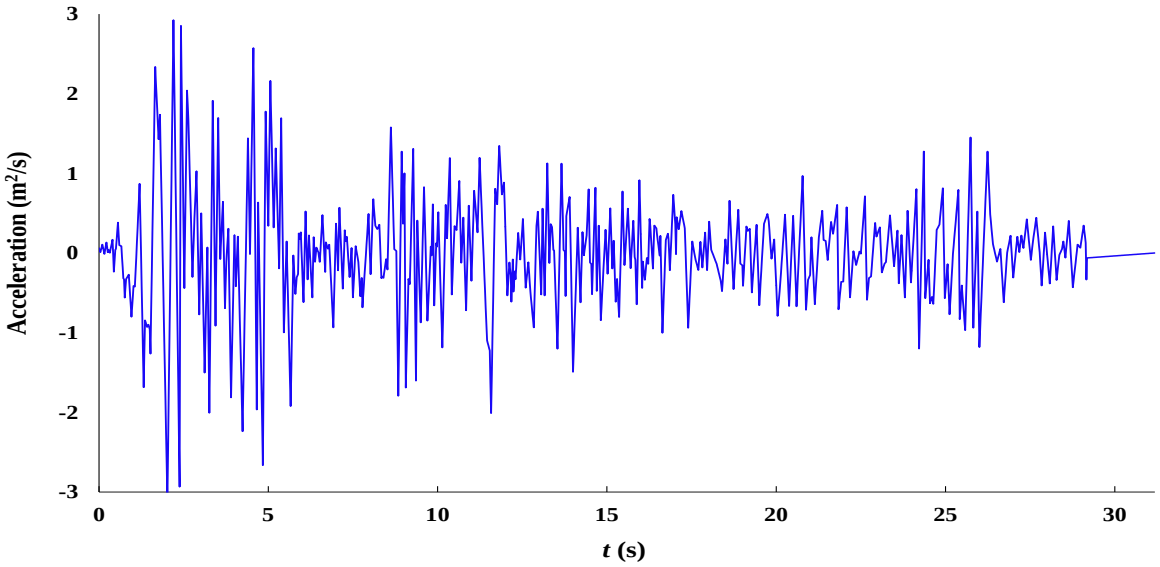

Fig. 23. Time history of north-south component of the El-Centro ground motion

The near-exact solution of this analysis is obtained by the fourth-order Runge-Kutta method using a very tiny time step $\Delta t_{ex} = 2\times10^{-5}$ s in the time interval of 31.18 s. To investigate the advantages of the new methods, the structure is analyzed with various time steps $\Delta t_1 = 2000\Delta t_{ex}$, $\Delta t_2 = 1000\Delta t_{ex}$ and $\Delta t_3 = 100\Delta t_{ex}$. Also, the results are compared to those from the generalized-α and SRK3 methods. Due to the explicitly of the new family, there is no need for iterative methods such as Newton-Raphson technique. However, the generalized-α and SRK3 schemes need Newton-Raphson iterations. The iterations are terminated if the incremental displacements reach a tiny value, 10^{-10} m. Figure 24 shows the lateral responses of the first story analyzed by various methods, which are obtained by using the second time step, Δt_2.

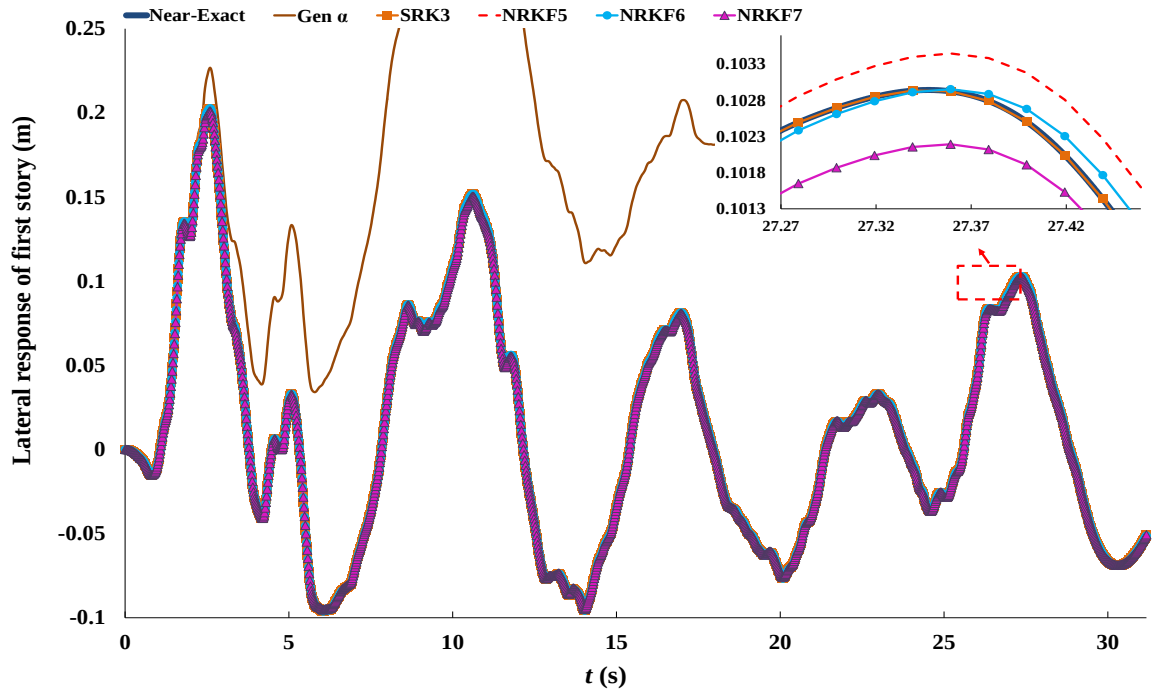

Fig. 24. lateral responses of the first story analyzed by various methods with the second time step, Δt_2

Table 7. Values of analysis error, CPU time, and storage for different methods

Scenario	Property	Gen. α	NRKF5	NRKF6	NRKF7	SRK3
Δt_1	*Err*	1.90×10^{1}	1.22	1.22	1.21	1.71×10^{-1}
	CPU Time (s)	1127	38	43	51	384
	Storage (Byte)	1,002,912	726,824	729,680	732,664	742,177
Δt_2	*Err*	8.26	6.51×10^{-3}	5.72×10^{-3}	7.06×10^{-3}	2.68×10^{-6}
	CPU Time (s)	2540	71	86	98	582
	Storage (Byte)	1,938,912	1,350,024	1,352,880	1,355,864	1,365,377
Δt_3	*Err*	2.63×10^{-1}	6.56×10^{-4}	5.75×10^{-4}	7.13×10^{-4}	5.85×10^{-8}
	CPU Time (s)	21980	676	821	961	4279
	Storage (Byte)	18,776,112	12,574,824	12,577,680	12,580,664	12,590,177

In order to compare analysis error (*Err*), CPU time, and storage values achieved by various time integration methods, Table 7 is prepared. In this table, the value of analysis error (*Err*) is calculated by using Eq. (45). Based on the results presented in Table 7, the generalized-α method with the highest values in *Err*, CPU time, and storage, has the weakest performance among the other methods. On the other hand, the NRKF5 method reaches the minimum values in CPU time and storage, in various analyzes. In the second and third scenarios (the cases of Δt_2 and Δt_3), among different orders of the new family, the NRKF6 method reaches solutions with the minimum values in *Err* and comparable values in CPU time and storage. Therefore, the NRKF6 method is chosen as the best order among different orders of the new family, which can reach better solutions in the nonlinear dynamic analysis. Compared to the SRK3 method, all suggested members of the new family have lower values in CPU time and storage. The values of *Err* obtained for the SRK3 method are small in different scenarios, whereas, compared to different members of the new family, the SRK3 method has larger values in CPU time.

By comparing the results obtained by the SRK3 method in the first scenario (Δt_1) and those by the NRKF6 method in the second scenario (Δt_2), it is obvious that the NRKF6 method has a better performance to obtain solutions with lower error values in a lower CPU time. In this comparison, the values of *Err* for the SRK3 and NRKF6 methods are 1.71×10^{-1} and 5.72×10^{-3}, respectively. Also, the values of CPU time for these methods are 384 s and 86 s, respectively. Aside from this, by comparing the values of CPU time between these two methods, one can see that the ratio of the CPU time values of the SRK3 and NRKF6 methods is 8.9 ($\frac{384}{43}$) in the first scenario. The ratio is equal to 6.8 ($\frac{582}{86}$) and 5.2 ($\frac{4279}{821}$) in the second and third scenarios, respectively. These comparisons illustrate that the SRK3 method needs a higher interval of time to perform nonlinear dynamic analyses compared to the NRKF6 method. On the other hand, the NRKF6 method can obtain good solutions with low error values in a shorter CPU time.

8. Conclusions

In this study, a higher-order explicit family of time integration methods was presented. The suggested formulation could analyze various linear and nonlinear dynamic systems. To develop this family, the Taylor series of the analytical amplification matrix was utilized. In this way, each time step of the integration procedure was divided into several stages. Different orders of the suggested family can be obtained by solving a system of nonlinear algebraic equations. The coefficients required (α) were shown for the orders $n=2$ to 10, in Table 1. It is worth mentioning that the higher-order methods can be achieved effortlessly. Therefore, the proposed methods form a comprehensive family. As a negative point, the stability of the proposed family is conditional. On the other

hand, as a positive point, the numerical accuracy and order of accuracy are improved as the order of the family increases.

One of the superiorities of the proposed Runge-Kutta family is the equality between the order of accuracy of the family and its number of stages used in a single time step. The results showed that the new family had the desired amplitude decay with a better performance in period error value compared to two well-known numerical integration methods, the Newmark linear acceleration and fourth-order Runge-Kutta. Furthermore, the performance of the family in amplitude decay and period error was enhanced as the order (n) rises.

The advantages of the authors' schemes were illustrated through various numerical experiments over several useful time integration methods, such as the Newmark linear acceleration technique, generalized-α, and explicit and implicit Runge-Kutta methods. The example undamped single degree of freedom oscillator showed the superiority of the proposed methods over the other techniques in analyzing linear mechanical systems. Furthermore, the results obtained by the proposed explicit family were more accurate than those achieved by the implicit CKRK and SRK3 methods. In Example 7-3, an impact load was applied to two degrees of freedom structure. The results demonstrated that the NRKF7 method has a better performance in analyzing a structure subjected to impact loading compared to the implicit SRK3 method. The methods NRKF6 and NRKF5 had more accurate results than the CKRK, fourth-order Runge-Kutta, and Newmark linear acceleration methods. The outcomes from Example 7-2 illustrated the ability of the new family in dealing with the non-classical damping behavior resulting from a five-story shear building. This example demonstrated that the method NRKF7 was the most accurate technique in analyzing shear building structures with non-classical dampers. Examples 7-4 and 7-5 showed that the suggested methods can solve plane and three-dimensional truss problems with high accuracy. In Example 7-5, the method NRKF6 and NRKF7 had the highest performance to solve the 3D truss problem in a low CPU time with very good accuracy. The results illustrated that Newmark linear acceleration and the fourth-order Rung-Kutta methods had the highest values in error and CPU time, respectively.

Example 7-6 showed that all orders of the proposed family can solve many degrees of freedom mass-spring-damper systems with nonlinear properties in stiffness and damping. In this experiment, the method NRKF7 analyzed the system with the lowest value in error, for large and medium time steps. However, if the time step is chosen a tiny value, the method NRKF6 can result in the more accurate analysis. As a weak point, if the time step is selected a large value, the results show that the lower orders of the family become unstable. However, as the order of the family is boosted, the stability, as well as, the accuracies of the answers are increased, which is a positive point.

In the last example, a tall shear building structure subjected to El-Centro ground motion was investigated. This structure had many degrees of freedom with nonlinear behavior in stiffness. According to the results, the existing implicit methods in this example, the generalized-α and SRK3 techniques had the highest values in error and CPU time, respectively. On the other hand, all members of the proposed family had the lowest values in CPU storage. As well, all orders of the proposed family had good performances in the accuracy of the solutions. Further to this, the NRKF6 method, which was chosen as the best order of the new family, could obtain accurate solutions with low values in CPU time and storage. This experiment illustrated that the new family methods are robust in analyzing tall building structures subjected to a realistic load, such as El-Centro ground motion.

9. Declarations

It is confirmed that the availability of data and material, funding, authors' contributions, acknowledgements, and all the subheadings of these and also the relevant information under each have been declared in this paper. Moreover, there is no conflict of interest.

10. References

Bathe, K.J. (1982). *Finite Element procedures in engineering analysis*, Prentice Hall, United Kingdom.

Bathe, K.J. and Wilson, E.L. (1972). "Stability and accuracy analysis of direct integration methods", *Earthquake Engineering and Structural Dynamics*, 1(3), 283-291, https://doi.org/10.1002/eqe.4290010308.

Braś, M., Izzo, G. and Jackiewicz, Z. (2017). "Accurate implicit-explicit general linear methods with inherent Runge-Kutta stability", *Journal of Scientific Computing*, 70(3), 1105-1143, https://doi.org/10.1007/s10915-016-0273-y.

Brogan, W.L. (1991). *Modern control theory*, Prentice Hall, United Kingdom.

Butcher, J.C. (2016). *Numerical methods for ordinary differential equations*, Wiley, Germany.

Chang, S.Y. (2013). "An explicit structure-dependent algorithm for pseudodynamic testing", *Engineering structures*, 46, 511-525, https://doi.org/10.1016/j.engstruct.2012.08.009.

Chung, J. and Hulbert, G. (1993). "A time integration algorithm for structural dynamics with improved numerical dissipation: the generalized-α method", *Journal of Applied Mechanics*, 60(2), 371-375, https://doi.org/10.1115/1.2900803.

Ezoddin, A., Kheyroddin, A. and Gholhaki, M. (2020). "Investigation of the effects of link beam length on the RC frame retrofitted with the linked column frame system", *Civil Engineering Infrastructures Journal*, 53(1), 137-159, https://doi.org/10.22059/CEIJ.2019.280596.1580.

Fok, P.W. (2016). "A linearly fourth order multirate Runge-Kutta method with error control", *Journal of Scientific Computing*, 66(1), 177-195, https://doi.org/10.1007/s10915-015-0017-4.

Ghassemieh, M. and Badrkhani Ajaei, B. (2018). "Impact of integration on straining modes and shear-locking for plane stress Finite Elements", *Civil Engineering Infrastructures Journal*, 51(2), 425-443, https://doi.org/10.7508/CEIJ.2018.02.011.

Goel, M.D., Kumar, M. and Matsagar, V.A. (2018). "Blast mitigation analysis of semi-buried structure", *Civil Engineering Infrastructures Journal*, 51(2), 445-460, https://doi.org/10.7508/CEIJ.2018.02.012.

Grote, M.J., Mehlin, M. and Mitkova, T. (2015). "Runge-Kutta-based explicit local time-stepping methods for wave propagation", *SIAM Journal on Scientific Computing*, 37(2), A747-A775, https://doi.org/10.1137/140958293.

Gu, Y. and Zhu, Y. (2021). "Adams predictor–corrector method for solving uncertain differential equation", *Computational and Applied Mathematics*, 40(2), 1-20, https://doi.org/10.1007/s40314-021-01461-2.

Hairer, E., Lubich, C. and Wanner, G. (2006). *Geometric numerical integration: Structure-preserving algorithms for ordinary differential equations*, Springer Berlin, Heidelberg.

Heun, K. (1900). "Neue Methoden zur approximativen integration der differentialgleichungen einer unabhängigen veränderlichen", *Zeitschrift für Angewandte Mathematik und Physik*, 45, 23-38.

Hughes, T.J. (2012). *The Finite Element method: Linear static and dynamic Finite Element analysis*, Dover Publications, United States.

Hulbert, G.M. and Chung, J. (1996). "Explicit time integration algorithms for structural dynamics with optimal numerical dissipation", *Computer Methods in Applied Mechanics and Engineering*, 137(2), 175-188, https://doi.org/10.1016/S0045-7825(96)01036-5.

Hulbert, G.M. and Hughes, T.J.R. (1987). "An error analysis of truncated starting conditions in step-by-step time integration: Consequences for structural dynamics", *Earthquake Engineering and Structural Dynamics*, 15(7), 901-910, https://doi.org/10.1002/eqe.4290150710.

Isherwood, L., Grant, Z.J. and Gottlieb, S. (2018). "Strong stability preserving integrating factor Runge-Kutta methods", *SIAM Journal on Numerical Analysis*, 56(6), 3276-3307, https://doi.org/10.1137/17M1143290.

Izzo, G. and Jackiewicz, Z. (2017). "Highly stable implicit–explicit Runge-Kutta methods", *Applied Numerical Mathematics*, 113(March), 71-92, https://doi.org/10.1016/j.apnum.2016.10.018.

Jørgensen, J.B., Kristensen, M.R. and Thomsen, P.G. (2018). "A family of ESDIRK integration methods", *arXiv preprint arXiv:1803.01613*, https://doi.org/10.48550/arXiv.1803.01613.

Kassam, A.K. and Trefethen, L.N. (2005). "Fourth-order time-stepping for stiff PDEs", *SIAM Journal on Scientific Computing*, 26(4), 1214-1233, https://doi.org/10.1137/S1064827502410633.

Kim, W. (2019). "A new family of two-stage explicit

time integration methods with dissipation control capability for structural dynamics", *Engineering Structures*, 195(15 September), 358-372, https://doi.org/10.1016/j.engstruct.2019.05.095.

Kordi, A. and Mahmoudi, M. (2022). "Damage detection in truss bridges under moving load using time history response and members influence line curves", *Civil Engineering Infrastructures Journal*, 55(1), 183-194, https://doi.org/10.22059/CEIJ.2021.314109.1723.

Kutta, W. (1901). "Beitrag zur näherungweisen Integration totaler Differentialgleichungen", *Zeitschrift für Angewandte Mathematik und Physik*, 46, 435-453.

Martín-Vaquero, J. and Kleefeld, A. (2019). "ESERK5: A fifth-order extrapolated stabilized explicit Runge-Kutta method", *Journal of Computational and Applied Mathematics*, 356(15 August), 22-36, https://doi.org/10.1016/j.cam.2019.01.040.

Lee, T.Y., Chung, K.J. and Chang, H. (2017). "A new implicit dynamic finite element analysis procedure with damping included", *Engineering Structures*, 147(15 September), 530-544, https://doi.org/10.1016/j.engstruct.2017.06.006.

Moler, C. and Van Loan, C. (2003). "Nineteen dubious ways to compute the exponential of a matrix, twenty-five years later", *SIAM Review*, 45(1), 3-49, https://doi.org/10.1137/S00361445024180.

Haj Najafi, L. and Tehranizadeh, M. (2016). "Distribution of building nonstructural components in height subjected to cost of damage for low-rise office buildings", *Civil Engineering Infrastructures Journal*, 49(2), 173-196, https://doi.org/10.7508/ceij.2016.02.001.

Newmark, N.M. (1959). "A method of computation for structural dynamics", *Journal of the Engineering Mechanics Division*, 85(3), 67-94, https://doi.org/10.1061/JMCEA3.0000098.

Noels, L., Stainier, L. and Ponthot, J.P. (2006). "Energy conserving balance of explicit time steps to combine implicit and explicit algorithms in structural dynamics", *Computer Methods in Applied Mechanics and Engineering*, 195(19-22), 2169-2192, https://doi.org/10.1016/j.cma.2005.03.003.

Ortigosa, R., Gil, A.J., Martínez-Frutos, J., Franke, M. and Bonet, J. (2020). "A new energy–momentum time integration scheme for non-linear thermo-mechanics", *Computer Methods in Applied Mechanics and Engineering*, 372(1 December), 113395, https://doi.org/10.1016/j.cma.2020.113395.

Paz, M. and Kim, Y.H. (2018). *Structural Dynamics: Theory and Computation*, Springer International Publishing, Germany.

Rezaie, F., Fakhradini, S.M. and Ghahremannejad, M. (2018). "Numerical evaluation of progressive collapse potential in reinforced concrete buildings with various floor plans due to single column removal", *Civil Engineering Infrastructures Journal*, 51(2), 405-424, https://doi.org/10.7508/ceij.2018.02.010.

Rezaiee-Pajand, M., Esfehani, S.A.H. and Karimi-Rad, M. (2018). "Highly accurate family of time integration method", *Structural Engineering and Mechanics*, 67(6), 603-616, https://doi.org/10.12989/sem.2018.67.6.603.

Rezaiee-Pajand, M., Esfehani, S.A.H. and Ehsanmanesh, H. (2021). "An efficient weighted residual time integration family", *International Journal of Structural Stability and Dynamics*, 21(08), 2150106, https://doi.org/10.1142/S0219455421501066.

Rezaiee-Pajand, M. and Karimi-Rad, M. (2017). "An accurate predictor-corrector time integration method for structural dynamics", *International Journal of Steel Structures*, 17(3), 1033-1047, https://doi.org/10.1007/s13296-017-9014-9.

Rossi, D.F., Ferreira, W.G., Mansur, W.J. and Calenzani, A.F.G. (2014). "A review of automatic time-stepping strategies on numerical time integration for structural dynamics analysis", *Engineering Structures*, 80, 118-136, https://doi.org/10.1016/j.engstruct.2014.08.016.

Shutov, A.V., Landgraf, R. and Ihlemann, J. (2013). "An explicit solution for implicit time stepping in multiplicative finite strain viscoelasticity", *Computer Methods in Applied Mechanics and Engineering*, 265(1 October), 213-225, https://doi.org/10.1016/j.cma.2013.07.004.

Soares, D. (2016). "A novel family of explicit time marching techniques for structural dynamics and wave propagation models", *Computer Methods in Applied Mechanics and Engineering*, 311(1 November), 838-855, https://doi.org/10.1016/j.cma.2016.09.021.

Soares, D. and Großeholz, G. (2018). "Nonlinear structural dynamic analysis by a stabilized central difference method", *Engineering Structures*, 173, 383-392, https://doi.org/10.1016/j.engstruct.2018.06.115.

Sun, Z. and Shu, C.W. (2019). "Strong stability of explicit Runge-Kutta time discretizations", *SIAM Journal on Numerical Analysis*, 57(3), 1158-1182, https://doi.org/10.1137/18M122892X.

Turaci, M.Ö. and Öziş, T. (2018). "On explicit two-derivative two-step Runge-Kutta methods", *Computational and Applied Mathematics*, 37(5), 6920-6954, https://doi.org/10.1137/18M122892X.

Turyn, L. (2013). *Advanced engineering mathematics*, CRC Press, United States.

Vejju, P., George, A. and Rahulkar, A.D. (2016). "Comparative study on the computation of state transition matrix using La-grange's interpolation

technique and Cayley-Hamilton theorem", *Proceedings of the 10th International Conference on Intelligent Systems and Control (ISCO)*, Coimbatore, India, 10.1109/ISCO.2016.7726936.

Yaghoubi, V., Abrahamsson, T. and Johnson, E.A. (2016). "An efficient exponential predictor-corrector time integration method for structures with local nonlinearity", *Engineering Structures*, 128, 344-361, https://doi.org/10.1016/j.engstruct.2016.09.024.

Zhang, L., Zhang, Q. and Sun, H.W. (2020). "Exponential Runge-Kutta method for two-dimensional nonlinear fractional complex Ginzburg-Landau equations", *Journal of Scientific Computing*, 83(3), 1-24, https://doi.org/10.1007/s10915-020-01240-x.

Zhao, S. and Wei, G.W. (2014). "A unified discontinuous Galerkin framework for time integration", *Mathematical Methods in the Applied Sciences*, 37(7), 1042-1071, https://doi.org/10.1002/mma.2863.

Appendices

A.1. The Uniqueness of the Coefficients α_j

One can consider $\mathbf{A}^n=\left\{\alpha_1^n,\alpha_2^n,\ldots,\alpha_{n-1}^n\right\}$ as a set of the coefficients α_j for $j=2,\ldots,n-1$ calculated from the nonlinear algebraic system given in Eq. (18) with the order of n. For every set of $\mathbf{A}^n$, there is another set, such as $\mathbf{B}^n=\left\{\beta_1^n,\beta_2^n,\ldots,\beta_{n-1}^n\right\}$ with the following relationships, which is a dual solution for the nonlinear algebraic system.

$$\begin{aligned}\beta_1^n&=\alpha_{n-2}^n\\ \beta_2^n&=\alpha_{n-3}^n\\ &\ldots\\ \beta_{n-2}^n&=\alpha_1^n\\ \beta_{n-1}^n&=\alpha_{n-1}^n\end{aligned}\qquad(A1)$$

One can easily check the equality of these dual sets ($\mathbf{A}^n$ and $\mathbf{B}^n$) for Eq. (18). It is worth mentioning that numerical characteristics of the new methods performed by the solutions $\mathbf{A}^n$ and $\mathbf{B}^n$, such as stability, order of accuracy, and numerical accuracy, are similar. For the new methods with the values of n equal to 2, 3, and 4, the sets $\mathbf{A}^n$ and $\mathbf{B}^n$ are equal. Therefore, the coefficients for $n=2$, 3, and 4, can be obtained uniquely.

A.2. The Existence of the Coefficients α_j

The coefficients α_{n-1}^n and α_{n-2}^n are obtained based on the second and last equations in Eq. (18). Form the equality $\frac{n-1}{1+\sum_{j=1}^{n-1}\frac{1}{\alpha_j}}=\frac{1}{2!}$, α_{n-1}^n is calculated using the other coefficients as follows.

$$\alpha_{n-1}^n=\frac{1}{2n-3-\sum_{j=1}^{n-2}\frac{1}{\alpha_j^n}}\qquad(A2)$$

Also, α_{n-2}^n can be obtained from the equalities $\frac{\prod_{v=1}^{n-2}\alpha_v}{1+\sum_{j=1}^{n-1}\frac{1}{\alpha_j}}=\frac{1}{n!}$ and $1+\sum_{j=1}^{n-1}\frac{1}{\alpha_j}=2!(n-1)$, as the below form.

$$\alpha_{n-2}^n=\frac{\left(\frac{2(n-1)}{n!}\right)}{\prod_{v=1}^{n-3}\alpha_v^n}\qquad(A3)$$

Using the third equality in Eq. (18), $\frac{\sum_{j=1}^{n-2}\alpha_j}{1+\sum_{j=1}^{n-1}\frac{1}{\alpha_j}}=\frac{1}{3!}$, as well as, Eqs. (A2) and (A3), one can calculate the coefficients for the methods with $n=2$, 3, and 4, easily. For other values of n, the authors utilized a heuristic procedure, which performs in an iterative manner shown in Figure A1. In this procedure, the coefficients α_j^n are calculated using the coefficients α_j^{n-1}. In order to stop iterations, the error introduced by Eq. (A4) should be computed at the end of each iteration.

$$Err=\sqrt{\sum_{k=1}^{n}\left(\frac{\frac{1}{k!}-R_k}{\left(\frac{1}{k!}\right)}\right)^2} \tag{A4}$$

$$R_k=\begin{cases}\dfrac{1+\sum_{j=1}^{n-1}\frac{1}{\alpha_j^{n,itr}}}{1+\sum_{j=1}^{n-1}\frac{1}{\alpha_j^{n,itr}}} & k=1\\ \dfrac{n-1}{1+\sum_{j=1}^{n-1}\frac{1}{\alpha_j^{n,itr}}} & k=2\\ \dfrac{\sum_{j=1}^{n-(k-1)}\prod_{v=0}^{k-3}\alpha_{j+v}^{n,itr}}{1+\sum_{j=1}^{n-1}\frac{1}{\alpha_j^{n,itr}}} & k\geq 3\end{cases} \tag{A5}$$

The error calculated by Eq. (A4) demonstrates the difference between the term on the left side of each equality in Eq. (18), which is estimated by the values of $\alpha_j^{n,itr}$, and the term on the right side of the equality. $\alpha_j^{n,itr}$ is indeed the estimated value of α_j^n in the iteration *itr*. ε, which is used to stop the iterations, has a very tiny value of 1×10^{-13}.

Figure A2 shows the values of *Err* obtained in calculating the coefficients α_j^n for $n=1$ to 100. The Results shown in Figure A2 illustrate the high ability of the authors' heuristic procedure in the calculation of α_j in a wide range of n.

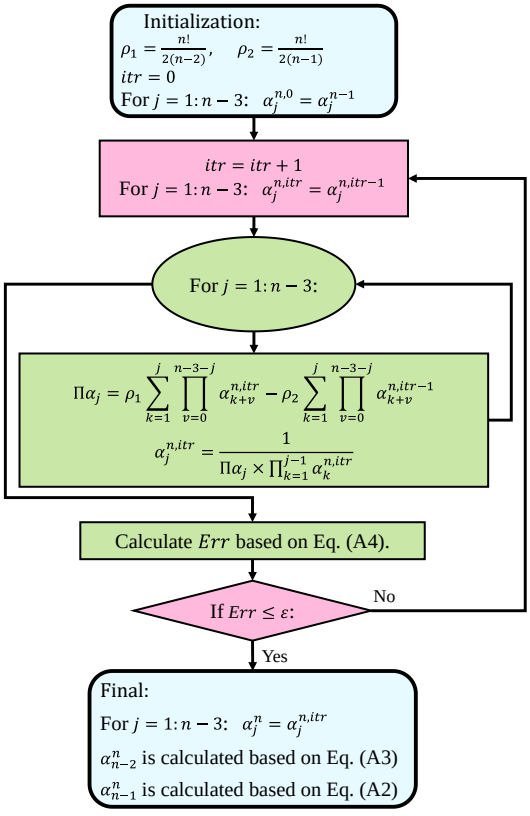

Fig. A1. The procedure for calculation of α_j^n for $n\geq5$

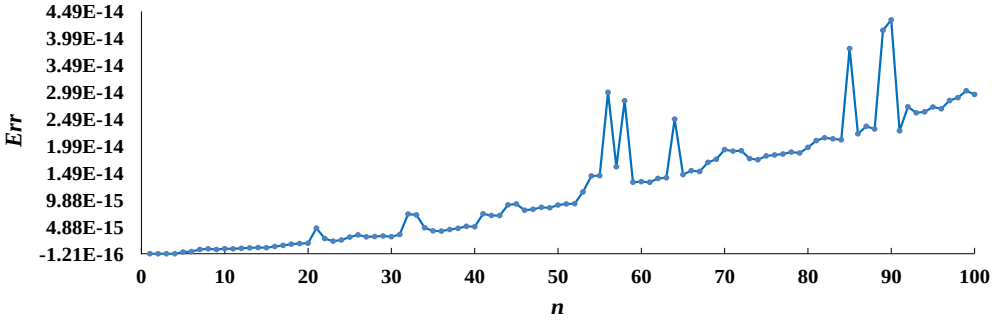

Fig. A2. *Err* for various values of n

Civil Engineering Infrastructures Journal 2023, 56(1): 79-103
DOI: 10.22059/CEIJ.2022.330808.1793

RESEARCH PAPER

Proposed Methodology and Comprehensive Design Process for Seismic Rehabilitation of Steel Structures with Supplemental Viscous Dampers

Bahmani, M.[1] and Zahrai, S.M.[2,3]*

[1] Assistant Professor, Department of Civil Engineering, Abadan Branch, Islamic Azad University, Abadan, Iran.
[2] Professor, School of Civil Engineering, College of Engineering, University of Tehran, Tehran, Iran.
[3] Adjunct Professor, Civil Engineering Department, University of Ottawa, Canada.

Received: 17 Sep. 2021; Revised: 06 Jul. 2022; Accepted: 17 Jul. 2022

ABSTRACT: Several types of steel-framed structures now require seismic retrofitting as a result of changes in their usage or modifications in seismic codes. During the last two decades, viscous dampers have been widely used for seismic rehabilitation of buildings because of their ease of application and significant reductions in structural response. The main objective of this research is to present a new comprehensive design process for seismic rehabilitation with non-linear viscous dampers and to introduce the concept of Optimal Retrofit Level (ORL) to control steel buildings. In this article, the inter-story drift as an important parameter of structural response is employed to estimate the failure cost and determine the limit state. Three-, nine- and twenty-story benchmark buildings are used to evaluate the proposed methodology. These buildings have considerably different dynamic properties. The earthquake records corresponding to three levels of seismic hazard are also applied for time-history analysis in order to investigate the trustworthiness of results obtained for zones with different seismicity. The numerical results indicate that the suggested method is able to drop lifecycle costs and creat an equilibrium between rehabilitation costs and failure costs after seismic rehabilitation.

Keywords: Lifecycle Cost, Optimal Retrofit Level, Seismic Retrofit, Steel Buildings, Viscous Dampers.

1. Introduction

The seismic design of buildings is based on life safety criteria or the collapse limit state, but extensive financial damage from recent earthquakes indicates the insufficiency of these criteria to protect the financial resources invested in construction (Shin and Singh, 2014). The financial consequences of recent earthquakes and the modifications to seismic codes highlight the increasing need for seismic retrofit of structures to improve their performance, conducted in two general methods. One is to increase the cross area of the structural member of the building by adding supports and strengthening the main members from the outside by adding steel sheets, fibre-enhanced polymer sheets or post-tensioning. The alternative is to use passive

* Corresponding author E-mail: mzahrai@ut.ac.ir

or active control methods such as energy dissipating devices, seismic isolation or tuned mass dampers (Guo et al., 2014).

Viscous Dampers (VD) are among energy dissipating devices that are commonly used in structures because of their ease of design, simple application in terms of minimum interference with existing building members and increase in damping without a significant increase in the stiffness or mass of the building. VDs are capable of absorbing large amounts of energy induced from earthquakes with little displacement and can decrease both the displacement and acceleration of a structure simultaneously because they are categorized as velocity-dependent dampers (Dall′ Asta et al., 2016).

Over the last two decades, because of the rewards of VDs for seismic rehabilitation of buildings, there have been numerous researches on their engineering and financial aspects. Overall, these studies could be categorized as follows:

- Design strategies for VDs (Kitayama and Constantinou, 2018; Rashid et al., 2022; Silvestri et al., 2010; Wani et al., 2021).
- Effect of nonlinear behaviour of VDs on reduced response of structures (Chopra and McKenna, 2016; Dall′ Asta et al., 2016; Edip et al., 2020; Golnargesi et al., 2022).
- Comparison of different methods for distributing VDs (Hwang et al., 2013);
- Application of VDs in rehabilitation of existing steel buildings (Guo et al., 2014; Sarkisian et al., 2013);
- Reducing the Life Cycle Cost (LCC) of buildings with supplemental VDs (Banazadeh et al., 2017; Ghasemof et al., 2021; Gidaris and Taflanidis, 2015; Salajegheh and Asadi, 2020; Sarcheshmehpour and Estekanchi, 2021; Shin and Singh, 2014);
- Experimental work for verifying proposed design relations (Seleemah and Constantinou, 1997; Sorace et al., 2016);
- Reliability-based optimal design of VDs (Altieri et al., 2018; Aydin et al., 2019; Dall'Asta et al., 2017);
- VDs configuration (Hwang et al., 2008).

Most recent studies on seismic retrofitting of existing structures using VDs focus separately on either the engineering or financial aspects of the matter, although decision-making on seismic retrofits of structures requires a simultaneous study of the engineering and financial effects of seismic retrofitting using passive control methods.

The objective of this study is to introduce a complete and simple design process for the seismic retrofit of steel frames with Non-Linear Viscous Dampers (NLVD) in which the technical and economic aspects of passive control of buildings are taken into account at the same time. The suggested comprehensive design process is presented as a scientific methodology of determining the retrofitting algorithm using NLVDs for professional design engineers. Note that the main research has been conducted in two companion papers: The first part reflected here presents the innovative methodology and detailed design procedure while the second one shows the application of this design process in existing steel buildings recently published elsewhere (Bahmani and Zahrai, 2018).

Compared to design procedures presented in other articles and codes, the proposed comprehensive design procedure has the following advantages: 1) The engineering and economic aspects of design of buildings equipped with VD are evaluated simultaneously; 2) The optimal retrofit level (ORL) is determined more easily and simply using the proposed formula and it is not required to apply optimization algorithms; 3) The design procedure of dampers is a simple and accurate approach and just the natural period of building and mass of each floor are used to specify the characteristics of VDs; 4) The results of comprehensive design procedure have acceptable accuracy for buildings where the distribution of mass and stiffness is not uniform over all floors.

2. Fundamentals of NLVD

This paper will focus on the retrofitting of benchmark building with added VDs. The effect of the added VDs to a benchmark building in resisting seismic force can be clearly explained from energy consideration. The event of a building responding to an earthquake ground motion is described using an energy concept in the follows.

Eq. (1) shows the supplementary force of NLVDs which represents a nonlinear force-velocity relation.

$$F_d = C|\dot{u}|^{\alpha} sgn(\dot{u}) \quad (1)$$

where *C*: is the VD damping coefficient, α: shows the velocity exponent for VD, $\dot{\boldsymbol{u}}$: represents the relative velocity between the two ends of VD, and sgn ( ): represents the sign function.

2.1. Supplemental Damping Ratio (DR) Provided by LVDs

The formulation of supplemental DR using LVDs is provided in chapter 9 of FEMA 356. The DR (ξ) provided by the LVDs for a single degree-of-freedom (SDOF) system vibrating under a cyclic harmonic load is:

$$\xi = \frac{W_D}{4\pi W_S} \quad (2)$$

where W_D: is the energy dissipated by LVDs and W_S: represents the maximum strain energy of the system. The experimental results show that for an increase in the DR of a multi-degree of freedom (MDOF) structure, the higher modes will be suppressed while the first mode will be dominant. Hence, only the first mode of MDOF structures is considered in simplified design methods. Thus, the energy dissipated by the LVDs and the maximum strain energy of the frame for the first mode are calculated as:

$$W_D = \sum_j W_{Dj} = \sum_j \pi C_j \left(\frac{2\pi}{T_m}\right)(u_{roof}\varphi_{mr,j} f_j)^2 \quad (3)$$

$$W_S = \frac{2\pi^2}{T_m^2}\sum_i m_i u_{roof}^2 \varphi_{mi}^2 \quad (4)$$

All the parameters for Eqs. (3) and (4) are described in the accompanying article (Bahmani and Zahrai, 2018). By applying Eqs. (3) and (4) to Eq. (2), the DR provided by LVD in the primary mode of the structure can be obtained as:

$$\xi_m = \frac{T_m \sum_j C_j \varphi^2{}_{mr,j} {f_j}^2}{4\pi \sum_i m_i \varphi_{mi}^2} \quad (5)$$

Eq. (5) is derived by assuming that the first mode of response of the structure is dominant (this assumption is true in most structures). This equation can be approximated in the following structures, where the effects of higher modes are also applied.

- Geometrically irregular buildings;
- A building with irregular mass distribution across its plan and height;
- A building with an irregular rigidity distribution across its plan and height;

2.2. Supplemental DR Provided by NLVDs

The energy dissipated by a NLVD for a SDOF system under cyclic harmonic vibration is as follows (Ramirez et al., 2000):

$$W_D = \int F_d du = \int C_N \dot{u}^{\alpha} du = \lambda C_N \left(\frac{2\pi}{T_m}\right)^{\alpha} u_0^{\alpha+1} \quad (6)$$

$$\lambda = 2^{2+\alpha}\frac{\Gamma^2(1+\frac{\alpha}{2})}{\Gamma(2+\alpha)} \quad (7)$$

in which F_d: represents the damping force, u: represents the displacement of the SDOF system, u_0: shows displacement amplitude or the maximum value of u, C_N: is the

damping coefficient of the NLVDs, α: refers to the velocity exponent for the NLVDs and Γ: is the gamma function. Eq. (6) could be developed for MDOF systems as:

$$W_D = \sum_j W_{D,j} = \sum_j \lambda_j C_{N,j} \left(\frac{2\pi}{T_m}\right)^{\alpha_j} (u_{roof}\varphi_{mr,j} f_j)^{\alpha_j+1} \quad (8)$$

By implementing Eqs. (8) and (4) in Eq. (2), the DR provided by the NLVDs in the primary mode of the building can be considered as (Ramirez et al., 2000):

$$\xi_m = \frac{\sum_j \lambda_j C_{N,j} \left(\frac{2\pi}{T_m}\right)^{\alpha_j-2} u_{roof}^{\alpha_j-1} \varphi_{mr,j}^{\alpha_j+1} f_j^{\alpha_j+1}}{2\pi \sum_i m_i \varphi_{mi}^2} \quad (9)$$

$$\lambda_j = 2^{\alpha_j+2} \frac{\Gamma^2(1+\frac{\alpha_j}{2})}{\Gamma(2+\alpha_j)} \quad (10)$$

in which $C_{N,j}$: is the damping coefficient for the j^{th} NLVD and α_j: refers to the velocity of the j^{th} NLVD.

2.3. Configurations of VDs

As shown in Figure 1, VDs can be installed in four various methods, of which the diagonal and chevron types are very common in practice.

3. Comprehensive Design Procedure

A comparison of the proposed comprehensive design procedure and those published in the literature discloses the relative innovation and straightforwardness of the proposed method given the following features:

- In the suggested comprehensive design procedure, the ORL is determined only by the results of Time-History Analysis (THA) without complicated computations;
- The performance levels, unlike other complex procedures, are explained using the damage states for simplicity;
- The building LCC is estimated for pre-retrofit and post-retrofit conditions using the results of steps two and eight of the technical section of the detailed design process;
- Unlike other studies where the ORL is specified through fragility analysis, the ORL is determined using the simple and clear formula proposed in this study;
- The shear strain energy method is used for the distribution of the damping coefficient. In this method, higher damping coefficient are assigned to floors with more strain energy. Therefore, the viscous dampers contribute to the reduction of the seismic response of the building more effectively.

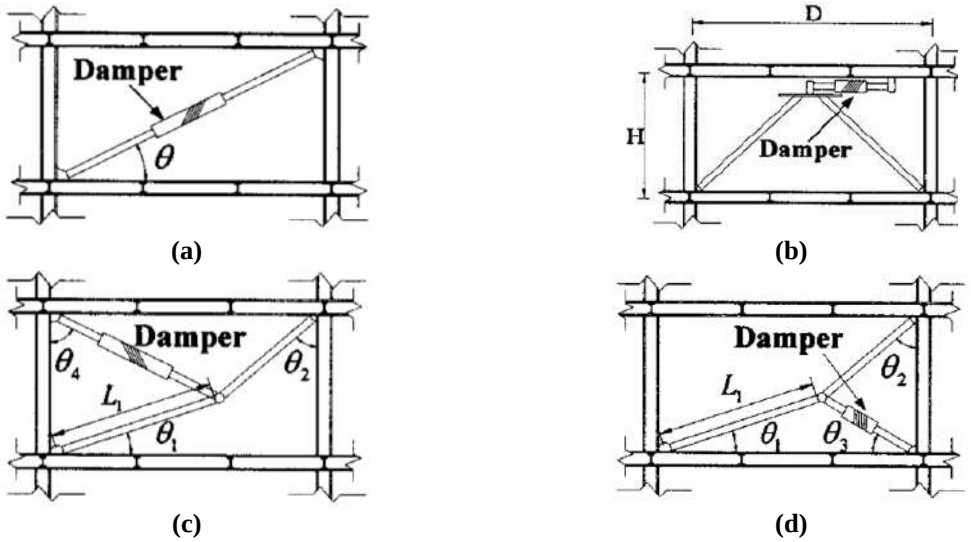

Fig. 1. Installation schemes of viscous dampers: a) Diagonal brace; b) Chevron; c) Upper toggle brace; and d) Lower toggle brace

3.1. Engineering Aspect of Comprehensive Design Procedure

As illustrated in Figure 2, the suggested design process consists of two sections: 1) the design of the NLVDs; and 2) the economic evaluation of the NLVD obtained from Section 1. The Engineering aspect of design process is composed of the following eight steps.

Step E1: Choosing Earthquake Records

Due to the simplicity of implementation, the common approach for seismic analysis of structures is to use the design code spectrum response; however, when a more accurate design is required, it is better to use real earthquake records. In order to assess the suggested comprehensive design process using benchmark structures, two far-field records and two near-field records from Ohtori et al. (2004). A detailed description of the earthquake records is available in Ohtori et al. (2004).

Step E2: FE Model Preparation for Building Without Dampers to Perform THA

Before retrofitting existing structures, for the purpose of evaluate the seismic performance of the bare frame, there is a requirement to build a Finite Element (FE) model and investigate the seismic behaviour of the structure using a FE program. In other words, the prerequisite to any retrofitting plan is to evaluate the existing seismic performance of the building.

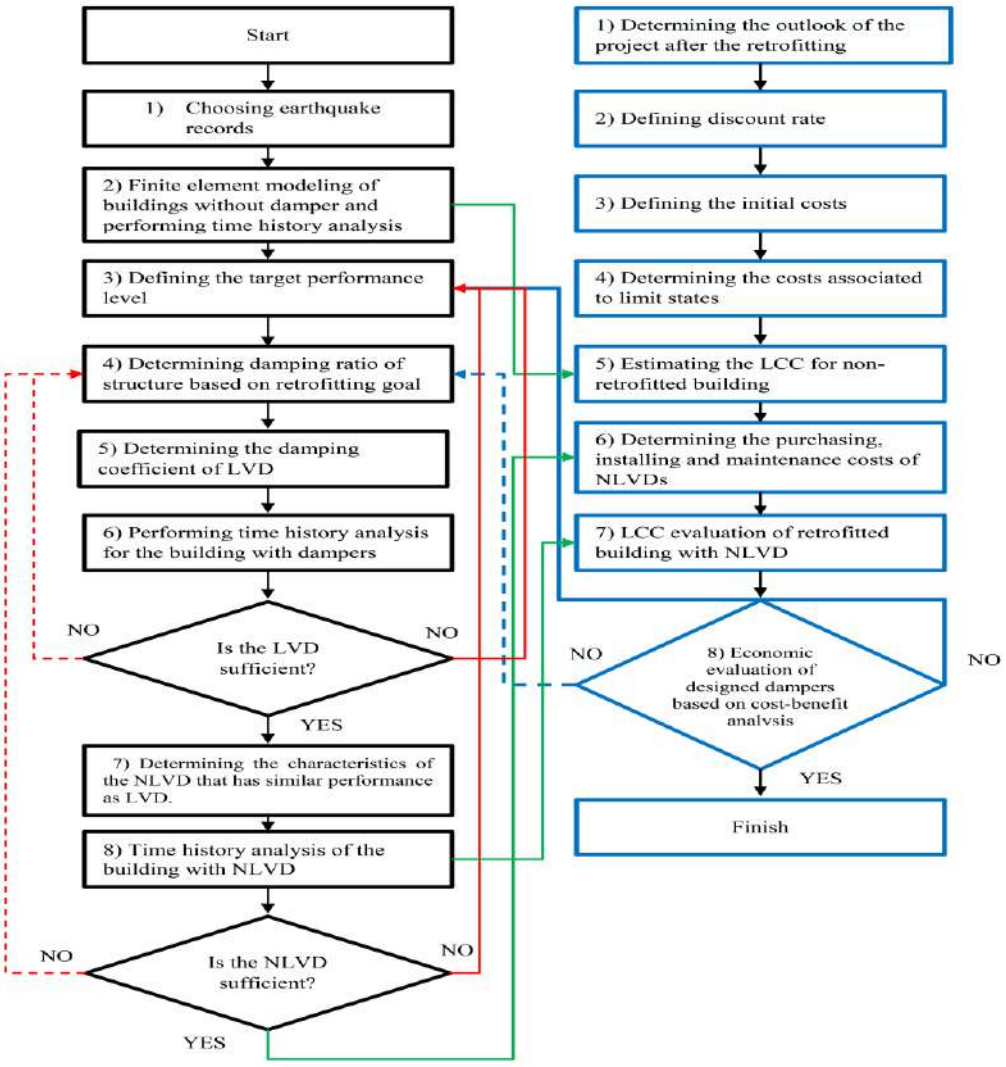

Fig. 2. The proposed comprehensive design procedure in this research for seismic retrofit of existing steel buildings with NLVDs

Step E3: Determining the Retrofitting Target

The upgrade target is based on customer requirements and seismic necessities provided by the design codes. To express performance levels of the structure, such as those shown in Table 1, the limit states presented by FEMA 227 are used in this study. Table 1 shows the maximum Inter-Story Drift (ISD) ratio, an essential parameter of building response that is an indicator of the performance level of the building. Immediate occupancy is the state at which the ISD ratio (Δ) for all buildings is less than 0.7. This is $\Delta \leq 2.5$ for the life safety state and $\Delta \leq 5$ for the collapse prevention state.

Step E4: Determine the Structural DR According to the Rehabilitation Target

Several researchers have provided relations (in engineering accuracy accepted zones) for the DR of dynamic systems (ξ) and its associated seismic response reduction coefficient ($\eta(\xi)$). The effect of ξ on the seismic response of a building is not totally similar at a constant acceleration, velocity or displacement zone, but it can be applied for a period range of typical buildings with acceptable accuracy. In this study, $\eta(\xi)$ of a building ($\eta_{\Delta}(\xi)$) is the result of the maximum ISD of that building retrofitted with NLVDs divided by the ISD of the building without dampers (inherent damping of$\xi = 0.05$). Here, the equation suggested by (Bommer et al., 2000) is used for defining the relation between the ξ of the structure after rehabilitation and the related reduction of the seismic response.

$$\eta_{\Delta}(\xi) = \frac{\Delta m_{max}}{\Delta_{max}} \tag{11}$$

$$\eta = \sqrt{\frac{10}{5 + \xi + \xi_m}} \tag{12}$$

Step E5: Determination of the LVD Damping Coefficient

Silvestri et al. (2010) suggested a simplified technique based on the uniform distribution of dampers along the height of building. He assumed the stiffness and weight of all stories to be the same. In the current study, using the comparisons by Hwang et al. (2013) of the various techniques of distributing dampers along height of the structure, the floor shear strain energy method is used. The damping distribution at different stories of the structure for the uniform distribution technique is not proportionate to the maximum dissipating force at each story during earthquake. Compared to other methods of damping distribution, this causes a decrease in the dissipation of the induced earthquake energy.

To assign a constant damping coefficient to the building, the effective DR of the building from the story shear strain energy method is more than that from the uniform distribution method. The VDs from the story shear strain energy method could improve the performance compared to those from the uniform distribution method lowering costs and easing application through decreased interference with the existing structure. Therefore, the use of the story shear strain energy method, a non-iterative method of distributing damping in the building, is more reasonable than the use of other methods because a higher damping coefficient is assigned to the stories of the building having higher shear strain energy, increasing the effectiveness of the dampers.

Table 1. Limit state and the corresponding performance levels

Limit state	Damage state	Story drift ratio (%)	Performance levels
1	None	$\Delta < 0.2$	
2	Slight	$0.2 < \Delta < 0.4$	Immediate occupancy
3	Light	$0.4 < \Delta < 0.7$	
4	Moderate	$0.7 < \Delta < 1.5$	Life safety
5	Heavy	$1.5 < \Delta < 2.5$	
6	Major	$2.5 < \Delta < 5.0$	Collapse prevention
7	Destroyed	$5.0 < \Delta$	

For shear buildings, the strain energy of the floor is proportional to $S_j\varphi_{mj}$; therefore, the damping coefficient at each level can be calculated as:

$$C_j = qS_j\varphi_{mj} \quad (13)$$

in which q: is the proportionality constant and $S_j = \sum_{i=j}^{roof} m_i\varphi_i$. The damping coefficient of the entire structure can be considered as:

$$\sum_i C_i = q\sum_i \varphi_{mi}S_i \quad (14)$$

Using Eqs. (13) and (14), the damping coefficient of each level can be obtained as:

$$C_j = \frac{\varphi_{mj}S_j}{\sum_i \varphi_{mi}S_i}\sum_i C_i \quad (15)$$

Placing Eq. (15) into Eq. (5) produces:

$$\xi_m = \frac{T_m\sum_j[\varphi_{mj}S_j(\sum_i C_i)(f_j\varphi_{mj})^2]}{4\pi(\sum_i m_i\varphi_i^2)(\sum_i \varphi_{mi}S_i)} \quad (16)$$

The damping coefficient of entire structure becomes:

$$\sum_i C_i = \frac{4\pi\xi_m(\sum_i m_i\varphi_i^2)(\sum_i \varphi_{mi}S_i)}{T_m\sum_i[\varphi_{mi}S_i(f_i\varphi_{mi})^2]} \quad (17)$$

Substituting Eq. (17) into Eq. (15) produces the damping coefficient of each level as:

$$C_j = \frac{4\pi\xi_m\varphi_{mj}S_j(\sum_i m_i\varphi_i^2)}{T_m\sum_i[\varphi_{mi}S_i(f_i\varphi_{mi})^2]} \quad (18)$$

Step E6: THA for Building with LVD

THA of the structure with LVDs is carried out using the earthquake records outlined in Step E1. The reason of this analysis is to validate the damping introduced to the structure by the LVDs and compare it to the target DR in Step E4 or, in other words, to calibrate the damping coefficient of LVD to achieve the target performance level as defined in Step E3. When comparing the structural performance of a bare frame and one equipped with dampers, ISD can be used as the effective parameter of structural response. If there is a considerable difference between the initial targets and the level of improvement in the structural behaviour or the DR, Step E4 or E3 should be revised.

Step E7: Determining the Characteristics of NLVDs to Provide Performance Similar to LVDs

The purpose of this step is to determine the features of NLVDs to provide performance similar to that of LVDs under the similar seismic excitation. To specify the damping coefficient of NLVDs using the energy approach, the average energy dissipated by the NLVD and LVD in a SDOF system subjected to all cycles of harmonic vibration is assumed to be equal:

$$\frac{1}{u_0}\int_0^{u_0} W_{DN}du = \frac{1}{u_0}\int_0^{u_0} W_{DL}du \quad (19)$$

$$\frac{1}{u_0}\int_0^{u_0} \lambda C_N\left(\frac{2\pi}{T_m}\right)^{\alpha} u^{\alpha+1}du = \frac{1}{u_0}\int_0^{u_0} \pi C\left(\frac{2\pi}{T_m}\right)u^2du \quad (20)$$

All the parameters of Eqs. (19) and (20) are introduced in the research of Lin et al. (2008). Unifying Eq. (20) produces the following for SDOF systems:

$$C = \frac{3\lambda C_N\left(\frac{2\pi}{T_m}\right)^{\alpha-1}u_0^{\alpha-1}}{\pi(2+\alpha)} \quad (21)$$

in which C: is the damping coefficient for a NLVD in a SDOF system.

For MDOF systems, $u$should be replaced by $u_{roof}\phi_{mr,j}f_j$ to produce:

$$C_j = \frac{3\lambda_j C_{N,j}\left(\frac{2\pi}{T_m}\right)^{\alpha_j-1}(u_{roof}\phi_{mr,j}f_j)^{\alpha_j-1}}{\pi(2+\alpha_j)} \quad (22)$$

where C_j: is the damping coefficient for the NLVD on the j^{th}floor of a MDOF system.

The DR given by NLVDs can be determined as the following when Eq. (22) is inserted into Eq. (5):

$$\xi_m = \frac{3\sum_j \frac{\lambda_j C_{N,j}}{(2+\alpha_j)} \left(\frac{2\pi}{T_m}\right)^{\alpha_j - 2} u_{roof}^{\alpha_j - 1} \varphi_{mr,j}^{\alpha_j + 1} f_j^{\alpha_j + 1}}{2\pi \sum_i m_i \varphi_{mi}^2} \quad (23)$$

Step E8: THA of Buildings with NLVD

THA is used to investigate the structural behaviour with NLVDs in order to develop a practical design. The goals of THA at this step are:

- To verify the similar energy dissipation for LVDs and NLVDs under the same seismic excitation;
- To assess the structural performance with NLVDs and compare it to the retrofitting target defined in Step E3;
- To assess the damping provided by the NLVDs and compare it to damping target defined in Step E4.

If the performance target of the structure is not met, Steps E3 and E4 should be revised.

3.2. Financial Aspect of Comprehensive Design Procedure

Decision-making about the seismic retrofit of structures requires concurrent study of the technical and economic effects of the retrofit. Therefore, providing a comprehensive design procedure which includes the design of viscous dampers and an economic assessment of the seismic retrofit is necessary. In other studies on the economic evaluation of seismic retrofit of structures using viscous dampers, two goals have been generally pursued: 1) Minimizing the lifecycle cost of a structure without conducting a feasibility study on the seismic retrofit; and 2) application of evolutionary algorithms to find the optimal parameters for viscous dampers and reduce retrofit costs.

In this study, the feasibility of seismic rehabilitation of structures with VDs is initially investigated through cost-benefit analysis (Eq. (37)). If the benefit-cost ratio is greater than 1, the seismic rehabilitation is economically feasible. If it is less than 1, the seismic retrofit is not recommended (the goal of retrofitting should be revised).

A new parameter called the Retrofit Level (RL) is introduced here which depends on the dynamic response of a structure at various levels of retrofitting to determine the ORL. This section addresses the level of retrofitting which should be chosen as the ORL if the benefit-cost ratio is greater than 1. In this study, Eq. (39) can be applied as a tool for decision-making to introduce an ORL where the initial cost of implementation of seismic retrofitting is balanced by a decrease in the costs of structural failure in future earthquakes.

Step F1: Determine the Design Timeline

Typical buildings have a design horizon of between 40 and 60 years. As obtained by Kappos and Dimitrakopoulos (2008), it is determined that increasing the time frame of the design horizon will increase the benefit-cost ratio. In this study, the design horizon is 50 years.

Step F2: Calculation of the Discount Rate

The discount rate converts the cost of future seismic damage to the net present worth. At a constant discount rate β over continuous time *t*, the discount rate factor can be expressed as:

$$D(t) = \left\{ \lim_{n\to\infty} \left(1 - \frac{\beta}{n}\right)^n \right\}^t = e^{-\beta t} \quad (24)$$

Step F3: Initial Cost Estimation

The initial costs of a building consist of the material, manufacturing and installation costs of building elements. For steel structures, this is normally considered proportional to the total weight of all structural elements. It also could be affected by parameters such as the cost of connections or other elements of the structure, which plays a role in its workability (Beheshti and Asadi, 2020; Fragiadakis et al., 2006).

Although there is no need to estimate the initial costs of a steel structure in order to determine the ORL, it is used to estimate the

costs of the limit states and failure cost. In this article, the 2016 RS Means Building Construction Costs are used to evaluate the initial costs of the building.

Step F4: Calculating the Costs Correlated with Limit States

The cost of the limit state includes the potential cost of damage caused by probable earthquakes in the building lifecycle. The limit state cost is the sum of the earthquake consequences and includes the cost of fixing the damage induced by the earthquake C_i^{dam}, damage to the contents of the building C_i^{con}, relocation C_i^{relo}, lost rent revenue C_i^{ren}, loss of commercial revenue C_i^{inc}, treatment of minor injuries $C_i^{m,inj}$, treatment of serious injuries $C_i^{s,inj}$, fatalities C_i^{fat} and other direct and indirect financial costs. The cost of the i^{th} limit state could be expressed as:

$$C_i^{LS} = C_i^{dam} + C_i^{con} + C_i^{relo} + C_i^{ren} + C_i^{inc} + C_i^{m,inj} + C_i^{s,inj} + C_i^{fat} \quad (25)$$

The details of cost calculations of each parameter with its basic cost for the Los Angeles area and the references for basic cost calculations are listed in Table 2. The third column in the table lists the basic costs according to the 2016 RSMeans Building Construction Costs, changed to present day costs using the following simple formula:

$$\text{Cost in Year A} = \frac{\text{Index for Year A}}{\text{Index for Year B}} \times \text{Cost in Year B} \quad (26)$$

As mentioned, the maximum ISD expresses seven different limit states as reported in FEMA 227. Table 3 lists the damage factors for the seven limit states and other information required to calculate limit states costs.

Table 2 Limit state costs calculation formulas

Cost category	Calculation formula	Adjusted cost	Unit	Reference
Damage	Replacement cost × floor area × damage factor	349.8	/m²	Whitney
Loss of contents	Unit contents cost × floor area × damage factor	756.2	/m²	FEMA 227
Relocation	Unit relocation cost × gross leasable area × restoration time	42.3	/month /m²	FEMA 178
Rental	Rental × rate gross leasable area × restoration time	15.5	/month /m²	FEMA 228
Income	Rental rate × gross leasable area × restoration time	218.2	/month /m²	FEMA 228
Minor injury	Minor injury × cost per person × floor area × occupancy rate × expected minor injury rate	2252	/person	FEMA 228
Serious injury	Serious injury × cost per person × floor area × occupancy rate × expected serious injury rate	22522	/person	FEMA 228
Human fatality	Human fatality × cost per person × floor area × occupancy rate × expected death rate	4110000	/life	FEMA 228

Table 3 Limit states, drift ratios, average damage factors, average loss of function, and percentage of minor and serious injuries and death per person occupancy as per ATC-13 and FEMA227

Limit state	Damage state	Story drift ratio (%)	Damage factor	Loss of function (Days)	Minor injury (%)	Serious injury (%)	Death (%)
1	None	$\Delta < 0.2$	0	0	0	0	0
2	Slight	$0.2 < \Delta < 0.4$	0.005	3.4	0.003	0.0004	0.0001
3	Light	$0.4 < \Delta < 0.7$	0.05	12.08	0.03	0.004	0.001
4	Moderate	$0.7 < \Delta < 1.5$	0.2	44.72	0.3	0.04	0.01
5	Heavy	$1.5 < \Delta < 2.5$	0.45	125.66	3	0.4	0.1
6	Major	$2.5 < \Delta < 5.0$	0.8	235.76	30	4	1
7	Destroyed	$5.0 < \Delta$	1	346.93	40	40	20

Step F5: Calculating LCC of Non-Rehabilitated Structure

The LCC of a structure is the cost necessary to maintain a presently occupied structure (during the life of the structure) in accordance with the design target. The LCC of a non-rehabilitated building includes the initial cost, maintenance costs and failure cost caused by design loads.

The initial cost has been explained in detail in Step F3. The maintenance costs include expenditures made to keep the building operational. The failure costs are the damage to structural and non-structural elements of the building due to a probable earthquake during building lifecycle. The failure costs include indirect costs related to the loss or replacement of goods in the building, loss of rental or commercial income, the treatment cost of minor and severe injuries and fatalities among residents. The failure costs associated with a limit state are equal to the limit state cost multiplied by the probability of the structure being exposed to loading of the limit state. Wen and Kang (2001) ignored maintenance costs because they are insignificant relative to initial and failure costs and introduced the following relationship for the LCC of a structure.

$$LCC_{NR} = C_{IN} + C_{FU_{NR}} \tag{27}$$

in which LCC_{NR}: is the LCC for a non-rehabilitated structure, C_{IN}: is the initial cost and $C_{FU_{NR}}$: is the failure cost for the non-rehabilitated structure. The relationship laid out by Wen and Kang (2001) for determining the failure costs of the non-rehabilitated structure is as follows:

$$C_{FU_{NR}} = \frac{\nu}{\beta}(1 - e^{-\beta t}) \sum_{i=1}^{N} C_i^{LS} P_i^{NR} \tag{28}$$

in which P_i^{NR}: is the possibility of the response of a non-rehabilitated structure being at the i^{th} limit state, C_i^{LS}: represents the costs associated with the i^{th} limit state (see Table 2), N: is the number of limit states, t: denotes the time of the project outlook, β: denotes the discount rate and ν represents the annual occurrence of substantial earthquakes as modelled by the Poisson distribution function. In this equation, P_i^{NR}: is determined as:

$$P_i^{NR} = P_i^{NR}(\Delta > \Delta_i) - P_{i+1}^{NR}(\Delta > \Delta_{i+1}) \tag{29}$$

$$P_i^{NR}(\Delta > \Delta_i) = (-\frac{1}{t}).ln[1 - \bar{P}_i^{NR}(\Delta > \Delta_i)] \tag{30}$$

in which $\bar{P}_i^{NR}(\Delta > \Delta_i)$: is the annual exceedance possibility (AEP) of maximum ISD ratio Δ_i. The AEP for the i^{th} limit state is derived as:

$$\bar{P}_i^{NR}(\Delta > \Delta_i) = \rho e^{-\psi \Delta_i} \tag{31}$$

in which ρ and ψ: are obtained by the best fit to the $\bar{P}_i^{NR} - \Delta_i$ pairs. These pairs correspond to earthquakes with probabilities of 2%, 10%, and 50% over 50 years. THA is used to produce the graphs. To conduct THA, three sets of earthquake records that contain longitudinal and traverse components from the Somerville and Collins (2002) database are used here.

Determination of P_i^{NR} for drift Δ_i^{NR} can be carried out by numerical calculation. After calculating P_i^{NR} for the drift percentage related with each limit state, the failure cost is obtained using the THA carried out in Step E2. As shown in Eq. (27), the LCC for a non-retrofitted structure is the sum of the failure cost from this step and the initial cost from Step F3.

Step F6: Determining the Total Cost of NLVDs

To determine the financial adequacy of the NLVDs in Step E8, the costs related to the parts associated to energy dissipation must be evaluated. This cost includes the purchase of NLVDs, their installation and maintenance to keep them in working order. The purchasing cost is proportional to the capacity and stroke range (Taylor, 1999). The installation cost of the dampers includes the bracing on which they are mounted and labour costs. The maintenance

cost includes keeping the damper in performance mode after each earthquake such that performance is not affected. The cost associated with dampers may be gained as:

$$C_D = C_0 + \frac{\nu}{\beta}(1 - e^{-\beta t}) \sum_{j=1}^{N} C_j^m P_j \quad (32)$$

in which C_D: refers to the total cost of protective devices, C_0: denotes the initial cost for protective devices, N: is the quantity of dampers, C_j^m: represents the cost for damper maintenance and P_j: is the possibility that the devices may need maintenance because of earthquakes.

Step F7: LCC for Rehabilitated Structure with NLVD

The LCC of a structure with NLVDs involves of the initial and failure costs of a structure that is rehabilitated with NLVDs as follows:

$$LCC_R = C_{IN} + C_{FU_R} \quad (33)$$

in which LCC_R: is the LCC of a rehabilitated building and C_{FU_R}: represents the failure cost for a rehabilitated structure. The difference among Eqs. (33) and (27) is determined by assessing the failure costs. The failure costs for rehabilitated structure are calculated by the results of THA (maximum ISDΔ_i^R) in Step E8 as:

$$C_{FU_R} = \frac{\nu}{\beta}(1 - e^{-\beta t}) \sum_{i=1}^{N} C_i^{LS} P_i^R \quad (34)$$

in which P_i^R: is the possibility of a rehabilitated structural seismic response falling into the i^{th} limit state. Determining P_i^R depends on Step E5, except that the probability of corresponding to Δ_i^R is derived from the THA of a retrofitted building to calculate P_i^R.

Step F8: Economic Assessment of Dampers Designed Based on Cost-Benefit Analysis

The calculations in Steps F5 and F7 are used to calculate the expected annual benefit by reducing the earthquake damage to retrofitted buildings as:

$$B_1 = LCC_{NR} - LCC_R \quad (35)$$

in which B_1: is the annual benefit expected due to a decrease in earthquake damage. In order to economically assess the retrofitting applied, the projected benefit in the project outlook is compared to expenditures for rehabilitation. The projected benefit in the design horizon is:

$$B_t = B_1 \frac{1 - (1 + \beta)^{-t}}{\beta} \quad (36)$$

in which B_t: is the expected benefit during the design period. For economic assessment of the applied rehabilitation, one can use B_t/C_D as:

$$\frac{B_t}{C_D} = \frac{B_1 \frac{1 - (1 + \beta)^{-t}}{\beta}}{C_0 + \frac{\nu}{\beta}(1 - e^{-\beta t}) \sum_{j=1}^{N} C_j^m P_j} \quad (37)$$

If the projected benefit during the design period is larger than the expenditure on rehabilitation the structure, then $B_t/C_D > 1$ and the rehabilitation applied is economical. Otherwise, revisions in Steps E3 and E4 will be necessary.

4. Determining the ORL

In prior sections, a comprehensive design method including the engineering and financial aspects of seismic rehabilitation of buildings with NLVDs has been presented. In the economic evaluation of retrofitted buildings using cost-benefit analysis, only the criterion of $B_t/C_D > 1$ is considered from a financial perspective and no action is taken to address ORL. As stated, most studies that examine the financial effects of seismic retrofitting of structures are focused on the use of evolutionary algorithms to determine optimum design which require time-consuming calculations and bring new complications into the design process for engineers. In this part, to complete this proposed design procedure, a simple method for determining the ORL of structures is introduced based on the LCC

of the structure. The flowchart in Figure 3 depicts the proposed method as a complement to comprehensive design procedure.

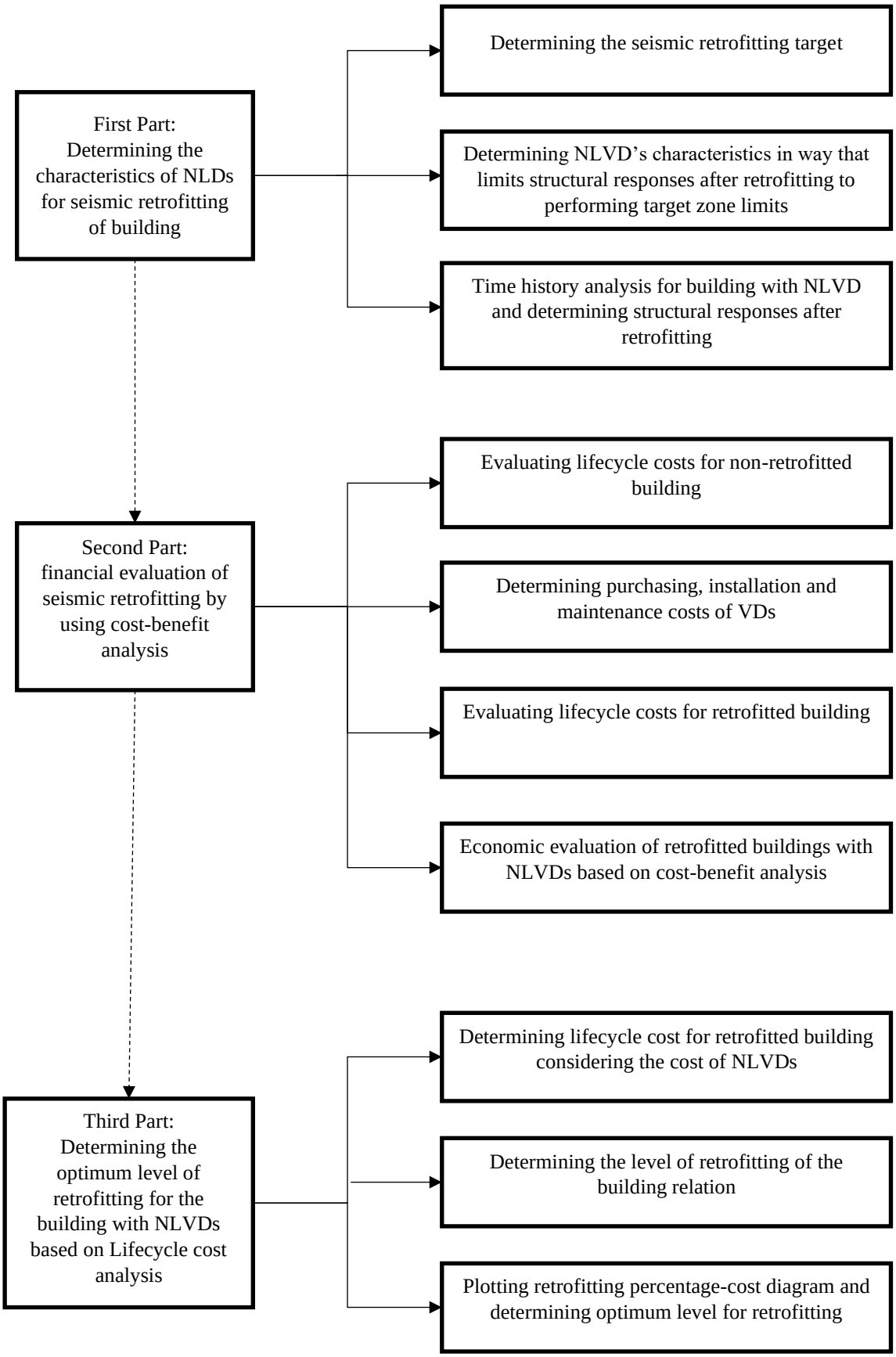

Fig. 3. Proposed method for determining ORL

4.1. Determining the total LCC

In a more general statement than what has been provided in Step F7, the total LCC of the retrofitted building during the design horizon can be calculated as the sum of the initial cost of the building, failure costs due to probable earthquakes in the design horizon and costs associated with the dissipation system. The expected total LCC can be expressed as a function of t and design variable vector X as follows:

$$E[C(t,X)] = C_{IN} + C_D(X) + C_{FU_R}(X) \quad (38)$$

in which $E[C(t,X)]$: is the total LCC over the design horizon. Although the use of NLVDs increases retrofitting costs, a decrease in the likelihood of a failure cost leads to a considerable drop in the costs that are induced by probable earthquakes in the building lifecycle.

4.2. Determining Retrofitting Level Relation

The proposed relation to determine the retrofitting level of the maximum ISD ratio of the stories is presented as:

$$RL = \frac{\Delta}{Before^{\Delta_{Before}^{max_{LS_1}}}_{max_{After}^{max}}} \quad (39)$$

in which RL: is the retrofitting level, Δ_{Before}^{max}: denotes the maximum ISD ratio for the state before retrofitting, Δ_{After}^{max}: represents maximum ISD ratio for the state after rehabilitation and Δ_{LS_1}: is the maximum ISD ratio in the first limit state.

The main difference between existing methods for economic assessment of seismic retrofitting and the proposed method is that existing methods seek to minimize the lifecycle cost of a structure at a constant retrofit level, while the RL is employed as an effective variable for the selection of optimal seismic retrofit strategy in the proposed method. In other words, the proposed method uses different *RL* values and the corresponding failure costs to determine ORL.

4.3. Plotting the RL-Cost Diagram and Determining ORL

The ORL is the result of minimizing the LCC of the structure and is the level of seismic retrofitting of a structure for which the total cost of the protective system plus the expected failure cost is minimized. By increasing the RL, the cost of retrofitting will increase, but the failure cost will also drop, because the damage due to probable earthquakes will decrease as well. As shown in Figure 4, the ORL is at the intersection of the diagrams of the damping system costs and expected failure costs due to probable earthquakes over the design horizon. In the design examples, attempts are made to use the proposed relation and design procedure to determine ORL for buildings with different dynamic characteristics under the effect of different earthquakes.

5. Design Examples

Without loss of generality, let's consider the three benchmark building structures represented in Figures 5 to 7. To assess the suggested comprehensive design process in this research, those three benchmark structures offered by Ohtori et al. (2004) are used. These three, nine, and twenty-story buildings were designed as part of the SAC Steel Project. The reason of selecting these structures for the design examples is to provide a clear basis for assessing the suggested comprehensive design procedure. All three buildings vary considerably in dynamic specifications and lateral strength capacity, thereby providing a broad basis for comparing different structural control strategies. They represent low, medium and high-rise buildings. The structural system for each of the three buildings consists of a perimeter moment-resisting frame and the interior pinned frames using the shear connection. The full description of the structure specifications includes the dimensions, size of members, loading and type of materials used in the study by Ohtori et al. (2004).

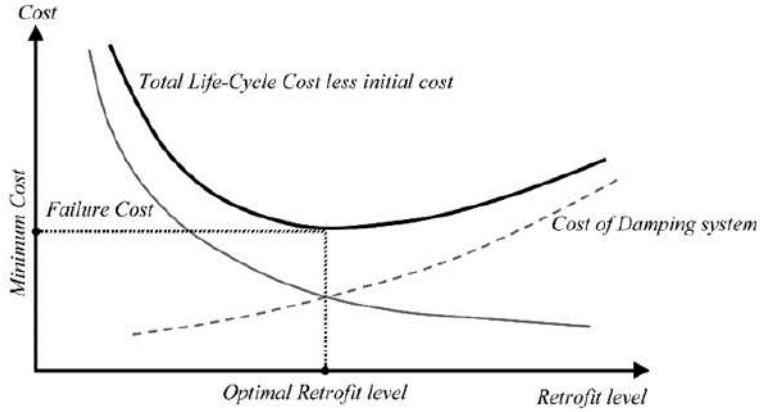

Fig. 4. Retrofitting level-cost diagram

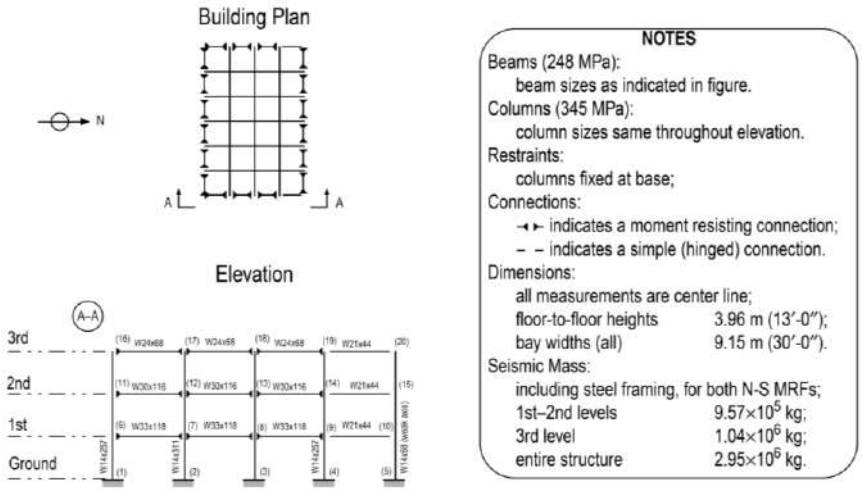

Fig. 5. 3-Story benchmark building N-S MRF (Ohtori et al., 2004)

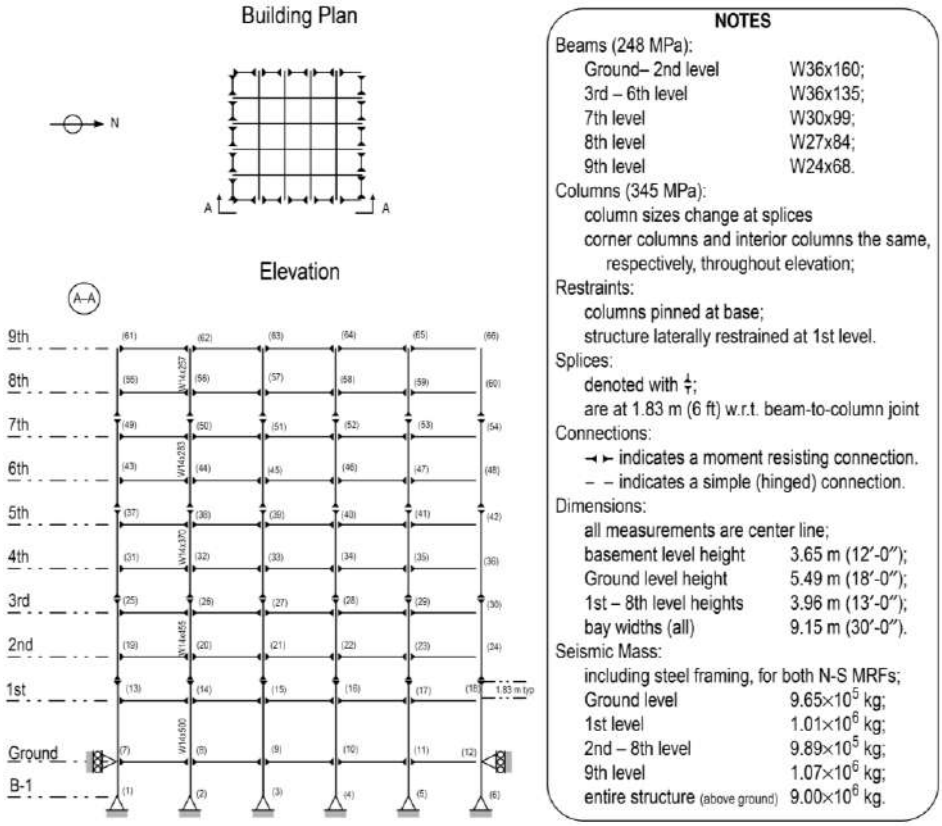

Fig. 6. 9-Story benchmark building N-S MRF (Ohtori et al., 2004)

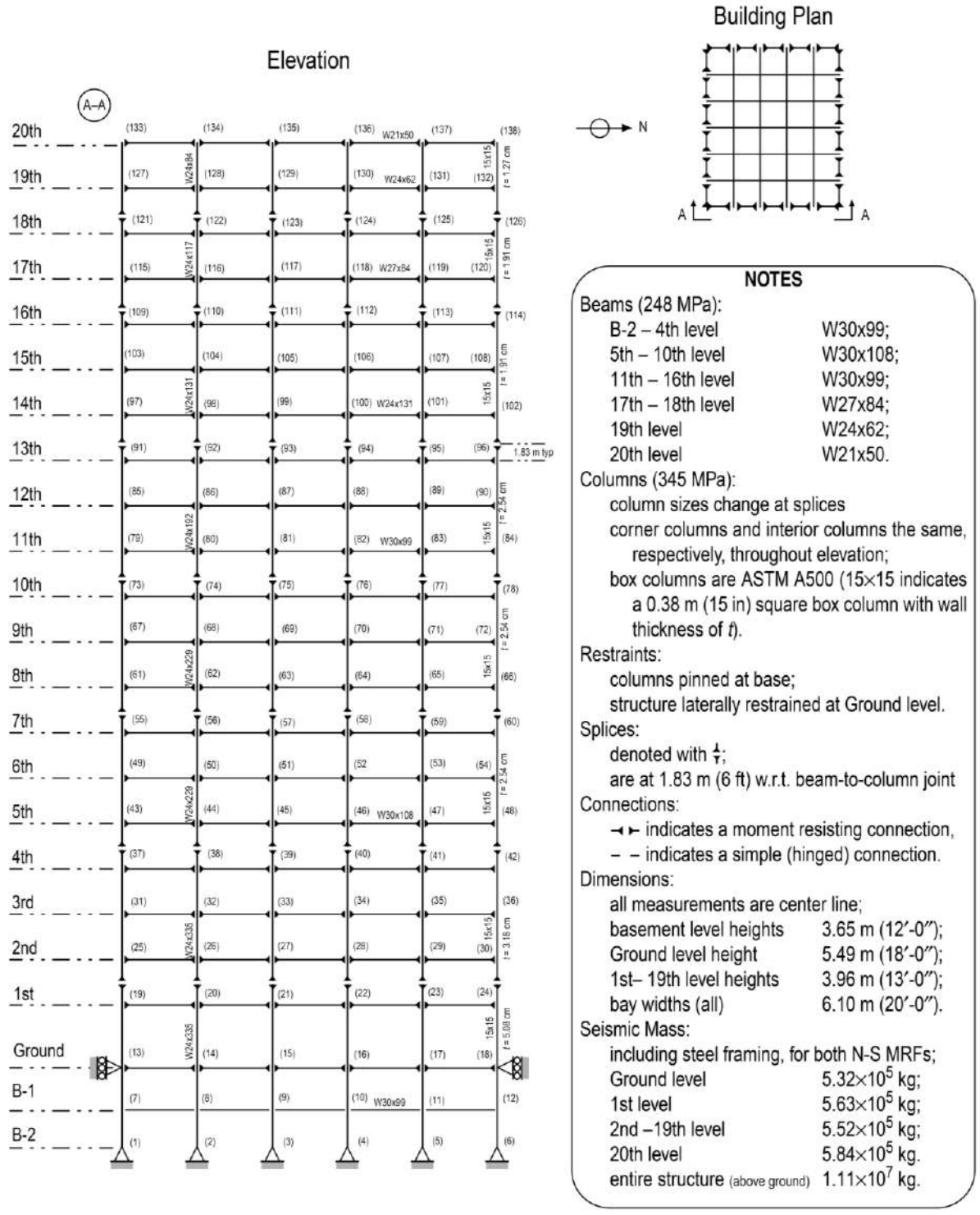

Fig. 7. 20-Story benchmark building N-S MRF (Ohtori et al., 2004)

5.1. Implementing Comprehensive Design Process for Benchmark Structures

In this research, only the important results of implementing the comprehensive design procedure for benchmark structures are presented and interpreted. The complete results of the step-by-step implementation and application of the comprehensive design procedure in the next phase of this research has recently been published in the companion paper (Bahmani and Zahrai, 2018). Based on the results of the THA on buildings without dampers for maximum ISD with different earthquake intensities (0.5, 1 and 1.5), the rehabilitation target is set to a 43% decrease in structural response. Eqs. (17) and (21) can be used to calculate

the damping coefficient of LVDs and NLVDs ($\alpha = 0.3$) as shown in Figure 8 for each story of the benchmark buildings. The lower stories are assigned more damping because the damping distribution in the structure is proportional to the strain energy of the building floors.

As shown in Figure 9, although the seismic retrofitting in all of the benchmark buildings led to the improved seismic performance, the reduction in the ISD for the 9-story structure is higher than that of other buildings.

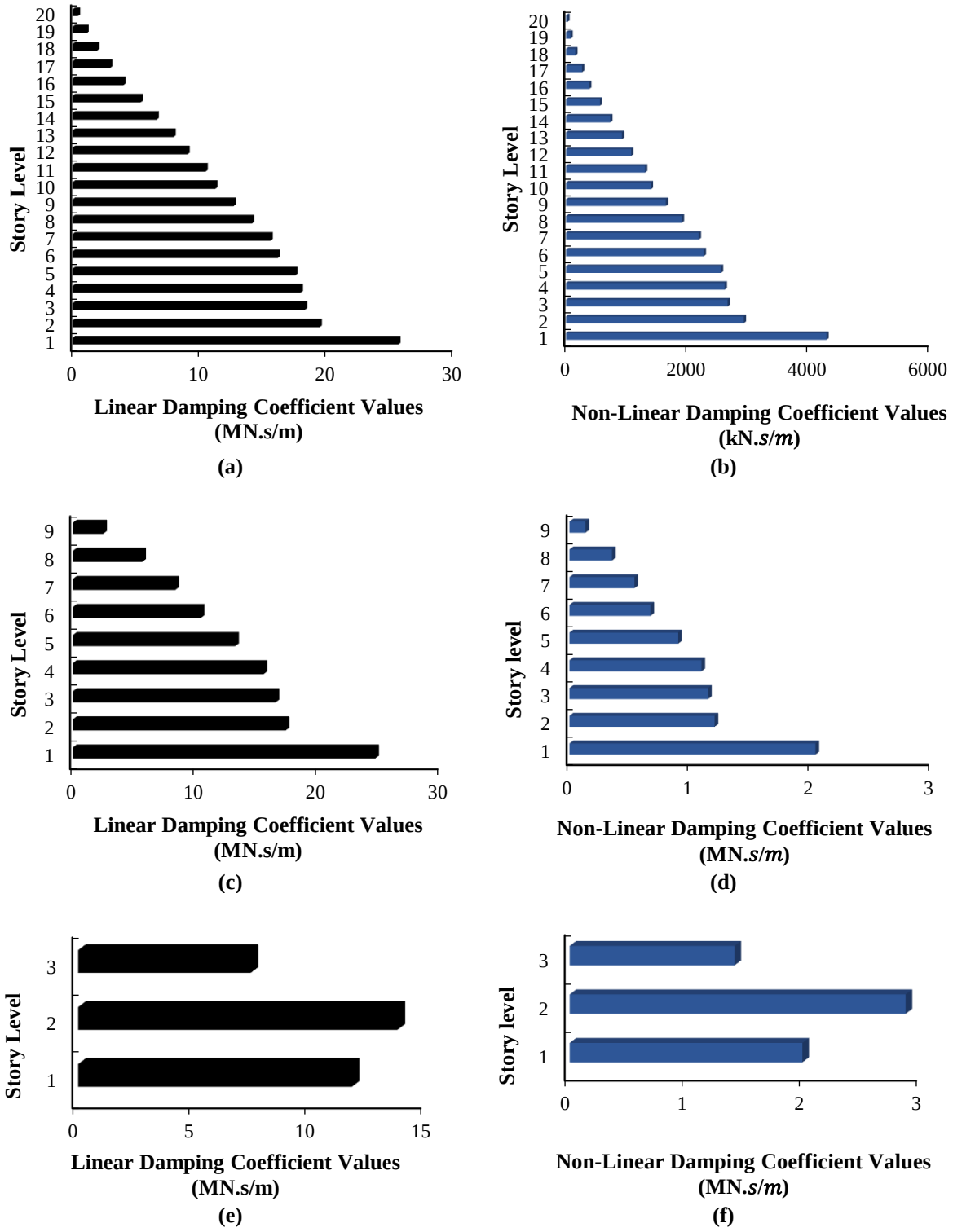

Fig. 8. Damping coefficients of LVDs and NLVDs for benchmark structures: a,b) 20-story; c,d) 9-story; and e,f) 3-story

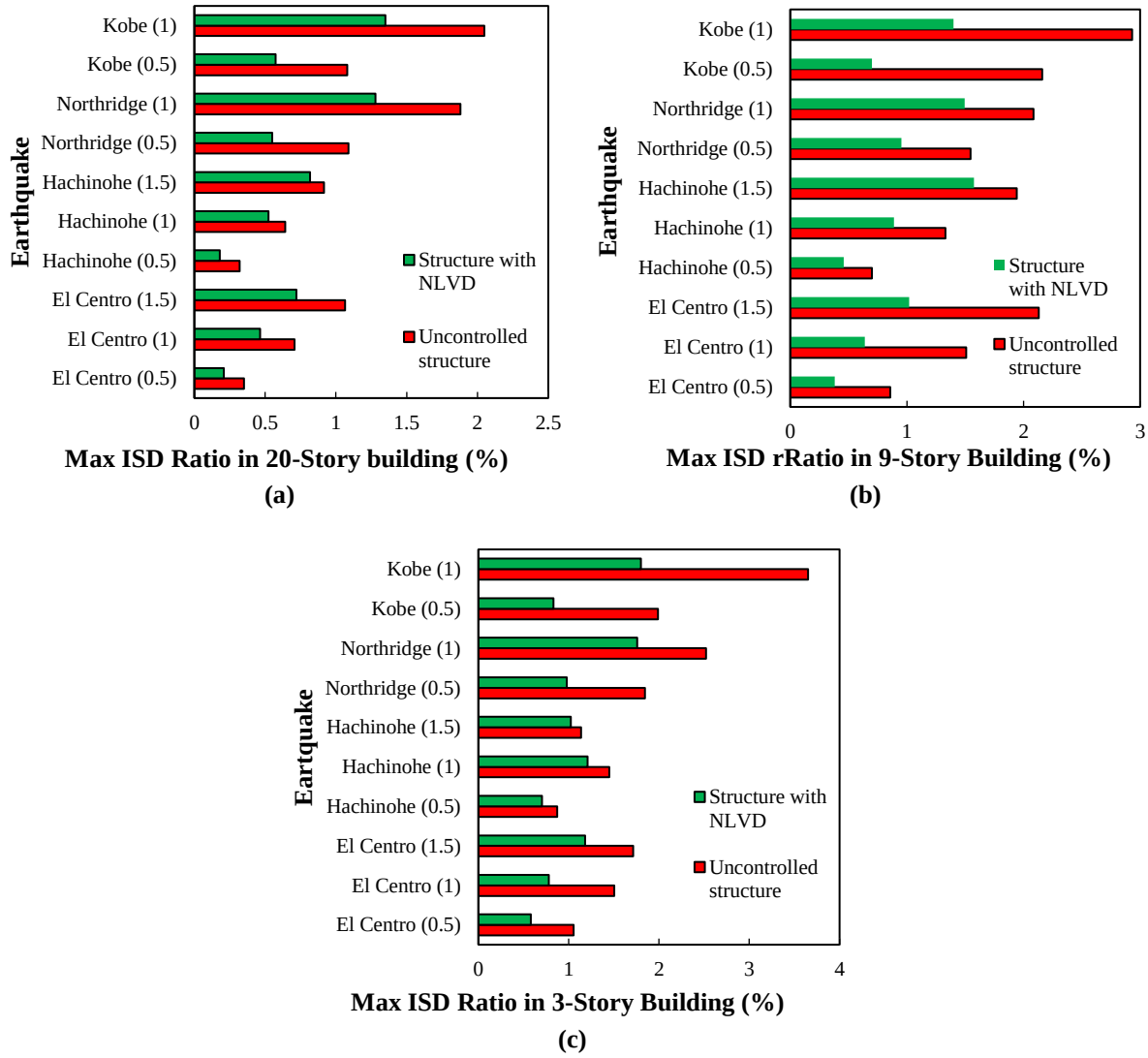

Fig. 9. Maximum ISD ratio in uncontrolled structures and structures with NLVDs: a) 20-story; b) 9-story; and c) 3-story

Figure 10 shows the maximum ISD ratios under each of those four earthquakes with coefficients of 1. As shown here, for each of four earthquake records, the maximum uncontrolled ISD ratios occurred at roof level. This suggests that the comprehensive design procedure is sufficiently capable of controlling the roof response.

Comparison of the results of the comprehensive design process on benchmark structures with NLVDs produced the following points:

- The buildings rehabilitated using the comprehensive design process performed better under low to medium intensity earthquakes than under severe earthquakes.
- Comparison of the results from the THA of the structures retrofitted with NLVDs for 3-, 9- and 20-story building shows that the comprehensive design procedure performed better for medium-rise buildings. In other words, the maximum decrease in seismic response (for an average of ten earthquake records) was in the 9-story building.

Figure 11 depicts the non-linear THA, three pairs of maximum ISD ratios and the AEP for non-retrofitted and retrofitted benchmark buildings. These pairs correspond to earthquakes with probabilities of 2, 10 and 50% over 50 years. As shown in Figure 11, the proposed comprehensive design procedure significantly reduced the ISD ratio of the benchmark buildings at all three levels of earthquake hazard.

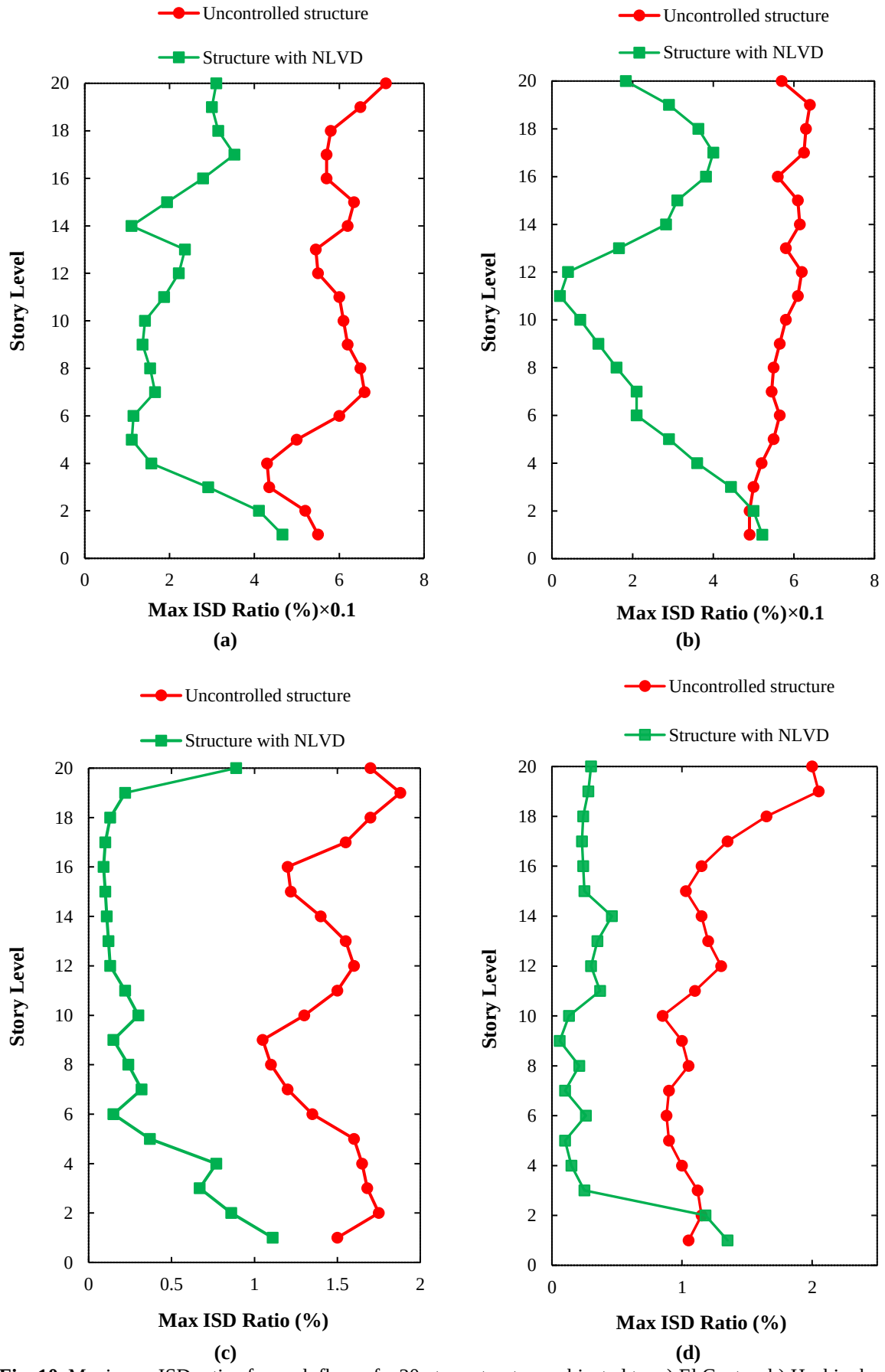

Fig. 10. Maximum ISD ratios for each floor of a 20-story structure subjected to: a) El Centro; b) Hachinohe; c) Northridge; and d) Kobe earthquakes

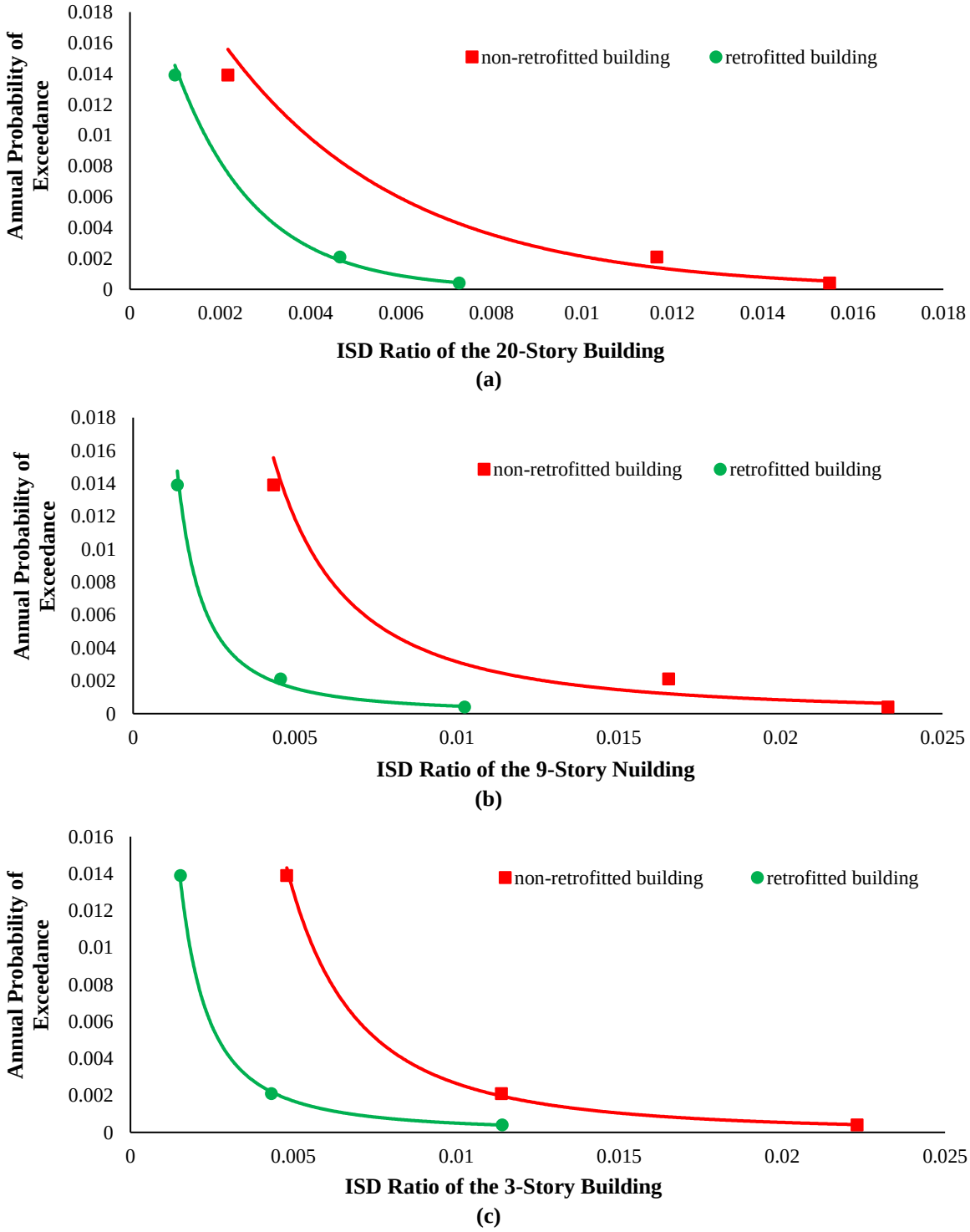

Fig. 11. Comparison of annual probability of exceedance for each damage state for retrofitted and non-retrofitted structures: a) 20-story; b) 9-story; and c) 3-story

The charts plotted for earthquake hazard levels for the probabilities of occurrence of 2%, 10% and 50% over 50 years indicated that the proposed design method significantly could reduce the ISD ratio at all levels of earthquake hazard.

Figure 12 shows that the return periods for 20-, 9- and 3-story buildings were 41, 5 and 16 years, respectively.

To determine the ORL, as mentioned, the failure cost curve is drawn against the cost of the protective system curve. An increase in RL will decrease the ISD and the failure cost. In order to plot the cost curves of the protective system and failure costs, all structures are modelled at three

retrofitting levels with NLVDs. Next, for each structure, THA is used with those ten earthquake records defined in Step E1. By determining the maximum ISD for each structure and the maximum auxiliary force of NLVDs at each level, the damping system cost diagram could be plotted for various retrofitting percentages.

Comparison of the retrofitting investment payback period diagrams indicates that the return period is shorter for medium-rise buildings.

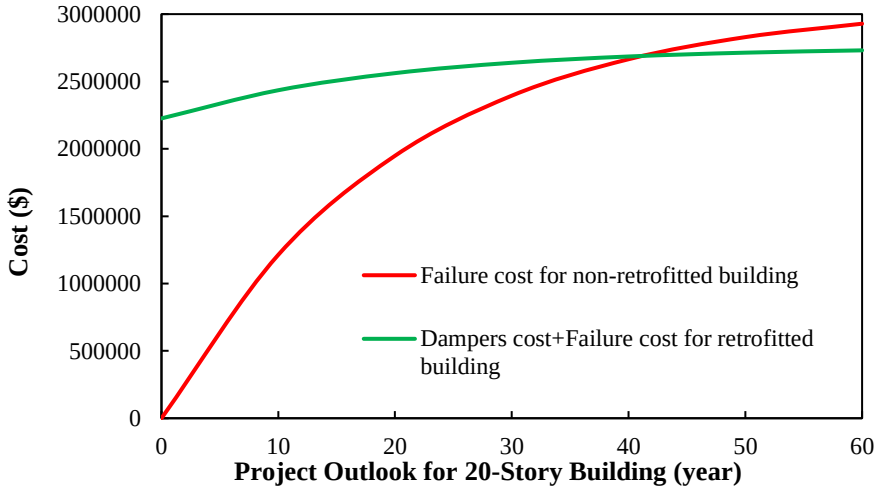

(a)

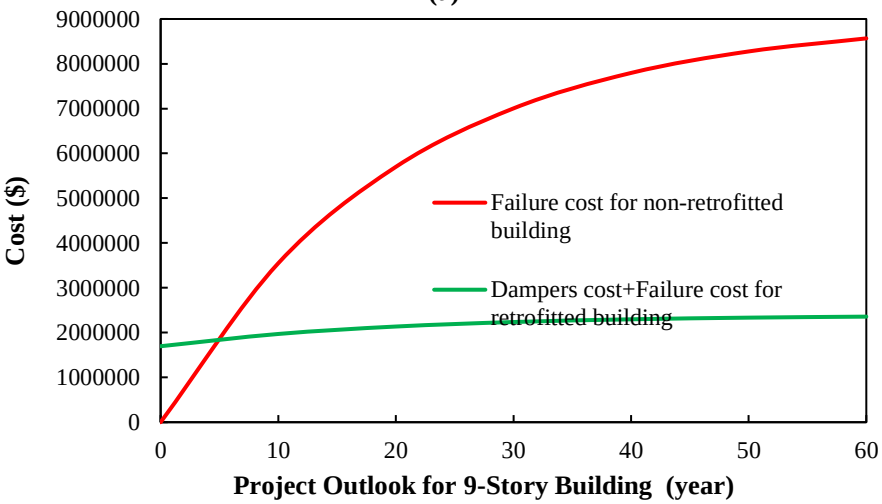

(b)

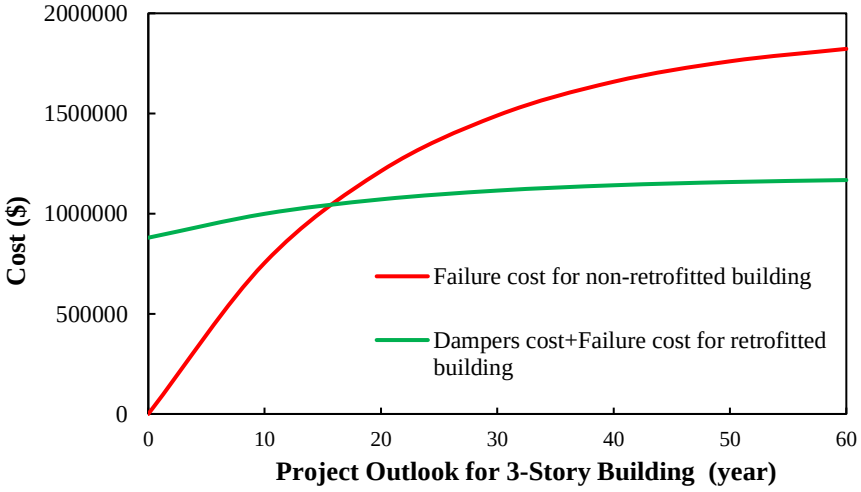

(c)

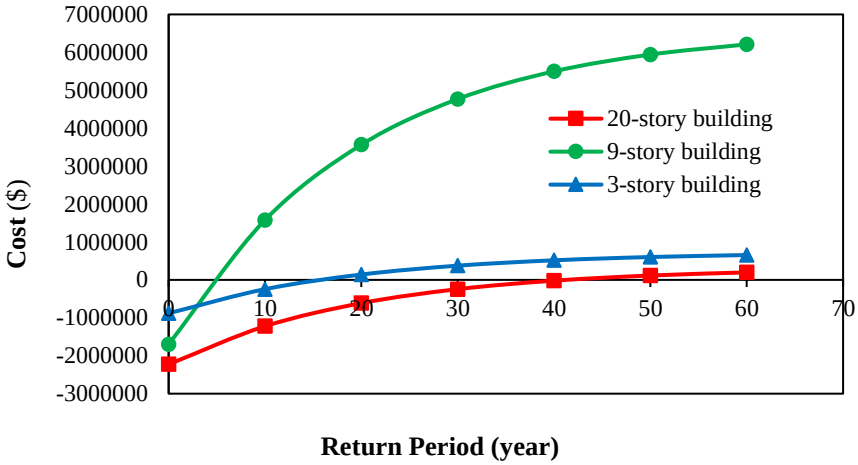

(d)

Fig. 12. Return period for retrofitting investments: a) 20-story; b) 9-story; and c) 3-story

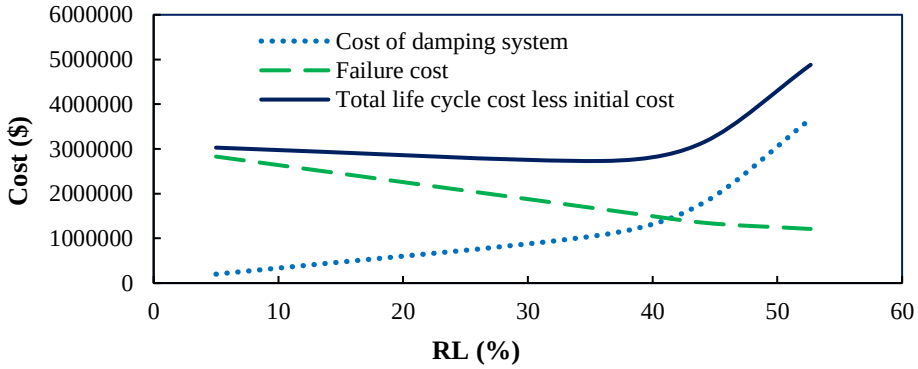

(a)

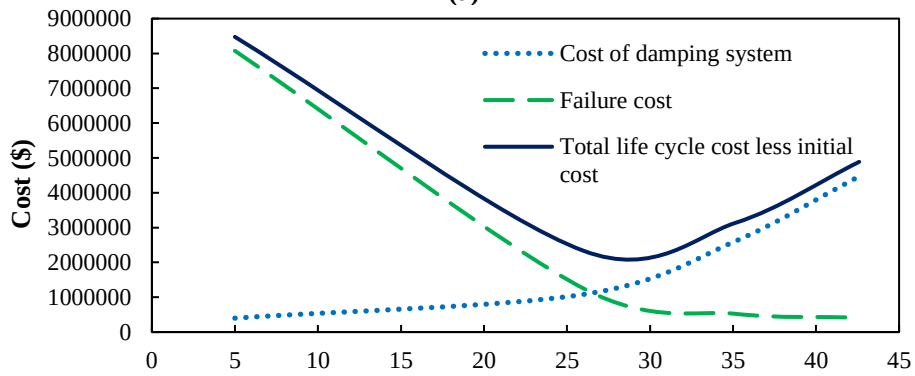

(b)

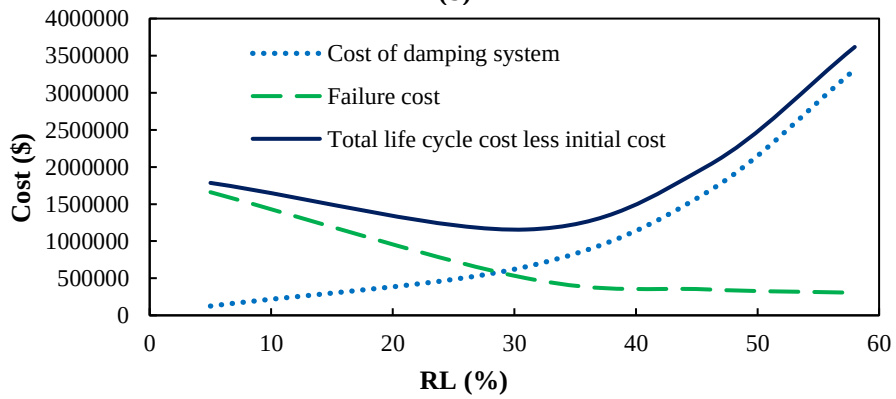

(c)

Fig. 13. ORL for: a) 20; b) 9; and c) 3-story buildings

After drawing the failure cost diagrams, each building is subjected to THA under the earthquake records defined in Step F5 and at the end the of Step F7. By determining the failure cost of the RLs, the failure cost diagram for various retrofitting percentages can be drawn. Figure 13 plots the functions of the damping system cost and failure costs for all buildings. As shown, the ORL values for 20-, 9- and 3-story buildings are 40%, 27% and 29%, respectively.

By investigating the curves for determining the ORL, it can be deduced that the ORL in medium-rise structures is lower than that of other structures. In other words, investing less created a greater decrease in the failure costs and the benefit-cost ratio is higher for medium-rise buildings (like the 9-story case) than for the other buildings; hence, implementation of a seismic rehabilitation in these structures has comparative advantages from a financial perspective. Moreover, the benefit-cost ratio increased as the project horizon time increased and the rate of increase in this ratio was rapid for less than 30 years but slowed after 40 years.

5.2. Sensitivity Analysis

The ORL depends on parameters which are often difficult to estimate. The effective parameters for determining ORL are the purchase, installation and maintenance costs of viscous dampers, structural failure costs in future earthquakes for different retrofit levels, design horizons and discount rates. The first two parameters are discussed in Section 5.2 (Figure 13) and sensitivity analysis is conducted here to determine the effect of changes in the design horizon and discount rate on the benefit-cost ratio in this section.

Figure 14 shows how changes in the design horizon and interest rate affect the economic assessment results of seismic retrofitting of the benchmark buildings. As shown, as the design horizon increases for $t < 30$, the benefit-cost ratio increases to a saturation point of about $t = 40$, after which the changes are small. Figure 14 also shows that, as the discount rate increases, the present value of the future benefit and benefit-cost ratio decrease. The high discount rate dramatically reduces the attractiveness of investment in the seismic retrofitting of structures.

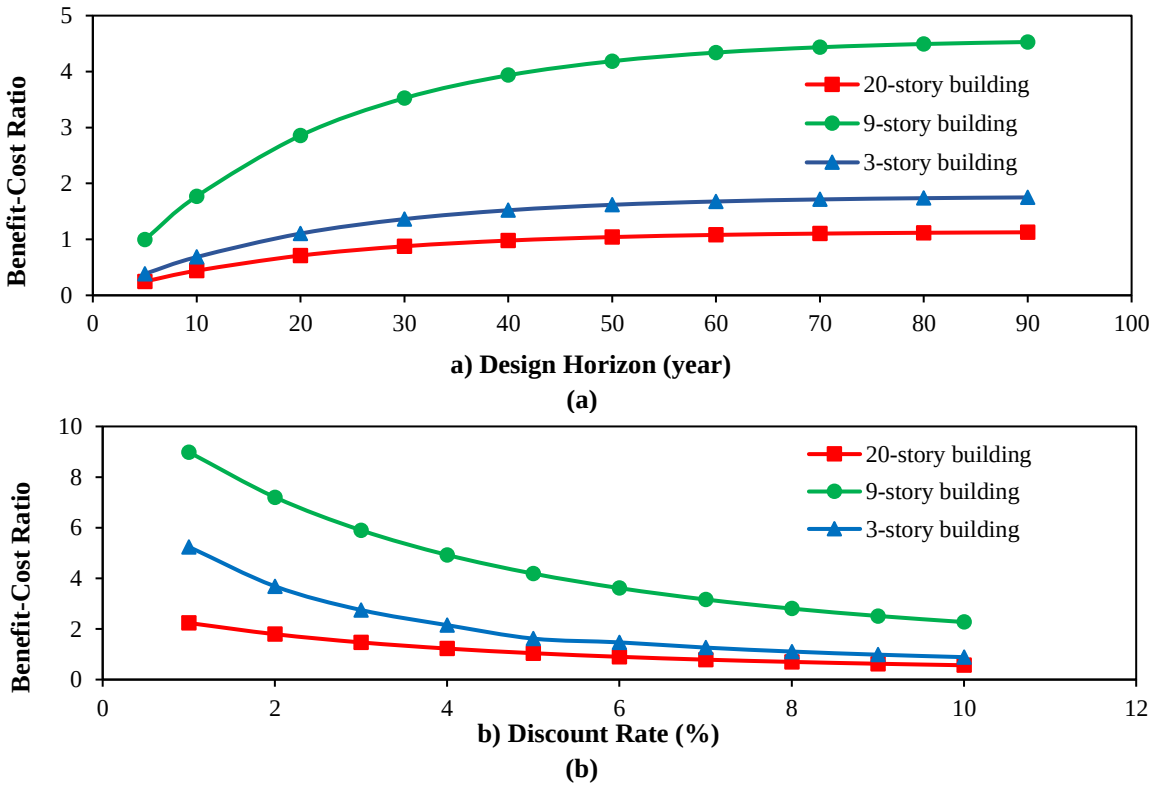

Fig. 14. Effect of: a) design horizon; and b) discount rate on cost-benefit assessment of benchmark structures

As observed in Figure 14 the benefit-cost ratio was sensitive to the discount rate and the high interest rate reduced this ratio dramatically along with the attractiveness of investment for seismic retrofit.

6. Conclusions

The significance of seismic retrofitting and the role of the long-term benefit of the expected failure cost reductions compared to seismic retrofit costs of existing structures are increasingly apparent for structural engineers. The use of NLVDs is an effective method of seismic retrofit of structures. These dampers have become increasingly attractive in recent years due to their comparatively simple design and installation.

Aimed to achieve a scientific design method for professional designer engineers, a comprehensive design process was presented for seismic retrofit of steel buildings in this study. The proposed procedure simultaneously assessed the engineering aspects and economic effects of seismic retrofit. The results of analysis of benchmark buildings revealed that the comprehensive design procedure is accurate enough for buildings with non-uniform distribution of mass and stiffness over the height in spite of other existing design procedures presented in other articles and codes. In the proposed procedure, the ISD ratio was used as the effective parameter of structural response in order to define limit states. The results of analysis of benchmark buildings indicated that the proposed procedure can reduce the response of structures and improve their performance. The numerical results also demonstrated that although the expected failure cost decreases for all structures and earthquakes with various intensities, the suggested design procedure is more influential to improve the performance of middle-rise structures and reduce the failure cost of earthquakes with moderate intensities.

LCC analysis showed that the ORL values for 20-, 9- and 3-story buildings are 40%, 27% and 29%, respectively, and the retrofitting cost return period is shorter for mid-rise buildings. However, the higher benefit-cost ratio in these structures compared to others was a relative financial advantage for seismic retrofitting in medium-rise buildings. Sensitivity analysis showed that the benefit-cost ratio for seismic retrofitting is sensitive to the time horizon of the project and the discount rate. Thus, an increase in the time horizon of the project and reducing the discount rate will increase the attractiveness of investment in seismic retrofitting.

6. References

Altieri, D., Tubaldi, E., De Angelis, M., Patelli, E. and Dall'Asta, A. (2018). "Reliability-based optimal design of nonlinear viscous dampers for the seismic protection of structural systems", *Bulletin of Earthquake Engineering*, 16, 963-982, https://doi.org/10.1007/s10518-017-0233-4.

Aydin, E., Noroozinejad Farsangi, E., Öztürk, B., Bogdanovic, A. and Dutkiewicz, M. (2019). *Improvement of building resilience by viscous dampers*, In: Resilient Structures and Infrastructure, Noroozinejad Farsangi E., Takewaki I., Yang T., Astaneh-Asl A., and Gardoni P., (eds.), Springer, 105-127, https://doi.org/10.1007/978-981-13-7446-3_4.

Bahmani, M. and Zahrai, S. M. (2018). "Application of a comprehensive seismic retrofit procedure for steel buildings using nonlinear viscous dampers", *International Journal of Civil Engineering*, 17(1 August), 1-19, https://doi.org/10.1007/s40999-018-0384-y.

Banazadeh, M., Gholhaki, M. and Parvini Sani, H. (2017). "Cost-benefit analysis of seismic-isolated structures with viscous damper based on loss estimation", *Structure and Infrastructure Engineering*, 13(8), 1045-1055, https://doi.org/10.1080/15732479.2016.1236131.

Beheshti, M. and Asadi, P. (2020). "Optimal seismic retrofit of fractional viscoelastic dampers for minimum life-cycle cost of retrofitted steel frames. *Structural and Multidisciplinary Optimization*, 61(5), 2021-2035, https://doi.org/10.1007/s00158-019-02454-w.

Bommer, J.J., Elnashai, A.S, and Weir, A.G. (2000). "Compatible acceleration and displacement spectra for seismic design codes", *Proceedings of the 12th World Conference on Earthquake Engineering*, Auckland, New Zealand.

Chopra, A. K. and McKenna, F. (2016). "Modeling viscous damping in nonlinear response history analysis of buildings for earthquake excitation", *Earthquake Engineering and Structural Dynamics*, 45(2), 193-211, https://doi.org/10.1002/eqe.2622.

Dall'Asta, A., Scozzese, F., Ragni, L. and Tubaldi, E. (2017). "Effect of the damper property variability on the seismic reliability of linear systems equipped with viscous dampers", *Bulletin of Earthquake Engineering*, 15(11), 5025-5053, https://doi.org/10.1007/s10518-017-0169-8.

Dall′ Asta, A., Tubaldi, E. and Ragni, L. (2016). "Influence of the nonlinear behavior of viscous dampers on the seismic demand hazard of building frames", *Earthquake Engineering and Structural Dynamics*, 45(1), 149-169, https://doi.org/10.1002/eqe.2623.

Edip, K., Bogdanovic, A., Stojmanovska, M., Poposka, A. and Farsangi, E.N. (2020). "A new approach in simulation of soil-structure interaction problems including damper effects", *International Journal of Earthquake and Impact Engineering*, 3(1), 1-14, https://doi.org/10.1504/IJEIE.2020.105377.

Fragiadakis, M., Lagaros, N. D. and Papadrakakis, M. (2006). "Performance-based multiobjective optimum design of steel structures considering life-cycle cost", *Structural and Multidisciplinary Optimization*, 32(1), 1-11, https://doi.org/10.1007/s00158-006-0009-y.

Ghasemof, A., Mirtaheri, M., Mohammadi, R.K. and Mashayekhi, M.R. (2021). "Multi-objective optimal design of steel MRF buildings based on life-cycle cost using a swift algorithm", *Structures*, 34, 4041-4059, https://doi.org/10.1016/j.istruc.2021.09.088.

Gidaris, I. and Taflanidis, A.A. (2015). "Performance assessment and optimization of fluid viscous dampers through life-cycle cost criteria and comparison to alternative design approaches", *Bulletin of Earthquake Engineering*, 13(4), 1003-1028, https://doi.org/10.1007/s10518-014-9646-5.

Golnargesi, S., Shariatmadar, H. and Golnargesi, B. (2022). "Structural control of building with ATMD through AN-IT2FLC under seismic excitation", *Civil Engineering Infrastructures Journal*, 55(2), 309-331, 10.22059/ceij.2021.325512.1760.

Guo, T., Xu, J., Xu, W. and Di, Z. (2014). "Seismic upgrade of existing buildings with fluid viscous dampers: Design methodologies and case study", *Journal of Performance of Constructed Facilities*, 29(6), 04014175, https://doi.org/10.1061/(ASCE)CF.1943-5509.0000671.

Hwang, J.-S., Huang, Y.-N., Yi, S.-L. and Ho, S.-Y. (2008). "Design formulations for supplemental viscous dampers to building structures", *Journal of Structural engineering*, 134(1), 22-31, https://doi.org/10.1061/(ASCE)0733-9445(2008)134:1(22).

Hwang, J.-S., Lin, W.-C. and Wu, N.-J. (2013). "Comparison of distribution methods for viscous damping coefficients to buildings", *Structure and Infrastructure Engineering*, 9(1), 28-41, https://doi.org/10.1080/15732479.2010.513713.

Kappos, A. J. and Dimitrakopoulos, E. (2008). "Feasibility of pre-earthquake strengthening of buildings based on cost-benefit and life-cycle cost analysis, with the aid of fragility curves", *Natural Hazards*, 45(1), 33-54, https://doi.org/10.1007/s11069-007-9155-9.

Kitayama, S. and Constantinou, M.C. (2018). "Seismic performance of buildings with viscous damping systems designed by the procedures of ASCE/SEI 7-16", *Journal of Structural engineering*, 144(6), 04018050, https://doi.org/10.1061/(ASCE)ST.1943-541X.0002048.

Lin, Y.-Y., Chang, K.-C. and Chen, C.-Y. (2008). Direct displacement-based design for seismic retrofit of existing buildings using nonlinear viscous dampers", *Bulletin of Earthquake Engineering*, 6(3), 535-552, https://doi.org/10.1007/s10518-008-9062-9.

Ohtori, Y., Christenson, R., Spencer Jr, B. and Dyke, S. (2004). "Benchmark control problems for seismically excited nonlinear buildings", *Journal of Engineering Mechanics*, 130(4), 366-385, https://doi.org/10.1061/(ASCE)0733-9399(2004)130:4(366).

Ramirez, O. M., Constantinou, M.C., Kircher, C.A., Whittaker, A., Johnson, M.W., Gomez, J.D. and Chrysostomou, C. (2000). *Development and evaluation of simplified procedures for the analysis and design of buildings with passive energy dissipation systems*, MCEER Reports, State University of New York at Buffalo.

Rashid, Z., Tantray, M. and Noroozinejad Farsangi, E. (2022). "Acceleration response-based adaptive strategy for vibration control and location optimization of magnetorheological dampers in multistoried structures", *Practice Periodical on Structural Design and Construction*, 27(1), 04021065, https://doi.org/10.1061/(ASCE)SC.1943-5576.0000648.

Salajegheh, S. and Asadi, P. (2020). "Life-cycle cost optimization of semiactive magnetorheological dampers for the seismic control of steel frames", *The Structural Design of Tall and Special Buildings*, 29(18), e1807, https://doi.org/10.1002/tal.1807.

Sarcheshmehpour, M. and Estekanchi, H. (2021). "Life cycle cost optimization of earthquake-resistant steel framed tube tall buildings", *Structures*, 30, 585-601,

https://doi.org/10.1016/j.istruc.2021.01.038.

Sarkisian, M., Lee, P., Hu, L., Garai, R., Tsui, A. and Reis, E. (2013). "Achieving enhanced seismic design using viscous damping device technologies", *Structures Congress 2013: Bridging Your Passion with Your Profession*, ASCE, 2729-2744, https://doi.org/10.1061/9780784412848.237.

Seleemah, A. and Constantinou, M.C. (1997). *Investigation of seismic response of buildings with linear and nonlinear fluid viscous dampers*, National Center for Earthquake Engineering Research, NCEER Publications.

Shin, H. and Singh, M. (2014). "Minimum failure cost-based energy dissipation system designs for buildings in three seismic regions, Part I: Elements of failure cost analysis", *Engineering Structures*, 74(September), 266-274, https://doi.org/10.1016/j.engstruct.2014.04.054.

Silvestri, S., Gasparini, G. and Trombetti, T. (2010). "A five-step procedure for the dimensioning of viscous dampers to be inserted in building structures", *Journal of Earthquake Engineering*, 14(3), 417-447, https://doi.org/10.1080/13632460903093891.

Somerville, P. and Collins, N. (2002). *Ground motion time histories for the Humboldt Bay Bridge*, Pasadena, CA, URS Corporation.

Sorace, S., Terenzi, G. and Mori, C. (2016). "Passive energy dissipation-based retrofit strategies for R/C frame water towers" *Engineering Structures*, 106(1), 385-398, https://doi.org/10.1016/j.engstruct.2015.10.038.

Taylor, D.P. (1999). "Buildings: Design for damping", *Proceedings of the Boston Society of Civil Engineers, BSCES*, Lecture Series: "Dynamics of Structures", USA.

Wani, Z.R., Tantray, M. and Farsangi, E.N. (2021). "Investigation of proposed integrated control strategies based on performance and positioning of MR dampers on shaking table", *Smart Materials and Structures*, 30(11), 115009, https://doi.org/10.1088/1361-665X/ac26e6.

Wen, Y.-K. and Kang, Y. (2001). "Minimum building life-cycle cost design criteria. I: Methodology", *Journal of Structural Engineering*, 127(3), 330-337, https://doi.org/10.1061/(ASCE)0733-9445(2001)127:3(330).

Civil Engineering Infrastructures Journal 2023, 56(1): 105-116
DOI: 10.22059/CEIJ.2022.328868.1794

RESEARCH PAPER

Evaluation of Seismic Designed Pipe Racks under Accidental Explosions with Finite Element Method

Roodpeyma, A.H.[1]* and Mahmoudzadeh Kani, I.[2]

[1] M.Sc., School of Civil Engineering, College of Engineering, University of Tehran, Tehran, Iran.
[2] Professor, School of Civil Engineering, College of Engineering, University of Tehran, Tehran, Iran.

Received: 29 Sep. 2021; Revised: 22 Feb. 2022; Accepted: 14 Mar. 2022

ABSTRACT: The safety of pipe racks in petrochemical sites or refineries needs to be considered to ensure a sustainable productivity and explosions would make these structures vulnerable. Non-building structures field have remained relatively intact in comparison with ordinary buildings for which state-of-the-art guidelines are regularly proposed and existing ones are renewed. To have comprehensive knowledge on non-building structures response to blast load, multiple factors are involved. This paper pinpoints how these variables affect the pipe racks and for this purpose, ABAQUS software undertakes the solving process as multi-degree of freedom (MDOF) and Finite Element method are required. Despite ordinary buildings, pipe racks are accompanied by non-structural components whose effects in design are evaluated not significant. Moreover, adequacy and accuracy of usual analysis including static and non-linear dynamic analysis are investigated. According to the calculations, static analysis is highly sensitive to irregularities and blast duration, therefore, it may lead to invalid results. Finally, a consequence analysis is suggested to be a contribution to engineers for outlining a well-arranged layout for different sectors.

Keywords: Blast Resistant Structures, Dynamics of Structures, FEM.

1. Introduction

In this era, the industrial productivity of most countries is highly dependent on oil-process facilities. The first successful oil extraction took place in Pennsylvania (1859) and since then, groundbreaking researches as well as new tools have facilitated the extraction and post-extraction mechanisms. This undoubtedly has a long way ahead to go because unprecedented environmental conditions or immeasurable probabilities of accidents alongside human errors make the re-investigation of design principles invaluable. This may be more of an importance for oil-led economies where raw oil or the export of the processed material constitutes a remarkable share of the annual budget. On the one hand, the related infrastructures should be designed resistant to routine loads. On the other hand, the supply chain should remain operational to a logic level for natural or accidental. In many regions inside the Middle East, the critical load is earthquake (Syed et al.,

* Corresponding author E-mail: amirh.roodpeyma@gmail.com

2017). So decades-long researches have been made to assess the performance of residential buildings in the face of earthquakes or, occasionally, blasts. For example, ACI-base-designed buildings were subjected to scrutiny with various explosion scenarios to verify the credibility of seismic design (Chiranjeevi and Simon, 2016; Syed et al., 2017).

Such studies have been carried out abundantly for buildings but much less in the case of non-building structures (Chiranjeevi and Simon, 2016). At the same time, the probability of explosion is high in refineries. The blasts may be triggered by external stimuli or accidents; for example, in an earthquake where the tremors may cause leakage and subsequently combustion (Kidam and Hurme, 2013; Planas et al., 2015; Suzuki, 2008). Accidents in the sites may also happen recurrently as a repercussion of a low safety culture (Aquino-Gaspara et al., 2021) and this situation may get exacerbated when coupling effect of blast wave and fragment would start a domino accident (Lai et al., 2021). Considering pipe racks vulnerable more than other sectors of a petrochemical site is not a faulty premise since among 364 accidents in specified petrochemical sites, pipe systems and racks were reported as repeatedly affected structures (Kidam and Hurme, 2013).

In the above-mentioned sites, three main categories can be observed: buildings, non-building structures, and non-building structures similar to buildings (ASCE, 2011; ISDPF, 2016). The latest was introduced at 1988 in UBC and improved by today in later revisions (Drake, 2004). Pipe racks are discerned as one of the best-known members of the non-building structures family (ASCE, 2011; Bedair, 2015; ISDPF, 2016). However, these advances have not been enough in comparison with those of ordinary buildings although a vast variety of daily-life demands, including clean water, electricity and sewage discharge, are feasible when pipe racks operate (Horold et al., 2000). Engineers often exploit buildings guidelines to design pipe racks. This approach not only may be non-conservative but also put the structures at serious risk. As an instance, the performance of the buildings frequently is defined due to life-safety or collapse prevention. Nevertheless, non-building structures based on their utilization status might not be allowed to reach a yield state (Horold et al., 2000). Furthermore, neither the nature of loads nor the occupation condition resembles residential buildings (Moharrami et al., 2015). The main role of racks is the distribution of pipes between levels and engaged parts in a facility. The conveyed pipes can

Significantly influence the stress distribution, deformation values and period of racks in seismic design (Roodpeyma and Mahmoudzadeh Kani, 2021). Also, previous researches confirm a 20% reduction in material consumption when the pipes are modeled simultaneously (Shahiditabar and Mirghaderi, 2013). In contrast with seismic analysis, the explosion analysis not only would be time-consuming but challenging, especially when it comes to details. CFD, coupled with competence in interpretation, is likely to end up with precise results, but the hardship in this path convinces engineers to take advantage of TNO, Baker-Sterlo or TNT equivalent dimensionless graphs (Hansen et al., 2010) . The selection of explosion type, affecting the structures in refineries, varies as the source of blast changes. It is commonly believed that vapor cloud explosions constitute the major cause of on-site blasts (ASCE, 2006). Far-field explosions, which are the main loads of this research, could be simulated with TNT equivalent method simply because neither the combustive source nor free distance is determined. The explosion would be originated from a gas leakage in other parts, post-earthquake induced fire or even reckless transportation of combustive materials (Bariha et al., 2016; Bloch and Wurst, 2010; Kong et al., 2018; Pula et al.,

2006; Moradi et al., 2021). Given the situation, consequence analysis is intended to provide credible data. With this in mind, an offshore site was subjected to vigorous studies, releasing useful information. As a result, it was concluded that a flash fire would affect a 60-meter-diameter circle. Meanwhile, at the very same location a BLEVE influences 20-meter-diameter circle (Pula et al., 2006).

There are no ubiquitously valid blast load parameters although two common scenarios are widely used in models that can be summarized as below:

- High pressure and short duration;
- Low pressure and long duration (Hansen et al., 2010; Pula et al., 2006).

Chen and Wang (2012) highlighted the shock wave absorption via EPS sandwich panels to safeguard the main structures, especially in offshore sites.

The attentions were drawn to DAF with regard to the pipes weight distribution in by Nelson et al. (2015). In this research, DAF equal to 1.5, proposed as the highest number in Biggs SDOF graphs, was acknowledged as a non-conservative coefficient for racks (Aarønaes et al., 2015). There are practical limitations when it comes to applying explosion on structures. Firstly, loads are not fully known, so that they are estimated unless the explosives are determined in both quality and quantity. Secondly, the operation is assigned as a linear correlation between time and pressure. Thirdly, dynamic interactions are usually neglected due to the complexity of details (Aarønaes et al., 2015; Su, 2012)

2. Material and Method

2.1. Material

2.1.1. Geometry and Physical Features of Racks

The modeled structure now is in operation at Khorasan-Iran petrochemical Complex and is to transport raw material between a few parts by steel pipes. The geometric features of the rack are summarized in Table 1. This rack was selected due to the complexity and diversity of sections which makes the results closer to the actual behavior of similar racks. Also, it would be a full-scale analysis compared to previous research in which simplifications have taken into account as sections were assimilated to a single section due to the complexity of analysis and also blast pressure was imposed on joints instead of the frames.

Table 1. Physical parameters

Feature	Definition
Length	102.85 m
Height	12.6 m
Span length	10 m
Lateral resistance system	Braced frames
Longitudinal resistance system	Ordinary frames
Intersection with other Racks	No

According to collected information, either from field inspection and as-built maps, the sections utilized in the construction are demonstrated in Table 2 as well as pipes' sections in Table 3. Also, the interconnected joints have been made from welding and bolts, which are reported highly fine. As like as most of Iran's infrastructures, the main design is dependent on the functionality of the rack under seismic loads, for which an importance factor equal to 1.25 was assigned (vital vessels).

2.1.2. Materials

The nominal yield stress of the steel is approximated 240 Mpa with ultimate stress of 370 Mpa and module of elasticity is estimated 203 Gpa. However, ASCE (2006) proposes, the nominal stress should be modified with coefficients because material gains additional strength in the face of dynamic loads. According to ASCE (2006), the more rapid a deformation shapes, the yield stress intensifies more. This increase is projected about 10% to 30%, dependent on the deformation rate (ASCE, 2006).

2.2. Method

2.2.1. Analysis Approach

Generally, MDOF analysis (Eq. (1)) is employed in the case of frames under blasts since the coincidence of axial forces and bending moments are calculated. MDOF can be utilized with 2D and 3D approaches.

Table 2. Elements sections

Beams type	Columns type	Braces type
W6 × 15	W6 × 20	L3 × 3 × 1/4
W8 × 21	W8 × 31	L4 × 4 × 1/4
W8 × 24	W10 × 45	2 L3-1/2 × 3-1/2 × 1/4
W8 × 35	W12 × 53	2 L4 × 3 × 1/ 4
W10 × 35	W12 × 87	2 L4 × 4 × 3/ 8
W12 × 79	W12 × 792	L4 × 4 × 1/4
W12 × 96	W14 × 78	2 L5 × 5 × 3/8
W14 × 74	W16 × 100	—-
W16 × 89	—-	—-
W16 × 100	—-	—-

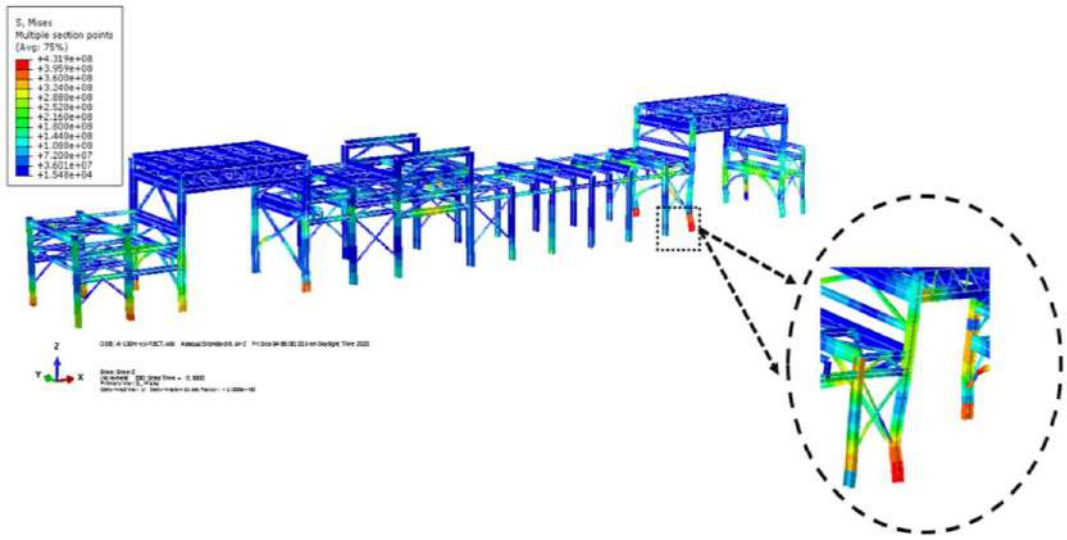

Fig. 1. The configuration of pipe rack and critical base sample

Table 3. Average of WOP/WP for critical nodes

Pipe diameter (inch)	Weight of contents (kg/m^2)	Weight of pipes (kg/m^2)
2	0.2	0.45
4	0.8	1.42
10	4.97	5.6
4	0.8	1.42
2	0.2	0.45
10	4.97	5.6
10	4.97	5.6
2	0.2	0.45
3	0.45	1.08
3	0.45	1.08
8	3.18	5.44
12	7.16	10.47
8	3.18	6.44
3	0.45	1.08

$$M\ddot{u}(t)+C\dot{u}(t)+F_{\text{int}}(t)=F_{ext}(t) \qquad (1)$$

where M: is mass, C: is damping, F_{int}: is internal force, F_{ext}: is external force, $\ddot{u}$: is acceleration, $\dot{u}$: is velocity and T: is time.

The geometric and mass symmetry dictate the necessity of 3D modeling in pipe racks; however, a complete symmetry seldom can be observed as height and plan irregularities govern (Aarønaes et al., 2015; ASCE, 2006; Su, 2012). Previous researchers have underlined the shape of pipe support but these supports were eliminated on the simulation (Aarønaes et al., 2015; Su, 2012). Observing details and surveying the geometry of the rack show that pipes go down and up despite previous studies in which pipes were assumed straight. These movements, which are about to be investigated closely, can constrain

frames together. For structural elements b31 type was selected because not only large axial strains as well as large rotations is formulated but also transverse shear strain is included. This eventually leads to distortion of the cross-section which is taken into calculation (Dassault Systèmes, 2015).

ABAQUS 6.14 (Simulia, 2015) was used for non-linear dynamic and static Finite Element analysis. Afterward, a python code with contribution of NUMPY, Pandas and Matplotlib libraries was developed to facilitate data extraction and pertinent graphs among a plethora of unprocessed information.

2.2.2. Blast Properties

When a blast wave propagates toward an object, three presumable hit-reflects may happen. If the stroked object (frames) has smaller dimension in one direction, the only effective load is dynamic pressure, as Figure 2 portraits (Aarønaes et al., 2015; Su, 2012).

There are copious notes on determining blast parameters and proposing closed-form equations for the calculation of pressure wave behavior. At first, Brode (1995) formed Eq. (2) as below.

$$P_{so} = \frac{0.975}{Z} + \frac{1.455}{Z^2} + \frac{5.85}{Z^3}, 0.1bar < P_{so} < 10bar$$
$$P_{so} = \frac{6.7}{Z}, 0.1bar < P_{so} < 10bar \quad (2)$$

where P_{so} : is peak side-on overpressure and Z: is distance from blast source.

Having brode documents, Newmark and Hansen (1961) devised another time-honored formula (Eq. (3)) in which W and R are explosive weight and object-to-source distance, respectively.

$$P_{so} = 6784\frac{W}{R^3} + (63\frac{W}{R^3})^{0.5} \quad (3)$$

Eventually, Henrych (1979) formulated pressure (Eq. (4)) magnitude based on Z as the scaled distance.

$$P_{so} = \frac{14.072}{Z} + \frac{5.54}{Z^2} + \frac{0.357}{Z^3} + \frac{0.00625}{Z^4}, 0.05bar < Z < 0.1$$
$$P_{so} = \frac{6.194}{Z} + \frac{0.326}{Z^2} + \frac{2.132}{Z^3}, 0.1bar < Z < 0.3$$
$$P_{so} = \frac{6.662}{Z} + \frac{4.05}{Z^2} + \frac{3.288}{Z^3}, 0.3bar < Z < 10 \quad (4)$$

The imposed dynamic pressure is classified into three major types that cover the suggested values of ASCE. There are a handful of formulas which are mostly based on experimental tests, but Table 4 is derived from UFC dimensionless graphs (Unified Facilities Criteria (UFC (3-340-02), 2008). Also, blast duration including 35 ms, 50 ms, 75 ms and 90 ms are extracted from UFC graphs.

Table 4. Selected blast magnitude

Blast type	Scaled distance	P (kPa)	Dynamic pressure (kPa)
A	7	137.9	55.2
B	8	103.4	27.56
C	10	68.95	13.8

3. Discussion and Results

3.1. Nonstructural Components

In this research, all of the columns were subjected to rigorous investigation since the abundance of beams provides the structure with high number of load transition paths. These columns, based on their elevations, were assorted to long and short elements. Short columns are in the range of 7 m to 9 m and long ones go in 10 m to 12 m length category. In all columns, the pipe layout exists at the apex. Long columns have been shaped to conduit pipes through a direction to not intersect with other equipment due to the rack location and restrictive access space. Because of divers sections and different levels, unlike available research, mesh sensitivity analysis ought to be conducted all over again and existing results are no longer viable. The results according to Figure 3 indicate the convergence with 3700 total elements with 0.8 cm mesh size.

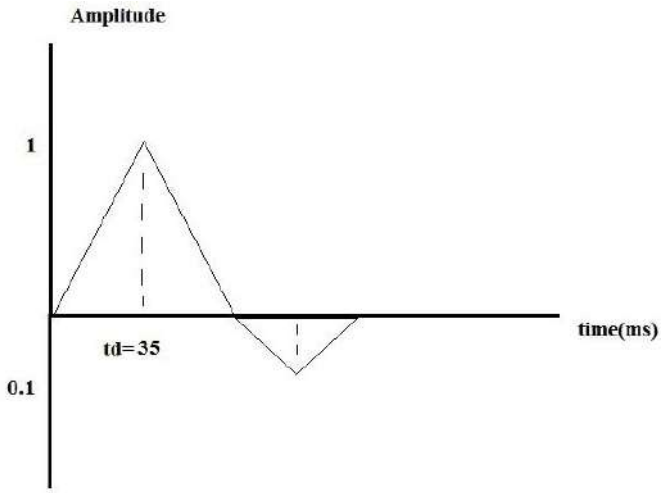

Fig. 2. Average pressure-time variation (UFC (3-340-02), 2008)

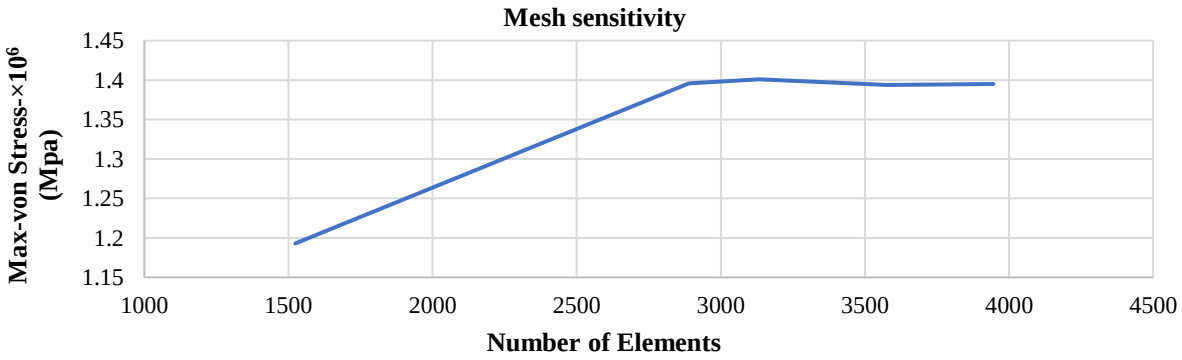

Fig. 3. Mesh sensitivity analysis

This finding will address a controversy in racks carrying pipes. Although important in material consumption, the pipe will not be playing a key role in the magnitude of stress at the critical elements in types A and B. Figure 3 clarifies the slight difference in one of the critical bases (Figure 1).

To pour into details, two sets of analysis, including WP (shorthand for with pipe) and WOP (shorthand for without pipe) were undertaken. The results in Table 5 imply that owners can ignore the pipes in models while remaining conservative. This table discloses the average of WOP/WP of critical nodes located at the bases.

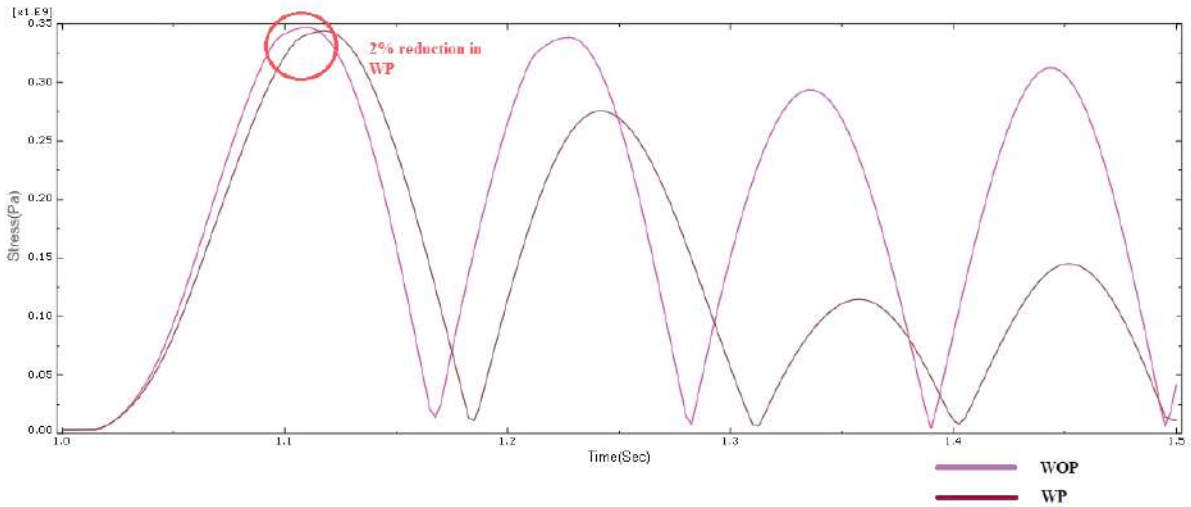

Fig. 3. Slight difference critical bases

Table 5. Average of WOP/WP for critical nodes

Type of explosion	Duration	Average (WOP/WP)
A	35	1.33
	50	1.2
	75	1.11
	90	1.06
B	35	1.02
	50	1
	75	1.03
	90	1.03
C	35	1.06
	50	1.02
	75	1.04
	90	1.02

Nonetheless, if the aim is an optimized design, one should have pipe racks modeled with pipes. Figures 4a-4f show the change of WOP/WP ratio in height and its dependence on the duration. This ratio, generally, rises when the elevation increases. In the following critical columns, WOP/WP for all types of blasts, at the bases, places around one. But as the height grows, the coefficient surges in two sharp steps. The first one is at the height of 6 m where the first floor, attached to the column, emerges. The second one happens at the top to which pipes are connected. For example, WOP/WP for column-1 experiences 100% increase followed by 50% growth. This pattern could be applied to other columns too.

In the case of explosion Type A, there is a plateau for WOP/WP around one, which is the direct consequence of transition into plasticity threshold as Figure 5a-5f depict, followed by changes.

Seemingly for all nodes which are not necessarily critical nodes, the interquartile range of columns' WOP/WP stands more than one with considerable positive skew; simultaneously, nodes below one are rare and located in non-critical areas.

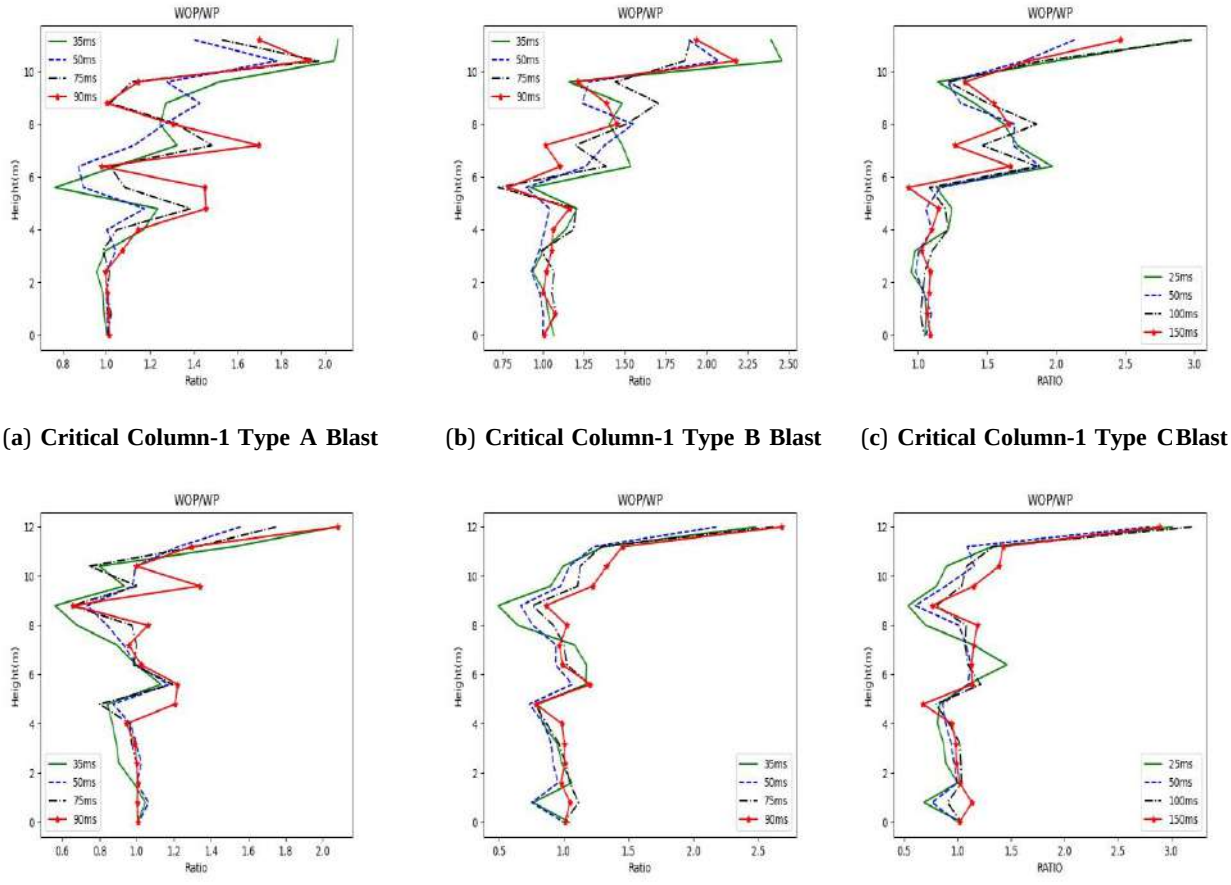

(a) Critical Column-1 Type A Blast (b) Critical Column-1 Type B Blast (c) Critical Column-1 Type CBlast

(d) Critical Column-2 Type A Blast (e) Critical Column-2 Type B Blast (f) Critical Column-2 Type CBlast

Fig. 4. WOP/WP for two critical columns

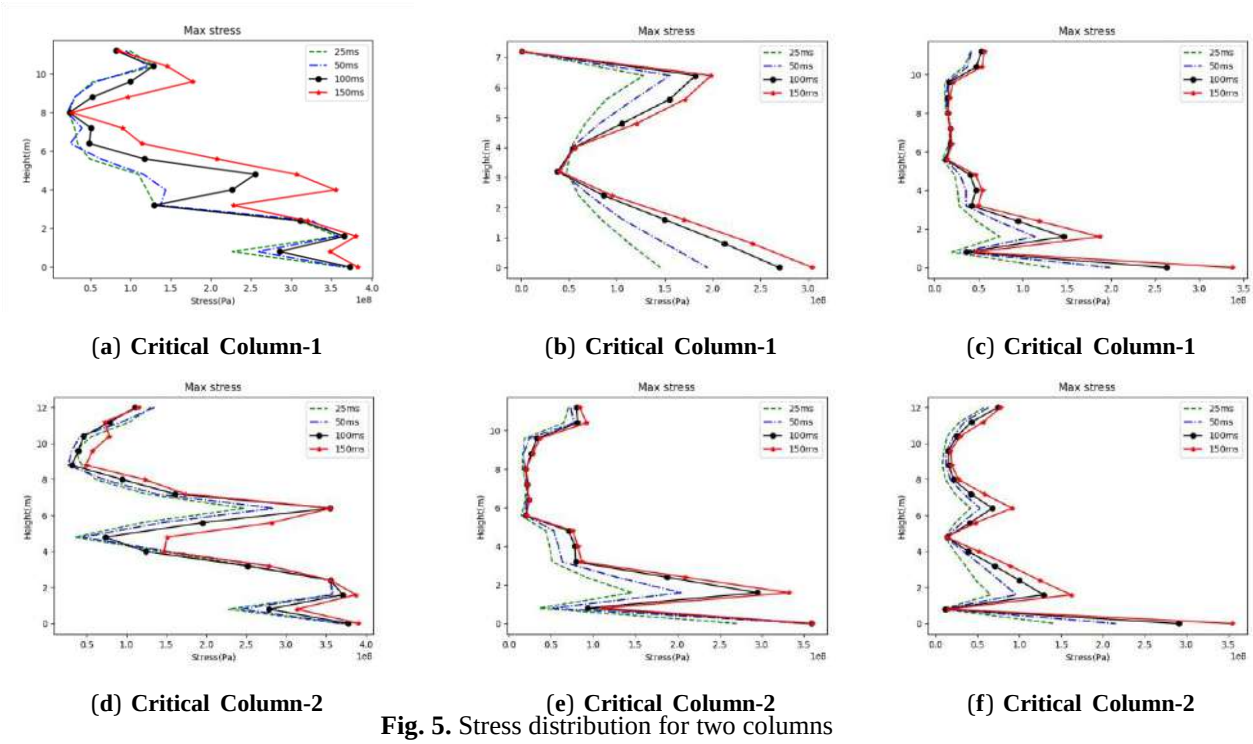

(a) Critical Column-1 (b) Critical Column-1 (c) Critical Column-1

(d) Critical Column-2 (e) Critical Column-2 (f) Critical Column-2

Fig. 5. Stress distribution for two columns

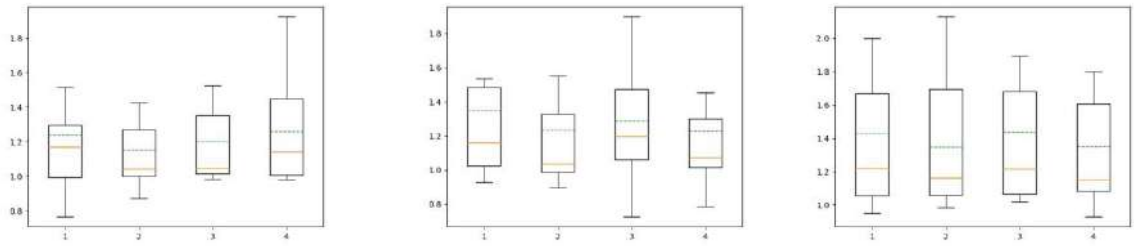

(a) WOP/WP Box Chart Critical (b) WOP/WP Box Chart Critical (c) WOP/WP Box Chart Critical

Fig. 6. Box chart

Furthermore, looking at displacements would be more practical and convenient than stress contours to base the primary judgment on since pipes in pipe racks bring intrinsic limitations on maximum tolerable deformation, becoming stricter where joints or flanges had been placed. Nevertheless, calculations (Table 6) reveal no meaningful difference between deformation on drift-controlled spots in WOP and WP conditions. This may stem from the rapid transience of propagated waves which pipes rarely find the chance to dissipate the initial momentum. So this slight contradiction could be overlooked. As this table depicts, this is predictable that both the duration and intensity of blasts have direct effect on the maximum deformation. The minimum lateral deformation in WOP caused by C-35 ms explosion is 1.7 cm, whereas the maximum appears to be 13.6 cm by A-90 ms. Meanwhile, the reduction percentage fluctuates between 9% and 14 % for B-50 ms and A-90 ms, respectively.

3.2. Static and Dynamic Approach

It is worth mentioning that the analysis method would put a burden on owners either financially or technically. In other words, providing the design team with fast-calculating computers and deft operators for interpretation would be unseen angles of an optimized design. So that a static analysis would be much more of predilection than non-linear dynamic (NL-dynamic). This is simply because of the convenience and rapidity of this method. To peruse the validation of static manner, an index in Eq. (5) was defined.

$$DAF = \frac{Stress_{NL-dynamic}}{Stress_{static}} \quad (5)$$

The index's values corroborate the credibility of static analysis in short durations (35 ms and 50 ms) for both types B and C in over 90% for critical elements. However, up until the stress is below the yield state, DAF rises where duration and intensity boost. Noteworthy to say, dynamic analysis remarkably differs from the static approach where stiffness irregularity occurs. Therefore, static analysis qualification defeats and the non-linear dynamic approach is strongly suggested if stiffness irregularity exists. DAF in columns' heights is depicted in Figures 7a-7f. As the height increases from the base, overall DAF grows. Meanwhile, this growth becomes significant in stiffness irregularities. This similar pattern in critical columns is constituted from three phases. Just one meter above the bases, strengthened by braces, the first irregularity boosts DAF by more than 50%. Then at the first-floor intersection, the second phase of escalation could be observed. Finally, at the tops, DAF, multiplies. The maximum DAF is approximately 6, which indicates the static analysis may underestimate the exact values by 600%.

Table 6. Reduction percent of WP to WOP

Type of explosion	WOP deformation (cm)	WP deformation (cm)	Reduction (%)
A-35 ms	4.67	4.18	10.4
B-35 ms	2.41	2.02	16.3
C-35 ms	1.17	1.03	11
A-50 ms	7.9	6.28	11.4
B-50 ms	3.3	3	9.03
C-50 ms	1.77	1.53	13.5
A-75 ms	9.46	8.31	12.1
B-75 ms	4.48	3.91	12.8
C-75 ms	2.2	1.9	12.6
A-90 ms	13.6	11.8	13.7
B-90 ms	5.7	5.05	11.4
C-90 ms	2.8	2.4	11.2

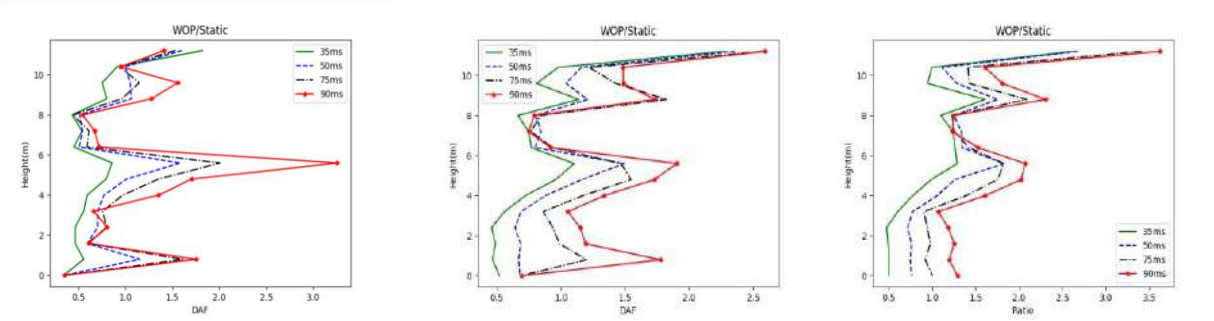

(a) Column-1 DAF in Height, Type A (b) Column-1 DAF in Height, Type B (c) Column-1 DAF in Height, Type C

(d) Column-2 DAF in Height, Type A (e) Column-2 DAF in Height, Type B (f) Column-2 DAF in Height, Type C

Fig. 7. DAF coefficient for two columns

3.3. Safe Distance

Arrangement of equipment, particularly those that may conduct or store combustive materials, should be checked as having a safe distance to pipe racks decreases the risk of severe damages. a list of scenarios and safe distances could be helpful to corresponding engineers or technicians locating other parts. If the safe distance verification is ignored, a tanker explosion may interrupt the daily activities of the whole process area as well as burdening the rehabilitation costs. Given how much safe distance is required, designers could acquire what location would be appropriate for putting other facilities such as gas reservoirs and tank. If the amplitude of potential blast is in the range of Type A, the corresponding immune distance for the pipe rack is determined between 50 m and 19.7 m according to Table7. This table might be more important in the case of designing main pipe racks or those that carry highly explosive and flammable materials. In regular racks, developing this table is optional but helpful in having a vivid overview of what is a well-arranged plan. The velocity (ft/sec) of wave is calculated with Eq. (6). In this equation P_{s0} should be in psi unit. The velocity and duration will determine the safe distance.

$$U = 1130(1 + 0.058P_{so})^{0.5} \quad (6)$$

4. Conclusions

In this paper, 3D Finite Element models were developed first, with ABAQUS software to simulate the behavior of a pipe rack under blast pressure. The models cover both non-linear material characteristics and non-linear geometrical parameters. According to the results main findings are listed as below:

- Non-structural components (pipes) have not meaningful effect on stress results at critical nodes and these pipes could be ignored in design process; however, if the aim is developing an optimized model, the pipes should be taken into design.
- The numerical outputs show that static analysis leads to conservative results only when the duration is less than 50 ms. In contrast, static analysis is not useful as considerable errors (even more than 100%) arise in long-duration blast waves. Thus non-linear dynamic analysis is necessary and more reliable. Also, DAF coefficient is significantly dependent on irregularities. So that non-linear dynamic analysis results in more accurate calculations and is suggested if irregularities exist.
- Finally, the safe distance table would be beneficial for engineers to have a well-organized arrangement of sectors. With this consequence analysis in hand, due to the location of pipe racks and importance of the vessels or highly combustive sectors could be outlined properly in order to mitigate the severity of damages in a confluence of accidents.

Table 7. Safe distance

Type of explosion	Duration (ms)	Dynamic pressure (kPa)	Distance from source (m)
A	35	55.15	19.77
B	35	27.57	18
C	35	13.78	16.5
A	50	55.15	27.6
B	50	27.57	25.75
C	50	13.78	23.6
A	75	55.15	41.5
B	75	27.57	39.7
C	75	13.78	35.5
A	90	55.15	50
B	90	27.57	46
C	90	13.78	42.6

5. References

Aarønaes, A., Nilsson, H. and Neumann, N. (2015). "Dynamic response of steel pipe rack structures subjected to explosion loads", *Steel Construction*, 8(3),162-166, https://doi.org/10.1002/stco.201510022.

ASCE. (2006). *Design of blast-resistant buildings in petrochemical facilities*, Second Edition. Reston, American Society of Civil Engineers, New York, USA, https://doi.org/10.1061/9780784410882.

ASCE. (2011). *Guidelines for Seismic Evaluation and Design of Petrochemical Facilities*, American Society of Civil Engineers, New York, USA, https://doi.org/10.1061/9780784411407.

Bariha, N., Mishra, I.M. and Srivastava, V.C. (2016). "Fire and explosion hazard analysis during surface transport of liquefied petroleum gas (LPG): A case study of LPG truck tanker accident in Kannur", *Journal of Loss Prevention in the Process Industries*, 40, 449-460, https://doi.org/10.1016/j.jlp.2016.01.020.

Bedair, O. (2015). "Rational design of pipe racks used for oil sands and petrochemical facilities", *Practice Periodical on Structural Design and Construction*, 20(2), 0401-4029, https://doi.org/10.1061/(ASCE)SC.1943-5576.0000224.

Bloch, K.P. and Wurst, D.M. (2010). "Process safety management lessons learned from a petroleum refinery spent caustic tank explosion", *Process Safety Progress*, 29(4), 332-339, https://doi.org/10.1002/prs.10381.

Brode, H.L. (1995). "Numerical solution of spherical blast waves", *Journal of Apply Physics*, 26(6), 766-775, https://doi.org/10.1063/1.1722085.

Chen, L. and Wang, Y.C. (2012). "Methods of improving survivability of steel beam-column connections in fire", *Journal of Construction Steel Research* (JCSR), 79, 127-139. https://doi.org/10.1016/j.jcsr.2012.07.025.

Chiranjeevi, M.D. and Simon, J. (2016). "Analysis of reinforced concrete 3D frame under blast loading and check for progressive collapse", *Indian Journal of Science and Technology*, 9(30), 1-6, https://doi.org/10.17485/ijst/2016/v9i30/99232.

Crowl, D.A. and Louvar, J.F. (2001). "Chemical process safety: Fundamentals with applications", 2nd (ed.), Pearson College Division, https://doi.org/10.1002/prs.12086.

Drake, R.M. (2004). "Seismic code developments for non-building structures similar to buildings", *Structures Congress*, (pp. 1-11), American Society of Civil Engineers, Reston, VA, https://doi.org/10.1061/ 40700(2004)93.

Hansen, O.R., Hinze, P., Engel, D. and Davis, S. (2010). "Using Computational Fluid Dynamics (CFD) for blast wave predictions", *Journal of Loss Prevention in the Process Industries*, 23(6), 885-906, https://doi.org/10.1016/j.jlp.2010.07.005.

Henrych, J. (1979). *The dynamics of explosion and its use*, 1st (ed.), Amsterdam: Elsevier Scientific Pub, https://doi.org/10.1002/eqe.4290080309.

Sprague, H.O. and Legatos, N.A. (2000). "Non-building structures seismic design code developments", *Earthquake Spectra*, 16(1), 127-140, https://doi.org/10.1193/1.1586087.

Kidam, K. and Hurme, M. (2013). "Analysis of equipment failures as contributors to chemical process accidents", *Process Safety and Environmental Protection*, 31(1-2), 61-78, https://doi.org/10.1016/j.psep.2012.02.001.

Kong, X., Zhao, D. and Hu, S. (2018). "Environment and safety risk analysis of storage tank accidents based on vulnerability, Process management and emergency management", *Chemical Engineering Transactions*, 67, 457-462. https://doi.org/10.3303/CET1867077.

Lai, E., Zhao, J., Li, X. and Guohua Chen, K. (2021). "Dynamic responses and damage of storage tanks under the coupling effect of blast wave and fragment impact", *Journal of Loss Prevention in the Process Industries*, 73(1 November), 104617, https://doi.org/10.1016/j.jlp.2021.104617.

Moharrami, H., Rashvandi, M. and Hajinouri, Y. (2016). "Evaluation of pipe racks design process and related codes", *Second National Structure Engineering Conference*, University of Amirkabir, Tehran, Iran, (in Persian), https://civilica.com/doc/535909.

Moradi, M., Tavakoli, H.R. and Abdollahzadeh, Gh. (2021). "Comparison of steel and reinforced concrete frames' durability under fire and post-earthquake fire scenarios", *Civil Engineering Infrastructure Journal*, 54(1), 145-168, 10.22059/ceij.2020.292639.1628.

Aquino-Gaspara, H.M., Díaz-Ovalle, C.O., López-Molinaa, A., Conde-Mejíaa, C. and Valenzuela-Gómeza, L.M. (2021). "Incident analysis of the "Pajaritos" petrochemical complex", *Journal of Loss Prevention in the Process Industries*, 70, 104404, https://doi.org/10.1016/j.jlp.2021.104404.

Newmark, N.M. and Hansen, R.J. (1961). *Design of blast resistant structures*, Vol. 3, New York, McGraw-Hill.

Iranian Seismic Design Code for Petroleum Facilities (ISDPF). (2016). *Seismic design of oil facilities code 038-3rd*, Oil ministry of Iran, Tehran, Iran, (in Persian).

Planas, E., Pastor, E., Casal, J. and Bonilla, J.M. (2015). "Analysis of the Boiling Liquid Expanding Vapor Explosion (BLEVE) of a liquefied natural gas road Tanker: The Zarzalico accident", *Journal of Loss Prevention in the Process*, 34(1 March), 127-138, https://doi.org/10.1016/ j.jlp.2015.01.026.

Pula, R., Khan, F.I., Veitch, B. and Amyotte, P.R. (2006). "A grid based approach for fire and explosion consequence analysis", *Process Safety and Environmental Protection*, 84(2B), 79-91. https://doi.org/10.1205/psep.05063.

Roodpeyma, A.H., and Mahmoudzadehkani, I. (2021). "Assessment of Nonstructural components on dynamic Parameters of pipe racks", *5th International Conference on Interdisciplinary Researches in Civil Engineering, Architecture and Urban Management in 21st Century*, Tehran, Iran, (in Persian), https://civilica.com/doc/1156994/.

Shahiditabar, A. and Mirghaderi, S.R. (2013). "Pipe and pipe rack interaction", *International Journal of Science and Technology*, 3(5), 39-44, https://www.ijastnet.com/journals/Vol_3_No_5_May_2013/4.pdf.

Simulia, D.S. (2015). *Abaqus analysis user manual*, Dassault Systemes, Pawtucket, USA.

Su, A. (2012). "Analysis of explosion load, Effects in pipe-racks", M.Sc. Thesis, Norwegian University of Science and Technology, http://hdl.handle.net/11250/238284.

Suzuki, K. (2008). "Earthquake damage to industrial facilities and development of seismic and vibration control technology", *Journal of System Design and Dynamics*, 2(1), 2-11, https://doi.org/10.1299/jsdd.2.2.

Syed, Z.I., Mohamed, O.A., Murad, K. and Kewalramani, M. (2017). "Performance of earthquake-resistant RCC frame structures under blast explosions", *Procedia Engineering*, 180, 82-90, https://doi.org/10.1016/j.proeng.2017.04.167.

Unified Facilities Criteria (UFC 3-340-02). (2008). *Structures to resist the effects of accidental explosions*, US Department of Defense, United States of America.

Civil Engineering Infrastructures Journal 2023, 56(1): 117-136
DOI: 10.22059/CEIJ.2022.334291.1802

RESEARCH PAPER

Distance Insensitive Concrete Crack Detection with Controlled Blurriness Using a Convolutional Neural Network

Su Fen, N.[1], Shokravi, H.[2], Bakhary, N.[3*], Padil, Kh.H.[2] and Zainal Abidin, A.R.[2]

[1] M.Sc., School of Civil Engineering, University Teknologi Malaysia, Johor, Malaysia.
[2] Assistant Professor, School of Civil Engineering, University Teknologi Malaysia, Johor, Malaysia.
[3] Associate Professor, School of Civil Engineering, University Teknologi Malaysia, Johor, Malaysia.

Received: 21 Nov. 2021; Revised: 16 Feb 2022; Accepted: 27 Feb. 2022

ABSTRACT: Crack detection is one of the critical tasks in health monitoring and inspection of civil engineering structures. The existence of major cracks may have detrimental effects on the integrity and performance of structures that need full consideration. Recent research into crack identification has shown an increasing interest in vision-based automated techniques, employing deep-learning computational methods such as Convolutional Neural Networks (CNNs). However, the wide range of real-world situations (e.g. camera or subject motion, misfocus, mist, and fog) can significantly compromise the accuracy of CNN-based crack identification due to a mismatched dataset in training and testing. Therefore, this study aims to establish an intelligent identification model using deep CNNs to automatically detect concrete cracks from real-world images. Moreover, the efficiency of the algorithm in identifying cracks based on blurred images in the training and validation dataset was investigated. The original dataset is replicated into various blurriness levels and split into eight different crack image sub-datasets. CNN models were trained and crack identification was carried out using different levels of image blurriness. The classification performance of the trained CNN was assessed using the concrete crack image dataset taken around Universiti Teknologi Malaysia. Sensitivity studies were also conducted to investigate the efficiency of the CNN method to identify damage under various image parameters. The results showed that the subset with the combination of sharp and slight blurriness level (blurriness Level 1) reached the highest training accuracy of 98.20%, and the network trained with blurriness Level 1 alone had the best accuracy, precision, and F1 score performance over eight training subsets. Moreover, the robustness of the networks was examined and verified under four different situations, which are; lighting, crack width, colour structures, and camera shooting angle conditions. It was observed that the presence of blurred images in the training dataset can enhance the CNN crack detection performance while high shooting angle and uneven illumination has a negative effect on the accuracy of the proposed CNN.

Keywords: Blurriness, Concrete, Convolutional Neural Network, Crack, Distance, Structural Health Monitoring.

* Corresponding author E-mail: hisham7348@gmail.com

1. Introduction

Concrete material has been widely used in civil structures. Over the service life, concrete structures may undergo many types of damage such as cracks, reduction of reinforcement bar diameter due to corrosion, loss of bond in the steel-concrete interface, corrosion of prestressed cables, and spalling. Lighter damage may have an impact on the aesthetic value of the structures, while severe damages could affect the durability and stability of the whole structure. Structural Health Monitoring (SHM) is the process of identifying damages during the service life of a structure (Abdulkareem et al., 2018; Abudallah Habib et al., 2021). Hence, the SHM practice, starting with early detection and followed by appropriate repair strategies, has a very important role in ensuring structural safety. Cracking is one of the most commonly reported defects that may threaten the structural health and integrity of concrete structures (Delatte, 2009).

Vision-based SHM has the potential to provide valuable information on structural monitoring (Ye et al., 2016). Conventionally, visual inspection is carried out by certified inspectors or structural engineers to detect and evaluate structural damage. However, the accuracy of human-based visual inspection is greatly influenced by the skill level and experience of the inspectors (Li et al., 2019). Additionally, this approach is not economical and more time-consuming, especially for large-scale structures. Recent advances in the quality of digital cameras and lenses, as well as their ability to be synchronised with other smart devices and vehicles, have made vision-based methods an attractive choice for SHM applications. Recently the joint application of computer-vision and deep-learning techniques are being widely incorporated in inspection, monitoring, and assessment of infrastructure.

Due to the high-capability in recognising patterns with extreme variability using convolutional and pooling layers, the Convolutional Neural Network (CNN) has revolutionised the paradigms of crack detection using computer vision and image processing (Wang et al., 2019). CNN is a deep neural network model utilising layers with convolving filters that are inspired by the visual cortex of animals (Ciresan et al., 2011). The utilisation of CNN for crack detection has been found in various civil engineering applications such as road pavements, masonry structures, buildings, roadway, bridges, and steel and concrete structures. Cha et al. (2018) developed a quasi-real-time structural damage detection method based on a faster region-based convolutional neural network. In their study, multiple types of structural damage images of concrete cracks, steel corrosion, bolts corrosion, and steel delamination with $500 \times 375 \times 3$ pixels resolution under uncontrolled conditions were used to train and validate the networks. The outcome of the study shows that 87.8% of structural damages were correctly detected and localised. Meanwhile, Atha and Jahanshahi (2018) demonstrated the applicability of CNN in detecting corrosion. To obtain the optimal CNN architecture, the authors have compared the performance of the existing pre-trained networks such as ZFNet and VGG16. The authors also investigated the effect of different input image parameters in terms of sizes and colour spaces. The study revealed that the input image size of 128×128 pixels resolution and the RGB or YCbCr is the most robust image input parameter. Later, Dorafshan et al. (2018) compared the performance of common edge detectors and CNN for crack detection in concrete structures. The study employed AlexNet CNN architecture in three different modes which are: i) fully train the network from scratch, ii) alter the last fully connected layers to match with the target labels, and iii) fine-tune the layers in AlexNet. It was found that fine-tuned AlexNet provides excellent crack detection accuracy. Recently, Zhang et al. (2020) successfully conducted an investigation on

autonomous bolt loosening detection based on faster R-CNN. Images with tight and loose bolts in 640 × 478 × 3 pixels resolution were used in the training and validating process. The study successfully demonstrated that the trained networks are able to detect the bolt damage accurately with input images from different conditions in terms of lighting, angles, and vibration. These studies described above demonstrate that the use of images together with CNN is a promising tool for damage detection and the versatility makes CNN potentially outperform most of the existing sensor-based damage detection methods.

In recent years, more detailed studies have been conducted to improve the performance of CNN for crack detection. For example, Cha et al. (2017) proposed a new CNN architecture for crack detection of concrete structures without calculating defect features. The study considered the image degradation effect due to the changes in lighting and shadow conditions. The results showed that considering the image degradation in the training data provides higher robustness and adaptability of the CNN-based method in finding concrete cracks in more realistic situations. Li et al. (2018) applied CNN for detecting cracks in real bridge inspections considering disturbance of noise and clutters. The result of the experimental work showed that the proposed algorithm outperforms the up-to-date methods in crack detection of civil structures. The higher success rate achieved in the experimental verification indicates the advantages of the proposed CNN-based method in crack detection of concrete surfaces.

Since the performance of CNN is highly dependent on the incorporated image quality, a more detailed study has been conducted to improve the performance of CNNs dealing with low-quality images. For example, Zhou and Song (2021) built and trained a novel CNN architecture that can analyse images with various types of disturbances such as low contrast and shallow cracks in roadway inspections, which led to better classification performance. Deng et al. (2020) carried out a comparative study to investigate the performance of three Faster R-CNNs, region-based fully convolutional networks, and feature pyramid network-based Faster R-CNN algorithms for detection of out of plane racks incorporating deformable modules. The results show that the addition of deformable modules improved the precision of crack detection in all three algorithms. Chen and Jahanshahi (2020) introduced a rotation-invariant fully convolutional network called active rotating filters to consider the rotation variation property of images for crack detection of concrete and pavements.

Currently, the extraction of information from blurred images is a popular research topic in the image processing field. Unmanned aerial vehicles which are capable of using a visual mounted camera are widely deployed to replace traditional human-based visual inspection of civil structures (Dorafshan and Maguire, 2018). One of the main challenges of unmanned aerial vehicles imagery is the blurriness caused by environmental and operational factors such as wind, mist, and fog (Sieberth et al., 2015). On the other hand, the application of smartphone cameras has been rapidly introduced to the visual monitoring of structures (Ratnam et al., 2019). Smartphones show great application prospects due to their unique combination of properties such as embedded hardware devices, intelligent antenna systems for transmitting and receiving data and, excellent optical properties. However, the pictures captured by mobile phones are prone to blurriness, probably due to operational factors such as camera movement and missed focus (Fankhauser et al., 2020).

Blurriness is one of the main qualitative attributes of images in computer vision systems. The qualitative attributes of images can be divided into three general categories of blurriness, noisiness, and blockiness (Shen et al., 2018). The

qualitative attributes of images and the reasons for their degradation are shown in Figure 1. Blur in images is one of the most common degradation phenomena that is mainly caused by several reasons such as camera shake, blurry background due to dust and debris, mist and fog, and missed focus. Blurriness is defined as the lack of spatial detail features resulting in a reduction in the sharpness of edges. Several solutions are introduced to deal with the blurriness of images. Dash et al. (2009) proposed restoration of images, while Han et al. (2018) and Sieberth et al. (2013) proposed removing the blurred images from the database. Though isolation of blurred images can improve the accuracy of the visual analysis and interpretation of data and reduce the rate of errors and false alarms, it may result in a partial loss of valuable information about the health state of a structure. Restoration of blurred images is another solution that is expensive due to the high computation burden and large execution time.

Several research studies have been carried out to enhance the quality of detecting cracks on concrete surfaces using computer-vision and deep-learning techniques. Jang et al. (2019) and Fan et al. (2018) studied methods to improve crack detectability while minimising false alarms. Cha, Choi, and Büyüköztürk (2017), Kim and Cho (2018) and Protopapadakis et al. (2019) investigated the accuracy, noise immunity, and versatility of the acquired images on CNN-based crack identification. However, the number of studies to discuss the quality of image attributes and enhancing the quality of acquired images is limited for damage detection of civil engineering structures, and detailed study of the effect of images degraded with blur is also quite limited. Therefore, this study investigates the applicability of a CNN in autonomously detecting concrete cracks at various levels of images blur. Images of concrete cracks pulled from open-source databases of *Mendeley Data* and *Data in Brief* are used in this study. Selected images were compiled into a single training database for training the CNN. Afterward, the original dataset is split into eight different crack image sub-datasets with the combinations of various blurriness levels for this purpose.

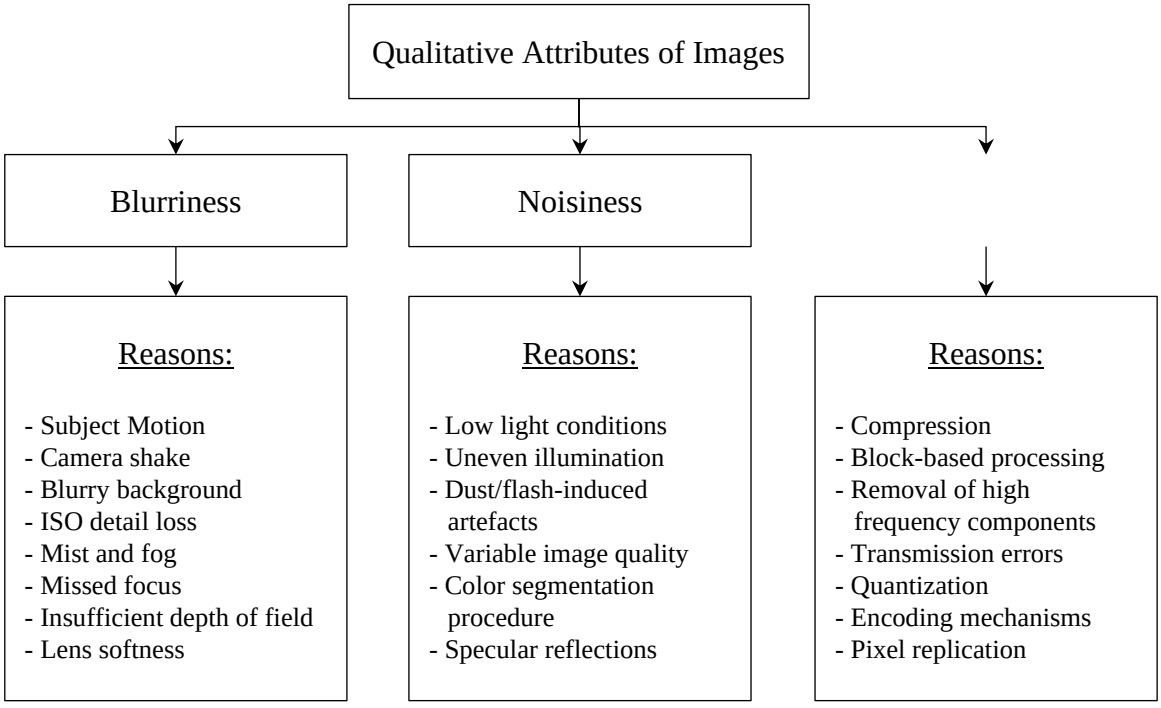

Fig. 1. The qualitative attributes of images and the reasons for the degradation of images

CNN models are trained and crack identifications are completed using different levels of image blurriness. A sensitivity study is also conducted to investigate the efficiency of the CNN in identifying cracks based on a different level of image blur in the training and validation datasets.

2. Research Methodology

This section describes the CNN configuration and the dataset used in this study. The approach is the combination of data collection, pre-processing, configuring the CNN and building the model.

2.1. Database Preparation

Existing open-source image databases of concrete cracks available in *Mendeley Data* and *Data in Brief* are compiled into a single training database to train the CNN in this research. Figure 2 shows the sample of images from the database. To ensure consistency and robustness of the training process, certain necessary image characteristics are specified, which are: i) the image must be sharp and can be seen without soft edges, ii) the distance between the camera lens and the concrete surface must be between 0.2 m to 1.0 m, and iii) the lighting condition of the image should be between 50 lux and 25,000 lux, which represents the dark to intensive lighting condition, respectively. Each of the images collected is then cropped into sub-images with a resolution of 227 × 227 pixels. The pixel of each image represents an element in the input matrix of the CNN. To prevent the occurrence of false annotations in the generation process of the database, cropped images with cracks on the edges are excluded. In total, 53,905 cropped small images were chosen which comprise 20,935 cracked and 32,970 non-cracked images. These images were stored in JPG format. As a supervised learning model, the trained CNN requires labelled information for all data. Hence, all of the 227 × 227 pixel images were labelled as "crack" or "positive" and "non-crack" or "negative" for classification purposes. The images were then randomly divided into training and validation sets with a ratio of 7:3.

In order to reduce the possibility of a network overfitting, data augmentation is performed with the use of the MATLAB software. An "*imageDataAugmenter*" is created to flip the training images horizontally and vertically. Subsequently, during the training process, an "*augmentedImageDatastore*" is responsible for transforming the training batches with the specified data augmentation options in the "*imageDataAugmenter*". It augments the training images randomly for each epoch without storing any images in memory. Thus, the transformed training datasets will be slightly different at every epoch. Once the network parameters are updated, the augmented images will be discarded. It should be noted that the actual number of training images remains unchanged at each epoch.

(a) **(b)**

Fig. 2. Sample of training images: a) Fine images; and b) Shadowed images

To identify the effect of the blurriness level and the performance of the CNN, various levels of blur are evaluated in this study. Each of the sub-images is blurred using a built-in function in MATLAB; 2-D Gaussian smoothing kernel with various standard deviations. The higher the value of standard deviation equals a higher level of blurriness. In this study, three levels of blurriness are examined where the standard deviation ranges from 1 to 3. Illustrations of different blurriness level on the images are depicted in Figure 3. The original dataset is replicated and split into eight different sub-datasets to train and validate the proposed CNN model in this study. These databases are composed of images with and without a blurriness level. Table 1 tabulates the image database combination used to train each network in this research. These databases are used to train different CNN models to detect damage which also consists of different levels of blurred images.

2.2. Convolutional Neural Network

Figure 4 shows the CNN architecture, which consists of multiple convolution blocks followed by the fully connected and classified layers. The input layer reads the image of 227 × 227 × 3 pixels resolution, and transfers it to the convolution blocks. Each convolution block is comprised of a convolution layer, an activation unit, and a pooling layer. The convolution operations with filters are performed to extract image features. Additionally, batch normalisation and dropout layers are introduced with the aforementioned layers in accordance with the purposes of use. After extracting the features of images in the learning layers, the output layer is responsible for classifying the images into their respective categories. Table 2 presents the detailed parameters of each layer and operation in the proposed CNN.

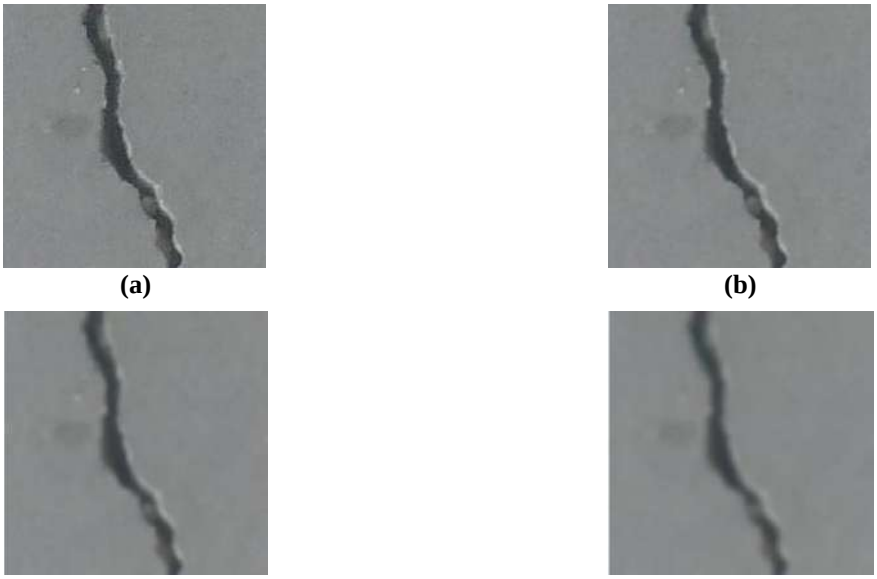

Fig. 3. Blurriness Level of: a) Sharp image; b) Level 1 blurred image; c) Level 2 blurred image; and d) Level 3 blurred image

Table 1. Image databases combination

Network	Datasets
A	Sharp
B	Blurriness level 1
C	Blurriness level 2
D	Blurriness level 3
E	Sharp + Blurriness level 1
F	Sharp + Blurriness level 2
G	Sharp + Blurriness level 3
H	Sharp + Blurriness level 1 + 2 + 3

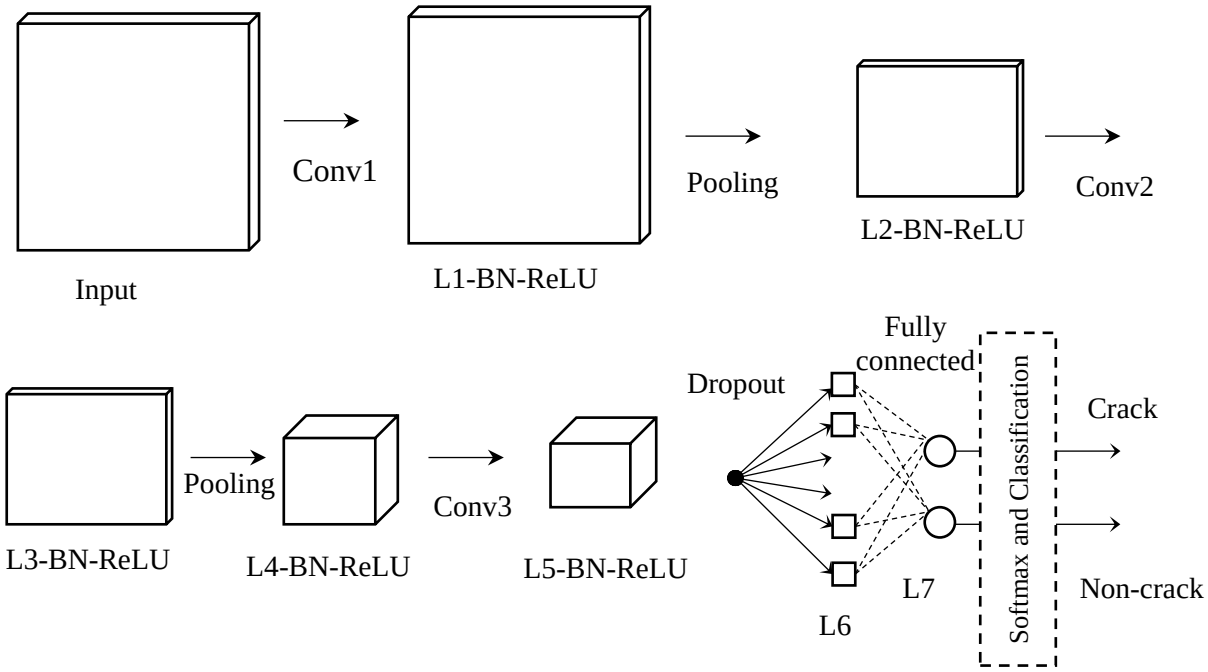

Fig. 4. Overview of CNN architecture

Table 2. Detailed parameters of each layer and operation in CNN

Layer	W/H	Channel	Operation	W/H	Channel	Number	Stride	Padding
Input	227	3	Conv1	3	3	8	1	1
L1	227	8	Pooling	3	3	-	2	0
L2	113	8	Conv2	3	8	16	1	1
L3	113	16	Pooling	3	3	-	2	0
L4	56	16	Conv3	3	16	32	1	1
L5	56	32	Dropout	-	-	-	-	-
L6	56	32	Fully Connected	1	-	2	-	-
L7	1	2	Softmax and Classification	-	-	-	-	-
L9	1	2	-	-	-	-	-	-

2.3. Sliding Window Technique

As depicted in Figure 5, during the sliding process, some of the cropped images may only have cracks on the edge spaces of images. These cracks can cause misclassification in the separation process. The sliding window technique is employed to overcome this problem in identifying the intact or cracked regions. The CNN architecture processes each receptive field and extracts features corresponding to weight kernels. The class of each region is recognized based on these weight dependent features. The features of the CNN architecture are automatically revised in every layer by the updated receptive fields' weights. The number of receptive fields of the designed architecture was 221, with 227 × 227 pixels. In this experiment's developed network, the three convolutional layers train the network. Features obtained from the first and second layers are only speculated as concrete surface cavities in the training data set. The visualized features are recognized and exploited by the trained network. The features from the last convolutional layer can be regarded as crack features. The segmentation results from the third layer are consistent, having low sensitivity to noise on the model's performance.

The sliding window searches over an image by shifting 227 pixels horizontally or vertically for a new region without overlapping. Since these kinds of images are disregarded in the generation of the database, the proposed CNN might not be able to detect such features as a crack or intact accurately. Therefore, based on Cha et al. (2017), an image is allowed to be

scanned twice with the designated sliding window approach, as illustrated in Figure 6. Directly, it can reduce the presence of such crack features and minimise misclassification.

2.4. Performance Indicator and Network Testing

The performance of the trained CNN is assessed using pictures of concrete cracks taken from Universiti Teknologi Malaysia. These pictures are referred to hereinafter as the test set. The test set is taken in such a way that they contain one or more of: i) different lighting conditions, ii) different crack widths, iii) different colour structures, iv) different shooting angles, and v) different image distances. The results are then compared to the actual observation in the test set. True Positives (TP) refer to the sub-image that is correctly labelled as a "crack" image by the network whilst False Positives (FP) indicate that the sub-image is falsely labelled as a "crack" image by the network. Furthermore, a True Negative (TN) test result denotes that the network correctly classified the sub-image as a "non-crack" image, and a False Negative (FN) happens when the network falsely classifies the sub-image as a "non-crack" image. Subsequently, the actual crack or Positive observation (P) is the sum of TP and FN in the testing image. In contrast, actual "non-crack" or Negative observation (N) is the sum of TN and FP in the test set.

Fig. 5. Presence of cracks on the edges of testing cropped image spaces

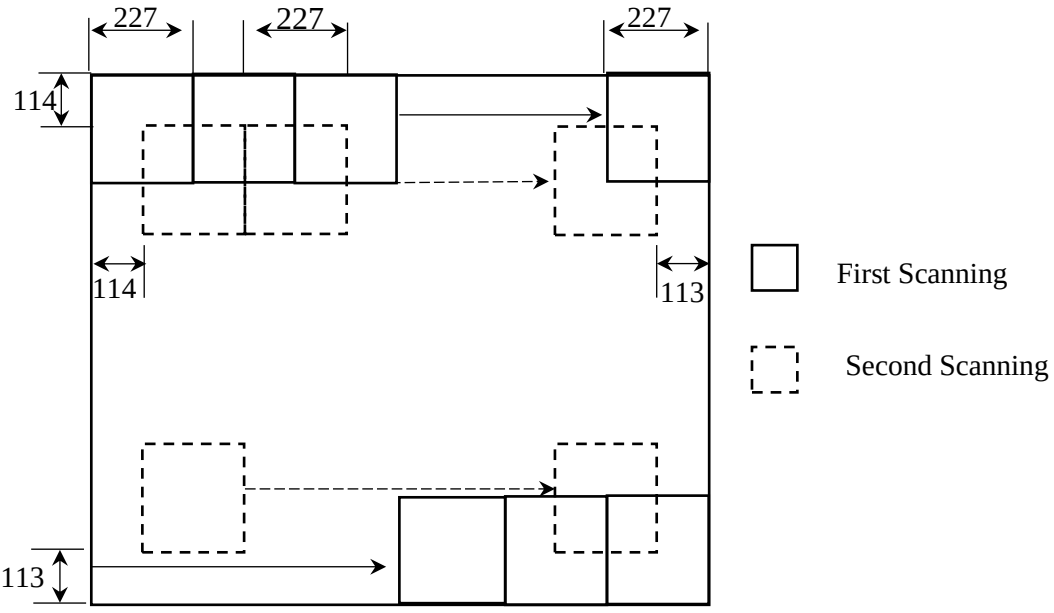

Fig. 6. Sliding window technique

In order to evaluate the performance of each network, performance indicators including accuracy, precision, recall, and F1 score will be deployed in this study. It should be noted that the accuracy does not always reflect the true performance of the CNN. The equations for the performance indicators are defined as:

$$Accracy = \frac{\sum TP + \sum TN}{\sum P + \sum N} \quad (1)$$

$$Precision = \frac{\sum TP}{\sum TP + \sum FP} \quad (2)$$

$$Recall = \frac{\sum TP}{\sum TP + \sum FN} \quad (3)$$

$$F1 = \frac{2 \times Recall \times Precision}{Recall + Precision} \quad (4)$$

where *TP*, *TN*, *P* and *N*: are true positive, true negative, positive observation and negative observation as mentioned earlier.

By taking into account the precision, recall, and F1, a better understanding of the effects of FN and FP regions can be provided on the performance of the CNN.

3. Prediction on Training Models

Under the same CNN architecture, eight different networks were used in the training process. These image datasets are made up of images with and without a blurriness level. This is to investigate the influence of the inclusion of blurred images on the performance of CNN. The corresponding datasets and detailed proportions of the training and validation sets for every network are listed in Table 3.

The validation accuracy is the indicator of the model response to new data and it is defined as the rate of correct classification of a newly seen image to the validation set at the iteration. The recorded training results including validation accuracy and training time for every network from the corresponding datasets are summarised in Table 4.

Stochastic gradient descent momentum was used to optimize CNN training with an initial learning rate of 0.01. The learning rate selection is a trade-off problem for accuracy and computation speed. A lower learning rate results in a longer training time, while a higher learning rate yields a shorter learning time. However, the network might reach a suboptimal result or diverge eventually. On the other hand, an epoch is a complete training cycle on the entire training dataset. The maximum number of epochs is the number of times the network has been updated for all of the images in the training set. In this study, the maximum epoch number considered is 10. The early stopping method was applied in the training process. Once there is little or no improvement on the loss of the validation set in ten consecutive times, the training progress will be stopped automatically. If the validation criterion is not met by the end of the 10th epoch, the training will be stopped at the maximum epoch number.

Table 3. Proportions of cracked and non-cracked images in training and validation sets

Network	No. of images					
	Crack			Non-crack		
	Training	Validation	Total	Training	Validation	Total
A	14655	6280	20935	23079	9891	32970
B	14655	6280	20935	23079	9891	32970
C	14655	6280	20935	23079	9891	32970
D	14655	6280	20935	23079	9891	32970
E	23909	12561	41870	46158	19782	65940
F	23909	12561	41870	46158	19782	65940
G	23909	12561	41870	46158	19782	65940
H	58618	25122	83740	92316	39564	131880

As shown in Table 4, the training time consumed for network A to network D is similar. As the number of images in the datasets increases, the training time increases. Network H was observed to have the longest training time since it was trained with the largest dataset. As for the validation accuracy, all networks achieved an accuracy above 95%. Network B and Network E yielded the highest accuracy as compared to the respective network made up of the same amounts of datasets. It should be noted that datasets from both networks consist of Level 1 blurriness images. On the other hand, Network H attained the lowest validation accuracy among all other networks. The lower validation accuracy can be due to the wide diversity of encompassed subclasses and a large number of training samples in Network H. Hence it can be noted that Network A performs as the optimum model based on the accuracy and training time results as shown in Table 4. Therefore, Network A is adopted for further performance investigation of the network under different conditions.

As shown in Table 4, increasing the number of training samples increased the training time. Generally, a larger training dataset could contribute more real-world scenarios, leading to a better generalization performance of the CNN algorithm. Overall, the total training time and computational overhead for performing one-time image training are not crucial if they help achieve enhanced accuracy. Hence, In real-world applications, increasing the number of training samples and training time is advisable if this increase could enhance the CNN's classification performance and detection accuracy in practical applications. In such a way, a trade-off between the training time and the accuracy should be set.

3.1. Performance of Network A under Different Conditions

Network A is used to detect concrete cracks on images in the test set. 23 raw images taken at a distance of 0.5 m are used to build the test set. It is noted that the images in the test set were not used in the training of Network A. Therefore, the images in the test set are entirely arbitrary to the trained Network A. Table 5 presents the summarised results of the testing images. As can be seen from Table 5, the highest accuracy reported is 100% in testing images No. 9 and 12. The test results are shown in Figures 7a and 7b, respectively. This may be due mainly to the absence of noisy features in these testing images. In contrast, the lowest accuracy reached is 40% in testing image No. 15 as shown in Figure 7c. It can be noticed that the existence of FP regions is mainly concentrated in the area of orange colour and spall concrete surfaces. Therefore, it leads to a lower number of TNs and eventually decreases the accuracy achieved. Overall, the network accurately detected these testing images with 83% accuracy, with less than approximately 14.82% degradation of accuracy obtained during the validation process, as shown in Table 4. Additionally, four different conditions in terms of lighting condition, crack width, colour structure, and angle are assessed during the testing process. The detailed detection results are displayed and discussed in the following subsections.

Table 4. Results for eight networks with different datasets

Network	Accuracy (%)	Training time (hr)
A	97.64	6.32
B	97.66	6.62
C	96.09	6.63
D	96.75	6.62
E	98.20	15.15
F	96.47	11.37
G	97.63	19.52
H	95.85	25.08

Table 5. Summarised result of scanned testing images

No.	P	N	TP	FP	TN	FN	Accuracy	Precision	Recall	F1	Remark
1	4	8	3	1	6	1	0.83	0.75	0.75	0.75	Figure 8a
2	33	188	33	27	161	0	0.88	0.55	1.00	0.71	-
3	32	189	31	24	165	1	0.89	0.56	0.97	0.71	-
4	24	129	14	9	120	10	0.88	0.61	0.58	0.59	-
5	29	192	28	53	139	1	0.76	0.35	0.97	0.51	-
6	23	198	10	4	194	13	0.92	0.71	0.43	0.54	-
7	26	195	3	6	189	23	0.87	0.33	0.12	0.18	-
8	21	200	21	63	137	0	0.71	0.25	1.00	0.40	Figure 9a
9	4	8	4	0	8	0	1.00	1.00	1.00	1.00	-
10	4	8	4	2	6	0	0.83	0.67	1.00	0.80	-
11	23	198	21	21	177	2	0.90	0.50	0.91	0.65	Figure 9b
12	4	8	4	0	8	0	1.00	1.00	1.00	1.00	Figure 8b
13	29	192	28	72	120	1	0.67	0.28	0.97	0.43	Figure 9a
14	28	193	28	24	169	0	0.89	0.54	1.00	0.70	Figure 8c
15	16	83	17	59	23	0	0.40	0.22	1.00	0.36	Figure 10a
16	18	177	17	14	163	1	0.92	0.55	0.94	0.69	-
17	34	187	32	71	116	2	0.67	0.31	0.94	0.47	Figure 11b
18	49	172	47	18	154	2	0.91	0.72	0.96	0.82	Figure 9c
19	16	205	11	14	191	5	0.91	0.44	0.69	0.54	Figure 8d
20	29	192	28	23	169	1	0.89	0.55	0.97	0.70	Figure 11c
21	38	183	38	9	174	0	0.96	0.81	1.00	0.90	-
22	9	9	7	3	6	2	0.72	0.70	0.78	0.74	-
23	17	82	16	27	55	1	0.72	0.37	0.94	0.53	Figure 10b
Average							0.83	0.56	0.87	0.64	

(a)

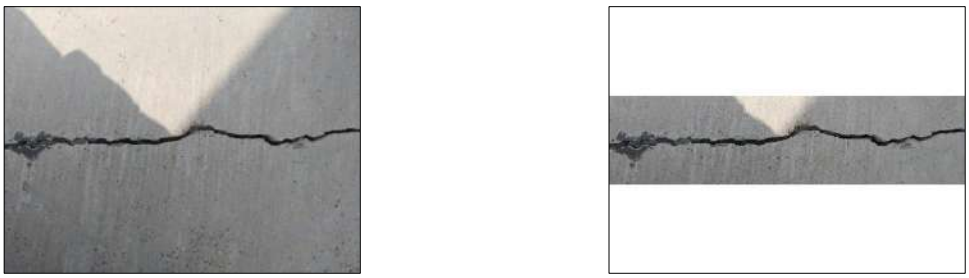

(b)

False Positive False Negative

(c)

Fig. 7. Images scanned using the trained CNN: a) No.9; b) No.12; and c) No.15

3.1.1. Crack Detection under Different Lighting

Figure 8 presents the detection result for the images with a shadowed area. As evidenced from Figure 8a, 1 out of 4 crack regions with the shadowed area is not successfully detected. In Figures 8b and 8c, the whole crack patterns are successfully identified by the proposed CNN. However, there are several FP regions distributed across the fine scratches and dirt stains of the image. As for Figure 8d, most of the crack regions are detected. Nevertheless, a few FN regions exist in the intensive lighting region, while FP regions are mainly distributed in the dark lighting region of the image. The test results for these images are tabulated in Table 6. It can be noted that the accuracy and recall for all testing images are sufficiently high. In contrast, precision and F1 are relatively low due to the high FP presence in Figures 8c and 8d. Figure 8d achieved the lowest precision followed by Figures 8c and 8a. This is owing to the existence of non-crack surfaces that are misclassified as crack surfaces. On the other hand, the presence of FN regions in Figures 8a and 8d reduced the recall to 0.75 and 0.65, respectively. Based on the results presented in Figure 8 and Table 6, it can be concluded that the proposed CNN is slightly sensitive to lighting conditions. Uneven illumination is an artefact classified as an image noisiness qualitative attribute of images. Figure 8d shows undetected crack regions in bright areas due to uneven illumination. The shadows or glow are created due to improper illumination mask the existing features. Several approaches are applicable for the correction of uneven illumination, including using illumination invariant features and illumination compensation approaches (Yang and Byun, 2007).

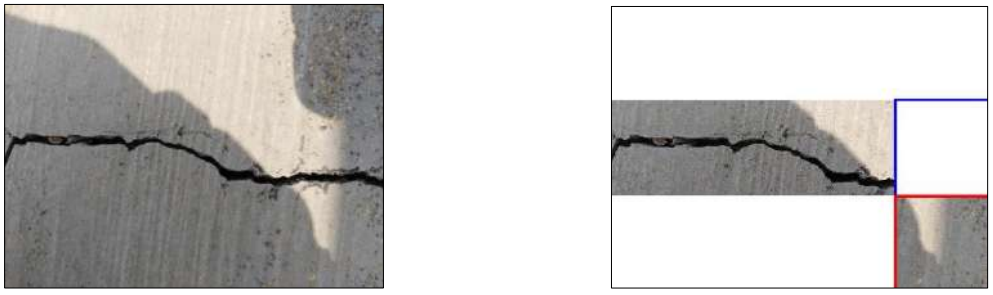

(a)

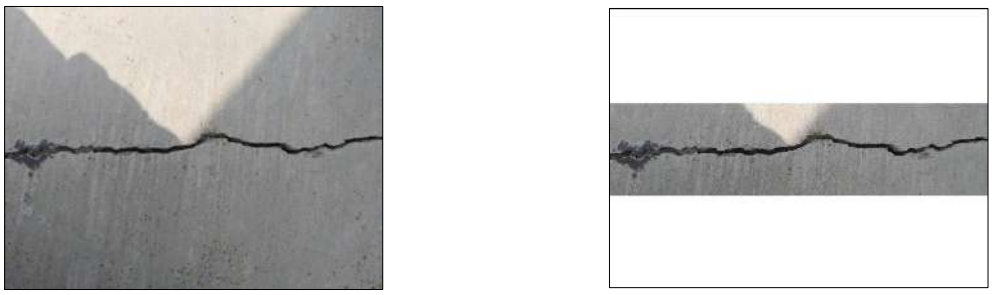

(b)

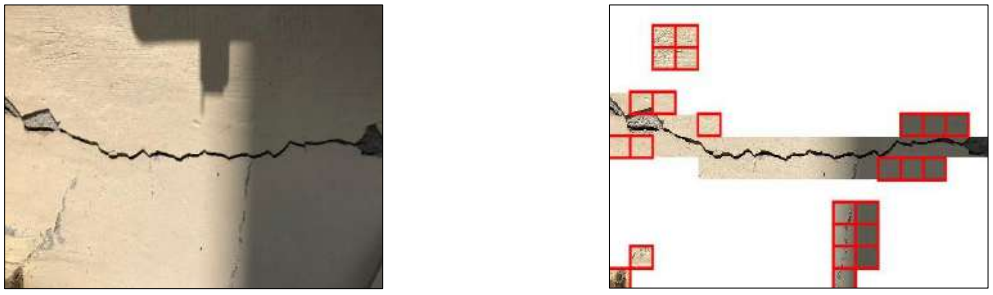

(c)

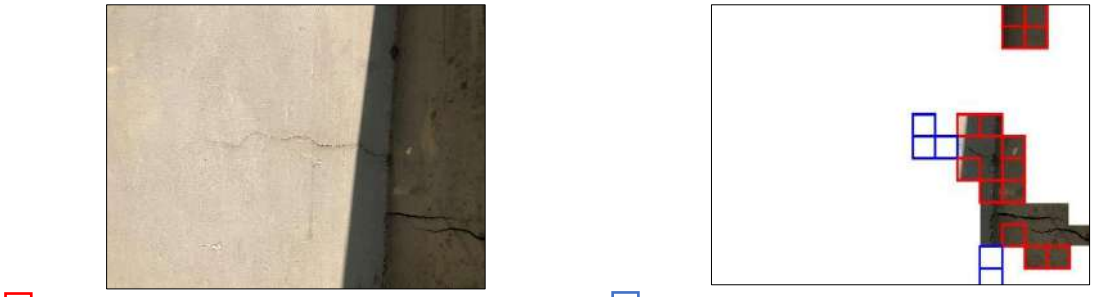

(d)

Fig. 8. Shadowed images scanned using the trained CNN: a) 908 × 681 pixels; b) 908 × 681 pixels; c) 3859 × 2951 pixels; and d) 3859 × 2951 pixels

Table 6. Detailed analysis of test images in Figure 8

Test image	TP	FP	TN	FN	Accuracy	Precision	Recall	F1
Figure 8a	3	1	7	1	0.83	0.75	0.75	0.75
Figure 8b	4	0	8	0	1.00	1.00	1.00	1.00
Figure 8c	28	24	169	0	0.89	0.54	1.00	0.70
Figure 8d	11	14	191	5	0.91	0.44	0.69	0.54
	Average				0.91	0.68	0.86	0.75

3.1.2. Crack Detection under Different Crack Width

Images containing various crack widths are also tested as depicted in Figure 9. The number of TP, FP, TN, and FN regions are summarised and tabulated in Table 7. It can be seen that the crack detection results for testing images are very effective regardless of crack width. The detection accuracy and recall are relatively high, which indicates that the majority of the cracks that theoretically exist are successfully spotted. Despite the successful detection, several FP regions occurred around the crack areas. Due to the high number of such regions, it will significantly reduce the precision and F1. As evidenced in Table 7, Figure 9a is reported to have the lowest precision as well as F1.

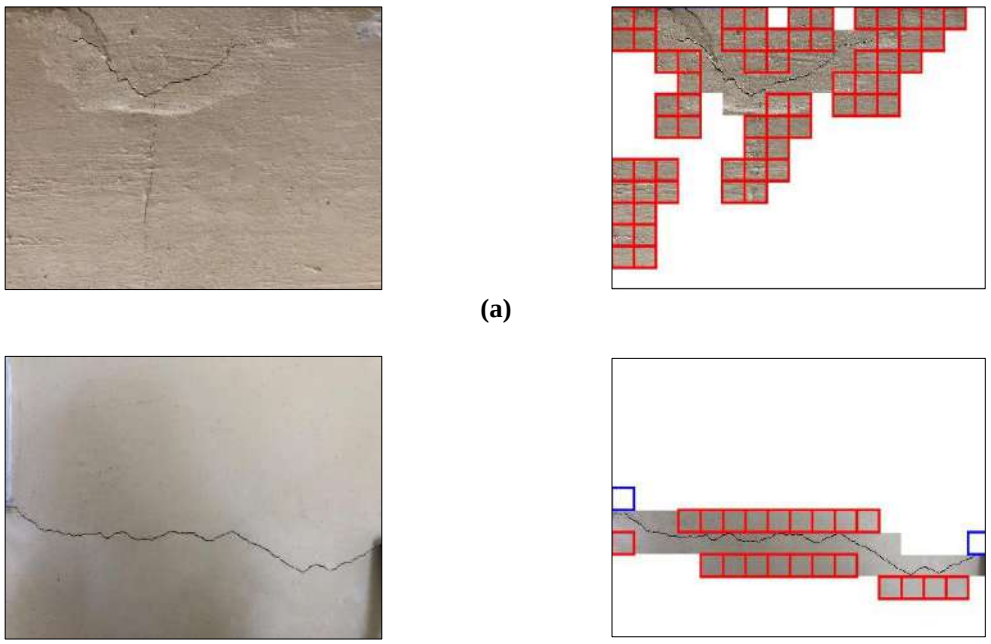

(a)

(b)

(c)

Fig. 9. Images scanned using the trained CNN: a) Thin crack; b) Medium crack; and c) Thick crack

Table 7. Detailed analysis of test images in Figure 9

Test image	TP	FP	TN	FN	Accuracy	Precision	Recall	F1
Figure 9a	21	63	137	0	0.71	0.25	1.00	0.40
Figure 9b	21	21	177	2	0.90	0.50	0.91	0.65
Figure 9c	47	18	154	2	0.91	0.72	0.96	0.82
	Average				0.84	0.49	0.96	0.62

3.1.3. Crack Detection under Different Colour Structures

Figure 10 shows the crack detection results with different colour structures with the proposed CNN model. It should be noted that they are made up of the same image yet different colours, in which Figure 10a is the RGB image while Figure 10b is a grayscale image. A close examination of Figures 10a and 10b reveals that the presence of orange colour resulted in a significant increase in the number of FP regions. Consequently, the accuracy, precision, and F1 for Figure 10a is much lower than that of Figure 10b as shown in Table 8. The occurrence of a large number of FP regions are due to the colour of the testing image which is radically different from the training images used in the database. This explicitly reflects the low generalisability of Network A.

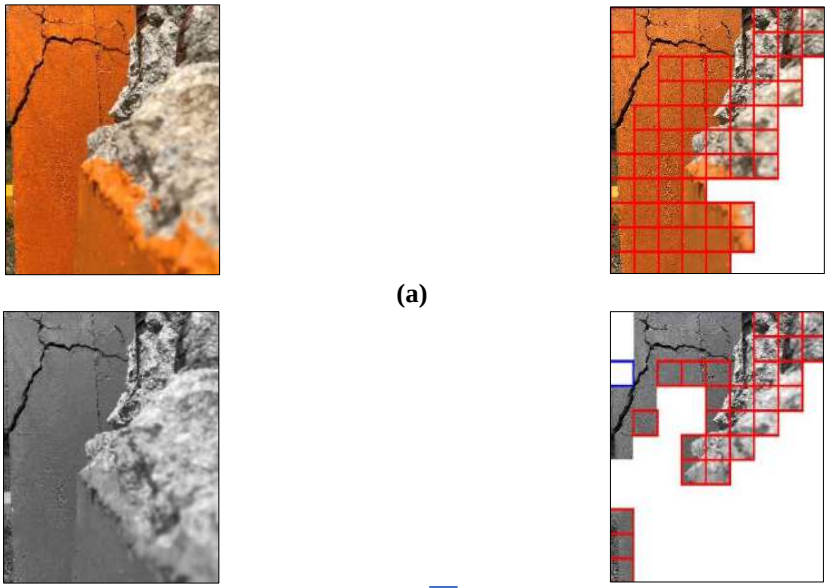

(a)

(b)

Fig. 10. Images scanned using the trained and validated CNN: a) Normal color; and b) Grayscale

Table 8. Detailed analysis of test images in Figure 10

Test image	TP	FP	TN	FN	Accuracy	Precision	Recall	F1
Figure 10a	16	60	23	0	0.39	0.21	1.00	0.35
Figure 10b	16	27	55	1	0.72	0.37	0.94	0.53
	Average				0.56	0.29	0.97	0.44

3.1.4. Crack Detection under Different Shooting Angles

Several testing images were photographed at different angles as illustrated in Figure 11. They can be divided into high angle (45° - 90°), medium angle (0° - 45°) and low angle (0°). Based on the results presented in Figure 11, it can be noted that the majority of the cracks in these images are successfully detected. The existence of FN regions is very minimal. However, the number of FP regions increases by increasing the shooting angle. Table 9 shows the detailed test results for Figure 11. The images acquired at the low angle achieved the highest accuracy, precision, recall, and F1. In contrast, the medium and high angle images showed lower values for all 4 performance indicators. Both of these images showed similar values for the four performance indicators. The high number of FP regions in these testing images greatly reduced the value of precision and F1. Notwithstanding that, it is clearly shown that the accuracy and recall based on the proposed CNN are in an acceptable range and true cracks can be identified and detected. Based on the results shown in Figure 11 and Table 9, it can be concluded that the shooting angle has a degree of influence on the precision of the proposed CNN. At a higher shooting angle, the proposed CNN is expected to give a higher number of FP regions. However, the proposed CNN still satisfied the requirement of identifying and locating the cracks in the testing images.

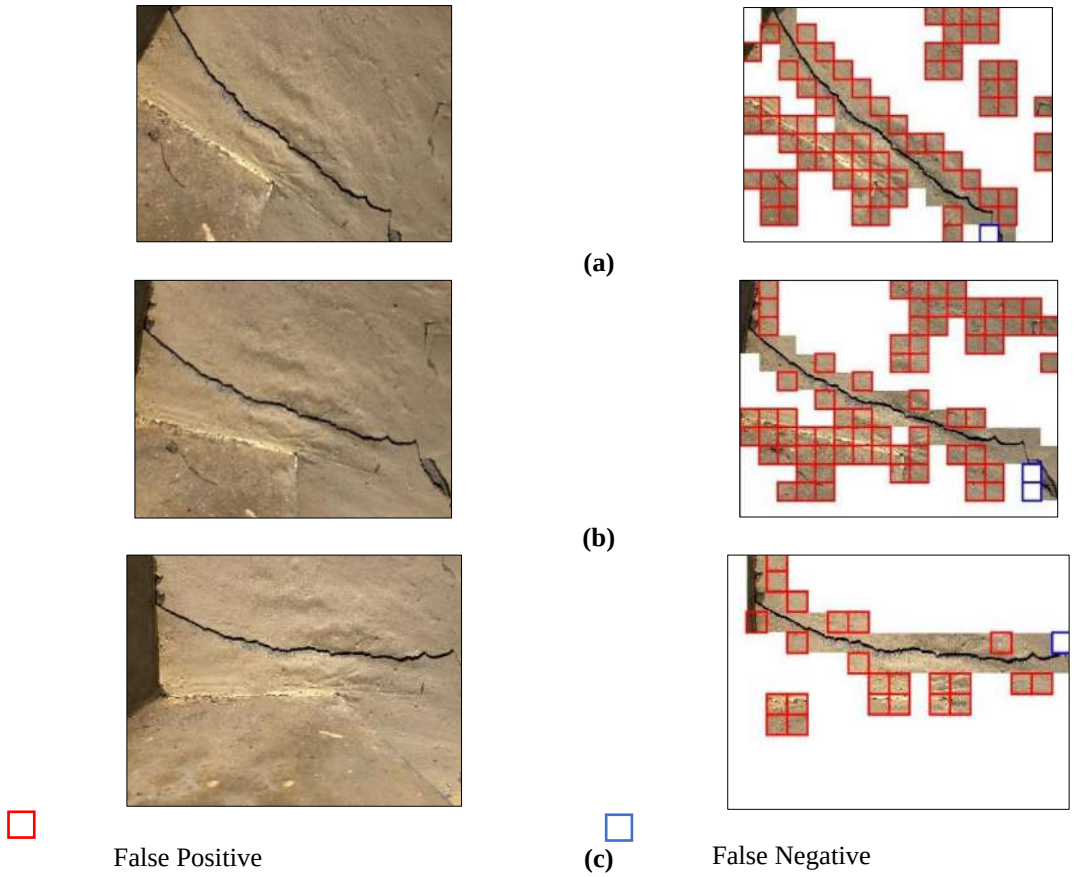

Fig. 11. Images scanned using the trained and validated CNN: a) High angle; b) Medium angle; and c) Low angle

Table 9. Detailed analysis of test images in Figure 11

Test image	TP	FP	TN	FN	Accuracy	Precision	Recall	F1
Figure 11a	28	72	120	1	0.67	0.28	0.97	0.43
Figure 11b	32	71	116	2	0.67	0.31	0.94	0.47
Figure 11c	28	23	169	1	0.89	0.55	0.97	0.70
	Average				0.74	0.38	0.96	0.53

3.2. Performance of the CNN under Various Image Distances

In real applications, the performance of the CNN on detecting cracks is influenced by the distance between the camera and object. In order to reduce such effects, eight networks with combinations of sharp and blurred images are trained using different datasets as shown in Table 2. Subsequently, these networks are then used to classify the images in the test sets as depicted in Figure 12. The test sets consist of four different classes of images taken in the distance of 0.5 m, 1.0 m, 1.5 m, and 2.0 m, respectively.

Figure 13 shows the performance indicators of all networks on the test sets. Among these networks, Network B appears to be the network with the best performance. The accuracy achieved by Network B increases gradually as the distance of the images in the test set increases from 0.5 m to 1.5 m. As the distance of the images increases from 1.5 m to 2.0 m, the accuracy of Network B shows a slight drop of 3.92%. The precision of Network B consistently outperformed most of the trained networks regardless of the image distances. This implies that the likelihood of misclassifying a non-crack as a crack is very minimal. The recall of Network B is slightly unsatisfactory as compared to other trained networks. This implies that Network B tends to miss more cracks as compared to the other trained networks. Since the F1 of Network B remains the highest among the trained networks, it can be said that the high precision outweighs the low recall of Network B and the low recall problem can be compensated by incorporating a larger volume of training data (Ryu, 2018). This suggests the highest robustness of Network B for crack detection across various distances of images from 0.5 m to 2.0 m. This detection performance is achieved due to the higher rate of TP diagnosis coupled with a lower number of FP in the detection of cracks incorporating replicated images of Level 1 blurriness for training.

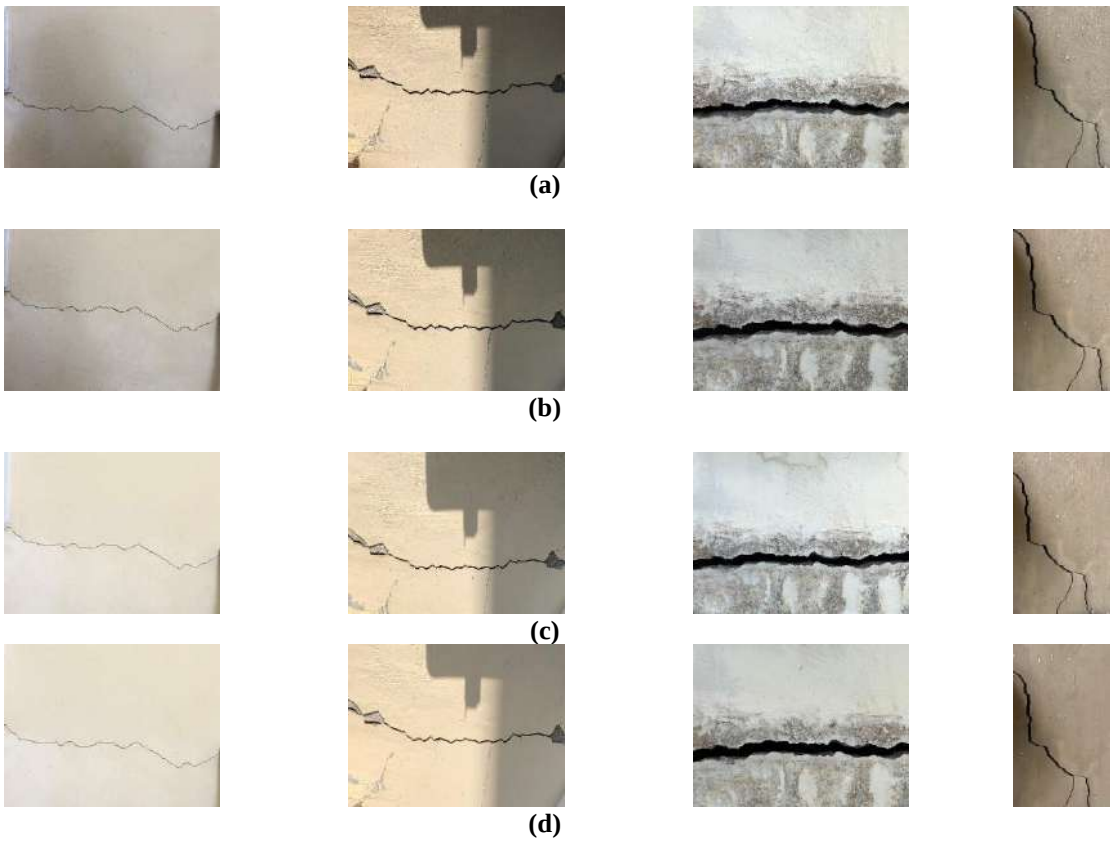

Fig. 12. Test sets taken in the distance of: a) 0.5 m; b) 1.0 m; c) 1.5 m; and d) 2.0 m

The accuracy achieved for Network A and Network H exhibited a similar trend as shown in Figure 13. Their accuracy rivals that of Network B. In fact, both Network A and Network H achieved slightly higher accuracy when the image distance was 0.5 m. However, Network A and Network H achieved different precision, recall, and F1 scores. By taking precision and recall into consideration, the F1 of Network A is significantly higher than that of Network H. Hence, it can be concluded that the true performance of Network A is better than Network H. As evidenced from Figure 13, the accuracy, precision, and F1 of Network C and D significantly increase as the distances of the images increases from 0.5 m to 2.0 m. This indicates that the performance of Networks C and D improves as the distances of the images increases. This is attributed to the fact that both of the networks were trained by using blurred images only. This finding also supports the idea that higher image distance can be captured by using a more blurred image training set. The consistently high recall achieved by Network D suggests that this network can accurately capture true cracks regardless of image distances. This implies that training with a blurred image can improve the ability of the network to capture cracks with various image distances.

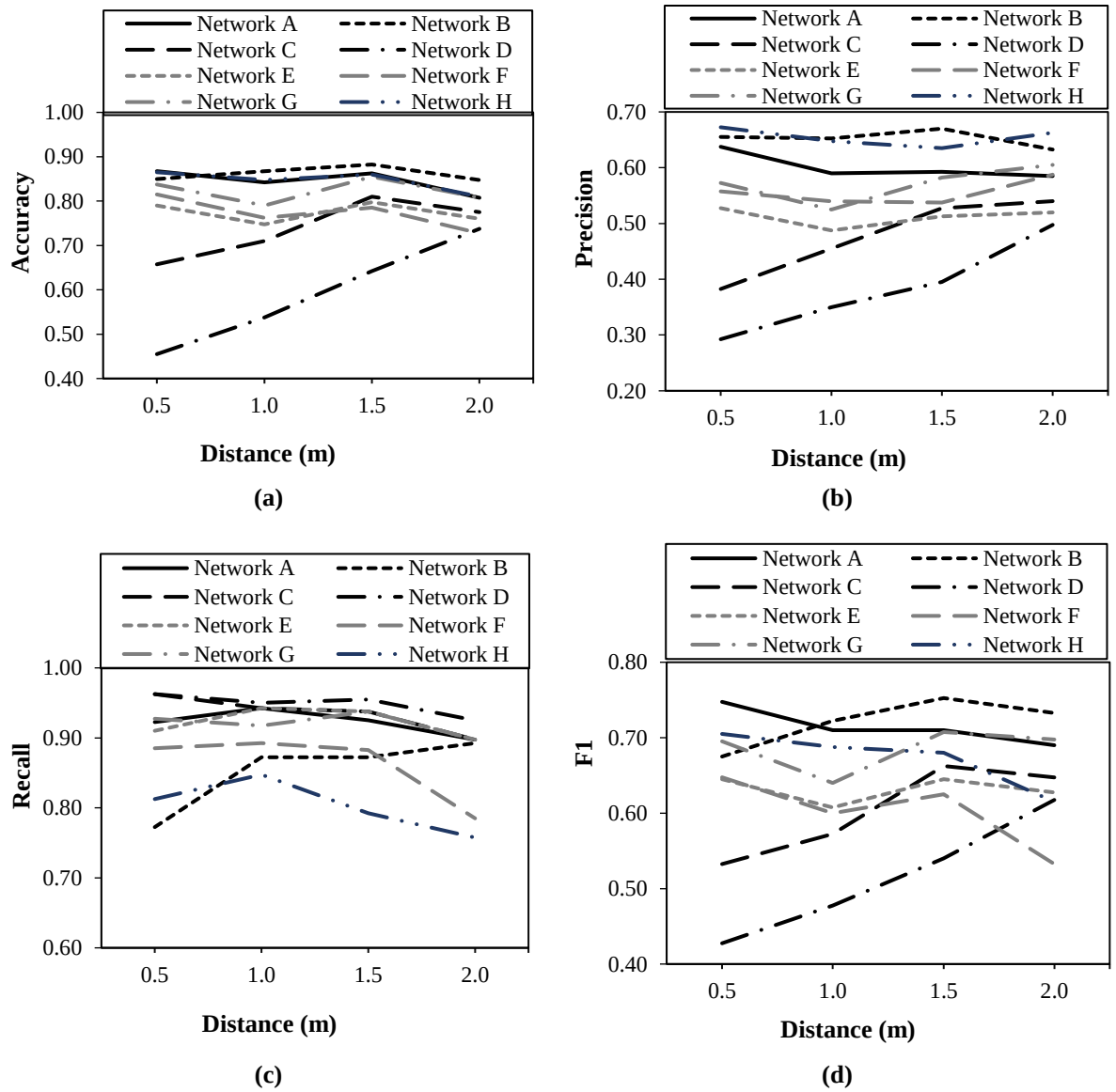

Fig. 13. Performance of all networks on the test sets: a) Accuracy; b) Precision; c) Recall; and d) F1

To further verify the performance of blurred images in the training database, Networks E, F, and G are compared. Among these three networks, it is noticeable that Network G attained the highest accuracy and F1 across various distances of images from 0.5 m to 2.0 m. It is also noted that the performance of Network F is better than Network E, and Network G is better than Network F. This means that the performance of the network improves when a higher blurriness level is used in the training database across various distances of images. Therefore, it can be said that Network G has a better true performance than the other two networks. It is noted that the performance of these networks is poorer than Networks A and H. This finding suggests that training the CNN with additional images with a single blurriness level cannot improve the performance of the network. Such a combination of training databases may result in a decrease in the performance of the network.

Different performance trends can be observed when comparing a network composed of merely blurred images with a network made up of both sharp images and blurred images. Network B consistently outperformed the accuracy and F1 of Network E for all distances of images. In contrast, Network G has a better performance on accuracy and F1 than that of Network D across various distances of images. Network C yielded a better performance as compared to Network F when the distances of images fall in the range of 1.5 m to 2.0 m. Although these networks achieved satisfactory accuracy during the training and validation process, the performance of the networks might suffer when used on images with significant deviations from the context represented in the training and validation set. Under these circumstances, the model could be improved by retraining with a wider range of databases.

4. Conclusions

This paper proposed a CNN-based framework for autonomous crack detection in concrete surfaces. The study aimed to increase the performance of the CNN algorithm that was least influenced by the mismatch of the dataset in training and testing caused by image blurriness artefacts. Hence, images of concrete cracks pulled from open-source databases *Mendeley Data* and *Data in Brief* were used in this study. Selected images were compiled into a single training database for training the CNN. A total of 53,905 images with 227 × 227 pixels were chosen based on the requirements set. Subsequently, each image was blurred with three levels of blurriness. Unlike previous research, data augmentation in this study was carried out automatically with the use of a built-in function in MATLAB. The training images were allowed to flip horizontally and vertically in a probabilistic approach. The proposed CNNs were successfully developed to detect concrete cracks autonomously from images, with validation accuracy attained by all networks exceeding 95%. The performance of the trained and validated CNN with the use of sharp images was evaluated using test sets with different pixels and under various lighting, crack widths, colour structures, and shooting angle conditions. A sliding window technique was deployed to perform the scanning of images larger than 227 × 227 pixels. The accuracy obtained by the trained and validated CNN was lower than the validation accuracy recorded due to the presence of FPs in the region of dark lighting, dirt stains, fine scratches, and visible light spectrum. Additionally, the intercorrelations between blurriness and image distance are summarised, including:

- As the distance of the images increases, the performance of the network trained with the use of blurred images significantly increases,
- The highest performing range of blurriness level is 1, followed by 2 and 3,

- CNNs trained with a sharp image and single blurriness level do not improve the performance of the network across varying image distances,
- Networks with the combination of sharp images and all blurriness level images exhibited similar accuracy trends compared to the network with only sharp images and
- The network with the sole use of blurriness level 1 images as the dataset outperforms all other networks across varying distances of the images.

It was observed that high shooting angle and uneven illumination has a negative effect on the accuracy of the proposed CNN. Therefore, this study concludes that the presence of blurred images in training data can solve the image distance issue associated with CNN. It could revolutionise automated inspection systems.

5. Acknowledgement

The authors would like to thank the Ministry of Higher Education, Malaysia, and Universiti Teknologi Malaysia (UTM) for their financial support through the HICoE Grant (4J224) and Transdisciplinary Research Grant (07G46).

6. References

Abdulkareem, M., Bakhary, N., Vafaei, M., Noor, N.M. and Padil, K.H. (2018). "Non-probabilistic wavelet method to consider uncertainties in structural damage detection", *Journal of Sound and Vibration*, 433(27 October), 77-98, https://doi.org/hdl.handle.net/11250/238284.

Abudallah Habib, I., Wan Mohtar, W.H.M., Muftah Shahot, K., El-shafie, A. and Abd Manan, T.S. (2021). "Bridge failure prevention: An overview of self-protected pier as flow altering countermeasures for scour protection", *Civil Engineering Infrastructures Journal*, 54(1), 1-22, https://doi.org/10.22059/CEIJ.2020.292296.1627.

Atha, D.J. and Jahanshahi, M.R. (2018). "Evaluation of deep learning approaches based on convolutional neural networks for corrosion detection", *Structural Health Monitoring*, 17(5), 1110-11128, https://doi.org/10.1177/1475921717737051.

Cha, Y.J., Choi, W. and Büyüköztürk, O. (2017). "Deep learning-based crack damage detection using convolutional neural networks", *Computer-Aided Civil and Infrastructure Engineering*, 32(5), 361-78, https://doi.org/10.1111/mice.12263.

Cha, Y.J., Choi, W., Suh, G., Mahmoudkhani, S. and Büyüköztürk, O. (2018). "Autonomous structural visual inspection using region-based deep learning for detecting multiple damage types", *Computer-Aided Civil and Infrastructure Engineering*, 33(9), 731-747, https://doi.org/10.1111/mice.12334.

Chen, F.C. and Jahanshahi, M.R. (2020). "ARF-crack: Rotation invariant deep fully convolutional network for pixel-level crack detection", *Machine Vision and Applications*, 31(6), 1-12, https://doi.org/10.1007/s00138-020-01098-x.

Ciresan, D.C., Meier, U., Masci, J., Gambardella, L.M. and Schmidhuber, J. (2011). "Flexible, high performance convolutional neural networks for image classification", *Twenty Second International Joint Conference on Artificial Intelligence*, Catalonia, Spain, https://doi.org/10.5591/978-1-57735-516-8/IJCAI11-210.

Dash, R., Sa, P. K., and Majhi, B. (2009). "RBFN based motion blur parameter estimation", *International Conference on Advanced Computer Control*, 327-331, IEEE, Singapore, https://doi.org/10.1109/ICACC.2009.98.

Delatte, N. (2009). *Failure, distress and repair of concrete structures*, Elsevier, https://doi.org/10.1533/9781845697037.

Deng, L., Chu, H.H., Shi, P., Wang, W. and Kong, X. (2020). "Region-based CNN method with deformable modules for visually classifying concrete cracks", *Applied Sciences*, 10(7), 2528, https://doi.org/10.3390/app10072528.

Dorafshan, S. and Maguire, M. (2018). "Bridge inspection: Human performance, unmanned aerial systems and automation", *Journal of Civil Structural Health Monitoring*, 8(July), 443-476.

Dorafshan, S., Thomas, R.J. and Maguire, M. (2018). "Comparison of deep convolutional neural networks and edge detectors for image-based crack detection in concrete", *Construction and Building Materials*, 186(20 October), 1031-1045, https://doi.org/10.1007/s13349-018-0285-4.

Fan, Y., Zhao, Q., Ni, S., Rui, T., Ma, S. and Pang, N. (2018). "Crack detection based on the mesoscale geometric features for visual concrete bridge inspection", *Journal of Electronic Imaging*, 27(5), 053011, https://doi.org/10.1117/1.JEI.27.5.053011.

Fankhauser, N., Kalberer, N., Müller, F., Leles, C.R., Schimmel, M. and Srinivasan, M. (2020). "Comparison of smartphone-camera and

conventional flatbed scanner images for analytical evaluation of chewing function", *Journal of oral rehabilitation*, 47(12), 1496-502, https://doi.org/10.1111/joor.13094.

Han, X., Thomasson, J.A., Bagnall, G.C., Pugh, N.A., Horne, D.W., Rooney, W.L., Jung, J., Chang, A., Molambo, L., Popescu, S.C., Gates, I.T. and Cope, D.A. (2018). "Measurement and calibration of plant-height from fixed-wing UAV images", *Sensors*, 18(12), 4092, https://doi.org/10.3390/s18124092.

Jang, K., Kim, N., and An, Y.-K. (2019). "Deep learning–based autonomous concrete crack evaluation through hybrid image scanning", *Structural Health Monitoring*, 18(5-6), 1722-1737, https://doi.org/10.3390/s18124092.

Kim, B. and Cho, S. (2018). "Automated vision-based detection of cracks on concrete surfaces using a deep learning technique", *Sensors*, 18(10), 3452, https://doi.org/10.3390/s18103452.

Li, S., Zhao, X. and Zhou, G. (2019). "Automatic pixel-level multiple damage detection of concrete structure using fully convolutional network", *Computer-Aided Civil and Infrastructure Engineering*, 34(7), 616-34, https://doi.org/10.1111/mice.12433.

Li, Y., Zhao, W., Zhang, X. and Zhou, O. (2018). "A two-stage crack detection method for concrete bridges using Convolutional Neural Networks", *IEICE Transactioons on Information and Systems*, 101(12), 3249-3252, https://doi.org/10.1587/transinf.2018EDL8150.

Protopapadakis, E., Voulodimos, A., Doulamis, A., Doulamis, N. and Stathaki, T. (2019). "Automatic crack detection for tunnel inspection using deep learning and heuristic image post-processing", *Applied intelligence*, 49(2), 2793-2806, https://doi.org/10.1007/s10489-018-01396-y.

Ratnam, M.M., Ooi, B.Y. and Yen, K.S. (2019). "Novel moiré-based crack monitoring system with smartphone interface and cloud processing", *Structural Control and Health Monitoring*, 26(10), e2420, https://doi.org/10.1002/stc.2420.

Ryu, P.-M. (2018). "Predicting the unemployment rate using social media analysis", *Journal of Information Processing Systems*, 14(4), 904-915, https://doi.org/10.3745/JIPS.04.0079.

Shen, L., Fang, R., Yao, Y., Geng, X. and Wu, D. (2018). "No-reference stereoscopic image quality assessment based on image distortion and stereo perceptual information", *IEEE Transactions on Emerging Topics in Computational Intelligence*, 3(1), 59-72, https://doi.org/10.1109/TETCI.2018.2804885.

Sieberth, T., Wackrow, R., and Chandler, J. (2013). "Automatic isolation of blurred images from UAV image sequences", *International Archives of the Photogrammetry, Remote Sensing and Spatial Information Sciences*, Rostock, Germany.

Sieberth, T., Wackrow, R. and Chandler, J. (2015). "UAV image blur-its influence and ways to correct it", *The International Archives of Photogrammetry, Remote Sensing and Spatial Information Sciences*, Toronto, Canada, https://doi.org/10.5194/isprsarchives-XL-1-W4-33-2015

Wang, Y., Fang, Z. and Hong, H. (2019). "Comparison of convolutional neural networks for landslide susceptibility mapping in Yanshan County, China", *Science of The Total Environment*, 666(20 May), 975-93, https://doi.org/10.1016/j.scitotenv.2019.02.263.

Yang, J. and Byun, H. (2007). "Illumination compensation algorithm using eigenspaces transformation for facial images", In: Gagalowicz, A., Philips, W. (eds.), *Computer Vision/Computer Graphics Collaboration Techniques* (MIRAGE 2007), Lecture Notes in Computer Science, Vol. 4418, Springer, Berlin, Heidelberg, https://doi.org/10.1007/978-3-540-71457-6_18.

Ye, X.-W., Dong, C.-Z. and Liu, T. (2016). "A review of machine vision-based structural health monitoring: methodologies and applications", *Journal of Sensors*, 2016, Article ID 7013039, https://doi.org/10.1155/2016/7103039.

Zhang, Y., Sun, X., Loh, K.J., Su, W., Xue, Z. and Zhao, X. (2020). "Autonomous bolt loosening detection using deep learning", *Structural Health Monitoring*, 19(1), 105-22, https://doi.org/10.1177/1475921719837509.

Zhou, S. and Song, W. (2021). "Deep learning-based roadway crack classification with heterogeneous image data fusion", *Structural Health Monitoring*, 20(3), 1274-1293, https://doi.org/10.1177/1475921720948434.

Civil Engineering Infrastructures Journal 2023, 56(1): 137-157
DOI: 10.22059/CEIJ.2022.334953.1803

RESEARCH PAPER

Prediction of Shear Strength of Reinforced Concrete Deep Beams Using Neuro-Fuzzy Inference System and Meta-Heuristic Algorithms

Mohammadizadeh, M.R.[1*], Esfandnia, F.[2] and Khatibinia, M.[3]

[1] Associate Professor, Department of Civil Engineering, University of Hormozgan, Bandar Abbas, Iran.
[2] Ph.D. Student, Department of Civil Engineering, University of Hormozgan, Bandar Abbas, Iran.
[3] Associate Professor, Department of Civil Engineering, University of Birjand, Birjand, Iran.

Received: 03 Dec. 2021; Revised: 16 Mar. 2022; Accepted: 10 Apr. 2022

ABSTRACT: It is generally accepted that the shear strength of Reinforced Concrete (RC) deep beams depends on the mechanical and geometrical parameters of the beam. The accurate estimation of shear strength is a substantial problem in engineering design. However, the prediction of shear strength in this type of beams is not very accurate. One of the relatively accurate methods for estimating shear strength of beams is Artificial Intelligence (AI) methods. Adaptive Neuro-Fuzzy Inference System (ANFIS) was presented as an AI method. In this study, the efficiency of ANFIS incorporating meta-heuristic algorithms for predicting shear strength of RC beams was investigated. Meta-heuristic algorithms were used to determine the optimum parameters of ANFIS for providing the efficient models of the prediction of the RC beam shear strength. To evaluate the accuracy of the proposed method, its results were compared with those of other methods. For this purpose, the parameters of concrete compressive strength, cross-section width, effective depth, beam length, shear span-to-depth beam ratio (a/d), as well as percentage of longitudinal and transverse reinforcement were selected as input data, and the shear strength of reinforced concrete deep beam as the output data. Here, K-fold validation method with k = 10 was used to train and test the algorithms. The results showed that the proposed model with second root mean square error of 25.968 and correlation coefficient of 0.914 is more accurate than other methods. Therefore, neural fuzzy inference system with meta-heuristic algorithms can be adopted as an efficient tool in the prediction of the shear strength of deep beams.

Keywords: Meta-Heuristic Algorithms, Neuro-Fuzzy Inference System, Reinforced Concrete Deep Beam, Shear Strength.

1. Introduction

Deep beams are widely used in civil engineering including tall buildings, tanks, rectangular silos, floor diaphragms, shear walls, slabs and offshore structures (Gandomi et al., 2013; Prayogo et al., 2020). Due to complicated behavior of

* Corresponding author E-mail: mrzmohammadizadeh@yahoo.com

these beams, there is no consensus on the definition of the deep beams to which is approved by all researchers. A criterion for the definition of deep beams is the ratio of its span length (L) to its depth (D) which is less than 5. However, this criterion is less than 2.5, 5 and 4 in European, Canadian and American standards, respectively. Due to the complexity of the shear mechanism of deep concrete beams and the various parameters affecting it, it is difficult to develop a general model for accurate estimation of shear strength, and therefore the exact shear strength of these beams cannot be calculated using a closed-form solution. For pervious decades, few studies have examined the shear strength and analyzed the behavior of reinforced concrete deep beams. Many studies have also attempted to predict the shear capacity of reinforced concrete (RC) deep beams using various experimental relationships and analytical models (Liu and Mihaylov, 2016). Improving prediction performance is very important in the design of RC deep beams. Therefore, an efficient model is required to accurately predict the shear capacity prediction for different types of RC beams. In recent years, Artificial Intelligence (AI) methods have been used for this purpose. The use of AI methods has been attracted as extensive research in many fields of civil engineering (Moosazadeh et al., 2019; Taghi Dastorani et al., 2018; Baghban et al. 2020; Chitgar and Berenjian 2021). AI methods have been successfully used in complex problems, so that these methods can provide a powerful prediction method. The use of AI methods has shown that a complex nonlinear relationship could be established between the shear capacity of RC deep beams and all the effective parameters. Therefore, the use of AI methods has been proposed as efficient methods in the field of civil engineering. Artificial Neural Network (ANN) as an AI method is extensively proposed in order to model complex relationships between input and output data or to find a pattern for data. Although, ANNs are used in many problems and applications, their development can be time consuming. Adaptive fuzzy-neural inference (ANFIS) as an AI method combines the prominent features of a Fuzzy Inference System (FIS) with ANNs. In this type of method, the fuzzy rules of the samples are determined through ANN (Toghroli et al., 2014). This system has also shown good efficiency in recent years in comparison with older methods such as ANNs for classifying and estimating functions.

In recent years, the prediction of the shear strength of RC beams using the AI methods has attracted much attention of researchers. Nguyen et al. (2021) presented a model for the prediction of the shear strength of RC deep beams based on ANN and using four training algorithms. This study showed that ANN is a suitable method for predicting the shear strength of RC deep beams (Nguyen et al., 2021). In the study of Suguna et al. (2018), high-strength concrete beams were modeled based on ANN. Yield load, deflection at yield load, service load, deflection at service load, final load, deflection at final load, and flexibility were the target parameters and were predicted by ANN (Suguna et al., 2018). The capability of AI techniques for the prediction of the behavior of an innovative type of C-shaped shear connectors, called Tilted Angle Connectors was investigated by Shariati et al. (2021). Armaghani and Asteris (2021) studied the application of AI techniques for the prediction of the compressive strength of cement-based mortar materials with or without Metakaolin (Armaghani and Asteris, 2021). Keshavarz and Torkian (2018) also studied the application of ANN and ANFIS models in the prediction of the compressive strength of concrete. The results showed that ANN and ANFIS methods are successful models for predicting compressive strength of concrete. The results also showed that ANFIS has higher accuracy in predicting the compressive strength of concrete than that of ANN (Keshavarz and Torkian, 2018). Dao et al.

(2019) used ANN and ANFIS models to predict the compressive strength of Geopolymer concrete. The results of the study showed that ANN and ANFIS models have great potential for predicting the compressive strength of Geopolymer concrete (Dao et al., 2019). Naderpour and Mirrashid (2020) studied and predicted shear strength of RC beams using ANFIS. The results showed that the neural fuzzy network system, especially the ANFIS method, is highly capable of predicting shear strength of RC beams (Naderpour and Mirrashid, 2020). Some studies were used AI methods with meta-algorithms for the prediction of shear strength of RC beams. Khatibinia and Mohammadizadeh (2017) presented ANFIS with GA and PSO for determining the bonding of FRP polymer fibers and masonry elements. The results showed that the use of ANFIS model with PSO and GA can be significantly improving prediction accuracy (Khatibinia and Mohammadizadeh, 2017). Also, the study of Pham et al. (2018) can be mentioned as one of the most comprehensive researches for the use of AI methods and machine learning in the field of civil engineering. In this research, the shear capacity of soft soil was predicted using machine learning algorithms such as PSO-ANFIS (PANFIS), GA-ANFIS (GANFIS), Support Vector Regression (SVR) and ANN. The results of this study showed that the PANFIS has the highest predictability (Pham et al., 2018).

According to past studies, the importance of shear strength of RC deep beams in the design of structures is necessary. Therefore, the purpose of this study is to predict the shear strength of reinforced concrete beams using ANFIS with meta-heuristic algorithms. The prediction methods are proposed based on a hybrid of ANFIS with GA, PSO, Ant Colony Optimization (ACO) method and Differential Evolution (DE) algorithm. Furthermore, for comparing the prediction accuracy of the shear strength of RC deep beams based on ANFIS with the metaheuristic algorithms, the results obtained from these models were compared with shear strength calculated from ACI and CSA regulations as well as those of ANNs (ACI, 2011; CSA, 1994).

2. Shear Strength of RC Deep Beams

Numerous methods have been used to design of RC deep beams. The American Concrete Institute Standard code-318 (ACI, 2011) is based on a model called the truss model, in which the concrete contribution is presented based on experimental results. Based on ACI, the shear strength of RC deep beams is calculated as:

$$V_c = v_c b_w d = \left(3.5 - 2.5\frac{M_u}{V_u d}\right) \times \left(1.9\sqrt{f_c^{'}} + 2.5\rho_w \frac{V_u d}{M_u}\right) b_w d \quad (1)$$

where $f_c^{'}$: is the 28-day compressive strength of the 30 × 15 cylindrical concrete sample, and ρ_w: is the ratio of the longitudinal bars which is defined as follows:

$$\rho_w = A_S / b_w d \quad (2)$$

where V_u and M_u: are shear force and bending moment at the critical point, respectively. b_w and d: are width and effective depth of the beam, respectively. For beams reinforced in transverse direction, the nominal shear strength of the deep beam V_n shall include the shear strength obtained from V_c concrete share and the shear strength obtained from V_s bars share:

$$V_n = V_c + V_s \quad (3)$$

where V_s: is expressed as follows:

$$V_s = [\frac{A_v}{12s}(1 + \frac{L_n}{d}) + \frac{A_{vh}}{12s_2}(11 - \frac{L_n}{d})]f_y d \quad (4)$$

where A_v: is the area of shear bars, f_y: is the yield stress of the stirrups, s: is the distance of center to center of the stirrups, and ρ_v: is the ratio of the shear bars. In CSA (Canadian, 1994), the total shear strength of RC deep beam consists of two shear strengths obtained from the share strength of concrete and the shear strengths of bars. In CSA, the concrete shear share V_c, depends on the amount of transverse reinforcement and d of beam and defined as:

$$V_c = \frac{V_c}{b_w d} = 0.2\sqrt{f_c'}\text{for}A_v \geq \frac{0.006\sqrt{f_c'}\,b_w s}{f_{yv}}\text{or}d \leq 300\text{mm}$$
$$V_c = \frac{V_c}{b_w d} = \frac{260}{1000+d}\sqrt{f_c'}\text{for}A_v < \frac{0.006\sqrt{f_c'}\,b_w s}{f_{yv}}\text{or}d > 300\text{mm} \quad (5)$$

The shear strength of bars is similar to the equation provided for V_s in the ACI Regulations. Some researchers used the design method based on the Strut-and-Tiefor for RC deep beams. In the Strut-and-Tie method, it was assumed that compressive forces was are tolerated by concrete struts, while tensile forces were tolerated by steel bars (Pal and Deswal, 2011).

3. Experimental Database

In the present study, 106 laboratory data were used to predict the shear strength of RC deep beams using ANFIS method with meta-heuristic algorithms. Data sets of RC deep beams include 19 data obtained from experiments on high strength RC beams impelimented by Tan et al. (1995), 52 data obtained from the results of study-related tests by Smith and Vantsiotis (1982), 35 laboratory data obtained from the study of Kong et al. (1970). Hence, all the experimental database and the brief details database are presented in Tables 1 and 2, respectively.

Table 1. Experimental database of RC deep beam

$V\ (kN)$	ρ_v	ρ_h	$f_c'(MPa)$	$\frac{d}{b_w}$	$\frac{L}{d}$	$\frac{a}{d}$
675	0.0048	0	58.80	4.2091	2.15	0.27
630	0.0048	0	51.60	4.2091	3.23	0.27
640	0.0048	0	53.90	4.2091	4.3	0.27
630	0.0048	0	57.30	4.2091	5.38	0.27
468	0.0048	0	56.00	4.2091	2.15	0.54
445	0.0048	0	47.00	4.2091	3.23	0.54
500	0.0048	0	53.90	4.2091	4.3	0.54
480	0.0048	0	53.00	4.2091	5.38	0.54
403	0.0048	0	51.02	4.2091	2.15	0.81
400	0.0048	0	44.00	4.2091	3.23	0.81
270	0.0048	0	48.20	4.2091	2.15	1.08
280	0.0048	0	44.10	4.2091	3.23	1.08
290	0.0048	0	46.80	4.2091	4.3	1.08
290	0.0048	0	48.00	4.2091	5.38	1.08
220	0.0048	0	50.80	4.2091	3.23	1.62
190	0.0048	0	44.50	4.2091	4.3	1.62
173	0.0048	0	45.30	4.2091	5.38	1.62
150	0.0048	0	41.10	4.2091	4.3	2.16
107	0.0048	0	42.08	4.2091	5.38	2.16
140	0	0	20.50	2.9902	2.67	1
136	0	0	20.90	2.9902	2.67	1
161	0.0028	0.0023	18.70	2.9902	2.67	1
149	0.0028	0.004	18.00	2.9902	2.67	1
141	0.0028	0.0068	16.10	2.9902	2.67	1

171	0.0028	0.0068	20.60	2.9902	2.67	1
184	0.0028	0.0091	21.10	2.9902	2.67	1
175	0.0063	0.0023	21.70	2.9902	2.67	1
171	0.0063	0.0045	19.80	2.9902	2.67	1
172	0.0063	0.0068	20.30	2.9902	2.67	1
162	0.0063	0.0091	19.10	2.9902	2.67	1
161	0.0125	0.0023	18.10	2.9902	2.67	1
173	0.0125	0.0045	19.20	2.9902	2.67	1
179	0.0125	0.0068	20.80	2.9902	2.67	1
168	0.0125	0.0091	19.90	2.9902	2.67	1
149	0	0	21.70	2.9902	3.08	1.21
148	0.0024	0.0023	22.10	2.9902	3.08	1.21
144	0.0024	0.0045	20.10	2.9902	3.08	1.21
141	0.0024	0.0068	20.80	2.9902	3.08	1.21
154	0.0024	0.0091	19.50	2.9902	3.08	1.21
129	0.0042	0.0023	19.20	2.9902	3.08	1.21
131	0.0042	0.0045	19.00	2.9902	3.08	1.21
126	0.0042	0.0068	17.50	2.9902	3.08	1.21
145	0.0042	0.0091	19.80	2.9902	3.08	1.21
131	0.0063	0.0023	16.20	2.9902	3.08	1.21
159	0.0077	0.0023	20.40	2.9902	3.08	1.21
159	0.0077	0.0045	19.00	2.9902	3.08	1.21
155	0.0077	0.068	19.20	2.9902	3.08	1.21
160	0.0077	0.0091	20.70	2.9902	3.08	1.21
154	0.0125	0.0023	17.10	2.9902	3.08	1.21
116	0	0	20.70	2.9902	3.67	1.5
119	0.0018	0.0023	19.20	2.9902	3.67	1.5
124	0.0018	0.045	21.90	2.9902	3.67	1.5
131	0.0018	0.0068	22.70	2.9902	3.67	1.5
123	0.0018	0.0091	21.80	2.9902	3.67	1.5
124	0.0031	0.0023	19.90	2.9902	3.67	1.5
104	0.0031	0.0045	19.20	2.9902	3.67	1.5
116	0.0031	0.0045	19.30	2.9902	3.67	1.5
125	0.0031	0.0068	20.40	2.9902	3.67	1.5
124	0.0031	0.0091	20.80	2.9902	3.67	1.5
141	0.0056	0.0023	21.00	2.9902	3.67	1.5
125	0.0056	0.0045	16.60	2.9902	3.67	1.5
128	0.0056	0.0068	18.30	2.9902	3.67	1.5
137	0.0056	0.0091	19.00	2.9902	3.67	1.5
147	0.0077	0.0023	19.60	2.9902	3.67	1.5
129	0.0063	0.0045	18.60	2.9902	3.67	1.5
153	0.0077	0.0045	19.20	2.9902	3.67	1.5
153	0.0077	0.0068	18.50	2.9902	3.67	1.5
160	0.0077	0.0091	21.20	2.9902	3.67	1.5
74	0	0	19.50	2.9902	4.83	2.08
88	0.0042	0.0023	16.10	2.9902	4.83	2.08
239	0.00245	0	21.50	9.5263	1.05	0.35
224	0.00245	0	24.60	7.8553	1.28	0.43
190	0.00245	0	21.20	6.1842	1.62	0.54
168	0.00245	0	21.20	4.5132	2.22	0.74
90	0.00245	0	21.70	2.8421	3.53	1.18
249	0.0086	0	19.20	9.5263	1.05	0.35
224	0.0086	0	18.60	7.8553	1.28	0.43
216	0.0086	0	19.90	6.1842	1.62	0.54
140	0.0086	0	22.80	4.5132	2.22	0.74
100	0.0086	0	20.10	2.8421	3.53	1.18
276	0	0.0245	22.60	9.5263	1.05	0.35
208	0	0.0245	19.20	6.1842	1.62	0.54
159	0	0.0245	21.90	4.5132	2.22	0.74
87	0	0.0245	22.60	2.8421	3.53	1.18

242	0	0.0086	22.00	9.5263	1.05	0.35
201	0	0.0086	21.00	7.8553	1.28	0.43
181	0	0.0086	20.10	6.1842	1.62	0.54
110	0	0.0086	22.00	4.5132	2.22	0.74
96	0	0.0086	22.60	2.8421	3.53	1.18
240	0.0061	0.0061	18.60	9.5263	1.05	0.35
208	0.0061	0.0061	19.20	7.8553	1.28	0.43
173	0.0061	0.0061	20.10	6.1842	1.62	0.54
127	0.0061	0.0061	21.90	4.5132	2.22	0.74
78	0.0061	0.0061	22.60	2.8421	3.53	1.18
308	0	0.005	26.10	9.5263	1.05	0.35
266	0	0.0061	25.10	7.8553	1.28	0.43
25	0	0.0077	26.10	6.1842	1.62	0.54
173	0	0.0102	26.10	4.5132	2.22	0.74
99	0	0.0153	25.10	2.8421	3.53	1.18
253	0	0	25.10	10.0263	1.05	0.5
300	0	0.0017	26.10	10.0263	1.05	0.35
260	0	0.0034	26.10	10.0263	1.05	0.35
264	0	0.0068	21.30	10.0263	1.05	0.35
297	0	0.0085	21.30	10.0263	1.05	0.35

Table 2. Brief of the experimental database of RC deep beams studied in the present study

Parameter	Minimum	Medium	Maximum	S.D
Width of the beam (*b*), (mm)	76	94.84	110	13.547
Effective depth (*d*), (mm)	216	401.57	762	108.465
The span-to-depth ratio (*a*/*d*)	0.27	1.006	2.16	0.468
Compressive stress of concrete (f_c'), (MPa)	16.20	25.80	58.80	15.93
Longitudinal reinforcement ratio (ρ_h)	0.00	0.0058	0.068	0.91
Shear Rebar Ratio (ρ_v)	0.00	0.004	0.0125	0.32
Ultimate shear strength (*V*), (kN)	25	201.48	675	2.15

Thus, the shear strength was considered as the output data. The 28-day compressive strength of 15 × 30 US cylinder specimen, cross-section width, effective depth, beam length, shear span-to-depth beam ratio, as well as the percentage of longitudinal and transverse reinforcement were adopted as the input data. The geometric dimensions and how the beam is loaded are shown in Figure 1.

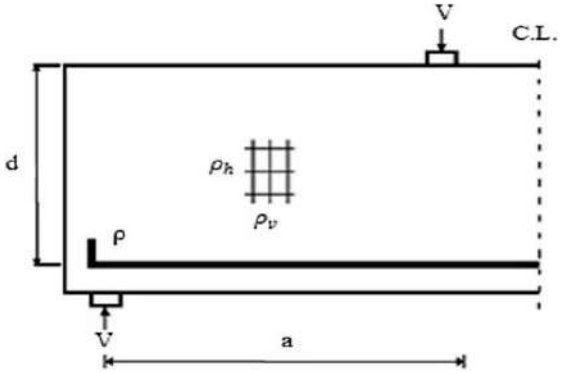

Fig. 1. Geometric dimensions of a reinforced concrete deep beam

4. Concept of ANFIS Model

A Fuzzy Inference System (FIS) was proposed as a nonlinear mapping approach from the input space to the output space (Jang, 1993; Jang et al., 1996). ANFIS uses a Sugeno type fuzzy system in a 5-layer network for two *x* and *y* inputs and one *f* output. ANFIS can optimize the performance of the fuzzy model by adjusting a parameter in the membership performance. This model combines the learning capabilities of a neural network with fuzzy logic inference to enhance predictability. This system has been so far used in a wide range of engineering fields and has shown considerable accuracy in estimating and predicting various engineering phenomena.

For simplicity a typical ANFIS shown in Figure 2 consists of two fuzzy if–then rules based on Takagi and Sugeno's type (Jang et al., 1996):

$$\begin{aligned} &Rule1{:}\ \text{If}\ x\ \text{is}\ A_1\ \text{and}\ y\ \text{is}\ B_1, \text{then}\ f_1 \\ &\qquad = p_1x + q_1y + r_1 \\ &Rule2{:}\ \text{If}\ x\ is\ A_2\ \text{and}\ y\ is\ B_2, \text{then}\ f_2 \\ &\qquad = p_2x + q_2y + r_2 \end{aligned} \quad (5)$$

where A_1, A_2, B_1, and B_2: stand for the labels of the representation of Membership Functions (MFs) for x and y inputs. Moreover, p_i, q_i, and r_i (i = 1, 2): refer to the variables of the output MFs (consequent variables).

As seen in Figure 2, an overall structure of ANFIS has 2 constant square nodes and adaptive circle nodes whose variables would be altered over the training procedure. A hybrid learning algorithm of ANFIS would be applied via the MFs parameters of input variables and linear parameters of the output variables. Gradient Descent (GD) strategies would be used to optimize the above parameters. The resulting output of the defined network with 1 output and 2 inputs with regard to these parameters may be computed in this way:

$$f = \sum_i \bar{w}_i f_i = \frac{\sum_{i=1}^{2} w_i f_i}{\sum_{i=1}^{2} w_i}, \text{for} i = 1,2 \quad (7)$$

$$w_i = \mu A_i(x) \times \mu B_i(x) \text{for} i = 1,2 \quad (8)$$

where w_i: represents the firing strength of the rule i. $\mu A_i(x)$ and $\mu B_i(x)$: refer to the membership degrees of x and y in A_i and B_i.

In ANFIS, membership function can be expressed by a number of the shape functions consisting of trapezoidal, triangular, generalized bell shaped and Gaussian functions. Sihag et al. (2017) shown that Gaussian membership function-based ANFIS had better performance than the other membership function. Hence, Gaussian membership function is used in this study. Gaussian functions are defined as:

$$\mu A_i(x) = \frac{1}{1 + (\frac{x - c_i}{a_i})^2} \quad (9)$$

$$\mu B_i(y) = \frac{1}{1 + (\frac{y - d_i}{e_i})^2} \quad (10)$$

where $\{a_i, c_i\}$ and $\{d_i, e_i\}$: represent the premise variable set applied for adjusting the MF shape.

5. Meta-Heuristic Algorithms

5.1. Particle Swarm Optimization

Particle Swarm Optimization (PSO) algorithm has been designed on the basis of the inspiration provided by the social behaviors of animals, including insects swarming, fish schooling, and birds flocking (Kennedy et al., 2001). Kennedy and Eberhart (2001) proposed PSO technique for simulating the elegant motions of the bird swarms as a part of a social and cognitive research. The technique contains some particles which are randomly selected in the search spaces of optimization problem. All particles of the swarm represent one of the probable solutions for the problem of optimization. The i^{th} particle in the t^{th} iteration has a relationship to a velocity vector (V_i^t) and a position vector (X_i^t):

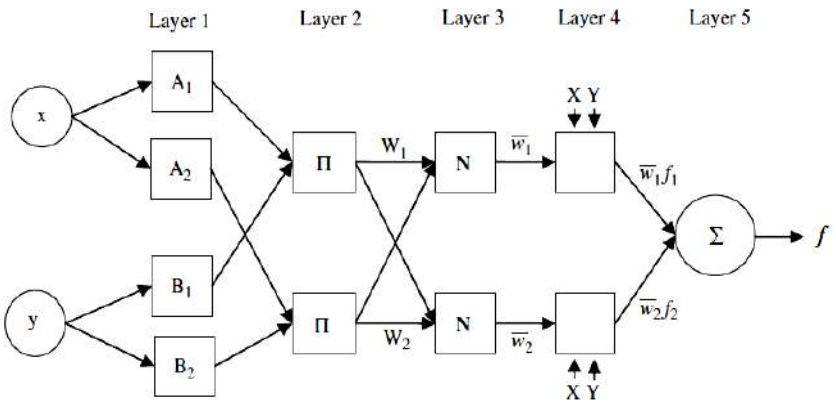

Fig. 2. The architecture of the ANFIS model

$$X_i^t = \{x_{i1}^t, x_{i2}^t, \ldots, x_{iD}^t\}$$
$$V_i^t = \{v_{i1}^t, v_{i2}^t, \ldots, v_{iD}^t\} \quad (11)$$

where *D*: refers to the volume of the solution space. As stated by researchers, the particles flying across the solution space, and its position would be updated with regard to the respective speed, global best position (***gbest***), and the best position particle (***pbest***) where swarms have met since the first iteration as:

$$V_i^{t+1} = \omega^t V_i^t + c_1 r_1(\text{pbest}_i^t - X_i^t) + c_2 r_2(\text{gbest}^t - X_i^t) \quad (12)$$

$$X_i^{t+1} = X_i^t + V_i^{t+1} \quad (13)$$

where r_1 and r_2: represent the uniform random sequences produced from intervals [0, 1]. C_1 and C_2: refer to the socio-cognitive scaling variables. ω: is the inertia weight that controls the influence of the previous velocity. Some researchers suggested that socio-cognitive scaling variables of c_1 and c_2 must be chosen as $c_1 = c_2 = 2$ for allowing the product c_1r_1 or c_2r_2 to be possessed a mean of 1. PSO is sensitivity to ω variable that possibly declines with the numbers of the iterations as follows (Shi et al., 2011):

$$\omega = \omega_{\max} - \frac{\omega_{\max} - \omega_{\min}}{t_{\max}}\, t \quad (14)$$

where ω_{max} and ω_{min}: represent the highest and least values of ω. t_{max}: refers to the limit numbers of optimization iteration. Table 3 represents the values of controlling parameters of PSO which is used in this study. The values of the parameters are selected based on a trial and error process.

Table 3. The value of controlling parameters for PSO algorithm

Parameter	Value
Number of population	40
Maximum number of iterations	1000
Ideal weight	1
Ideal slope to weight ratio	0.99
Private learning coefficient	1
Public learning coefficient	2

5.2. ACO for Continuous Domains (ACO_R)

First, Ant Colony Optimization (ACO) was proposed for solving the discrete problems of optimization (Socha and Dorigo, 2008). This algorithm has been proposed based on the inspiration via investigating the behaviours of the real ants for their food source. For finding an optimal solution for problem with continuous domains, ACO for continuous domains (ACO_R) is implemented based on the basis of two stages (Socha and Dorigo, 2008). At the first stage, a number of *k* artificial ants make solutions for problem via taking samples of a Probability Density Function (PDF) that is extracted from the pheromone data. At the second stage, the solutions would be applied for modifying the pheromone so that the construction probability of high-quality solutions would be enhanced. In the ACO_R procedure, the number of the solutions memorized in the archive *P* are adjusted at *M*; that is, $X^j = \{x_1^j, x_2^j, \ldots, x_d^j\}^T, j = 1, \ldots, M$. The solutions are consistently sorted with regard to their value of the objective function; that is:

$$f(X^1) \leq f(X^2) \leq \ldots \leq f(X^M) \quad (15)$$

For each variable $x_i (i = 1, \ldots, d)$, *T*: is used to derive the Gaussian kernel PDF as:

$$G_i(x) = \sum_{j=1}^{M} \zeta_j \frac{1}{\sigma_i^j \sqrt{2\pi}} exp(- \frac{(x - \mu_i^j)^2}{2\sigma_i^{j2}}), -\infty < x < +\infty \quad (16)$$

Furthermore, this kernel is used for guiding the ants in the respective search procedure. The weight ζ_j: is computed based on:

$$\zeta_j \propto \frac{1}{\gamma M \sqrt{2\pi}} exp(- \frac{(j-1)^2}{2\gamma^2 M^2}), j = 1, \ldots, M \quad (17)$$

where γ: is a parameter of the algorithm.

The small value of γ strongly causes the best solutions, and for its large value the probability becomes more uniform. The value of the *i*th variable in the *j*th solution is chosen as the mean, i.e. $\mu_i^j = x_i^j$. The standard deviation is obtained using the average distance of the other solutions from the *j*th solution which is multiplied by a parameter ρ:

$$\sigma_i^j = \frac{\rho}{M-1}\sum_{m=1}^{M}\left|x_i^m - x_i^j\right| \quad (18)$$

The lower the value of ρ the higher the convergence speed of the algorithm.

At each iteration of ACO_R, each artificial ant performs *d* steps from *i* = 1 to *d*. By sampling the PDF $G_i(x)$, the *k*th ant at step *i* is used for providing a partial solution of the optimization problem. By reaching the steps to the value *d*, a new solution, $X^k = \{x_1^k, x_2^k, .\rightleftarrows., x_d^k\}$, is constructed. All *k* solutions are added to the archive *T*, and the same number of the worst solutions is removed from it. Table 4 represents the values of the parameters of the ACO_R algorithm. The values of the parameters were selected based on a trial and error process.

Table 4. The value of the parameters of the ACO_R algorithm

Parameter	Value
Number of population	20
Maximum number of iterations	200
Resonance coefficient	0.5
Deviation distance ratio	1

5.3. Real-Coded Ga with SBX Crossover

According to Gen and Cheng (2000), Genetic Algorithms (GAs) commonly contain 5 elements (Gen and Cheng, 2000):

- A genetic expression of the problem solutions;
- An operator to establish an early population of the solutions;
- A mechanism to evaluate the function rating solution with regard to its fitness;
- A mechanism to select parent and genetic operators altering the genetic compositions of the children over the reproduction process;
- The variables affecting GAs.

Real-coded GA (RCGA) was proposed as one of the acceptable methods for optimization problems with continuous variables. Real number encoding has more acceptable performance compared to the binary or gray encoding for such problems. Conventionally, the tournament selection in RCGA is used as a selection operator. Moreover, polynomial mutation and Simulated Binary Crossover (SBX) are chosen as other operators of RCGA.

In the SBX crossover operator, two children solutions is established from two parents (Subbaraj et al., 2011). Therefore, a random number, $u_i \in [0.1]$, is initially selected, and β_{qi}: is computed as follows:

$$\beta_{qi} = \begin{cases} (2u_i)^{\frac{1}{\eta_c+1}} u_i \le 0.5 \\ \left(\frac{1}{2(1-u_i)}\right)^{\frac{1}{\eta_c+1}} otherwise \end{cases} \quad (19)$$

where η_c: is the crossover index. Moreover, a spread factor β_{qi}: is described as the absolute difference ratio in the offspring values to that of the parents. Afterwards, two children solutions are achieved as:

$$\begin{aligned} X_i^{(1,t+1)} &= 0.5\left[(1+\beta_{qi})X_i^{(1+t)} + (1-\beta_{qi})X_i^{(2+t)}\right] \\ X_i^{(2,t+1)} &= 0.5\left[(1-\beta_{qi})X_i^{(1+t)} + (1+\beta_{qi})X_i^{(2+t)}\right] \end{aligned} \quad (20)$$

In the next stage of RCGA, new produced offspring experiences polynomial mutation operation. Moreover, instead of a normal distribution, the distribution of probability may be a polynomial function. This new offspring $Y_i^{(1,t+1)}$ would be estimated as follow (Deb, 2011):

$$Y_i^{(1,t+1)} = X_i^{(1,t+1)} + \left(X_i^U - X_i^L\right)\delta_i \quad (21)$$

where X_i^U and X_i^L: represent the upper and

lower limit values. The parameter δ_i: is achieved from the polynomial probability distribution.

$$P(\delta) = 0.5(\eta_m + 1)(1 - |\delta|)^{\eta_m} \quad (22)$$

Table 5 represents the values of the parameters of RCGA. The value of the parameters was selected based on a trial and error process.

Table 5. Parameters related to GA algorithm

Parameter	Value
Number of population	100
Maximum number of iterations	500
Mutation percentage	0.5
Period percentage	0.7
Mutation rate	0.1
Selection pressure	8
Gamma	0.2

5.4. Differential Evolution Algorithm

Differential Evolution (DE) algorithm has been proposed by Storn and Price (1997). DE is considered as one of the stochastic optimization algorithms, which applies vector difference for perturbing the vector populations (Storn and Price, 1997). At initial stages, DE begins with a population containing N n-dimensional vectors as:

$$X_i(t) = \{x_i^1, x_i^2, \dots, x_i^n\}, i = 1,2,\dots,N \quad (23)$$

In this method, the vectors is randomly chosen on the intervals a $[X^{Li}, X^{Ui}], i = 1,2,\dots,n$. Furthermore, e vectors are updated via mutation, crossover, and selection operations during the DE procedure.

Mutation operation: Based on the operation, three vectors $\boldsymbol{X}_{r1}(t)$, $\boldsymbol{X}_{r2}(t)$, and $\boldsymbol{X}_{r3}(t)$ are randomly selected for each certain $\boldsymbol{X}_i(t)$ vector at iteration t. However, $r1$, $r2$ and $r3$ indicators should be different. Consequently, the weighted differences of two vectors are added to the 3rd vector for forming a mutant vector $\bar{V}_i(t) = \{\bar{v}_i^1, \bar{v}_i^2, \dots, \bar{v}_i^n\}$:

$$\bar{V}_i(t) = X_{r1}(t) + F(X_{r2}(t) - X_{r3}(t)) \quad (24)$$

Crossover operation: In this stage, the trial vector $\boldsymbol{U_i(t)}$ is designed through the components of the target vector, $\boldsymbol{X_i(t)}$ and components of the mutant vector $\bar{V}_i(t)$ through a binomial crossover operation:

$$u_i^j(t) = \begin{cases} \bar{v}_i^j(t) \; if \; rand_j \le C_r or j = j_{rand} \\ x_i^j(t) otherwise \end{cases} \quad (25)$$

where j_{rand}: represents a random integer in a range between 1 and n. $rand_j$: refer to the i^{th} assessment of an equal random number generator and $C_r \in (0,1)$. The $j = j_{rand}$ condition makes sure that the trial vector $\boldsymbol{U}_i(t)$ gets not less than 1 component from its mutant vector $\bar{V}_i(t)$.

Selection operation: By the comparison of the trial vector $\boldsymbol{U}_i(t)$ with the target vector $\boldsymbol{X}_i(t)$, the solution with the lowest objective function value is survived into the next generation:

$$X_i(t+1) = \begin{cases} U_i(t) \; if \quad fit(U_i(t)) \le fit(X_i(t)) \\ X_i(t) otherwise \end{cases} \quad (26)$$

It is noted that the DE method is implemented and continued using the mutation, crossover and selection operations until some criterion of the method stop is reached. In addition, the control parameters of the DE method contain the population size, N, the scaling factor, F, and the crossover constant, C_r. Table 6 represents the values of the parameters of the DE algorithm. The values of the parameters were selected based on a trial and error process.

Table 6. The value of the parameters of the DE algorithm

Parameter	Value
Number of population	20
Maximum number of iterations	200
Lowest scale coefficient	0.2
Highest scale coefficient	0.8
Crossover rate	0.1

6. The Proposed Intelligent ANFIS Technique

As presented in previous section, the ANFIS technique uses the advantages of both fuzzy systems and neural networks. Nonetheless, training the ANFIS model are considered as one of the major challenges for the real problems. Moreover, the GD strategies are used as the training techniques of ANFIS, which are known as local search strategies, and their functions commonly are contingent on the variables initial values. As it is possible to consider the optimum design of fuzzy systems (FSs) in the framework of an optimization problem, numerous authors suggested meta-heuristic strategies, including Genetic Algorithms (Jang, 1993; Savrun and İnci, 2021; Zhang, 2020) and PSO (Khoshbin et al., 2016; Lin et al., 2017) for designing optimum FSs. It is widely accepted that the accuracy and function of the ANFIS model is dependent on the premise variables and consequent variables that should be taught. For improving and increasing the ANFIS model accuracy in the present study, the PSO, ACO_R, RCGA and DE methods were used for finding the premise variables $\{a_i, b_i, c_i\}$. These parameters are adopted as the design variables of the optimization problem. In addition, the root mean squared error (*RMSE*) obtained based on actual output and desired outputs is considered as the objective function, which can be defined as follows.

$$RMSE = \sqrt{\frac{\sum_{i=1}^{n}(y_i - p_i)^2}{n}} \quad (27)$$

where y and p: stand for the measurement values and the predicted values. n: refers to the total numbers of the test data. Indeed, the errors variation in the suggested model may be calculated by *RMSE*, which would be too helpful in the case of undesirability of great errors.

In a conventional fuzzy inference system, the number of fuzzy rules is assigned by the user's experience. In ANFIS simulation, the number of MFs assigned to each input variable of problem is also selected by trial and error procedure. Therefore the Subtractive Algorithm (SA) (Chiu, 1997) is used for finding the optimum number of the fuzzy rules. The fuzzy inference system for the antecedents and consequents is also constructed by the fuzzy c-means (FCM) approach (Bezdek, 1981). The flowchart of the proposed ANFIS incorporating meta-heuristic algorithms is depicted in Figure 3.

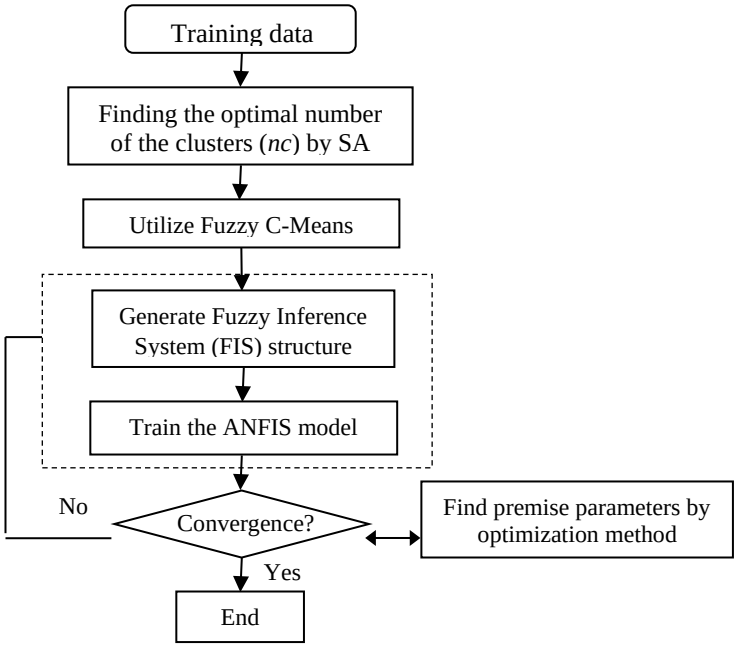

Fig. 3. Flowchart of the proposed ANFIS method with optimization methods

7. Numerical Results

In this study, a database containing 106 samples of RC deep beams were used to develop ANFIS with meta-heuristic algorithms (i.e. PSO, GA, ACO and DE) for the prediction of the shear strength of RC deep beams. For producing the prediction model, it is required that database is randomly divided into two sets of training and testing data. Simple procedures were proposed for splitting the data into training and testing data. These methods do not express the performance of the model well. Because each of them is highly dependent on data which is selected for training and testing data. This dependence sometimes results in higher model accuracy, and the other times in lower accuracy. To solve this problem and obtain the high accuracy of the proposed model, k-fold validation method was used. In this validation method, the number of partitions is usually proportional to the number of data points. By selecting *k* data points, it must be ensured that the number of data points in the training subset and the validation subset can contain proportional variation and show the same distribution. In this study, 90% of the data is used as the proportion of the training subsets and 10% for the validation subsets, which can be obtained by performing the ten-digit validation method to ensure that all subsets have the same distribution.

Using the cross-validation approach, the training data were randomly grouped into ten unique cross-subsets. In each iteration, one subset was used for the validation process and not another subset for the training process. Thus, each set of data is used at least once in both the training and validation phases. In the present study, the ten-fold cross-validation method (k = 10) was used, each set was trained ten times in the optimization process of parameters. Therefore, ten different values of the mean validation error for the objective function were obtained. Thus, the average of the results obtained from these ten subsets represents a useful method for predicting the overall performance of the ANFIS, ANFIS-GA, ANFIS-PSO, ANFIS-ACO and ANFIS-DE models.

It is noted that the values of the parameters presented in Tables 3 to 6 were selected based on a trial and error process. In fact, first, the different combinations of the values of the parameters were considered. Then, the optimization method was implemented for each combination. Thus, the combination with the minimum objective function is considered as the best combination of the values of the parameters.

7.1. Scaling and Dividing Database

For assessing the effectiveness and accuracy of the proposed ANFIS incorporating meta-heuristic algorithms, the values of the input variables were scaled. For this purpose, the values of the input variables were normalized between 0.2 and 0.8 and before dividing database as follows.

$$\bar{x}_i = b_1 \frac{x_i - x_{min}}{xmin_{max} + b_2} \tag{28}$$

where $\bar{x}_i$, x_{max} and x_{min}: are the normalized, maximum and minimum values of the input variables, respectively. In this study, b_1 and b_2: were assumed to be equal to 0.6 and 0.2 based on the study of Khatibinia and Mohammadizadeh (2017), respectively. Then, the database was randomly divided into training and testing sets including 75 and 32 samples, respectively.

7.2. Results of the Proposed ANFIS Model

To explore and evaluate the accuracy of the proposed ANFIS with meta-heuristic in estimating the shear strength of RC beams, different statistical criterions were utilized. The second Root Mean Square Error (*RMSE*) (Eq. (27)), coefficient of determination (R^2) and Absolute Mean Error (*MAE*) were considered as the statistical criteria. These *MAE* and R^2 are defined as (Kaveh et al., 2017):

$$MAE = \frac{\sum_{i=1}^{n}[p_i - y_i]}{n} \quad (29)$$

$$R^2 = \frac{(\sum_{i=1}^{n}(y_i - y_{ave})\,(p_i - p_{ave}))^2}{\sum_{i=1}^{n}(y_i - y_{ave})^2 \sum_{i=1}^{n}(p_i - p_{ave})^2} \quad (30)$$

where p_i: is the predicted value and y_i: is the real value for n samples. y_{ave} and p_{ave}: are the mean of the measurement and predicted values in the data samples.

According to the statistical criteria, the statistical results ANFIS, ANFIS-GA, ANFIS-PSO, ANFIS-ACO and ANFIS-DE were presented in Table 7 for testing phase and were compared with those of ACI, CSA, ANN and GEP models.

As can be seen from Table 7, the proposed ANFIS model with meta-heuristic methods predicts the shear strength parameter with much higher accuracy than other developed models. The predicted shear strength values obtained from ANFIS, ANFIS-GA, ANFIS-PSO, ANFIS-ACO and ANFIS-DE models are presented in Figures 4a to 4e, in terms of the shear strength obtained from the experimental results.

Table 7. Comparison of the statistical results using different models for testing phase

Model	Reference	*RMSE* (KN)	R^2	*MAE* (KN)
ACI	(Gandomi et al., 2013)	140.62	0.870	113.54
CSA	(Gandomi et al., 2013)	114.70	0.820	91.34
ANN	(Gandomi et al., 2013)	42.27	0.950	30.28
GEP	(Gandomi et al., 2013)	51.57	0.930	40.99
ANFIS	Present study	38.252	0.849	40.284
ANFIS-GA	Present study	31.357	0.944	23.931
ANFISA-ACO	Present study	37.095	0.925	26.429
ANFIS-PSO	Present study	36.058	0.885	20.540
ANFIS-DE	Present study	25.968	0.914	24.487

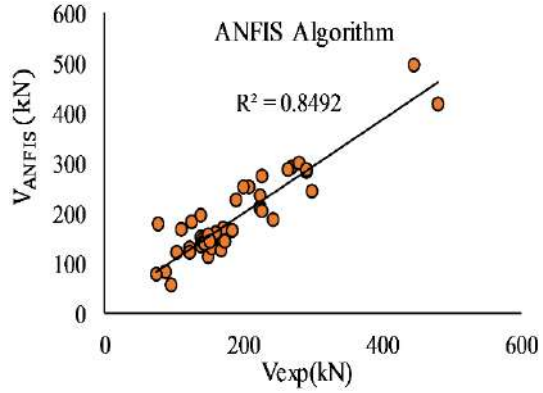

(a) ANFIS (*RMSE* = 40.35 kN)

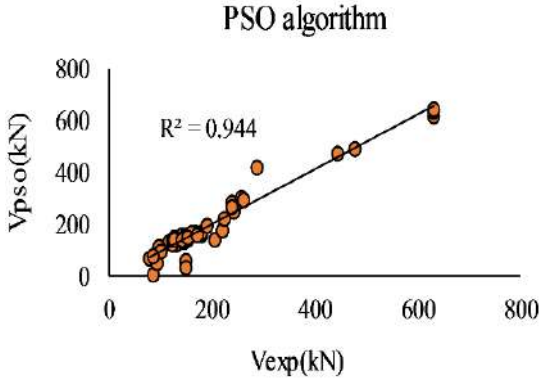

(b) ANFIS-PSO (*RMSE* = 36.06kN)

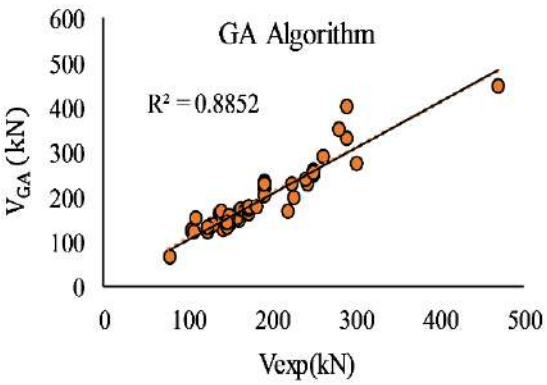

(c) ANFIS-GA (*RMSE* = 31.35 kN)

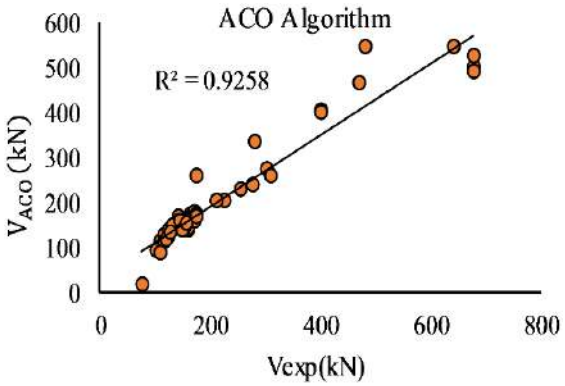

(d) ANFIS-ACO algorithm (*RMSE* = 37.095 kN)

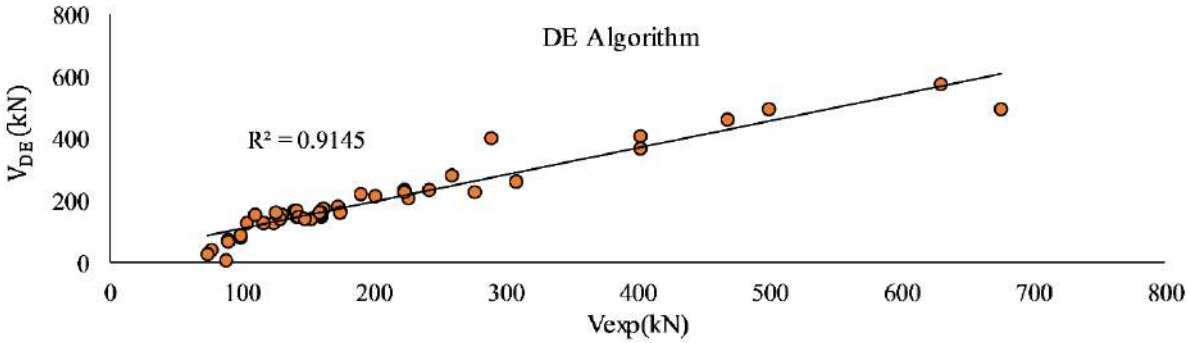

(e) ANFIS-DE (*RMSE* = 25.96 kN)

Fig. 4. Experimental shear strength results in terms of predicted shear strength

The results show that the shear strength predicted by the proposed ANFIS with meta-heuristic algorithms is in good agreement with the shear strength obtained from the experimental results. In order to clarify an overall comparison, the statistical criteria used in testing phase were combined to create a normalized Reference Index (*RI*) as follows (Chou et al., 2011):

$$RI = \frac{\overline{RMSE} + \overline{MAE}}{2} \quad (31)$$

where $\overline{RMSE}$ and $\overline{MAE}$: are the normalized *RMSE* and *MAE*, respectively.

Table 8 shows the results based on *RI* for the proposed method, the original ANFIS, ANN, GEP, ACI and CSA techniques for comparison purposes. Based on the value *RI* obtained in the testing process, the proposed method outperforms the other techniques. It can also be observed from Table 8 that the ANFIS-DE model can be considered as an efficient technique with high accuracy in comparison with the other techniques.

7.3. Influence of Parameters on the Ratio of Predicted to Experimental Shear Strength

7.3.1. Beam Span Length to Effective Depth (*L/d*)

The changes of the ratio of the experimental shear strength to the predicted shear strength (V_{exp}/V_{pre}) using ANFIS, ANFIS-GA, ANFIS-PSO, ANFIS-ACO and ANFIS-DE models in terms of different ratios of L/d are shown in Figures 5a to 5e, respectively.

Table 8. Performance measurement results of various prediction techniques

Model	Reference	$\overline{RMSE}$	$\overline{MAE}$	*RI*
ACI	(Gandomi et al., 2013)	0.00	0.00	0.00
CSA	(Gandomi et al., 2013)	0.24	0.23	0.15
ANN	(Gandomi et al., 2013)	0.90	0.86	0.58
GEP	(Gandomi et al., 2013)	0.78	0.78	0.52
ANFIS	Present study	0.79	0.89	0.56
ANFIS-GA	Present study	0.96	0.95	0.64
ANFISA-ACO	Present study	0.94	0.90	0.61
ANFIS-PSO	Present study	1.00	0.91	0.64
ANFIS-DE	Present study	0.96	1.00	0.65

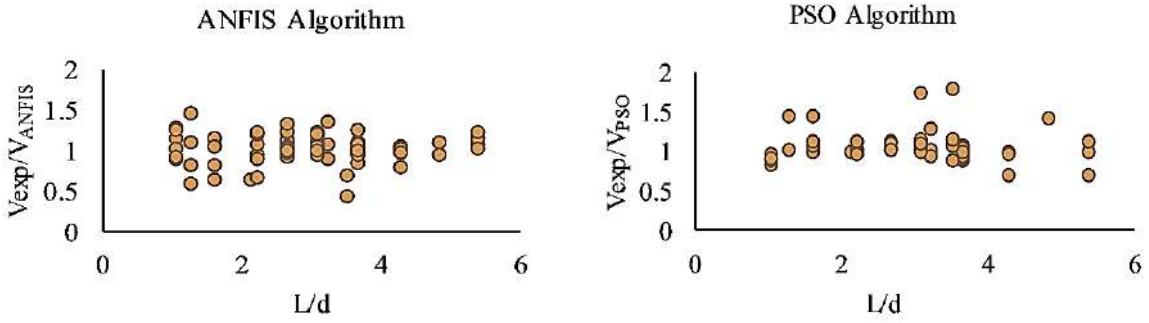

(a) ANFIS **(b) ANFIS-PSO**

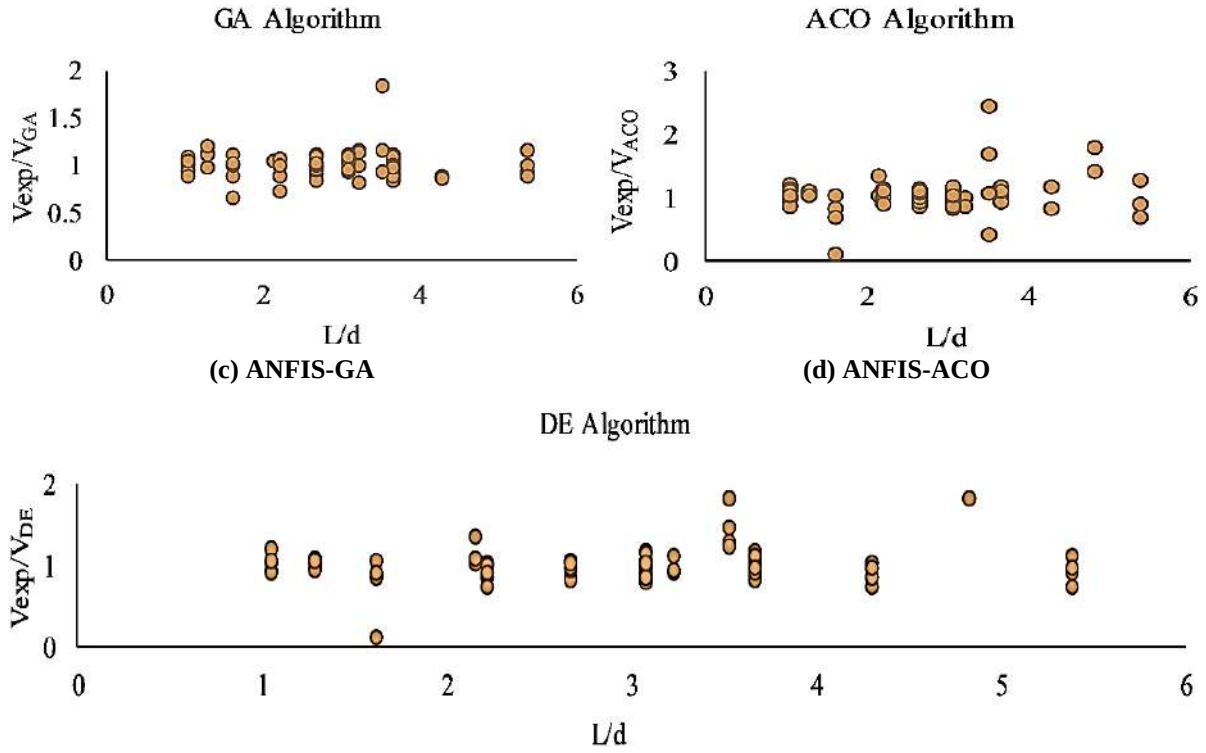

(c) ANFIS-GA **(d) ANFIS-ACO**

(e) ANFIS-DE

Fig. 5. The changes of the ratio of the experimental shear strength to the predicted shear strength in term of *L/d* parameter

In other words, these figures show the accuracy of the proposed methods with respect to the geometrical properties of the examined beams. It can be seen from Figures 5c and 5e that the values of V_{exp}/V_{pre} for the ANFIS-GA and ANFIS-DE models have higher accuracy than that of the other models. It can also be concluded that the regardless of the geometrical type of the deep beam, the prediction of shear strength in these two models shows the high accurate for the different types of deep beams with arbitrary geometry. While ANFIS-PSO, and ANFIS-ACO models only have high accuracy in predicting shear strength of the beam in a range of $2 < L/d < 4$.

7.3.2. Shear Span to Effective Depth (*a/d*)

The changes of V_{exp}/V_{pre} obtained from ANFIS, ANFIS-PSO, ANFIS-GA, ANFIS-ACO and ANFIS-DE are shown in terms of different *a*/*d* ratios in Figures 6a to 6e, respectively. The results of these figures show that the values of V_{exp}/V_{pre} are more accurate in the ANFIS-GA and ANFIS-DE models and have less dispersion than those of the other examined models.

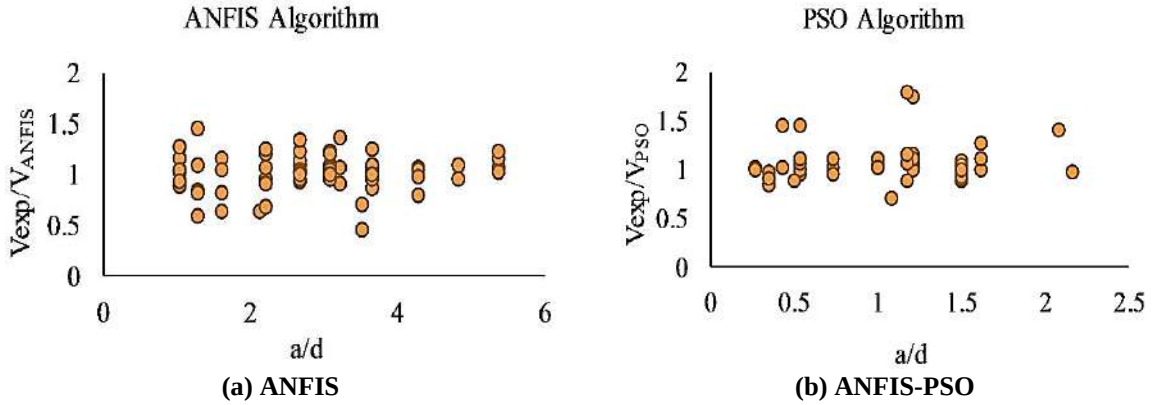

(a) ANFIS **(b) ANFIS-PSO**

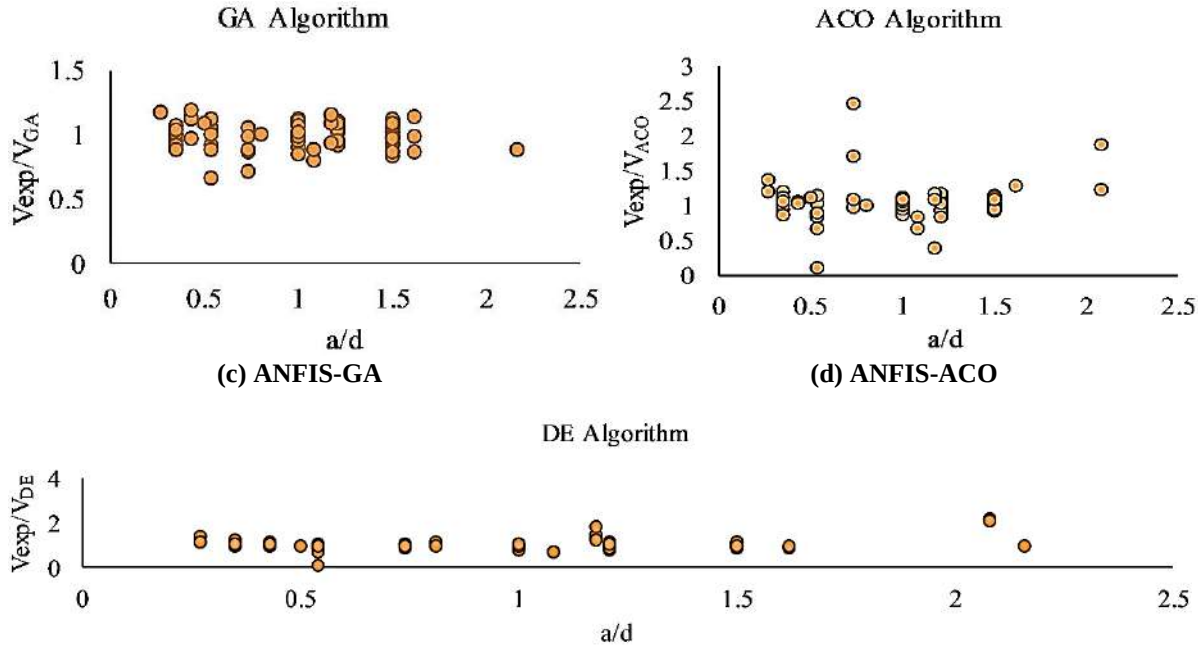

(c) ANFIS-GA **(d) ANFIS-ACO**

(e) ANFIS-DE

Fig. 6. The changes in the ratio of experimental shear strength to predicted shear strength in terms of a/d parameter

7.3.3. Compressive Strength of Concrete

The changes of V_{exp}/V_{pre} in terms of the compressive strength values (28-day US Cylinder specimen) for different models of ANFIS, ANFIS-GA, ANFIS-PSO, ANFIS-ACO and ANFIS-DE are presented in Figures 7a to 7e, respectively. The compressive strength of concrete is considered as an import parameter in the design of RC beams. As can be seen from Figure 7e, the prediction of shear strength with the ANFIS-DE method is less affected by the changes in the compressive strength of concrete and has higher accuracy than the other methods. Thus, the ANFIS-DE method shows high accuracy for a wide range of concrete compressive strengths.

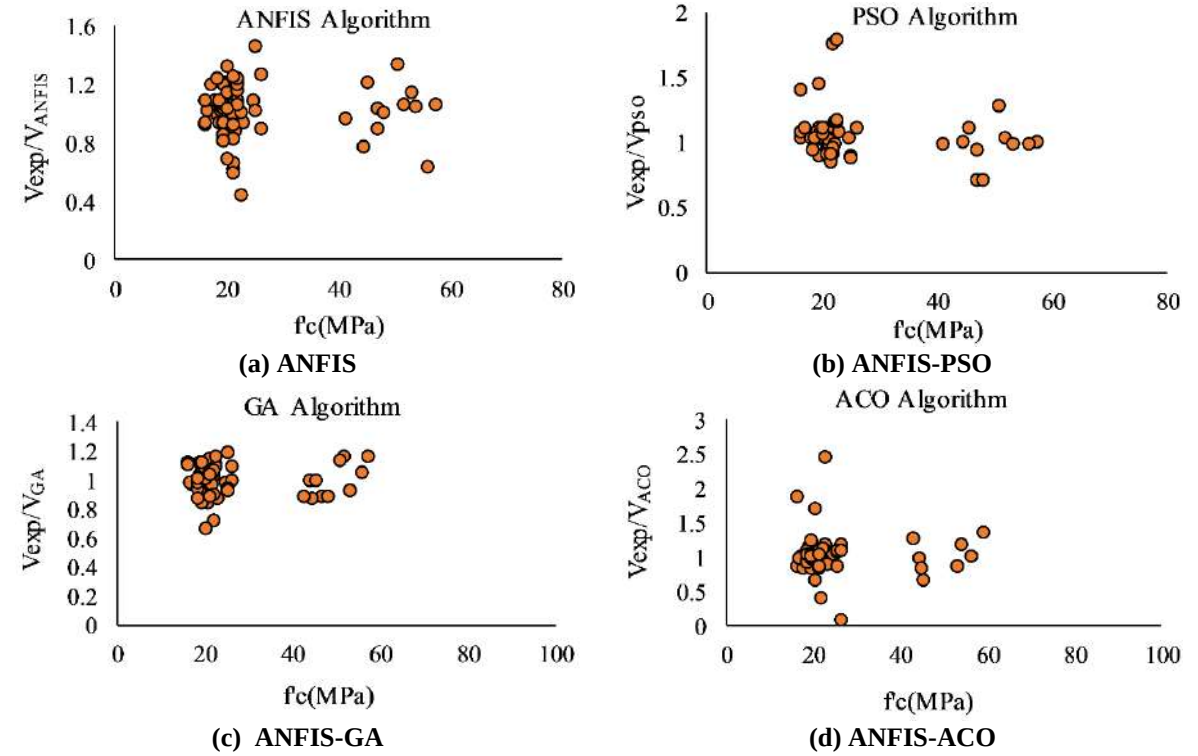

(a) ANFIS **(b) ANFIS-PSO**

(c) ANFIS-GA **(d) ANFIS-ACO**

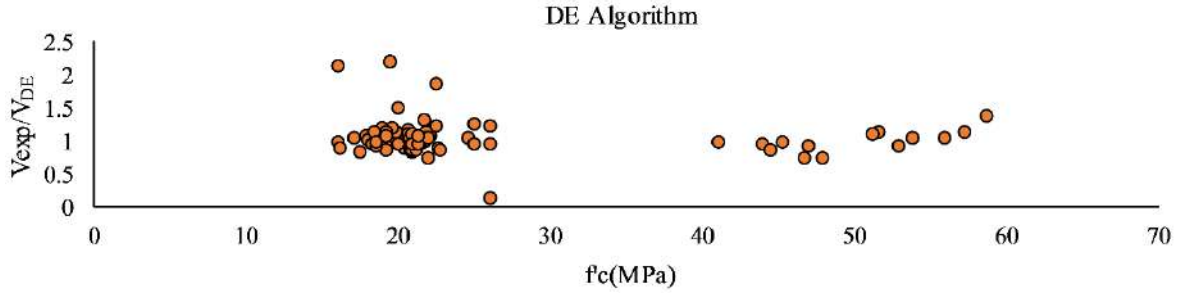

(e) ANFIS-DE

Fig. 7. The changes in the ratio of the experimental shear strength to the predicted shear strength in terms of f_c'

7.3.4. Longitudinal Reinforcement Percentage in Deep Beams

The changes of V_{exp}/V_{pre} for RC deep beams obtained from ANFIS, ANFIS-PSO, ANFIS-GA, ANFIS-ACO and ANFIS-DE models in term of the longitudinal reinforcement percentage are shown in Figures 8a to 8e, respectively. The results show that the values of V_{exp}/V_{pre} are closer to 1 in the ANFIS-GA and ANFIS-DE models. The higher accuracy is more pronounced in predicting the shear strength in term of longitudinal rebar percentage between 0.2 and 1%. These figures also show that ANFIS model has the highest data dispersion. Therefore, it can be seen from Figures 8c and 8e that for the prediction of the shear strength of deep beam, using ANFIS-GA, ANFIS-DE, ANFIS methods have more accurate.

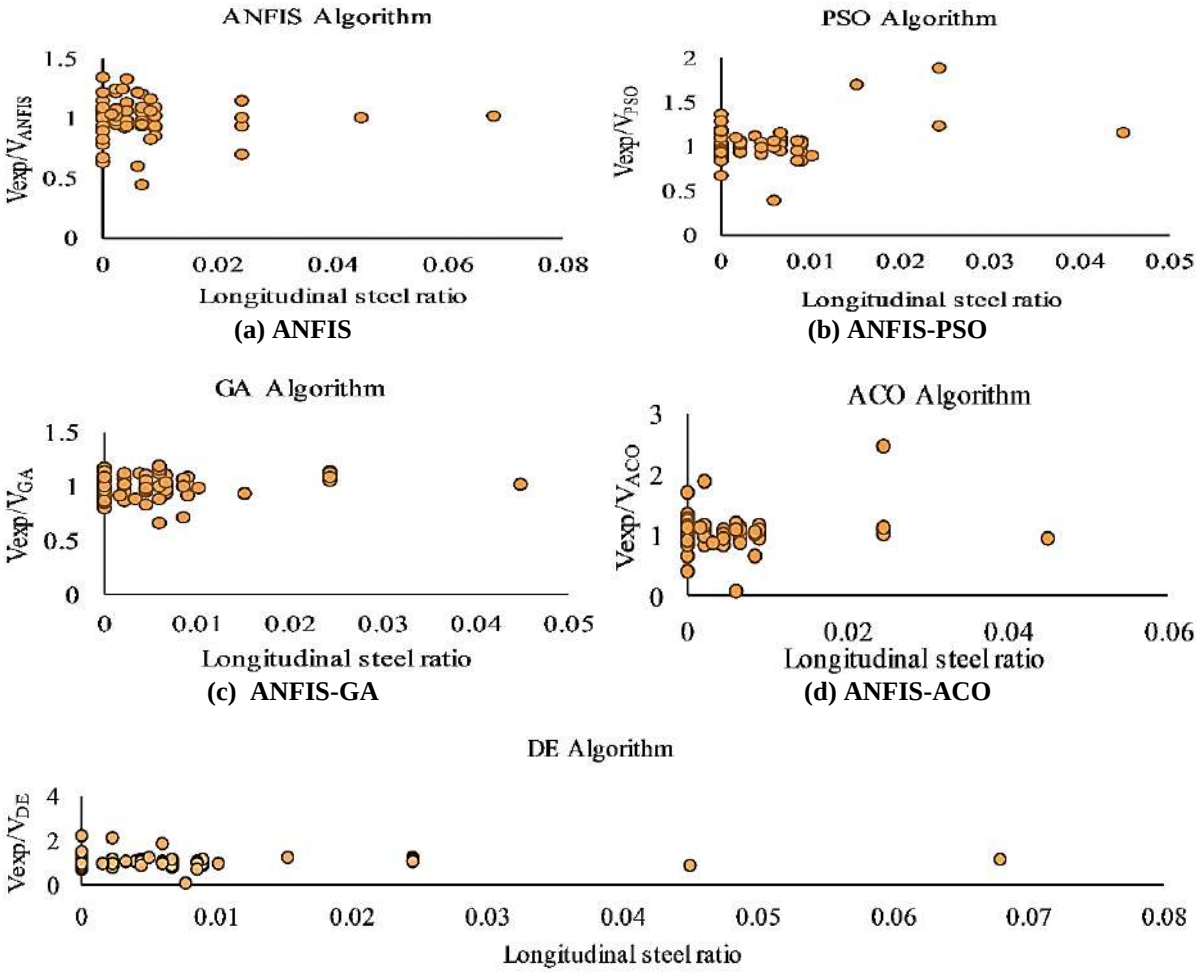

(a) ANFIS **(b) ANFIS-PSO**

(c) ANFIS-GA **(d) ANFIS-ACO**

(e) ANFIS-DE

Fig. 8. The changes in the ratio of experimental shear strength to predicted shear strength in terms of the longitudinal rebar

7.3.5. Shear Reinforcement Percentage in Deep Beams

The changes of V_{exp}/V_{pre} obtained from ANFIS, ANFIS-PSO, ANFIS-GA, ANFIS-ACO and ANFIS-DE models in term of the shear reinforcement percentage of RC deep beams are shown in Figures 9a to 9e, respectively. The results show that the values of V_{exp}/V_{pre} in ANFIS-GA and ANFIS-DE models are closer to 1 than the other models, and have high accurate. The higher accuracy is more evident in the prediction of the shear strength in term of shear reinforcement percentage in a range of 0.3 to 0.6 percent. Figure 9a also shows that the ANFIS model has the highest data dispersion. Therefore, in the prediction of the shear strength of deep beam in the presence of the shear reinforcement percentage, ANFIS-GA, ANFIS-DE and ANFIS methods can lead to higher accuracy. As a general conclusion, it can be expressed that ANFIS-GA and ANFIS-DE models give the best results for estimating the shear strength of RC deep beam with shear reinforcement ratio of 0.3 to 1.2%.

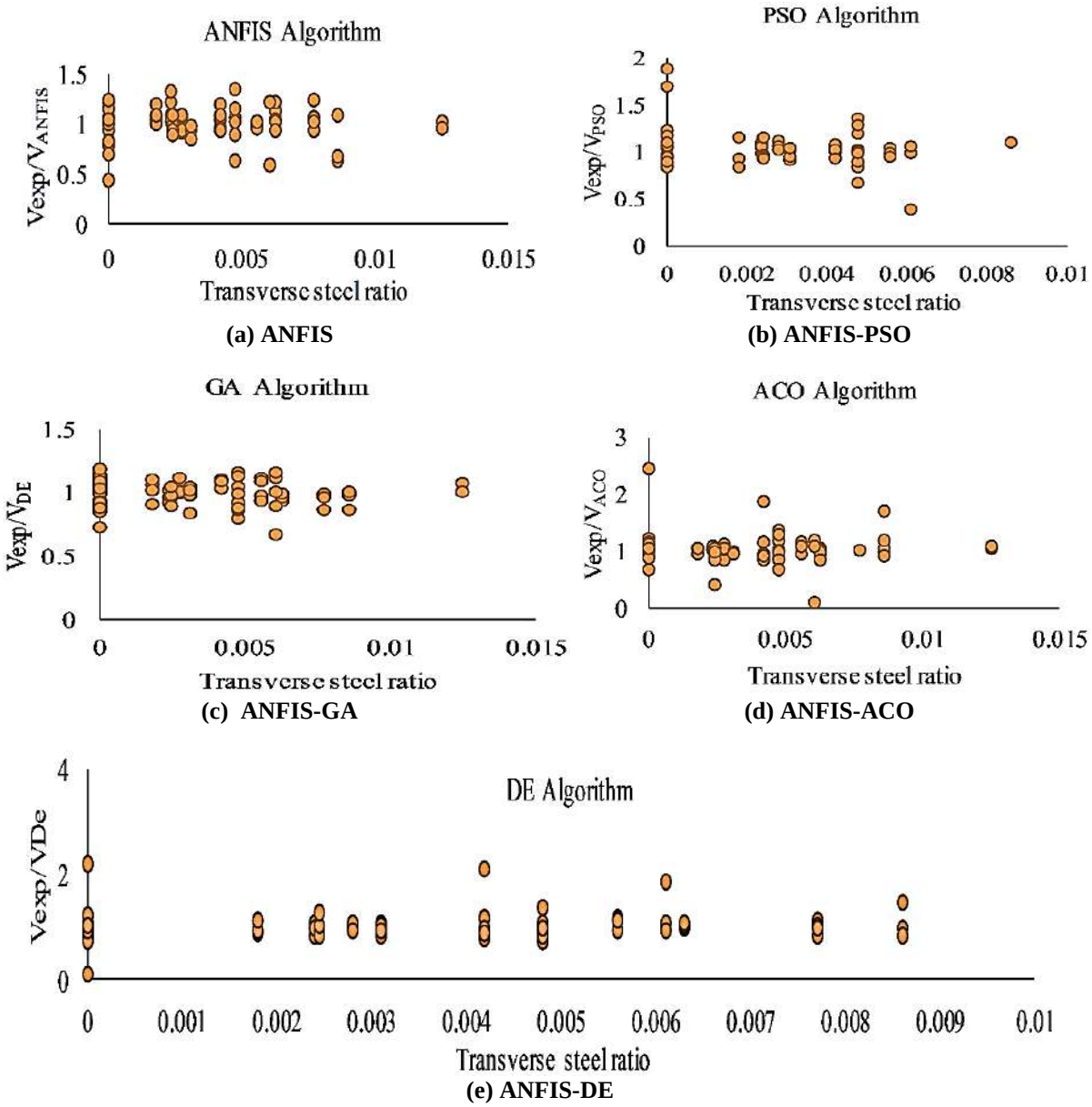

Fig. 9. The changes in the ratio of experimental shear strength to predicted shear strength in terms of the shear reinforcement percentage in deep beam

8. Conclusions

This study developed an ANFIS with meta-heuristic methods to predict the shear strength of RC deep beams. In the proposed approach, the meta-heuristic methods were employed to find the optimal parameters for membership functions and fuzzy rules in the ANFIS model which can generate a model for the shear strength of RC deep beams with high accuracy. The results reveals that the ANFIS method with meta-heuristic algorithms, as a powerful computational tool, can be used to analyze the complex relationships between different parameters in predicting shear strength of RC deep beams. The proposed ANFIS methods had better performance than the conventional ANFIS tuned based on the gradient decent approach. This efficient performance was obtained based on the stronger ability of the global search of the meta-heuristic algorithms. The comparison of these methods and the Strut-and-Tie method as well as the ACI approaches shows that the accuracy of the proposed ANFIS models is high. Furthermore, the results demonstrate that the ANFIS with meta-heuristic algorithms can be used as an alternative method to predict the shear strength of RC deep beams in comparison of ANN, GEP and other empirical approaches. The parametric studies show that shear strength of deep beams increases with the increase of concrete strength, and decreases with the increase of shear span to effective depth ratio. The results also show that among the different meta-heuristic methods, the DE method has the higher accuracy than other methods.

Although the computational cost of the proposed ANFIS method is higher than that for the conventional ANFIS. In future research, other optimization techniques may be developed to replace the GA, PSO, ACO and DE techniques used in this study for further comparison. It is also noted that the proposed ANFIS model considered in this study can certainly be used to accurately predict the shear strength of ordinary beams. However, due to the fact that the mechanism of ultimate fracture of ordinary beams is different from deep beams. Hence, for predicting the shear strength of ordinary beams, the database of the same beams should be used.

9. References

ACI. (2011). *Building code requirements for structural concrete (ACI 318-11)*, American Concrete Institute.

Armaghani, D.J. and Asteris, P.G. (2021). "A comparative study of ANN and ANFIS models for the prediction of cement-based mortar materials compressive strength", *Neural Computing and Applications*, 33(9), 4501-4532, https://doi.org/10.1007s00521-020-05244-4.

Baghban, A., Karamodin, A., and Haji Kazemi, H. (2020). "Fault-tolerant damage control of nonlinear structures using artificial intelligence", *Civil Engineering Infrastructures Journal*, 53(2), 395-406, https://doi.org/10.22059/CEIJ.2020.287804.1609.

Bezdek, J.C. (1981). *Pattern recognition with fuzzy objective function algorithms*, Plenum Press, New York, https://doi.org/10.1007/978-1-4757-0450-1.

CSA. (1994). *Building code, design of concrete structures: Structures (Design)-A National Standard of Canada (CAN-A23. 3-94), Clause 11.1. 2*, Canadian Standards Association, Toronto.

Gholamzadeh Chitgar, A. and Berenjian, J. (2021), "Performance evaluation of RBF networks with various variables to forecast the properties of SCCs", *Civil Engineering Infrastructures Journal*, 54(1), 59-73, https://doi.org/10.22059/CEIJ.2020.288257.1611.

Chiu, S. (1997). "Fuzzy model identification based on cluster estimation", *Journal of Intelligent and Fuzzy Systems*, 2(3), 267-278, https://doi.org/10.3233/ifs-1994-2306.

Chou, J.S., Chiu, C.K., Farfoura, M. and Al-Taharwa, I. (2011). "Optimizing the prediction accuracy of concrete compressive strength based on a comparison of data-mining techniques", *Journal of Computing in Civil Engineering*, 25(3), 242-253, https://doi.org/10.1061/(ASCE)CP.1943-5487.0000088.

Dao, D.V., Ly, H.B., Trinh, S.H., Le, T.T. and Pham, B.T. (2019). "Artificial intelligence approaches for prediction of compressive strength of geopolymer concrete", *Materials*, 12(6), 983, https://doi.org/10.3390/ma12060983.

Deb, K. (2011). "Multi-objective optimisation using

evolutionary algorithms: an introduction", In: Wang, L., Ng, A., Deb, K. (eds), *Multi-Objective Evolutionary Optimisation for Product Design and Manufacturing*, pp. 3-34, Springer: London.

Gandomi, A.H., Yun, G.J. and Alavi, A.H. (2013). "An evolutionary approach for modeling of shear strength of RC deep beams", *Materials and Structures*, 46(12), 2109-2119, https://doi.org/10.1007/978-0-85729-652-8_1.

Gen, M. and Cheng, R. (2000). *Genetic algorithms and engineering optimization*, John Wiley & Sons, Inc., USA, https://doi.org/10.1002/9780470172261.

Jang, J.S. (1993). "ANFIS: adaptive-network-based fuzzy inference system", *IEEE Transactions on Systems, Man, and Cybernetics*, 23(3), 665-685, https://doi.org/10.1109/21.256541.

Jang, J.S.R., Sun, C.T. and Mizulani, E. (1996). *Neuro–fuzzy and soft computing: a computational approach to learning and machine intelligence*, Prentice-Hall, https://doi.org/10.1109/tac.1997.633847.

Kaveh, A., Hamze-Ziabari, S.M. and Bakhshpoori, T. (2017). "M5'algorithm for shear strength prediction of hsc slender beams without web reinforcement", *International Journal of Modeling and Optimization*, 7(1), 48-53, https://doi.org/10.24200/sci.2017.4509.

Kennedy, J., Eberhart, R.C., and Shi, Y. (2001). *Swarm intelligence*, Morgan Kaufmann Publishers, San Francisco, https://doi.org/10.1007/s00897020553a.

Keshavarz, Z. and Torkian, H. (2018). "Application of ANN and ANFIS models in determining compressive strength of concrete", *Journal of Soft Computing in Civil Engineering*, 2(1), 62-70, https://doi.org/10.22115/SCCE.2018.51114.

Khatibinia, M. and Mohammadizadeh, M.R. (2017). "Intelligent fuzzy inference system approach for modeling of debonding strength in FRP retrofitted masonry elements", *Structural Engineering and Mechanics*, 6(2), 283-293, https://doi.org/10.12989/sem.2017.61.2.283.

Khoshbin, F., Bonakdari, H., Ashraf Talesh, S.H., Ebtehaj, I., Zaji, A.H. and Azimi, H. (2016). "Adaptive neuro-fuzzy inference system multi-objective optimization using the genetic algorithm/singular value decomposition method for modelling the discharge coefficient in rectangular sharp-crested side weirs", *Engineering Optimization*, 48(6), 933-948, https://doi.org/10.1080/0305215x.2015.1071807.

Kong, F.K., Robins, P.J. and Cole, D.F. (1970). "Web reinforcement effects on deep beams", *Journal Proceedings*, 67(12), 1010-1018, https://doi.org/10.14359/7336.

Lin, J.C.W., Yang, L., Fournier-Viger, P., Hong, T.P. and Voznak, M. (2017). "A binary PSO approach to mine high-utility itemsets", *Soft Computing*, 21(17), 5103-5121, https://doi.org/10.1007/s00500-016-2106-1.

Liu, J. and Mihaylov, B.I. (2016). "A comparative study of models for shear strength of reinforced concrete deep beams", *Engineering Structures*, 112, 81-89, https://doi.org/10.1016/j.engstruct.2016.01.012.

Moosazadeh, S., Namazi, E., Aghababaei, H., Marto, A., Mohamad, H. and Hajihassani, M. (2019). "Prediction of building damage induced by tunnelling through an optimized artificial neural network", *Engineering with Computers*, 35(2), 579-591, https://doi.org/10.1007/s00366-018-0615-5.

Naderpour, H. and Mirrashid, M. (2020). "Shear strength prediction of RC beams using adaptive neuro-fuzzy inference system", *Scientia Iranica*, 27(2), 657-670, https://doi.org/10.24200/sci.2018.50308.1624.

Nguyen, T.A., Ly, H.B., Mai, H.V.T., and Tran, V.Q. (2021). "On the training algorithms for artificial neural network in predicting the shear strength of deep beams", *Complexity*, 3(1), 1-18, https://doi.org/10.1155/2021/5548988.

Pal, M. and Deswal, S. (2011). "Support vector regression based shear strength modelling of deep beams", *Computers and Structures*, 89(13-14), 1430-1439, https://doi.org/10.1016/j.compstruc.2011.03.005.

Prayogo, D., Cheng, M.Y., Wu, Y.W. and Tran, D.H. (2020). "Combining machine learning models via adaptive ensemble weighting for prediction of shear capacity of reinforced-concrete deep beams", *Engineering with Computers*, 36(3), 1135-1153, https://doi.org/10.1007/s00366-019-00753-w.

Savrun, M.M. and İnci, M. (2021). "Adaptive neuro-fuzzy inference system combined with genetic algorithm to improve power extraction capability in fuel cell applications", *Journal of Cleaner Production*, 299(25 May), 126944, https://doi.org/10.1016/j.jclepro.2021.126944.

Shariati, M., Mafipour, M. S., Mehrabi, P., Shariati, A., Toghroli, A., Trung, N.T. and Salih, M.N.A. (2021). "A novel approach to predict shear strength of tilted angle connectors using artificial intelligence techniques", *Engineering with Computers*, 37(3), 2089-2109, https://doi.org/10.1007/s00366-019-00930-x.

Shi, Y., Liu, H., Gao, L. and Zhang, G. (2011). "Cellular particle swarm optimization", *Information Sciences*, 181(20), 4460-4493, https://doi.org/10.1016/j.ins.2010.05.025.

Sihag, P., Tiwari, N.K. and Ranjan, S. (2019). "Prediction of unsaturated hydraulic conductivity using adaptive neuro-fuzzy inference system (ANFIS)", *ISH Journal of Hydraulic Engineering*, 25(2), 132-142, https://doi.org/10.1080/09715010.2017.138186

1.
Smith, K.N. and Vantsiotis, A.S. (1982). "Shear strength of deep beams", *Journal Proceedings*, 79(3), 201-213, https://doi.org/10.14359/10899.
Socha, K. and Dorigo, M. (2008). "Ant colony optimization for continuous domains", *European Journal of Operational Research*, 185(3), 1155-1173, https://doi.org/10.1016/j.ejor.2006.06.046.
Storn, R. and Price, K. (1997). "Differential evolution, A simple and efficient heuristic for global optimization over continuous spaces", *Journal of Global Optimization*, 11(4), 341-359, https://doi.org/10.1023/a:1008202821328.
Subbaraj, P., Rengaraj, R. and Salivahanan, S. (2011). "Enhancement of self-adaptive real-coded genetic algorithm using Taguchi method for economic dispatch problem", *Applied Soft Computing*, 11(1), 83-92, https://doi.org/10.1016/j.asoc.2009.10.019.
Suguna, K., Raghunath, P.N., Karthick, J. and Uma Maheswari, R. (2018). "ANN based modeling for high strength concrete beams with surface mounted FRP laminates", *International Journal of Optimization in Civil Engineering*, 8(3), 453-467, http://ijoce.iust.ac.ir/article-1-355-en.htm.
Tan, K.H., Kong, F.K., Teng, S. and Guan, L. (1995). "High-strength concrete deep beams with effective span and shear span variations", *Structural Journal*, 92(4), 395-405, https://doi.org/10.14359/991.
Taghi Dastorani, M., Mahjoobi, J., Talebi, A. and Fakhar, F. (2018). "Application of machine learning approaches in rainfall-runoff modeling (Case Study: Zayandeh_Rood Basin in Iran)", *Civil Engineering Infrastructures Journal*, 51(2), 293-310, https://doi.org/10.7508/CEIJ.2018.02.004.
Toghroli, A., Mohammadhassani, M., Suhatril, M., Shariati, M. and Ibrahim, Z. (2014). "Prediction of shear capacity of channel shear connectors using the ANFIS model", *Steel and Composite Structures*, 17(5), 623-639, https://doi.org/10.12989/scs.2014.17.5.623.
Zhang, C. (2020). "Classification rule mining algorithm combining intuitionistic fuzzy rough sets and genetic algorithm", *International Journal of Fuzzy Systems*, 22, 1694-1715, https://doi.org/10.1007/s40815-020-00849-2.
Zhou, Q., Zhu, F., Yang, X., Wang, F., Chi, B. and Zhang, Z. (2017). "Shear capacity estimation of fully grouted reinforced concrete masonry walls using neural network and adaptive neuro-fuzzy inference system models", *Construction and Building Materials*, 153, 937-947, https://doi.org/10.1016/j.conbuildmat.2017.07.171.

Civil Engineering Infrastructures Journal 2023, 56(1): 159-172
DOI: 10.22059/CEIJ.2022.337777.1811

RESEARCH PAPER

Predicting Compressive Strength of Concrete Using Histogram-Based Gradient Boosting Approach for Rapid Design of Mixtures

Al Adwan, J.[1], Alzubi, Y.[1*], Alkhdour, A.[1] and Alqawasmeh, H.[1]

[1] Assistant Professor, Civil Engineering Department, Faculty of Engineering Technology, Al-Balqa Applied University, Amman, Jordan.

Received: 21 Jan. 2022; Revised: 14 Mar. 2022; Accepted: 04 Apr. 2022

ABSTRACT: Applications of machine learning techniques in concrete properties' prediction have great interest to many researchers worldwide. Indeed, some of the most common machine learning methods are those based on adopting boosting algorithms. A new approach, histogram-based gradient boosting, was recently introduced to the literature. It is a technique that buckets continuous feature values into discrete bins to speed up the computations and reduce memory usage. Previous studies have discussed its efficiency in various scientific disciplines to save computational time and memory. However, the algorithm's accuracy is still unclear, and its application in concrete properties estimation has not yet been considered. This paper is devoted to evaluating the capability of histogram-based gradient boosting in predicting concrete's compressive strength and comparing its accuracy to other boosting methods. Generally, the results of the study have shown that the histogram-based gradient boosting approach is capable of achieving reliable prediction of concrete compressive strength. Additionally, it showed the effects of each model's parameters on the accuracy of the estimation.

Keywords: Compressive Strength, Concrete, Histogram-Based Gradient Boosting, Machine Learning.

1. Introduction

There is no doubt that concrete is one of the most widely used materials all over the world (Elzokra et al., 2020; Habib et al., 2021). Generally, it has high compressive strength and stiffness, making it suitable for various construction works (Malkawi et al., 2020). Concrete mixture design as a vital and recondite problem is the method of identifying the kind and amount of individual components to produce concrete that fits desired properties, such as workability and strength, for a particular purpose and is also economically acceptable (Yeh, 2007; Wardeh et al., 2015). Optimal design of concrete composition proportions with the lowest cost and needed performance is considered a challenge of designers and decision-makers (DeRousseau et al., 2018). In reality, the strength of this material is one of its significant parameters for mixture design and optimization, yet obtaining it at a mature age requires a relatively long experimental process (Ni and Wang, 2000; Al Houri et al., 2020).

Mathematical modeling of concrete

* Corresponding author E-mail: yazan.alzubi@yahoo.com

characteristics has become a fundamental issue in recent years, owing to the rapid developments of novel concrete types stimulated by the ever-challenging requirements of the construction industry (Chaabene et al., 2020). The used techniques to design concrete characteristics are separated into two categories: conventional and artificial intelligence-augmented methods (Ziolkowski and Niedostatkiewicz, 2019; Gholamzadeh Chitgar and Berenjian, 2021). In general, various data-driven mathematical methods have been applied to estimate the properties of concrete rapidly, including multiple linear regression (Khademi et al., 2017), fuzzy logic (Topcu and Sarıdemir, 2008), genetic programming (Chopra et al., 2016), artificial neural networks (Lee, 2003; Habib and Yildirim, 2021), bagging machine learning techniques (Han et al., 2019; Farooq et al., 2020), boosting machine learning methods (Nguyen-Sy et al., 2020; Salimbahrami and Shakeri, 2021).

Due to its superior accuracy, the gradient-boosting decision tree is a commonly used machine learning algorithm in many disciplines (Guryanov, 2019). For instance, Feng et al. (2020) utilized an adaptive boosting approach to estimate concrete's compressive. Kaloop et al. (2020) used the gradient tree boosting machine to predict the compressive strength of high-performance concrete. Moreover, Nguyen-Sy et al. (2020) developed a machine learning model using extreme gradient boosting to design concrete mixtures using constituent materials and age at testing. Even though the gradient boosting algorithm performs very well, massive ensembles will likely be slow in training and inference (Lu et al., 2020). This difficulty in developing gradient-boosting models for large datasets, tens of thousands of observations or more, emerges from the time consumed to find the best split points (Shepovalov and Akella, 2020).

In contrast, a histogram-based technique can decrease computation time and memory usage by converting continuous data into discrete bins to build attribute histograms instead of finding the split points (Cai et al., 2021). Recently, three major Python coding libraries that wrap up many modern efficiency approaches for training gradient-boosting algorithms have permitted the development of histogram-based models, including scikit-learn (Pedregosa et al., 2011), XGBoost (Chen and Guestrin, 2016), and LightGBM (Ke et al., 2017). The importance of histogram-based gradient boosting (HGBoost) comes from its ability to considerably reduce the computational efforts and memory usage required to train machine learning models for large datasets. Previous studies have focused on the technique's performance regarding the time and memory needed to develop the estimation models. Besides, the capability of HGBoost in predicting concrete characteristics is still unclear, and the studies investigating its accuracy for adaptation in the civil engineering discipline are scarce.

Therefore, this article evaluates the accuracy and reliability of the histogram-based gradient boosting technique in predicting the compressive strength of concrete mixtures. As a part of the study, a parametric assessment will be conducted to highlight the influence of each of the method's parameters on the model's accuracy. In addition, the results of the HGBoost will be compared against that of various boosting approaches to benchmark and understand the algorithm's performance. This information is missing from the literature and is helpful for many engineers and researchers working in the field.

2. Materials and Methods

Researchers have invented artificial intelligence-based solutions for many real-time scenarios in recent years, thanks to advances in the application of machine learning algorithms across a wide range of fields (Amidi et al., 2021; Ahmad et al.,

2022; Kim et al., 2022). The roots of gradient boosting may be traced back to the discovery by statistician Leo Breiman that it can help diminish bias, resulting in increased performance (Mease and Wyner, 2008). Adaptive Boosting (AdaBoost) was the first convenient embodiment of the boosting concept. It was developed by Yoav Freund and Robert Schapire in 1995, and it has been shown to help enhance the behavior of various learning techniques (Freund and Schapire, 1997). When it comes to training machine learning algorithms for massive datasets, HGBoost is very valuable because of its ability to minimize the amount of computing effort and memory needed significantly (Guryanov, 2019). The general methodology followed in this research for quantifying the accuracy of HGBoost is illustrated in Figure 1.

The fundamental purpose of concrete mixture design is to determine the appropriate quantity of constituents in the mix. Therefore, the mixture components must be chosen precisely to obtain the highest possible concrete performance while keeping costs down. This behavior is manifested by several features in which compressive strength is the most important. In this research, machine learning techniques will be applied to design a concrete mixture using the HGBoost model and an enormous dataset for estimating the strength of concrete. The histogram-based gradient boosting method predicts the compressive strength of a concrete mix relied on the quantity of the seven primary ingredients and age at testing of concrete, more accurately cement, fine and coarse aggregate, superplasticizer, fly ash, silica fume, and water, as shown in Figure 2.

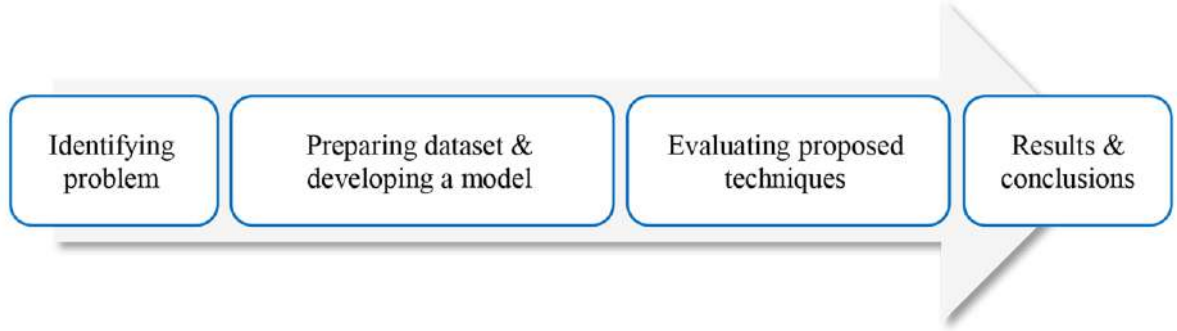

Fig. 1. Graphical description of the research methodology

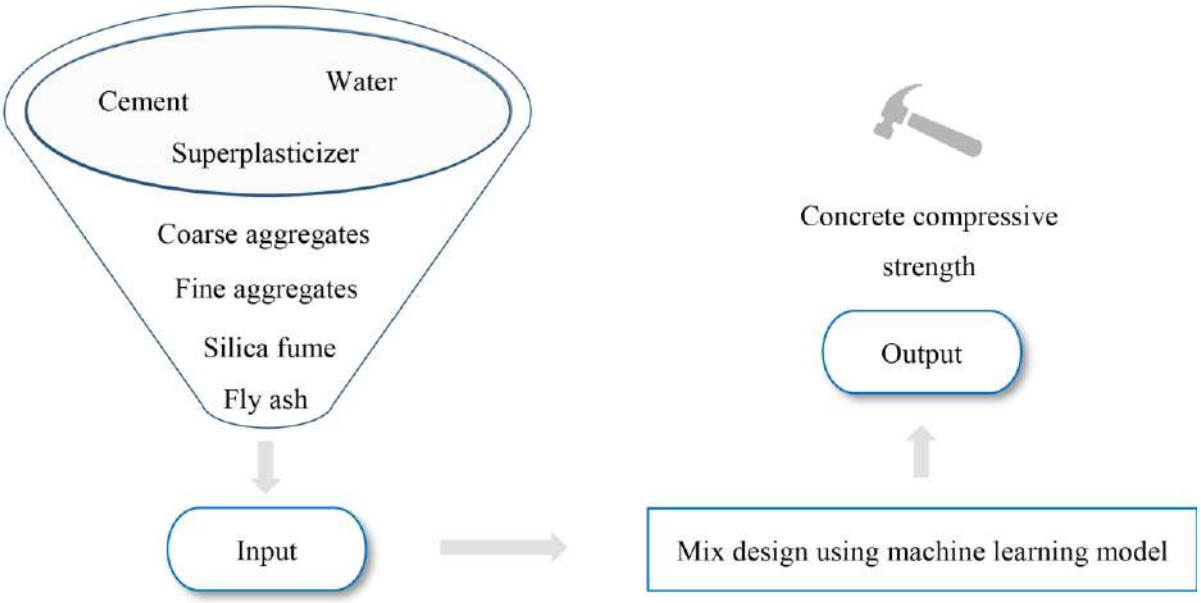

Fig. 2. Stages of a process for concrete mixture design using a machine learning

2.1. Dataset Acquisition

As stated before, this research focuses solely on the accuracy of HGBoost rather than its time and memory consumption. Accordingly, developing a significantly large dataset with tens of thousands of observations is not required. Thus, a relatively large set of experimental results for various concrete mixtures was utilized to investigate the HGBoost model's capability against other machine learning techniques. This dataset was first developed by Yeh (1998) from many resources and then used in various researches for developing numerical models (Yeh, 2006; Asteris et al., 2021; Ke and Duan, 2021). Generally, the database comprises 1005 observations (Table 1 and Figure 3). The compressive strength of the mixtures is accounted for 15 cm cylinder specimens. Yeh (1998) stated that the dataset often contains some unexpected inaccuracies regarding the class of fly ash or that of the cement, the gradation of the aggregates, and the type of superplasticizer. While this issue might cause difficulty to the machine learning model due to the fluctuation of the materials' sources, it will simulate the cause of constructing a generalized machine learning model for designing concrete mixtures, which is one of the major potentials of the HGBoost model. Indeed, the concrete's constituent materials and age were used as the input parameters, while its compressive strength was the output of the estimation models. Additionally, it can be noticed from Table 1 that the fly ash and age have higher standard deviations than the average values, which is attributed to having high vibration between the values and abnormal distribution of the data.

2.2. Boosting Machine Learnings Techniques

A decision tree is a learning technique that is widely used in data mining. It is applied for classification and regression issues. According to this process, the estimation model is often created by recursively splitting the dataset, fitting a basic predicting algorithm in each of these divisions, and ultimately depicting each model as a decision tree (Loh, 2011). At a given node m, the data is represented by Q_m with N_m samples. This data is partitioned into two subsets $Q_m^{left}(\theta)$, Eq. (1), and $Q_m^{right}(\theta)$, Eq. (2), where for each candidate split $\theta = (j, t_m)$ compose of a j feature and t_m threshold.

$$Q_m^{left}(\theta) = \{(x, y)|x_i \leq t_m\}$$
$$Q_m^{right}(\theta) = Q_m / Q_m^{left}(\theta) \quad (1)$$

The quality of the candidate split at the given node m is calculated through the loss function $H()$.

$$G(Q_m, \theta) = \frac{N_m^{left}}{N_m} H\left(Q_m^{left}(\theta)\right) + \frac{N_m^{right}}{N_m} H\left(Q_m^{right}(\theta)\right) \quad (2)$$

Thereafter, those parameters that minimize the loss are selected using Eq. (3), and the process is repeated for $Q_m^{left}(\theta)$ and $Q_m^{right}(\theta)$ until reaching the maximum allowable depth $N_m < min_{samples}$ or $N_m = 1$.

Table 1. Descriptive statistics of the utilized database

	Variable	Average	Standard deviation	Min.	First quintile	Median	Third quintile	Max.
Input	Cement (kg/m^3)	278.63	104.34	102	190.7	265	349	540
	Blast furnace slag (kg/m^3)	72.04	86.17	0	0	20	142.5	359.4
	Fly ash (kg/m^3)	55.54	64.21	0	0	0	118.3	200.1
	Water (kg/m^3)	182.08	21.34	121.8	166.6	185.7	192.9	247
	Superplasticizer (kg/m^3)	6.033	5.92	0	0	6.1	10	32.2
	Coarse aggregate (kg/m^3)	974.38	77.58	801	932	968	1032	1145
	Fine aggregate (kg/m^3)	772.69	80.34	594	724.3	780	823.1	992.6
	Age (days)	45.86	63.73	1	7	28	56	365
Output	Compressive strength (MPa)	35.25	16.285	2.33	23.52	33.8	44.975	82.6

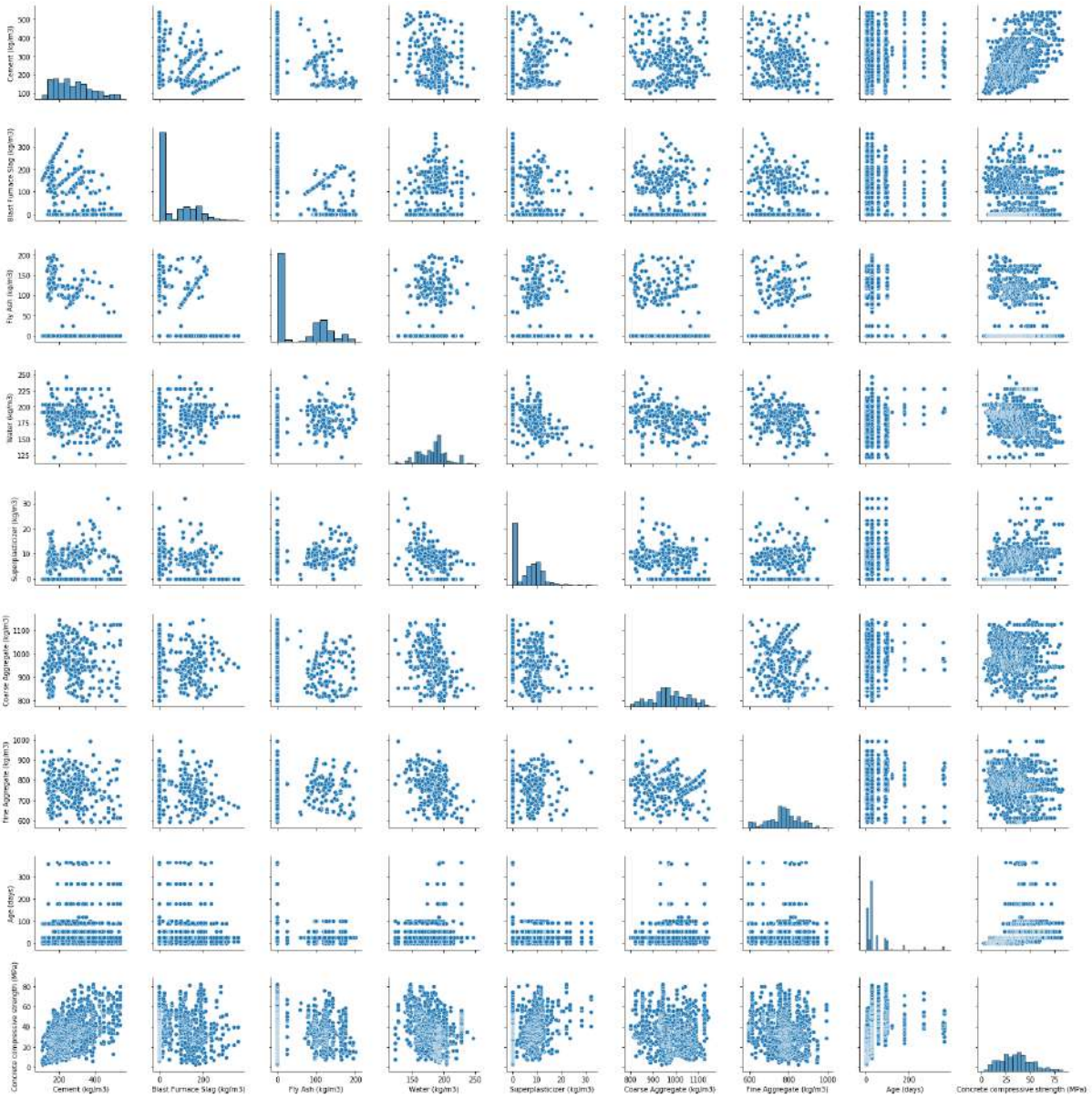

Fig. 3. Visualization of the utilized database

$$\theta^* = argmin_\theta G(Q_m, \theta) \quad (3)$$

On the other hand, Adaptive boosting, as described by Freund and Schapire (1997), is a method that works by fitting new copies of the regression model using the same training dataset through adjusting its weights from the error of the prior trial. The implantation of this algorithm is performed according to Drucker (1997). In the beginning, the AdaBoost is trained on a base estimator (weak learner) $f(x)$, and the error e_i is obtained for the entire set. Thereafter, a series of weak learners $f_k(x), k = 1,2, \dots, N$ is produced and combined to develop a strong model $H(x)$ through the strategy in Eq. (4).

$$H(x) = v \sum_{k=1}^{N} \left(ln \frac{1}{\alpha_k} \right) g(x) \quad (4)$$

where v: is the learning rate, α_k: is the weight of the base estimators calculated from Eq. (5), and $g(x)$: is median of all $\alpha_k f_k(x)$.

$$\alpha_k = \frac{e_i}{1 - e_i} \quad (5)$$

Stochastic gradient boosting (SGBoost) is similar to the AdaBoost approach that works by adding a new model ensemble but with a significant difference based on minimizing the learner's loss function. In addition, the weak estimator in the gradient

boosting is a larger decision tree with multiple levels compared to the regressor in the AdaBoost model. The training set $\{(x_1, y_1), \ldots, (x_n, y_n)\} \subset \chi \times R$ will be determined with a sample size n and space of input variables χ. Specify $\hat{y}_i$ as the prediction of a gradient boosting machine method with x_i input variable as indicated in Eq. (6).

$$\hat{y}_i = F_M(x_i) = \sum_{m=1}^{M} h_m(x_i) \quad (6)$$

in which M: is the total number of predictors provided in the algorithm and h_m: is a weak learner.

The gradient boosting is developed greedily, as stated in Eq. (7).

$$F_m(x) = F_{m-1}(x) + \underset{h \in H}{argmin} \sum_{i=1}^{n} L[y_i, F_{m-1}(x_i) + h(x_i)] \quad (7)$$

where $h(x)$: is the base estimator, $L(\cdot)$: is the loss function with the negative gradient identified in Eq. (8).

$$g_m = -\frac{\partial L[y, F_{m-1}(x)]}{\partial F_{m-1}(x)} \quad (8)$$

The SGBoost is formulated by modifying the gradient boosting model to fit the base learner randomly on a subsample with fraction $f < 1$.

Histogram-based gradient boosting (HGBoost) is a recently introduced machine learning approach (Chen and Guestrin, 2016). Unlike other techniques, it buckets continuous feature values into discrete bins and uses these bins to construct feature histograms during training. This method speeds up the training stage and reduces the memory consumption of the model. The algorithm developed herein is based on the one available in the scikit-learn library (Cai et al., 2021).

eXtreme gradient boosting (XGBoost) is an efficient and scalable machine learning algorithm applied for tree boosting (Pedregosa et al., 2011). In general, both gradients boosting and XGBoost follow the principle of gradient boosting, but XGBoost uses a more regularized model to control the over-fitting issues to achieve better results. Additionally, the XGBoost model uses the exact greedy tree method compared to the optimized approximate one adopted in the HGBoost model. The objective function of this algorithm is given in Eq. (9).

$$Obj = \sum_{i=1}^{n} L[\hat{y}_i, y_i)] + \sum_{i=1}^{n} \omega(f_t) \quad (9)$$

where $L(\cdot)$: is the loss function for the model's bias, and ω: is a regular term used for suppressing the complexity of the model.

2.6. Model Development and Hyperparameters Tunning

The machine learning algorithm's performance is greatly affected by the chosen hyperparameter values that must be tuned. This article used the grid search method with k-fold cross-validation in the training stage to optimize the approaches' hyperparameters. Hence, the proposed process for developing the machine learning techniques, Figure 4, has started by first dividing the dataset into 70% training and 30% testing ones. The proper parameter selection of each approach was performed utilizing a 10-folds cross-validation procedure. Once the hyperparameters of each technique are defined, the performance of the final tuned algorithm is validated on the test dataset by comparing different scoring parameters.

2.7. Quality Assessment

Statistical measures and visual representations are adopted for analyzing the HGBoost performance, as revealed in Figure 5. The goodness-of-fit is checked using the coefficient of determination, Eq. (10), and A20-index, Eq. (11). The Root Mean Square Error (RMSE), Eq. (12), and Mean Absolute Error (MAE), Eq. (13), were used for the error analysis.

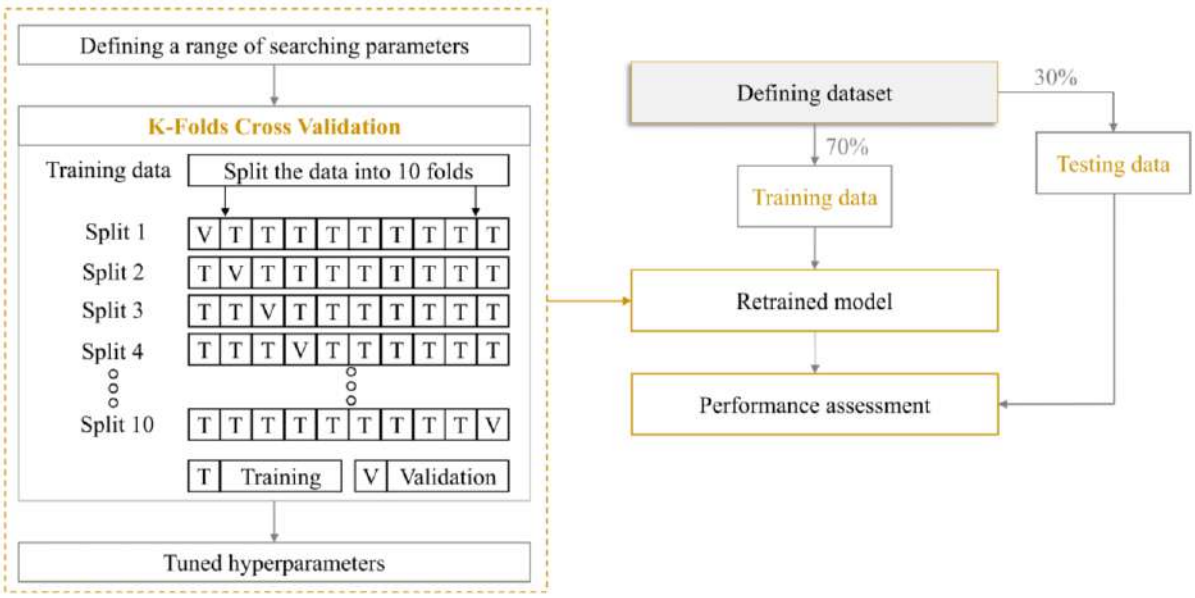

Fig. 4. Schematic diagram for developing machine learning algorithms

$$R^2 = 1 - \frac{\sum(x_i - y_i)^2}{\sum(x_i - \bar{x}_i)^2} \quad (10)$$

$$A20 - Index = \frac{m_{20}}{n} \quad (11)$$

$$RMSE = \sqrt{\frac{\sum_{i=1}^{n}(x_i - y_i)^2}{n}} \quad (12)$$

$$MAE = \frac{1}{n}\sum_{i=1}^{n}|y_i - \bar{y}_i| \quad (13)$$

where x_i: is the measured value, $\bar{x}_i$: is the mean of the measured values, y_i: is the predicted value $\bar{y}_i$: is the mean of the predicted values, n: is the number of observations, and m_{20}: is the number of samples with a measured to the predicted ratio between 0.8 and 1.20.

3. Results and Discussions

Indeed, hyperparameter tuning of machine learning models is critical for achieving superior estimation capabilities. In this section, a parametric study was conducted to evaluate the impacts of each of the HGBoost parameters on the model performance. The effect of the tree depth is clarified in Figure 6. Generally, it can be seen that shallow trees result in reduced performance of the HGBoost model. Whereas, deep ones, especially over ten edges from the root to the deepest leaf, provide superior testing results in which the A10-index, R^2, RMSE, and MAE 0.85, 0.92, 22, and 3.2, respectively. Similar outcomes were reported for the unconstrained trees. Accordingly, the unconstrained tree is adopted for this study. Also, in Figure 7, increasing the number of bins beyond ten affects the estimation results slightly and yields high accuracy with an average R^2 of 0.92. Thus, any value after 10 is suitable for the HGBoost model, yet in this study, the one with the least error value was used. On the other hand, the least essential variable while generating the model was the L2 regularization parameter, Figure 8, since it showed a fluctuation at low values and slightly impacted both the fitting rates and errors of the algorithm and later ones. Furthermore, for the investigated dataset, the learning rate with a value of 0.3 yields the best performance of the HGBoost method with an A10-index of about 1, as indicated in Figure 9. Additionally, the least-squares loss function improved the model's accuracy compared to the slightest absolute deviation, as shown in Figure 10. Therefore, the least-squares loss function was utilized for developing the HGBoost model.

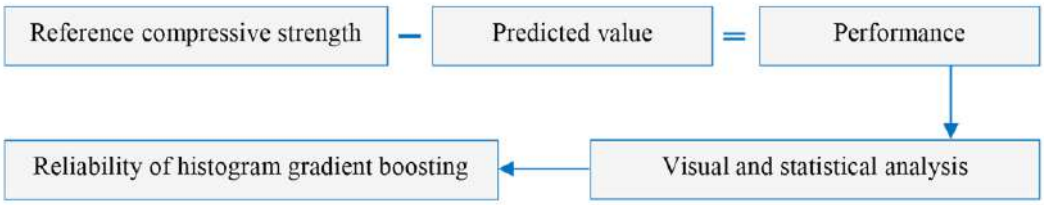

Fig. 5. Benchmarking proposed model

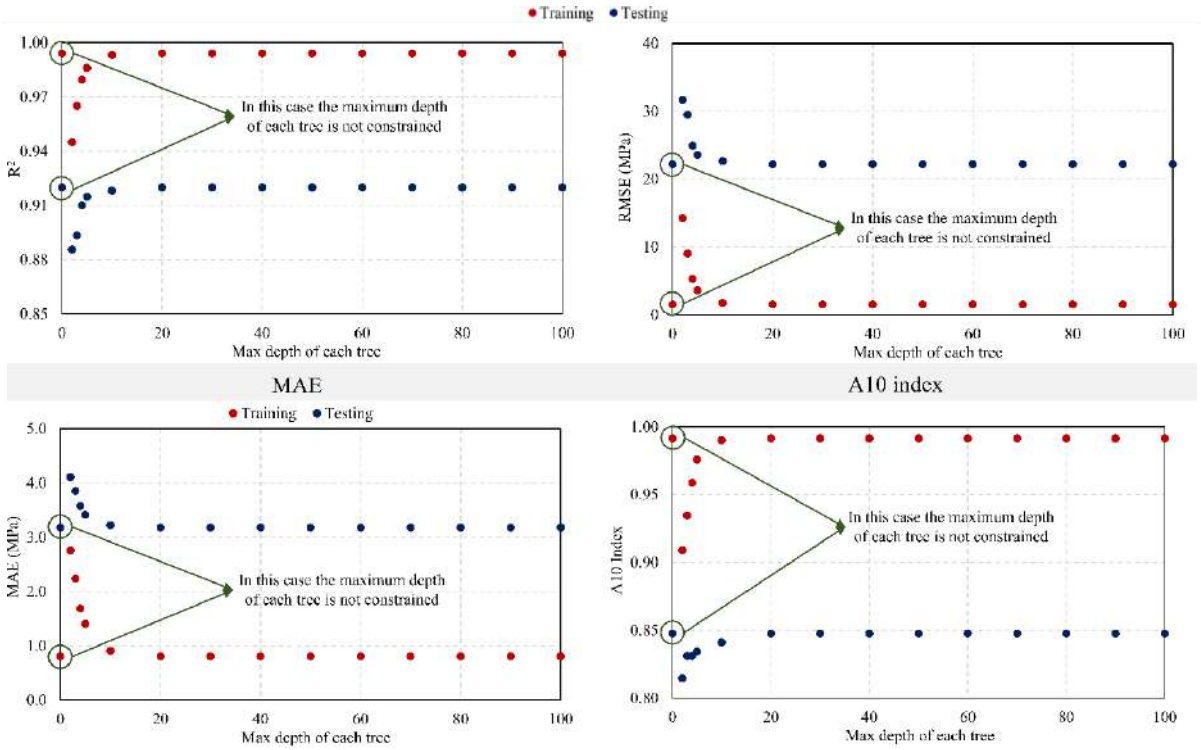

Fig. 6. Influence of the depth of each tree on the HGBoost performance

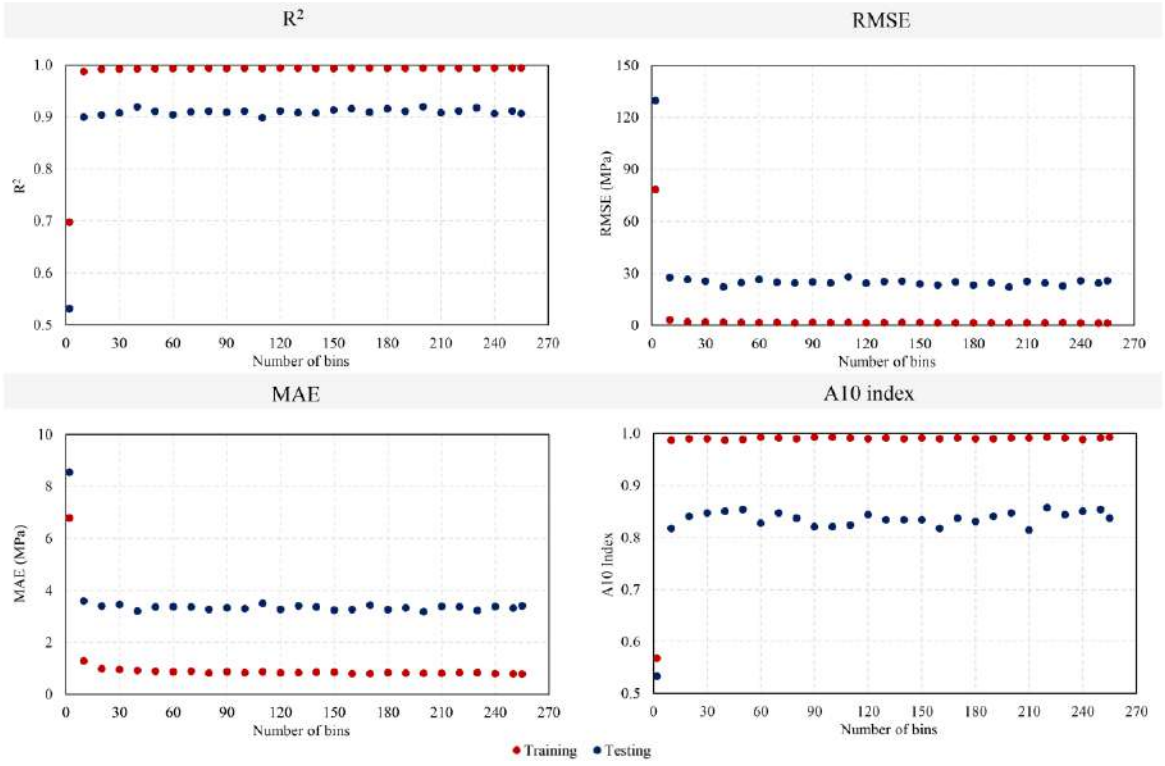

Fig. 7. Role of number of bins in HGBoost on the model performance

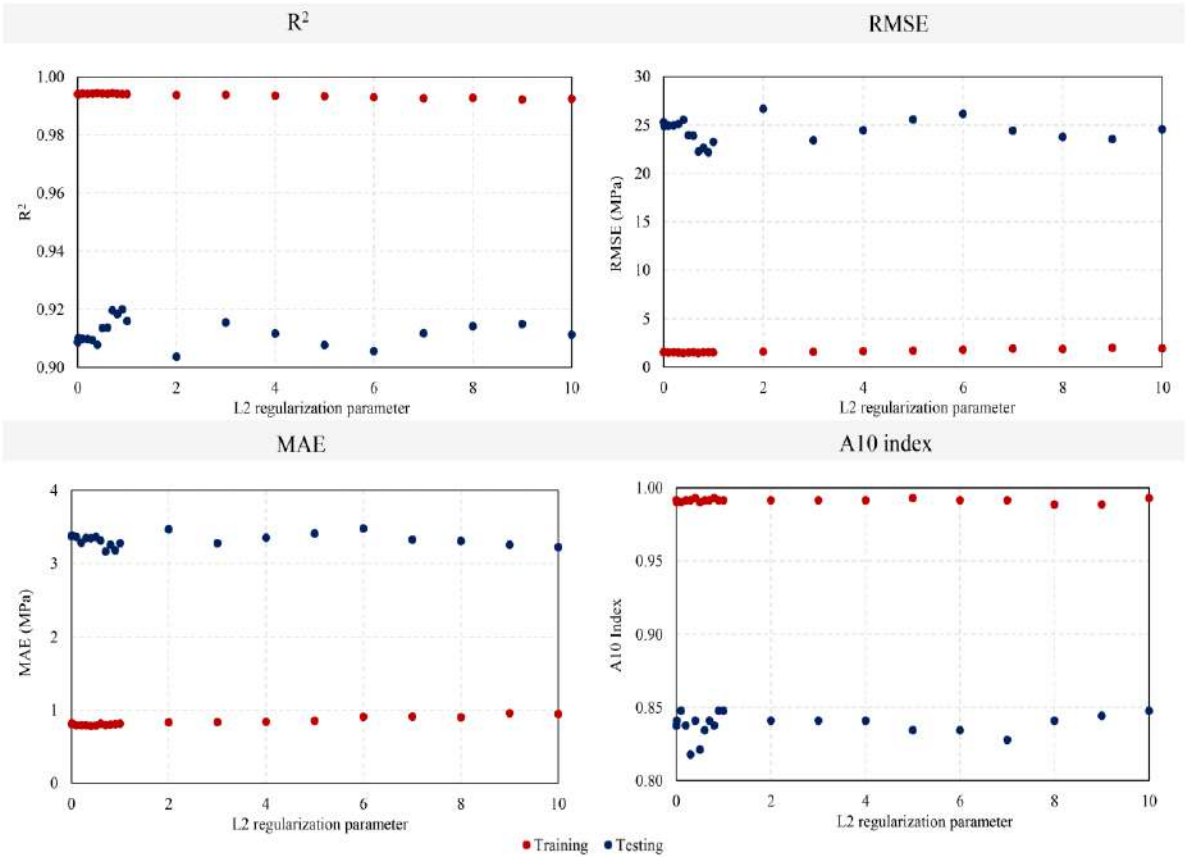

Fig. 8. Impact of the L2 regularization parameter on the HGBoost quality

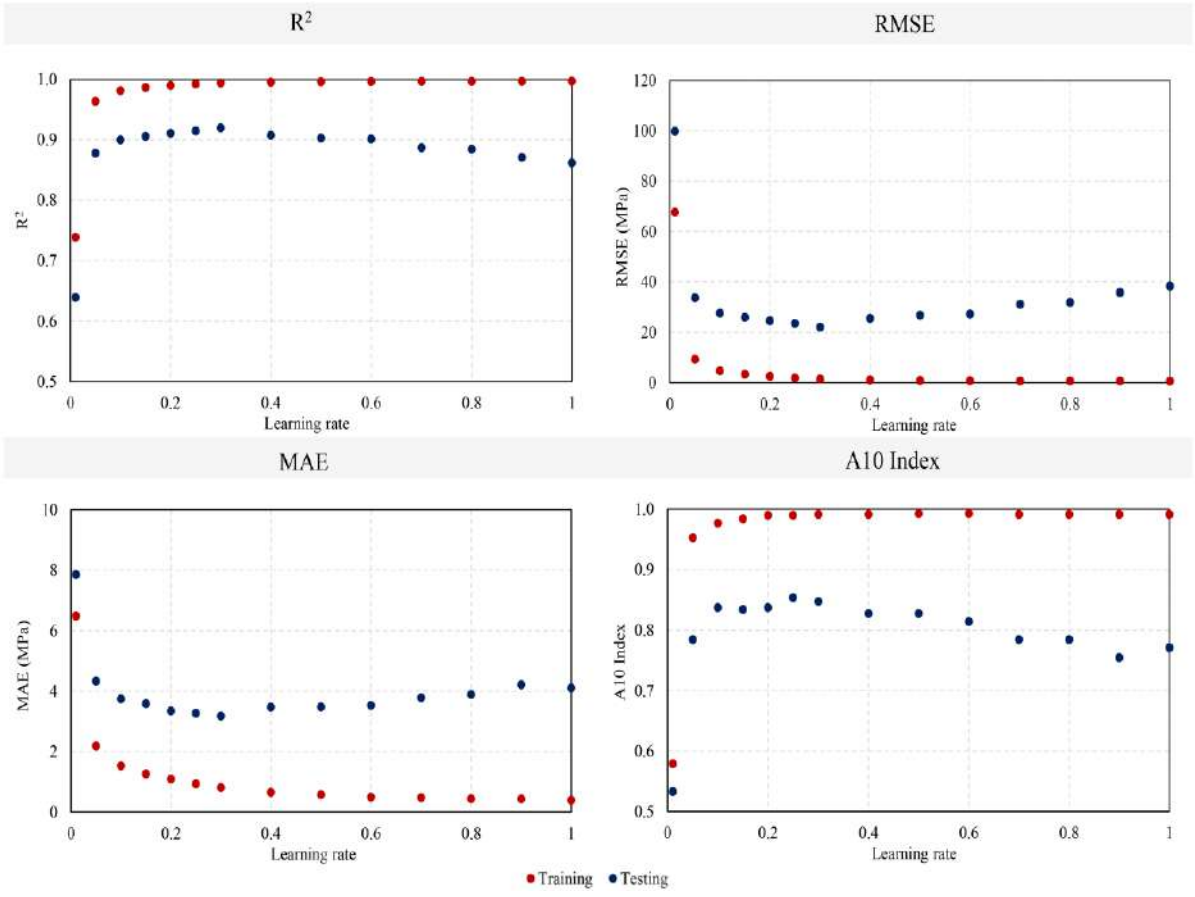

Fig. 9. Influence of learning rate in HGBoost on the performance of the model

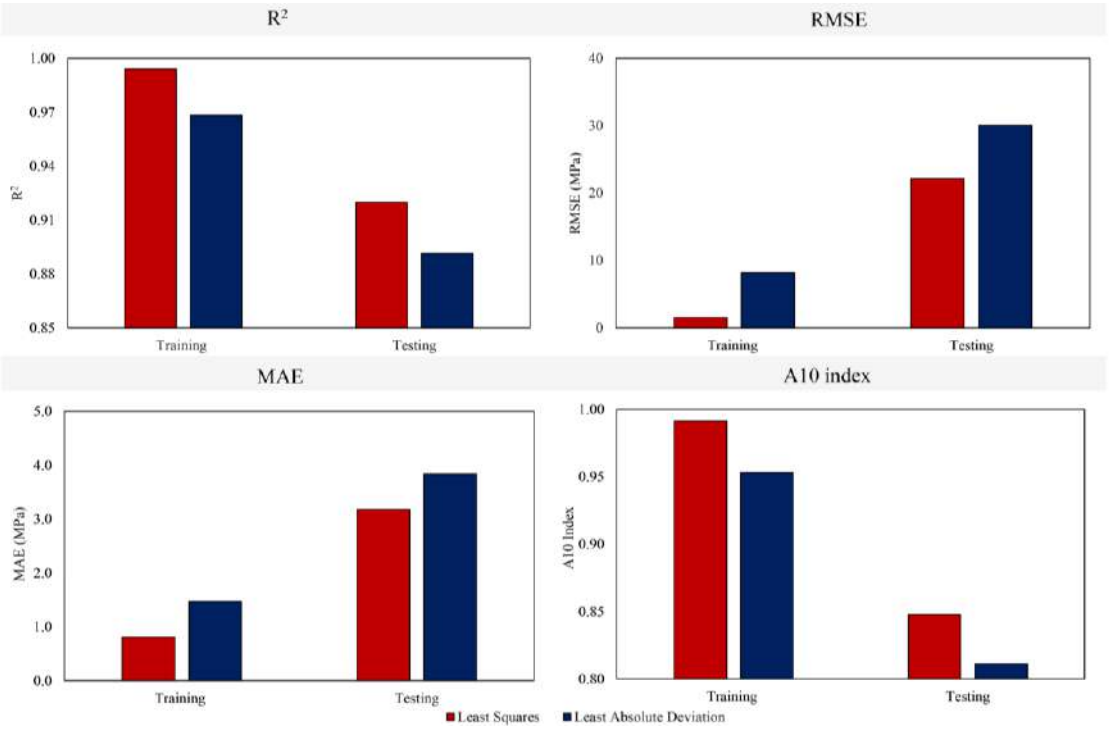

Fig. 10. Influence of the type of loss function on the performance of the HGBoost model

As mentioned previously, several machine learning and statistical models were proposed for predicting the compressive strength of concrete mixtures. However, the literature still lacks a study that evaluates the accuracy of HGBoost models. Therefore, a comparative assessment of boosting algorithms in machine learning will be presented. The estimation results, Figure 11, show that the AdaBoost model gives a minimal performance. At the same time, SGBoost, HGBoost, and XGBoost approaches yielded similar outcomes. This observation is further illustrated in the residual plot as shown in Figure 12a. As a matter of fact, the box plots in Figure 12b highlights that for the case of the training dataset, the average, median, first quartile, and third quartile were all predicted accurately in all models. On the other hand, these values were best estimated in the testing dataset by the HGBoost model followed by the SGBoost and XGBoost. Indeed, the capabilities of the methods are not affected by the value of the compressive strength in which the models revealed good efficiency for both low and high strength mixtures.

Table 2 represents the fitting rates and the errors values of the addressed algorithm. In general, the coefficient of determination for the training dataset is higher than that of the testing data. The performance of the AdaBoost technique in the testing case has dropped significantly compared to the training set directed towards an overfitting issue. Also, the A20 index of HGBoost has reduced by 4.9% and 6% against SGBoost and XGBoost models, respectively, while the AdaBoost generates the lowest A20 index and highest testing errors. On the other hand, the HGBoost achieves higher testing errors than the SGBoost and XGBoost because the latter techniques use the exact greedy tree method while the HGBoost adopts an optimized approximate one.

Table 2. Performance assessment of the models

Model	Training				Testing			
	R^2	RMSE	MAE	A20 Index	R^2	RMSE	MAE	A20 Index
AdaBoost	1.00	1.41	0.54	0.97	0.87	35.54	4.17	0.78
SGBoost	1.00	0.54	0.22	0.99	0.92	23.01	2.96	0.88
HGBoost	0.99	1.51	0.79	0.99	0.91	24.97	3.28	0.84
XGBoost	0.99	1.60	0.84	1.00	0.93	20.61	2.94	0.89

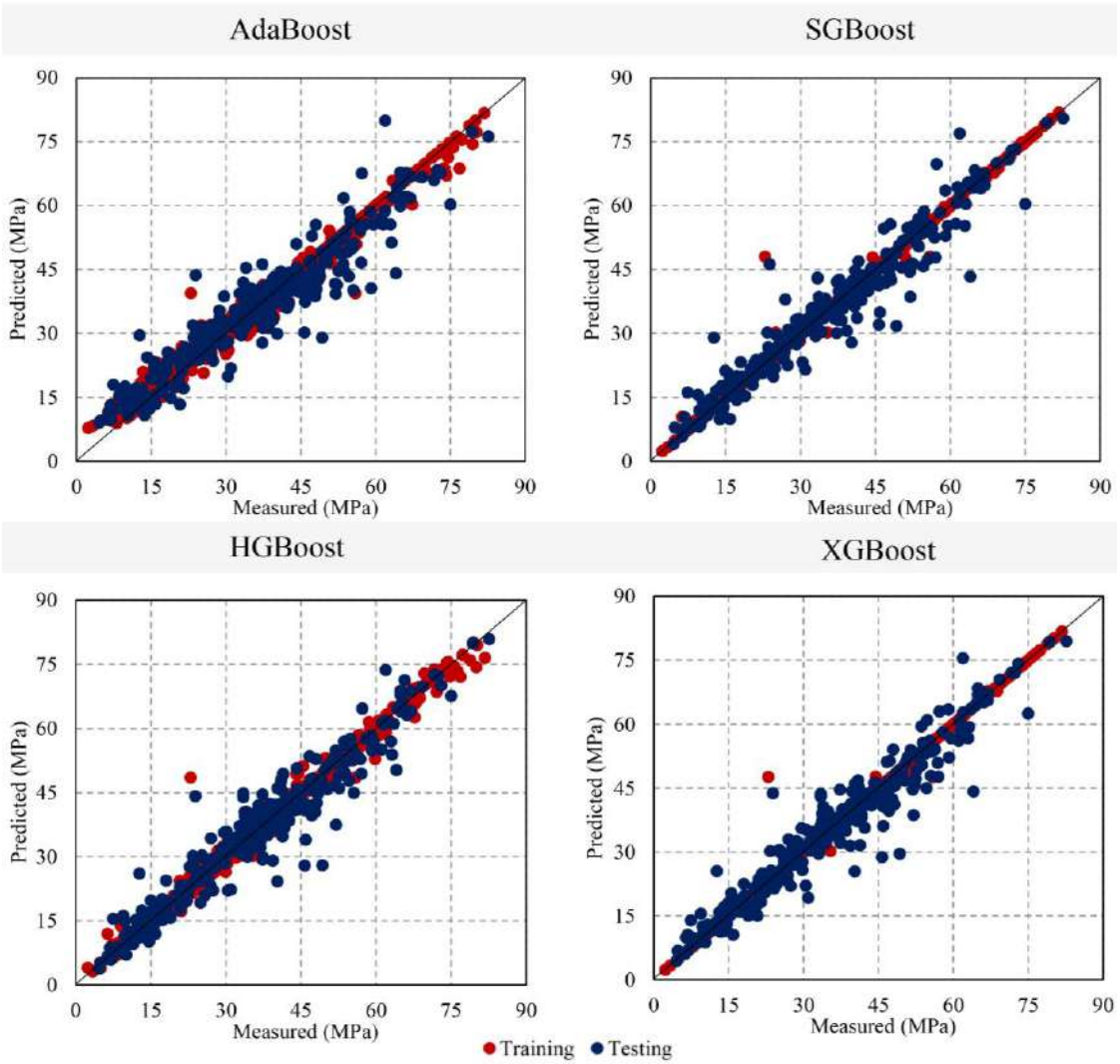

Fig. 11. Compressive strength estimation using boosting technique

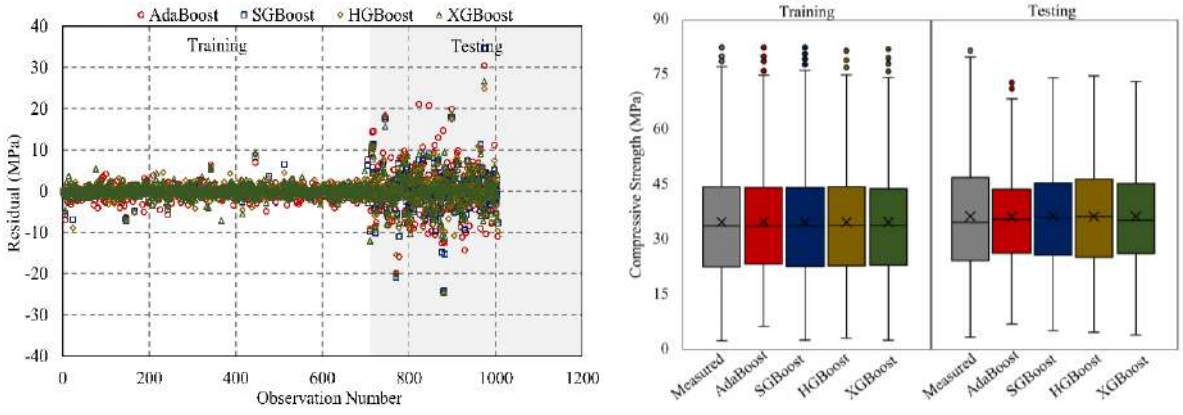

Fig. 12. a) Residual plot; and b) Box plots of the machine learning techniques

4. Conclusions

Traditionally, decision-makers have been mainly concerned with meeting needed objectives for specific concrete characteristics, such as obtaining a defined early-age compressive strength besides keeping a workable concrete when developing concrete mixtures. At present, this situation has changed after emerging modern technologies that offer advanced methods to quantify and fine-tune the

properties of concrete. This investigation is primarily focused on using machine learning in concrete mixture design and developing a helpful tool to be applied in engineering practices. It evaluated the quality of histogram-based gradient boosting algorithms in estimating the compressive strength of the concrete mix. The performance analysis of the HGBoost model indicated that it returns high accuracy, but a slight reduction was produced compared to SGBoost and XGBoost in the testing case, as previously stated. Further works are still needed in this field to propose more generalized models capable of estimating other properties of concrete, such as its durability and dynamic behavior. In addition, it is crucial to report the performance of other newly developed models in the rapidly growing field of machine learning, including those approaches that can be built to serve specified tasks.

5. References

Ahmad, A., Ahmad, W., Aslam, F. and Joyklad, P. (2022). "Compressive strength prediction of fly ash-based geopolymer concrete via advanced machine learning techniques", *Case Studies in Construction Materials*, 16(1 June), e00840, https://doi.org/10.1016/j.cscm.2021.e00840.

Al Houri, A., Habib, A., Elzokra, A. and Habib, M. (2020). "Tensile testing of soils: History, equipment and methodologies", *Civil Engineering Journal*, 6(3), 591-601, https://doi.org/10.28991/cej-2020-03091494.

Amidi, Y., Nazari, B., Sadri, S. and Yousefi, A. (2021). "Parameter estimation in multiple dynamic synaptic coupling model using Bayesian Point Process State-Space Modeling framework", *Neural Computation*, 33(5), 1269-1299, https://doi.org/10.1162/neco_a_01375.

Asteris, P.G., Skentou, A.D., Bardhan, A., Samui, P. and Pilakoutas, K. (2021). "Predicting concrete compressive strength using hybrid ensembling of surrogate machine learning models", *Cement and Concrete Research*, 145(1 July), 106449, https://doi.org/10.1016/j.cemconres.2021.106449.

Cai, J., Li, X., Tan, Z. and Peng, S. (2021). "An assembly-level neutronic calculation method based on LightGBM algorithm", *Annals of Nuclear Energy*, 150(1 January), 107871, https://doi.org/10.1016/j.anucene.2020.107871.

Chaabene, W.B., Flah, M. and Nehdi, M.L. (2020). "Machine learning prediction of mechanical properties of concrete: Critical review", *Construction and Building Materials*, 260(10 November), 119889, https://doi.org/10.1016/j.conbuildmat.2020.119889.

Chen, T., and Guestrin, C. (2016). "Xgboost: A scalable tree boosting system", *Proceedings of the 22nd ACM Sigkdd International Conference on Knowledge Discovery and Data Mining* (pp. 785-794), San Francisco, California, USA.

Chopra, P., Sharma, R.K. and Kumar, M. (2016). "Prediction of compressive strength of concrete using artificial neural network and genetic programming", *Advances in Materials Science and Engineering*, 2016(10 January), Article ID 7648467, https://doi.org/10.1155/2016/7648467.

DeRousseau, M.A., Kasprzyk, J.R. and Srubar III, W.V. (2018). "Computational design optimization of concrete mixtures: A review", *Cement and Concrete Research*, 109(1 July), 42-53, https://doi.org/10.1016/j.cemconres.2018.04.007.

Drucker, H. (1997). Improving regressors using boosting techniques", 97th International Conference on Machine Learning (ICML), Vol. 97, pp. 107-115, https://doi.org/10.1155/2016/7648467.

Elzokra, A., Al Houri, A., Habib, A., Habib, M. and Malkawi, A.B. (2020). "Shrinkage behavior of conventional and nonconventional concrete: A review", *Civil Engineering Journal*, 6(9), 1839-1851, https://doi.org/10.28991/cej-2020-03091586.

Farooq, F., Nasir Amin, M., Khan, K., Rehan Sadiq, M., Faisal Javed, M., Aslam, F. and Alyousef, R. (2020). "A comparative study of random forest and genetic engineering programming for the prediction of compressive strength of high strength concrete (HSC)", *Applied Sciences*, 10(20), 7330, https://doi.org/10.3390/app10207330.

Feng, D.C., Liu, Z.T., Wang, X.D., Chen, Y., Chang, J.Q., Wei, D.F. and Jiang, Z.M. (2020). "Machine learning-based compressive strength prediction for concrete: An adaptive boosting approach", *Construction and Building Materials*, 230(10 January), 117000, https://doi.org/10.1016/j.conbuildmat.2019.117000.

Freund, Y., and Schapire, R.E. (1997). "A decision-theoretic generalization of on-line learning and an application to boosting", *Journal of Computer and System Sciences*, 55(1), 119-139, https://doi.org/10.1006/jcss.1997.1504.

Gholamzadeh Chitgar, A. and Berenjian, J. (2021). "Performance evaluation of RBF networks with

various variables to forecast the properties of SCCs", *Civil Engineering Infrastructures Journal*, 54(1), 59-73.

Guryanov, A. (2019). "Histogram-based algorithm for building gradient boosting ensembles of piecewise linear decision trees", *International Conference on Analysis of Images, Social Networks and Texts* (pp. 39-50), Springer, Cham, https://doi.org/10.1007/978-3-030-37334-4_4.

Habib, A., Houri, A.A., Habib, M., Elzokra, A. and Yildirim, U. (2021). "Structural performance and Finite Element modeling of roller compacted concrete dams: A review", *Latin American Journal of Solids and Structures*, 18(13 May), https://doi.org/10.1590/1679-78256467.

Habib, A. and Yildirim, U. (2021). "Prediction of the dynamic properties in rubberized concrete", *Computers and Concrete*, 27(3), 185-197, https://doi.org/10.12989/cac.2021.27.3.185.

Han, Q., Gui, C., Xu, J. and Lacidogna, G. (2019). "A generalized method to predict the compressive strength of high-performance concrete by improved random forest algorithm", *Construction and Building Materials*, 226(30 November), 734-742, https://doi.org/10.1016/j.conbuildmat.2019.07.315.

Kaloop, M.R., Kumar, D., Samui, P., Hu, J.W. and Kim, D. (2020). "Compressive strength prediction of high-performance concrete using gradient tree boosting machine", *Construction and Building Materials*, 264(20 December), 120198, https://doi.org/10.1016/j.conbuildmat.2020.120198.

Ke, G., Meng, Q., Finley, T., Wang, T., Chen, W., Ma, W., Ye, Q. and Liu, T.Y. (2017). "Lightgbm: A highly efficient gradient boosting decision tree", *NeurIPS Proceedings, Advances in Neural Information Processing Systems (NIPS 2017)*, 30, 3146-3154.

Ke, X., and Duan, Y. (2021). "A Bayesian machine learning approach for inverse prediction of high-performance concrete ingredients with targeted performance", *Construction and Building Materials*, 270(8 February), 121424, https://doi.org/10.1016/j.conbuildmat.2020.121424.

Khademi, F., Akbari, M., Jamal, S.M. and Nikoo, M. (2017). "Multiple linear regression, artificial neural network, and fuzzy logic prediction of 28 days compressive strength of concrete", *Frontiers of Structural and Civil Engineering*, 11(1), 90-99, https://doi.org/10.1007/s11709-016-0363-9.

Kim, B., Lee, D. E., Hu, G., Natarajan, Y., Preethaa, S. and Rathinakumar, A.P. (2022). "Ensemble machine learning-based approach for predicting of FRP-concrete interfacial bonding", *Mathematics*, 10(2), 231, https://doi.org/10.3390/math10020231.

Lee, S.C. (2003). "Prediction of concrete strength using artificial neural networks", *Engineering Structures*, 25(7), 849-857, https://doi.org/10.1016/S0141-0296(03)00004-X.

Loh, W.Y. (2011). "Classification and regression trees", *Wiley Interdisciplinary Reviews: Data Mining and Knowledge Discovery*, 1(1), 14-23.

Lu, H., Karimireddy, S.P., Ponomareva, N. and Mirrokni, V. (2020). "Accelerating gradient boosting machines", *International Conference on Artificial Intelligence and Statistics,* (pp. 516-526), PMLR.

Malkawi, A.B., Habib, M., Aladwan, J. and Alzubi, Y. (2020). "Engineering properties of fibre reinforced lightweight geopolymer concrete using palm oil biowastes", *Australian Journal of Civil Engineering*, 18(1), 82-92, https://doi.org/10.1080/14488353.2020.172195.

Mease, D. and Wyner, A.J. (2008). "Evidence contrary to the statistical view of boosting", *Journal of Machine Learning Research*, 9, 131- 156.

Nguyen-Sy, T., Wakim, J., To, Q.D., Vu, M.N., Nguyen, T.D. and Nguyen, T.T. (2020). "Predicting the compressive strength of concrete from its compositions and age using the extreme gradient boosting method", *Construction and Building Materials*, 260(10 November), 119757, https://doi.org/10.1016/j.conbuildmat.

Ni, H.G. and Wang, J.Z. (2000). "Prediction of compressive strength of concrete by neural networks", *Cement and Concrete Research*, 30(8), 1245-1250, https://doi.org/10.1016/S0008-8846(00)00345-8.

Salimbahrami, S.R. and Shakeri, R. (2021). "Experimental investigation and comparative machine-learning prediction of compressive strength of recycled aggregate concrete", *Soft Computing*, 25(2), 919-932, https://doi.org/10.1007/s00500-021-05571-1.

Shepovalov, M. and Akella, V. (2020). "FPGA and GPU-based acceleration of ML workloads on Amazon cloud-A case study using gradient boosted decision tree library", *Integration*, 70(1 January), 1-9, https://doi.org/10.1016/j.vlsi.2019.09.007.

Topcu, I.B. and Sarıdemir, M. (2008). "Prediction of compressive strength of concrete containing fly ash using artificial neural networks and fuzzy logic", *Computational Materials Science*, 41(3), 305-311, https://doi.org/10.1016/j.commatsci.2007.04.009.

Pedregosa, F., Varoquaux, G., Gramfort, A., Michel, V., Thirion, B., Grisel, O., Blondel, M., Prettenhofer, P., Weiss, R., Dubourg, V. and

Vanderplas, J. (2011). "Scikit-learn: Machine learning in Python", *The Journal of Machine Learning Research*, 12(1 November), 2825-2830.

Wardeh, G., Ghorbel, E. and Gomart, H. (2015). "Mix design and properties of recycled aggregate concretes: applicability of Eurocode 2", *International Journal of Concrete Structures and Materials*, 9(1), 1-20, https://doi.org/10.1007/s40069-014-0087-y.

Yeh, I.C. (1998). "Modeling of strength of high-performance concrete using artificial neural networks", *Cement and Concrete Research*, 28(12), 1797-1808, https://doi.org/10.1016/j.commatsci.2007.04.009.

Yeh, I.C. (2006). "Analysis of strength of concrete using design of experiments and neural networks", *Journal of Materials in Civil Engineering*, 18(4), 597-604, https://doi.org/10.1061/(ASCE)0899-1561(2006)18:4(597).

Yeh, I.C. (2007). "Computer-aided design for optimum concrete mixtures", *Cement and Concrete Composites*, 29(3), 193-202, https://doi.org/10.1016/j.cemconcomp.2006.11.001.

Ziolkowski, P. and Niedostatkiewicz, M. (2019). "Machine learning techniques in concrete mix design", *Materials*, 12(8), 1256, https://doi.org/10.3390/ma12081256.

Civil Engineering Infrastructures Journal 2023, 56(1): 173-192
DOI: 10.22059/CEIJ.2022.339138.1819

RESEARCH PAPER

Development of Bearing Capacity Equation for Rectangular Footing under Inclined Loading on Layered Sand

Panwar, V.[1]* and Dutta, R.K.[2]

[1] Ph.D. Candidate, Department of Civil Engineering, National Institute of Technology Hamirpur, Hamirpur, Himachal Pradesh, India.
[2] Professor, Department of Civil Engineering, National Institute of Technology Hamirpur, Hamirpur, Himachal Pradesh, India.

Received: 21 Feb. 2022; Revised: 15 May 2022; Accepted: 15 Jun. 2022

ABSTRACT: This study provides an equation of bearing capacity for a rectangular footing placed on dense sand overlying loose sand and subjected to inclined concentric loading using the limit equilibrium followed by projected area method. The parameters varied were thickness ratio (0.00 to 2.00) of the upper dense sand layer, embedment ratio (0 to 2), friction angle of upper dense (41° to 46°) sand and lower loose (31° to 36°) sand layer, and applied load inclination (0° to 30°) for the parametric study. The highest and lowest increase in the bearing capacity were observed for a friction angle combination of 46°-36° and 41°-31°, respectively, at different thickness ratios. The bearing capacity obtained from the proposed equation was approximately 4.97 and 10.5 times its initial value at embedment ratios of 1 and 2, respectively. Bearing capacity was reduced by 20.55%, 54.58% and 87.90% for load inclinations of 5°, 15°, and 30° for friction angles of upper dense and lower loose sand layer combinations of 46° and 36° and at a thickness ratio of 2. The bearing capacity obtained from the proposed equation decreased by 99.89%, 66.04%, and 61.5% as the load inclination increased from 0° to 30° for embedment ratios of 0, 1, and 2. With respect to finite element results, the average deviation of the bearing capacity obtained from the proposed equation at embedment ratios 0, 1, and 2 was 14.56%, 18.71% and 23.56%, respectively. The proposed bearing capacity equation produced results that were consistent with those reported in the literature, with an average deviation of 10.71%.

Keywords: Bearing Capacity, Inclined Loading, Layered Sand, Projected Area Approach, Rectangular Footing.

1. Introduction

The load of the superstructure through the footing is shifted to the soil underneath it. The depth-to-width ratio determines whether a footing is shallow or deep. The load must be transferred underneath the footing in a way that avoids settling and shear failure. In the literature, a number of studies have been reported by the researchers (Meyerhof, 1974; Meyerhof and Hanna, 1978; Hanna, 1981, 1982, 1987; Oda and Win, 1990; Michalowski and Shi, 1995; Kenny and Andrawes, 1997;

* Corresponding author E-mail: vipsarahan17@gmail.com

Okamura et al., 1998; Merifield et al., 1999; Shiau et al., 2003; Farah, 2004; Massih et al., 2005; Kumar et al., 2007; Johnson et al., 2015; Mosadegh and Nikraz, 2015; Rao et al., 2015; Ibrahim, 2016; Khatri et al., 2017a; Misir and Laman, 2017; Saha et al., 2018; Reddy and Kumar, 2018; Eshkevari et al., 2018; Eshkevari et al., 2019; Zheng et al., 2019; Biswas and Krishna, 2019; Ullah et al., 2020; Chwała and Puła, 2020; Al-Ameri et al., 2020; Benmoussa et al., 2021; Mandeel et al., 2021; Panwar and Dutta, 2021; Singh and Rao, 2021; Nujid et al., 2021; Ibrahim et al., 2021; Das and Khatri, 2021; Gupta and Mital, 2021; Hajitaheriha et al., 2021 and Das et al., 2022) to evaluate the bearing capacity of footings on single layer or layered soils and subjected to vertical or inclined loads.

Meyerhof (1974), Khatri et al. (2017a), Eshkevari et al. (2019) and Das and Khatri (2021) investigated the bearing capacity of strip and circular footing on layered soil (dense sand over loose sand) under vertical load. Further, Oda and Win (1990), Meyerhof (1974), Michalowski and Shi (1995), Okamura et al. (1998), Farah (2004), Kumar et al. (2007), Mosadegh and Nikraz (2015), Misir and Laman (2017), Reddy and Kumar (2018), Saha et al. (2018), Biswas and Krishna (2019), Al-Ameri et al. (2020), Chwała and Puła (2020) and Nujid et al. (2021) studied the bearing capacity of the strip, circular and square/rectangular footing on layered soil (dense sand over soft clay) under vertical load. The bearing capacity of the strip, circular and rectangular footing on layered soil (stiff clay over soft clay, stiff over soft clay and stiff clay over loose sand) was conducted by Rao et al. (2015), Ullah et al. (2020), Benmoussa et al. (2021) and Ibrahim et al. (2021) under vertical loading. In addition, there were studies (Meyerhof and Hanna, 1978; Hanna, 1981, 1982; Massih et al., 2005; Mosadegh and Nikraz, 2015) on bearing capacity for strip and circular footings on layered soil (dense sand over loose sand; loose sand over dense sand; and dense sand over soft clay) available in the literature. Under vertical (Meyerhof, 1974; Kenny and Andrawes, 1997; Okamura et al., 1998) and inclined (Meyerhof and Hanna, 1978) loads, the limit equilibrium approach was employed to investigate the bearing capacity of the strip and circular footings.

Using the punching shear coefficient for the vertical and inclined loading, an equation for the ultimate bearing capacity of strip and circular footings on layered soil (dense sand over loose sand) was suggested by Meyerhof (1974) and Meyerhof and Hanna (1978). Comparison of the findings of Meyerhof (1974), Meyerhof and Hanna (1978) and Kenny and Andrawes (1997) was attempted by Shoaei et al. (2012) and concluded that the findings of Meyerhof (1974) and Meyerhof and Hanna (1978) overestimate the bearing capacity at greater depths. Michalowski and Shi (1995) used a Kinematic approach for estimation of average pressure below the strip footing under vertical loading. Projected area approach was followed by Kenny and Andrawes (1997), Okamura et al. (1998) and Farah (2004) to estimate the bearing capacity of the strip, circular and square/rectangular footing on layered soil under vertical loading.

In order to predict the ultimate bearing capacity for strip, circular and square/rectangular footing on layered soil (dense sand over soft clay) using punching shear coefficients, load dispersion angle and soil properties under vertical loading, an equation was proposed by Farah (2004) and it was found to overestimate the bearing capacity as compared to previous studies Meyerhof (1974). Further, the researchers Misir and Laman (2017) and Al-Ameri et al. (2020) developed the bearing capacity equation using regression analysis based on the limit equilibrium analysis and finite element analysis for circular and square footing. The results were in a very good agreement to predict the bearing capacity when compared with the past works. Recently Finite Element modelling was used to assess the bearing capacity of strip

(Hanna, 1987; Mosadegh and Nikraz, 2015; Khatri et al., 2017a; Eshkevariet al., 2018; Das and Khatri, 2021; Nujid et al., 2021), circular (Khatri et al., 2017a; Reddy and Kumar, 2018; Singh and Rao, 2021; Das and Khatri, 2021; Benmoussa et al., 2021), square (Saha et al., 2018; Mandeel et al., 2021) and rectangular (Ullah et al., 2020; Panwar and Dutta, 2021; Ibrahim et al., 2021) footings on layered soil (dense sand over loose sand, dense sand over soft clay, soft clay over dense sand and soft clay over stiff clay), respectively.

Gupta and Mital (2021) investigated the effect of multilayer of geogrid reinforced sand on the bearing capacity of rectangular footing under inclined as well as eccentric loading experimentally. The effect of various parameters such as number of reinforced layers, eccentricity and load inclination were investigated using laboratory tests and finite element analysis. The ultimate bearing capacity observed to be increased with the increase in geogrid reinforced layers. Das et al. (2022) investigated the effect of geogrid sheet reinforced at the interface of dense sand and loose sand for the ultimate bearing capacities of embedded strip and circular footing and concluded that the effect of geogrid sheet was marginal when compared with the ultimate bearing capacity of unreinforced foundation.

Using the Finite Element analysis, Hajitaheriha et al. (2021) examined the impact on drag stress of the circular and square section piles placed in soft clay overlaid on dense sand. In the circular sections, the value of the drag load was always greater when compared with the results for the square-shaped sections pile. The ultimate bearing capacity was calculated using numerical and experimental methods in all the above studies. However, no equation of ultimate bearing capacity for the rectangular footing under inclined loading has been published since then, especially on layered soil (dense sand over loose sand). As a result, using the punching shear mechanism and limit equilibrium methodology, an equation for the bearing capacity of rectangular footing on dense sand underlain by loose sand under inclined loading was derived in the current study. To get a fair estimate of bearing capacity, the load spread mechanism in the upper dense sand layer was selected using finite element analysis. The bearing capacity of the rectangular footing over layered sand was calculated for various friction angles of upper dense and lower loose sand layer, load inclination and varied thickness of upper dense sand layer at different footing depths. The findings were compared to those found in the literature.

2. Methodology

Following the limit equilibrium approach reported by Meyerhof and Hanna (1978), the load from the footing was assumed to spread through the upper dense sand to the lower loose sand. The failure surface for rectangular footing under load (q_u) with load inclination (θ) is shown in Figure 1a. The footing is placed at a depth (D) below the surface of ground level and the passive pressure (Pp) was assumed to act on the failure surface by making angle δ normal to the failure surface. The failure was assumed to occur at the interface of the upper dense and lower loose sand layer. Figure 1b shows a plan view of the assumed failure mechanism under inclined loading (q_u) for the rectangular footing with load dispersion angle $\alpha 1$ and $\alpha 2$ across the width and $\alpha 3$ and $\alpha 4$ across the length of the footing. The assumptions made for mathematical derivation are as follows.

- The footing is assumed to have rigid and rough base lying at some depth (D) in upper dense sand layer.
- The sand above the footing base has negligible shear strength and it acts as a surcharge load.
- The interface of the layered sand and the ground surface is assumed to be horizontal.
- No effect of the water table on the

ultimate bearing capacity of the rectangular footing was considered in the analysis. It was assumed that the water table is at great depth below the lower loose sand layer.

- The upper dense and lower loose sand layer were supposed to be fully drained with friction angle of φ_1 and φ_2 respectively.
- Full mobilization of the shear strength of the upper dense and lower loose sand is assumed along the failure surface.
- Applied load (q_u) is acting at the centre of the rectangular footing at a load inclination (θ).
- Passive pressure generated on all sides of the projected area was assumed to be equal as per Meyerhof and Hanna (1978).

The stress distribution under inclined loading is shown in Figure 2. If stress (σ) develops on the surface of the footing, it reflects a slight increase in stress ($\Delta\sigma$) at the layered sand interface under inclined loading. For the derivation of the equation based on the above, a small strip (abcdefgh) of thickness (ΔZ) at a distance Z from the footing base was considered as shown in the Figure 2. For the analysis, the free body diagram is shown in Figures 3a and 3b along width (abef) and length (bcfg) of a rectangular footing for the small strip of thickness (ΔZ). The passive pressure (ΔPp) acted on the failure surface at an angle δ normal of failure surface (ae, bf, cg). It is pertinent to mention here that the dimensions $L1$ and $W1$ are the length and width of the strip of thickness (ΔZ) at a distance Z below the base of the footing.

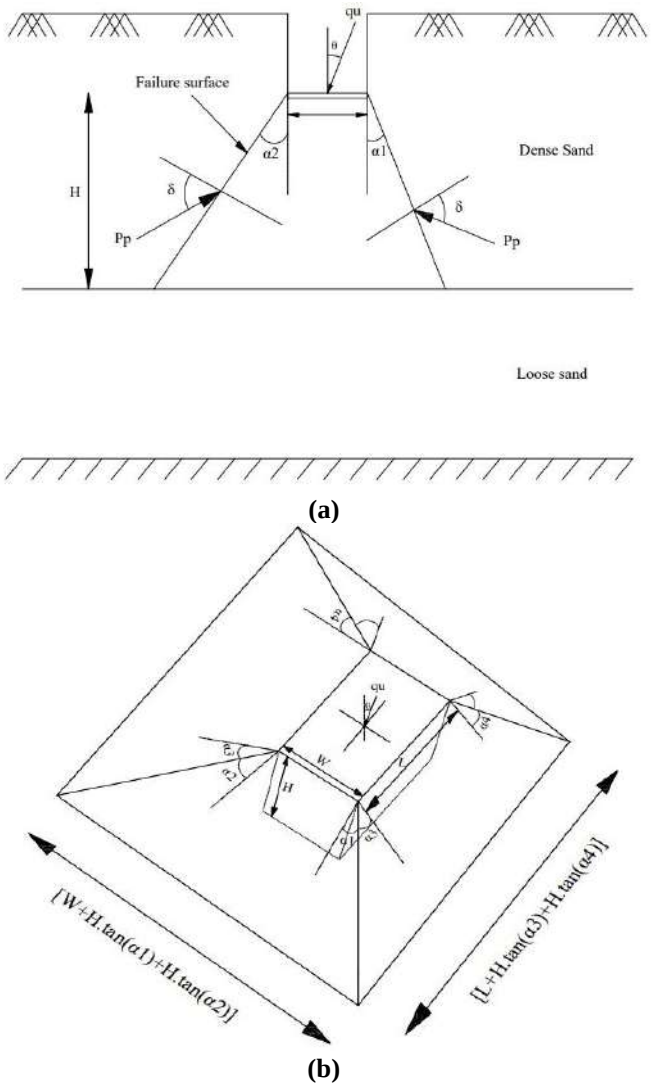

Fig. 1. Assumed failure surface for rectangular footing under inclined loading: a) Alevation; and b) Plan view

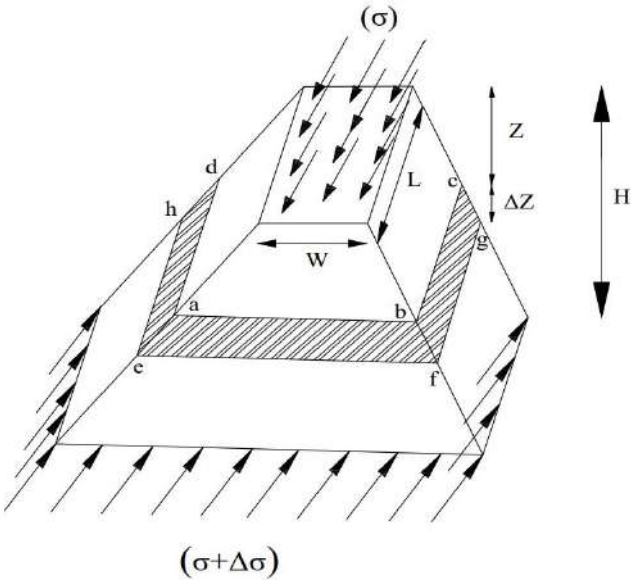

Fig. 2. Stress distribution under inclined loading

Table 1. Variation of load spread angle with thickness ratio and load inclination at different embedment ratio

H/W	θ (Deg.)	φ_2/φ_1	α at D/W=0			α at D/W=1			α at D/W=2		
			α_{01}	α_{02}	α_{03}	α_{11}	α_{12}	α_{13}	α_{21}	α_{22}	α_{23}
0.0			37	37	15	12	12	12	11	11	11
0.5			32	32	12	10	10	11	10.5	10.5	10
1.0			28	28	10	8	8	9	10	10	9
1.5	0	0.756	32	32	11	7	7	8	9	9	9
2.0			35	35	12	13	13	11	11	11	10
0.0			20	46	14	8	19	13	7	17	10
0.5			17	43	12	5	18	11	5.5	14	9
1.0	5	0.761	14	41	11	4	10	10	4	12	8
1.5			12	37	12	3	15	10	3	11	7.5
2.0			27	40	13	6	16	12	5	12	10
0.0			5	61	12	-4	26	13	-4	21.5	12
0.5			2	57	10	-3.5	18	11	-2	17.5	11
1.0	10	0.767	-1	51	9.5	-3	16	10	0	15	10
1.5			-4	48	9	0	19	12	2	17.5	11
2.0			-5	43	9	1	27	12.5	3	21	12
0.0			-32	72	13	-10	31	12	-10	28.9	11
0.5			-29	64	12	-8	29	11	-9	27	10
1.0	15	0.772	-24	57	11	-5	27	10	-8.5	23	10
1.5			-20	51	9	-2	24	9	-10	26	10
2.0			-29	62	10	-4	33	13	-11	30	11
0.0			-54	81	14	-21	45	12	-17.5	39	14
0.5			-52	73	12	-19	41	10	-15	33.5	13
1.0	20	0.777	-45	71	11	-15	38	9	-12.5	30	10
1.5			-48	73	12	-18	43	11	-13	32.3	11.5
2.0			-53	80	13	-20	47	12	-13.5	37	13
0.0			-70	90	14	-32	57	14	-26	51	15
0.5			-60	90	13	-29	51	12	-23	48	14
1.0	25	0.782	-58	90	10	-28	47	11	-22	37	12
1.5			-69	90	12	-24	43	12	-17.5	45	13
2.0			-69	90	13	-29	54	15	-20	56	14
0.0			-80	90	14	-42	74	13	-40	61	12
0.5			-75	90	13	-34	61	10	-37	56	12
1.0	30	0.756	-69	90	11	-29	55	10	-26	49	9
1.5			-68	90	10	-30	58	11	-28	55	11
2.0			-71	90	13	-44	75	12.5	-33	59	13

Table 2. Comparison of results with finite element analysis

H/W	D/W	φ_1, φ_2 (Degree)	Dimensionless bearing capacity ($q_{ult}/\gamma_1 W$)					
			θ =0°		θ =15°		θ =30°	
			Present equation	F.E.M. analysis	Present equation	F.E.M. analysis	Present equation	F.E.M. analysis
0.00			7.50	10.21	1.99	6.78	0.008	1.025
0.50			21.93	14.06	11.53	8.72	3.74	5.14
1.00	0	41,31	39.88	21.27	20.91	13.84	3.74	9.75
1.50			51.99	33.47	20.91	16.42	3.74	9.75
2.00			51.99	38.18	20.91	22.44	3.74	9.75
0.00			11.01	15.48	3.27	9.59	0.09	5.00
0.50			30.39	25.67	16.09	12.91	7.08	7.69
1.00	0	43,33	54.32	53.91	31.53	20.07	7.28	12.33
1.50			79.69	85.91	33.78	26.67	7.28	17.43
2.00			79.69	91.97	33.78	40.27	7.28	17.43
0.00			19.27	29.77	6.55	14.82	0.53	6.20
0.50			49.84	53.88	26.58	28.39	11.55	12.28
1.00	0	46,36	87.82	102.45	50.54	49.83	18.5	18.48
1.50			130.75	159.29	69.47	74.75	18.5	28.72
2.00			152.98	167.29	69.47	97.79	18.5	28.72
0.00			37.34	44.25	22.15	33.83	12.68	17.66
0.50			67.93	65.93	40.99	51.88	22.73	23.75
1.00	1	41,31	100.49	85.78	60.28	60.22	31.91	34.83
1.50			134.55	140.33	79.84	69.52	40.78	45.12
2.00			170.02	157.52	99.62	93.39	49.51	56.81
0.00			51.61	52.72	30.66	37.85	17.25	21.19
0.50			92.62	83.49	55.54	60.04	30.21	34.78
1.00	1	43,33	136.44	131.39	81.08	77.99	42.15	44.83
1.50			182.38	177.51	106.98	108.87	53.72	58.93
2.00			226.24	218.28	132.47	138.62	65.83	74.29
0.00			83.44	91.34	49.78	46.11	27.47	34.67
0.50			149.43	156.93	88.64	76.57	46.71	52.34
1.00	1	46,36	220.45	234.01	128.73	125.11	64.66	70.47
1.50			295.30	358.29	169.46	177.29	82.06	97.99
2.00			373.65	410.80	210.70	220.67	99.23	125.70
0.00			75.75	74.29	48.25	63.03	29.16	46.78
0.50			122.53	98.60	76.81	76.55	45.29	56.14
1.00	2	41,31	168.91	153.45	104.51	104.96	59.94	68.16
1.50			214.69	198.50	131.40	145.21	73.49	79.11
2.00			259.30	244.65	157.35	175.46	86.26	97.39
0.00			104.21	83.72	66.38	70.38	39.74	56.78
0.50			166.61	131.40	103.60	93.37	59.63	66.63
1.00	2	43,33	228.48	201.40	139.57	152.09	77.48	85.68
1.50			289.44	251.91	174.30	171.05	93.93	111.60
2.00			348.52	338.19	207.60	199.77	109.41	131.39
0.00			167.43	131.44	106.76	115.93	63.23	80.16
0.50			268.016	252.68	164.41	146.52	91.21	100.64
1.00	2	46,36	367.92	384.29	219.82	233.96	116.00	128.52
1.50			466.24	508.37	272.96	321.40	138.85	157.46
2.00			561.00	659.83	323.48	412.34	160.47	218.31

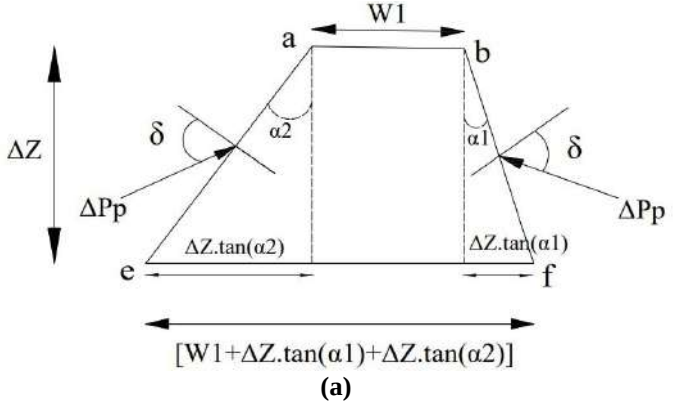

(a)

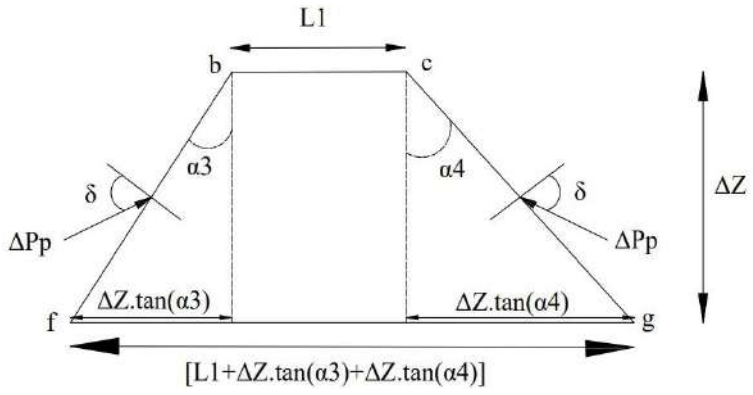

(b)

Fig. 3. Free body diagram across the footing (a) width (b) length

Summation of all the forces in the vertical direction for a small strip of thickness (ΔZ) leads to Eq. (1).

$$\sum F_V = 0$$
$$\sigma_V.\cos(\theta).(L1.W1) + \gamma_1.\left(\frac{\Delta Z}{3}\right).\left\{[W1 + \Delta Z.\tan(\alpha1) + \Delta Z.\tan(\alpha2)].[L1 + \Delta Z.\tan(\alpha3) + \Delta Z.\tan(\alpha4)] + (L1.W1) + \sqrt{\begin{matrix}(L1.W1).\\ [W1 + \Delta Z.\tan(\alpha1) + \Delta Z.\tan(\alpha2)].\\ [L1 + \Delta Z.\tan(\alpha3) + \Delta Z.\tan(\alpha4)]\end{matrix}}\right\} - \Delta P_{pv} - (\sigma_V + \Delta\sigma_V).\cos(\theta).[W1 + \Delta Z.\tan(\alpha1) + \Delta Z.\tan(\alpha2)].[L1 + \Delta Z.\tan(\alpha3) + \Delta Z.\tan(\alpha4)] = 0 \quad (1)$$

where γ_1: is the unit weight of the upper dense sand layer, and σv and ΔP_{pv}: are the vertical component of applied stress and the passive pressure, respectively. It worth noting here that the passive pressure on all sides of the projected area is not equal, however, following Meyerhof and Hanna (1978), it was assumed to be the same in this analysis. The passive pressure (ΔPp_v) in the vertical direction can be written as:

$$\Delta P_{pv} = \Delta P_p.\sin(\delta) \quad (2)$$

$$\Delta P_{pv} = \gamma_1.K_p.\left(D + Z + \frac{\Delta Z}{2}\right).\Delta Z.[2L1 + 2W1 + \Delta Z.\tan(\alpha1) + \Delta Z.\tan(\alpha2) + \Delta Z.\tan(\alpha3) + \Delta Z.\tan(\alpha4)].\sin(\delta) \quad (3)$$

in which K_p: depends upon the product of passive earth pressure coefficient as per Caquot and Kerisel (1949) and punching shear inclination factor as per Meyerhof and Hanna (1978).

Rewriting the Eq. (1):

$$\sigma_v.\cos(\theta).(L1.W1) + \gamma_1.\left(\frac{\Delta Z}{3}\right).\left\{\begin{matrix}(L1.W1) + \\ W1.[(\Delta Z.\tan(\alpha3) + \Delta Z.\tan(\alpha4)] \\ +L1.[(\Delta Z.\tan(\alpha1) + \Delta Z.\tan(\alpha2)] \\ +\Delta Z^2.\begin{bmatrix}\tan(\alpha1).\tan(\alpha3) + \\ \tan(\alpha1).\tan(\alpha4) + \\ \tan(\alpha2).\tan(\alpha3) + \\ \tan(\alpha2).\tan(\alpha4)\end{bmatrix} + \\ \sqrt{(L1.W1).\begin{bmatrix}L1.W1 + \\ W1.[(\Delta Z.\tan(\alpha3) + \Delta Z.\tan(\alpha4)] \\ +L1.[(\Delta Z.\tan(\alpha1) + \Delta Z.\tan(\alpha2)] \\ +\Delta Z^2.\begin{bmatrix}\tan(\alpha1).\tan(\alpha3) + \\ \tan(\alpha1).\tan(\alpha4) + \\ \tan(\alpha2).\tan(\alpha3) + \\ \tan(\alpha2).\tan(\alpha4)\end{bmatrix}\end{bmatrix}}\end{matrix}\right\} - \Delta P_{pv} - (\sigma_v + \Delta\sigma_v).\cos(\theta).\left\{\begin{matrix}(L1.W1) + W1.[\Delta Z.\tan(\alpha3) + \Delta Z.\tan(\alpha4)] \\ +L1.[\Delta Z.\tan(\alpha1) + \Delta Z.\tan(\alpha2)] + \\ \Delta Z^2.\begin{bmatrix}\tan(\alpha1).\tan(\alpha3) + \tan(\alpha1).\tan(\alpha4) \\ +\tan(\alpha2).\tan(\alpha3) + \tan(\alpha2).\tan(\alpha4)\end{bmatrix}\end{matrix}\right\} \quad (4)$$

Since ΔZ and $\Delta\sigma v$ are very small, so their square or their product would be also very small. Thus neglecting the terms such as $(\frac{\Delta Z^2}{3}.\tan(\alpha1).\tan(\alpha3)$, $\frac{\Delta Z^2}{3}.\tan(\alpha2).\tan(\alpha4)$,$(\sigma v + \Delta\sigma v).\cos(\theta).\Delta Z.\tan(\alpha3)$,$(\sigma v + \Delta\sigma v).\cos(\theta).\Delta Z^2.\tan(\alpha1).\tan(\alpha3)$ etc…),

Eq. (5) is obtained.

$$\sigma_V.\cos(\theta).(L1.W1) + \gamma_1.\left(\frac{\Delta Z}{3}\right).[2(L1.W1) + (L1.W1)] - \Delta P_{pv} - (\sigma_V + \Delta\sigma_V).\cos(\theta).(L1.W1) = 0 \quad (5)$$

Similarly, neglecting the terms such as $\frac{1}{2}.[(2W1 + 2L1).\Delta Z^2 + \Delta Z^3.[\tan(\alpha1) + \tan(\alpha2) + \tan(\alpha3) + \tan(\alpha4)]$ after expanding the Eq. (3), because $\Delta Z^2, \Delta Z^3$ are very small, results in new Eq. (6).

$$\Delta P_{pv} = 2\gamma_1.K_p.(D + Z).(L1 + W1).\Delta Z.\sin(\delta) \quad (6)$$

Eq. (7) is obtained by substituting the ΔP_{pv} in Eq. (5).

$$\sigma_V.\cos(\theta).(L1.W1) + \gamma_1.\left(\frac{\Delta Z}{3}\right).[3(L1.W1)] - 2\gamma_1.K_p.(D + Z).(L1 + W1).\Delta Z.\sin(\delta) - (\sigma_V + \Delta\sigma_V).\cos(\theta).(L1.W1) = 0 \quad (7)$$

Simplification of Eq. (7) leads to Eq. (8).

$$\Delta\sigma_V.\cos(\theta).(L1.W1) = \gamma_1.\left[(L1.W1) - 2K_p.(D + Z).(L1 + W1).\sin(\delta)\right].\Delta Z \quad (8)$$

Dividing Eq. (8) on both sides with ($W1.L1$) results in Eq. (9).

$$\Delta\sigma_V.\cos(\theta) = \gamma_1.\left[1 - \frac{2K_p.(D+Z).(L1+W1).\sin(\delta)}{(L1.W1)}\right].\Delta Z \quad (9)$$

Integrating Eq. (9) as shown in Eq. (10) on both sides, results in Eq. (11).

$$\int \Delta\sigma_V.\cos(\theta) = \int \gamma_1.\left[1 - \frac{2K_p.(D + Z).(L1 + W1).\sin(\delta)}{(L1.W1)}\right].\Delta Z \quad (10)$$

$$\Delta\sigma_V.\cos(\theta) = \gamma_1.Z - \left[\frac{2\gamma_1.K_p.\left(D.Z+\frac{Z^2}{2}\right).(L1+W1).\sin(\delta)}{(L1.W1)}\right] + C \quad (11)$$

where C: is constant of integration.

In order to find C, the following boundary conditions are applied to Eq. (11). At $Z = 0$, $L1 = L$, $W1 = W$ and $\sigma v = q_u$, which results in Eq. (12).

$$C = q_u.\cos(\theta) \quad (12)$$

where q_u: is the ultimate load bearing capacity of the rectangular footing in the layered sand.

Further, at $Z = H$, $L1 = [L + H.\tan(\alpha3) + H.\tan(\alpha4)]$, $W1 = [W + H.\tan(\alpha1) + H.\tan(\alpha2)]$ and $\sigma v = q_L$, will result into Eq. (13) is obtained from Eq. (11).

$$q_L.\cos(\theta) = \gamma_1.H - \left\{\frac{2\gamma_1.K_p.H.\left(D + \frac{H}{2}\right).\left[\begin{matrix}(W + H.\tan(\alpha1) + \mathrm{H}.\tan(\alpha2)) \\ +(L + H.\tan(\alpha3) + \mathrm{H}.\tan(\alpha4))\end{matrix}\right].\sin(\delta)}{[W + H.\tan(\alpha1) + \mathrm{H}.\tan(\alpha2)].[L + H.\tan(\alpha3) + \mathrm{H}.\tan(\alpha4)]}\right\} + q_u.\cos(\theta) \quad (13)$$

where q_L: is the bearing capacity of the lower loose sand layer, $q_L.\cos(\theta)$ and $q_u.\cos(\theta)$: is the vertical component of the bearing capacity q_L and q_u which were further designated as q_{Lv} and q_{uv}, respectively in this derivation. As per IS 6403 (1981), for the sand under inclined loading, the bearing capacity is given by Eq. (14).

$$q_{Lv} = \gamma_1.(D + H).N_{q2}.S_{q2}.d_{q2}.i_{q2} + \left(\frac{1}{2}\right).\left(\gamma_2.W.N_{\gamma2}.S_{\gamma2}.d_{\gamma2}.i_{\gamma2}\right) \quad (14)$$

where d_{q2}, $d_{\gamma2}$, i_{q2}, $i_{\gamma2}$ and S_{q2}, $S_{\gamma2}$: are the depth, inclination and shape factors. The equation for the inclination and shape factors are given in Eqs. (15a) and (15b) and Eqs. (16a) and (16b), respectively.

$$i_{q2} = \left(1 - \frac{\theta}{90^0}\right)^2 \quad (15a)$$

$$i_{\gamma2} = \left(1 - \frac{\theta}{\varphi_2}\right)^2 \quad (15b)$$

and

$$S_{q2} = \left(1 + \frac{0.2W}{L}\right) \quad (16a)$$

$$S_{\gamma 2} = \left(1 - \frac{0.4W}{L}\right) \quad (16b)$$

Substituting Eqs. (14, 15a, 15b, 16a and 16b) in Eq. (13) and after rearranging it, Eq. (17) is resulted.

$$q_{uv} = \left[\gamma_1.\left(1+\frac{0.2W}{L}\right).(D+H).N_{q2}.d_{q2}.i_{q2}\right] + \left[\left(\frac{1}{2}\right).\left(1-\frac{0.4W}{L}\right).\gamma_2.W.N_{\gamma 2}.d_{\gamma 2}.i_{\gamma 2}\right] - \gamma_1.H + \left\{\frac{2\gamma_1.K_p.H.\left(D+\frac{H}{2}\right).\left[\begin{matrix}W+L+H.\tan(\alpha 1)+\mathrm{H}.\tan(\alpha 2)\\ +H.\tan(\alpha 3)+\mathrm{H}.\tan(\alpha 4)\end{matrix}\right].\sin(\delta)}{\begin{matrix}[W+H.\tan(\alpha 1)+\mathrm{H}.\tan(\alpha 2)].\\ [L+H.\tan(\alpha 3)+\mathrm{H}.\tan(\alpha 4)]\end{matrix}}\right\} \quad (17)$$

Further, by simplification of Eq. (17), Eq. (18) is obtained.

$$\begin{aligned}(q_{uv}) &= (\gamma_1).(N_{\gamma 2}).\left[\left(1+\frac{0.2W}{L}\right).(D+H).\left(\frac{N_{q2}}{N_{\gamma 2}}\right).d_{q2}.i_{q2} + \left(\frac{1}{2}\right).\left(\frac{\gamma_2}{\gamma_1}\right).\left(1-\frac{0.4W}{L}\right).W.d_{\gamma 2}.i_{\gamma 2}\right] - \gamma_1.H \\ &+ \left\{\frac{\begin{matrix}2\gamma_1.K_p.H.\\ \left(D+\frac{H}{2}\right).\\ \left[\begin{matrix}W+L+\\ H.\tan(\alpha 1)+\mathrm{H}.\tan(\alpha 2)+\\ H.\tan(\alpha 3)+\mathrm{H}.\tan(\alpha 4)\end{matrix}\right].\sin(\delta)\end{matrix}}{\begin{matrix}[W+H.\tan(\alpha 1)+\mathrm{H}.\tan(\alpha 2)]\\ .[L+H.\tan(\alpha 3)+\mathrm{H}.\tan(\alpha 4)]\end{matrix}}\right\}\end{aligned} \quad (18)$$

To convert Eq. (18) into a dimensionless form, it is divided with $\gamma_1 W$ on both sides. Then Eq. (19) is obtained.

$$\left(\frac{q_{uv}}{\gamma_1 W}\right) = \left(\frac{\gamma_2}{\gamma_1}\right).(N_{\gamma 2}).\left[\left(\frac{\gamma_1}{\gamma_2}\right).\left(1+\frac{0.2W}{L}\right).\left(\frac{D}{W}+\frac{H}{W}\right).\left(\frac{N_{q2}}{N_{\gamma 2}}\right).d_{q2}.i_{q2} + \left(\frac{1}{2}\right).\left(1-\frac{0.4W}{L}\right).d_{\gamma 2}.i_{\gamma 2}\right] - \left(\frac{H}{W}\right) + \left\{\begin{matrix}2K_p.\left(\frac{H}{W}\right).\\ \left[\begin{matrix}1+\left(\frac{L}{W}\right)\\ +\left(\frac{H}{W}\right).\\ \left[\begin{matrix}\tan(\alpha 1)+\tan(\alpha 2)\\ +\tan(\alpha 3)+\tan(\alpha 4)\end{matrix}\right]\end{matrix}\right].\\ \frac{\left(\frac{D}{W}+\frac{H}{2W}\right).\sin(\delta)}{\left\{\left(\begin{matrix}1+\left(\frac{H}{W}\right).\\ [\tan(\alpha 1)+\tan(\alpha 2)]\end{matrix}\right)\right\}}\\ .\left\{\begin{matrix}\left(\frac{L}{W}\right)+\left(\frac{H}{W}\right).\\ [\tan(\alpha 3)+\tan(\alpha 4)]\end{matrix}\right\}\end{matrix}\right\} \leq q_t \quad (19)$$

The dimensionless ultimate bearing capacity ($q_{uv}/\gamma_1 W$) derived as per Eq. (19) is valid only up to the bearing capacity of the upper sand layer (q_t), after which bearing capacity remains constant and was primarily dependent on the upper dense sand layer. Further, from Eq. (19), the bearing capacity of rectangular footing on layered sand under inclined load depends on: 1) Embedment depth of footing (D); 2) Thickness of dense sand layer (H); 3) Unit weight and friction angle of the upper dense (γ_1, φ_1) and lower loose (γ_2, φ_2) sand layer; 4) Dimensions of the footing (L and W); and 5) Load inclination (θ) with respect to vertical. It is pertinent to mention here that the angle $\alpha 1$, $\alpha 2$, $\alpha 3$ and $\alpha 4$ associated with the load spread mechanism too depends on the above parameters. For strip and circular footings, the angles $\alpha 1$ and $\alpha 2$ were both considered equal to the inclination of the applied load in the work of Meyerhof and

Hanna (1978). In the present study, to have a reasonable estimate of bearing capacity using the limit equilibrium methodology, the magnitude of the all load spread angles were determined for surface ($\alpha 01, \alpha 02, \alpha 03, \alpha 04$) as well as for embedment ratio (D/W) of 1($\alpha 11, \alpha 12, \alpha 13, \alpha 14$) and 2($\alpha 21, \alpha 22, \alpha 23, \alpha 24$), respectively by performing Finite Element analysis in the ABAQUS software using C3D8R element. For the numerical study, the load inclination angle (θ) was varied from 0^0 to 30^0 at an interval of 5^0. The impact of soil density was considered in the analysis. The relation between the unit weights and friction angles used for modelling were considered as per Bowles (1977) for the upper dense and the lower loose sand layer and are shown in Tables 3 and 4, respectively.

It is pertinent to mention here that Dawarci et al. (2014) reported a friction angle of 36^0 and 42^0 for the sand corresponding to a unit weight of 15.44 kN/m^3 and 16.65 kN/m^3, respectively. Khatri et al. (2017b) obtained a friction angle of sand as 33.4° corresponding to a unit weight of 13.87 kN/m^3. Das et al. (2021) used a friction angle for the loose (31°-36°) and dense (41°-46°) sand for performing the numerical study of the ring footing on layered sand. Furthermore, Hanna (1981) and Farah (2004) used a punching shearing mechanism to acquire the bearing capacity of the strip footing on layered soil, obtaining a friction angle of 47.7° and 34°, respectively, corresponding to a unit weight of 16.33 kN/m^3 and 13.78 kN/m^3. Given the foregoing, the mechanism, as well as the unit weights and friction angles (Tables 3 and 4) selected for modelling, are justified.

Further, for the numerical study, the dilation angles for the upper dense and lower loose sand layers were calculated as per Szypcio and Dołżyk (2006). Modulus of elasticity for the upper dense and lower loose sand layers were derived from 1200(N+6) kPa as per El-Kasaby (1991). The standard penetration resistance (N) was calculated as per IS 6403 (1981) corresponding to the friction angles for the upper dense and lower loose sand layers used for modelling. Numerical study was conducted for different thickness ratio (H/W) which were varied from 0.00 to 2.00. More details of the numerical study can be seen in Panwar and Dutta (2021). It is pertinent mention here that the Finite Element analysis was performed both for the surface and embedded footing.

Figure 4 shows the failure surface movement with the variation in load inclination in the form of vectorial displacement at different embedment ratio. The failure surface of the rectangular footing resting on upper dense sand overlying lower loose sand under inclined load was observed to make different angles α1 and α2 across the width, but angles α3 and α4 were found to be the same across the length for surface as well as for embedded footing. Figures 5a and 5b shows the load spread angle α1, α2 and α3 across the width and length of the rectangular footing. All the load spread angles were measured with respect to the vertical axis below the base edges of the rectangular footing in the direction of load inclination as well as in the opposite direction as shown in the Figure 5.

Table 1 shows the variation of the load spread angle with the thickness ratio (H/W) load inclination (θ) and soil friction ratio (φ_2/φ_1) at different embedment ratio (D/W). From the present study, for surface footing (D/W = 0) it was observed that with the increase in the thickness ratio, all the load spread angles were found to decrease as long as the bearing capacity was dependent on the properties of both the sand layers. But when the failure surface confined to the upper dense sand layer, all load spread angles were observed to increase for each load inclination. Similar behaviour observed when the embedment ratio increased from 1 to 2. It is pertinent to mention here that the sign convention for the α1 was considered negative when measured towards left of the vertical axis otherwise it was considered positive. As the

soil defining parameters changed, there was change in all load spread angles. Load spread angle variation with thickness ratio, load inclination and soil friction ratio were presented both for the surface and embedded footing through Eqs. (20(a-c), 21(a-c) and 22(a-c)).

For surface footing (D/W = 0),

$$\alpha 01 = -3.45 * \left(\frac{H}{W}\right) - 3.69 * (\theta) - 137.53 * \left(\frac{\varphi_2}{\varphi_1}\right) + 139.78 \quad (20a)$$

$$\alpha 02 = \exp * \left(-0.036 * \left(\frac{H}{W}\right) + 0.033 * (\theta) + 1.77 * \left(\frac{\varphi_2}{\varphi_1}\right) + 2.23\right) \quad (20b)$$

$$\alpha 03 = \alpha 04 = -1.24\left(\frac{H}{W}\right) + 0.04 * (\theta) + 12.58 \quad (20c)$$

For embedded footing (D/W = 1),

$$\alpha 11 = \left[\left(-0.10 * \left(\frac{H}{W}\right)^3\right) - (0.051 * (\theta)^2) - \left(114.64 * \left(\frac{\varphi_2}{\varphi_1}\right)\right) + 94.20\right] \quad (21a)$$

$$\alpha 12 = \exp * \left(0.072 * \left(\frac{H}{W}\right) + 0.057 * (\theta) - 0.32 * \left(\frac{\varphi_2}{\varphi_1}\right) + 2.72\right) \quad (21b)$$

$$\alpha 13 = \alpha 14 = -0.85 * \left(\frac{H}{W}\right) + 0.08 * (\theta) + 11.23 \quad (21c)$$

For embedded footing (D/W = 2),

$$\alpha 21 = \left[\left(0.21 * \left(\frac{H}{W}\right)^3\right) - \left((0.043 * (\theta)^2)\right) - \left(206.50 * \left(\frac{\varphi_2}{\varphi_1}\right)\right) + 163.33\right] \quad (22a)$$

$$\alpha 22 = \exp * \left(0.061 * \left(\frac{H}{W}\right) + 0.055 * (\theta) + 4.85 * \left(\frac{\varphi_2}{\varphi_1}\right) - 1.42\right) \quad (22b)$$

$$\alpha 23 = \alpha 24 = -0.80 * \left(\frac{H}{W}\right) + 0.02 * (\theta) + 138.27 * \left(\frac{\varphi_2}{\varphi_1}\right) - 94.63 \quad (22c)$$

Table 3. Upper dense sand layer properties used for modelling

φ_1	γ_1 (kN/m^3)
41°	19.5
42°	20.0
43°	20.5
44°	21.0
45°	21.5
46°	22.0

Table 4. Lower loose sand layer properties used for modelling

φ_2	γ_2 (kN/m^3)
31°	14.5
32°	15.0
33°	15.5
34°	16.0
35°	16.5
36°	17.0

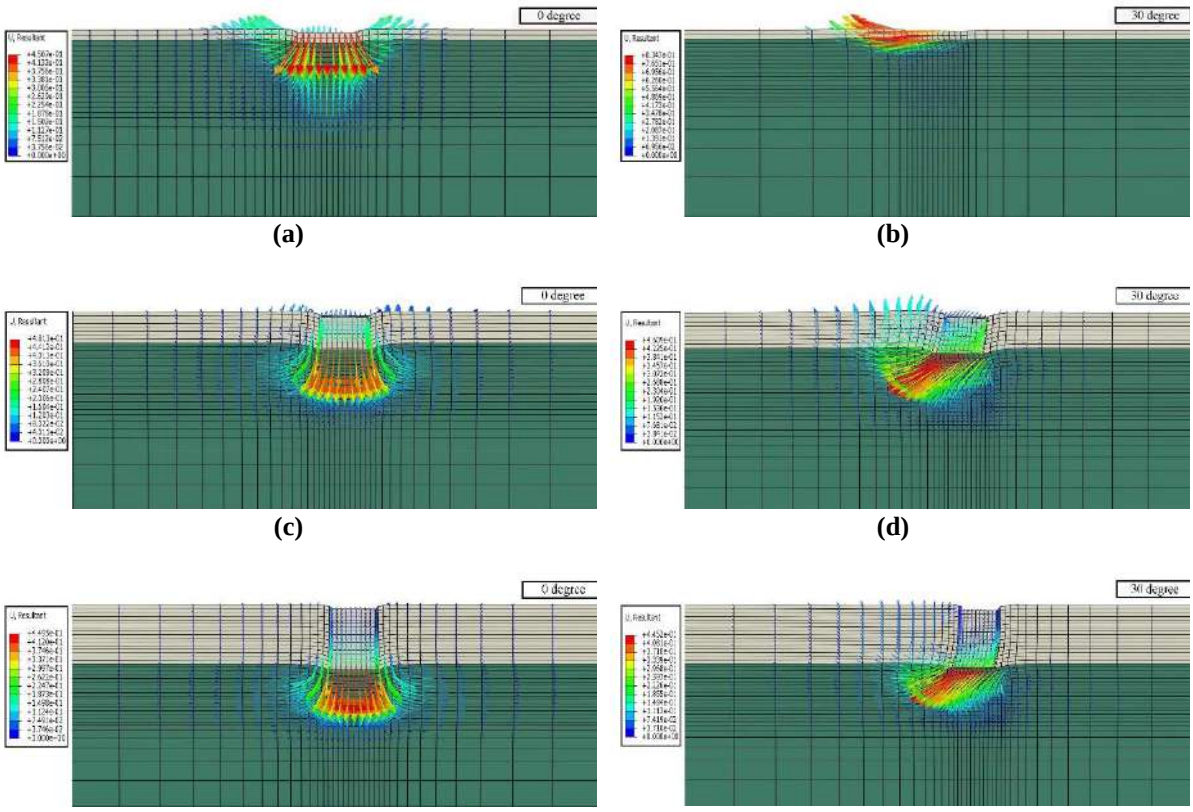

Fig. 4. Vectorial displacement failure: a) and b) For surface footing; c) and d) For embedment ratio 1; and e) and f) For embedment ratio 2 under a load inclination of 0^0 and 30^0

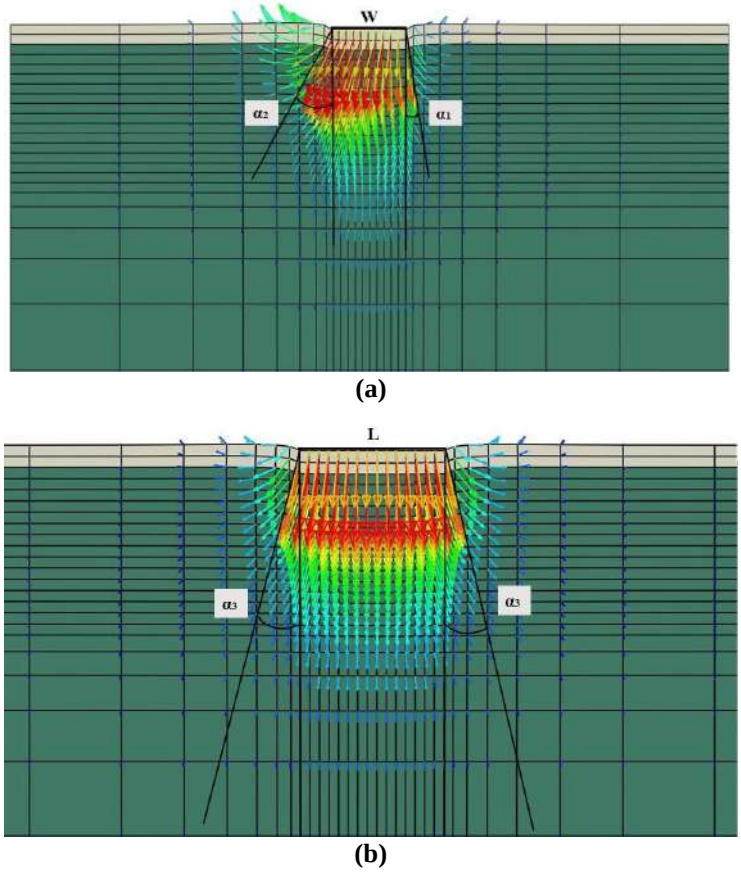

Fig. 5. Load spread angle across the: a) Width (W); and b) Length (L) of the footing

3. Validation with the FEM Results

Numerical study was performed as per Panwar and Dutta (2021) for the calculation of load spread angle $\alpha 1$, $\alpha 2$, $\alpha 3$, and $\alpha 4$ for the surface ($D/W = 0$) and embedded ($D/W = 1$ and 2) footing. The proposed Eq. (19) also depends on these loads spread angles. A validation of the proposed equation with the numerical study was performed corresponding to varying thickness ratio (0.00 to 2.00), load inclination (0^0 to 30^0) and friction angles of upper dense (41^0 to 46^0) and lower loose (31^0 to 36^0) sand layers under the inclined load. Comparison of the results was tabulated in Table 2 for the specific parameter of the friction angles, thickness ratio and load inclination at different embedment ratio.

Study of Table 2 reveals that when the load inclination increased from 0^0 to 30^0, the results obtained from the proposed equation were in line with the results obtained from the finite element analysis. The overall average deviation was observed to increase with the increase in the embedment ratio and found to be 14.56%, 18.71% and 23.56% at an embedment ratio of 0, 1 and 2, respectively. This difference in the results is attributed to the use of passive earth pressure coefficient as per Caquot and Kerisel (1949) and punching shear inclination factors as per Meyerhof and Hanna (1978) in the derived Eq. (19). It is worth noting that the bearing capacity determined in the numerical study corresponded to a peak in the pressure relative settlement plot or determined using the double tangent method, whichever came first.

4. Results and Discussions

With the use of Eq. (19), the bearing capacity of rectangular footing on layered sand was calculated by varying the parameters such as thickness ratio (H/W), friction angle of sands, embedment ratio (D/W) and load inclination (θ). Further, the bearing capacity was expressed in a dimensionless form ($q_{uv}/\gamma_1 W$). The results of this parametric study are described below.

4.1. Effect of Thickness Ratio, Sand Friction Angle and Embedment Ratio on the Dimensionless Bearing Capacity

In order to study the effect of the thickness ratio, sand friction angle and embedment ratio on the dimensionless bearing capacity, the results were plotted in Figure 6 corresponding to upper dense friction angle (41^0 and 46^0) and lower loose sand (31^0-36^0) layer friction angle at varying thickness ratio (0.25 to 2.00) for rectangular footing under vertical loading. Study of Figure 6a reveals that when thickness ratio increased from 0.00 to 2.00 for combination of the φ_1 (41^0) and φ_2 (31^0-36^0), there was an increase in the dimensionless bearing capacity. This may be due to the increase in the thickness of the upper dense sand layer. Further, study of Figure 6a reveals that with the increase in the thickness ratio, the dimensionless bearing capacity reached to the value of q_t (ultimate bearing capacity of upper dense sand) at a particular thickness ratio and becomes constant corresponding to the rest of the thickness ratio and similar behaviour observed in Figures 6b, 6c and 6e. This may be attributed to the fact that beyond a specific thickness ratio the failure surface remains in the upper dense sand and no contribution was observed of the lower loose sand layer beyond that specific thickness ratio. The trend was same corresponding to all φ_1 and φ_2 at varying thickness ratio.

Further, study of Figure 6 reveals that corresponding to $\varphi_{1=}$ 46^0 and $\varphi_{2=}$ 31^0, the dimensionless bearing capacity for surface footing obtained from the proposed equation for a thickness ratio of 0.00 was about 7.50 which increased to 26.27, 52.05 and 116.90 for a thickness ratio of 0.50, 1.00 and 2, respectively. It implies that the bearing capacity at a thickness ratio of 0.50, 1.00 and 2 was about 3.50, 6.94 and 15.58 times of its initial value. Figure 6 further reveals that with the increase in the friction

angle of upper dense sand layer from 41^0 to 46^0, the dimensionless bearing capacity increased due to increase in the frictional resistance. A close examination of Figures 6c, 6d and 6e, 6f reveals that with the increase the embedment ratio (1 and 2), the dimensionless bearing capacity also increases. This may be due to increase in the additional surcharge load besides the increase in upper dense sand layer. The increase in the dimensionless bearing capacity obtained from the proposed equation was 4.97 and 10.5 times the dimensionless bearing capacity of surface footing for an embedment ratio 1 and 2 respectively. Figure 6 further reveals that the highest and the lowest increase in the dimensionless bearing capacity was observed at a friction angle combination of 46^0-36^0 and 41^0-31^0 and at an embedment ratio 2 and 0 respectively at varying thickness ratio.

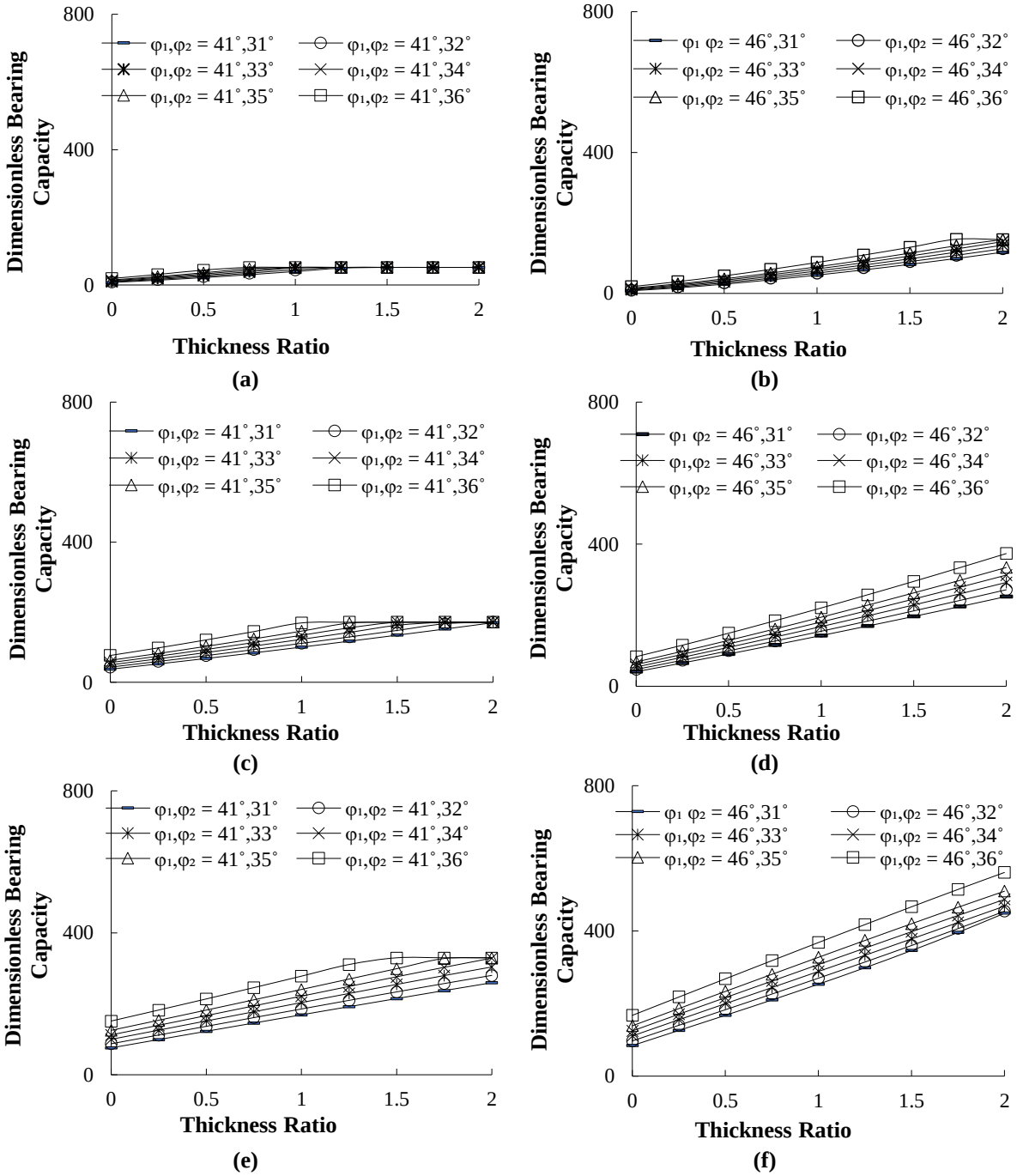

Fig. 6. Plot of dimensionless bearing capacity: a) and b) At D/W = 0; c) and d) At D/W = 1; and e) and f) At D/W = 2 with varying φ_1 (41^0 and 46^0) and φ_2 (31^0-36^0) at varying thickness ratio

4.2. Effect of Load Inclination and Embedment Ratio on the Dimensionless Bearing Capacity

In order to study the effect of the load inclination on the dimensionless bearing capacity, the results were plotted in Figure 7 corresponding to upper dense sand friction angle (41^0 to 46^0) and lower loose sand layer friction angle (31 and 36^0) at varying load inclination (0^0 to 30^0) for specific thickness ratio (H/W=2) with the increase in embedment ratio (0 to 2). Study of Figures 7a, 7b reveals that at thickness ratio of 2, with the increase in the load inclination from 0^0 to 30^0, there was decrease in the dimensionless bearing capacity for all friction angle combination and this may be due to the movement of the failure surface in the direction of load application. Also, the vertical and horizontal displacement found to decrease and increase respectively resulting failure of the footing. For $\varphi_1 = 46^0$ and $\varphi_2 = 36^0$ and at a thickness ratio of 2.00, the dimensionless bearing capacity of surface footing obtained from the proposed equation for a load inclination of 0^0 was about 152.98 which decreased to 121.53, 69.47 and 18.50 for a load inclination of 5^0, 15^0 and 30^0 respectively. It implies that the dimensionless bearing capacity at a load inclination of 5^0, 15^0 and 30^0 decreased about 20.55%, 54.58% and 87.90% of its initial value. Further study of Figures 7c, 7d 7e and 7f shows that as the embedment ratio increased from 0 to 1 and 2, the dimensionless bearing capacity increased but with a decreasing trend with the increase in the load inclination. This is attributed to the increase in the thickness of the upper dense sand layer and additional increase of surcharge load. Similar trend was observed at other thickness ratios as evident from Figure 7. The maximum decrease in the dimensionless bearing capacity obtained from the proposed equation was 99.89 %, 66.04 % and 61.5 % with the increase in the load inclination from 0^0 to 30^0 for an embedment ratio 0, 1 and 2, respectively. A close examination of Figure 7 reveals that highest and the lowest increase in the dimensionless bearing capacity was observed at embedment ratio (D/W) of 2.00 and 0, respectively for different friction angle and load inclination combinations.

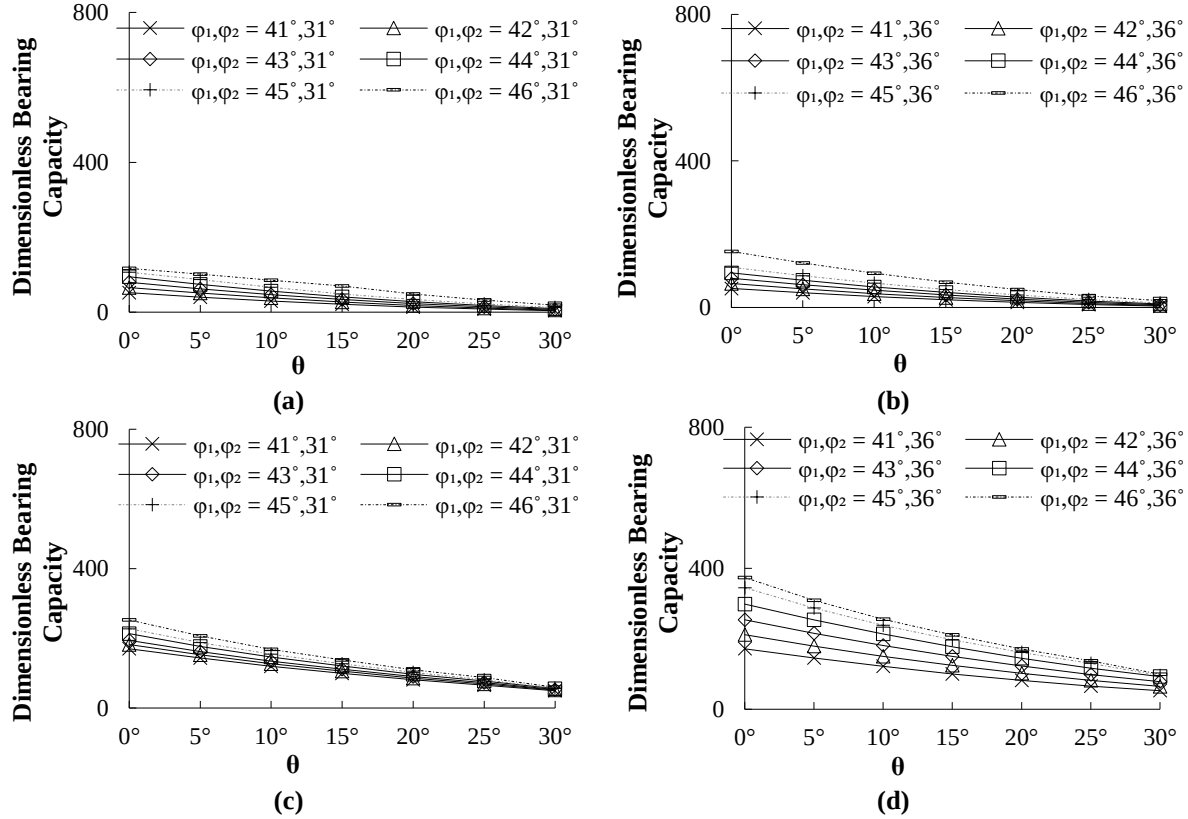

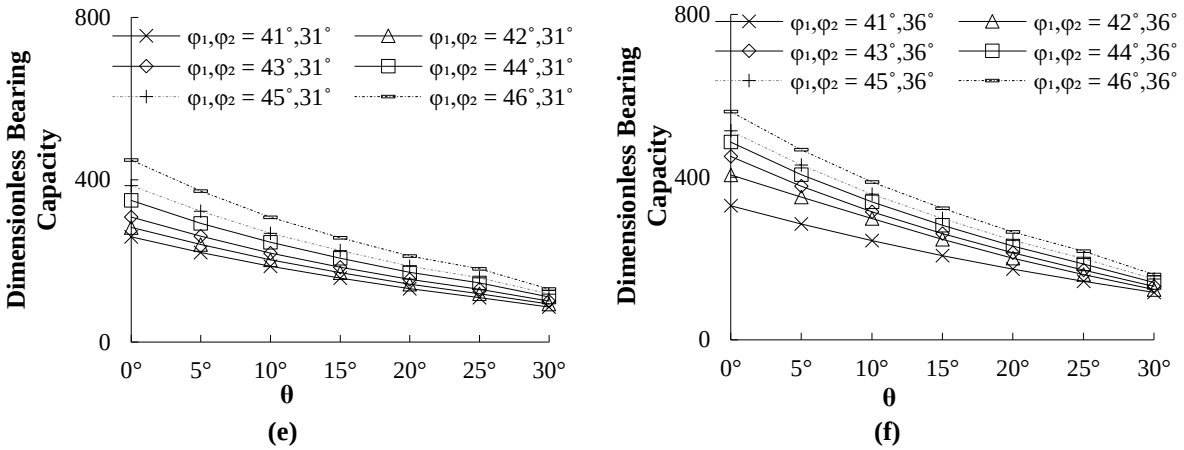

Fig. 7. Plot of dimensionless bearing capacity: a) and b) At D/W = 0l; c) and d) at D/W = 1; and e) and f) At D/W = 2 with varying load inclination ($\theta = 0^0$ to 30^0) for soil combination of φ_1 (41^0-46^0) and φ_2 (31^0 and 36^0) at some specific thickness ratio

4.3. Comparison

The experimental results reported by Meyerhof and Hanna (1978) were compared with the results obtained from the proposed Eq. (19). The dimensionless bearing capacity obtained from Eq. (19) for *L/W* = 1 was calculated and compared with the results reported by Meyerhof and Hanna (1978) for the circular footing as both the footings have similar shape factor. It is pertinent to mention here that Meyerhof and Hanna (1978) used the friction angle and unit weight of the upper dense and lower loose sand layer as 47.5° and 34°, 16.33 kN/m^3 and 13.78 kN/m^3, respectively. The comparison was shown in Figure 8 corresponding to a load inclination (θ) of 0^0, 10^0, 20^0 and 30^0 for varying thickness ratio (*H/W*) with embedment ratio (*D/W*) = 0 and 1. Study of Figure 8a reveals that for the surface footing, the results obtained from the proposed Eq. (19) at smaller thickness ratio were found to be conservative in comparison to the results of Meyerhof and Hanna (1978).

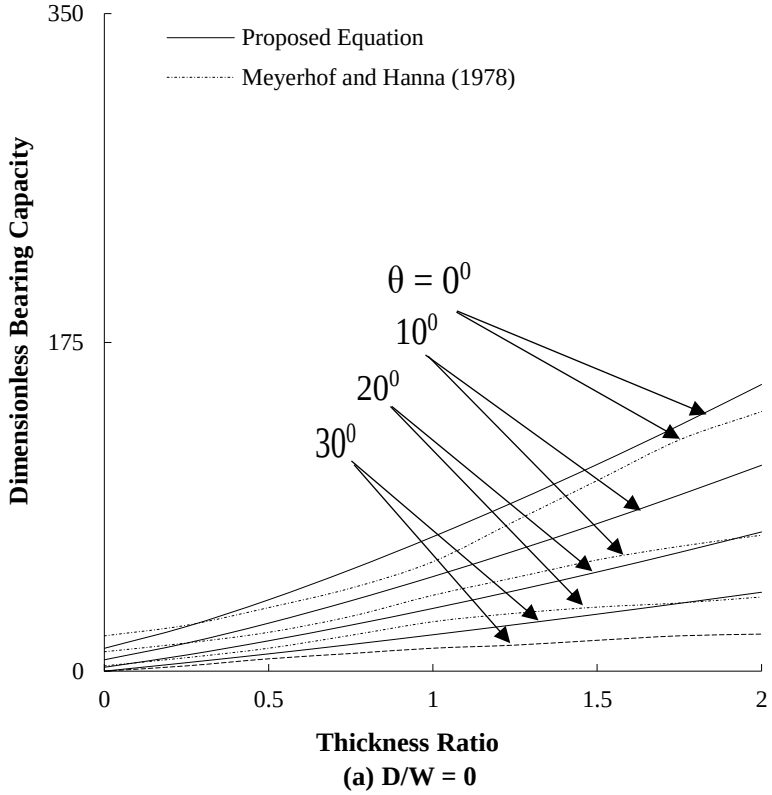

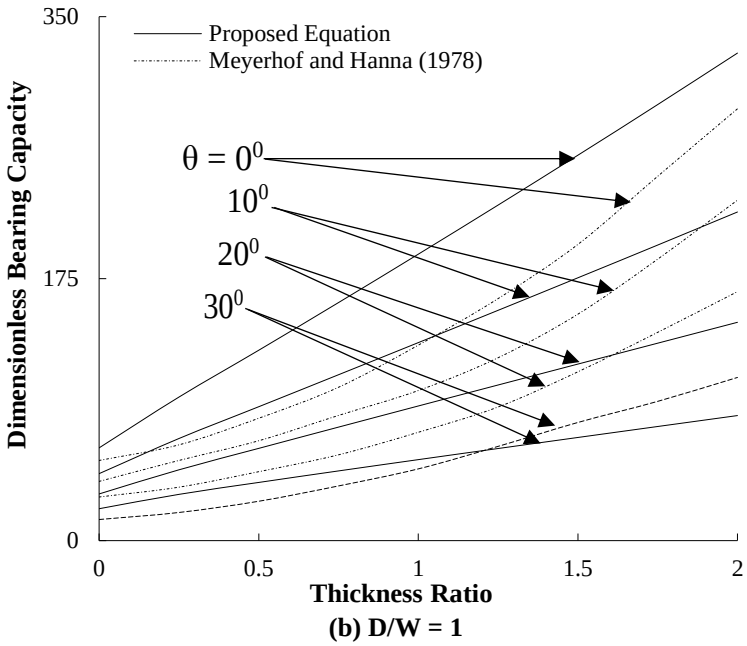

Fig. 8. Comparison of the rectangular footing at L/W=1 with circular footing

The results obtained from the proposed Eq. (19) were higher than the results obtained from Meyerhof and Hanna (1978) for higher thickness ratios (> 0.25). The average deviation in the results obtained from the proposed Eq. (19) was about 15.61% in comparison to the results reported by Meyerhof and Hanna (1978). Further, from Figure 8b, at *D/W* = 1, the results obtained from the proposed Eq. (19) were more conservative in comparison to the results obtained at *D/W* = 0 when compared with the results of Meyerhof and Hanna (1978). Further, study of Figure 8b reveals that the average deviation in the dimensionless bearing capacity was about 10.71% in case of embedded footing. All discrepancy may be due to the difference in the actual shape of the footings used in the comparison at the same shape factor, as well as the fact that the load spread angle used by Meyerhof and Hanna (1978) was assumed to be equal to the angle of load inclination.

5. Conclusions

In the present study, the bearing capacity equation for rectangular footing subjected to inclined load and resting on the layered sand (dense sand overlying loose sand) was derived using a well-known limit equilibrium methodology along with load spread mechanism. The results obtained from this study bring forth the following conclusions:

- The highest and the lowest increase in the bearing capacity was observed at a friction angle combination of 46^0-36^0 and 41^0-31^0 respectively, at varying thickness ratio.
- The bearing capacity obtained from the proposed equation was approximately 4.97 and 10.5 times of its initial value at an embedment ratio 1 and 2, respectively.
- For $\varphi_1 = 46^0$ and $\varphi_2 = 36^0$ and at a thickness ratio of 2.00, the bearing capacity at a load inclination of 5^0, 15^0 and 30^0 decreased about 20.55%, 54.58% and 87.90% of its initial value.
- The decrease in the bearing capacity obtained from the proposed equation was 99.89%, 66.04% and 61.5% with the increase in the load inclination from 0^0 to 30^0 for an embedment ratio 0, 1 and 2, respectively.
- In comparison to the proposed equation estimates, the average deviation was 14.56%, 18.71% and 23.56% for embedment ratio 0, 1 and 2, respectively with respect to finite element results.

- The results obtained from the derived bearing capacity equation was found to be comparable with those reported in literature with an average deviation of about 10.71% at different embedment ratio.

6. List of Symbols

φ_1, φ_2	Soil friction angle for upper dense sand and lower loose sand soil, in degree
γ_1, γ_2	Unit weight of the upper dense sand soil and lower loose sand soil, kN/m^3
$\alpha 1$, $\alpha 2$, and $\alpha 3$, $\alpha 4$	Load dispersion angle across width and length of the footing in general form, degree
E_1,E_2	Elastic moduli for upper dense sand and lower loose sand layer
υ_1, υ_2	Poisons ratio for upper layer and lower layer
W	Width of the footing
L	Length of the footing
Δz	Small strip thickness
θ	Concentric load inclination angle with respect to vertical acting on the rectangular footing, in degree
σ	Stress applied on the footing, kN/m^2
σv	Vertical component of the applied stress, kN/m^2
q_u	Concentrated inclined load acting, kN
H	Thickness of the upper dense sand layer
D	Depth of the embedded footing from ground surface
P_p	Total passive earth pressure acting normal to the failure plane
P_{pv}	Vertical component of passive earth pressure
ΔP_p	Small passive earth pressure acting on small strip soil
K_p	Passive earth pressure coefficient
q_{uv}	Ultimate load bearing capacity of the rectangular footing in the layered sand (vertical component)
q_{Lv}	Ultimate bearing capacity of lower loose sand (vertical component)
q_t	Ultimate bearing capacity of upper dense sand (vertical component)
i_q , i_γ	Inclination factors
S_γ, S_q	Shape factors
N_q, N_γ	Bearing capacity
d_q, d_γ	Depth factors
C	Constant of integration
$\left(\frac{q_{uv}}{\gamma_1 W}\right)$	Dimensionless ultimate bearing capacity of the footing
δ	Mobilised shearing resistance angle at failure, degree
Z	Distance where small strip of soil lies below rectangular footing
H/W	Thickness ratio
D/W	Embedment ratio
$\varphi 2/\varphi 1$	Soil friction ratio

7. Acknowledgment

The authors would like to express special thanks to Central Building Research Institute (CSIR-CBRI) Roorkee for providing the opportunity to utilize the ABAQUS software for this work.

8. References

Al-Ameri, A.F.I., Hussein, S.A. and Mekkiyah, H. (2020). "Estimate the bearing capacity of full-scale model shallow foundations on layered-soil using PLAXIS", *Solid State Technology*, 63(1), 1775-1787, http://solidstatetechnology.us/index.php/JSST/article/view/568.

Benmoussa, S., Benmebarek, S. and Benmebarek, N. (2021). "Bearing capacity factor of circular footings on two-layered clay soils", *Civil Engineering Journal*, 7(5), 775-785, https://doi.org/10.28991/cej-2021-03091689.

Biswas, A. and Krishna, A.M. (2019). "Behaviour of circular footing resting on layered foundation: sand overlying clay of varying strengths", *International Journal of Geotechnical Engineering*, 13(1), 9-24, https://doi.org/10.1080/19386362.2017.131424.

Bowles, J.E. (1977). *Foundation analysis and design*, McGraw-Hill, NewYork.

Caquot, A., and Kerisel, L. (1949). *T~aite de mecanique des sols*, Gauthier-Villars, Paris, France.

Chwała M. and Puła W. (2020). "Evaluation of shallow foundation bearing capacity in the case of a two-layered soil and spatial variability in soil strength parameters", *Plos One*, 15(4), e0231992, https://doi.org/10.1371/journal.pone.0231992.

Das, P. and Khatri V. (2021). "Bearing capacity estimation of shallow foundations on layered sand strata using finite elements analysis", *Lecture Notes in Civil Engineering book series*, 137, 401-412, https://doi.org/10.1007/978-981-33-6466-0_37.

Das, P.P., Khatri, V.N. and Dutta, R.K. (2021). "Bearing capacity of ring footing on a weak sand layer overlying a dense sand deposit", *Geomechanics and Geoengineering*, 16(4), 249-262, https://doi.org/10.1080/17486025.2019.1664775.

Das, P.P., Khatri, V.N. and Kumar, J. (2022). "Bearing capacity of strip and circular footing on layered sand with geogrid at the interface", *Arabian Journal of Geosciences*, 15(1), 361, https://doi.org/10.1007/s12517-022-09614-1.

Dawarci, B., Ornek, M. and Turedi, Y. (2014). "Analysis of multi-edge footings rested on loose and dense sand", *Periodica Politechnica Civil Engineering*, 58(4), 355-370, https://doi.org/10.3311/PPci.2101.

El-Kasabi, E.A.A. (1991). "Estimation of guide values for the modulus of elasticity of soil", *Bulletin of Faculty of Engineering HRBC Journal*, 19(1), 1-7.

Eshkevari, S.S., Abbo, A.J. and Kouretzis, G.P. (2018). "Bearing capacity of strip footings on sand over clay", *Canadian Geotechnical Journal*, 56(5), 1-33, https://doi.org/10.1139/cgj-2017-0489.

Eshkevari, S.S., Abbo, A.J. and Kouretzis, G. (2019). "Bearing capacity of strip footings on layered sands", *Computers and Geotechnics*, 114(1 October), 103101, https://doi.org/10.1016/j.compgeo.2019.103101.

Farah, C.A. (2004). "Ultimate bearing capacity of shallow foundations on layered soils", MSc Thesis, Civil and Environmental Engineering, Concordia University, Quebec.

Gupta, S. and Mital, A. (2021). "A comparative study of bearing capacity of shallow footing under different loading conditions", *Geomechanics and Geoengineering*, 17(4), 1338-1349, https://dot.org/10.1080/17486025.2021.1940310.

Hajitaheriha, M.M., Jafari, F., Hassanlourad, M. and Motlagh, A.H. (2021). "Investigating the reliability of negative skin friction on composite piles", *Civil Engineering Infrastructures Journal*, 54(1), 23-42, https://dot.org/10.22059/CEIJ.2020.287489.1607.

Hanna, A.M. (1981). "Foundations on strong sand overlying weak sand", *Journal of the Geotechnical Engineering,* 107(7), 915-927.

Hanna, A.M. (1982). "Bearing capacity of foundations on a weak sand layer overlying a strong deposit", *Canadian Geotechnical Journal,* 19(3), 392-396, https://ascelibrary.org/doi/10.1061/AJGEB6.0001169.

Hanna, A.M. (1987). "Finite element analysis of footings on layered soils", *Mathematical Modelling,* 9(11),813-819, https://doi.org/10.1139/t82-043.

Ibrahim, K.M.H.I. (2016). "Bearing capacity of circular footing resting on granular soil overlying soft clay", *Housing and Building National Research Center Journal,* 1(1), 71-77, https://doi.org/10.1016/j.hbrcj.2014.07.004.

Ibrahim, M.M., and Al-Obaydi, M.A. (2021). "Numerical analysis of a rectangular footing resting on two inclined layers of soil", *IOP Conference Series: Earth and Environmental Science*, (Vol. 856, No. 1, p. 012039), IOP Publishing, https://doi.org/10.1088/1755-1315/856/1/012039.

IS 6403 (1981). *Code of practice for determination of breaking capacity of shallow foundations*, Bureau of Indian Standard, New Delhi, India.

Johnson, K., Christensen, M., Sivakugan, N. and Karunasena, W. (2015). "Simulating the response of shallow foundations using finite element modelling", *Proceedings of the MODSIM 2003 International Congress on Modelling and Simulation*, Townsville, QLD, Australia (pp. 14-17), https://www.mssanz.org.au/MODSIM03/Volume_04/C15/03_Johnson_Simulating.pdf.

Kenny, M.J. and Andrawes, K.Z. (1997). "The bearing capacity of footings on a sand layer overlying soft clay", *Geotechnique,* 47(2), 339-345, https://doi.org/10.1680/geot.1997.47.2.339.

Khatri, V.N., Debbarma, S.P., Dutta, R.K. and Mohanty, B. (2017b). "Pressure-settlement behaviour of square and rectangular skirted footings resting on sand", *Geomechanics and Engineering*, 12(4),689-705, https://doi.org/10.12989/gae.2017.12.4.689.

Khatri, V.N., Kumar, J. and Akhtar, S. (2017a). "Bearing capacity of foundations with inclusion of dense sand layer over loose sand strata", *International Journal of Geomechanics*, 17(10), 06017018, https://doi.org/10.1061/(ASCE)GM.1943-5622.0000980.

Kumar, A., Ohri, M.L. and Bansal R.K. (2007). "Bearing capacity tests of strip footings on reinforced layered soil", *Geotechnical and Geological Engineering,* 25(2), 139-150, https://doi.org/10.1007/s10706-006-0011-6.

Mandeel, S.A.H., Mekkiyahb H.M. and Al-Americ, A.F.I. (2021). "Bearing Capacity of square footing resting on layered soil", *Al-Qadisiyah Journal for Engineering Sciences,* 13, 306-313, https://doi.org/10.30772/qjes.v13i.700.

Massihv, D.Y.A., Hachem, E.E. and Soubra, A.H. (2005). "Bearing capacity of eccentrically and/or obliquely loaded strip footing over two-layer foundation soil by a kinematical approach", *VIII International Conference on Computational Plasticity (COMPLAS VIII)*, Barcelona.

Merifield, R.S., Sloan, S.W. and Yu, H.S. (1999). "Rigorous plasticity solutions for the bearing capacity of two-layered clays", *Géotechnique,* 49(4), 471-490, https://doi.org/10.1680/geot.1999.49.4.471.

Meyerhof, G.G. (1974). "Ultimate bearing capacity of footings on sand layer overlying clay",

Canadian Geotechnical Journal, 11(2), 223-229, https://doi.org/10.1139/t74-018.

Meyerhof, G.G. and Hanna, A.M. (1978). "Ultimate bearing capacity of foundations on layered soils under inclined load", *Canadian Geotechnical Journal,* 15(4), 565-572, https://doi.org/10.1139/t78-060.

Michalowski, R.L. and Shi, L. (1995). "Bearing capacity of footings over two-layer foundation soil", *Journal of the Geotechnical Engineering,* 121(5), 421-428, https://ascelibrary.org/doi/10.1061/%28ASCE%290733-9410%281995%29121%3A5%28421%29.

Misir, G. and Laman, M. (2017). "A modern approach to rstimate the bearing capacity of layered soil", *Periodica Polytechnica Civil Engineering*, 61(3), 434-446, https://doi.org/10.3311/PPci.9578.

Mosadegh, A. and Nikraz, H. (2015). "Bearing capacity evaluation of footing on a layered-soil using ABAQUS", *Journal of Earth Science and Climatic Change*, 6(3), 264, http://dx.doi.org/10.4172/2157-7617.1000264.

Nujid, M.M., Idrus, J., Bawadi, N.F. and Firoozi, A. A. (2021). "Evaluating the effect of embedment depth on collapse failure analysis of strip foundation", *Civil Engineering and Architecture*, 9(5A), 1-9, https://doi.org/10.13189/cea.2021.091301.

Oda, M. and Win, M. (1990). "Ultimate bearing-capacity tests on sand with clay layer", *Journal of the Geotechnical Engineering,* 116(12), 1902-1906, https://doi.org/10.1061/(asce)0733-9410(1990)116:12(1902).

Okamura, M., Takemura, J. and Kimura, T. (1998). "Bearing capacity predictions of sand overlying clay based on limit equilibrium methods", *Soils and Foundations,* 38(1), 181-194, https://doi.org/10.3208/sandf.38.181.

Panwar, V. and Dutta, R.K. (2021). "Bearing capacity of rectangular footing on layered sand under inclined loading", *Journal of Achievements in Materials and Manufacturing Engineering,* 108(2), 49-62, https://doi.org/10.5604/01.3001.0015.5064.

Rao, P., Liu, Y. and Cuia, J. (2015). "Bearing capacity of strip footings on two-layered clay under combined loading", *Computers and Geotechnics,* 69, 210-218, https://doi.org/10.1016/j.compgeo.2015.05.018.

Reddy, V.S.K. and Kumar D.T.K. (2018)," Behaviour of foundation in layered soils", *International Journal of Science and Research,* 7(1), 1075-1078, https://doi.otg/10.21275/ART20179556.

Saha, A., Patra, S., Das, A. and Bera, A.K. (2018). "Bearing capacity of footing on sand overlay by soft soil using Abaqus: A numerical based study", *Geotechnics for Infrastructure Development,* Indian Geotechnical Society, Kolkata Chapter.

Shiau, J.S., Lyamin, A.V. and Sloan, S.W. (2003). "Bearing capacity of a sand layer on clay by finite element limit analysis", *Canadian Geotechnical Journal,* 40(5), 900-915, https://doi.org/10.1139/t03-042.

Shoaei, M.D., Alkarni, A., Noorzaei, J., Jaafar, M.S. and Huat, B.B.K. (2012). "Review of available approaches for ultimate bearing capacity of two-layered soils", *Journal of Civil Engineering and Management,* 18(4), 469-482, https://doi.org/10.3846/13923730.2012.699930.

Singh, S.P. and Roy, A.K. (2021). "Numerical study of the behaviour of a circular footing on a layered granular soil under vertical and inclined loading", *Civil and Environmental Engineering Reports,* 1(31), 29-43, https://doi.org/10.2478/ceer-2021-0002.

Szypcio, Z. and Dołżyk, K. (2006). "The bearing capacity of layered subsoil", *Studia Geotechnica et Mechanica,* XXVIII(1), 45-60.

Ullah, S.N., Hossain, M.S., Hu, Y. and Fourie, A. (2020). "Numerical modelling of rectangular footing on a sand embankment over mine tailings", In: Wang, C., Ho, J., Kitipornchai, S. (eds.), *ACMSM25,* Lecture Notes in Civil Engineering, Springer, Singapore; 37, 1027-1036, https://doi.org/10.1007/978-981-13-7603-0_97.

Zheng, G., Zhao, J., Zhou, H. and Zhang, T. (2019). "Ultimate bearing capacity of strip footings on sand overlying clay under inclined loading", *Computers and Geotechnics,* 106(1 February), 266-273, https://doi.org/10.1016/j.compgeo.2018.11.003.

Civil Engineering Infrastructures Journal 2023, 56(1): 193-204
DOI: 10.22059/CEIJ.2022.341199.1827

RESEARCH PAPER

Assessment of Fire Load and Probabilistic Temperature for Office Buildings in Pakistan

Noman, M.[1*], Hilal Ahmad, H.[2], Hamza, A.[2], Yaqub, M.[3], Saad Ali, M.[2] and Khattak, A.[4]

[1] Ph.D., Department of Civil Engineering, Faculty of Engineering and Technology, International Islamic University, Islamabad, Pakistan.
[2] M.Sc., Department of Civil Engineering, Faculty of Engineering and Technology, International Islamic University, Islamabad, Pakistan.
[3] Professor, Department of Civil Engineering, University of Engineering and Technology Taxila, Pakistan.
[4] Postdoctoral Researcher, College of Transportation Engineering, Tongji University Jiading Campus, Shanghai, China.

Received: 05 Apr. 2022; Revised: 12 Jul. 2022; Accepted: 13 Aug. 2022

ABSTRACT: This paper presents the results from 92 fire load density surveys conducted in 52 office buildings of Pakistan. The combination method of surveying that includes both inventory and weighing methods is used to determine the fire load of 92 office rooms, including 44 private and 48 government offices. Multiple linear regression analysis techniques are applied to assess the relationship of Fire Load Density (FLD) with variables according to the characteristics of the office rooms, such as office type, category, combustible materials, room dimensions, and ventilation conditions. Probabilistic models for FLD are developed using the regression analysis of the survey data. The survey data is further used to determine the maximum fire intensity in office buildings in Pakistan. The survey results show that the FLD increases with the increase in the area of the office. The percentage of wood is found to be the most contributing factor in the fire load. It has been noted that the fire load values are different for government and private offices, whereas the Building Code of Pakistan (BCP) has the same value for both. Statistical results presented in this study will be helpful in the fire safety and fire-resistant structure design of buildings in Pakistan.

Keywords: Fire Load Density, Office Buildings, Pakistan Building Code, Regression Analysis.

1. Introduction

Fire load can be seen as the basis for evaluating the duration and intensity of fire when combined with building characteristics such as openings for ventilation and the size of the compartment. Once these are known, other factors such as heat release and the extent and spread of smoke can be determined to a certain extent. The smoke production is a crucial factor in determining the available time for occupants to evacuate the building, whereas the heat intensity and duration determine

* Corresponding author E-mail: muhammad.noman@iiu.edu.pk

the residual strength of the structure. The fire spread may lead to various failures that can be in the form of structural failure (Mazza, 2015; Moradi et al., 2022, 2021; Noman et al., 2022; Sharma et al., 2014; Tavakoli and Kiakojouri, 2015), or other failures like material failure (Mazza, 2016; Noman et al., 2022; Tufail et al., 2016), element failure (Mazza, 2017; Noman and Yaqub, 2021), cracks in the walls and floors, insulation failure (the increased temperature at the unexposed side of the fire compartment), and spread through openings (e.g., windows and doors). To know about the resistance of the structure to the fire, the probable period of the fire should be known, which can be calculated from the fire load and desired conditions.

Fire load is the total combustible materials present in a compartment (Fontana et al., 2016). Usually, fire loads are uneven, and therefore the term Fire Load Density (FLD) is used, which is the total amount of combustible material per unit floor area of a compartment (MJ/m^2) (Buchanan and Abu, 2017b). Fire load data is used by a range of professionals, including architects, building control officers, fire modelers, fire investigation bodies, fire risk assessors, fire safety engineers, and insurance assessors. These are instrumental for many reasons, such as evaluating active and passive protection systems required in a building, conducting fire scene investigations, modelling the movement of fire, smoke, and gases in buildings, and assessing insurance premiums.

Fire load can be determined using several methods. The NFPA 557 (NFPA, 2023) recommends two ways for the determination of fire load; the weighing method (weighing of the combustible items) and the inventory method (determination of the mass of an object based on its measured volume and corresponding density). A combination of both methods can also be used. Fire load surveys in the past have used different survey methodologies (Culver, 1978; Kumar, 1995; Zalok and Eduful, 2013), including the inventory method (Culver, 1978; Issen, 1980; Korpela, 2000; Kumar, 1995), the weighing method (Baldwin et al., 1970; Ingberg et al., 1957), a combination of inventory and weighing (Barnett, 1984; Doyle and Macilwraith, 2019; Green, 1977), use of questionnaires (Bwalya, 2008; Bwalya et al., 2010), and web-based photographs of real estate sites. Each of the survey methods is associated with some uncertainties and shows a difference in results. However, a combination of inventory and weighing methods is found to provide more accurate results and the least uncertainty of fire loads (Zalok and Eduful, 2013). In this study, the combination method is used for determination of the FLD.

One of the very initial and detailed works on FLD was carried out by Culver (1976), whose work was further analyzed by Khorasani et al. (2014), proposing a probabilistic FLD model. Xie et al. (2019) further updated the FLD model of Khorasani et al. (2014), using the Bayesian approach by incorporating the data from recent fire load surveys. Ingberg et al. (1957) reported the FLD of 1270 MJ/m^2 in office buildings of America. Baldwin et al. (1970) reported the FLD of 400 MJ/m^2 in the office buildings of the UK. Bryson and Gross (1968) reported the FLD of 527 MJ/m^2. Culver's (1978) survey resulted in a much closer value of FLD (960 MJ/m^2) compared to that of Ingberg et al. (1957). On the other hand, Barnet (1984) reported a FLD of 440 MJ/m^2 for office buildings in New Zealand. The average FLD for office buildings in India was 348 MJ/m^2, as reported by Kumar and Rao (1997). Caro and Milke (1996), Milke and Caro (1996), Korpela and Kushner (2000), and Yii (2000) also determined the average FLD of offices as 1298 MJ/m^2, 1000 MJ/m^2, and 950 MJ/m^2 respectively. Some of the recent studies conducted in France (Thauvoye et al., 2008), Canada (Eduful, 2012), and China (Zhai, 2013) provided the information of average FLD in office

buildings to be 657 MJ/m^2, 852 MJ/m^2, and 652 MJ/m^2, respectively. Elhami-Khorasani et al. (2020) and Gernay et al. (2019) developed a new methodology for facilitating FLD. The methodology consists of four steps including digital inventory, organization of data, items matching using computer vision, and fuel load estimation. The values (1468 MJ/m^2) from the new methodology of the fire load survey were found to be much larger than the old survey methods. The main reasons for variation in survey results are regional differences, the difference in surveying techniques, and advancements in technology (new gadgets replacing paper and large desktop computers etc.).

Pakistan is a developing country, and with its development in the commercial sector, medium and large-sized shopping malls, office buildings, hotels, and other facilities are emerging, which has led to an increase in the number of fire incidents. Statistical data from Pakistan's National Disaster Management Authority (NDMA) indicates a steep upward trend in fire incidents (NDMA, 2016). Pakistan-Fire Safety Provisions in the Building Code of Pakistan (Pakistan, 2016) were formally launched in 2017. However, most of the portion is adapted from the National Fire Protection Authority (NFPA) standards. A proper FLD survey and its probabilistic models are not investigated.

In this paper, FLD for office buildings of Pakistan is investigated by surveying a representative model of the office buildings of concern and making a list of the compartments' sizes, fixed and movable combustibles, ventilation conditions, and their relevant features using the combination method. The study also differentiates government offices from private offices. The data is analyzed using regression analysis, and probabilistic models are developed. The information is further used to determine the maximum intensity of fires in office buildings in Pakistan. The results are then compared with various survey results across the world.

2. Fire Load Survey

The survey was conducted for the determination of fire load in office buildings in different sectors of Islamabad, Pakistan. A total of 92 office rooms were surveyed from 52 buildings, including 44 private offices and 48 government offices. The survey method adopted for this research was the combination method (Džolev et al., 2021) that includes the weighing method (direct weighing) and inventory method (determining the volume and multiplying with the unit weight) of the combustible items. The FLD in MJ/m^2 was calculated using the corresponding material's net calorific value using the following equation.

$$FLD = weight \times \frac{Calorific\_value}{Area} \quad \left(\frac{MJ}{m^2}\right) \tag{1}$$

Fire load of combustible materials that could be easily handled, such as paper, plastic, furniture, etc., are determined using the direct weighing method, whereas the inventory method was used for the fire load of the combustible ceiling, wooden partitions, or woodwork on walls, doors, window frames, and heavy furniture.

A survey form was developed to record the data collected during the survey and organise all room characteristics to calculate fire load density in an office room (Appendix). The survey sheet was based on the required data for the evaluation of FLD for office buildings in Pakistan that can be incorporated into the building code of Pakistan. The survey form was divided into three sections:

i. The first section consisted of building information such as the name of the building, category and type of room, and room characteristics such as room area, ceiling height (m), fuel load arrangement, and the number of openings. These all characteristics of the

room were recorded in the form during the survey.

ii. The second section consisted of the weight of combustible items that exist in an office room. It was further divided according to the type of combustible material like wood, plastic, papers, and other combustible items. This section also included a column for the number of elements. This column was for heavy and fixed combustible items that could not be weighed directly and had to be converted into several elements. These elements exist separately to determine their volume by length, width, height, and the total volume of the elements. The weight of the combustible items was calculated using the following equation.

$$Weight\ (kg) = volume\ (m^3) * density\ \left(\frac{kg}{m^3}\right) \quad (2)$$

In the last column, the fire load density of an item was calculated using the calorific value of the corresponding material of an item and divided by the total area of the office room.

iii. The third section consists of information regarding members that conduct the survey and general notes for the material of combustible items such as density and calorific value. The time and date of the survey conduction are also mentioned in this section.

The buildings were selected from each sector of Islamabad, depending upon availability and permissions to conduct surveys. It was made sure that at least two offices for each category be surveyed from each sector in the Capital. The parameters of interest during the survey include the fire load, type of office (general, clerical, and storage), office category (Government, private), room dimensions, room ventilation, and fire safety equipment. The buildings were selected from each sector of Islamabad, depending upon availability and permissions to conduct surveys. It was made sure that at least two offices for each category must be surveyed from each sector in the Capital. SPSS software (Frey, 2017) was used for the statistical analysis of the surveyed data. Multiple linear regression analysis techniques were applied to the survey data using different variables according to the characteristics of the office room like office type, category (government or private), combustible materials, room dimensions, and ventilation conditions.

3. Descriptive Statistics

3.1. Relationship Between FLD and Office Type

The office rooms are distributed into three types, i.e., general office rooms, clerical office rooms, and storage and file rooms. The impact of various types of office rooms on fire load (including range, mean and standard deviation) is given in Table 1. Clerical office rooms are usually small but congested and loaded with record material; therefore, these office rooms are separated from other general office rooms. The maximum mean fire load (1322 MJ/m^2) was found in storage and file rooms. The reason for this high fire load is the huge bulk of files and papers, which are mostly placed in storage rooms for a much longer time. Clerical office rooms have a higher standard deviation value, possibly due to the huge difference in FLD between government office rooms and private office rooms.

Table 1. Impact of office room type on fire load density

Office type	Fire load (MJ/m^2)			
	Mean	Minimum	Maximum	Standard deviation
General	386	247	617	103
Clerical	681	256	1184	246
Storage and file rooms	1322	1125	1468	146
All office rooms	602	247	1468	322

3.2. Relationship between FLD and Office Category (Private/Government)

The office setups and distribution of fire load vary a lot while considering the difference between government and private sector offices. The survey results in Table 2 show a mean difference of 1.8 times more for government offices than that for private offices. The difference is probably because the small private sector is well managed and properly arranged compared to government offices that are more congested and not well managed. Apart from that, government offices are still using old techniques of file systems and lots of paperwork which stays in offices for a longer period, whereas in the private sector, most of the paperwork is replaced by computers and data storage is shifted to computer or cloud storage. A comparison of fire load for various types of office rooms concerning government and private office rooms is presented in Figure 1.

3.3. Relationship between FLD and Combustibles Items

Fire occurs when combustible items come into contact with oxygen in the presence of heat. The fire, which usually starts with burning one item, gradually spreads to other nearby items and grows in size and intensity as pre flashover fire (Buchanan and Abu, 2017a). The combustible items provide valuable information about the trend of fire load. Wood, paper, and plastic are the major contributing items to the fire load in an office building. The survey results were analyzed for these combustible items to find their relationship with different categories of office buildings.

Figure 2 shows the impact on fire load due to the percentage of wood present in office rooms. Although having a larger amount of fire load, the government office rooms have a lesser contribution from wood than private office rooms where the wood is a major contributing combustion material towards the fire load. The percentage of wood in government offices mostly lies between 30% to 70%, with a dispersed spread of fire load in the graph. However, in the case of private offices, the data is more concentrated, and the percentage of wood in fire load varies between 55% and 90%. The reason for the difference is that government office rooms have less furniture, but huge piles of paper as compared to the private office room where the offices are well furnished with wooden furniture.

Table 2. Impact of office category on fire load density

Office category	Fire load (MJ/m^2)			
	Mean	Minimum	Maximum	Standard deviation
Private	431	256	612	108
Government	763	247	1468	368

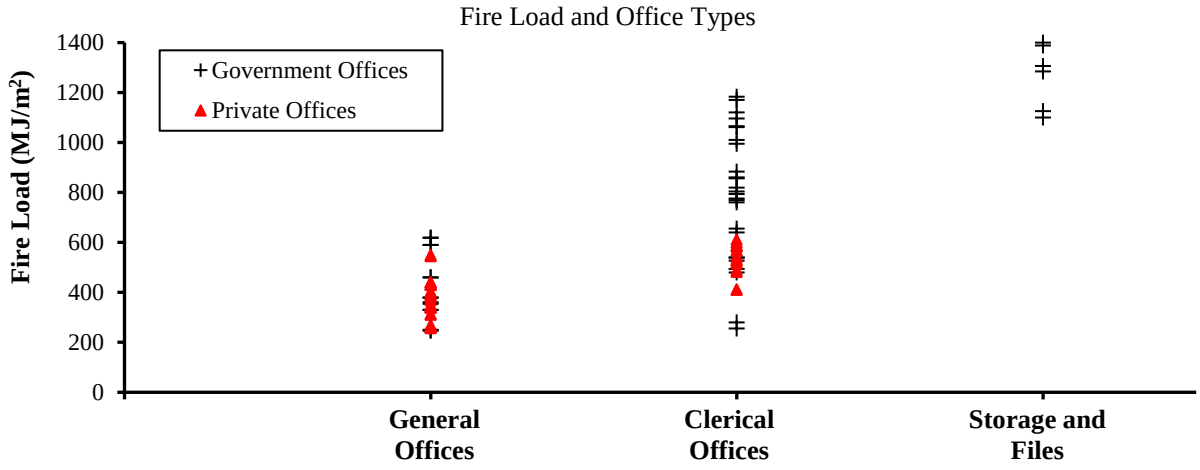

Fig. 1. Fire load in different types of office rooms

The percentage of plastic in comparison to fire load for private and government offices is shown in Figure 3. The contribution of plastic is found to be lesser as compared to the percentage of wood. Most of the plastic load lies below 40% of the total fire load. Despite the large fire load in government office rooms, the contribution of plastic is less. Pakistan is a developing country and is still using outdated methods (paper files, folders, shelves, cardboards, etc.) for record-keeping. It is expected that with time, the plastic load in offices will increase and replace the paper and wood in the offices.

The survey results in Figure 4 show the contribution of paper percentage to the total fire load. Private office rooms in Figure 4 show the lesser contribution of paper in fire load due to the reason that the private office rooms are already moved or are in the process of moving towards digitalization. However, the government office rooms are still abundant with paper and file work. The percentage of paper in most of the private office rooms is not more than 30% whereas, in the case of government office rooms, the percentage exceeds more than 60%.

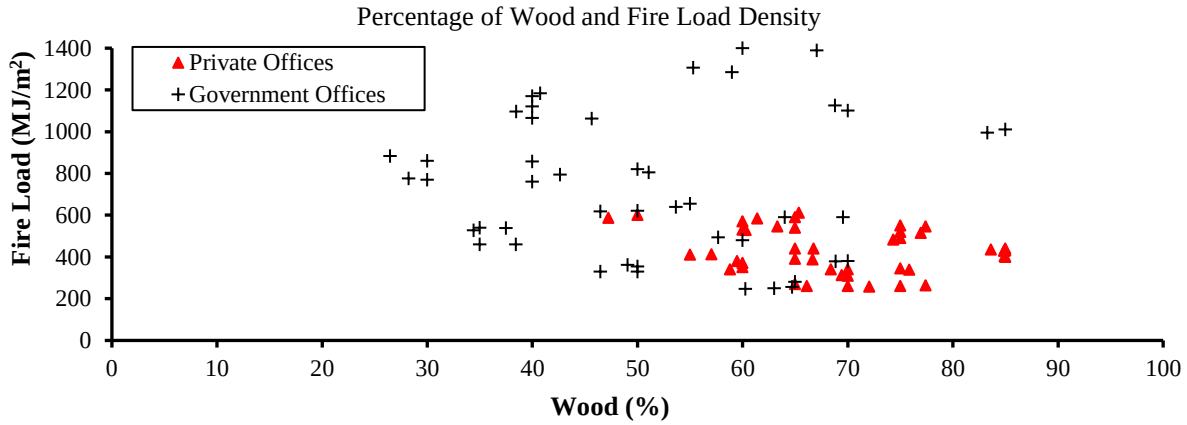

Fig. 2. FLD and percentage of wood for both government and private offices

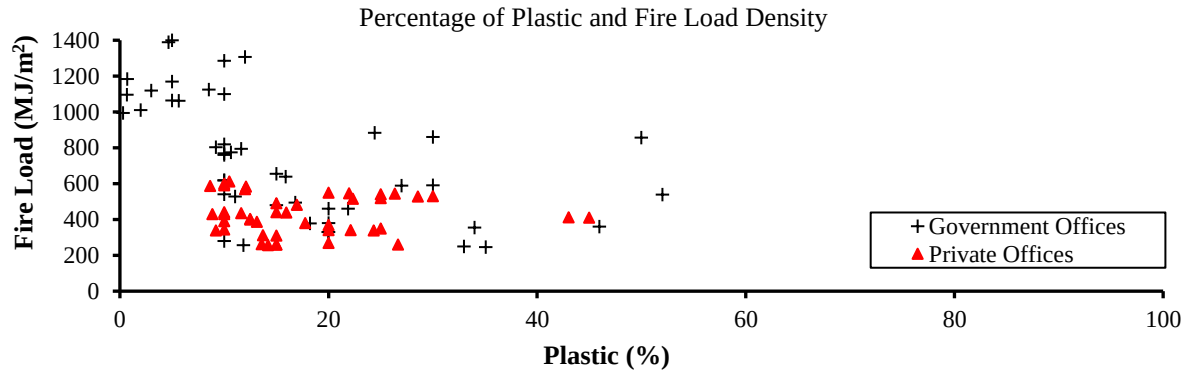

Fig. 3. FLD and percentage of plastic government and private offices

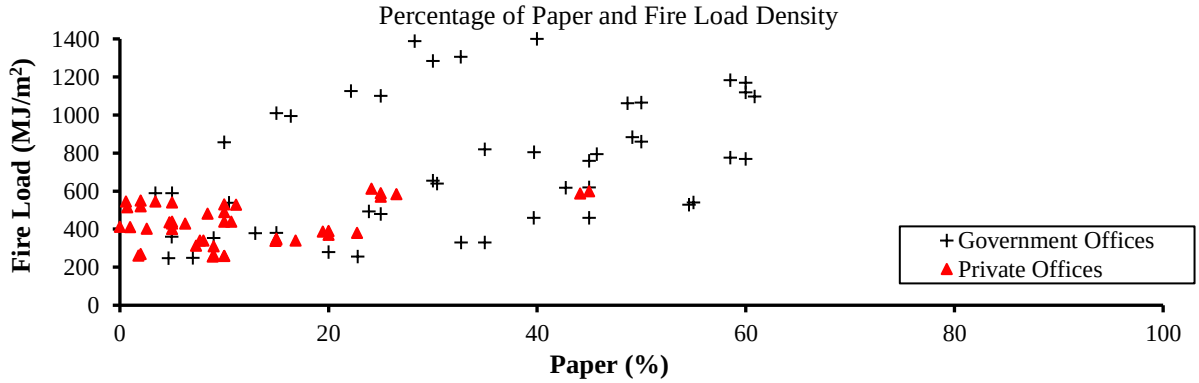

Fig. 4. FLD and percentage of paper for government and private office rooms

4. Regression Analysis

4.1. Model Summary

The surveyed offices were divided into three categories such as: i) Private Offices (PO), ii) Government Offices (GO), and iii) A Combination of Government and Private offices (CGP). Multiple linear regression analysis techniques were applied to surveyed data from 44 private office rooms, 48 government rooms, and a combination of both.

Fire load density was considered as a dependent variable in the office room, whereas Wood Percentage (WP), Office Type (OT), and Area of the Room (AR) were considered independent variables. An additional variable Office Category (OC) was considered for the combination of both offices. The reason for selecting the WP as an independent variable instead of paper or plastic is due to the results from the descriptive statistics showing a higher contribution of wood in FLD as compared to others. In the analysis, the categorical variable OT is found to be the most significant factor for all government offices, private offices, and a combination of both offices. Apart from office type, the office category is found to be a significant factor for the CGP offices. This is most probably because the difference between the FLD of government and private offices is quite large; therefore, changing this variable affects the model equation.

In the development of the model for office rooms, three independent variables were compared with a dependent variable, FLD. The categorical variable x_1 represent the percentage of wood in the office room, x_2 represent the office type (for general office rooms x_2 = 1, for clerical office x_2 = 2, and for storage and file rooms x_2 = 3) and x_3 represent the area of the office room in m^2. The coefficients show the weightage of each variable. At the assumed level of significance as α equal to 0.05 (see in Table 3), the coefficient value for variable OT is significant for both private offices and government offices. In the case of the combined government and private offices, the OT and OC show maximum weightage. The OT variable is much more significant than the other independent variables.

4.2. Model Equations (Variance of Analysis)

Table 4 shows the portion of variance analysis, including the sum of squares, the degree of freedom, and the mean square were given in the columns. The F-statistic value is found based on these data. The P-value is less than 0.005, proving that the whole model equation is significant. The confidence level for private offices, government offices, and combined government and private offices are 54%, 59%, and 67%, respectively.

Table 3. Effect of variables on fire load density

	Constant and variables of model	Coefficients (B)	T-statistic	P-value
Private offices	Constant	149.38	0.91	0.38
	Wood Percentage (WP)	0.71	0.37	0.72
	Office Type (OT)	197.58	4.96	0
	Area of office Rooms (AR)	-1.91	-1.42	0.17
Government offices	Constant	-0.67	-0.003	0.99
	Wood Percentage (WP)	0.04	0.01	0.99
	Office Type (OT)	443.41	5.97	0
	Area of office Rooms (AR)	-2.96	-0.64	0.53
Combine government and private offices	Constant	-285.96	-1.3	0.2
	Wood Percentage (WP)	1.49	0.67	0.51
	Office Type (OT)	373.04	7.59	0
	Category (OC)	179.69	2.55	0.015
	Area of rooms	-3.67	-1.59	0.12

Table 4. Model summary for offices

	Model	Sum of Squares (SS)	Degrees of freedom (df)	Mean Square (MS)	F-statistic	P-value
Private offices	Regression	155416.6	3	51805.5	9.1	0.001
	Residual	102262.2	18	5681.2		
	Total	257678.8	21			
Government offices	Regression	2011418.5	3	670472.8	12.0	0
	Residual	1110109.6	20	55505.4		
	Total	3121528.1	23			
Combine offices (Government + Private)	Regression	3282782.6	4	820695.6	24.1	0
	Residual	1394036.2	41	34000.8		
	Total	4676818.9	45			

The equation developed from the regression analysis for the fire load density of private office rooms is:

$$f(x) = 149.38 + 0.71x_1 + 197.58x_2 - 1.91x_3 \quad (3)$$

The R-square value for the equation is 0.60, and the adjusted R-square value is 0.54. The mean and standard deviation of fire load density for all the surveyed private offices was found as 427.18 MJ/m^2 and 110.77 MJ/m^2, respectively.

The equation for the fire load density of government office rooms is:

$$f(x) = -0.67 + 0.04x_1 + 443.41x_2 - 2.96x_3 \quad (4)$$

The R-square value for the equation is 0.64, and the adjusted R-square value is 0.59. The mean and standard deviation of fire load density for all the surveyed government offices was found as 763.41 MJ/m^2 and 368.40 MJ/m^2, respectively.

The equation for the fire load density of combined government and private offices is:

$$f(x) = -285.96 + 1.49x_1 + 373.04x_2 + 179.69x_3 - 3.67x_4 \quad (5)$$

where $f(x)$: represent the fire load density in MJ/m^2, variable x_1: represent the percentage of wood in the office room, x_2: represent the office type (for general office rooms x_2 = 1, for clerical office x_2 = 2, and for storage and file rooms x_2 = 3) and x_3: represent the area of the office room in m^2. A new variable x_4 is added for the category of government and private office buildings.

The R-square value is increased to (0.70), and the adjusted R-square value is (0.67) when combined offices are considered. The mean and standard deviation of fire load density for all the surveyed offices was found as 602.61 MJ/m^2 and 322.38 MJ/m^{2,} respectively.

5. Analysis for Maximum Temperature

Using the survey data, including fire loads, office types, categories, office dimensions, and ventilations, maximum temperature T_{max} °C was calculated by using an empirical equation developed by Law (Buchanan and Abu, 2017a). The equations consider the total internal room area (m^2), area of the openings (m^2), and height of the openings (m). The ventilation conditions during the survey included the measuring breadth, depth, and height of each opening from the floor level. The ventilation provides a supply of oxygen, thus increasing the intensity of the fire. The average maximum temperatures determined for various office types of the survey data are presented in Table 5. The average temperature and standard deviation for all the rooms were found to be 1176.88 °C and 52.14 °C, respectively. Despite having the maximum fire load, the storage rooms showed the minimum temperature (930.55 °C) because of the least ventilation. The maximum temperature exists in the clerical office rooms (1210.81 °C) because it has more space and is well ventilated. A graphical comparison of office types with maximum temperature and ventilation factors is shown in Figures 5a and 5b, respectively.

The survey conducted in Pakistan (Islamabad) for total fire load density is 603 MJ/m^2 found by the combination method. The difference in fire load density for government and private offices is found to be much greater (763.42 MJ/m^2 for government offices and 431.49 MJ/m^2 for private offices) and thus cannot be treated as the same while designing an office building for fire safety and fire resistance. The comparison of fire load densities of Pakistan with other worldwide FLD surveys is presented in Figure 6.

6. Conclusions

In this paper, the fire load density for office buildings in Pakistan is investigated by surveying a representative model of the office buildings of concern and making a list of the compartments' sizes, fixed and movable combustibles, ventilation conditions, and their relevant features using the combination method. A total of 92 office rooms were surveyed for fire load, including government and private office rooms in the different sectors of Islamabad. The data were analyzed using the multiple linear regression techniques to develop fire FLD models for private, government, and combination of both types of offices. The analytical methods were also used to analyze data to find the characteristics of fire like temperature, etc., in an office due to the total fire load in the office rooms. The results were compared with various codes across the world, including the building code of Pakistan, to show the fire load values. Based on the survey results following conclusions can be drawn.

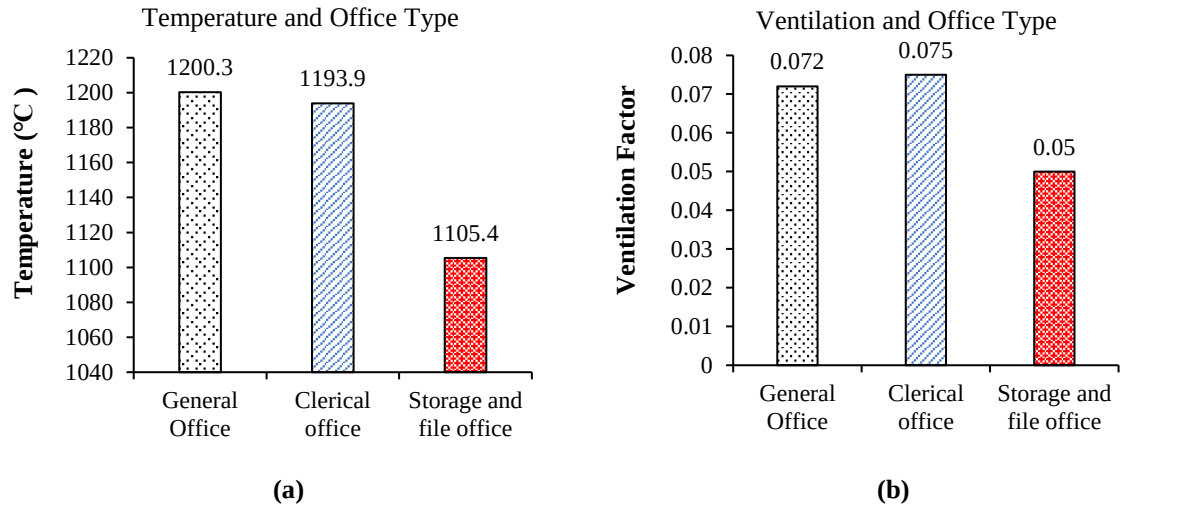

Fig. 5. Comparison of office type with: a) Average maximum temperatures; and b) Ventilation factors

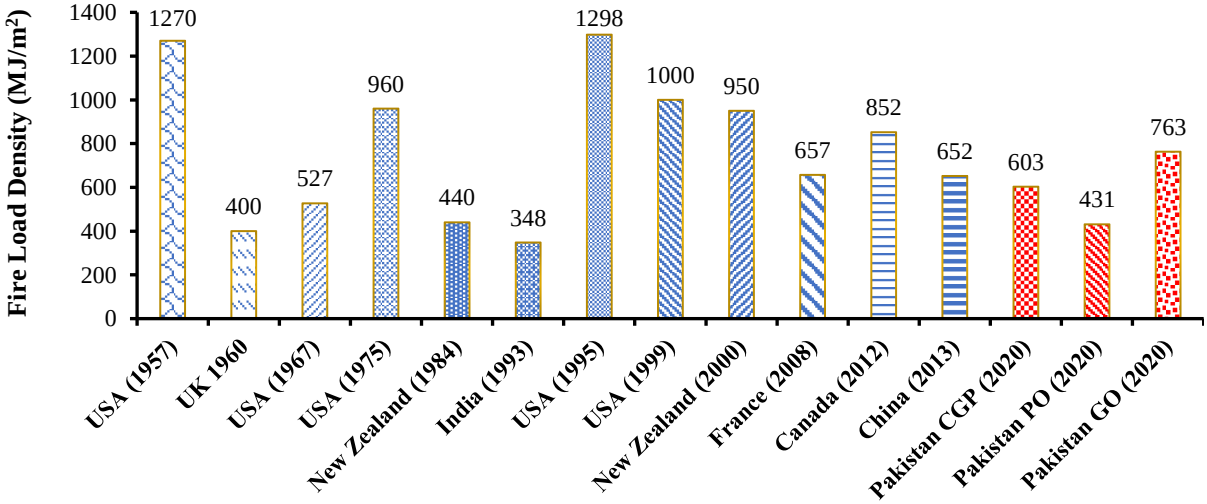

Fig. 6. Comparison of fire load densities from various surveys around the world

Table 5. Office temperatures for various office types using the survey data

Office type	Temperature (℃)			
	Minimum	Maximum	Mean	Standard deviation
General office	1062.18	1210.50	1189.45	34.01
Clerical office	1093.12	1210.81	1177.93	35.24
Storage and file office	930.55	1209.95	1105.36	129.79
All office type	930.55	1210.81	1176.88	52.14

a. The average and standard deviation of the fire load for all the office rooms were 603 MJ/m^2 and 322.38 MJ/m^{2,} respectively. The present building code of Pakistan lacks this information.
b. The survey results found that the value of fire load changes for office room use. Storerooms contain the heaviest fire load, which was 1468.02 MJ/m^2. The minimum fire load in general office rooms was 247.05 MJ/m^2.
c. Two types of office buildings were surveyed, private office buildings and government office buildings. The survey result shows that the fire load values are different for government and private offices, whereas the building code of Pakistan (which is adapted from NFPA codes) has the same value for both government and private offices.
d. The impact of the percentage of the wood material is more than the other combustible material in the office room. In some office rooms, the wood percentage was found to be more than 80%. The result also shows that the percentage of paper in the office room has less impact on fire load. The plastic contribution is below 30% of the total fire load.
e. The fire load depends on the area and amount of combustible material present in the office room. When the area of the room increases, the fire load also increases because it has the more combustible material in the room and the fire load decrease when the area of the room decreases but has the less combustible materials in the office room. This finding is contrary to other surveys conducted worldwide.

7. References

Baldwin, R., Law, M., Allen, G. and Griffiths, L.G. (1970). *Survey of fire-loads in modern office buildings, Some preliminary results*, JFRO, Fire Research Note No. 808.

Barnett, C.R. (1984). *Pilot fire load survey*, Project Report No 3580, New Zealand Fire Protection Association, MacDonald Barnett Partners, Auckland.

Bryson, J.O. and Gross, D. (1968). *Techniques for the survey and evaluation of live floor loads and fire loads in modern office buildings*, U.S. Department of Commerce, National Bureau of Standards, (Vol. 9698), Washington, DC.

Buchanan, A.H. and Abu, A.K. (2017a). *Structural design for fire safety*, John Wiley and Sons.

Buchanan, A.H. and Abu, A.K. (2017b). *Structural design for fire safety* (Second), United Kingdom: Wiley.

Bwalya, A. (2008). "An overview of design fires for building", *Fire Technology*, 44(June), 167-184. https://doi.org/10.1007/s10694-007-0031-7.

Bwalya, A.C., Gibbs, E., Lougheed, G.D. and Kashef, A. (2010). *Characterization of fires in multi-suite residential dwellings: Phase 1- Room fire experiments with individual furnishings*, Institute for Research in Construction, National Research Council Canada, Research Report, IRC-RR-302, Ottawa, Canada.

Caro, T.C. and Milke, J.A. (1996). *A survey of fuel loads in contemporary office buildings*, US Department of Commerce, Technology Administration.

Culver, C. (1976). *Fire loads and live loads in buildings*, US Department of Commerce, National Bureau of Standards, 111-119.

Culver, C.G. (1978). "Characteristics of fire loads in office buildings", *Fire Technology*, 14(1), 51-60. https://doi.org/10.1007/BF01997261.

Doyle, G.M. and Macilwraith, A. (2019). "A survey of fire loads for different room types found in a third level educational building", *Collaborative European Research Conference (CERC)*, 387-396.

Džolev, I., Laban, M. and Draganić, S. (2021). "Survey based fire load assessment and impact analysis of fire load increment on fire development in contemporary dwellings", *Safety Science*, 135(1 March), 105094.

Eduful, J. (2012). "Correlation of fire load survey methodologies towards design fires for office

buildings", Ph.D. Thesis, Carleton University.

Elhami-Khorasani, N., Castillo, J.G.S., Saula, E., Josephs, T., Nurlybekova, G. and Gernay, T. (2020). "Application of a digitized fuel load surveying methodology to office buildings", *Fire Technology*, 57(January), 101-122, https://doi.org/10.1007/S10694-020-00990-2.

Fontana, M., Kohler, J., Fischer, K. and Sanctis, G. De. (2016). *Fire load density*, SFPE Handbook of Fire Protection Engineering, 1131-1142.

Frey, F. (2017). SPSS (software), *The International Encyclopedia of Communication Research Methods*, 1-2.

Gernay, T., Van Coile, R., Elhami Khorasani, N. and Hopkin, D. (2019). "Efficient uncertainty quantification method applied to structural fire engineering computations", *Engineering Structures*, 183(15 March), 1-17, https://doi.org/10.1016/j.engstruct.2019.01.002.

Green, M. (1977). "A survey of fire loads in modern office nuilding, Some preliminary results", *Fire Technology*, 13(1), 42- 52.

Ingberg, S.H., Dunham, J.W. and Thompson, J.P. (1957). *Combustible contents in buildings*, Building Materials and Structures Report 149, National Bureau of Standards, Washington, DC.

Issen, L.A. (1980). *Single family residential fire live loads survey*, Washington, D.C.: US Department of Commerce, National Bureau of Standards Washington, DC.

Khorasani, N.E., Garlock, M. and Gardoni, P. (2014). "Fire load: Survey data, recent standards, and probabilistic models for office buildings", *Engineering Structures*, 58(1 January), 152-165. https://doi.org/10.1016/j.engstruct.2013.07.042.

Korpela, K. and K.J. (2000). "Fire loads in office buildings", *Proceedings of the 3rd International Conference on Performance-Based Codes and Fire Safety Design Methods*, Society of Fire Protection Engineers, Bethesda, MD.

Korpela, K. and Kushner, J. (2000). "Fire loads in office buildings", *Proceedings of the 3rd International Conference on Performance-Based Codes and Fire Safety Design Methods*, Society of Fire Protection Engineers (SFPE), Bethesda, USA.

Kumar, K.R. (1995). "Fire load in residential nuildings", *Building and Environment*, 30(2), 299-305.

Kumar, S. and Rao, C.V.S.K. (1997). "Fire loads in office buildings", *Journal of Structural Engineering*, 123(3), 365-368. https://doi.org/10.1061/(ASCE)0733-9445(1997)123:3(365).

Mazza, F. (2015). "Seismic vulnerability and retrofitting by damped braces of fire-damaged rc framed buildings", *Engineering Structures*, 101(15 October), 179-192.

Mazza, F. (2016). "Effects of near-fault vertical earthquakes on the nonlinear incremental response of RC base-isolated structures exposed to fire", *Bulletin of Earthquake Engineering*, 14(2), 433-454.

Mazza, F. (2017). "Residual seismic load capacity of fire-damaged rubber bearings of RC base-isolated buildings", *Engineering Failure Analysis*, 79(15 October, 951-970.

Milke, J.A. and Caro, T.C. (1996). "A survey of occupant load factors in contemporary office buildings", *Journal of Fire Protection Engineering*, 8(4), 169-182, https://doi.org/10.1177/104239159600800402.

Moradi, M., Tavakoli, H.R. and Abdollahzade, G.R. (2022). "Collapse probability assessment of a 4-story RC frame under post earthquake fire scenario", *Civil Engineering Infrastructures Journal*, 55(1), 121-137, https://doi.org/10.22059/CEIJ.2021.313241.1718.

Moradi, M., Tavakoli, H.R. and Abdollahzadeh, G. (2021). "Comparison of steel and reinforced concrete frames' durability under fire and post-earthquake fire scenario", *Civil Engineering Infrastructures Journal*, 51(1), 145-168. https://doi.org/10.22059/CEIJ.2020.292639.1628.

NDMA. (2016). *National Disaster Management Authority*, NDMA Annual Report, Government of Pakistan Engineering Council.

NFPA. (2023). *NFPA 557, Standard for determination of fire loads for use in structural fire protection design*, In National Fire Protection Association (NFPA 557), 2023 Edition, Quincy, MA 02169.

Noman, M. and Yaqub, M. (2021). "Restoration of dynamic characteristics of RC T-beams exposed to fire using post fire curing technique", *Engineering Structures*, 249(15 December), 113339, https://doi.org/10.1016/j.engstruct.2021.113339.

Noman, M., Yaqub, M., Abid, M., Musarat, M.A., Vatin, N.I. and Usman, M. (2022). "Effects of low-cost repair techniques on restoration of mechanical properties of fire-damaged concrete", *Engineering Structures*, 8(27 January), 1-14, https://doi.org/10.3389/fmats.2021.801464.

Noman, M., Yaqub, M., Fahad, M., Butt, F. and Khalid, B. (2022). "Dynamic characteristics of RC structures in short and long duration real fires", *Case Studies in Construction Materials*, 16(1 June), e01058, https://doi.org/10.1016/j.cscm.2022.e01058.

Pakistan, G. (2016). *Fire safety provisions 2016*, In Building Code of Pakistan.

Sharma, U.K., Kumar, V., Kamath, P., Singh, B., Bhargava, P., Singh, Y., Usmani, A., Torero, J., Gillie, M. and Pankaj, P. (2014). "Testing of full-scale RC frame under simulated fire following earthquake", *Journal of Structural Fire*

Engineering, 5(3), 215-228, https://doi.org/10.1260/2040-2317.5.3.215.

Tavakoli, H.R. and Kiakojouri F. (2015). "Threat-independent column removal and fire-induced progressive collapse: Numerical study and comparison", *Civil Engineering Infrastructures Journal*, 48(1), 121-131.

Thauvoye, C., Zhao, B., Klein, J. and Fontana, M. (2008). "Fire load survey and statistical analysis", *Fire Safety Science*, 9(9 December), 991-1002, https://doi.org/10.3801/IAFSS.FSS.9-991.

Tufail, M., Shahzada, K., Gencturk, B.,and Wei, J. (2016). "Effect of elevated temperature on mechanical properties of limestone, quartzite and granite concrete", *International Journal of Concrete Structures and Materials*, 10(1), 1-6, https://doi.org/10.1007/s40069-016-0175-2.

Xie, Q., Xiao, J., Gardoni, P. and Hu, K. (2019). "Probabilistic analysis of building fire severity based on fire load density models", *Fire Technology*, 55(4), 1349-1375.

Yii, H.W. (2000). "Effect of surface area and thickness on fire loads", M.E. Dissertation, School of Engineering, University of Canterbury, New Zealand.

Zalok, E. and Eduful, J. (2013). "Assessment of fuel load survey methodologies and its impact on fire load data", *Fire Safety Journal*, 62(1 November), 299-310, https://doi.org/10.1016/j.firesaf.2013.08.011.

Zhai, Y. (2013). "Survey and statistical parameters of office building fire load", *Build Science*, 29(07), 122-123, https://doi.org/10.13614/j.cnki.11-1962/tu.2013.07.027.

Appendix

Data collection for fire load (FYP)

Data releated to building

Room Type		Room Length (meter)		Building Name	
Room Category		Room Width (meter)			
Fire protection systen		Ceiling Height (meter)		Fire Load Arrangement	
Floor		Area Of Room (m^2)			

An item which is weighing by combining Weighing and Inventory technique

Item	Type	No	No of element	Length (m)	width (m)	Hight (m)	Volume (m^3)	Density (kg/m^3)	Weight (kg)	Total Weight (kg)	net Total weight (kg)	Calorific Value (MJ/kg)	Fire Load (MJ/m^2)
Wood													
Plastic													
Papers													
Others													
											Total Fire Load (MJ/m^2)		0.000

Conducted by: Approved by:

Date:_____ Time:_____ No:_____

Civil Engineering Infrastructures Journal 2023, 56(1): 205-219
DOI: 10.22059/CEIJ.2022.318133.1739

RESEARCH PAPER

Innovative Efficient Element for Analysis of FGM Plates Using FEM

Shahnavaz, F.[1], Attarnejad, R.[2*], Shaloudegi, K.[3] and Kazemi Firouzjaei, R.[4]

[1] M.Sc., Researcher, School of Civil Engineering, College of Engineering, University of Tehran, Tehran, Iran.
[2] Professor, School of Civil Engineering, College of Engineering, University of Tehran, Tehran, Iran.
[3] M.Sc., Researcher, School of Civil Engineering, Clarkson, Potsdam, USA.
[4] M.Sc., Researcher, School of Civil Engineering, Polytechnic University of Catalonia (UPC), Barcelona, Spain.

Received: 29 Jan. 2021; Revised: 04 Dec. 2021; Accepted: 04 Dec. 2021

ABSTRACT: In order to obtain accurate results from displacement-based Finite Element Method (FEM), it is crucial to introduce accurate shape functions that interpolate the displacement field within an element. This paper attempts to provide such a new component by using Finite Element method using Basic Displacement Function (BDFs) for the free vibration analysis of plates with in-plane Functionally Graded Material (FGM). The first step is to introduce displacement functions and compute them using the energy method. Later, new shape functions are developed based on stiffness and force methods used to model the mechanical behavior of the element, wherein the shape functions benefit from the generality and accuracy of the stiffness and force methods. Last, the plate is analyzed using Finite Element method to derive the structural matrices from new shape functions. Several numerical examples demonstrate the accuracy and efficiency of the method, and a special material graded index named Ns is introduced.

Keywords: Basic Displacement Functions (BDFs), Finite Element Method (FEM), Free Vibration, Functionally Graded Materials (FGMs), Kirchhoff-Love Plate Theory.

1. Introduction

There are many applications of thin rectangular plates in modern engineering, such as in civil engineering, mechanical engineering, marine industry, and aeronautical engineering. (Hamrit and Necib, 2018). Over the last century, many research studies have been conducted on plates. A mathematical model of the membrane theory of plates was first presented by Euler in the eighteenth century (Naumenko and Eremeyev, 2017). In later years, Lagrange devised differential equations to describe plate free vibrations (Ramkumar et al., 1987). Over the years, a great deal of investigation has been conducted on the dynamic analysis of thin plates (Wang et al., 2017) as well as dynamic analyses of variable thickness plates such as sandwich panels (Vatani Oskouei and Kiakojouri, 2015). Leissa provides a thorough documentation of many of them (Leissa, 1969). The Kirchhoff

* Corresponding author E-mail: Attarnjd@ut.ac.ir

hypothesis dictates that thin plates will vibrate as a result of their classical vibration behavior. The use of structural elements with variable thickness reduces the weight of structure elements and improves material utilization, resulting in more economic design of structures. Static and stability analysis is an essential component of the design of these structures (Tenenbaum et al., 2020).

Material properties of Functionally Graded Materials (FGMs) are continuously variable according to spatial coordinates. FGMs display gradual variations in material properties, unlike laminated composites that can suffer from interfacial stresses leading to delamination and crack propagation (Das, 2010). Changing the thickness direction or changing the in-plane material can be used to achieve this. Initially, the idea of FGMs was proposed by Bever and Shen (1997) to produce polymer (Bever. Since there is no blunt conversion in material properties across the confluence of dissimilar materials, FGMs avoid problems associated with conventional composites, such as large inter-laminar stresses, crack initiation, and delamination (Gupta, 2020). Afterward application of FGMs noteworthy increased in aerospace engineering and micro-electrical industry. Since the mid-1990s, FGMs have been applied in many fields, such as optics, human implants, engine components, turbine blades, and many others. Researchers have also given these FGMs considerable attention (Miyamoto et al., 1999). According to the wide application of FGMs, the behavior of FGM structures has been studied in several studies such as beams, plates, and shells (Vidal et al., 2021). However, most of these studies deal with FGMs with material indices changing in thickness direction merely (Njim et al., 2021).

In recent years, many researchers have investigated the static and dynamic analyses of plates with different plate theories in conjunction with the study of their material property variation. For example, the static analysis of functionally graded rectangular plates using third-order shear deformation theory was presented by Reddy (2000). Based on Reddy's theory, Cheng and Batra (2000) investigated the identical eigenvalues between the functionally graded plates and those of membranes subjected to uniform in-plane loads. They also related the deflection of FGM plates predicted by the first-order and the third-order shear deformation theory to that of an substitute compatible Kirchhoff plate. Moreover, several studies have been done on bi-directional FGM beams (Şimşek, 2016). Among them, Goupee and Vel (2006) developed a methodology for the simulation and optimization of the vibration response of bi-directional functionally graded beams. To the best of the author's knowledge, there are a few papers in the literature that have considered the in-plane material inhomogeneity. For instance, Liu et al. (2010) presented the free vibration of FGM plates with in-plane material inhomogeneity and obtained a Levy-type solution in the specific case where the plate is merely supported alongside to the material gradient direction. In addition, an elastoplastic Mindlin-Reissner plate is analyzed using a non-layered Finite Volume formulation (Fallah et al., 2017). Recently, with the inclusion of porosity, free vibration analysis was carried out on tapered Functionally Graded Material (FGM) plates (Kumar et al., 2021). Numerical method is also used to analyse the performance of walls (Shahir and Delfan, 2021). Based on modal strain energy and Dempster-Shafer evidence theory, a damage detection method is presented for finding damage in two-layer grids using only a few mode shapes (Teimouri et al., 2021). An asymptotic framework for layered plates is developed with piecewise uniform problem parameters. As well as functionally graded shells, coatings and interfacial layers, it allows various extensions (Kaplunov et al., 2021). A two-parameter model of Winkler-Pasternak's elastic medium with Aluminum

and Alumina porosity is used to model the interaction between FGM plate and elastic foundation (Saidi and Sahla, 2019). Considering porosities that may occur inside functionally graded materials (FGMs) during their fabrication, a higher-order shear deformation model is developed for static and free vibration analyses of functionally graded beams (Hadji et al., 2019). Also, the nonlinear bending of functionally graded (FG) circular sector plates has been investigated when they are subjected to transverse mechanical loading (Fallah and Karimi, 2019).

In the case of general variations of the material and geometry of the plate, there is no closed-form solution, so alternative numerical techniques are required, e.g. the Rayleigh-Ritz method (Kumar, 2018), Differential Quadrature Method (DQM) (Bacciocchi et al., 2016), Differential Least-Square-based Finite Difference (LSFD) (Liu et al., 2021), Differential Quadrature Element Method (DQEM) (Makvandi et al., 2019), Transformed Differential Quadrature Method (TDQM) (Malekzadeh, 2018), generalized differential quadrature rule (Lal and Siani, 2020), methods based on the Green Functions (Mora et al., 2016), 2D Differential Transform Method (2D-DTM) (Chiba, 2019). FEM is one of these techniques.

The goal of this paper is to present an effective tool for analyzing plates with in-plane Functionally Graded Materials (FGMs) using the FEM. A unit load method is used to derive Basic Displacement Functions (BDFs). Afterward, in terms of BDFs, new shape functions have been derived from a mechanical perspective. The Finite Element method is finally used in order to derive structural stiffness and a consistent mass matrix for the in-plane FGM plate. The present method has been illustrated using numerical examples and graphs to illustrate both its accuracy and economy. Moreover, a special material graded index has been presented, namely *Ns*. This method is really efficient for analyzing FGM plates and makes it possible to do a Finite Element analysis with lower segments. Thus, it will result to have the answers more quickly on a medium computer.

2. Materials and Methods

A general case is considered in this study. In Figure 1, a rectangular FGM plate with length *a* and width *b* is shown in a Cartesian coordinate system. Also, $h(x,y)=h_0\times H(x)\times H(y)$: is the variable thickness of the plate, where h_0: is plate thickness at the coordinate center, and $H(x)$ and $H(y)$: stand for thickness abnormality along x and y directions, respectively. Figure 2 depicts positive signs for the shear forces and bending moments. The material properties, such as the elastic modulus, E and mass density, ρ are varying in-plane as follows:

$$E = V_l E_l + V_r E_r \tag{1}$$

$$\rho = V_l \rho_l + V_r \rho_r \tag{2}$$

in which:

$$V_l + V_r = 1 \tag{3}$$

where V_l and V_r: are the volumes of fraction in the left and right sides of the plate along the direction with material inhomogeneity which y : is the direction in this study.

In order to understand Kirchhoff-Love plate theory, the following assumptions has been made (Szilard, 2004):

1. z is not affected by displacement along z-direction;
2. Before deformation, portions of the plate that were parallel to its middle surface remain parallel to it after deflection;
3. Deformation due to shear is ignored;
4. The deflections and rotations of plates are small compared to their dimensions;
5. Transverse stresses in the plate surface direction can be ignored.

As a result of Kirchhoff-Love plate theory, the following relationships can be written as follows.

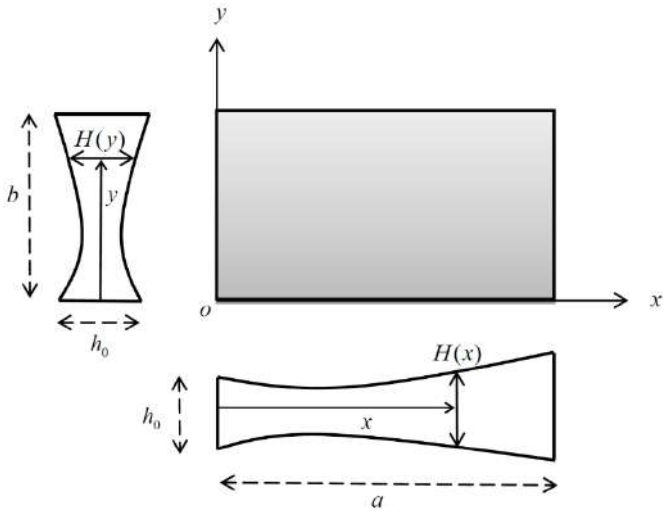

Fig. 1. FGM rectangular plate in a Cartesian coordinate system

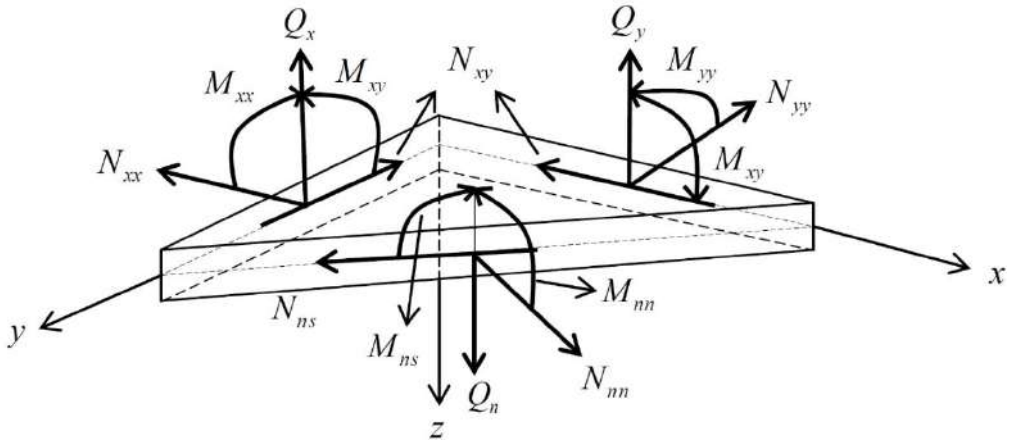

Fig. 2. Positive sign conventions for shear forces and bending moments

Deranication in x, y and z directions are given as:

$$u_x = -z\theta_x = -z\frac{\partial w_0}{\partial x}, \quad u_y = -z\theta_y = -z\frac{\partial w_0}{\partial y}, \quad u_z = w_0 \tag{4}$$

where θ_x and θ_y: stand for bending rotations about x and y axis, respectively, in the following manner:

$$\theta_x = \frac{\partial w_0}{\partial x}, \qquad \theta_y = \frac{\partial w_0}{\partial y} \tag{5}$$

and w_0: is the displacement function. Strain/displacement relations give:

$$\varepsilon_{xx} = -z\frac{\partial^2 w_0}{\partial x^2}, \quad \varepsilon_{yy} = -z\frac{\partial^2 w_0}{\partial y^2}, \quad \varepsilon_{xy} = -2z\frac{\partial^2 w_0}{\partial x \partial y}, \quad \varepsilon_{xz} = \varepsilon_{yz} = \varepsilon_{zz} = 0 \tag{6}$$

Constitutive equations give:

$$\sigma_{xx} = \frac{E}{1-\nu^2}(\varepsilon_{xx} + \nu\varepsilon_{yy}) = \frac{-Ez}{1-\nu^2}\left(\frac{\partial^2 w_0}{\partial x^2} + \nu\frac{\partial^2 w_0}{\partial y^2}\right) \tag{7}$$

$$\sigma_{yy} = \frac{E}{1-\nu^2}(\varepsilon_{yy} + \nu\varepsilon_{xx}) = \frac{-Ez}{1-\nu^2}\left(\frac{\partial^2 w_0}{\partial y^2} + \nu\frac{\partial^2 w_0}{\partial x^2}\right) \tag{8}$$

$$\sigma_{xy} = \frac{E}{1-\nu^2}\left(\frac{1-\nu}{2}\varepsilon_{xy}\right) = \frac{-Ez}{1+\nu}\left(\frac{\partial^2 w_0}{\partial x \partial y}\right) \tag{9}$$

Applying Eqs. (7) to (9), moments per unit length are represented by

$$M_{xx} = \int_{-h/2}^{h/2} z\,\sigma_{xx}\,dz = -D\left(\frac{\partial^2 w_0}{\partial x^2} + \nu\frac{\partial^2 w_0}{\partial y^2}\right) \tag{10}$$

$$M_{yy} = \int_{-h/2}^{h/2} z\,\sigma_{yy}\,dz = -D\left(\frac{\partial^2 w_0}{\partial x^2} + \nu\frac{\partial^2 w_0}{\partial y^2}\right) \tag{11}$$

$$M_{xy} = \int_{-h/2}^{h/2} z\,\sigma_{xy}\,dz = -D(1-\nu)\left(\frac{\partial^2 w_0}{\partial x \partial y}\right) \tag{12}$$

where $D = \frac{E}{12(1-\nu^2)}h(x,y)^3$: is the bending rigidity of the plate and ν: is Poisson's ratio which is consistent.

Based on a harmonic abnormality of $w_0(x,y,t)$ as the transverse displacement of the FGM plate, Eq. (13) can be written.

$$w_0(x,y,t) = w(x,y)e^{i\omega t} \tag{13}$$

where ω: denotes natural frequency. FGM variable thickness thin plates obey the following differential equation (Van Vinh et al., 2021):

$$\frac{\partial^2}{\partial x^2}\left[-D\left(\frac{\partial^2 w}{\partial x^2}+v\frac{\partial^2 w}{\partial y^2}\right)\right] + 2\frac{\partial^2 w_0}{\partial x\partial y}\left[-D(1-v)\left(\frac{\partial^2 w}{\partial x\partial y}\right)\right] + \frac{\partial^2}{\partial y^2}\left[-D\left(\frac{\partial^2 w}{\partial y^2}+v\frac{\partial^2 w}{\partial yx^2}\right)\right] = -\rho h w\omega^2+\frac{\rho h^3\omega^2}{12}\left(\frac{\partial^2 w}{\partial x^2}+\frac{\partial^2 w}{\partial y^2}\right) \quad (14)$$

2.1. BDFs Definition

Various types of beams have been used in different ways with Basic Displacement Functions (BDFs) (Attarnejad et al., 2010). It discusses how to calculate BDFs for tapered FGM plates, followed by a discussion of their applications in deriving nodal flexibility matrices.

Pachenari and Attarnejad (2014a) interpreted BDFs to be the nodal displacements of FGM plates whose boundary conditions are Clamped-Clamped-Free-Free (C-C-F-F). Since it has only one free node and other conditions derived from it, they assumed this condition. An element's x- or y-axis transverse displacement or rotation angle is the result of a unit load acting at x- or y-distance. It is possible to specify detail BDFs for node i as below (the edges adjacent to node i are free, whereas the edges adjacent to the other are clamped):

b_{wi}: is load acting at *x*, *y* causes a transverse displacement of node *i* (Figure 3a); $b_{\theta xi}$: is a unit load acting at *x*, *y* bends rotation of node *i* in the *x*-direction (Figure 3b); $b_{\theta yi}$: is a unit load acting at *x*, *y* bends the rotation of node *i* in the *y*-direction (Figure 3c). nodes *i* = 1, 2, 3 and 4 are respectively shown in Figure 3. The reciprocal theorem is applied to all the BDFs in order to determine their equivalent systems. BDFs are the transverse displacements of an element due to a unit nodal load or moment. An arbitrary point (such as point(x, y)) on the element is considered. As a result, BDFs in node i are equivalent since edges that end at node i are free, but others are clamped:

b_{wi}: is an acting unit load at node *i* causes transverse displacement at distances *x* and *y* (Figure 4a); $b_{\theta xi}$: is an *x*-directed moment acting on node *i* for distance *x* and *y* will result in a transverse displacement at distances *x* and *y*; $b_{\theta yi}$: is the *y*-axis motion of the unit moment at node *i* at distances *x* and *y* is the result of transverse displacement at distances *x* and *y* (Figure 4c).

2.2. Nodal Flexibility Matrices

According to the concept of equivalent definitions of BDFs, nodal flexibility matrices can be derived for node *i* of the FGM plate element.

On the basis of the equivalent definitions of BDFs and its first derivative, nodal flexibility matrices can be determined for all nodes in terms of BDFs:

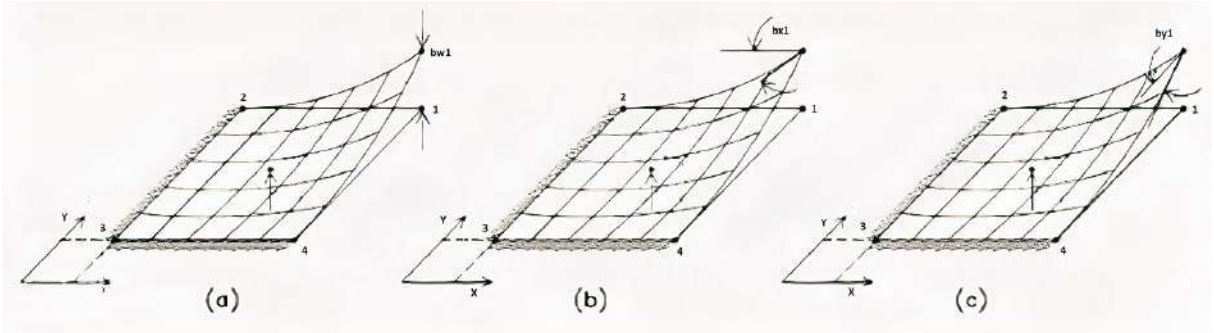

Fig. 3. The transverse displacements of an arbitrary point due to a unit nodal load: a) Load acting at x, y causes a transverse displacement of node; b) Unit load acting at x, y bends rotation of node 1 in the x-direction; and c) unit load acting at x, y bends the rotation of node 1 in the y-direction

$$F_{ii}=\begin{bmatrix} b_{wi(x,y)} & b_{\theta xi(x,y)} & b_{\theta yi(x,y)} \\ \frac{db_{wi(x,y)}}{dx}|_{xi,yi} & \frac{db_{\theta xi(x,y)}}{dx}|_{xi,yi} & \frac{db_{\theta yi(x,y)}}{dx}|_{xi,yi} \\ \frac{db_{wi(x,y)}}{dy}|_{xi,yi} & \frac{db_{\theta xi(x,y)}}{dy}|_{xi,yi} & \frac{db_{\theta yi(x,y)}}{dy}|_{xi,yi} \end{bmatrix}$$

By multiplication of flexibility matrix and force matrix, the displacement of each node obtains.

2.3. BDFs Computation

BDFs can be calculated for each node using methods based on energy because they contain pure mechanical essence. In this study the unit load method (virtual work) is employed as follow (Zakeri et al., 2016):

Node 1:

$$b_{w1(x,y)}=\frac{1}{m}\int_{\beta B}^{y}\int_{\alpha A}^{x}\frac{(A-s)(x-s)}{s^{3r}t^{3l}}\left(\frac{x-A}{k}\right)^{c}\left(\frac{y-B}{j}\right)^{d}dsdt+\frac{1}{m}\int_{\beta B}^{y}\int_{\alpha A}^{x}\frac{(B-t)(y-t)}{s^{3r}t^{3l}}\left(\frac{x-A}{k}\right)^{c}\left(\frac{y-B}{j}\right)^{d}dsdt$$

$$b_{\theta 1(x,y)}=\frac{1}{m}\int_{\beta B}^{y}\int_{\alpha A}^{x}\frac{(x-s)}{s^{3r}t^{3l}}(\frac{x-A}{k})^{c}(\frac{y-B}{j})^{d}\,dsdt$$

$$b_{\theta 1(x,y)}=\frac{1}{m}\int_{\beta B}^{y}\int_{\alpha A}^{x}\frac{(y-t)}{s^{3r}t^{3l}}(\frac{x-A}{k})^{c}(\frac{y-B}{j})^{d}\,dsdt$$

Node 2:

$$b_{w2(x,y)}=\frac{1}{m}\int_{\beta B}^{y}\int_{x}^{A}\frac{s(x-s)}{s^{3r}t^{3l}}\left(\frac{x-A}{k}\right)^{c}\left(\frac{y-B}{j}\right)^{d}dsdt+\frac{1}{m}\int_{\beta B}^{y}\int_{\alpha A}^{x}\frac{(B-t)(y-t)}{s^{3r}t^{3l}}\left(\frac{x-A}{k}\right)^{c}\left(\frac{y-B}{j}\right)^{d}dsdt$$

$$b_{\theta x2(x,y)}=\frac{1}{m}\int_{\beta B}^{y}\int_{\alpha A}^{x}\frac{(x-s)}{s^{3r}t^{3l}}(\frac{x-A}{k})^{c}(\frac{y-B}{j})^{d}\,dsdt$$

$$b_{\theta y2(x,y)}=\frac{1}{m}\int_{\beta B}^{y}\int_{x}^{A}\frac{(y-t)}{s^{3r}t^{3l}}(\frac{x-A}{k})^{c}(\frac{y-B}{j})^{d}\,dsdt$$

Node 3:

$$b_{w3(x,y)}=\frac{1}{m}\int_{y}^{B}\int_{x}^{A}\frac{s(x-s)}{s^{3r}t^{3l}}\left(\frac{x-A}{k}\right)^{c}\left(\frac{y-B}{j}\right)^{d}dsdt+\frac{1}{m}\int_{\beta B}^{y}\int_{\alpha A}^{x}\frac{-t(y-t)}{s^{3r}t^{3l}}\left(\frac{x-A}{k}\right)^{c}\left(\frac{y-B}{j}\right)^{d}dsdt$$

$$b_{\theta x3(x,y)}=\frac{1}{m}\int_{y}^{B}\int_{x}^{A}\frac{(x-s)}{s^{3r}t^{3l}}(\frac{x-A}{k})^{c}(\frac{y-B}{j})^{d}\,dsdt$$

$$b_{\theta y3(x,y)}=\frac{1}{m}\int_{y}^{B}\int_{x}^{A}\frac{(y-t)}{s^{3r}t^{3l}}(\frac{x-A}{k})^{c}(\frac{y-B}{j})^{d}\,dsdt$$

Node 4:

$$b_{w4(x,y)}=\frac{1}{m}\int_{y}^{B}\int_{\alpha A}^{x}\frac{(A-s)(x-s)}{s^{3r}t^{3l}}\left(\frac{x-A}{k}\right)^{c}\left(\frac{y-B}{j}\right)^{d}dsdt+\frac{1}{m}\int_{\beta B}^{y}\int_{\alpha A}^{x}\frac{-t(y-t)}{s^{3r}t^{3l}}\left(\frac{x-A}{k}\right)^{c}\left(\frac{y-B}{j}\right)^{d}dsdt$$

$$b_{\theta x4(x,y)}=\frac{1}{m}\int_{y}^{B}\int_{\alpha A}^{x}\frac{(x-s)}{s^{3r}t^{3l}}(\frac{x-A}{k})^{c}(\frac{y-B}{j})^{d}\,dsdt$$

$$b_{\theta y4(x,y)}=\frac{1}{m}\int_{y}^{B}\int_{\alpha A}^{x}\frac{(y-t)}{s^{3r}t^{3l}}(\frac{x-A}{k})^{c}(\frac{y-B}{j})^{d}\,dsdt$$

where A: is the length, B: is the width of the plate, s and t: are integral variables, r and l: are thickness parameters, k and j: are stiffnesses (EI) in the x-direction and y-direction, c/d: is the inhomogeneous ratio in x and y directions (E_x/E_y and c+d=1. The following properties are assumed for the FGM plate:

$$h(x,y)=h_1(\frac{x}{A})^{r}(\frac{y}{B})^{l}\text{ and }r\neq\frac{1}{3},1,\ l\neq\frac{1}{3},1$$

$$c,d=\frac{1}{2}$$

m is defined as:

$$m=\frac{E_0h_1^3/A^{3r}B^{3l}}{12(1-\nu^2)} \tag{16}$$

Figure 4 shows the parameters of Eq. (15).

Thus, the equations could be rewritten as:

Node 1:

$$b_{w1(x,y)} = \frac{1}{m}\frac{x^2(x-k)^{-3r}}{(1-3r)(3-3r)}\frac{(2A-x)y(y-j)^{-3l}}{1-3l} + \frac{1}{m}\frac{y^2(y-j)^{-3r}}{(1-3l)(3-3l)}\frac{(2B-y)x(x-k)^{-3r}}{1-3r}$$

$$b_{\theta x1(x,y)} = \frac{1}{m}\frac{x^2(x-k)^{-3r}}{(2-3r)(1-3r)}\frac{y(y-j)^{-3l}}{(1-3l)}$$

$$b_{\theta y1(x,y)} = \frac{1}{m}\frac{x(x-k)^{-3r}}{(1-3r)}\frac{y^2(y-j)^{-3l}}{(1-3l)(2-3l)}$$

Node 2:

$$b_{w2(x,y)} = \frac{1}{m}(A^{2-3r}\left(\frac{A}{3-3r}-\frac{x}{2-3r}\right) + \frac{x^3(x-k)^{-3r}}{(3-3r)(2-3r)})\frac{y(y-j)^{-3l}}{(1-3l)} + \frac{1}{m}\frac{y^2(y-j)^{-3r}}{(2-3l)}\left(\frac{B}{1-3l}-\frac{y}{3-3l}\right) + \frac{A^{1-3r}-x^3(x-k)^{-3r}}{(1-3l)}$$

$$b_{\theta x2(x,y)} = \frac{1}{m}(A^{1-3r}\left(\frac{-A}{2-3r}+\frac{x}{1-3r}\right) + \frac{x^2(x-k)^{-3r}}{(2-3r)(1-3r)})\frac{y(y-j)^{-3l}}{(1-3l)}$$

$$b_{\theta y2(x,y)} = \frac{1}{m}\frac{A^{1-3r}-x(x-k)^{-3r}}{(1-3r)}\frac{y^2(y-j)^{-3l}}{(1-3l)(2-3l)}$$

Node 3:

$$b_{w3(x,y)} = \frac{1}{m}(A^{2-3r}\left(\frac{A}{3-3r}-\frac{x}{2-3r}\right) + \frac{x^3(x-k)^{-3r}}{(3-3r)(2-3r)})\frac{B^{1-3l}y(y-j)^{-3l}}{(1-3l)} + \frac{1}{m}(B^{2-3l}\left(\frac{B}{3-3l}-\frac{y}{2-3l}\right) + \frac{y^3(y-j)^{-3r}}{(3-3l)(2-3l)})(\frac{A^{1-3r}-x^3(x-k)^{-3r}}{(1-3l)})$$

$$b_{\theta x3(x,y)} = \frac{1}{m}(A^{1-3r}\left(\frac{-A}{2-3r}+\frac{x}{1-3r}\right) - \frac{x^2(x-k)^{-3r}}{(2-3r)(1-3r)})\frac{B^{1-3l}-y(y-j)^{-3l}}{(1-3l)}$$

$$b_{\theta y3(x,y)} = \frac{1}{m}\frac{A^{1-3r}-x(x-k)^{-3r}}{(1-3r)}(B^{1-3l}(\frac{-B}{2-3l} - \frac{y}{1-3l})\frac{y^2(y-j)^{-3l}}{(1-3l)(2-3l)})$$

Node 4:

$$b_{w4(x,y)} = \frac{1}{m}(\frac{Ax^2(x-k)^{-3r}}{(1-3r)(2-3r)} - \frac{x^3(x-k)^{-3r}}{(3-3r)(2-3r)})\frac{B^{1-3l}y(y-j)^{-3l}}{(1-3l)} + \frac{1}{m}(B^{2-3l}\left(\frac{B}{3-3l}-\frac{y}{2-3l}\right) + \frac{y^3(y-j)^{-3r}}{(3-3l)(2-3l)})(\frac{x(x-k)^{-3r}}{(1-3r)})$$

$$b_{\theta x4(x,y)} = \frac{1}{m}\frac{x^2(x-k)^{-3r}}{(2-3r)(1-3r)}\frac{B^{1-3l}-y(y-j)^{-3l}}{(1-3l)}$$

$$b_{\theta y4(x,y)} = \frac{1}{m}\frac{x^2(x-k)^{-3r}}{(1-3r)}(B^{1-3l}(\frac{-B}{2-3l} - \frac{y}{1-3l})\frac{y^2(y-j)^{-3l}}{(1-3l)(2-3l)})$$

Considering a tapered FGM plate under transverse load *q(x,y)*, a two-determinate analysis can be used to calculate the support reactions, i.e. *C-C-F-F* plates (Figure 5). It can be written using the superposition principle:

$$\begin{Bmatrix} w_1 \\ \theta_{x1} \\ \theta_{y1} \end{Bmatrix}^{(a)} = \begin{Bmatrix} w_1 \\ \theta_{x1} \\ \theta_{y1} \end{Bmatrix}^{(b)} + \begin{Bmatrix} w_1 \\ \theta_{x1} \\ \theta_{y1} \end{Bmatrix}^{(c)} = 0 \qquad (17)$$

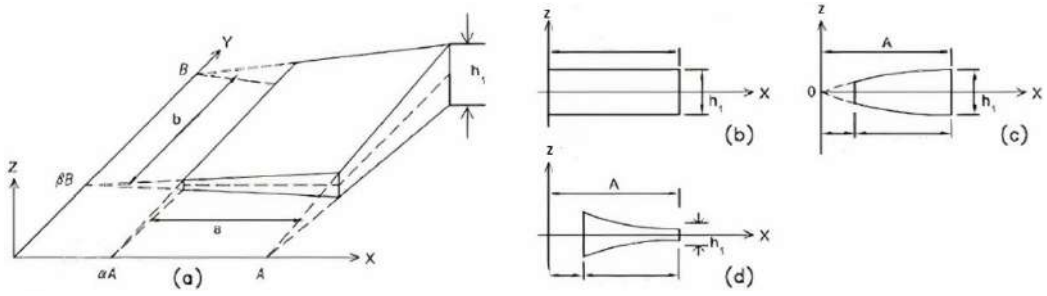

Fig. 4. Plate parameters: a) Three-dimensional view of the plate; b) Plate with fixed thickness; c) Plate with gradually increasing thickness; and d) Plate with gradually decreasing thickness

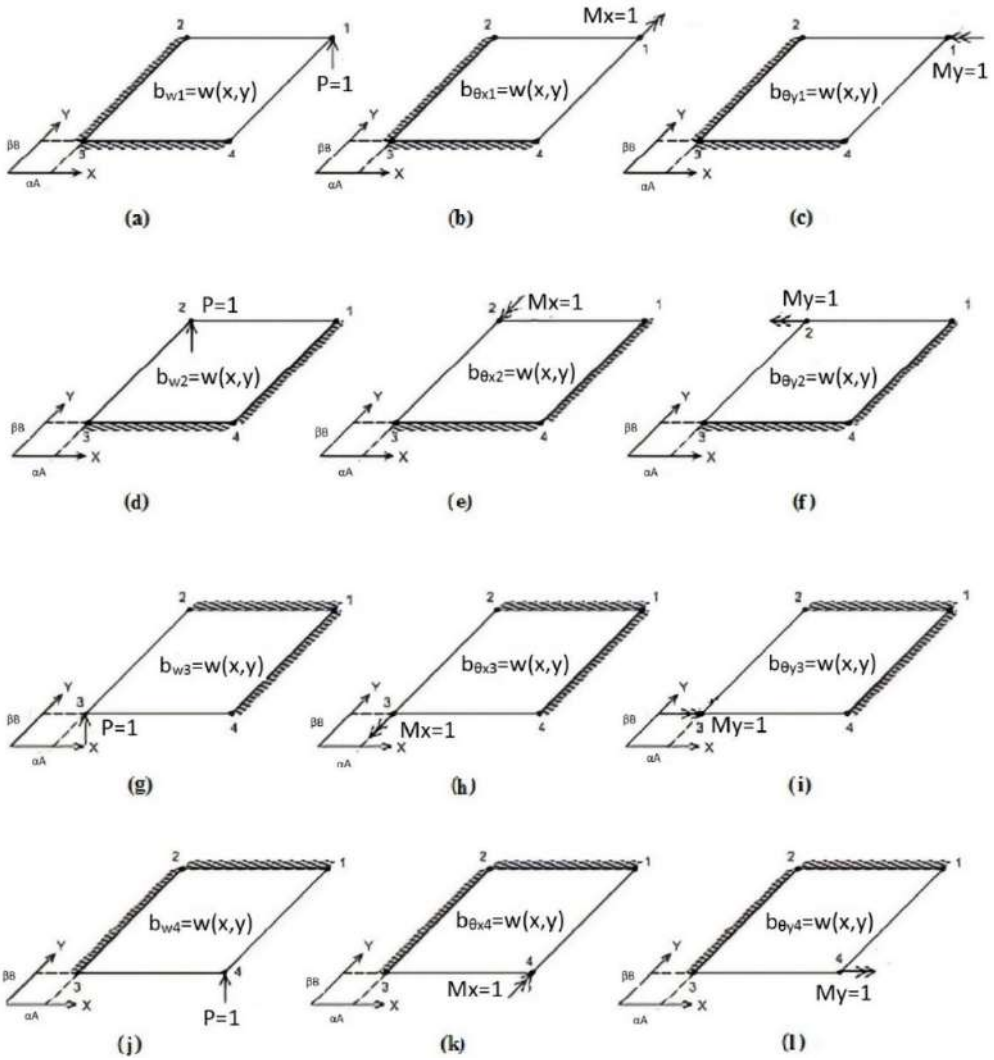

Fig. 5. Positive directions: a) Load acting at x, y causes a transverse displacement of Node 1; b) Unit load acting at x, y bends rotation of Node 1 in the x-direction; c) Unit load acting at x, y bends the rotation of Node 1 in the y-direction; d) Load acting at x, y causes a transverse displacement of Node 2; e) Unit load acting at x, y bends rotation of Node 2 in the x-direction; f) Unit load acting at x, y bends the rotation of Node 2 in the y-direction; g) Load acting at x, y causes a transverse displacement of Node 3; h) Unit load acting at x, y bends rotation of Node 3 in the x-direction; i) Unit load acting at x, y bends the rotation of Node 3 in the y-direction; j) Load acting at x, y causes a transverse displacement of Node 4; k) unit load acting at x, y bends rotation of Node 4 in the x-direction; and l) Unit load acting at x, y bends the rotation of Node 4 in the y-direction

in cases (a) - (c), w_1, θ_{x1}: stand for the nodal displacements at node *i* in Figures 5a-5c, respectively. BDFs can be used to measure nodal displacements at node 1:

$$\begin{Bmatrix} w_1 \\ \theta_{x1} \\ \theta_{y1} \end{Bmatrix}^{(b)} = \int_{\beta B}^{B}\int_{\alpha A}^{A} q_z(x,y) \begin{Bmatrix} b_{w1}(x,y) \\ b_{\theta x1}(x,y) \\ b_{\theta y1}(x,y) \end{Bmatrix} dxdy \quad (18)$$

$$\begin{Bmatrix} w_1 \\ \theta_{x1} \\ \theta_{y1} \end{Bmatrix}^{(c)} = F_{11} \begin{Bmatrix} F^1 \\ M_x^1 \\ M_y^1 \end{Bmatrix} \quad (19)$$

The matrix F_{11} represents the nodal flexibility of node 1 in Eq. (8). By using Eqs. (18) to (20), one obtains:

$$\begin{Bmatrix} F^1 \\ M_x^1 \\ M_y^1 \end{Bmatrix} = -F_{11}^{-1} \int_{\beta B}^{B}\int_{\alpha A}^{A} q_z(x,y) \begin{Bmatrix} b_{w1}(x,y) \\ b_{\theta x1}(x,y) \\ b_{\theta y1}(x,y) \end{Bmatrix} dxdy \quad (20)$$

in which F_{11}^{-1} is the nodal stiffness matrix of node 1. Similarly, other nodes also receive support reactions. Thus the support reactions of node *i* (*i* =1, .., 4) are:

$$\begin{Bmatrix} F^i \\ M_x^i \\ M_y^i \end{Bmatrix} = -F_{ii}^{-1} \int_{\beta B}^{B} \int_{\alpha A}^{A} q_z(x,y) \begin{Bmatrix} b_{wi}(x,y) \\ b_{\theta xi}(x,y) \\ b_{\theta yi}(x,y) \end{Bmatrix} dxdy \tag{21}$$

Support reactions with opposite signs have the same magnitude as nodal equivalent forces, so the vector F containing nodal equivalent forces is equal:

$$F = \sum \int_{\beta B}^{B} \int_{\alpha A}^{A} q_z(x,y) b dxdy \tag{22}$$

where $\sum$ and $b = \begin{bmatrix} b_{w1} & b_{\theta x1} & b_{\theta y1} & b_{w2} & b_{\theta x2} & b_{\theta y2} & b_{w3} & b_{\theta x3} & b_{\theta y3} & b_{w4} & b_{\theta x4} & b_{\theta y4} \end{bmatrix}^T$ are the matrices indicating nodal stiffness and nodal BDFs for nodes 1 to 4.

Comparing Eq. (7) with Eq. (22), based on the BDFs, new shape functions are created:

$$N = b^T \sum \tag{23}$$

The stiffness matrices are determined by using Eq. (7) to Eq. (9). Any analysis should follow these steps. A program developed in MATLAB to do these steps automatically and make it practical and economical.

The shape function of Figure 5a is shown in MATLAB as an example in Figure 6. Based on Figure 6 the displacement of node 1 is the superposition of the three forces (P, M_x and M_y) that are calculated by this multiplication. In the case of rotation, the derivative is needed. The nodal stiffness matrix is evaluated after inverting the nodal flexibility matrix. Using a superposition of the shape functions, each edge's movement can be calculated.

FEM can calculate shapes such as circular, triangular, or trapezoidal by using rectangular elements. (Bramble and Zlámal, 1970). The examples of the other shapes are outside the scope of this paper.

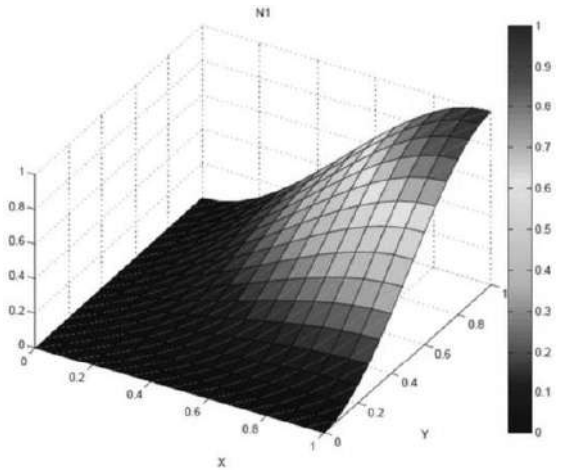

Fig. 6. First Shape function of Node 1

3. Results and Discussion

A step-by-step procedure is described below for performing a structural analysis of FGM plates using BDFs:

Step 1: Calculation of BDFs using Section 2.2.

Step 2: Matrix analysis of nodal flexibility using Eq. (15).

Step 3: Computation of $\sum$ using Eq. (22).

Step 4: Reaching the shape functions using Eq. (23).

Step 5: Formulation of stiffness matrices using Eq. (7) to Eq. (9).

Demonstrating the accuracy and applicability of 2D-DTM in free vibration analysis of Kirchhoff plate with in-plane functionally graded material, the following examples are given numerically as a validation test of the method. To achieve this, consider a rectangular in-plane FGM plate, with a length of a and a width of b, is shown in Figure 1. The material properties such as the elastic modulus E and mass density ρ are varying in-plane as mentioned in Section 2.1.

$$E = V_l E_l + V_r E_r \tag{24}$$

$$\rho = V_l \rho_l + V_r \rho_r \tag{25}$$

$$V_l + V_r = 1 \tag{26}$$

The most appropriate and simplest distribution of materials property is power-low distribution as follows

$$V_l = (y/b)^n \quad , \quad V_r = [1-(y/b)^n] \tag{27}$$

where *n*: is the material graded index which is a real number such as 0, 0.5, 1, 2. Consequently, Eq. (24) and Eq. (25) can be represented as:

$$\begin{aligned} E &= (y/b)^n E_l + [1-(y/b)^n] E_r \\ \rho &= (y/b)^n \rho_l + [1-(y/b)^n] \rho_r \end{aligned}, \tag{28}$$

Assuming the constant Poisson's ratio and substituting Eq. (28) in Eq. (24), Eq. (25) can be rewritten as follows, which is the general differential equation of the FGM plates, after replacing all parameters:

$$\begin{aligned} &\frac{\partial^2}{\partial\xi^2}\left[-\frac{\left(\frac{y}{b}\right)^n E_1 + \left[1-\left(\frac{y}{b}\right)^n\right]E_r}{12(1-v^2)} hy^3 \left(b^4 \frac{\partial^2 w}{\partial\xi^2} + va^2b^2\frac{\partial^2 w}{\partial\eta^2}\right)\right] \\ &+2\frac{\partial^2}{\partial\xi\partial\eta}\left[-\frac{\left(\frac{y}{b}\right)^n E_1 + \left[1-\left(\frac{y}{b}\right)^n\right]E_r}{12(1-v^2)} hy^3a^2b^2(1-v)\left(\frac{\partial^2 w}{\partial\xi\partial\eta}\right)\right] \\ &+\frac{\partial^2}{\partial\eta^2}\left[-\frac{\left(\frac{y}{b}\right)^n E_1 + \left[1-\left(\frac{y}{b}\right)^n\right]E_r}{12(1-v^2)} hy^3 \left(a^4 \frac{\partial^2 w}{\partial\eta^2} + va^2b^2\left(\frac{\partial^2 w}{\partial\xi^2}\right)\right)\right] \\ &+\left[\left(\frac{y}{b}\right)^n \rho_1 + \left[1-\left(\frac{y}{b}\right)^n\right]\rho_r\right] hwa^4b^4\omega^2 \\ &-\frac{\left(\frac{y}{b}\right)^n \rho_1 + \left[1-\left(\frac{y}{b}\right)^n\right]\rho_1}{12} h^3\omega^2\left(a^2b^4\frac{\partial^2 w}{\partial\xi^2} + a^4b^2\frac{\partial^2 w}{\partial\eta^2}\right) = 0 \end{aligned} \tag{29}$$

The FGM plate considered here is made from ceramic and metal, in which the material is fully ceramic (E_c = 7.65 × 10^{10} P_a and ρ_c = 2.5 × 10^3 kg/m^3) at $y = 0\,(\eta = 0)$ and fully metal (E_m = 2.06×10^{11} P_a and ρ_m = 7.85 × 10^3 kg/m^3) at $y = b\,(\eta = 1)$ and the constant Poisson's ratio is assumed as $\nu = 0.3$.

Considering different boundary conditions of the various edges of a square plate such as Simply supported (S), Clamped (C) and Free edge (F), the presented general procedure has been employed to calculate the first non-dimensional transverse natural frequency (Ω which is followed up $\Omega^2 = \omega l^2\sqrt{\frac{h\rho_0}{D_0}}$ in which $D_0 = \frac{E_0}{12(1-\nu^2)}h^3$, $\rho_0 = \rho_c$ and $E_0 = E_c$) of the considered plate for different values of the n material graded index, and a, plate width. The results are shown in Tables 1-4 and compared with those reported by Liu et al. (2010). In these tables, all the plates are simply supported $x = 0$ and $x = a$ which are denoted by the two first letters. Similarly, the boundaries conditions at $y = 0$ and $y = b$ are shown by the third and fourth letters respectively. As it is demonstrated in the tables, the results have excellent agreement with those of Levy-type solution obtained by Liu et al. (2010). This close agreement clearly demonstrates the capability of the present general method in calculating the non-dimensional natural frequency of in-plane FGM plates. This general method can be applied for any other recursive formula which is obtained from the governing differential equation of the plate with arbitrary material and geometrical properties.

Table 1. The values of non-dimensional natural frequency Ω for different boundary conditions

		α = 1								
n	**Method**	**SSCS**	**SSCF**	**SSCC**	**SSSF**	**SSSC**	**SSSS**	**SSFS**	**SSFC**	**SSFF**
0	Differ. Eq.	4.863	3.562	5.381	3.418	4.863	4.443	3.418	3.562	3.104
	BDFs	4.863	3.563	5.380	3.419	4.863	4.443	3.417	3.562	3.103
0.5	Differ. Eq.	4.644	3.369	5.143	3.419	4.717	4.277	3.380	3.555	3.940
	BDFs	4.645	3.370	5.143	3.418	4.718	4.275	3.382	3.556	3.942
1	Differ. Eq.	4.641	3.349	5.199	3.243	4.777	4.306	3.433	3.624	3.016
	BDFs	4.643	3.348	5.202	3.245	4.780	4.307	3.432	3.623	3.016
2.5	Differ. Eq.	4.769	3.347	5.408	3.247	4.941	4.413	3.480	3.671	3.039
	BDFs	4.768	3.347	5.410	3.248	4.941	4.412	3.481	3.672	3.042

Table 2. The values of non-dimensional natural frequency Ω for different boundary conditions

α = 5										
n	**Method**	**SSCS**	**SSCF**	**SSCC**	**SSSF**	**SSSC**	**SSSS**	**SSFS**	**SSFC**	**SSFF**
0	Differ. Eq.	3.964	1.963	4.753	1.159	3.964	3.204	1.160	1.964	0.614
	BDFs	3.964	1.964	4.756	1.162	3.964	3.205	1.162	1.965	0.614
0.5	Differ. Eq.	3.707	1.727	4.531	1.160	3.894	3.095	1.178	2.097	0.595
	BDFs	3.706	1.730	4.533	1.160	3.893	3.095	1.178	2.097	0.595
1	Differ. Eq.	3.703	1.665	4.583	1.068	3.960	3.101	1.209	2.198	0.597
	BDFs	3.706	1.667	4.585	1.071	3.962	3.103	1.212	2.199	0.598
2.5	Differ. Eq.	3.801	1.652	4.806	1.059	4.112	3.139	1.230	2.246	0.602
	BDFs	3.803	1.584	4.805	1.062	4.113	3.141	1.229	2.246	0.603

Table 3. The values of non-dimensional natural frequency Ω for different boundary conditions

α = 20										
n	**Method**	**SSCS**	**SSCF**	**SSCC**	**SSSF**	**SSSC**	**SSSS**	**SSFS**	**SSFC**	**SSFF**
0	Differ. Eq.	3.929	1.881	4.732	0.562	3.929	3.146	0.568	1.881	0.153
	BDFs	3.930	1.883	4.735	0.563	3.930	3.146	0.568	1.882	0.153
0.5	Differ. Eq.	3.669	1.631	4.511	0.569	3.863	3.040	0.579	2.028	0.148
	BDFs	3.671	1.632	4.513	0.570	3.863	3.042	0.580	2.031	0.148
1	Differ. Eq.	3.665	1.562	4.562	0.522	3.929	3.045	0.595	2.133	0.149
	BDFs	3.667	1.565	4.565	0.523	3.930	3.046	0.596	2.136	0.149
2.5	Differ. Eq.	3.760	1.547	4.785	0.517	4.081	3.075	0.606	2.183	0.150
	BDFs	3.761	1.546	4.784	0.519	4.084	3.075	0.608	2.183	0.150

Table 4. The values of non-dimensional natural frequency Ω for different boundary conditions

α = 1000										
n	**Method**	**SSCS**	**SSCF**	**SSCC**	**SSSF**	**SSSC**	**SSSS**	**SSFS**	**SSFC**	**SSFF**
0	Differ. Eq.	3.926	1.875	4.730	0.080	3.927	3.142	0.080	1.875	0.003
	BDFs	3.927	1.875	4.730	0.080	3.927	3.142	0.080	1.875	0.003
0.5	Differ. Eq.	3.666	1.624	4.509	0.080	3.861	3.036	0.082	2.023	0.003
	BDFs	3.666	1.626	4.510	0.080	3.862	3.036	0.082	2.024	0.003
1	Differ. Eq.	3.662	1.555	4.561	0.074	3.927	3.041	0.084	2.129	0.003
	BDFs	3.663	1.556	4.561	0.074	3.927	3.042	0.084	2.129	0.003
2.5	Differ. Eq.	3.757	1.539	4.784	0.073	4.078	3.071	0.086	2.178	0.003
	BDFs	3.757	1.539	4.785	0.073	4.078	3.071	0.086	2.179	0.003

For testing, results are compared to those of Liu et al. (2010) shown in Table 1 to Table 4. Nevertheless, new results had to be presented that had not been computed before. For this reason, the added boundary conditions CCFF and CCCC which were not shown in Liu et al. (2010) are calculated in this research.

The results in this paper confirm that the free vibrations of the FGM plate match the homogeny plate in specific N_s. This is the frequency that equals that of the homogeny plate. This can be useful for replacing some cheaper material in the specific Ω_0, if it is needed. The results of the N_s, for several cases, are shown in Table 7.

Another important issue is convergence. Figures 7 and 8 show how many elements are needed in FEM in order to arrive at the answer for n = 1 and 2.5, respectively. For both of them, α is equal to one and they are in SSSS condition. Upon selecting 48 elements, the graph begins to converge to the answer after a dramatic growth while in n = 2.5, a fracturing can be observed.

The graph of Ω based on α is represented in Figure 9. It shows a significant drop in the frequency before α = 5 but a slight decrease after that.

Table 5. The values of non-dimensional natural frequency Ω for different CCFFs

CCFF		**α**			
n		1	5	20	1000
0	BDFs	3.136	2.786	2.757	2.692
0.5	BDFs	2.997	2.640	2.629	2.566
1	BDFs	3.030	2.671	2.658	2.596
2.5	BDFs	3.125	2.791	2.748	2.682

Table 6. The values of non-dimensional natural frequency Ω for different CCCCs

CCCC		α			
n		1	5	20	1000
0	BDFs	8.021	6.915	6.896	6.611
0.5	BDFs	7.781	6.854	6.825	6.492
1	BDFs	7.866	6.934	6.902	6.576
2.5	BDFs	8.282	7.921	7.639	7.388

Table 7. The values of N_s for different boundary conditions

N_s	Boundary Conditions (BCs)					
α	**SSCS**	**SSCC**	**SSSC**	**SSSS**	**CCCC**	**CCFF**
1	3.64	2.28	1.77	2.94	1.55	2.67
5	5.19	2.14	1.02	5.02	0.97	2.43
20	5.17	2.16	1	6.17	0.98	2.65
1000	5.17	2.13	1	6.17	1.08	2.67

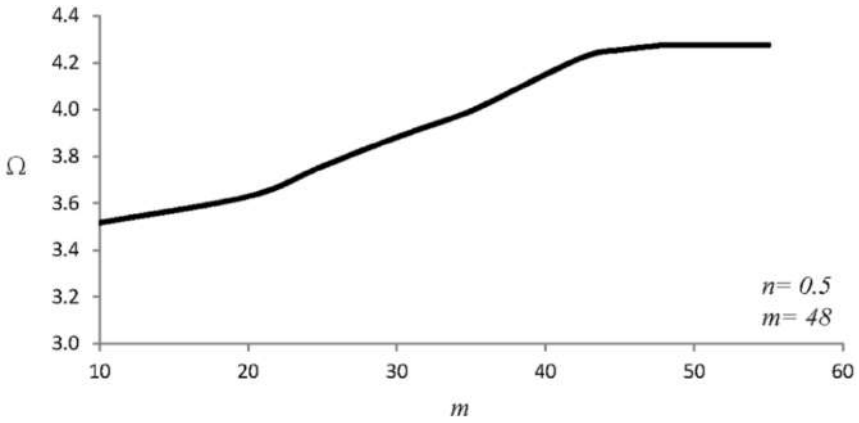

Fig. 7. Convergence of frequency for α =1, n = 0.5 and SSSS condition

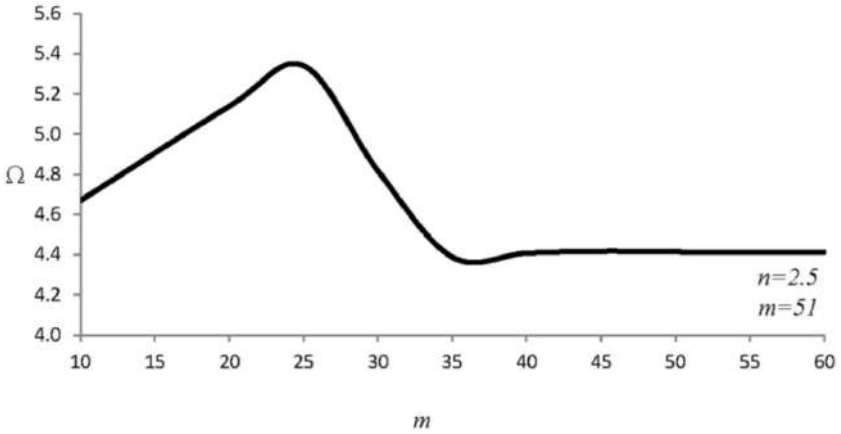

Fig. 8. Convergence of frequency for α = 1, n = 2.5 and SSSS condition

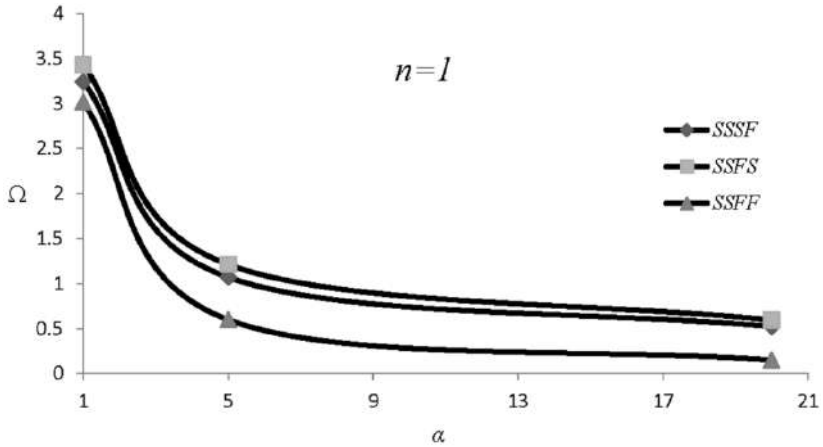

Fig. 9. The impact of α on Ω

4. Conclusions

Using the Finite Element Method (FEM) and Basic Displacement Functions (BDFs), this paper presented an efficient element for in-plane Functionally Graded Materials (FGMs) plates vibration analysis. The first step was to define and generate BDFs. New shape functions could be derived mechanically by expressing them as derived BDFs. Furthermore, the Finite Element method was used to compute the structural stiffness and the mass matrix of the considered beams. This method was tested on several numerical examples, which showed excellent agreement with the literature with regard to accuracy and economy. Several examples demonstrated that the method is super-convergent for either free vibration or bent beams with different boundary conditions.

The following benefits can be attributed to this method:

- Through the presented method, any variations in the taper ratio and mechanical properties of the plate can be incorporated into the design.
- The generality of stiffness methods and the accuracy of forces methods are combined to create a new element.
- Implementing the new element, free vibration analyses are performed with lower elements. As a result, the time and cost of the analyses are significantly reduced.

Different structural applications have proven the concept of BDFs' competency. In order to facilitate the study of these other complex structural elements as well as the application of BDFs and other advanced materials, such as functionally graded materials (FGMs), the authors are extending BDFs to shells.

5. Symbol List

a	length of the plate along x direction
b	length of the plate along y direction
b	vector of BDFs
E	modulus of elasticity
F	vector of nodal forces
F_{ii}	nodal flexibility matrices of ith node
$h(x_j, y_j)$	thickness of the plate at point j (x_j, y_j)
K	stiffness matrix
M	mass matrix
N	vector of shape functions
N_s	special material graded-index
$q_z(x,y)$	external transverse load
r	taper factor of the plate in x direction
s	taper factor of the plate in y direction
w	transverse displacement
w_0	the displacement function
x, y	longitudinal coordinates along plate
θ	angle of rotation
Σ	matrix containing nodal stiffness matrices
Ω	non-dimensional Eigen frequency
ω	Eigen frequency

6. References

Attarnejad, R., Semnani, S.J. and Shahba, A. (2010). "Basic displacement functions for free vibration analysis of non-prismatic Timoshenko beams", *Finite Elements in Analysis and Design*, 46(10), 916-929, https://doi.org/10.1016/j.finel.2010.06.005.

Bacciocchi, M., Eisenberger, M., Fantuzzi, N., Tornabene, F. and Viola, E. (2016). "Vibration analysis of variable thickness plates and shells by the generalized differential quadrature method", *Composite Structures*, 156, 218-237, https://doi.org/10.1016/j.compstruct.2015.12.004.

Bramble, J. H. and Zlámal, M. (1970). "Triangular elements in the finite element method", *Mathematics of Computation*, 24(112), 809-820, https://doi.org/10.1090/S0025-5718-1970-0282540-0.

Cheng, Z.Q. and Batra, R.C. (2000). "Three-dimensional thermoelastic deformations of a functionally graded elliptic plate", *Composites Part B: Engineering*, 31(2), 97-106, https://doi.org/10.1016/S1359-8368(99)00069-4.

Chiba, R. (2019). "Natural convection analysis of water near its density extremum between finite vertical plates: A differential transform

approach", *International Journal of Mathematical Modelling and Numerical Optimisation*, 9(4), 429-448, https://doi.org/10.1504/IJMMNO.2019.102601.

Das, R.R. (2010). "Adhesion failure and delamination of bonded tubular joints made with laminated FRP composites and functionally graded materials", Doctoral Dissertation, IIT Kharagpur, http://dx.doi.org/10.1016/j.compstruct.2020.113386.

Fallah, F. and Karimi, M. (2019). "Non-linear analysis of functionally graded sector [lates with simply supported radial edges under transverse loading", *Mechanics of Advanced Composite Structures*, 6(1), 65-74, https://doi.org/10.22075/macs.2019.16171.116.

Fallah, N., Parayandeh-Shahrestany, A. and Golkoubi, H. (2017). "A Finite Volume formulation for the elasto-plastic analysis of rectangular Mindlin-Reissner plates, a non-layered approach", *Civil Engineering Infrastructures Journal*, 50(2), 293-310, https://doi.org/ 10.7508/ceij.2017.02.006.

Goupee, A.J. and Vel, S.S. (2006). "Optimization of natural frequencies of bidirectional functionally graded beams", *Structural and Multidisciplinary Optimization*, 32(6), 473-484, https://doi.org/10.1007/s00158-006-0022-1.

Gupta, A. (2020). "Functionally graded structures: Design and analysis of tailored advanced composites", In *Characterization, Testing, Measurement, and Metrology*, (pp. 33-55), CRC Press.

Hadji, L., Zouatnia, N. and Bernard, F. (2019). "An analytical solution for bending and free vibration responses of functionally graded beams with porosities: Effect of the micromechanical models", *Structural Engineering and Mechanics*, 69(2), 231-241, https://doi.org/10.12989/sem.2019.69.2.231.

Hamrit, F. and Necib, B. (2018). "Analysis of mechanical structures using plate finite element method under different boundary conditions", *Diagnostyka*, 19(2), 3-9, http://dx.doi.org/10.29354/diag/86257.

Kaplunov, J., Erbas, B. and Ege, N. (2021). "An asymptotic theory for a functionally graded plate", *BGSIAM'21*, 32, Bulgaria.

Kumar, V., Singh, S.J., Saran, V.H. and Harsha, S.P. (2021). "Vibration characteristics of porous FGM plate with variable thickness resting on Pasternak's foundation", *European Journal of Mechanics-A/Solids*, 85(1 January), 104124, https://doi.org/10.1016/j.euromechsol.2020.104124.

Kumar, Y. (2018). "The Rayleigh–Ritz method for linear dynamic, static and buckling behavior of beams, shells and plates: A literature review", *Journal of Vibration and Control*, 24(7), 1205-1227, https://doi.org/10.1177/1077546317694724.

Lal, R. and Saini, R. (2020). "Vibration analysis of FGM circular plates under non-linear temperature variation using generalized differential quadrature rule", *Applied Acoustics*, 158(15 January), 107027, https://doi.org/10.1016/j.apacoust.2019.107027.

Leissa, A.W. (1969). "Vibration of plates", Washington: NASA SP-160, US Government Printing Office,

Liu, D.Y., Wang, C.Y. and Chen, W.Q. (2010). "Free vibration of FGM plates with in-plane material inhomogeneity", *Composite Structures*, 92(5), 1047-1051, https://doi.org/10.1016/j.compstruct.2009.10.001.

Liu, Y.Y., Shu, C., Zhang, H.W., Yang, L.M. and Lee, C. (2021). "An efficient high-order least square-based finite difference-finite volume method for solution of compressible Navier-Stokes equations on unstructured grids", *Computers and Fluids*, 222(30 May), 104926, https://doi.org/10.1016/j.compfluid.2021.104926.

Makvandi, H., Moradi, S., Poorveis, D. and Heidari Shirazi, K. (2019). "Crack identification in postbuckled plates using differential quadrature element method and sequential quadratic programming", *Amirkabir Journal of Mechanical Engineering*, 51(3), 51-60, https://doi.org/10.22060/mej.2018.13543.5660.

Malekzadeh, P., Setoodeh, A.R. and Shojaee, M. (2018). "Vibration of FG-GPLs eccentric annular plates embedded in piezoelectric layers using a transformed differential quadrature method", *Computer Methods in Applied Mechanics and Engineering*, 340(1 October), 451-479, https://doi.org/10.1016/j.cma.2018.06.006.

Miyamoto, Y., Kaysser, W.A., Rabin, B.H., Kawasaki, A. and Ford, R.G. (Eds.). (2013). *Functionally graded materials: design, processing and applications*, Vol. 5, Springer Science & Business Media.

Mora, P., Ducasse, E. and Deschamps, M. (2016). "Interaction of guided waves with cracks in an embedded multilayered anisotropic plate by using a Boundary Element approach", *Physics Procedia*, 70, 326-329, https://doi.org/10.1016/j.phpro.2015.08.217.

Naumenko, K. and Eremeyev, V.A. (2017). "A layer-wise theory of shallow shells with thin soft core for laminated glass and photovoltaic applications", *Composite Structures*, 178, 434-446, https://doi.org/10.1016/j.compstruct.2017.07.007.

Njim, E.K., Al-Waily, M. and Bakhy, S.H. (2021).

"A critical review of recent research of free vibration and stability of functionally graded materials of sandwich plate", In *IOP Conference Series: Materials Science and Engineering*, Vol. 1094, No. 1, p. 012081, IOP Publishing, https://doi.org/10.1088/1757-899x/1094/1/012081.

Pachenari, Z. and Attarnejad, R. (2014a). "Free vibration of tapered Mindlin plates using basic displacement functions", *Arabian Journal for Science and Engineering*, 39(6), 4433-4449, https://doi.org/10.1007/s13369-014-1071-1.

Pachenari, Z. and Attarnejad, R. (2014b). "Analysis of tapered thin plates using basic displacement functions", *Arabian Journal for Science and Engineering*, 39(12), 8691-8708, https://doi.org/10.1007/s13369-014-1407-x.

Ramkumar, R.L., Chen, P.C. and Sanders, W.J. (1987). "Free vibration solution for clamped orthotropic plates using Lagrangian multiplier technique", *AIAA Journal*, 25(1), 146-151, https://doi.org/10.2514/3.9594.

Reddy, J. (2000). "Analysis of functionally graded plates" *International Journal for Numerical Methods in Engineering*, 47(1-3), 663-684, https://doi.org/10.1002/(SICI)1097-0207(20000110/30)47:1/3%3C663::AID-NME787%3E3.0.CO;2-8.

Saidi, H. and Sahla, M. (2019). "Vibration analysis of functionally graded plates with porosity composed of a mixture of Aluminum (Al) and Alumina (Al_2O_3) embedded in an elastic medium", *Frattura ed Integrità Strutturale*, 13(50), 286-299, https://doi.org/10.3221/IGF-ESIS.50.24.

Shahir, H. and Delfan, S. (2021). "Numerical investigation of nailing pattern effect on nailed wall performance", *Civil Engineering Infrastructures Journal*, 54(2), 331-350, https://doi.org/10.22059/ceij.2021.298632.1659.

Şimşek, M. (2016). "Buckling of Timoshenko beams composed of two-dimensional functionally graded material (2D-FGM) having different boundary conditions", *Composite Structures*, 149(1 August), 304-314, https://doi.org/10.1016/j.compstruct.2016.04.034.

Szilard, R. (2004). "Theories and applications of plate analysis: Classical, numerical and engineering methods", *Applied Mechanics Reviews*, 57(6), B32-B33, https://doi.org/10.1115/1.1849175.

Teimouri, H., Davoodi, M.R., Mostafavian, S.A. and Khanmohammadi, L. (2021). "Damage detection in double layer grids with modal strain energy method and Dempster-Shafer theory", *Civil Engineering Infrastructures Journal*, 54(2), 253-266, https://doi.org/10.22059/ceij.2020.294512.1644.

Tenenbaum, J., Deutsch, A. and Eisenberger, M. (2020). "Analytical buckling loads for rectangular orthotropic and symmetrically laminated plates", *AIAA Journal*, 58(2), 907-917, https://doi.org/10.2514/1.J058536.

Van Vinh, P., Dung, N.T. and Tho, N.C. (2021, February). "Modified single variable shear deformation plate theory for free vibration analysis of rectangular FGM plates", *Structures*, 29(1 February), 1435-1444, https://doi.org/10.1016/j.istruc.2020.12.027.

Vatani Oskouei, A. and Kiakojouri, F. (2015). "Non-linear dynamic analysis of steel hollow I-core sandwich panel under air blast loading", *Civil Engineering Infrastructures Journal*, 48(2), 323-344, https://doi.org/10.7508/ceij.2015.02.008.

Vidal, P., Gallimard, L., Polit, O. and Valot, E. (2021). "Analysis of functionally graded plates based on a variable separation method", *Mechanics of Advanced Materials and Structures*, 29(26), 4890-4901, https://doi.org/10.1080/15376494.2021.1942597.

Wang, X., Liang, X. and Jin, C. (2017). "Accurate dynamic analysis of functionally graded beams under a moving point load", *Mechanics Based Design of Structures and Machines*, 45(1), 76-91, https://doi.org/10.1080/15397734.2016.1145060.

Zakeri, M., Modarakar Haghighi, A. and Attarnejad, R. (2016). "On the analysis of FGM beams: FEM with innovative element", *Journal of Solid Mechanics*, 8(2), 348-364, https://dorl.net/dor/20.1001.1.20083505.2016.8.2.9.9.

AIMS AND SCOPE

Since the College of Engineering (Former Faculty of Engineering, FOE) of the University of Tehran has renewed its policy toward scientific publication, the Civil Engineering transaction of the well- built 45 years old Persian journal of *"Nashrieh Daneshkadeh Fanni"* is to be published in English and as separate independent journal with the name of ***Civil Engineering Infrastructures Journal***.

Civil Engineering Infrastructures Journal is an international journal which publishes high quality scientific papers in all areas of engineering and management of civil infrastructures. The civil infrastructures include, but are not limited to: buildings, bridges, dams, transportation systems, geotechnical structures, underground constructions, water distribution systems, offshore platforms, pipelines, ocean structures, airports and power plants.

The scope of this journal encompasses, but is not restricted to the following aspects of engineering and management of infrastructures:

- Mathematical modeling
- Computational and experimental methods
- Environmental Impact assessment
- Passive defense and security issues
- Monitoring and assessment
- Construction and design for durability
- Deterioration modeling and aging
- Failure analysis
- Field testing
- Financial planning
- Inspection and diagnostics
- Life-cycle analysis and prediction

- Maintenance, rehabilitation, repair and replacement strategies
- Non-destructive testing
- Optimization of maintenance and management
- Specifications and codes
- Reliability and risk management
- Supervisory Control and Data Assimilation (SCADA)
- Automation and Robotics in Construction
- Smart civil infrastructure Systems
- Sustainable civil infrastructure systems
- Case studies

Audiences of ***Civil Engineering Infrastructures Journal*** are researchers and practitioners as well as people working in infrastructure design, construction, maintenance and operation. Papers considered for publication must contain a clear and well-defined engineering component and make a significant contribution to the engineering and management of civil infrastructures. All articles submitted to this journal will undergo a rigorous peer review by anonymous independent experts.

Additional information can be obtained from:

Civil Engineering Infrastructures Journal
College of Engineering,
University of Tehran
P.O. Box: 11155- 4563
Tehran, Iran
Tel/ Fax: +98-21-88956097
Web Site: www.ceij.ir
Email: ceij@ut.ac.ir

University of Tehran
College of Engineering

Copyright Transfer Agreement

In order to protect the author(s), from the consequences of unauthorized use, the publisher requests that all author(s) sign the appropriate statement below:
The author(s) undersigned hereby approves submission of this work and all subsequent revisions for publication and transfers, assigns, or otherwise conveys copyright ownership to the Civil Engineering Infrastructures Journal (CEIJ). I (we) acknowledge that i) the submitted material represents original material, ii) does not infringe upon the copyright of any third party, and iii) that no part of the work has been published or under consideration for publication elsewhere unless and until it is rejected by Civil Engineering Infrastructures Journal (CEIJ). I (we) agree to indemnify the publisher against any loss or damages arising out of a breach of this agreement. In the event that my (our) submission is not published, copyright ownership shall revert to the author (s).

Manuscript Title:

Corresponding Author

Author:
Date: Signature;

Author:
Date: Signature:

Author:
Date: Signature:

Author:
Date: Signature:

Please submit the signed agreement with the final manuscript to:
Civil Engineering Infrastructures Journal (CEIJ)
School of Civil Engineering,
College of Engineering, University of Tehran
Enghelab Ave., P.O. Box: 11155-4563, Tehran, Iran.
Tel: 88956097
Fax: 66498981
E-mail: ceij@ut.ac.ir
Website: www.ceij.ir

CIVIL ENGINEERING INFRASTRUCTURES JOURNAL (CEIJ)

is indexed and abstracted in the bibliographical databases including:

Web of Science (ESCI)
http://science.thomsonreuters.com

Scopus
https://www.scopus.com

Islamic World Science Citation Center;
http://www.isc.gov.ir

Directory of Open Access Journals (DOAJ)
https://doaj.org

Google Scholar
https://scholar.google.com

General Impact Factor (GIF)
http://generalimpactfactor.com

Scientific Indexing Services (SIS)
http://www.sindexs.org

International Institute of Organized Research (I2OR)
http://www.i2or.com

Information Matrix for the Analysis of Journals (MAIR)
http://miar.ub.edu

ROAD: the Directory of Open Access scholarly Resources
http://road.issn.org

Scientific World Index
http://www.sciwindex.com

International Innovative Journal Impact Factor (IIJIF)
http://www.iijif.com

Science library index
http://scinli.com

Journal Factor
http://www.journalfactor.org

Open Academic Journals Index (OAJI)
http://oaji.net

Electronic Journals Library (EZB)
https://rzblx1.uni-regensburg.de

Systematic Impact Factor (SIF)
http://www.sifactor.org

COSMOS IMPACT FACTOR
http://www.cosmosimpactfactor.com

Polish Ministry of Science and Higher Education (MSHE)
https://journals.indexcopernicus.com

Magiran
http://www.magiran.com

Scientific Information Database (SID); Iran;
http://www.Sid.ir

Ministry of Science, Research and Technology of Iran has granted the Science and Research (Elmi-Pajouheshi) credit to CEIJ according to the letter No. 3/252445 at 25 Feb. 2012.

College of Engineering

Civil Engineering Infrastructures Journal

Volume 56, Number 1, June 2023

CONTENTS:

Civil Engineering Infrastructures Journal (CEIJ)

Volume 56, Number 1, June 2023